Springer Series in Solid-State Sciences 182

Miron Ya. Amusia
Konstantin G. Popov
Vasily R. Shaginyan
Vladimir A. Stephanovich

Theory of Heavy-Fermion Compounds

Theory of Strongly Correlated Fermi-Systems

Springer

Springer Series in Solid-State Sciences

Volume 182

The Springer Series in Solid-State Sciences consists of fundamental scientific books prepared by leading researchers in the field. They strive to communicate, in a systematic and comprehensive way, the basic principles as well as new developments in theoretical and experimental solid-state physics.

More information about this series at http://www.springer.com/series/682

Miron Ya. Amusia · Konstantin G. Popov
Vasily R. Shaginyan · Vladimir A. Stephanovich

Theory of Heavy-Fermion Compounds

Theory of Strongly Correlated Fermi-Systems

Springer

Miron Ya. Amusia
Racah Institute of Physics
The Hebrew University
Jerusalem
Israel

and

A. F. Ioffe Physical-Technical Institute
St. Petersburg
Russian Federation

Konstantin G. Popov
Ural Division Komi Science Center
Russian Academy of Sciences
Syktyvkar
Russia

Vasily R. Shaginyan
Petersburg Nuclear Physics Institute
Gatchina
Russia

and

CTSPS
Clark Atlanta University
Atlanta
USA

Vladimir A. Stephanovich
Institute of Physics
Opole University
Opole
Poland

ISSN 0171-1873 ISSN 2197-4179 (electronic)
ISBN 978-3-319-10824-7 ISBN 978-3-319-10825-4 (eBook)
DOI 10.1007/978-3-319-10825-4

Library of Congress Control Number: 2014950681

Springer Cham Heidelberg New York Dordrecht London

© Springer International Publishing Switzerland 2015
This work is subject to copyright. All rights are reserved by the Publisher, whether the whole or part of the material is concerned, specifically the rights of translation, reprinting, reuse of illustrations, recitation, broadcasting, reproduction on microfilms or in any other physical way, and transmission or information storage and retrieval, electronic adaptation, computer software, or by similar or dissimilar methodology now known or hereafter developed. Exempted from this legal reservation are brief excerpts in connection with reviews or scholarly analysis or material supplied specifically for the purpose of being entered and executed on a computer system, for exclusive use by the purchaser of the work. Duplication of this publication or parts thereof is permitted only under the provisions of the Copyright Law of the Publisher's location, in its current version, and permission for use must always be obtained from Springer. Permissions for use may be obtained through RightsLink at the Copyright Clearance Center. Violations are liable to prosecution under the respective Copyright Law.
The use of general descriptive names, registered names, trademarks, service marks, etc. in this publication does not imply, even in the absence of a specific statement, that such names are exempt from the relevant protective laws and regulations and therefore free for general use.
While the advice and information in this book are believed to be true and accurate at the date of publication, neither the authors nor the editors nor the publisher can accept any legal responsibility for any errors or omissions that may be made. The publisher makes no warranty, express or implied, with respect to the material contained herein.

Printed on acid-free paper

Springer is part of Springer Science+Business Media (www.springer.com)

Preface

Heavy-Fermion compounds comprise a great variety of strongly correlated systems such as two-dimensional (2D) quantum liquids (2D ^{3}He and electrons in metal oxide semiconductor field effect transistor (MOSFETs)), heavy fermion (HF) metals, high-temperature superconductors, quantum spin liquids confined in insulators, quasicrystals, and even the Universe itself. Numerous experimental facts unveiling the thermodynamic, transport, relaxation, etc., properties are collected on all these objects, and these facts represent all fields of the condensed matter physics. One might say that the physics of HF compounds represents a new edition of the condensed matter physics, for the observed behavior is quite unique while the edition is still under construction. Therefore, the problem of presenting a theory of HF compounds is both arduous and of great importance.

In this book, we construct the theory and illustrate it by numerous applications dealing with various physical phenomena and processes and explaining the corresponding experimental facts. To make the book understandable as much as possible, for the reader's convenience we, when considering a problem of the HF compounds, give the necessary elements of the theory within a particular place. Because of huge diversity in the considered topics, we hope that such a presentation allows the reader to learn the particular physical process without a laborious recursion to special chapters of the book.

One of the most fruitful concepts of modern solid state physics is a paradigm of quasiparticles. This concept permits to represent any solid as certain ground state and its elementary excitations in the form of quasiparticles. In the quasiparticle language, a complex system of strongly interacting electrons and ions is reduced to a gas of low-energy excitations, whose behavior could be described by various (primarily perturbative) well-established techniques. The quasiparticles paradigm permits to achieve a significant standardization of the description of different types of quantum solids and, by this virtue, similar formalism can be applied across a wide range of Condensed Matter systems.

Rapid development of condensed matter physics at the end of the twentieth century put many challenges to the conventional wisdom in this discipline, elaborated for previous 50 years. Such discoveries as high-T_c superconductivity, integer and fractional quantum Hall effects, as well as a multitude of quantum phase transitions still do not find their satisfactory and complete theoretical explanation. Moreover, many modern experimental findings in solids put such fundamental concepts of “classical” condensed matter physics, as quasiparticle, under scrutiny. As a result, there has been a growing body of theoretical and experimental studies showing that the conventional picture of quasiparticles is not always correct for systems with strongly interacting fermions. Examples of systems exhibiting significant deviations from the above quasiparticle picture are chemical compounds with heavy fermions (heavy-fermion compounds), whose experimental behavior is strongly different from that predicted by ordinary Fermi liquid theory. The body of these “strange” experimental facts is now commonly attributed to as non-Fermi liquid (NFL) behavior. As quasiparticle paradigm is inherent in other branches of condensed matter physics, the same NFL behavior is exhibited at low temperatures by two-dimensional electron gas and even ^{3}He, where its neutral atoms are fermions with spin 1/2. We believe that to meet the above challenges adequately, the new points of view on old ideas are necessary.

This monograph is written to explain how the standard quasiparticle paradigm can be modified to describe the striking NFL anomalies in the above classes of strongly correlated fermionic systems. The main emphasis is on physics of HF compounds and other systems with essentially NFL behavior. We show how revised quasiparticle concept can describe all the above systems in a unified manner. Here we present a comprehensive analysis of existing theoretical and experimental results for all listed systems with NFL behavior such as HF metals, high-temperature superconductors, quantum spin liquids, quasicrystals, and two-dimensional Fermi systems. The common feature of these systems is that their physical properties can hardly be understood within the framework of the Landau Fermi liquid theory and their behavior is so unusual that the traditional Landau quasiparticles paradigm fails to describe it. The important speciality of our monograph is that we compare a great deal of our theoretical observations with numerous experimental facts. As a result, the monograph contains more than 150 figures that facilitate understanding both the presented theory and the experimental facts collected on very different HF compounds.

In this book, we present a theoretical approach, which, based on modified and extended quasiparticles paradigm, permits to naturally describe the basic properties and the scaling behavior of the above substances. The essence of the approach is that due to the altering of Fermi surface topology, the substance undergoes so-called fermion condensation quantum phase transition, where Landau quasiparticles survive but completely change their properties. In contrast to the Landau statement that the quasiparticle effective mass is a constant, the effective mass of the above new quasiparticles strongly depends on temperature, magnetic field, pressure, and other external parameters. As a signal of such a fermion condensation quantum phase transition (FCQPT) serves unlimited increase in the effective mass of quasiparticles that determines the excitation spectrum and creates both flat bands and a fermion condensate; while FCQPT represents the unique quantum phase transition that occurs only at zero temperature.

Upon reading the book, it can be asserted, that strongly correlated Fermi systems with quite different microscopic nature exhibit the same NFL behavior, while the data collected on very different strongly correlated fermionic systems manifest a universal scaling behavior so that these substances are unexpectedly identical despite their diversity. For the reader's convenience, the analysis is carried out in the broad context of the explanation of salient and unusual experimental results. The numerous calculations of the thermodynamic, relaxation and transport properties, being in good agreement with experimental facts, offer the reader solid grounds to learn the FCQPT theory implications and applications. Finally, the reader will learn that FCQPT develops unexpectedly simple, yet complete and uniform description of the NFL behavior of many different classes of substances. As a result, these different classes are unified to create a new state of matter.

The book is organized as follows. The first chapter is of introductory character and gives the definition and classification of strongly correlated systems. The theoretical approaches to strongly correlated systems like Landau theory of Fermi-liquid (LFL) are introduced. It is shown that LFL theory is insufficient to describe NFL properties of HF compounds. For such description, the notion of FCQPT is introduced. To make the book self-contained, Chap. 2 gives a brief overview of Landau Fermi liquid theory, introducing famous Landau quasiparticles. Chapter 3 gives the explanation of our theory of fermion condensation. The theory relies on Landau approach to Fermi liquids description, outlined in Chap. 2. The essence of this theory is that under certain conditions, the Landau interaction (and Fermi surface topology, which is described in Chap. 4) alters so that at FCQPT point the quasiparticle effective mass starts to depend on temperature, magnetic field, and other external parameters. We show that this theory has deep implications on the properties of HF compounds and other strongly correlated electron systems. Chapters 5–8 show how the FCQPT concept works for specific HF compounds. Here we analyze and describe the thermodynamic, transport and relaxation properties of HF compounds. Extensive comparison with experimental data is performed. We show that many unexplained and puzzling experimental facts related to NFL behavior can be well explained within the above concept. We emphasize here that contrary to "ordinary" (like Kondo lattice) theoretical approaches ascribing the NFL properties of the HF compounds to the "death" of Landau quasiparticles, our FCQPT approach shows convincingly that quasiparticles survive, although their properties are strongly modified, for instance, their effective mass becomes temperature, magnetic field, and other external parameters dependent. We also demonstrate that the extended quasiparticles paradigm permits to naturally explain the scaling behavior of HF compounds.

In Chap. 9, it is demonstrated that the fermion condensation gives floor to the quasi-classical physics in HF compounds. This observation permits us to gain more insights into the puzzling NFL physics of HF compounds and explain challenging experimental facts. In Chaps. 10 and 11, we consider the paradoxical behavior of the residual resistivity of HF metals in magnetic fields and under pressure. Chapter 13 is devoted to asymmetric conductivity of strongly correlated compounds revealed by the methods of scanning tunneling microscopy and point-contact spectroscopy.

In Chap. 14, a violation of the Wiedemann–Franz law in HF metals is considered. In Chap. 15, we present the theoretical analysis of thermodynamics of HF compounds at high magnetic fields. Chapters 12 and 16 show non-typical applications of FCQPT approach. Namely, Chap. 12 shows that a new phenomenon called “merging,” analogous to FCQPT, occurs in systems with finite number of fermions (so-called finite Fermi systems) like atomic nuclei and in two-dimensional electron systems in silicon. Chapter 16 deals with the baryon asymmetry in the early Universe, where FCQPT may also be realized. This shows that the phenomenon of Fermion condensation is ubiquitous in Nature. In Chaps. 17 and 18 we consider the quantum criticality of very different heavy-fermion compounds, such as quantum spin liquids, quasicrystals, high-T_c superconductors, HF metals, and 2D ^{3}He. Chapter 19 contains concluding remarks.

This monograph is written on the basis of the results of the present authors’ theoretical investigations as well as on theoretical and experimental studies of other researchers. The book is intended for undergraduate and graduate students and researchers in condensed matter physics. Also, the material of the book has widely been presented in the form of lectures in Clark Atlanta University (USA), Hebrew University of Jerusalem (Israel), St. Petersburg University (Russia), Syktyvkar University (Russia), Opole University (Poland).

We are indebted to many our colleagues for long-lasting collaboration of the subject of our present monograph. To name a few, they are S.A. Artamonov, A. Bulgac, J.W. Clark, V.T. Dolgopolov, J. Dukelsky, V.I. Isakov, G.S. Japaridze, V.A. Khodel, A.Z. Msezane, Yu.G. Pogorelov, P. Schuck, A.A. Shashkin, M.V. Zverev, G.E. Volovik.

Saint Petersburg

Miron Ya. Amusia
Konstantin G. Popov
Vasily R. Shaginyan
Vladimir A. Stephanovich

Acknowledgments

This work was partly supported by the RFBR # 14-02-00044, the Saint Petersburg State University # 11.38.658.2013, U.S. DOE, Division of Chemical Sciences, Office of Energy Research and AFOSR.

Contents

1 Introduction 1
1.1 Introductory Remarks 1
1.1.1 General Consideration: Strong Versus Weak Correlations 1
1.1.2 Theoretical Approaches to Strongly Correlated Systems 3
1.1.3 Quantum Phase Transitions and NFL behavior of HF compounds 12
1.1.4 Limits and Goals of the Book 16
References 18

2 Landau Fermi Liquid Theory and Beyond 21
2.1 Quasiparticle Paradigm 21
2.2 Pomeranchuk Stability Conditions 23
2.3 Thermodynamic and Transport Properties 24
2.3.1 Equation for the Effective Mass and the Scaling Behavior 25
References 29

3 Fermi Liquid with Fermion Condensate 31
3.1 The Fermion-Condensation Quantum Phase Transition 31
3.1.1 The FCQPT Order Parameter 33
3.1.2 Quantum Protectorate Related to FCQPT 35
3.1.3 The Influence of FCQPT at Finite Temperatures 36
3.1.4 Phase Diagram of Fermi System with FCQPT 38
3.2 Two Scenarios of the Quantum Critical Point 40
References 49

4 The Topological Phase Transitions Related to Fermion Condensate 51
4.1 Topological Phase Transitions Related to FCQPT 51
References 59

5 Appearance of Fermion-Condensation Quantum Phase Transition in Fermi Systems 61
5.1 The Superconducting State with FC at $T = 0$ 61
    5.1.1 Green's Function of the Superconducting State with FC at $T = 0$ 63
    5.1.2 The Superconducting State at Finite Temperatures . . . 64
    5.1.3 Bogolyubov Quasiparticles 66
    5.1.4 The Dependence of Superconducting Phase Transition Temperature T_c on Doping 68
    5.1.5 The Gap and Heat Capacity Near T_c 69
5.2 The Dispersion Law and Lineshape of Single-Particle Excitations 70
5.3 Electron Liquid with FC in Magnetic Fields 73
    5.3.1 Phase Diagram of Electron Liquid in Magnetic Field 73
    5.3.2 Magnetic Field Dependence of the Effective Mass in HF Metals and High-T_c Superconductors 78
5.4 Appearance of FCQPT in Fermi systems 81
References 84

6 Highly Correlated Fermi Liquid in Heavy-Fermion Metals: The Scaling Behavior 87
6.1 Magnetic Field Dependence of the Quasiparticle Effective Mass 87
6.2 Quasiparticles and the Temperature Dependence of the Effective Mass 90
6.3 Scaling Behavior of the Effective Mass and Energy Scales 93
    6.3.1 Schematic Phase Diagram of a HF Metal 95
    6.3.2 Non-Fermi Liquid Behavior of $YbRh_2Si_2$ 97
    6.3.3 Heat Capacity and the Sommerfeld Coefficient 98
6.4 General Properties of the Phase Diagrams of Heavy-Fermion Metals 99
References 109

7 Highly Correlated Fermi Liquid in Heavy-Fermion Metals: Magnetic Properties 111
7.1 Magnetization 111
7.2 Magnetoresistance 113

7.2.1 Longitudinal Magnetoresistance 113
7.2.2 Transverse Magnetoresistance in the HF Metal $CeCoIn_5$ 114
7.2.3 Electric Resistivity of HF Metals 119
7.3 Magnetic Entropy 120
7.4 Magnetic Susceptibility 121
7.4.1 Magnetic Susceptibility and Magnetization Measured on $CeRu_2Si_2$ 121
7.5 Magnetic-Field-Induced Reentrance of the LFL Behavior and Spin-Lattice Relaxation Rates. 123
7.6 The Relations Between Critical Magnetic Fields B_{c0} and B_{c2} in HF Compounds. 127
7.7 Scaling Behavior of the HF $CePd_{1-x}Rh_x$ Ferromagnet. 130
References. 136

8 Metals with a Strongly Correlated Electron Liquid 139
8.1 Entropy, Linear Expansion, and Grüneisen's Law 139
8.1.1 Entropy, Linear Expansion, and Grüneisen's Law 140
8.2 The $T - B$ Phase Diagram, the Hall Coefficient, and the Magnetic Susceptibility 142
8.3 The Impact of FCQPT on Ordinary Continuous Phase Transitions in HF Metals 146
8.3.1 The Comparison of $T - B$ Phase Diagrams for $YbRh_2Si_2$ and $CeCoIn_5$ 147
8.3.2 The Tricritical Point in the $B - T$ Phase Diagram of $YbRh_2Si_2$ 150
8.3.3 Low Temperature Entropy of $YbRh_2Si_2$ 152
References. 153

9 Quasi-classical Physics Within Quantum Criticality in HF Compounds 155
9.1 Second Wind of the Dulong-Petit Law at a Quantum Critical Point 155
9.2 Transport Properties Related to the Quasi-classical Behavior 162
9.3 Quasi-classical Physics and T-Linear Resistivity 168
References. 176

10 Magnetoresistance in the HF Metal at Zero Temperature. 179
10.1 Introduction 179
10.2 The HF Metal $CeCoIn_5$ 180
10.3 The HF Metal $YbRh_2Si_2$ 187
10.4 Main Results 196
References. 197

11 Zero Temperature Magnetoresistance of the HF Metal: Enigma of $Sr_3Ru_2O_7$ 199
11.1 Introduction: Flat Bands and Enigma of Metamagnetic Quantum Critical Regime in $Sr_3Ru_2O_7$ 199
11.2 Magnetoresistivity 201
11.3 Fermion Condensation 203
11.4 Phase Diagram 204
11.5 Jumps 205
11.6 Entropy 209
11.7 Scaling Behavior 210
11.8 Main Results 212
References 212

12 Fermion Condensation in Finite Systems 215
12.1 Finite Systems 215
12.2 Merging of Landau Levels in Two-Dimensional Electron System in Silicon 226
References 232

13 Asymmetric Conductivity of Strongly Correlated Compounds 235
13.1 Normal State 235
13.1.1 Suppression of the Asymmetrical Differential Resistance in $YbCu_{5-x}Al_x$ in Magnetic Fields 240
13.2 Superconducting State 241
13.3 Relation to the Baryon Asymmetry in the Early Universe 247
References 249

14 Violation of the Wiedemann-Franz Law in HF Metals 251
References 259

15 High Magnetic Fields Thermodynamics of Heavy Fermion Metals 261
15.1 Introduction 261
15.2 Phase Diagram 265
15.3 Results and Discussion 266
15.3.1 Kinks 269
15.4 Main Results 271
References 272

16 Baryon Asymmetry Resulting from FCQPT in the Early Universe 273
16.1 Introduction 273
16.2 Model 274

16.3 The Asymmetry of the Universe 279
References. 282

17 Quantum Criticality of Spin Liquids in Novel Insulators and Magnets. 285
17.1 Thermodynamic Properties of Quantum Spin Liquid in Insulators 286
17.1.1 Model 286
17.1.2 Phase Diagram 290
17.1.3 The Thermodynamic Properties 290
17.2 Scaling in Dynamic Susceptibility of Herbertsmithite and HF Metals 297
17.2.1 Theory of Dynamic Spin Susceptibility of Quantum Spin Liquid and Heavy-Fermion Metals 298
17.2.2 Scaling Behavior of the Dynamic Susceptibility 300
17.3 Spin–Lattice Relaxation Rate of Quantum Spin Liquid 304
17.4 Heat Transport in Magnetic Fields by Quantum Spin Liquid in Insulators 306
References. 314

18 Quantum Criticality of Heavy-Fermion Compounds. 317
18.1 Quantum Criticality of High-Temperature Superconductors and HF Metals 317
18.2 Quantum Criticality of Quasicrystals 321
18.3 Quantum Criticality at Metamagnetic Phase Transitions 329
18.3.1 Typical Properties of the Metamagnetic Phase Transition in $Sr_3Ru_2O_7$ 329
18.3.2 Metamagnetic Phase Transition in HF Metals 331
18.4 Universal Behavior of Two-Dimensional ^{3}He at Low Temperatures 332
18.5 Scaling Behavior of HF Compounds and Kinks in the Thermodynamic Functions 340
18.6 New State of Matter 342
References. 343

19 Conclusions 345
References. 348

Index 351

Acronyms

$2D$	Two-dimensional
$\mathbf{A_q}$	The hyperfine coupling constant of the muon or nucleus with the spin excitation at wave vector **q**
A_{HT}, A_{LT}	High- and low-temperature resistance coefficients
a_B	Bohr radius
$A_w(B,T)$, A_w	The constants of temperature T and magnetic field B-dependent parts of thermal resistance
a	Lattice constant
AC, ac	Alternating current
AF, AFM	Antiferromagnet, antiferromagnetic
B, H	Magnetic field strength
B_{c0}, H_{c0}	The critical field at which the magnetic field-induced QCP takes place
B_{c2}, H_{c2}	The upper critical fields for superconductors
B_{eff}	Effective magnetic field
B_c	Critical magnetic field
B_{inf}	The magnetic field taken at the inflection point
$C(T)$	Heat capacity
C, C_{mag}	Specific heat of quantum spin liquid
$c_{i\sigma}$, $c_{i\sigma}^{\dagger}$	Creation and annihilation operators for electron on-site i with spin index $\sigma = \uparrow, \downarrow$
$C_n(T)$, $C_s(T)$	Heat capacity in the normal and superconducting state
c_s, c_t	Sound and zero sound velocities respectively
c	The speed of light
$D(k,\omega)$	Boson propagator
DC	Direct current
DFT	Density Functional Theory

DMFT	Dynamic Mean-Field Theory
DOS	Density of states
DP	Dulong–Petit
$E_{DMFT}[\rho(\mathbf{r}), G]$	Total energy functional in DMFT theory
$E_{gs}(\kappa(\mathbf{p}), n(\mathbf{p}))$	Ground-state energy
$E_0(A)$	Ground-state energy of atomic nucleus as a function of mass number
e	The charge of electron
$\mathscr{F}(\mathbf{p}, \mathbf{p}_1)$, $F_{\sigma,\sigma_1}(\mathbf{p}, \mathbf{p}_1, n)$, $F(\mathbf{p}, \mathbf{p}_1, n)$, $f(\mathbf{p}, \mathbf{p}_1)$, $U(\lvert\mathbf{p} - \mathbf{p}'\rvert)$	Landau interaction (amplitude)
f_1	First harmonic of Landau interaction (amplitude)
F_L^s, F_L^a	Dimensionless spin-symmetric and spin-antisymmetric parts of Landau interaction (amplitude)
$\bar{f}_i$	Occupation number in two-dimensional electron system
$s-$, $p-$, $d-$ and $f-$ electron shells	Electron shells with orbital quantum number from 0 to 3 respectively
$F(n(\mathbf{p}, T))$	Free energy as a functional of electron occupation number $n(\mathbf{p}, T)$
$F^+(\mathbf{p}, \omega)$, F^+, $G(\mathbf{p}, \omega)$, G	Gorkov Green's functions of a superconductor
FC	Fermi condensate or Fermi condensation
FCQPT	Fermion condensation quantum phase transition
FL	Fermi liquid
FM	Ferromagnet, ferromagnetic
G_A, G_R	The advanced and retarded quasiparticle Green's functions respectively
$\hbar = h/2\pi$	Planck constant
HF	Heavy fermions
^{3}He, ^{4}He	Helium isotopes with three and four nucleons
$I_{n_\mathbf{p}}$	Collision integral as a function of quasiparticles occupation number $n_\mathbf{p}$
I	The electric current
I^s, I^{as}	Symmetric and asymmetric parts of the electric current
k_B	Boltzmann constant
K	Compressibility and also Kadowaki–Woods ratio
$L(T)$, L_0	Lorentz number at $T \neq 0$ and $T = 0$ respectively
LFL	Landau Fermi Liquid
LMR	Longitudinal magnetoresistance

LSDA	Local spin density approximation
$\hat{\mathbf{M}}$, $\underline{\mathbf{M}}$	Average magnetization vector
$\mathscr{M}$	Magnetization modulus
M, $M(T,B)$	Magnetization as a function of temperature T and magnetic field B
M^*, M^*_{mag}, M^*_{FC}, m^*	Quasiparticle effective mass
m, m_e, M	Free electron mass
M_{nor}	Normalized magnetization
MOSFET	Metal Oxide Semiconductor Field Effect Transistor
MR, $R^{\rho}_{M}(B,T)$	Magnetoresistance
n	Charge carrier concentration
n_i	Density of electrons at the site i
n_s	Density of electrons in two-dimensional electron system
$n(\mathbf{p},T)$	Quasiparticle occupation number (or distribution function) as a function of their momentum $\mathbf{p}$ and temperature T
$N(\xi,T)$	The density of states
$N_S(E)$	The density of states of a superconductor
$N(E_F)$ or $N(0)$	The density of states at the Fermi surface
NFL	Non-Fermi Liquid
$\mathbf{p_i}$, $\mathbf{p_f}$	The borders of Fermi volume, where fermion condensate is localized
$\mathbf{p}^{\uparrow}$, $\mathbf{p}^{\downarrow}$	Momenta of Fermi surfaces with spin up and spin down
p_F	Fermi momentum
P	Pressure
PM	Paramagnet, paramagnetic
QC, QCs	Quasicrystals
QCL	Quantum critical line
QCP	Quantum critical point
QPT	Quantum Phase Transition
QSL	Quantum spin liquid
$R_{nl}(r)$	Radial part of wave functions, determined by two quantum numbers n (main) and l (orbital)
$R_H(B)$	Hall coefficient
r_s	Wigner–Seitz radius
$\mathscr{S}(T_c)$	Stoner factor
$S(n(\mathbf{p},T))$, $S(T)$	The entropy as a function of quasiparticles occupation number $n_{\mathbf{p}}$ and temperature T
S_{AF}, $S_{NFL}(T)$	Entropy in the antiferromagnetic and non-Fermi liquid phases respectively; latter is a function of temperature T

S_0	The residual entropy of Fermi condensate at $T = 0$
$S(T)$	Seebeck coefficient
SC	Superconducting
SCDFT	Superconducting Density Functional Theory
SCQSL	Strongly correlated quantum spin liquid
SDA	Spin density approximation
SUSY	Supersymmetry
$\mathscr{T}(\mathbf{j}, \omega = 0)$	Vertex part of a diagram
t_{ij}	The hopping matrix element for electrons between sites i and j (e.g. in Hubbard model)
T_c	Critical Temperature
$T_D,\ \Omega_D,\ \Omega_t$	Debye temperature
$T\ [\rho, G]$	Kinetic energy term in DMFT theory
T	Tesla
$T^*, T^*(B)$	Crossover/transition temperature
T_p^*	The temperature at which the pseudogap is closed
T_{inf}	The temperature taken at the inflection point
TMR	Transversal magneto-resistance
T_{NL}	The Néel temperature
TPT	Topological phase transition
TT	Topological transitions
$1/T_1$	The spin-lattice relaxation rate
$1/T_1^{\mu},\ 1/T_{1N}^{\mu}$	Muon (ordinary and normalized respectively) spin-lattice relaxation rates
$U,\ U_i$	Local Coulomb repulsion between two electrons occupying the same site i (e.g., in Hubbard model)
vHs	van Hove singularity
V_{KS}	Kohn–Sham potential
$V_{xc}[\rho, G]$	Exchange-correlation potential in DMFT theory
V	Applied voltage
V	Volume
v_t	The velocity of transverse zero sound
$w(B, T),\ w$	Thermal resistivity
w_0	Residual thermal resistivity
WF	Wiedemann–Franz
x_{FC}	Critical number density in *FCQPT* point
x	Electron (hole) number density, doping
$z(\mathbf{p}),\ z$	Quasiparticle weight, renormalization factor, so-called z-factor

$\alpha_{FC}(T)$	Thermal expansion coefficient for the system with fermion condensate
$\alpha_R,\ \alpha_R(T,B)$	Exponent in power-law of resistance temperature dependence
$\alpha(T)$	Thermal expansion coefficient
$\alpha,\ \beta,\ g$	Coupling constant, Landau interaction constant
$\alpha_{cr},\ b_c,\ g_c$	Critical value of Landau interaction constant
α	Critical exponent
$\chi_{AC}(B,T)$	AC magnetic susceptibility
χ	Magnetic susceptibility, spin susceptibility
$\chi_0(\mathbf{q},\omega)$	The linear response function for the non-interacting Fermi liquid
$\chi(\mathbf{q},\omega,g)$	The response function of the system
$\chi(\mathbf{q},\ \omega\to 0)$	Low-frequency dynamical magnetic susceptibility
$\chi'(\mathbf{p},\omega,T),\ \chi''(\mathbf{p},\omega,T)$	The real and imaginary part of the spin susceptibility, respectively
$\delta\mathbf{p}=\mathbf{p_f}-\mathbf{p_i}$	Momentum interval occupied by fermion condensate
$\delta(x)$	Dirac delta function
$\varDelta(\mathbf{p}),\ \varDelta(\phi)$	Superconducting gap as a function of momentum and angle respectively
$\varDelta\rho_L(B,T)$	Classical contribution to magnetoresistance
$\varDelta\sigma_d(V)$	The asymmetric part of the differential conductivity
$\varepsilon_F,\ E_F$	Fermi energy
ε_i	Single-electron energy
$\varepsilon(\mathbf{p},T),\ \varepsilon(\mathbf{p},T,n)$	Quasiparticle single-particle energy as a function of momentum **p**, temperature *T* and occupation number *n*
γ_0	Sommerfeld coefficient
$\varGamma(T)$	Grüneisen ratio
$\gamma,\ \gamma(T)$	The quasiparticle damping or width of quasiparticle state
$\varGamma$	The scattering amplitude
$\varGamma^\omega$	The ω-limit of the scattering amplitude
$\varGamma^k$	The *k*-limit of the scattering amplitude
$\kappa(\mathbf{r},\mathbf{r}_1),\ \kappa(\mathbf{p})$	Anomalous density or the order parameter
$\kappa(B,T),\ \kappa$	Thermal (heat) conductivity as a function of magnetic field *B* and temperature *T*
$I(B,T)=(\kappa(B,T)-\kappa(0,T))/\kappa(0,T)$	The reduced heat conductivity
κ_d	Dielectric constant
$I_N(B,T)$	The normalized reduced heat conductivity

λ_0	Coupling constant of superconducting (pairing) interaction
$\lambda_0 V(\mathbf{p}_1, \mathbf{p}_2)$	Pairing interaction
μ, $\mu(T)$, μ_σ, $\mu(A)$	Chemical potential, also as a function of temperature T, spin σ and mass number A
μ_B	Bohr magneton
∇	Nabla operator
v_F	Fermi velocity
Ω_F	The volume of Fermi sphere
Ω_{FC}	The volume occupied by fermion condensate
Ω_0	The characteristic frequency of zero sound
$\hbar\omega_c = \hbar eB/m^* c$	Cyclotron splitting
Φ_{lm}	Angular part of wave functions
Φ, $\Phi[n(\mathbf{r}, \kappa(\mathbf{r}, \mathbf{r}_1))]$	Thermodynamic potential as a function of quasiparticle occupation number n
$\Pi(\mathbf{j})$	Polarization operator
π	Pi-number
$\Psi_\sigma(\mathbf{r})$	Field operator for annihilation of an electron with spin $\sigma = \uparrow, \downarrow$ at the position $\mathbf{r}$
$\psi_i(\mathbf{r})$	Single-electron wave function
ρ_∞	Critical density
$\rho(T)$	Electric resistance
ρ_0	Residual (electric) resistance
ρ_0^{LFL}, ρ_0^{NFL}, ρ_0^{nem}	Residual resistance in the Landau Fermi liquid state, non-Fermi liquid state and in the nematic phase
$\rho(\mathbf{r})$, ρ_x	Electronic charge density
ρ	The number density of a system
ρ_{inf}	The magnetoresistance taken at the inflection point
σ_{tr}	Transport cross-section
$\sigma_d(V)$	Differential tunnel conductivity
$\Sigma(\mathbf{p}, \varepsilon)$	Self-energy part
$\sigma(T)$, σ	The electrical conductivity
τ_q	The lifetime of quasiparticles
τ	The collision time
$\theta(p)$	Theta function or Heaviside function
$\varphi_\lambda(\mathbf{r})$	Wave functions

Chapter 1
Introduction

Abstract This chapter has introductory character and gives the definition and classification of strongly correlated systems. We outline the difference between strongly and weakly correlated systems and show that the former cannot be described adequately in the framework of ubiquitous methods like e.g., band theory of solids. We familiarize the reader with theoretical approaches to strongly correlated systems and to Landau theory of Fermi-liquid in particular. We show that Landau theory is insufficient to describe so-called non Fermi liquid properties of several strongly correlated substances like heavy fermion compounds. For such description, the notion of fermion condensation quantum phase transitions has been introduced. The aims and goals of the book are also discussed.

1.1 Introductory Remarks

1.1.1 General Consideration: Strong Versus Weak Correlations

When we are dealing with an ensemble of particles, which do not interact with each other, the problem can be completely solved analytically. The situation is drastically different, when even weak interparticle interaction is "turned on": In this case the problem ceases to be single-particle and many body effects enter the scene. As modern physics is dealing primarily with the ensembles of interacting particles, it is not an exaggeration to say, that its central problem is the many-body theory. Indeed, all our surroundings, from cosmic bodies to tiny objects like molecules, are made of many constituents. This statement is also valid for microscopic particles like atoms and nuclei. Several decades ago it became clear that, perhaps, only quarks and leptons can be considered as truly elementary particles, which cannot be splitted into smaller entities.

To form a body of any size, the constituent particles have to interact with each other. Such an interaction is achieved by exchange of these particles by quanta of interaction field—photons, gluons , and mesons. However, if the speed of interacting particles is much less than the speed of light, the interaction can be limited to either some phenomenological potentials, or, for charged objects and not too small distances, to pure Coulomb interaction.

M.Y. Amusia et al., *Theory of Heavy-Fermion Compounds*, Springer Series in Solid-State Sciences 182, DOI 10.1007/978-3-319-10825-4_1

The materials, that are well understood, usually contain the ensemble of free or almost free weakly interacting (or weakly correlated) particles. To understand the latter materials, band theory, which represent electrons in the form of extended plane waves, is a good starting point. That theory helps capture the delocalized nature of electrons in metals. It is valid provided that the Coulomb interaction energy of electrons is much smaller than their kinetic energy. However there are important physical systems for which interactions between the electrons are not weak, and these interactions play a major role in determining the properties of such systems. They are usually called strongly correlated systems. The examples here can be metals with open $d-$ and $f-$ electron shells, where electrons occupy narrow bands. There, electrons experience strong Coulomb repulsion because of their spatial confinement in those bands. The effect of correlations on the physical properties of such objects is often profound. The interplay of the d and f electrons internal degrees of freedom like spin, charge, and orbital moment can exhibit a lot of exotic phenomena at low temperatures. That interplay makes strongly correlated electron systems extremely sensitive to small variations of external parameters, such as temperature, pressure, or magnetic field.

In materials called heavy fermion systems, mobile electrons at low temperatures behave as if their masses were a hundred times the mass of an electron in a silicon or simple metal. Such systems exhibit a great variety of interesting phenomena like anomalies in electric and thermal conductivity, quantum phase transitions between magnetically ordered state and superconductivity, emergence and dissociation of local magnetic moments etc. This rich variety of the phenomena makes their experimental and theoretical studies all the more difficult. Quantum mechanical study of strongly correlated fermionic systems is done by two approaches: ab-initio numerical electronic structure simulations and model theoretical treatment. In the first case real materials can be described with all details of their chemical composition and crystal structure fully taken into account. In model approaches, such subtleties are usually neglected in favor of more rigorous mathematical treatment of the problem. The result yields the dependencies (in graphical and sometimes in analytical form) of system physical properties upon external parameters like temperature, pressure and/or external fields. But nowadays even in latest theoretical treatment, the solutions of derived equations could be obtained by means of numerical calculations only.

In this context we mention so-called optical lattices, consisting of boson atoms ensemble in a periodic potential. At low temperatures such Bose particles can condense: i.e. most of the particles can be found in a state of zero momentum, which helps to minimize their kinetic energy. Below we will see that related phenomenon can occur in the systems with strongly correlated fermions, giving rise to completely new physics, which is the same for many seemingly different systems. We will see also that the notion of fermion condensation permits to elegantly explain the whole bunch of puzzling experimental facts in systems with strongly correlated fermions. At this moment, a good general approach accepted for understanding strongly correlated systems does not exist. For example, certain aspects of systems exhibiting quantum Hall effect or some magnetic materials are already understood. But the other systems are understood very poorly. For instance, the nature of high temperature superconductivity remains mysterious despite decades of intensive work. Most importantly we do not have a unified view on the fermionic systems for which interparticle interactions not only cannot be neglected but play a decisive role in the formation of their observable properties.

1.1.2 Theoretical Approaches to Strongly Correlated Systems

A natural question appear: How to solve a many-body problem? In other words, how to describe a system of large number of interacting constituents knowing how to deal with single free particle motion and its interaction with the other particle and environment? This problem is not new and by far not specific to quantum systems. Indeed, this problem existed already at the time when Newton created his mechanics and discovered the law of gravitation. However, in the case of relatively weak gravitational interaction only two-body dynamics is essential so that the rest of particle ensemble could be treated as small perturbation. For instance, the Moon and all other planets of Solar system affect the Earth rotation around the Sun as a small, although noticeable perturbation. Only recently it became clear that in some cases even weak gravitational interaction can lead to prominent many-body effects, so called resonance phenomena.

In quantum mechanics, the many-body problem became essential almost immediately after discovery of the Schrödinger equation [1] in 1926. The motivation was the fact that the potential, in which the given quantum particle (say, electron) moves, is created by the rest of the particles, where this electron resides. At that time it had already been recognized, that the electron-electron interaction in atoms plays less important role than their interaction with the atomic nucleus. This hierarchy is similar to that in Solar system in regard of inter-planet and Sun-planet interactions. Already in 1928 D. Hartree suggested the concept of self-consistent field [2, 3] that permitted to consider many—electron atoms treating their electrons as moving in a field essentially modified as compared to the pure Coulomb field of an atomic nucleus. Tho years later V. A. Fock took into account the fact that all electrons are identical Fermi particles so that their wave function has to be antisymmetric under permutation of any two electrons [4, 5]. As a result, prominent Hartree-Fock equation had been formulated. This equation is in use until now, being applied not only to single atoms, but to multi-atomic objects like molecules, clusters, fullerenes and even bulk solids. The application of the Hartree-Fock equation is not limited to the systems with Coulomb interparticle interaction. The same equation can be successfully applied to nucleus as a system consisting of protons and neutrons. Actually Hartree-Fock equation considers only non-perturbative part of interparticle interaction; it can also be applied to the systems of Bose particles where it is called Gross-Pitaevskiy equation.

The remaining part of interparticle interaction that is neglected in the Hartree-Fock framework is usually called *residual interaction*. This part of interaction leads to so-called *correlation effects*, or *interparticle correlations*. Obviously, the Hartree-Fock equation is able to describe many-body system satisfactorily only if correlations are negligible. However, as it is known now, there exist a number of many body systems, where correlations lead to decisively important *collective phenomena*.

We note here, that Hartree-Fock approach along with little earlier Thomas-Fermi approach [6, 7] were the first representative of so-called first principle (*ab initio*) methods to incorporate the above collective phenomena in the physical properties of solids and strongly correlated systems in particular. The aim of such methods is to calculate the macroscopic, observable properties of a body having in disposal its microscopic characteristics like its crystalline symmetry and interatomic interaction potentials. If all microscopic details were known, the problem would be solved exactly utilizing (many-particle) Schrödinger equation. Unfortunately, this is not the case for majority of real systems. Only molecules consisting of small number of atoms as well as single atoms can be more or less satisfactorily treated by this straightforward method. In this approach, their wave functions are represented as linear combinations of corresponding Slater determinants.

Further development of ab-initio methods was related to the breakthrough, made by Hohenberg-Kohn theorem, which puts a foundation to the Density Functional Theory (DFT) [8–11]. The Hohenberg-Kohn theorem states that a system's wave function is defined uniquely by its charge density. The idea of DFT is a direct generalization of Hartree-Fock self-consistent field approach. Namely, in DFT, the differential equations called Kohn-Sham equation for single-electron wave functions are solved with certain effective potential, which, in turn, is determined self-consistently by that equation's solutions. This Kohn-Sham equation is derived by variation of the energy functional $E[\rho]$, depending on the local electronic charge density $\rho = \rho(\mathbf{r})$. This functional, expressing the total energy of many-body system, has the form [10]

$$E[\rho] = T[\rho] + \int \rho(\mathbf{r}) V_{ext}(\mathbf{r}) d^3r + \int d^3r\, d^3r' \frac{\rho(\mathbf{r})\rho(\mathbf{r}')}{|\mathbf{r} - \mathbf{r}'|} + E_{xc}[\rho], \tag{1.1}$$

where $T[\rho]$ is kinetic energy, $V_{ext}(\mathbf{r})$ is the external potential acting on the electrons, third term is the Hartree contribution to the Coulomb interaction between the charges, and the last term is the so-called exchange and correlation energy contributions $E_{xc}[\rho]$. The exchange contribution takes into account the partial suppression of Coulomb repulsion between electrons in the same spin state due to Pauli principle. The DFT method would be exact if the explicit form of the term E_{xc} in (1.1) would be known. However, this is not the case, as for that one needs to solve the system of functional equations exactly [12].

To handle this problem, the DFT self-consistent approach along with approximations (like, for instance, local density approximation (LDA) and its spin counterpart local spin density approximation (LSDA), see [13] for details) for exchange- correlation energy E_{xc} had been utilized in DFT. Also, as particular representation of wave functions corresponding to $\rho(\mathbf{r})$ cannot be defined uniquely in DFT, this quantity is expressed usually via single-electron wave functions $\psi_i(\mathbf{r})$

$$\rho(\mathbf{r}) = \sum_{i=1}^{N} |\psi_i(\mathbf{r})|^2, \tag{1.2}$$

where N is the number of electrons in a system.

Minimizing the functional (1.1) over the functions $\psi_i(\mathbf{r})$ (with respect to the normalization conditions for ψ_i) generates Kohn–Sham equations:

$$\left[-\frac{\nabla^2}{2m} + V_{KS}[\rho(\mathbf{r})]\right]\psi_i = \varepsilon_i \psi_i, \tag{1.3}$$

where ε_i are the single-electron eigenvalues, Kohn-Sham potential V_{KS} represents a static mean field (signifying the explicit neglecting of correlation effects when all electrons feel the same potential) of the electrons and has to be determined in a self-consistent way

$$V_{KS}[\rho(\mathbf{r})] = V_{ext}(\mathbf{r}) + V_{xc}[\rho(\mathbf{r})] + 2\int \frac{\rho(\mathbf{r}')d^3r'}{|\mathbf{r}-\mathbf{r}'|},\ V_{xc}[\rho(\mathbf{r})] = \frac{\delta E_{xc}[\rho(\mathbf{r})]}{\delta\rho(\mathbf{r})}, \tag{1.4}$$

where $\delta/\delta\rho$ means the variational derivative. The (1.4) allows one to calculate electronic charge density and total energy for the ground state of a system. The DFT with LDA and/or LSDA approximations for $E_{xc}[\rho]$ had been successfully applied to describe the electronic properties of atoms, molecules and solids, where correlation effects are not too strong. In the systems with strong correlations like transition metal oxides, the DFT gave incorrect metallic ground state in the absence of long-range magnetic order.

As in 1960-ties the computational power was too feeble to calculate real things by ab initio methods, the so-called model Hamiltonian approach comes into play. Namely, the full many-body Hamiltonian is simplified to account for only a few relevant degrees of freedom—typically, the valence electron orbitals near the Fermi level. One of the simplest models of correlated electrons is the Hubbard Hamiltonian [14], which takes into account the interplay between electron hopping and local on-cite repulsion:

$$\mathscr{H} = \sum_{i,j,\sigma} t_{ij} c^\dagger_{i\sigma} c_{j\sigma} + U \sum_i n_{i\uparrow} n_{i\downarrow}, \tag{1.5}$$

where $c_{i\sigma}$ and $c^\dagger_{i\sigma}$ are creation and annihilation operators for electron on site i with spin index $\sigma = \uparrow, \downarrow$, $n_i = c^\dagger_{i\sigma} c_{i\sigma}$ is the density of electrons at site i, U is a local Coulomb interaction between two electrons occupying the same site i. The matrix element t_{ij} describes hopping of electrons with between sites i and j. It is usually supposed that hopping is not zero for nearest neighbors (with number z_n) only. Such simplified treatment of electron–electron Coulomb repulsion turns out to be very convenient to study the itinerant electron systems, especially their magnetic states. A wide variety of analytical and numerical methods have been utilized to study the strongly correlated electron systems in the framework of Hubbard model. But despite that, the Hubbard model (1.5) could be solved only for limited number of cases.

It had been observed in 1989 [15] that the consideration of the electron correlations on the lattices with large (actually infinite) number of nearest neighbors z_n, simplifies the problem essentially so that it can be solved exactly for any strength of Coulomb repulsion. The simplification at $z_n \to \infty$ occurs due to the fact that in this case one can neglect the spatial fluctuations leaving only time dependent on-site fluctuations. This fact laid the foundation of Dynamical Mean-Field Theory (DMFT), which mapped lattice models (like Hubbard one [16, 17]) to effective impurity problem with correlated electrons feeling mean field which this time is dynamic, i.e. time or energy dependent. Solution of the latter effective impurity problem can be further used to construct the self-energy for lattice Green's function G that, in turn, gives new approximation for above dynamic mean-field. The DMFT solutions become exact as the number of neighbors increases. Similar to DFT, the DMFT also relies on energy functional $E_{DMFT}[\rho(\mathbf{r}), G]$, which in this case depends on the above local Green's function G:

$$E_{DMFT}[\rho(\mathbf{r}), G] = T[\rho(\mathbf{r}), G] + \int \rho(\mathbf{r}) V_{ext}(\mathbf{r}) d^3r + \int d^3r\, d^3r' \frac{\rho(\mathbf{r})\rho(\mathbf{r}')}{|\mathbf{r} - \mathbf{r}'|} + E_{xc}[\rho(\mathbf{r}), G], \tag{1.6}$$

where $G = G_{i\sigma}(t - t') = - < c_{i\sigma}(t) c^{\dagger}_{i\sigma}(t') >$ specifies the probability to create an electron with spin index σ at a site i at time t' and annihilate it at the same site at a time $t > t'$. In practical calculations this function is found self-consistently from the above effective single-impurity problem, where the rest of the electrons are considered as the bath for given impurity one. The theory is called "dynamic" as Green's function depends explicitly on time or frequency argument. Also, the approximations for $E_{xc}[\rho(\mathbf{r}), G]$ are provided.

Although dynamical mean-field methods clearly represent a new advance in many-body physics, they are still unable to capture many effects in strongly correlated systems, e.g., the divergent behavior of the effective mass. That is why generalizations of DFMT to account for real materials is an active area of research. The above consideration shows that only ab-initio methods in principle cannot give sufficient insights in the physics of strongly-correlated systems because of their computational complexity, still beyond reach of modern computer's possibilities. The more insight has been achieved on the way of model assumptions and simplification of initial many-body Hamiltonian, leaving in them only the most essential terms, which, on the other hand, could be assessed both analytically and numerically. Nonetheless, these methods meet with enormous difficulties while being applied to consideration of excitation spectra of a many-body system, while these spectra define the thermodynamic, transport and relaxation properties.

The complimentary approach essential break-through in the understanding of many-body systems was the introduction of so-called *quasiparticles*. Namely, the real interacting (with potential V) particle ensemble is substituted by quasiparticles, that interact via some *effective* interaction V_{eff} and represent the excitation on top of some vacuum ground state.

Then the question appears how to construct the quasiparticles and their effective interaction. At a first glance, this is a simple problem, if the interaction is weak. But what is the meaning of weakness if, roughly speaking, the effect of interaction includes in some cases a large number generated by the corresponding phase transition. So, the weakness can be overwhelmed by the large number, leading to macroscopic correlated coherent phenomena like superfluidity and/or superconductivity.

The first attempt in this direction was undertaken by Landau in 1956 [18], when he assumed the existence of quasiparticles, and afterwards, when he, together with his colleagues gave a proof of the developed approach on the general grounds of many-body theory [19]. He suggested that for systems where the interaction is strong, quasiparticles can be introduced as well defined objects. The ground state energy E in that case is assumed to be a functional of the quasiparticle distribution function $n(\mathbf{p})$, $E[n(\mathbf{p})]$, with the single particle spectrum (or the dispersion law) $\varepsilon(\mathbf{p}) = \delta E[n(\mathbf{p})]/\delta n(\mathbf{p})$. According to conventional usual practice a quasiparticle is presumed to be well-defined until proven not to be. The textbook picture of quasiparticles as long-living excitations weakly interacting with each other works very well for many objects. This system of quasiparticles forms the Landau quasiparticle paradigm. Nevertheless, in a number of recently studied strongly correlated systems the above quasiparticles neither interact weakly nor remain well-defined even at zero temperature. As we shall see in Chap. 2, this paradigm is to be substituted by an extended one. As an example, Landau treated the liquid ^{3}He, which is a liquid, whose constituents are Fermi particles—two-electron atoms with ^{3}He nuclei. He demonstrated that at low temperatures the excitations of such a system could be described as those of a quasiparticle gas.

It is worth noting, that at temperature $T = 0$ in spite of strong interparticle interaction the distribution of quasiparticles $n(\mathbf{p})$ as a function of their momentum p can be presented as a Fermi-step of noninteracting fermions:

$$n(\mathbf{p}) = \begin{cases} 1, & p \le p_F \\ 0, & p > p_F, \end{cases} \tag{1.7}$$

where p_F is the so-called Fermi-momentum of the system. It is essential that the densities (i.e. total numbers per unit volume) of particles and quasiparticles coincide. E.g., in three dimensional (3D) case they both equal to

$$\rho = \frac{p_F^3}{3\pi^2}. \tag{1.8}$$

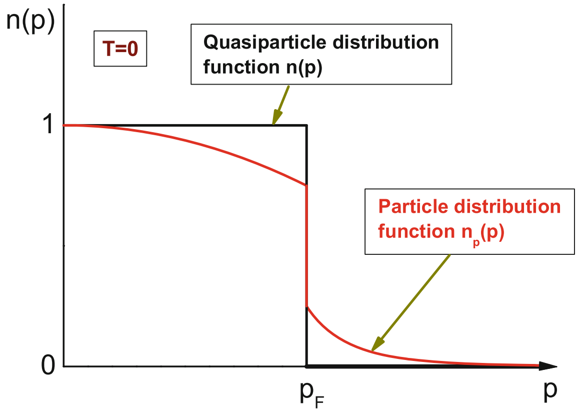

Fig. 1.1 Quasiparticle $n(\mathbf{p})$ and particle $n_p(\mathbf{p})$ distribution functions at $T = 0$ are shown by the *arrows*. $n(\mathbf{p})$ is given by (1.7) and $n_p(\mathbf{p})$ by (1.9) with the jump at $p = p_F$

Throughout, *if otherwise do not stated*, we adopt the atomic system of units, where $\hbar = c = 1$, where c is the speed of light. In this book, we consider a different branches of the condensed matter physics. As a result, in some chapters we use those systems of units which are commonly accepted in the considered area. For example, as it is done in Chap. 12.

As to the momentum dependence of the *particle* distribution function $n_p(\mathbf{p})$, it has, according to Migdal [20], a tail at $p > p_F$, in contrast to the distribution function of quasiparticles. This tail decreases as p increases. This decrease is fast, but not exponential. In the same paper [20], it had been demonstrated that at $p = p_F$ the function $n_p(\mathbf{p})$ has a step:

$$0 < n_p(p_F) = z < 1. \tag{1.9}$$

It is seen from (1.7), (1.9) and Fig. 1.1, that both the quasiparticles and the particles distribution functions have jumps at the Fermi momentum p_F.

The single-particle spectrum $\varepsilon(\mathbf{p})$ for Landau quasiparticle at $(p - p_F)/p_F \ll 1$ is similar to that of an excitation of a gas of non-interacting Fermi-particles at low temperatures T

$$\varepsilon(p) - \mu = \frac{p_F(p - p_F)}{M^*}, \tag{1.10}$$

where μ is the chemical potential and M^* is the effective mass that, from case to case, differs from the mass M in a different degree. Here M is the bare mass of the particles constituting the many-body system under consideration. In the many-body theory, one usually investigates systems consisting of single-particle type, having the same mass, spin and charge. Generalization to multi-component systems is very often not a simple and straightforward task.

A quasiparticle excitation can decay by creating two and more quasiparticles. If this decay proceeds sufficiently fast, the concept of quasiparticle as well defined system's excitation faces difficulties. More precisely, before the decay process quasiparticle lives for time (so-called *quasiparticle lifetime*), which is reciprocal to its width γ. It had been also demonstrated by Migdal [20], that the quasiparticle width can be estimated by the following relation

$$\gamma \sim \frac{(p - p_F)^2}{2M^*}. \tag{1.11}$$

Note that $\gamma \ll \varepsilon(p) - \mu = p_F(p - p_F)/M^*$ at $(p - p_F)/p_F \ll 1$ and therefore quasiparticle can be considered to be reasonably stable, if they are close enough to the Fermi-surface at any inter-particle interaction strength. The simplest excitation of a Fermi-system, which interacts strongly with an external field, can be viewed as an absorbtion of its quanta with low excitation energy ω and small (as compared to p_F) momentum k by a combination of a quasi-particle of energy $\varepsilon(p)$ (with $p > p_F$) and quasi-hole $\varepsilon(p')$ (with $p' \le p_F$). Note that the energy and momentum conservation is valid:

$$\omega(k) = \varepsilon(p) - \varepsilon(p'), \ \mathbf{k} = \mathbf{p} - \mathbf{p}'. \tag{1.12}$$

The presence of effective interaction, transforming one electron-hole pair into the second, third and so on, leads to collective response of the Fermi-system on the external field. Due to the presence of V_{eff}, so-called coherent collective excitations in the Fermi-system are formed. One of examples is a sound-like excitation with $\omega = c_t k$ termed *zero sound* with propagation velocity $c_t \ge p_F/M^*$ [19]. General expressions to determine the dependence of excitation energy ω upon momentum k had been derived in [19, 21]. It is essential to have in mind that there exists a profound analogy between quasi-hole in condensed matter and antiparticle in elementary particles theory.

The concept of relatively weakly interacting quasiparticles permits to express the low-temperature thermodynamic and electrodynamic properties of the Fermi-system under consideration via several numbers characterizing the quasiparticles and their effective interaction. For instance, the specific heat C turned out to be simply proportional to M^*, which in turn generates its proportionality to the system's temperature T

$$C \propto M^* T. \tag{1.13}$$

At some parameters of the effective interaction a Fermi-liquid can undergo *phase transitions* to other states like ferromagnetic and antiferromagnetic. This corresponds to solutions of Landau equation determining collective excitations that have zero or pure imaginary energy for non-zero momentum. I. Ya. Pomeranchuk derived the conditions [22] yielding the value and sign of V_{eff}, which is necessary for the susceptibility towards a fictitious external field to become infinite. This means that the system is unstable with respect to transition to certain fundamentally different (than the initial one) ground state, which is already stable for above V_{eff}. The phase transitions are of particular interest, since they describe possible system evolution under the action of above weak perturbations. The stability conditions itself can only signal on possible instability of initially chosen system's ground state. But they are not enough for finding the state of a system formed after instability has been developed.

It was common wisdom for many years, that if we augment the above Pomeranchuk conditions by the one, determining the transition to the superconducting state, we are able to describe all possible phase transitions of a Fermi-system. However, for ^{3}He the experimental situation is not that clear. The investigation of the heat capacity C at temperature dropping from tenths of Kelvins down to millikelvin start to contradict the linear law (1.13). The data, instead of temperature independence, demonstrated a more complex law like $M^* = a + b \ln T$ with very strange at that time possibility of diverging in the limit $T = 0$ [23]. Starting from millikelvin, new phases, including a superfluid one, were discovered in liquid ^{3}He [24]. Arguments appear that for any system a superfluidity is inevitable for sufficiently low T and therefore strictly speaking the above presented quasiparticle concept in liquid ^{3}He is not valid at low temperatures.

The Fermi liquid approach along with quasiparticles paradigm have been successfully applied to studies of electrons in solids and in metals in particular [19, 21]. It appeared that vast majority of properties of electron liquid in metals can be well understood in the framework of the temperature independent Landau-type quasiparticles so that this approach becomes almost universal in quantum liquids description in condensed matter. However, further development of the condensed matter physics shows convincingly that more and more properties of solids either cannot be satisfactorily described by the ordinary Fermi-liquid picture and/or require complete revision of the quasiparticle paradigm. It turned out that latter revision is highly nontrivial task. It appeared, however, that additionally to above Fermi liquid instabilities (i.e. those related to Pomeranchuk's conditions and to transition to superfluid (superconducting) state, another instability was overlooked. Indeed, it has never been discussed what happens to the system if some interparticle interaction generates the divergence of the effective mass $M^* \to \infty$ rather than the susceptibility. In this case, as we will see in Chap. 2, all quasiparticle excitation energies equal to zero so that the system resembles a condensate of Fermi particles or Fermi condensation/condensate (FC) [12, 25–28]. Numerous studies has confirmed the possibility of the FC state that exists for certain interparticle interaction potentials and demonstrates its unusual properties. The possibility of the fermion condensation quantum phase transition (FCQPT), preceding FC, does not abandon the concept of quasiparticles. On the contrary, it demonstrates that during this phase transition the quasiparticle effective mass M^* become dependent on external parameters like temperature, pressure and/or external field. This situation opposes the Landau Fermi-liquid picture, where the effective mass never depend on the above external parameters, being a constant, determined by particle density and their interaction. The above consideration makes it clear that FCQPT has a quantum nature, determining a non-Fermi liquid (NFL) behavior or quantum criticality in strongly correlated systems.

At the beginning, the idea of FC has not been considered by the community too seriously. It was interpreted as a mathematical trick rather than an approach to describe real phenomena. It turns out, however, that above idea is capable to deliver the adequate description of a huge body of otherwise unexplained experimental data. It has been demonstrated several times that classical Landau theory of Fermi liquid is insufficient and too narrow to encompass many experimentally important cases. A variety of these effects appeared in a number of newly discovered systems, including those, explained in the framework of FC picture (see e.g., [26–28]). Abundance of data stimulates to present these results in a form of a book, what makes data better accessible to not only to experts, but also to graduate students who will, hopefully, use this approach in their future research. This approach can be considered as complimentary, but also in many case as an unique tool to treat and describe real systems, exhibiting the quantum criticality.

The physics of quantum matter occupies a substantial part of modern physics. In contrast to the general belief, a quantum matter can show up even at room temperature, as it takes place for electrons in metals, which behave in accordance with the above the famous Landau Fermi liquid (LFL) theory based on the quasiparticle paradigm [18, 19, 24]. We consider the quantum criticality in HF compounds begotten by quantum phase transitions with their quantum critical points located at $T = 0$. The quantum criticality describes a new quantum state of matter which exhibits a universal behavior, and can hardly be understood within the framework of the LFL theory. Thus, quantum criticality in materials of significant theoretical and practical interest requires a new theoretical input. Furthermore, there are indications that the relevant new physics demands a departure from the quasiparticle paradigm of LFL theory. One could also expect that we have to confine our consideration to ultra low temperatures. This is not the case since HF compounds, for instance, reveal significant deviation from LFL properties, termed as NFL behavior, for the temperatures as high as tens of Kelvins. On the other hand, as we shall see, HF compounds at their quantum criticality can exhibit a quasi-classical behavior.

From now on, we call HF compounds “strongly correlated Fermi systems” as well. Strongly correlated Fermi-systems, represented by HF compounds, high-T_c superconductors, strongly correlated insulators with spin liquid, quasicrystals, and two-dimensional (2D) Fermi liquids, are among the most intriguing and best experimentally studied fundamental systems in physics, however until very recently these lacked theoretical description [26–28]. The properties of these materials differ dramatically from those of ordinary Fermi-systems [26–39]. For instance, in the case of HF metals, the strong electron-electron correlations lead to a renormalization of M^*, which may exceed the ordinary, so called “bare” electron mass by several orders of magnitude or even become infinitely large. The effective mass strongly depends on temperature, pressure, or applied magnetic field. HF metals exhibit NFL behavior and unusual power laws of the temperature dependence of the thermodynamic properties at low temperatures. To describe this NFL behavior, the ideas based on the concept of quantum, thermal fluctuations, and Kondo lattice in a quantum critical point (QCP) have been utilized, see e.g., [29, 31, 40–43]. These ideas, however, could not provide a universal description of NFL properties. This generated a real crisis in physics of HF systems and to overcome this crisis, a new quantum phase transition, responsible for the observed behavior was suggested [26–28, 34–38, 40, 44]. Below we will show that FCQPT based concept of quantum criticality permits to resolve many puzzles of physics of strongly correlated fermion systems, and HF metals in particular.

1.1.3 Quantum Phase Transitions and NFL behavior of HF compounds

The unusual properties and NFL behavior observed in high-T_c superconductors, HF metals, 2D Fermi-systems and other HF compounds, such as novel insulators and quasicrystals, are assumed to be determined by various magnetic quantum phase transitions [26–36, 38–41]. Since a quantum phase transition occurs at $T = 0$, the control parameters are all but temperature, i.e. composition, electron (hole) number density x, pressure, magnetic field strength B, etc. A quantum phase transition occurs at a quantum critical point, which separates the ordered phase (emerging as a result of quantum phase transition) from disordered one. It is usually assumed that magnetic (e.g., ferromagnetic and antiferromagnetic) quantum phase transitions with the corresponding critical fluctuations are responsible for the NFL behavior. The critical point of such a phase transition can be shifted to $T = 0$ by varying the above control parameters.

Universal behavior can be expected only if the system under consideration is sufficiently close to a quantum critical point, e.g., when the correlation length is much larger than the microscopic length scale, so that critical quantum and thermal fluctuations determine the anomalous contribution to the thermodynamic functions of a substance. Quantum phase transitions of this type are so widespread [30–32, 36–40] that we call them ordinary quantum phase transitions [45]. In this case, the physics is determined by thermal and quantum fluctuations of the critical state, while quasiparticle excitations are destroyed by these fluctuations. Conventional arguments that quasiparticles in strongly correlated Fermiliquids “get heavy and die” at a quantum critical point commonly employ the well-known formula based on the assumptions that the z-factor (the quasiparticle weight in the single-particle state, see above) vanishes at the points of second-order phase transitions [44]. However, it has been shown that this scenario is problematic, see Chap. 3, Sect. 3.2 [46, 47].

The order parameter fluctuations, developing an infinite correlation range, and the vanishing of quasiparticle excitations are considered to be the main reason for the NFL behavior of heavy-fermion metals, 2D fermion systems and high-T_c superconductors [31, 32, 36, 39, 40, 48]. However, this approach faces certain difficulties. Critical behavior in HF metals is observed experimentally at high temperatures comparable to the effective Fermi temperature T_k. For instance, the thermal expansion coefficient $\alpha(T)$, which is a linear function of temperature for normal LFL, $\alpha(T) \propto T$, demonstrates the experimental $\sqrt{T}$ temperature dependence in $CeNi_2Ge_2$ as the temperature decreases from 6 K to at least 50 mK (i.e. varies by two orders of magnitude) [41]. Such behavior can hardly be explained within the framework of the above critical fluctuation theory. Obviously, such a situation is realizable only at a low-temperature regime, $T \to 0$, when the critical fluctuations make the leading contribution to the entropy and when the correlation length is much longer than the microscopic length scale. At a certain temperature T_k, this macroscopically large correlation length must be destroyed by ordinary thermal fluctuations and the corresponding universal behavior must disappear.

Another difficulty is in explaining the restoration of the LFL behavior under the application of magnetic field B, as observed in HF metals and in high-T_c superconductors [29, 41, 49]. At $T \to 0$ for the LFL state the following relations are valid for the electric resistivity $\rho(T) = \rho_0 + AT^2$, the heat capacity $C(T) = \gamma_0 T$, and the magnetic susceptibility $\chi = const$. It turns out that the coefficients in the above laws depend on the magnetic field strength B. Namely, $A = A(B)$, the Sommerfeld coefficient $\gamma_0(B) \propto M^*$, and the magnetic susceptibility $\chi = \chi(B)$. These quantities depend on B in such a way that $A(B) \propto \gamma_0^2(B)$ and $A(B) \propto \chi^2(B)$, which implies that the Kadowaki-Woods relation $K = A(B)/\gamma_0^2(B)$ [50] is B-independent and is preserved [41]. Such universal behavior, quite natural when quasiparticles with the effective mass M^* play the main role, can barely be explained within the framework that assumes the absence of quasiparticles or Kondo lattice. We emphasize here, that quasiparticles are absent in ordinary quantum phase transitions in the vicinity of QCP. Indeed, there is no reason to expect that γ_0, χ and A are affected by the fluctuations in a such a correlated fashion that preserves the Kadowaki-Woods ratio.

For instance, the Kadowaki-Woods relation does not agree with the spin density wave scenario [41] and with the results of research in quantum criticality based on the renormalization-group approach [51]. Moreover, measurements of charge and heat transfer have shown that the Wiedemann-Franz law holds in some high-T_c superconductors [49, 52] and HF metals [53–56]. All this suggests that quasiparticles do exist in such metals, and this conclusion is also corroborated by photoemission spectroscopy results [57, 58]. The inability to explain peculiarities of behavior of HF metals mentioned above in the framework of theories based on ordinary quantum phase transitions implies that another important concept introduced by Landau, the order parameter, also ceases to operate (see, e.g., [36, 38, 40, 44]). Thus, we are left without the most fundamental principles of many-body quantum physics [18, 19, 24], and many interesting phenomena associated with the NFL behavior of strongly correlated Fermi-systems remain unexplained.

NFL behavior manifests itself in the power-law behavior of the physical quantities of strongly correlated Fermi-systems located close to their QCPs, with exponents different from those of ordinary Fermi liquids [59, 60]. It is common belief that the main output of theory is the explanation of these exponents which are at least dependent on the magnetic character of QCP and dimensionality of the system. On the other hand, the NFL behavior cannot be captured by these exponents as seen from Fig. 1.2. Indeed, the specific heat C/T exhibits a behavior that is to be described as a function of both temperature T and magnetic B field rather than by a single exponent. One can see that at low temperatures C/T demonstrates the LFL behavior which is changed by the transition regime at which C/T reaches its maximum and finally

Fig. 1.2 Electronic specific heat of YbRh$_2$Si$_2$, C/T, versus temperature T as a function of magnetic field B [59] shown in the legend

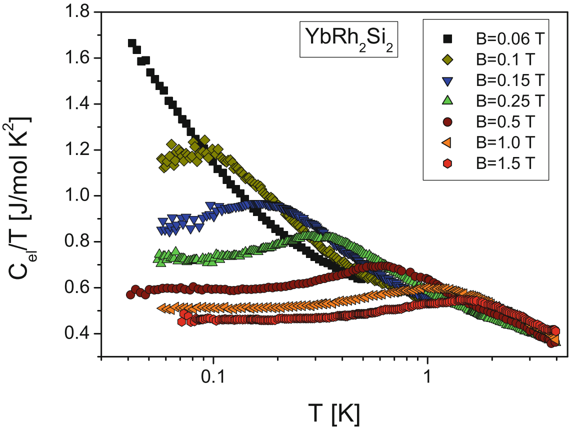

C/T decays into NFL behavior as a function of T at fixed B. It is clearly seen from Fig. 1.2 that, in particularly in the transition regime, these exponents may have little physical significance.

To show that the behavior of C/T reported in Fig. 1.2 is of generic character, we recollect that in the QCP vicinity it is helpful to use "internal" scales to measure the effective mass $M^* \propto C/T$ and temperature T [26–28, 61, 62]. As it is seen from Fig. 1.2, a maximum structure in $C/T \propto M^*_M$ at temperature T_M appears under the application of magnetic field B and T_M shifts to higher T as B is increased. The value of the Sommerfeld coefficient $C/T = \gamma_0$ is saturated towards lower temperatures decreasing at elevated magnetic field. To obtain the normalized effective mass M^*_N, we use M^*_M (maximal value of the effective mass) and T_M as above "internal" scales: The maximum value of C/T has been used to normalize C/T, and T was normalized by T_M. In Fig. 1.3 the obtained $M^*_N = M^*/M^*_M$ as a function of normalized

Fig. 1.3 The normalized effective mass M^*_N versus normalized temperature T_N. M^*_N is extracted from the measurements of the specific heat C/T on YbRh$_2$Si$_2$ in magnetic fields B [59] listed in the legend. Constant effective mass M^*_L inherent in normal Landau Fermi liquids is depicted by the *solid line*

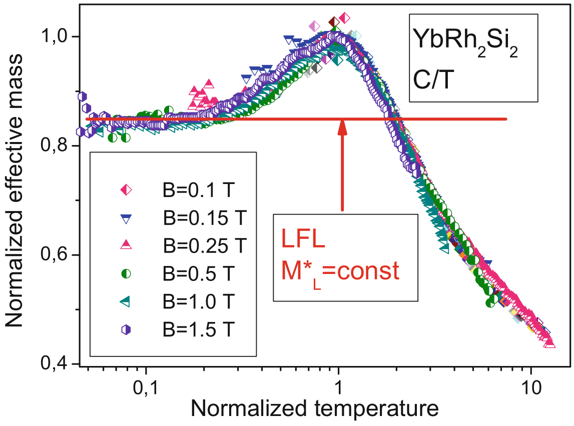

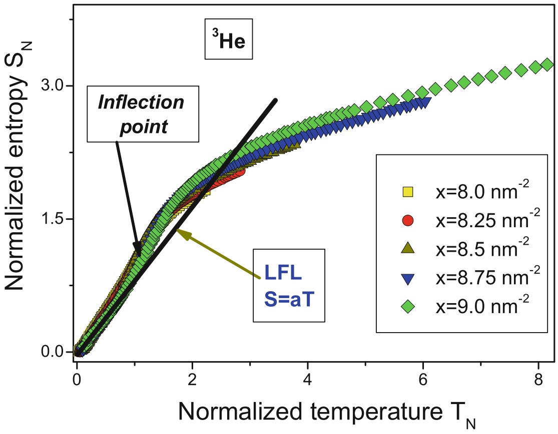

Fig. 1.4 The normalized entropy S_N versus normalized temperature T_N. S_N is extracted from the measurements of the entropy S on ^{3}He at different number densities x [63] shown in the legend. The behavior of the entropy $S \propto T$ inherent in normal Landau Fermi liquids is represented by the *solid line*

temperature $T_N = T/T_M$ is shown by symbols. Note that we have excluded the experimental data for magnetic field $B = 0.06$ T. In that case, as will be shown, $T_M \to 0$ and the corresponding T_M and M^*_M are unavailable. It is seen that the LFL and NFL states are separated by the transition (or crossover) regime (or region) where M^*_N reaches its maximal value. Figure 1.3 reveals the scaling behavior of the normalized experimental curves—the curves at different magnetic fields B merge into a single one in terms of the normalized variable $y = T/T_M$. As it is seen from Fig. 1.3, the normalized effective mass $M^*_N(y)$ extracted from the measurements is not a constant, as would be for LFL, and shows the scaling behavior over three decades in normalized temperature y. It is seen from Figs. 1.2 and 1.3 that the NFL behavior and the associated scaling extend at least to temperatures up to few Kelvins. Scenario, where order parameter fluctuations with infinite (or sufficiently large) correlation length and time develop the NFL behavior, can hardly occur at such high temperatures. We now briefly discuss how the scaling behavior of the normalized entropy, reported in Fig. 1.4 and revealing the quantum criticality observed in 2D ^{3}He [63]. This quantum criticality is extremely significant as it allows us to detect the scaling behavior in the 2D system formed by ^{3}He atoms which are essentially different from electrons. As we shall see, the dependence of some observable like the entropy, obviously, do not have "peculiar points" like maxima. The normalization is to be performed in the other points like the inflection point at $T = T_{inf}$ shown in Fig. 1.4 by the arrow, for details see Chap. 18 and Sect. 18.4. It is seen from Fig. 1.4 that the normalized experimental curves $S(T)$ taken at different values of the number densities x merge into single curve $S_N(T_N) = S(T/T_{inf})/S(T_{inf})$. The observed behavior of S_N strongly deviates from that of the LFL one, and cannot be described by a function $S_n(T_N) \simeq T_N^{\beta}$.

Thus, we conclude that the proper explanation of scaling behavior of both $M^*_N(y)$ and $S_N(y)$ shown in Figs. 1.3 and 1.4 is a challenge for theories of critical behavior of HF metals. While the existing theories are primarily dealing with calculations of so-called critical exponents β that characterize $M^*_N(y)$ and S_N at $y \gg 1$, they overlook the regime, signifying transition from LFL to NFL behavior, and are unable to explain both the LFL and scaling behavior, emerging under the application of magnetic field. As we mentioned above, this transition regime is indeed related to the quantum criticality of systems located near FCQPT. Another part of the problem is the remarkably large temperature ranges over which the NFL behavior is observed. Thus, we conclude that the influence of the critical point extends over a wide range in $T > 0$. This is the regime of quantum criticality, which is crucial for interpreting a wide variety of experiments. As we will see below, the above large temperature ranges are precursors of the quantum critical point related with FCQPT and the emergence of new quasiparticles. The latter fact, in turn, generates the scaling behavior of the normalized effective mass that allows to explain the thermodynamic, transport and relaxation properties of HF compounds at the LFL, transition and NFL regimes.

Taking into account the simple behavior shown in Figs. 1.3 and 1.4, we ask the question: what theoretical concepts can replace the Fermi-liquid paradigm with the notion of the effective mass in cases where the LFL theory breaks down? So far such a concept within the framework of ordinary quantum phase transitions approach is not available [26–28, 31]. Therefore, here in this book we focus on the FCQPT concept that preserves the notion of quasiparticles and is intimately related to the unlimited growth of the effective mass M^*. We shall show that this approach is capable to reveal the scaling behavior of the effective mass and to deliver an adequate theoretical explanation of a vast majority of experimental results collected on strongly correlated Fermi systems like HF metals, quasicrystals, quantum spin liquids, 2D fermi-systems, etc. As we shall see, all these HF compounds exhibit a universal scaling behavior at their quantum criticality, and constitute a new state of matter. Thus whichever mechanism drives the system to FCQPT, the system demonstrates the universal behavior, while there are lot of such mechanisms or tuning parameters like the pressure, number density, magnetic field, chemical doping, frustration and etc.

In contrast to the Landau paradigm based on the assumption that M^* is a constant as shown by the solid line in Fig. 1.3, in FCQPT approach the effective mass M^* of new quasiparticles depends strongly on T, x, B etc. Therefore, to explain numerous experimental data, the extended quasiparticles paradigm is to be introduced. The main point here is that the new well-defined quasiparticles (with M^* depending on external parameters) determine, as before, the thermodynamic, relaxation and transport properties of strongly correlated Fermi-systems in wide temperature range. The FCQPT approach had been already successfully applied to describe the thermodynamic properties of such different strongly correlated systems as ^{3}He on the one hand and complicated HF compounds and insulators with spin liquid on the other [26–28, 46, 64–67].

1.1.4 Limits and Goals of the Book

This monograph presents a theory of strongly correlated compounds, i.e. HF metals, high-T_c superconductors, substances with quantum spin liquids, quasicrystals, and 2D systems like ^{3}He. As we have seen above, this extremely wide diversity of strongly correlated fermion systems represents, or introduces a new state of matter, demonstrating in many cases the universal scaling behavior. Our aim is to show that diverse strongly correlated Fermi-systems such as 3D HF metals, 2D Fermi liquids, compounds with spin liquid and quasicrystals exhibit the quantum criticality, which can be described within a unified approach based on FCQPT theory [12, 25–28]. We discuss the construction of the theory and show that it is capable to explain the vast majority of experimental facts in strongly correlated Fermi-systems. Our analysis is in the context of salient experimental results. Our calculations of the non-Fermi liquid behavior, the scales and thermodynamic, relaxation and transport properties are in good agreement with experimental facts. We shall focus on the scaling behavior of the thermodynamic, transport and relaxation properties that can be revealed both from experimental facts and theoretical analysis. We do not discuss, however, the specific features of strongly correlated systems in full; instead, we focus on the universal behavior of such systems. We also do not discuss the physics of Fermi-systems, that are not related to condensed matter. Namely, these are neutron stars, atomic clusters and nuclei, quark plasma, and ultra-cold gases in traps, where, according to our views, the fermion condensate induced by FCQPT can also exist [68–73]. Ultra-cold gases in traps are interesting because their easy tuning allows selecting the values of the parameters required for observations of quantum critical point and FC. We also do not discuss the specific microscopic mechanisms of quantum criticality related to the emergence of FCQPT in a specific compound. Such mechanisms rely heavily on crystalline structure of a specific substance and development of these mechanisms seems not feasible in a near future. In contrast, we consider general mechanisms leading to the formation of flat bands, and analyze the common properties of strongly correlated Fermi-systems in close connection with accessible experimental facts. For example, the mechanism of quantum criticality, observed in f-electron materials, can take place in the systems when the centers of merged single-particle levels "get stuck" at the Fermi surface. One observes that this could provide a simple mechanism for pinning narrow bands in solids to the Fermi surface [73]. Also, we consider high-T_c superconductors within a coarse-grained model based on the FCQPT theory just to illuminate their generic relationships with HF metals. When studying quasicrystals, quantum spin liquids and 2D systems, we propose the corresponding mechanisms as well. To stress the ubiquitous features of FCQPT, in Chap. 16 we consider its possible role in the emergence of the Universe.

Experimental studies of the properties of quantum phase transitions and their quantum critical points are very important for understanding the physical nature of strongly correlated Fermi-systems. The experimental data, gathered on different strongly correlated Fermi-systems, complement each other. In the case of high-T_c superconductors, only few experiments dealing with their QCPs have been conducted. This is because the corresponding QCPs are in the superconductivity range at low temperatures and the physical properties of the respective quantum phase transition are altered by the superconductivity. As a result, high magnetic fields are needed to destroy the superconducting state. Such experiments can be conducted for HF metals. Experimental research provides data for HF metals behavior, shedding light on the nature of their critical points and phase transitions [41, 49, 52, 54].

Hence, a complete understanding of unusual physical properties related to NFL behavior, can be achieved on the base of simultaneous and comparative experimental studies of high-T_c superconductors, HF metals and other correlated Fermi-systems [55, 57, 58].

Since we are concentrated on the properties that are non-sensitive to the detailed crystalline structure of the system, we avoid difficulties associated with the anisotropy generated by the crystal lattice of solids, its special features, defects, etc., We study the universal behavior of high-T_c superconductors, HF metals, quasicrystals, quantum spin liquids, and 2D Fermi-systems at low temperatures using the model of a homogeneous HF liquid [26–28, 61, 62]. The model is quite meaningful as we consider the low-temperature scaling behavior of these compounds. This behavior is closely related to the scaling of quantities like effective mass, heat capacity, thermal expansion coefficient, etc. The aforementioned scaling is determined, primarily, by long wave length properties of corresponding compound. In other words, they are dealing with transfers of momenta with wave vectors, that are small compared to those of the reciprocal lattice constant. The high momentum contributions can therefore be ignored by substituting the lattice for the jelly model.

We analyze the universal properties of HF compounds systems using the FCQPT theory [12, 25–28, 74], because the behavior of HF metals already suggests that their unusual properties can be associated with the QPT related to the infinite increase in the effective mass at the critical point. Moreover, we shall see that both the scaling behavior and the quantum criticality displayed in Figs. 1.3 and 1.4 can be quite naturally captured within the framework of the above FCQPT related extended quasiparticle paradigm, which gives explanations of the NFL behavior observed in wide range of HF compounds.

References

1. E. Schrödinger, Naturwissenschaften **14**, 664 (1926)
2. D.R. Hartree, Math. Proc. Cambridge Philos. Soc. **24**, 89 (1928)
3. D.R. Hartree, Math. Proc. Cambridge Philos. Soc. **24**, 111 (1928)
4. V.A. Fock, Z. Phys. **61**, 126 (1930)
5. V.A. Fock, Z. Phys. **62**, 795 (1930)
6. L.N. Thomas, Proc. Cambridge Philos. Soc. **23**, 542 (1927)
7. E. Fermi, Rend. Accad. Lincei **6**, 602 (1927)
8. P. Hohenberg, W. Kohn, Phys. Rev. **136**, B864 (1964)
9. W. Kohn, L.J. Sham, Phys. Rev. **140**, A1133 (1965)
10. H. Eschrig, *Fundamentals of Density Functional Theory* (Teubner, Stuttgart, 1996)
11. W. Kohn, Rev. Mod. Phys. **71**, 1253 (1999)
12. V.A. Khodel, V.R. Shaginyan, V.V. Khodel, Phys. Rep. **249**, 1 (1994)
13. R. Jones, O. Gunnarson, Rev. Mod. Phys. **61**, 689 (1989)
14. J. Hubbard, Proc. Roy. Soc. Lond. **276**, 238 (1963)
15. W. Metzner, D. Vollhardt, Phys. Rev. Lett. **62**, 324 (1989)
16. A. Georges, G. Kotliar, Phys. Rev. B **45**, 6479 (1992)
17. M. Jarrell, Phys. Rev. Lett. **69**, 168 (1992)
18. L.D. Landau, Zh Eksp, Teor. Fiz. **30**, 1058 (1956)

19. E.M. Lifshitz, L.P. Pitaevskii, Statisticheskaya Fizika (Statistical Physics), part 2, in *Course of Theoretical Physics* (Moscow, Nauka, 1978)
20. A.B. Migdal, Sov. Phys. JETP. **5**, 333 (1957)
21. A.A. Abrikosov, L.P. Gorkov, I.E. Dzyaloshinski, *Methods of Quantum Field Theory in Statistical Physics* (Dover, New York, 1975)
22. I.Y. Pomeranchuk, Zh Eksp, Teor. Fiz. **35**, 524 (1958)
23. M.Y. Amusia, V.E. Starodubsky, Phys. Lett. A **35**, 115 (1971)
24. D. Pines, P. Noziéres, *Theory of Quantum Liquids* (Benjamin, New York, 1966)
25. V.A. Khodel, V.R. Shaginyan, JETP Lett. **51**, 553 (1990)
26. V.R. Shaginyan, M.Y. Amusia, K.G. Popov, Phys. Usp. **50**, 563 (2007)
27. V.R. Shaginyan, M.Y. Amusia, K.G. Popov, Usp. Fiz. Nauk **177**, 586 (2007)
28. V.R. Shaginyan, M.Y. Amusia, A.Z. Msezane, K.G. Popov, Phys. Rep. **492**, 31 (2010)
29. G.R. Stewart, Rev. Mod. Phys. **73**, 797 (2001)
30. C.M. Varma, Z. Nussionov, W. van Saarloos, Phys. Rep. **361**, 267 (2002)
31. H.v Löhneysen, A. Rosch, M. Vojta, P. Wölfle, Rev. Mod. Phys. **79**, 1015 (2007)
32. M. Vojta, Rep. Prog. Phys. **66**, 2069 (2003)
33. V.I. Belyavsky, Y.V. Kopaev, Phys. Usp. **49**, 441 (2006)
34. J. Custers, P. Gegenwart, H. Wilhelm, K. Neumaier, Y. Tokiwa, O. Trovarelli, C. Geibel, F. Steglich, C. Pépin, P. Coleman, Nature **424**, 524 (2003)
35. T. Senthil, M.P.A. Fisher, Phys. Rev. B **62**, 7850 (2000)
36. T. Senthil, M. Vojta, S. Sachdev, Phys. Rev. B **69**, 035111 (2004)
37. T. Senthil, S. Sachdev, M. Vojta, Physica B **359–361**, 9 (2005)
38. T. Senthil, A. Vishwanath, L. Balents, S. Sachdev, M.P.A. Fisher, Science **303**, 1490 (2004)
39. P. Coleman, in *Lectures on the Physics of Highly Correlated Electron Systems VI*, ed. by F. Mancini (American Institute of Physics, New York, 2002), p. 79
40. P. Coleman, A.J. Schofield, Nature **433**, 226 (2005)
41. R. Kúchler, N. Oeschler, P. Gegenwart, T. Cichorek, K. Neumaier, O. Tegus, C. Geibel, J.A. Mydosh, F. Steglich, L. Zhu, Q. Si, Phys. Rev. Lett. **91**, 066405 (2003)
42. N.E. Hussey, Nat. Phys. **3**, 445 (2007)
43. P. Gegenwart, T. Westerkamp, C. Krellner, Y. Tokiwa, S. Paschen, C. Geibel, F. Steglich, E. Abrahams, Q. Si, Science **315**, 969 (2007)
44. P. Coleman, C. Pépin, Q. Si, R. Ramazashvili, J. Phys. Condens. Matter **13**, R723 (2001)
45. V.R. Shaginyan, J.G. Han, J. Lee, Phys. Lett. A **329**, 108 (2004)
46. V.A. Khodel, J.W. Clark, M.V. Zverev, Phys. Rev. B **78**, 075120 (2008)
47. V.A. Khodel, JETP Lett. **86**, 721 (2007)
48. P. Coleman, **1**, 1 (2010). arXiv:1001.0185v1
49. C. Proust, E. Boaknin, R.W. Hill, L. Taillefer, A.P. Mackenzie, Phys. Rev. Lett. **89**, 147003 (2002)
50. K. Kadowaki, S.B. Woods, Solid State Commun. **58**, 507 (1986)
51. A.J. Millis, A.J. Schofield, G.G. Lonzarich, S.A. Grigera, Phys. Rev. Lett. **88**, 217204 (2002)
52. R. Bel, K. Behnia, Y. Nakajima, K. Izawa, Y. Matsuda, H. Shishido, R. Settai, Y. Onuki, Phys. Rev. Lett. **92**, 217002 (2004)
53. J. Paglione, M. Tanatar, D. Hawthorn, E. Boaknin, R.W. Hill, F. Ronning, M. Sutherland, L. Taillefer, C. Petrovic, P. Canfield, Phys. Rev. Lett. **91**, 246405 (2003)
54. J. Paglione, M.A. Tanatar, D.G. Hawthorn, F. Ronning, R.W. Hill, M. Sutherland, L. Taillefer, C. Petrovic, Phys. Rev. Lett. **97**, 106606 (2006)
55. F. Ronning, R.W. Hill, M. Sutherland, D.G. Hawthorn, M.A. Tanatar, J. Paglione, L. Taillefer, M.J. Graf, R.S. Perry, Y. Maeno, A.P. Mackenzie, Phys. Rev. Lett. **97**, 067005 (2006)
56. F. Ronning, C. Capan, E.D. Bauer, J.D. Thompson, J.L. Sarrao, R. Movshovich, Phys. Rev. B **73**, 064519 (2006)
57. J.D. Koralek, J.F. Douglas, N.C. Plumb, Z. Sun, A.V. Fedorov, M.M. Murnane, H.C. Kapteyn, S.T. Cundiff, Y. Aiura, K. Oka, H. Eisaki, D.S. Dessau, Phys. Rev. Lett. **96**, 017005 (2006)
58. S. Fujimori, A. Fujimori, K. Shimada, T. Narimura, K. Kobayashi, H. Namatame, M. Taniguchi, H. Harima, H. Shishido, S. Ikeda, D. Aoki, Y. Tokiwa, Y. Haga, Y. Onuki, Phys. Rev. B **73**, 224517 (2006)

59. N. Oeschler, S. Hartmann, A. Pikul, C. Krellner, C. Geibel, F. Steglich, Physica B **403**, 1254 (2008)
60. P. Gegenwart, T. Westerkamp, C. Krellner, M. Brando, Y. Tokiwa, C. Geibel, F. Steglich, Physica B **403**, 1184 (2008)
61. V.R. Shaginyan, M.Y. Amusia, K.G. Popov, Phys. Lett. A **373**, 2281 (2009)
62. V.R. Shaginyan, M.Y. Amusia, K.G. Popov, S.A. Artamonov, JETP Lett. **90**, 47 (2009)
63. M. Neumann, J. Nyéki, B. Cowan, J. Saunders, Science **317**, 1356 (2007)
64. V.R. Shaginyan, A.Z. Msezane, K.G. Popov, V.A. Stephanovich, Phys. Rev. Lett. **100**, 096406 (2008)
65. V.R. Shaginyan, A.Z. Msezane, K.G. Popov, Phys. Rev. B **84**, 060401(R) (2011)
66. V.R. Shaginyan, A.Z. Msezane, K.G. Popov, G.S. Japaridze, V.A. Stephanovich, Europhys. Lett. **97**, 56001 (2012)
67. V.R. Shaginyan, A.Z. Msezane, K.G. Popov, V.A. Khodel, Phys. Lett. A **376**, 2622 (2012)
68. V.A. Khodel, J.W. Clark, M.V. Zverev, Phys. Rev. Lett. **87**, 031103 (2001)
69. M.Y. Amusia, A.Z. Msezane, V.R. Shaginyan, Phys. At. Nuclei **66**, 1850 (2003)
70. V.A. Khodel, J.W. Clark, L. Hoachen, M.A. Zverev, Pisma v ZHETF **84**, 703 (2006)
71. G.E. Volovik, Acta Phys. Slov. **56**, 49 (2006)
72. G.E. Volovik, in Quantum Analogues: From Phase Transitions to Black Holes and Cosmology, ed. by W.G. Unruh, R. Schutzhold, *Springer Lecture Notes in Physics*, vol. 718 (Springer, Orlando, 2007), p. 31
73. V.A. Khodel, J.W. Clark, H. Li, M.V. Zverev, Phys. Rev. Lett. **98**, 216404 (2007)
74. V.R. Shaginyan, JETP Lett. **79**, 286 (2004)

Chapter 2
Landau Fermi Liquid Theory and Beyond

Abstract In this chapter we consider the Landau theory of the Fermi liquid that has a long history and remarkable results in describing a numerous properties of the electron liquid in ordinary metals and Fermi liquids of the ^{3}He type. The theory is based on the assumption that elementary excitations determine the physics at low temperatures, resembling that of weakly interacting Fermi gas. These excitations behave as quasiparticles with a certain effective mass. The effective mass M^* exhibits a simple universal behavior, for it is independent of the temperature, pressure, and magnetic field strength and is a parameter of the theory. Microscopically deriving the equation determining the effective mass, we go beyond Landau approach and analyze more complicated universal behavior of M^* at the fermion condensation quantum phase transition.

2.1 Quasiparticle Paradigm

One of the most complex problems of modern condensed matter physics is the problem of the structure and properties of Fermi systems with strong interparticle interaction. The first consistent theory of above systems had been proposed by Landau. The main idea of Landau theory of Fermi liquids, later called “normal”, was to describe the strongly interacting multi-fermion system in terms of some ground state and its elementary excitations, which, being quantized, generate so-called Landau quasiparticles. Contrary to ordinary particles in a Fermi liquid, which are strongly interacting fermions, the quasiparticles are fictitious particles which are indeed the quanta of above elementary excitations. In such a picture, the real physical interaction between fermions (which in general case is unknown) is substituted by some effective phenomenological interaction between quasiparticles, formulated in terms of so-called Landau interaction (or amplitudes). This paradigm permits to reduce the problem formally to the weakly-interacting Fermi gas, and introduces the effective interaction between quasiparticles [1–3]. The Landau approach can be regarded as an effective low-energy theory with the high-energy degrees of freedom being eliminated by introducing the above quasiparticle interaction, which substitute the strong interaction between real particles. The invariability of the ground state of the

M.Y. Amusia et al., *Theory of Heavy-Fermion Compounds*, Springer Series
in Solid-State Sciences 182, DOI 10.1007/978-3-319-10825-4_2

Landau Fermi liquid (LFL) is determined by the Pomeranchuk stability conditions: A system becomes unstable when at least one Landau interaction becomes negative and reaches its critical value [2–4]. We note that the new phase, in which stability is restored can also be described, in principle, by the LFL theory.

To make the presentation self-contained, here we briefly recapitulate the main ideas of the LFL theory [1–3, 5]. The theory is based on the quasiparticle paradigm, which states that quasiparticles are elementary weakly excited states of Fermi liquids and are therefore specific excitations determining their low-temperature thermodynamic and transport properties. In the case of the electron liquid, the quasiparticles are characterized by the electron quantum numbers and the effective mass M^*. The ground state energy of the system is a functional of the quasiparticle occupation numbers (or the quasiparticle distribution function) $n(\mathbf{p}, T)$, and the same is true for the free energy $F(n(\mathbf{p}, T))$, the entropy $S(n(\mathbf{p}, T))$, and other thermodynamic functions. We can find the distribution function from the minimum condition for the free energy $F = E - TS$ (hereafter we use atomic units, where $k_B = \hbar = 1$)

$$\frac{\delta(F - \mu N)}{\delta n(\mathbf{p}, T)} = \varepsilon(\mathbf{p}, T) - \mu(T) - T \ln \frac{1 - n(\mathbf{p}, T)}{n(\mathbf{p}, T)} = 0. \tag{2.1}$$

Here μ is the chemical potential fixing the number density x:

$$x = \int n(\mathbf{p}, T) \frac{d\mathbf{p}}{(2\pi)^3} \tag{2.2}$$

and

$$\varepsilon(\mathbf{p}, T) \; = \; \frac{\delta E(n(\mathbf{p}, T))}{\delta n(\mathbf{p}, T)} \tag{2.3}$$

is the quasiparticle energy. The quasiparticle energy, similar to the energy E, is a functional of $n(\mathbf{p}, T)$: $\varepsilon = \varepsilon(\mathbf{p}, T, n)$. The entropy $S(n(\mathbf{p}, T))$ related to quasiparticles is given by the well-known expression [1–3]

$$\begin{aligned} S(n(\mathbf{p}, T)) = -2 \int \Big[& n(\mathbf{p}, T) \ln(n(\mathbf{p}, T)) + (1 - n(\mathbf{p}, T)) \\ & \times \ln(1 - n(\mathbf{p}, T)) \Big] \frac{d\mathbf{p}}{(2\pi)^3}, \end{aligned} \tag{2.4}$$

which follows from combinatorial reasoning. Equation (2.1) is usually written in the standard form of the Fermi-Dirac distribution,

$$n(\mathbf{p}, T) = \left\{ 1 + \exp\left[\frac{(\varepsilon(\mathbf{p}, T) - \mu)}{T} \right] \right\}^{-1}. \tag{2.5}$$

At $T \to 0$, (2.1) and (2.5) reduce to $n(p, T \to 0) \to \theta(p_F - p)$ if the derivative $\partial\varepsilon(p \simeq p_F)/\partial p$ is finite and positive. Here p_F is the Fermi momentum and $\theta(p_F - p)$ is the unit step function. The single particle energy can be approximated as $\varepsilon(p \simeq p_F) - \mu \simeq p_F(p - p_F)/M_L^*$, where M_L^* is the effective mass of the Landau quasiparticle,

$$\frac{1}{M_L^*} = \frac{1}{p}\frac{d\varepsilon(p, T = 0)}{dp}|_{p=p_F}. \tag{2.6}$$

In turn, the effective mass M_L^* is related to the bare electron mass m by the well-known Landau equation [1–3, 5]

$$\frac{1}{M_L^*} = \frac{1}{m} + \sum_{\sigma_1}\int \frac{\mathbf{p}_F\mathbf{p}_1}{p_F^3} F_{\sigma,\sigma_1}(\mathbf{p_F}, \mathbf{p}_1) \times \frac{\partial n_{\sigma_1}(\mathbf{p}_1, T)}{\partial p_1}\frac{d\mathbf{p}_1}{(2\pi)^3}. \tag{2.7}$$

where $F_{\sigma,\sigma_1}(\mathbf{p_F}, \mathbf{p}_1)$ is the Landau interaction, which depends on the momenta $\mathbf{p_F}$ and $\mathbf{p}$ and spin indices σ, σ_1. For simplicity, we suppress the spin indices in the effective mass as M_L^* is almost completely spin-independent in the case of a homogeneous liquid and weak magnetic fields. The Landau interaction F is given by

$$F_{\sigma,\sigma_1}(\mathbf{p}, \mathbf{p}_1, n) = \frac{\delta^2 E(n)}{\delta n_\sigma(\mathbf{p})\delta n_{\sigma_1}(\mathbf{p}_1)}. \tag{2.8}$$

2.2 Pomeranchuk Stability Conditions

The stability of the ground state of LFL is determined by the Pomeranchuk stability conditions: The considered system becomes unstable when at least one harmonic of Landau interaction becomes negative and reaches its critical value [2–5]

$$F_L^{a,s} = -(2L + 1). \tag{2.9}$$

Here F_L^a and F_L^s are the dimensionless spin-symmetric and spin-antisymmetric Landau interactions, L is the angular momentum related to the corresponding Legendre polynomials P_L,

$$F_{\sigma,\sigma_1}(\mathbf{p}, \mathbf{p}_1) = \frac{1}{N}\sum_{L=0}^{\infty} P_L(\Theta)\left[F_{L\ \sigma,\sigma_1}^a + F_L^s\right]. \tag{2.10}$$

Here Θ is the angle between momenta $\mathbf{p}$, and the dimensionless Landau interaction reads

$$F_{\sigma,\sigma_1}(\mathbf{p},\mathbf{p}_1) = NF_{\sigma,\sigma_1}(\mathbf{p},\mathbf{p}_1,n), \tag{2.11}$$

where the density of states $N = M^*_L p_F/(2\pi^2)$ and the Landau interaction F_{σ,σ_1} $(\mathbf{p},\mathbf{p}_1,n)$ is given by (2.8). It follows from (2.7) that

$$\frac{M^*_L}{m} = 1 + \frac{F^s_1}{3}. \tag{2.12}$$

In accordance with the Pomeranchuk stability conditions it is seen from (2.12) that $F^s_1 > -3$, otherwise the effective mass becomes negative leading to unstable state when it is energetically favorable to excite quasiparticles near the Fermi surface. Below we again suppress the spin indices σ for simplicity.

2.3 Thermodynamic and Transport Properties

To deal with the transport properties of Fermi systems, one needs a transport equation describing slowly varying disturbances of the quasiparticle distribution function $n_{\mathbf{p}}(\mathbf{r},t)$ which depends on position $\mathbf{r}$ and time t. As long as the transferred energy ω and momentum q of the external field quanta are much smaller than the energy and momentum of the quasiparticles, $qp_F/(TM^*_L) \ll 1$, the quasiparticle distribution function $n(\mathbf{q},\omega)$ satisfies the transport equation [1–3, 5]

$$\frac{\partial n_{\mathbf{p}}}{\partial t} + \nabla_{\mathbf{p}}\varepsilon_{\mathbf{p}}\nabla_{\mathbf{r}}n_{\mathbf{p}} - \nabla_{\mathbf{r}}\varepsilon_{\mathbf{p}}\nabla_{\mathbf{p}}n_{\mathbf{p}} = I[n_{\mathbf{p}}]. \tag{2.13}$$

The left-hand side of (2.13) describes the dissipationless dynamic of quasiparticles in phase space. The quasiparticle energy $\varepsilon_{\mathbf{p}}(\mathbf{r},t)$ now depends on its position and time, and the collision integral $I[n_{\mathbf{p}}]$ measures the rate of the distribution function variation due to collisions. The transport equation (2.13) allows one to calculate all the transport properties of a Fermi-system. It should be emphasized here the role of Umklapp processes discussed in Sect. 10.2. In particulary, these processes lead to a nonzero contribution of FC to ρ_0, and is associated with the presence of the crystal lattice, more precisely, with the Umklapp processes, violating momentum conservation [6]. We assume the presence of Umklapp processes in all cases when the violation of momentum conservation is of importance.

It is common belief that the equations of this subsection are phenomenological and inapplicable to describe Fermi systems where the effective mass M^* depends strongly on temperature T, external magnetic fields B, pressure P etc. At the same time, many experimental data collected for HF metals reveal that the quasiparticle effective mass strongly depends on T, B and doping (or the number density) x. Moreover, in those cases the effective mass M^* can reach very high values or even diverge. As we have seen in Sect. 1.1, such a behavior is so unusual that the traditional Landau quasiparticles paradigm fails to describe it. Therefore, to reconcile the

Landau quasiparticle picture with the experimental situation in the real substances, the extended quasiparticles paradigm is to be introduced with still well-defined quasiparticles determining as before the thermodynamic and transport properties of strongly correlated Fermi-systems. In this paradigm, the effective mass M^* becomes a function of T, x, B so that just this dependence gives rise to the experimentally observed NFL behavior [7–13]. As we shall see in the following Sect. 2.3.1, the extended quasiparticle paradigm permits to derive (2.7) microscopically.

2.3.1 Equation for the Effective Mass and the Scaling Behavior

To derive the equation determining the effective mass, we consider the model of a homogeneous HF liquid and employ the density functional theory for superconductors (SCDFT) [14] which allows us to consider E as a functional of the occupations numbers $n(\mathbf{p})$ [10, 15–17]. As a result, the ground state energy E of the normal state becomes the functional of the occupation numbers and the function of the number density x, $E = E(n(\mathbf{p}), x)$, while (2.3) gives the single-particle spectrum. Upon differentiating both sides of (2.3) with respect to $\mathbf{p}$ and after some algebra involving integration by parts, we obtain [9, 10, 15, 16]

$$\frac{\partial\varepsilon(\mathbf{p})}{\partial\mathbf{p}} = \frac{\mathbf{p}}{m} + \int F(\mathbf{p}, \mathbf{p}_1, n)\frac{\partial n(\mathbf{p}_1)}{\partial\mathbf{p}_1}\frac{d\mathbf{p}_1}{(2\pi)^3}. \tag{2.14}$$

To calculate the derivative $\partial\varepsilon(\mathbf{p})/\partial\mathbf{p}$, we employ the functional representation

$$\begin{aligned} E(n) = &\int \frac{p^2}{2m} n(\mathbf{p}) \frac{d\mathbf{p}}{(2\pi)^3} \\ &+ \frac{1}{2}\int F(\mathbf{p}, \mathbf{p}_1, n)_{|n=0}\, n(\mathbf{p})n(\mathbf{p}_1)\frac{d\mathbf{p}d\mathbf{p}_1}{(2\pi)^6} + \cdots \end{aligned} \tag{2.15}$$

It is seen directly from (2.14) that the effective mass is given by the well-known Landau equation

$$\frac{1}{M^*} = \frac{1}{m} + \int \frac{\mathbf{p}_F\mathbf{p}_1}{p_F^3} F(\mathbf{p}_\mathrm{F}, \mathbf{p}_1, n)\frac{\partial n(p_1)}{\partial p_1}\frac{d\mathbf{p}_1}{(2\pi)^3}. \tag{2.16}$$

Here we suppress the spin indices for simplicity. To calculate M^* as a function of T, we construct the free energy $F = E - TS$, where the entropy S is given by (2.4). Minimizing F with respect to $n(\mathbf{p})$, we arrive at the Fermi-Dirac distribution, (2.5). The above derivation shows that (2.14) and (2.16) are exact and allow to calculate the behavior of both $\partial\varepsilon(\mathbf{p})/\partial\mathbf{p}$ and M^* which now is a function of temperature T, external magnetic field B, number density x and pressure P rather than a constant.

As we shall see, it is just this feature of M^* that forms both the scaling and the NFL behavior observed in measurements on HF metals.

It is assumed in LFL theory that M^*_L is positive, finite and independent of external factors like field and/or temperature. As a result, the temperature-dependent corrections to M^*_L, the quasiparticle energy $\varepsilon(\mathbf{p})$ and other quantities begin with the term proportional to T^2 in 3D systems. In this case, the effective mass is given by (2.16), and the specific heat C is as follows [1]

$$C = \frac{2\pi^2 NT}{3} = \gamma_0 T = T\frac{\partial S}{\partial T}, \tag{2.17}$$

and the spin susceptibility

$$\chi = \frac{3\gamma_0\mu_B^2}{\pi^2(1+F_0^a)}, \tag{2.18}$$

where μ_B is the Bohr magneton and $\gamma_0 \propto M^*_L$. In the LFL case, upon using the transport (2.13) one finds for the electrical resistivity at low T [5]

$$\rho(T) = \rho_0 + AT^{\alpha_R}, \tag{2.19}$$

where ρ_0 is the residual resistivity, the exponent $\alpha_R = 2$ and $A \propto (M^*)^2$ is the coefficient determining the charge transport. This coefficient is proportional to the quasiparticle-quasiparticle scattering cross-section. Equation (2.19) symbolizes and defines the LFL behavior observed in normal metals.

Due to the normalization condition used in (2.11), (2.12) defines the implicit dependence of the effective mass M^* on the Landau interaction. Taking into account (2.12) and introducing the density of states of a free Fermi gas, $N_0 = mp_F/(2\pi^2)$, we obtain the effective mass M^* as an explicit function of the Landau interaction and the bare mass m [18–20]

$$\frac{M^*}{m} = \frac{1}{1 - F^1/3}, \tag{2.20}$$

where $F^1 = N_0 f^1$, and $f^1(p_F, p_F)$ is the p-wave component of the Landau interaction. Since $x = p_F^3/3\pi^2$ in the LFL theory, the Landau interaction can be written as $F^1(p_F, p_F) = F^1(x)$. Provided that at a certain critical point x_{FC}, the denominator $(1 - F^1(x)/3)$ tends to zero, i.e. $(1 - F^1(x)/3) \propto (x - x_{FC}) + a(x - x_{FC})^2 + \cdots \to 0$, we find that [21, 22]

$$\frac{M^*(x)}{m} \simeq a_1 + \frac{a_2}{x - x_{FC}} \propto \frac{1}{r}, \tag{2.21}$$

where a_1 and a_2 are constants and $r = (x - x_{FC})/x_{FC}$ is the "distance" from QCP x_{FC} where $M^*(x \to x_{FC}) \to \infty$. We note that the divergence of the effective mass given by (2.21) does preserve the Pomeranchuk stability conditions for $F^1 > -1$, see (2.9). As it was discussed above, (2.21) represents the explicit formula for the effective mass, for $F^1 \propto m$, while $F_1^s \propto M^*$ and (2.12) represents an implicit formula for the effective mass.

The behavior of $M^*(x)$ described by formula (2.21) is in good agreement with the results of experiments [23–27] and calculations [28, 29]. In the case of electron systems, (2.21) holds for $x > x_{FC}$, while for 2D ^{3}He we have $x < x_{FC}$ so that always $r > 0$. Such behavior of the effective mass is observed in HF metals, which have a fairly flat and narrow conduction band corresponding to a large effective mass, with a strong correlation and the effective Fermi temperature $T_k \sim p_F^2/M^*(x)$ of the order of several dozen kelvins or even lower [30].

The effective mass as a function of the electron density x in a silicon MOSFET (Metal Oxide Semiconductor Field Effect Transistor), approximated by (2.21), is shown in Fig. 2.1. The constants a_1, a_2 and x_{FC} are taken as fitting parameters. We see that (2.21) provides a good description of the experimental results.

The divergence of the effective mass $M^*(x)$ discovered in measurements involving 2D ^{3}He [26, 27] is illustrated in Fig. 2.2. Figures 2.1 and 2.2 shows that the description provided by (2.21) does not depend on the nature of constituting fermions and is in good agreement with the experimental data.

To illustrate the ability of the extended quasiparticle paradigm to capture the observed scaling behavior of M^*, it is instructive to explore it briefly here, while more detailed consideration is reserved for Chap. 6. For that, we write the quasiparticle distribution function as $n_1(\mathbf{p}) = n(\mathbf{p}, T) - n(\mathbf{p})$, with $n(\mathbf{p})$ being the step function, and (2.16) then becomes

$$\frac{1}{M^*(T)} = \frac{1}{M^*} + \int \frac{\mathbf{p}_F\mathbf{p_1}}{p_F^3} F(\mathbf{p_F}, \mathbf{p}_1) \frac{\partial n_1(p_1, T)}{\partial p_1} \frac{d\mathbf{p}_1}{(2\pi)^3}. \tag{2.22}$$

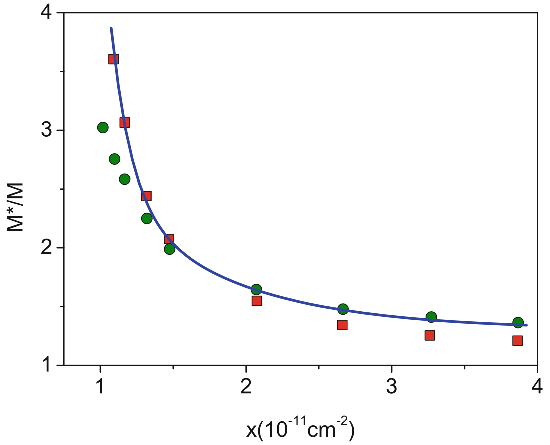

Fig. 2.1 The ratio M^*/M in a silicon MOSFET as a function of the electron number density x. The *squares* mark the experimental data on the Shubnikov-de Haas oscillations. The data obtained by applying a parallel magnetic field are marked by *circles* [23–25]. The *solid line* represents the function (2.21)

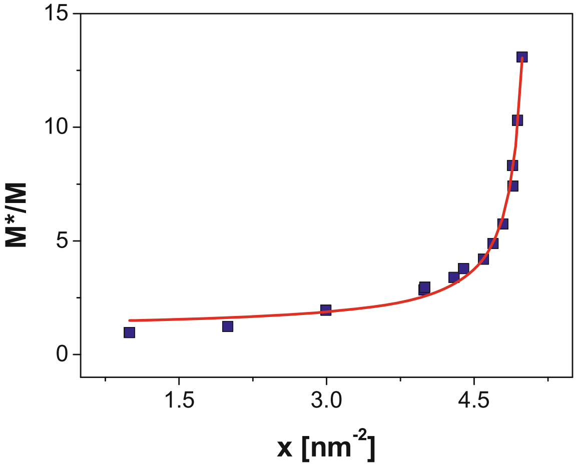

Fig. 2.2 The ratio M^*/M in 2D ^{3}He as a function of the density x of the liquid, obtained from heat capacity and magnetization measurements. The experimental data are marked by *black squares* [26, 27], and the *solid line* represents the function given by (2.21), where $a_1 = 1.09$, $a_2 = 1.68\,\mathrm{nm}^{-2}$, and $x_{FC} = 5.11\,\mathrm{nm}^{-2}$

At QCP $x \to x_{FC}$, the effective mass $M^*(x)$ diverges and (2.22) becomes homogeneous determining M^* as a function of temperature while the system exhibits the NFL behavior. If the system is located before QCP, M^* is finite so that at low temperatures the integral on the right hand side of (2.22) represents a small correction to $1/M^*$ and the system demonstrates the LFL behavior seen in Figs. 1.2 and 1.3. The LFL behavior assumes that the effective mass is independent of temperature, $M^*(T) \simeq const$, as shown by the horizontal line in Fig. 1.3. Obviously, the LFL behavior takes place only if the second term on the right hand side of (2.22) is small in comparison with the first one. In the case of common metals the effective mass $M^* \sim m$ and the Fermi energy is $E_F \sim 1$ eV. Then, the integral I on the right hand side of (2.22) satisfies the condition $M^*I \ll 1$ even at room temperatures. As a result, $M^*(T) \simeq M^*(T = 0)$. As soon as the effective mass $M^*(x)$ diverges, as it is shown in Fig. 2.2 the condition $M^*I \ll 1$ ceases to be valid at some temperature $T \sim T_M$. Thus, at temperatures $T \sim T_M$ the system enters the transition regime: M^* grows, reaching its maximum M^*_M at $T = T_M$, with subsequent diminishing. As seen from Fig. 1.3, near temperatures $T \geq T_M$ the last "traces" of LFL regime disappear, the second term in (2.22) starts to dominate, and again this equation becomes homogeneous so that the NFL behavior is restored, manifesting itself in decreasing M^* as a function of T. As we shall see below, the above solution of (2.22) generates the scaling behavior of the effective mass, resulting in the experimentally observed universal (i.e. independent on microscopic structure of specific substance) properties of HF compounds at their quantum criticality.

References

1. L.D. Landau, Zh Eksp, Teor. Fiz. **30**, 1058 (1956)
2. E.M. Lifshitz, L.P. Pitaevskii, *Statisticheskaya Fizika (Statistical Physics), part 2*. Course of Theoretical Physics (Nauka, Moscow, 1978)
3. E.M. Lifshitz, L.P. Pitaevskii, *Statisticheskaya Fizika (Statistical Physics), part 2*. Course of Theoretical Physics (Pergamon Press, Oxford, 1980)
4. I.Y. Pomeranchuk, Zh Eksp, Teor. Fiz. **35**, 524 (1958)
5. D. Pines, P. Noziéres, *Theory of Quantum Liquids* (Benjamin, New York, Amsterdam, 1966)
6. E.M. Lifshitz, L.P. Pitaevskii, *Physical Kinetics* (Pergamon Press, Oxford, 1981)
7. V.R. Shaginyan, M.Y. Amusia, K.G. Popov, Phys. Usp. **50**, 563 (2007)
8. V.R. Shaginyan, M.Y. Amusia, A.Z. Msezane, K.G. Popov, Phys. Rep. **492**, 31 (2010)
9. V.A. Khodel, J.W. Clark, M.V. Zverev, Phys. Rev. B **78**, 075120 (2008)
10. V.R. Shaginyan, M.Y. Amusia, K.G. Popov, Phys. Lett. A **373**, 2281 (2009)
11. J. Dukelsky, V. Khodel, P. Schuck, V. Shaginyan, Z. Phys. **102**, 245 (1997)
12. V.A. Khodel, V.R. Shaginyan, in *Condensed Matter Theories 12*, ed. by J. Clark, V. Plant (Nova Science Publishers Inc., NY, 1997), p. 221
13. J.W. Clark, V.A. Khodel, M.V. Zverev, Phys. Rev. B **71**, 012401 (2005)
14. L.N. Oliveira, E.K.U. Gross, W. Kohn, Phys. Rev. Lett. **60**, 2430 (1988)
15. V.R. Shaginyan, Phys. Lett. A **249**, 237 (1998)
16. M.Y. Amusia, V.R. Shaginyan, Phys. Lett. A **269**, 337 (2000)
17. V.R. Shaginyan, JETP Lett. **68**, 527 (1998)
18. D. Vollhardt, Rev. Mod. Phys. **56**, 99 (1984)
19. M. Pfitzner, P. Wölfle, Phys. Rev. B **33**, 2003 (1986)
20. D. Vollhardt, P. Wölfle, P.W. Anderson, Phys. Rev. B **35**, 6703 (1987)
21. V.M. Yakovenko, V.A. Khodel, JETP Lett. **78**, 850 (2003)
22. V.R. Shaginyan, JETP Lett. **77**, 104 (2003)
23. A.A. Shashkin, S.V. Kravchenko, V.T. Dolgopolov, T.M. Klapwijk, Phys. Rev. B **66**, 073303 (2002)
24. A.A. Shashkin, M. Rahimi, S. Anissimova, S.V. Kravchenko, V.T. Dolgopolov, T.M. Klapwijk, Phys. Rev. Lett. **91**, 046403 (2003)
25. S.V. Kravchenko, M.P. Sarachik, Rep. Prog. Phys. **67**, 1 (2004)
26. A. Casey, H. Patel, J. Nyeki, B.P. Cowan, J. Saunders, Low Temp. Phys. **113**, 293 (1998)
27. A. Casey, H. Patel, J. Cowan, B.P. Saunders, Phys. Rev. Lett. **90**, 115301 (2003)
28. Y. Zhang, V.M. Yakovenko, S.D. Sarma, Phys. Rev. B **71**, 115105 (2005)
29. Y. Zhang, S.D. Sarma, Phys. Rev. B **70**, 035104 (2004)
30. G.R. Stewart, Rev. Mod. Phys. **73**, 797 (2001)

Chapter 3
Fermi Liquid with Fermion Condensate

Abstract Here we discuss the general properties of FCQPT leading to the emergence of FC. We present a microscopic derivation of the main equations of FC, and show that Fermi systems with FC form an entirely new class of Fermi liquids with its own topological structure, protecting the FC state. We construct the phase diagram, and explore the order parameter of these systems. We show that the fermion condensate has a strong impact on the observable physical properties of systems, where it is realized, up to relatively high temperatures of a few tens kelvin. Two different scenarios of the quantum critical point (QCP), a zero-temperature instability of the Landau state, related to the divergence of the effective mass, are also investigated. Flaws of the standard scenario of the QCP, where this divergence is attributed to the occurrence of some second–order phase transition, are demonstrated.

3.1 The Fermion-Condensation Quantum Phase Transition

As it is shown in Sect. 2.2, the Pomeranchuk stability conditions do not encompass all possible types of instabilities and that at least one related to the divergence of the effective mass given by (2.21) was overlooked [1]. This type of instability corresponds to a situation where the effective mass, the most important characteristic of a quasiparticle, can become infinitely large. As a result, the quasiparticle kinetic energy is infinitely small near the Fermi surface and the quasiparticle distribution function $n(\mathbf{p})$ minimizing $E(n(\mathbf{p}))$ is determined by the potential energy. This leads to the formation of a new class of strongly correlated Fermi liquids with fermion condensate (FC) [1–4], separated from the normal Fermi liquid by FCQPT [5–7].

It follows from (2.21) that at $T = 0$ and $r \to 0$ the effective mass diverges, $M^*(r) \to \infty$. Beyond the critical point x_{FC}, the distance r becomes negative and, correspondingly, so does the effective mass. To avoid an unstable and physically meaningless state with a negative effective mass, the system must undergo a quantum phase transition at the critical point $x = x_{FC}$, which, as we will see shortly, is FCQPT [5–7]. As the kinetic energy of quasiparticles near the Fermi surface is proportional to the inverse effective mass, their potential energy determines the ground-state one as $x \to x_{FC}$. Hence, a phase transition reduces the energy of the system and transforms

M.Y. Amusia et al., *Theory of Heavy-Fermion Compounds*, Springer Series
in Solid-State Sciences 182, DOI 10.1007/978-3-319-10825-4_3

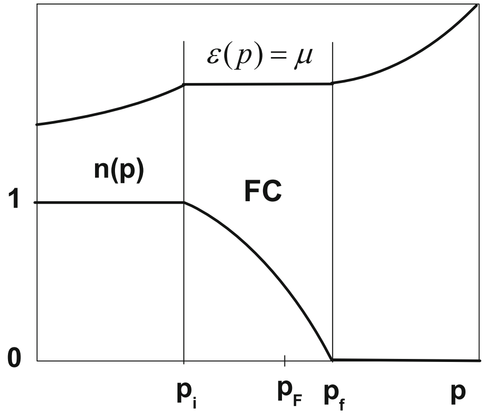

Fig. 3.1 The single-particle spectrum $\varepsilon(p)$ and the quasiparticle distribution function $n(p)$. Because $n(p)$ is a solution of (3.1), we have $n(p < p_i) = 1, 0 < n(p_i < p < p_f) < 1$, and $n(p > p_f) = 0$, while $\varepsilon(p_i < p < p_f) = \mu$. The Fermi momentum p_F satisfies the condition $p_i < p_F < p_f$

the quasiparticle distribution function. Beyond QCP $x = x_{FC}$, the quasiparticle distribution is determined by the ordinary equation for a minimum of the energy functional [1]:

$$\frac{\delta E(n(\mathbf{p}))}{\delta n(\mathbf{p}, T = 0)} = \varepsilon(\mathbf{p}) = \mu; \;\; p_i \leq p \leq p_f. \tag{3.1}$$

Equation (3.1) yields the quasiparticle distribution function $n_0(\mathbf{p})$ that minimizes the ground-state energy E. This function found from (3.1) differs from the step function in the interval from p_i to p_f, where $0 < n_0(\mathbf{p}) < 1$, and coincides with the step function outside this interval. In fact, (3.1) coincides with (2.3) provided that the Fermi surface at $p = p_F$ transforms into the Fermi volume at $p_i \leq p \leq p_f$ suggesting that the single-particle spectrum is absolutely "flat" within this interval. A possible solution $n(\mathbf{p})$ of (3.1) and the corresponding single-particle spectrum $\varepsilon(\mathbf{p})$ are depicted in Fig. 3.1. Quasiparticles with momenta within the interval $(p_f - p_i)$ have the same single-particle energies equal to the chemical potential μ and form FC, while the distribution function $n_0(\mathbf{p})$ describes the new state of the Fermi liquid with FC [1, 2, 4]. In contrast to the Landau, marginal, or Luttinger Fermi liquids [8–10], which exhibit the same topological structure of the Green's function, in systems with FC, where the Fermi surface spreads into a strip, the Green's function belongs to a different topological class. The Green's function of systems with FC is considered in Sects. 3.2 and 5.1.1. The topological class of the Fermi liquid is characterized by the invariant [4, 11, 12]

$$N_t = \mathrm{tr} \oint_C \frac{dl}{2\pi i} G(i\omega, \mathbf{p}) \partial_l G^{-1}(i\omega, \mathbf{p}), \tag{3.2}$$

where "tr" denotes the trace over the spin indices of the Green's function and the integral is taken along an arbitrary contour C encircling the singularity of the Green's function. The invariant N_t in (3.2) takes integer values even when the singularity is not of the pole type, cannot vary continuously, and is conserved in a transition from the Landau Fermi liquid to marginal liquids and under small perturbations of the Green's function. As it was shown by Volovik [4, 11, 12], the situation is quite different for systems with FC, where the invariant N_t becomes a half-integer and the system with FC transforms into an entirely new class of Fermi liquids with its own topological structure, thus forming a new state of matter protected by the topological invariant given by (3.2).

A few remarks are in order here. As it was shown above, the solutions of (3.1) describe the topologically protected new state of matter. Equation (3.1) represents an ordinary one to search the minimum of functional E. In the case of Bose system the equation $\delta E/\delta n(p) = \mu$ describes a common instance. In the case of Fermi systems such an equation, generally speaking, were not correct. Thus, it is the FC state, taking place behind FCQPT, that makes (3.1) applicable for Fermi systems. Thus, Fermi quasiparticles in the region $p_i < p < p_f$ can behave as Bose one, occupying the same energy level $\varepsilon = \mu$, and (3.1) yields the quasiparticle distribution function $n_0(\mathbf{p})$ that minimizes the ground-state energy E. This state can be viewed as the state possessing the supersymmetry (SUSY) that interchanges bosons and fermions eliminating the difference between them. In the strongly coupling limit when the Pauli restriction $n(p) < 1$ is automatically met and all the quasiparticles form the FC state, p_f is determined by the condition

$$x = \int_0^{p_f} n_0(p) \frac{p^2 dp}{\pi^2}. \tag{3.3}$$

In that case SUSY is restored over all the configuration space. We shall see that SUSY emerges naturally in condensed matter systems known as HF compounds. In Chap. 13, we shall see that emerging the FC state accompanied by SUSY violates the time invariance symmetry, while in Chap. 16 we demonstrate that emerging SUSY violates the baryon symmetry of the Universe. Thus restoring one important symmetry, the FC state violates another essential symmetry.

3.1.1 The FCQPT Order Parameter

We start with visualizing the main properties of FCQPT. To this end, again consider the density functional theory for superconductors (SCDFT) [13]. SCDFT states that the thermodynamic potential Φ is a universal functional of the number density $n(\mathbf{r})$ and the anomalous density (or the order parameter) $\kappa(\mathbf{r}, \mathbf{r}_1)$, providing a variational principle to determine the densities. At the superconducting transition temperature

T_c a system undergoes the second order phase transition into superconducting state. Our goal now is to construct a quantum phase transition which evolves from the superconducting one.

Let us recall that the vanishing of coupling constant λ_0 of the BCS-like pairing interaction [14] implies the disappearance of the superconducting gap at any finite temperature, see Chap. 5. In that case, $T_c \to 0$ and the superconducting state occurs at $T = 0$ so that at finite temperatures there is a normal state only. This means that at $T = 0$ the anomalous density

$$\kappa(\mathbf{r}, \mathbf{r_1}) = \langle \Psi_\uparrow(\mathbf{r})\Psi_\downarrow(\mathbf{r_1})\rangle \tag{3.4}$$

is finite, while the superconducting gap

$$\Delta(\mathbf{r}) = \lambda_0 \int \kappa(\mathbf{r}, \mathbf{r_1}) d\mathbf{r_1} \tag{3.5}$$

is infinitely small [15–17]. In (3.4), the field operator $\Psi_\sigma(\mathbf{r})$ annihilates an electron of spin $\sigma, \sigma = \uparrow, \downarrow$ at the position $\mathbf{r}$. For the sake of simplicity, we consider the model of homogeneous HF liquid [15, 16]. Then at $T = 0$, the thermodynamic potential Φ reduces to the ground state energy E which turns out to be a functional of the occupation number $n(\mathbf{p})$ since in that case the order parameter $\kappa(\mathbf{p}) = v(\mathbf{p})u(\mathbf{p}) = \sqrt{n(\mathbf{p})(1 - n(\mathbf{p}))}$. Latter expression relates the order parameter κ to the coefficients $u(\mathbf{p})$ and $v(\mathbf{p})$ of Bogoluybov transformation, diagonalizing the corresponding Hamiltonian in electron (fermion) creation and annihilation operators, see e.g., [18]. More precisely,

$$n(\mathbf{p}) = v^2(\mathbf{p}), \quad \kappa(\mathbf{p}) = v(\mathbf{p})u(\mathbf{p}), \tag{3.6}$$

where for fermions the parameters $u(\mathbf{p})$ and $v(\mathbf{p})$ are normalized so as $v^2(\mathbf{p}) + u^2(\mathbf{p}) = 1$, see also [18].

Minimization of E over $n(\mathbf{p})$ yields (3.1). If (3.1) has nontrivial solution $n_0(\mathbf{p})$ then instead of the Fermi step we have $0 < n_0(\mathbf{p}) < 1$ in certain range of momenta $p_i \le p \le p_f$. In this case, as $n_0(\mathbf{p})$ is neither 0 nor 1, the order parameter $\kappa(\mathbf{p}) = \sqrt{n_0(\mathbf{p})(1 - n_0(\mathbf{p}))}$ becomes finite in this range, while the single particle spectrum $\varepsilon(\mathbf{p})$ is flat. Thus, the step-like Fermi occupation restructures inevitably and forms FC when (3.1) possesses the nontrivial solution at some $x = x_c$. This solution is indeed a QCP of FCQPT. In QCP point one has $p_i \to p_f \to p_F$ so that the effective mass M^* diverges [1, 15, 16, 19]

$$\left[M^*(x \to x_c)\right]^{-1} = \frac{1}{p_F} \frac{\partial \varepsilon(\mathbf{p})}{\partial \mathbf{p}}\bigg|_{\substack{p \to p_F \\ x \to x_c}} \to 0. \tag{3.7}$$

At any small but finite temperature the order parameter (anomalous density) κ decays and this state undergoes the first order phase transition converting into a normal state with thermodynamic potential Φ_0. Indeed, at $T \to 0$, the entropy $S = -\partial \Phi_0 / \partial T$

of the normal state is given by (2.4). It is seen from (2.4) that the normal state is characterized by the temperature-independent entropy S_0 [15, 16, 19, 20]. Since the entropy of the superconducting ground state is zero, we conclude that the entropy is discontinuous at the phase transition point with the gap $\delta S = S_0$. Thus, the system undergoes the first order phase transition. The heat q of this transition is $q = T_c S_0 = 0$ since $T_c = 0$. Because of the stability condition at the point of the first order phase transition, we have $\Phi_0(n(\mathbf{p})) = \Phi(\kappa(\mathbf{p}))$. Obviously the condition is satisfied since $q = 0$. We postpone more detailed discussion of the superconductivity (and related Green's functions) of the systems with FC to Chap. 5.

3.1.2 Quantum Protectorate Related to FCQPT

Like any other phase transition, the FCQPT comprises strong interparticle interaction so that there is no way to describe reliably all its details within approaches based on a perturbation theory or some schemes using diagrams. On the other hand, as we have seen above, SCDFT represents reliable theory. Then, the next way to confirm the FC existence is to study the model systems, which admit the exact solutions. Such theoretical studies should be augmented by careful examination of experimental data that could be interpreted in favor (or to the detriment) of FC existence. Exactly solvable models unambiguously suggest that Fermi systems with FC exist (see, e.g., [21–24]). Taking the results of topological investigations into account, we can affirm that the new class of Fermi liquids with FC is nonempty, actually exists, and represents an extended family of new states of Fermi systems [4, 11, 12].

We note that the solutions $n_0(\mathbf{p})$ of (3.1) are new solutions of the well-known equations of the Landau Fermi-liquid theory. Indeed, at $T = 0$, the standard solution given by a step function, $n(\mathbf{p}, T \to 0) \to \theta(p_F - p)$, is not the only possible one. Anomalous solutions $\varepsilon(\mathbf{p}) = \mu$ of (2.1) can exist if the logarithmic expression on its right-hand side is finite. This is possible if $0 < n_0(\mathbf{p}) < 1$ for $p_i \le p \le p_f$. Then, this logarithmic expression remains finite within this interval as $T \to 0$, the product $T \ln[(1 - n_0(\mathbf{p}))/n_0(\mathbf{p})]_{|T\to 0} \to 0$, and we again arrive at (3.1).

Thus, as $T \to 0$, the quasiparticle distribution function $n_0(\mathbf{p})$, which is a solution of (3.1), does not tend to the step function $\theta(p_F - p)$ and, correspondingly, in accordance with (2.4), the entropy $S(T)$ of this state tends to a finite value S_0 as $T \to 0$:

$$S(T \to 0) \to S_0. \tag{3.8}$$

As the density $x \to x_{FC}$ (or as the interaction force increases), the system reaches QCP where FC is formed. This means that $p_i \to p_f \to p_F$ and that the deviation $\delta n(\mathbf{p})$ from the step function is small. Expanding the function $E(n(\mathbf{p}))$ in Taylor series in $\delta n(\mathbf{p})$ and keeping only the leading terms, we can use (3.1) to obtain the following relation that is valid for $p_i \le p \le p_f$:

$$\mu = \varepsilon(\mathbf{p}) = \varepsilon_0(\mathbf{p}) + \int F(\mathbf{p}, \mathbf{p}_1)\delta n(\mathbf{p_1})\frac{d\mathbf{p}_1}{(2\pi)^2}. \tag{3.9}$$

Both quantities, the Landau interaction $F(\mathbf{p}, \mathbf{p}_1)$ and the single-particle energy $\varepsilon_0(\mathbf{p})$, are calculated at $n(\mathbf{p}) = \theta(p_F - p)$.

Equation (3.9) has nontrivial solutions for densities $x \le x_{FC}$ if the corresponding Landau interaction, which is density-dependent, is positive and sufficiently large for the potential energy to be higher than the kinetic energy. For instance, such a state is realized in a low-density electron liquid. The transformation of the Fermi step function $n(\mathbf{p}) = \theta(p_F - p)$ into a smooth function determined by (3.9) then becomes possible [1, 2, 25].

It follows from (3.9) that the quasiparticles of FC form a collective state, because their state is determined by the macroscopic number of quasiparticles with momenta $p_i < p < p_f$. The shape of the FC single-particle spectrum is independent of the Landau interaction details, which in general is determined by the microscopic properties of the system like chemical composition, collective states, structure irregularities and the presence of impurities. The only characteristic determined by the Landau interaction is the length of interval (from p_i to p_f) of FC existence. Of course, the interaction must be strong enough for FCQPT to occur. Therefore, we conclude that spectra related to FC have a universal shape. In Sects. 3.1.3 and 5.1 we show that these spectra depend on temperature and the superconducting gap and that this dependence is also universal. The existence of such spectra can be considered a characteristic feature of a "quantum protectorate", in which the properties of the material, including the thermodynamic properties, are determined by a certain fundamental principle [26, 27]. In our case, the state of matter with FC is also a quantum protectorate, since the new type of quasiparticles of this state determines the special universal thermodynamic and transport properties of Fermi liquids with FC.

3.1.3 The Influence of FCQPT at Finite Temperatures

According to (2.1), the single-particle energy $\varepsilon(\mathbf{p}, T)$ is linear in T for $T \ll T_f$ for $p_f < p < p_i$ [28]. Expanding $\ln((1 - n(\mathbf{p}))/n(\mathbf{p}))$ in series in $n(\mathbf{p})$ at $p \simeq p_F$, we arrive at the expression

$$\frac{\varepsilon(\mathbf{p}, T) - \mu(T)}{T} = \ln\frac{1 - n(\mathbf{p})}{n(\mathbf{p})} \simeq \left.\frac{1 - 2n(\mathbf{p})}{n(\mathbf{p})}\right|_{p \simeq p_F}, \tag{3.10}$$

where T_f is the temperature above which the effect of FC is insignificant [29]:

$$\frac{T_f}{\varepsilon_F} \sim \frac{p_f^2 - p_i^2}{2m\varepsilon_F} \sim \frac{\Omega_{FC}}{\Omega_F}. \tag{3.11}$$

Here Ω_{FC} is the volume occupied by FC, ε_F is the Fermi energy and Ω_{FC} is the volume of the Fermi sphere. Taking $\Omega_F/\Omega \sim 0.1$ and $\varepsilon_F \sim 100\,\mathrm{K}$, we obtain $T_f \sim 10\,\mathrm{K}$, and conclude that the NFL behavior can take place up temperatures of several 10 K. We note that for $T \ll T_f$, the occupation numbers $n(\mathbf{p})$ obtained from (3.1) are almost perfectly independent of T [28–30]. At finite temperatures, according to (3.10), the dispersionless plateau $\varepsilon(\mathbf{p}) = \mu$ shown in Fig. 3.1 is slightly rotated counterclockwise relatively to μ, so that $\varepsilon(\mathbf{p}) - \mu = T \ln[(1 - n_p)/n_p]$. As a result, the plateau is slightly tilted and rounded off at its end points. According to (2.6) and (3.10), the effective mass M^*_{FC} of the FC quasiparticles is given by

$$M^*_{FC} \simeq p_F \frac{p_f - p_i}{4T}. \tag{3.12}$$

To derive (3.12), we approximate $dn(p)/dp \simeq -1/(p_f - p_i)$. Equation (3.12) shows clearly that for $0 < T \ll T_f$, the electron liquid with FC behaves as if it were placed at a QCP since the electron effective mass diverges as $T \to 0$. Actually, as we shall see in Sect. 5.3, the system is at a quantum critical line as critical behavior is observed behind QCP with $x = x_{FC}$ of FCQPT as $T \to 0$. In Chap. 8, we show that the behavior of such a system differs dramatically from that of a system at QCP.

The (3.11) and (3.12) permit to estimate the effective mass M^*_{FC} in the form

$$\frac{M^*_{FC}}{M} \sim \frac{N(0)}{N_0(0)} \sim \frac{T_f}{T}, \tag{3.13}$$

where $N_0(0)$ is the density of states of a noninteracting electron gas and $N(0)$ is the density of states at the Fermi surface. Equations (3.12) and (3.13) yield the temperature dependence of M^*_{FC}.

Multiplying both sides of (3.12) by $p_f - p_i$, we obtain an expression for the characteristic energy,

$$E_0 \simeq 4T, \tag{3.14}$$

which determines the momentum interval $p_f - p_i$ having the low-energy quasiparticles with the energy $|\varepsilon(\mathbf{p}) - \mu| \le E_0/2$ and the effective mass M^*_{FC}. The quasiparticles that do not belong to this momentum interval have an energy $|\varepsilon(\mathbf{p}) - \mu| > E_0/2$ and an effective mass M^*_L that is weakly temperature-dependent [6, 7, 31]. Equation (3.14) shows that E_0 is independent of the condensate volume. We conclude from (3.12) and (3.14) that for $T \ll T_f$, the single-electron spectrum of FC quasiparticles has a universal shape and has the features of a quantum protectorate.

The above discussion shows that a system with FC is characterized by two effective masses, M^*_{FC} and M^*_L. This fact manifests itself in the abrupt variation of the quasiparticle dispersion law, which for quasiparticles with energies $\varepsilon(\mathbf{p}) \le \mu$ can be approximated by two straight lines intersecting at $E_0/2 \simeq 2T$. Figure 3.1 shows that at $T = 0$, the straight lines intersect at $p = p_i$. This also occurs when the system is in its superconducting state at temperatures $T_c \le T \ll T_f$, where T_c is the critical temperature of the superconducting phase transition, which agrees with the experimental data of [32]. We will see in Sect. 5.1 that this behavior also agrees with the experimental data at $T \leq T_c$. At $T > T_c$, the quasiparticles are well-defined as their width γ is small compared to their energy and is proportional to the temperature, $\gamma \sim T$ [29, 33]. The quasiparticle excitation curve (see Sect. 5.2) can be approximately described by a simple Lorentzian [31], which also agrees with the experimental data [32, 34–36].

We now estimate the density x_{FC} at which FCQPT occurs. We show in Sect. 5.4 that an unlimited increase of the effective mass precedes the appearance of a density wave or a charge density wave formed in electron systems at $r_s = r_0/a_B = r_{cdw}$, where r_0 is the average distance between electrons, and a_B is the Bohr radius. Hence, FCQPT certainly occurs at $T = 0$ when r_s reaches its critical value r_{FC} corresponding to x_{FC}, with $r_{FC} < r_{cdw}$ [25]. We note that the increase of the effective mass at the electron number density decrease has been observed experimentally, see Figs. 2.1 and 2.2.

Thus, the formation of FC can be considered as a general property of different strongly correlated systems rather than an exotic phenomenon corresponding to the anomalous solution of (3.1). Beyond FCQPT, the condensate volume is proportional to $r_s - r_{FC}$, with $T_f/\varepsilon_F \sim (r_s - r_{FC})/r_{FC}$, at least when $(r_s - r_{FC})/r_{FC} \ll 1$. This implies that [15, 16]

$$\frac{r_s - r_{FC}}{r_{FC}} \sim \frac{p_f - p_i}{p_F} \sim \frac{x_{FC} - x}{x_{FC}}. \tag{3.15}$$

Since a state of a system with FC is highly degenerate, FCQPT serves as a stimulator of phase transitions that could lift the degeneracy of the spectrum at the interval $p_f - p_i$. For instance, FC can stimulate the formation of spin density waves, antiferromagnetic and/or ferromagnetic state etc., thus strongly stimulating the competition between phase transitions eliminating the degeneracy. The presence of FC facilitates a transition to the superconducting state as both phases have the same order parameter.

3.1.4 Phase Diagram of Fermi System with FCQPT

At $T = 0$, a quantum phase transition is driven by a nonthermal control parameter like number density x. As we have seen, at QCP, $x = x_{FC}$, the effective mass diverges. It follows from (2.21) that beyond QCP, the effective mass becomes negative. As such a physically meaningless state cannot be realized, the system undergoes FCQPT leading to the FC formation.

The schematic phase diagrams of the systems which are driven to the FC state by variation of x are reported in Fig. 3.2. The panel a displays the case when FCQPT takes place at growing densities. As we have seen in Sect. 3.1, FCQPT occurs as soon as the potential energy of the quasiparticles near the Fermi surface determines the ground-state energy. Therefore, the panel a represents the phase diagram of a system composed of particles interacting with each other by van-der-Waals forces

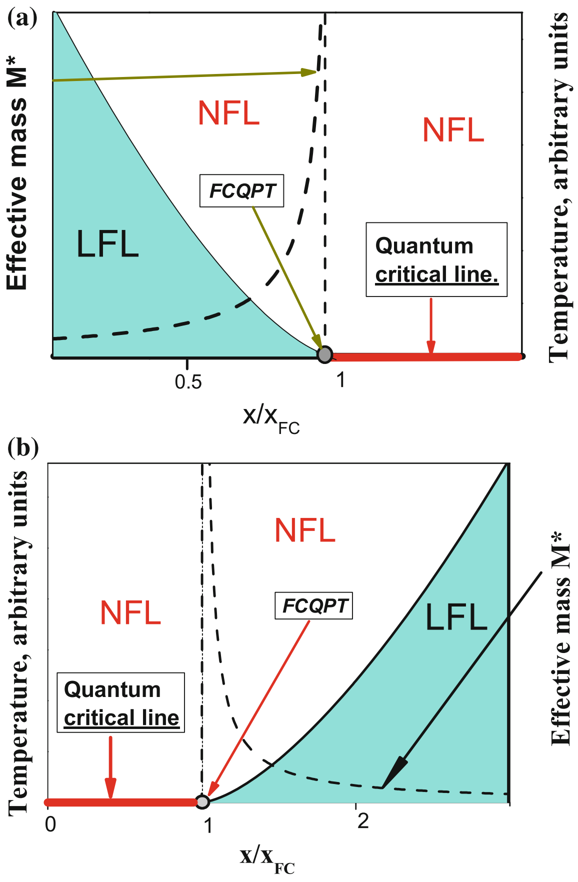

Fig. 3.2 Schematic temperature—number density phase diagrams of the systems with FC. The panel **a** displays the phase diagram for the case when the FCQPT takes place at growing densities, while the panel **b** displays the opposite case. The number density x is taken as the control parameter and depicted as x/x_{FC}. The *dashed line* shows $M^*(x/x_{FC})$ as the system approaches FCQPT, marked by the *arrow*. The *shadowed* area in the panel **a** corresponds to the case $x/x_{FC} < 1$ and sufficiently low temperatures, where the system is in the LFL phase. This case in the panel **b** corresponds to $x/x_{FC} > 1$. At $T = 0$ and beyond the FCQPT critical point, the system is at the quantum *critical line* as shown in the legend. This *critical line* is characterized by the FC state with finite superconducting order parameter κ. At any finite temperature $T > T_c = 0$, κ is destroyed so that the system undergoes the first order phase transition, possesses finite entropy S_0 and exhibits the NFL behavior at any finite temperatures $T < T_f$

with strong hardcore repulsion. At elevated densities the potential energy overcomes the kinetic one leading to FC emergence, which is the case for 2D ^{3}He films, see Sect. 18.4. The panel b displays the opposite case which occurs in electronic systems, when the potential energy dominates at lowering densities, see Sect. 5.4 for details. The similarity of the both diagrams reflects the universal behavior of systems located near FCQPT, as it is discussed in Chap. 18.

Figure 3.2 demonstrates that upon approaching the critical density x_{FC} the system remains in the LFL region at sufficiently low temperatures as it is shown by the shadowed area. The temperature range of the shadowed area shrinks as the system approaches FCQPT, and $M^*(x/x_{FC})$ diverges as shown by the dashed line and (2.21). At FCQPT x_{FC} shown by the arrow in Fig. 3.2, the system demonstrates the NFL behavior down to the lowest temperatures. Beyond the critical point at finite temperatures the behavior remains the NFL and is determined by the temperature-independent entropy S_0 [15, 16, 20]. In that case at $T \to 0$, the system is approaching a quantum critical line (shown in the legend) rather than a quantum critical point. Upon reaching the quantum critical line from the above at $T \to 0$ the system undergoes the first order quantum phase transition, which is FCQPT taking place at $T_c = 0$. At the same time, at temeparture lowering for x before QCP (which is $x < x_{FC}$ in panel a and $x > x_{FC}$ in panel b) the system does not undergo a phase transition and transits smoothly from NFL to LFL phase.

It is seen from Fig. 3.2 that at finite temperatures there is no boundary (or phase transition) between the states of systems located before or after FCQPT. Therefore, at elevated temperatures the properties of systems with $x/x_{FC} < 1$ or with $x/x_{FC} > 1$ become indistinguishable. On the other hand, at $T > 0$ the NFL state above the critical line and in the QCP vicinity is strongly degenerate so that the degeneracy stimulates different phase transitions, which finally lift it. The lifting of the degeneracy means that the NFL state can be obscured by the other states like superconducting (for example, in $CeCoIn_5$ [17, 20]) or antiferromagnetic (for example in $YbRh_2Si_2$ [37]) etc. The diversity of low-temperature phase transitions is one of the most spectacular features of the physics of many of HF metals. The scenario of ordinary quantum phase transitions makes it hard to understand why they are so different and why their critical temperatures are so small. However, such diversity is endemic to systems with a FC [19].

Upon varying nonthermal tuning parameters like the number density, pressure or magnetic field, the NFL behavior could be destroyed and the LFL one is restored as we shall see in Chaps. 6 and 8. For example, the application of magnetic field $B > B_{c0}$ drives a system to QCP and destroys the AF state restoring the LFL behavior. Here, B_{c0} is a critical magnetic field, such that at $B > B_{c0}$ the system is driven towards its LFL state. In some cases as in the HF metal $CeRu_2Si_2$, $B_{c0} = 0$, see e.g., [38], while in $YbRh_2Si_2$, $B_{c0} \simeq 0.06$ T [39].

3.2 Two Scenarios of the Quantum Critical Point

The statement that the Landau quasiparticle picture breaks down at points of second–order phase transitions has become a truism. The violation of this picture is attributed to vanishing of the quasiparticle weight z in the single-particle state. In nonsuperfluid Fermi systems, the z-factor is determined by the formula $z = [1-(\partial\Sigma(p,\varepsilon)/\partial\varepsilon)_0]^{-1}$ where the subscript 0 indicates that the respective derivative of the mass operator Σ

is evaluated at the Fermi surface. This factor enters a textbook formula

$$\frac{M}{M^*} = z\left[1 + \left(\frac{\partial \Sigma(p,\varepsilon)}{\partial \varepsilon_p^0}\right)_0\right] \tag{3.16}$$

for the ratio M^*/M of the effective mass M^* to the mass M of a free particle. As seen from this formula, where $\varepsilon_p^0 = p^2/2M$, the effective mass diverges at a critical density ρ_c, where z vanishes provided the sum $1 + \left(\partial\Sigma(p, \varepsilon = 0)/\partial\varepsilon_p^0\right)_0$ has a *positive and finite value* at this point. Nowadays, when studying critical fluctuations of arbitrary wave-lengths $k < 2p_F$ has become popular, this restriction is often assumed to be met without stipulations. E.g., a standard scenario of the quantum critical point where M^* diverges is formulated as follows: in the vicinity of an impending second-order phase transition, "quasiparticles get heavy and die" [40].

However, as seen from (3.16), M^* may diverge not only at the points of the second-order phase transitions, but also at a critical density ρ_∞, where the sum $1 + \left(\frac{\partial\Sigma(p,\varepsilon)}{\partial\varepsilon_p^0}\right)_0$ changes its sign. Furthermore, we will demonstrate that except for the case of the ferromagnetic instability, M^* cannot diverge at ρ_c without violation of stability conditions [41].

In what follows we restrict ourselves to one-component three-dimensional (3D) homogeneous Fermi liquids, where the particle momentum is conserved, and the Landau equation, connecting the quasiparticles group velocity $\partial\varepsilon/\partial\mathbf{p}$ to their momentum distribution $n(p)$ in terms of the interaction function f, has the form [18]

$$\frac{\partial\varepsilon(p)}{\partial\mathbf{p}} = \frac{\mathbf{p}}{M} + \int f(\mathbf{p}, \mathbf{p_1})\,\frac{\partial n(p_1)}{\partial\mathbf{p_1}}\,\frac{d^3p_1}{(2\pi)^3}\,. \tag{3.17}$$

Setting here $p = p_F$ and introducing the notation $v_F = (d\varepsilon(p)/dp)_0 = p_F/M^*$, one obtains

$$v_F = \frac{p_F}{M}\left(1 - \frac{p_F M}{3\pi^2} f_1\right)\,, \tag{3.18}$$

implying that

$$\frac{M}{M^*} = 1 - \frac{1}{3}\frac{p_F M}{\pi^2} f_1\,. \tag{3.19}$$

Hereafter we employ notations of Fermi liquid (FL) theory where f_1 is the first harmonic of the interaction function $f(\theta) = z^2\Gamma^\omega(p_F, p_F; \theta)$, with Γ^ω being the ω-limit of the scattering amplitude Γ of two particles, whose energies and incoming momenta $\mathbf{p}_1, \mathbf{p}_2$ lie on the Fermi surface, with $\cos\theta = \mathbf{p}_1\cdot\mathbf{p}_2/p_F^2$, while the 4-momentum transfer $(\mathbf{q}, \omega)$ approaches zero, such that $qp_F/\omega \to 0$. In what

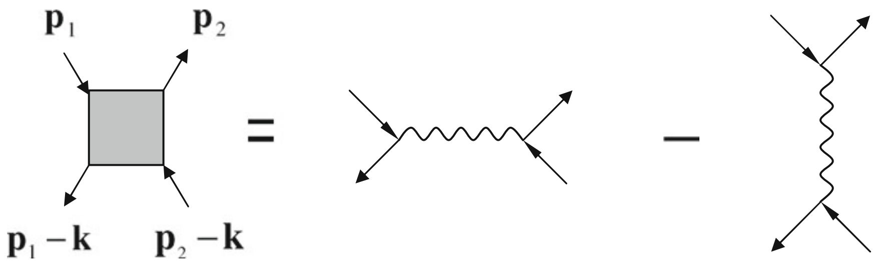

Fig. 3.3 This figure illustrates the singular contributions to the scattering amplitude in the vicinity of the second–order phase transition

follows we shall use Γ^k, that is the k-limit of the scattering amplitude Γ. In that case the energy transfer $(\mathbf{q}, \omega)$ approaches zero, such that $\omega/qp_F \to 0$.

It is instructive to rewrite (3.19) in terms of the k-limit of the dimensionless scattering amplitude $\nu\Gamma^k = A + B\sigma_1\sigma_2$ where $\nu = z^2 p_F M^*/\pi^2$ is the quasiparticle density of states. Simple algebra then yields

$$\frac{M}{M^*} = 1 - \frac{1}{3}A_1. \tag{3.20}$$

This formula stems from (3.19) and relation [18] $A_1 = \Phi_1/(1 + \frac{\Phi_1}{3})$, where Φ_1 is the spin-independent part of the product $\nu\Gamma^\omega$. Thus at the density ρ_∞ where the effective mass diverges one has

$$A_1(\rho_\infty) = 3\,, \quad \Phi_1(\rho_\infty) = \infty\,. \tag{3.21}$$

In the following we focus on critical density fluctuations with $k_c \neq 0$. First we notice that there is a strong dependence of the amplitude $\Gamma_{\alpha\beta,\gamma\delta}(\mathbf{p}_1, \mathbf{p}_2, \mathbf{k}, \omega = 0)$ on the momentum transfer k close to the critical momentum k_c, specifying the spectrum of density fluctuations. That fact stems from the asymmetry of Γ with respect to the interchange of momenta and spins of colliding particles. In this case, upon neglecting regular components one finds (see as illustration Fig. 3.3),

$$A(\mathbf{p}_1, \mathbf{p}_2, \mathbf{k}, \omega = 0; \rho \to \rho_c) = -D(\mathbf{k}) + \frac{1}{2}D(\mathbf{p}_1 - \mathbf{p}_2 + \mathbf{k}), \tag{3.22}$$

with

$$D(k \to k_c, \omega = 0) = \frac{g}{\xi^{-2}(\rho) + (k - k_c)^2}\,, \tag{3.23}$$

the correlation length $\xi(\rho)$ diverging at $\rho = \rho_c$.

Within the quasiboson approximation (for details see e.g., [42]), the derivative $(\partial\Sigma(p,\varepsilon)/\partial\varepsilon)_0$ diverges at $\rho \to \rho_c$ as $\xi(\rho)$, while the derivative $\left(\partial\Sigma(p,\varepsilon)/\partial\varepsilon_p^0\right)_0$

remains finite at any k_c. If these results were correct, then the densities ρ_∞ and ρ_c would coincide, in agreement with the standard scenario of the QCP. However, calculations of harmonics $A_k(\rho)$ of the amplitude $A(p_F, p_F, \cos\theta)$ from (3.22) to (3.23) yield

$$A_0(\rho\to\rho_c) = g\frac{\pi}{2}\frac{k_c\xi(\rho)}{p_F^2}, \;\; A_1(\rho\to\rho_c) = g\frac{3\pi}{2}\frac{k_c\xi(\rho)}{p_F^2}\cos\theta_0. \tag{3.24}$$

We see that the sign of $A_1(\rho \to \rho_c)$, coinciding with that of $\cos\theta_0 = 1 - k_c^2/2p_F^2$, turns out to be *negative* at $k_c > p_F\sqrt{2}$. According to (3.20) this implies that at the point of the second–order phase transition, the ratio $M^*(\rho_c)/M < 1$. Thus we infer that at $k_c > p_F\sqrt{2}$, the densities ρ_c and ρ_∞ *cannot coincide*. In its turn, this implies that vanishing of the z-factor at ρ_c is compensated by the divergence of the derivative $(\partial\Sigma(p,\varepsilon)/\partial\varepsilon_p^0)_0$ at this point, otherwise (3.16) fails.

To verify this assertion let us write down the fundamental LFL relation [43] between the k- and ω-limits of the vertex $\mathscr{T}$ that has the symbolic form $\mathscr{T}^k = \mathscr{T}^\omega + \big(\Gamma^k((G^2)^k - (G^2)^\omega)\mathscr{T}^\omega\big)$ where external brackets mean integration and summation over all intermediate momentum and spin variables. We note that the k- and ω-limits of the vertex $\mathscr{T}$ are defined in the same way as it was done when defining k- and ω-limits of the scattering amplitude Γ. In dealing with the bare vertex $\mathscr{T}^0 = \mathbf{p}$ the extended form of this relation is

$$-\frac{\partial G^{-1}(p)}{\partial \mathbf{p}} = \frac{\partial G^{-1}(p)}{\partial\varepsilon}\frac{\mathbf{p}}{M} + Sp_\sigma\int \Gamma^k(p,q)\left(\left(G^2(q)\right)^k - \left(G^2(q)\right)^\omega\right)\frac{\partial G^{-1}(q)}{\partial q_0}\frac{\mathbf{q}}{M}\frac{d^4q}{(2\pi)^4 i}, \tag{3.25}$$

In writing this equation the Pitaevskii identities [43]

$$\mathscr{T}^k(\mathbf{p}) = -\frac{\partial G^{-1}(p,\varepsilon)}{\partial\mathbf{p}}\;, \quad \mathscr{T}^\omega(\mathbf{p}) = \frac{\partial G^{-1}(p,\varepsilon)}{\partial\varepsilon}\mathbf{p} \tag{3.26}$$

are employed. Upon inserting the LFL formula

$$\left(G^2(q)\right)^k = \left(G^2(q)\right)^\omega - 2\pi^3 i\frac{\nu}{p_F^2}\delta(\varepsilon)\delta(p-p_F) \tag{3.27}$$

into (3.25) and the standard replacement of the spin-independent part of $\nu\Gamma^k$ by A, after some algebra we are led to equation

$$1 + \left(\frac{\partial\Sigma(p,\varepsilon)}{\partial\varepsilon_p^0}\right)_0 = \left(1 - \left(\frac{\partial\Sigma(p,\varepsilon)}{\partial\varepsilon}\right)_0\right)\left(1 - \frac{1}{3}A_1\right)\,. \tag{3.28}$$

Remembering that $-\partial G^{-1}(p,\varepsilon)/\partial \mathbf{p} = z^{-1}d\varepsilon(p)/dp$ one arrives [43] at (3.20). On the other hand, as seen from (3.25), at $k_c > p_F\sqrt{2}$ where $A_1 < 0$, the derivative $\left(\partial\Sigma(p,\varepsilon)/\partial\varepsilon_p^0\right)_0$ does diverge at the same density, as the derivative $(\partial\Sigma(p,\varepsilon)/\partial\varepsilon)_0$, in contrast to the result [42]. To correct the defect of the quasiboson approximation, the spin-independent part of the scattering amplitude Γ entering the formulas for the derivatives of the mass operator Σ should be replaced by that of the amplitude Γ^{ω}.

We will immediately see that at finite $k_c < p_F\sqrt{2}$, vanishing of the z-factor is *incompatible* with the divergence of M^* as well. Indeed, as seen from (3.24), the harmonics $A_0(\rho_c)$ and $A_1(\rho_c)$ are related to each other by equation $A_0(\rho_c) = A_1(\rho_c)/(3\cos\theta_0)$. If $M^*(\rho_c)$ were infinite, then according to (3.20), $A_1(\rho_c)$ would equal 3, and $A_0(\rho_c) = 1/\cos\theta_0$. However, the quantity $A_0 = \Phi_0/(1+\Phi_0)$ cannot be in excess of 1, otherwise the Pomeranchuck stability condition [43] $\Phi_0 > -1$ is violated, and the compressibility turns out to be negative. Thus the QCP cannot be reached without the violation of the stability condition. If so, approaching the QCP, the system undergoes a first–order phase transition, as in the case of 3D liquid ^{3}He.

The finiteness of M^* at the points of vanishing of the z-factor requires an alternative explanation of the logarithmic enhancement of the specific heat $C(T)$, observed in many heavy fermion metals and attributed to contributions of critical fluctuations.

Let us now turn to the analysis of another opportunity for the occurrence of the QCP, addressed first in microscopic calculations of the single-particle spectrum of 3D electron gas. It is associated with the change of the sign of the sum $1+\left(\frac{\partial\Sigma(p,\varepsilon)}{\partial\varepsilon_p^0}\right)_0$ at $\rho_\infty \neq \rho_c$. In this case, the z-factor keeps its finite value, and hence, the quasiparticle picture holds on both sides of the QCP. In standard Landau theory, equation

$$\varepsilon(p, T=0) = \mu \tag{3.29}$$

with μ, being the chemical potential, has the single root, determining the Fermi momentum p_F. Suppose, at a critical coupling constant g_T, a bifurcation in (3.29) emerges, then beyond the critical point, at $g > g_T$, this equation acquires, at least, two new roots that triggers a *topological* phase transition. In many-body theory, equation, determining critical points of the topological phase transitions, has the form

$$\varepsilon_p^0 + \Sigma(p, \varepsilon=0) = \mu. \tag{3.30}$$

Significantly, terms, proportional to $\varepsilon\ln\varepsilon$, existing in the mass operator Σ of marginal Fermi liquids, do not enter this equation.

The bifurcation p_b in (3.29) and (3.30) can emerge at any point of momentum space. If p_b coincides with the Fermi momentum p_F, then at the critical density the sum $1+\left(\frac{\partial\Sigma(p,\varepsilon)}{\partial\varepsilon_p^0}\right)_0$ vanishes, and one arrives at the *topological* quantum critical point. In connection with this scenario, it is instructive to trace the evolution of the group velocity $v_F = (d\varepsilon/dp)_0$ versus the first harmonic f_1. As follows from (3.18),

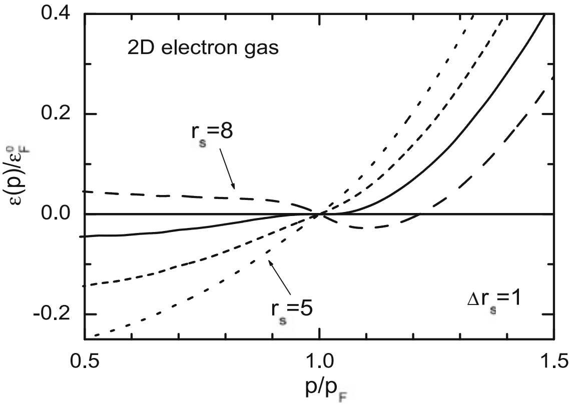

Fig. 3.4 Single-particle spectrum $\varepsilon(p)$ of a homogeneous 2D electron gas in units of $\varepsilon_F^0 = p_F^2/2M$, evaluated at $T = 0$ for different values of the dimensionless parameter $r_s = \sqrt{2}Me^2/p_F$ [41]

v_F keeps its positive sign as long as $F_1^0 = p_F M f_1/3\pi^2 < 3$, and the Landau state with the quasiparticle momentum distribution $n_F(p) = \theta(p - p_F)$ remains stable. However, at $F_1^0 > 3$, the sign of v_F changes, and the Landau state is necessarily rearranged. This conclusion is in agreement with results of microscopic calculations of the single-particle spectrum $\varepsilon(p, T = 0)$ of 2D electron gas, [41] shown in Fig. 3.4. As seen, the sign of v_F holds until the dimensionless parameter r_s attains a critical value $r_{sc} \simeq 7.0$. At greater r_s, the derivative $(d\varepsilon(p)/dp)_0$, evaluated with the momentum distribution $n_F(p)$, becomes negative, and the Landau state loses its stability, since the curve $\varepsilon(p)$ crosses the Fermi level more than one time.

At $T = 0$, two types of the topological transitions are known, see Chap. 4. One of them, giving rise to the multi-connected Fermi surface, was uncovered and studied later in calculations of the single-particle spectrum $\varepsilon(p)$ on the base of (3.17), with the interaction function $f(k)$, having no singularities at $k \to 0$. In this case, beyond the QCP, (3.29) has three roots $p_1 < p_2 < p_3$, i.e. the curve $\varepsilon(p)$ crosses the Fermi level three times, and occupation numbers are: $n(p) = 1$ at $p < p_1$, $n(p) = 0$ at $p_1 < p < p_2$, while at $p_2 < p < p_3$, once again $n(p) = 1$, and at $p > p_3$, $n(p) = 0$. As the coupling constant g increases, the number of the roots of (3.29) rapidly grows, however, their number remains countable at any $g > g_T$.

The situation changes in Fermi liquids with a singular attractive long-range current-current term

$$\Gamma^0(\mathbf{p}_1, \mathbf{p}_2, \mathbf{k}, \omega = 0) = -g\frac{\mathbf{p}_1\mathbf{p}_2 - (\mathbf{p}_1\mathbf{k})(\mathbf{p}_2\mathbf{k})/k^2}{k^2}, \tag{3.31}$$

since in these systems, e.g., in dense quark-gluon plasma, solutions with the multi-connected Fermi surface are unstable. Indeed, the group velocity $d\varepsilon(p)/dp$ evaluated with $n_F(p) = \theta(p - p_F)$ from (3.17) has the form $d\varepsilon(p)/dp = p_F/M - g\ln(2p_F/|p_F - p|)$, implying that (3.29) has three different roots p_1, p_2, p_3, corresponding to the Fermi surface, having three sheets at any $g > 0$. However, at the next iteration step, the new Fermi surface has already five sheets, the Fermi surface has seven sheets and so on. With increasing the number of iterations, the distance between neighbor sheets rapidly shrinks. In this situation, a minute elevation of temperature renders the momentum distribution $n(p, T)$ a smooth T-*independent* function $n_*(p)$, different from 0 and 1 in a domain $\mathscr{C}$ between the sheets. In this case, the ground–state stability condition,

$$\delta E = \int (\varepsilon(p) - \mu)\, \delta n(p) \frac{d^3 p}{(2\pi)^3} > 0, \tag{3.32}$$

requiring the nonnegativity of the variation δE of the ground state energy E at any admissible variation of $n_*(p)$, is met, provided

$$\varepsilon(p) = \mu\,, \quad p \in \mathscr{C}. \tag{3.33}$$

As a result, we arrive at another type of the topological transitions, the so-called fermion condensation, where the roots of (3.29) form an *uncountable* set, called the fermion condensate (FC). Since the quasiparticle energy $\varepsilon(p)$ is nothing but the derivative of the ground state energy E with respect to the quasiparticle momentum distribution $n(p)$, (3.33) can be rewritten as variational condition

$$\frac{\delta E}{\delta n(p)} = \mu, \quad p \in \mathscr{C}. \tag{3.34}$$

The FC Green function has the form

$$G(p, \varepsilon) = \frac{1 - n_*(p)}{\varepsilon + i\delta} + \frac{n_*(p)}{\varepsilon - i\delta}\,, \quad p \in \mathscr{C}, \tag{3.35}$$

and coincides with that of (5.14), if we recall that $n^*(p) = v^2(p)$. As seen, only the imaginary part of the FC Green function differs from that of the ordinary LFL Green function. As we have seen in Sect. 3.1, this difference exhibits itself in a *topological charge*, given by the integral (3.2). We recall, that for conventional Fermi liquids and systems with the multi-connected Fermi surface, the topological charge N_t is integer, while for the states with a FC, its value is *half-integer*.

For illustration of the phenomenon of fermion condensation, let us address the dense quark-gluon plasma. Upon inserting into (3.17) only leading divergent terms in the interaction function f, constructed from (3.31), one finds

$$0 = 1 - \lambda \int \ln \frac{1}{|x - x_1|} \frac{\partial n_*(x_1)}{\partial x_1} dx_1\,, \quad x, x_1 \in \mathscr{C}\,, \tag{3.36}$$

where dimensionless variables $x = (p_F - p)/2p_F$ and λ are introduced. (3.36) has a numerical solution; to find its solutions we simplify (3.36), replacing the kernel

$\ln(1/|x - x_1|)$ by $\ln(1/x)$ provided $x > x_1$, and by $\ln(1/x_1)$, otherwise, to obtain

$$0 = 1 + \lambda n_*(x) \ln x + \lambda \int_{x}^{x_m} \ln x_1 \frac{\partial n_*(x_1)}{\partial x_1} dx_1 \quad x, x_1 \in \mathscr{C}. \tag{3.37}$$

An approximate solution of this equation is $n_*(x) = x/x_m$ where $x_m = e^{-\frac{1}{\lambda}}$ is determined from condition $n(x_m) = 1$. We see that the range of the interval $[0, x_m]$ of fermion condensation, adjacent to the Fermi surface, is exponentially small.

Nontrivial smooth solutions $n_*(p)$ of (3.34) exist even in weakly interacting Fermi systems. However, in these systems, the Pauli restriction $n_*(p) < 1$ is violated, rendering such solutions meaningless. Even at the QCP, where the nonsingular interaction function f is already sufficiently strong, no consistent FC solutions $n_*(p)$ exist, satisfying the requirement $n(p) < 1$ wherever. These solutions emerge at a critical constant g_{FC}, and at $g > g_{FC}$, they win the contest with any other solutions. Thus on the phase diagram of systems with nonsingular repulsive interaction functions f, the standard LFL phase occupies the interval $g < g_T$, the phase with the multi-connected Fermi surface, the interval $g_T < g < g_{FC}$, while the phase with the FC exists at $g > g_{FC}$.

In dealing with the $(T - g)$ phase diagram of such systems, we notice that the temperature evolution of the quasiparticle momentum distribution, associated at $T = 0$ with the multi-connected Fermi surface, depends on the departure of the difference $|\varepsilon(p) - \mu|$ from 0 in the domain $\mathscr{C}$. Its maximum value ε_m determines a new energy scale $\varepsilon_m \simeq d^2/M^*(0)$, where d is the average distance between the sheets of the Fermi surface that rapidly falls with the increase of the sheets number. If temperature T attains values, comparable with ε_m, then, as seen from the Landau formula $n(p) = [1 + \exp{(\varepsilon(p) - \mu)/T)}]^{-1}$, the distribution $n(p)$ becomes a smooth function of p. Employing the FC notation $n_*(p)$ for this function, one finds that at $T \geq \varepsilon_m$ the spectrum

$$\varepsilon(p, T) - \mu = T \ln \frac{1 - n_*(p)}{n_*(p)}\ , \quad p \in \mathscr{C} \tag{3.38}$$

does coincide with the FC spectrum, and in good agreement with the study of the FC state carried out within the Hubbard model [44]. We infer that at $T \simeq \varepsilon_m$, a crossover from a state with the multi-connected Fermi surface to a state with the FC occurs. As a result, FL thermodynamics of the systems with the multi-connected Fermi surface completely alters at $T \simeq \varepsilon_m$, since properties of systems with the FC resemble those of a gas of localized spins. Such a transition was recently observed in the heavy–fermion metal $\mathrm{YbIr_2Si_2}$, transition temperature being merely 1 K.

Let us now turn to systems of fermions, interacting with a “foreign” bosonic mode, e.g., phonons or photons. In the Frölich model [14], aimed for the elucidation of electron and phonon spectra in solids, electrons share momentum with the lattice due to the electron-phonon interaction. The non-conservation of the electron momentum results in the *violation* of the second of the relations (3.26), and (3.19) acquires the form

$$\frac{M}{M^*} = z\frac{(\mathbf{n}\mathscr{T}^{\omega}(\mathbf{p}))_0}{p_F}\left(1-\frac{1}{3}A_1\right), \tag{3.39}$$

where $\mathbf{n}=\mathbf{p}/p$. The deviation of the ratio M/M^* from the Landau value (3.19), is well pronounced in the limit of small sound velocities $c_s << v_F$. For illustration, let us consider the weak coupling limit of the Frölich model, where the first harmonic A_1, evaluated from the phonon propagator $D(|\mathbf{p}_1-\mathbf{p}_2|,\omega=0)$ equals 0 due to its isotropy. If (3.19) were correct, then M^*/M would equal 1. However, this is not the case: $M^*/M = 1+g^2 p_F M/2\pi^2$ where g is the electron-phonon coupling constant [45]. Evidently, if the ratio v_F/c_s drops, then the departure from (3.19) falls due to weakening of the contribution of the pole of the boson propagator. Such a situation occurs just in the vicinity of the QCP, since at this point $v_F = p_F/M^* = 0$.

So far information on the QCP properties of Fermi liquids is extracted from measurements, carried out in 2D electron gas, 2D liquid ^{3}He and heavy–fermion metals. Accurate measurements of the effective mass M^* in dilute 2D electron gas are made on (100)- and (111)-silicon MOSFET's. In principle, the divergence of M^*, see Fig. 2.1, observed in these experiments, can be associated with critical spin-density fluctuations. However, experimental data rules out a significant enhancement of the Stoner factor. The Stoner factor $\mathscr{S}=\chi/\chi_0$ indicates the enhancement or suppression of ferromagnetic fluctuations. Here χ is the magnetic susceptibility, and χ_0 is the magnetic susceptibility of noninteracting system. In many theories, the enhancement of M^* is related to disorder effects. However, the effective masses, specifying the electron spectra of (100)- and (111)-silicon MOSFET's, where disorder is different, almost coincide with each other provided dimensionless parameters r_s of the 2D Coulomb problem, are the same. On the other hand, this coincidence that agrees with results of microscopic calculations is straightforwardly elucidated within the topological scenario of the QCP. There are reports on the divergence of the effective mass in 2D liquid ^{3}He, see Fig. 2.2. Furthermore it is reported that at the density $\rho > 9.00$ nm^{-2}, the low-temperature limit of the product $T\chi(T)$ quickly increases with increasing ρ. In addition, the ratio of the specific heat $C(T)$ to T does not obey LFL theory in this density region, since it increases with lowering T. These facts can be interpreted as evidence for the presence of the FC. Unfortunately, so far the accuracy of extremely difficult measurements of the ratio $C(T)/T$ at $T \leq 1K$, is insufficient to properly evaluate a low-temperature part of the entropy S and compare it with the respective FC entropy, extracted from data on $\chi(T)$. The divergence of the ratio $C(T)/T$, associated with the QCP, is observed in several heavy–fermion compounds. Authors of the experimental article claim that data on the Sommerfeld-Wilson ratio $R_{SW}=\chi(T)/C(T)$ in a doped compound $\mathrm{YbRh_2(Si_{0.95}Ge_{0.05})_2}$ point to an enhancement of the Stoner factor that has to be infinite at the point of the ferromagnetic phase transition. However, evaluation of the Stoner factor from experimental data in heavy–fermion metals encounters difficulties. Furthermore, with a correct normalization experimental data are explained without any enhancement of the Stoner factor that rules out the relevance of the ferromagnetic phase transition to the QCP in this metal.

Thus, two different scenarios of the quantum critical point, a low-temperature instability of the Landau state, related to the divergence of the density of states $N(0) \sim M^*$, are analyzed. Shortcomings of the conventional scenario of the QCP, where the divergence of the effective mass M^* is attributed to vanishing of the quasiparticle weight z in the single-particle state, are elucidated. In a different, topological scenario, associated with the change of the topology of the Fermi surface at the QCP, the quasiparticle picture holds on both the sides of the QCP. This scenario is in agreement with microscopic calculations of the QCP in 2D electron gas and does not contradict relevant experimental data on 2D liquid ^{3}He and heavy–fermion metals.

References

1. V.A. Khodel, V.R. Shaginyan, JETP Lett. **51**, 553 (1990)
2. V.A. Khodel, V.R. Shaginyan, V.V. Khodel, Phys. Rep. **249**, 1 (1994)
3. V.A. Khodel, J.W. Clark, H. Li, M.V. Zverev, Phys. Rev. Lett. **98**, 216404 (2007)
4. G.E. Volovik, JETP Lett. **53**, 222 (1991)
5. V.R. Shaginyan, J.G. Han, J. Lee, Phys. Lett. A **329**, 108 (2004)
6. M.Y. Amusia, V.R. Shaginyan, JETP Lett. **73**, 232 (2001)
7. M.Y. Amusia, V.R. Shaginyan, Phys. Rev. B **63**, 224507 (2001)
8. C.M. Varma, Z. Nussionov, W. van Saarloos, Phys. Rep. **361**, 267 (2002)
9. C.M. Varma, P.B. Littlewood, S. Schmittrink, E. Abrahams, A.E. Ruckenstein, Phys. Rev. Lett. **63**, 1996 (1989)
10. C.M. Varma, P.B. Littlewood, S. Schmittrink, E. Abrahams, A.E. Ruckenstein, Phys. Rev. Lett. **64**, 497 (1990)
11. G.E. Volovik, Acta Phys. Slov. **56**, 49 (2006)
12. G.E. Volovik, in *Quantum Analogues: From Phase Transitions to Black Holes and Cosmology*, eds. by W.G. Unruh, R. Schutzhold. Springer Lecture Notes in Physics, vol. 718 (Springer, Orlando, 2007), p. 31
13. L.N. Oliveira, E.K.U. Gross, W. Kohn, Phys. Rev. Lett. **60**, 2430 (1988)
14. J. Bardeen, L.N. Cooper, J.R. Schrieffer, Phys. Rev. **108**, 1175 (1957)
15. V.R. Shaginyan, M.Y. Amusia, K.G. Popov, Phys. Usp. **50**, 563 (2007)
16. V.R. Shaginyan, M.Y. Amusia, A.Z. Msezane, K.G. Popov, Phys. Rep. **492**, 31 (2010)
17. V.R. Shaginyan, JETP Lett. **77**, 104 (2003)
18. E.M. Lifshitz, L.P. Pitaevskii, *Statisticheskaya Fizika (Statistical Physics), part 2*. Course of Theoretical Physics (Pergamon Press, Oxford, 1980)
19. V.A. Khodel, J.W. Clark, M.V. Zverev, Phys. Rev. B **78**, 075120 (2008)
20. V.A. Khodel, M.V. Zverev, V.M. Yakovenko, Phys. Rev. Lett. **95**, 236402 (2005)
21. D.V. Khveshchenko, R. Hlubina, T.M. Rice, Phys. Rev. B **48**, 10766 (1993)
22. I.E. Dzyaloshinskii, J. Phys. I (France) **6**, 119 (1996)
23. D. Lidsky, J. Shiraishi, Y. Hatsugai, M. Kohmoto, Phys. Rev. B **57**, 1340 (1998)
24. V.Y. Irkhin, A.A. Katanin, M.I. Katsnelson, Phys. Rev. Lett. **89**, 076401 (2002)
25. V.A. Khodel, V.R. Shaginyan, M.V. Zverev, JETP Lett. **65**, 242 (1997)
26. R.B. Laughlin, D. Pines, Proc. Natl. Acad. Sci. USA **97**, 28 (2000)
27. P.W. Anderson, Science **288**, 480 (2000)
28. V.A. Khodel, J.W. Clark, V.R. Shaginyan, Solid Stat. Comm. **96**, 353 (1995)
29. J. Dukelsky, V. Khodel, P. Schuck, V. Shaginyan, Z. Phys. **102**, 245 (1997)

30. V.A. Khodel, V.R. Shaginyan, in *Condensed Matter Theories*, vol. 12, ed. by J. Clark, V. Plant (Nova Science Publishers Inc., New York, 1997), p. 221
31. S.A. Artamonov, V.R. Shaginyan, JETP **92**, 287 (2001)
32. P.V. Bogdanov, A. Lanzara, S.A. Kellar, X.J. Zhou, E.D. Lu, W.J. Zheng, G. Gu, J.I. Shimoyama, K. Kishio, H. Ikeda, R. Yoshizaki, Z. Hussain, Z.X. Shen, Phys. Rev. Lett. **85**, 2581 (2000)
33. J.D. Koralek, J.F. Douglas, N.C. Plumb, Z. Sun, A.V. Fedorov, M.M. Murnane, H.C. Kapteyn, S.T. Cundiff, Y. Aiura, K. Oka, H. Eisaki, D.S. Dessau, Phys. Rev. Lett. **96**, 017005 (2006)
34. A. Kaminski, M. Randeria, J.C. Campuzano, M.R. Norman, H. Fretwell, J. Mesot, T. Sato, T. Takahashi, K. Kadowaki, Phys. Rev. Lett. **86**, 1070 (2001)
35. T. Valla, A.V. Fedorov, P.D. Johnson, B.O. Wells, S.L. Hulbert, Q. Li, G.D. Gu, N. Koshizuka, Science **285**, 2110 (1999)
36. T. Valla, A.V. Fedorov, P.D. Johnson, Q. Li, G.D. Gu, N. Koshizuka, Phys. Rev. Lett. **85**, 828 (2000)
37. V.R. Shaginyan, M.Y. Amusia, K.G. Popov, Phys. Lett. A **373**, 2281 (2009)
38. D. Takahashi, S. Abe, H. Mizuno, D. Tayurskii, K. Matsumoto, H. Suzuki, Y. Onuki, Phys. Rev. B **67**, 180407(R) (2003)
39. P. Gegenwart, J. Custers, C. Geibel, K. Neumaier, K.T.T. Tayama, O. Trovarelli, F. Steglich, Phys. Rev. Lett. **89**, 056402 (2002)
40. P. Coleman, C. Pépin, Q. Si, R. Ramazashvili, J. Phys. Condens. Matter **13**, R723 (2001)
41. V.A. Khodel, JETP Lett. **86**, 721 (2007)
42. A.V. Chubukov, V.M. Galitski, V.M. Yakovenko, Phys. Rev. Lett. **94**, 046404 (2005)
43. A.A. Abrikosov, L.P. Gorkov, I.E. Dzyaloshinski, *Methods of Quantum Field Theory in Statistical Physics* (Dover, New York, 1975)
44. D. Yudin, D. Hirschmeier, H. Hafermann, O. Eriksson, A.I. Lichtenstein, M.I. Katsnelson, Phys. Rev. Lett. **112**, 070403 (2014)
45. A.B. Migdal, *Theory of Finite Fermi Systems and Applications to Atomic Nuclei* (Wiley, New York, 1967)

Chapter 4
The Topological Phase Transitions Related to Fermion Condensate

Abstract In this chapter, we consider so-called topological phase transitions, taking place in normal Fermi liquid. In other words, here we are dealing with different instabilities of normal Fermi liquids relative to several kinds of perturbations of initial quasiparticle spectrum $\varepsilon(p)$ and occupation numbers $n(p)$ associated with the emergence of a multi-connected Fermi surface. Depending on the parameters and analytical properties of the Landau interaction, such instabilities lead to several possible types of restructuring of initial Landau Fermi liquid ground state. This restructuring generates topologically distinct phases. One of them is the FC discussed above, another one belongs to a class of topological transitions (TT) and will be called "iceberg" phase, where the sequence of rectangles ("icebergs") $n(p) = 0$ and $n(p) = 1$ is realized at $T = 0$. At elevated temperatures the "icebergs melt down" and the behavior of the system becomes similar to that with the fermion condensate.

4.1 Topological Phase Transitions Related to FCQPT

In Chap. 3, we have investigated the structure of the Fermi surface beyond FCQPT within the extended quasiparticle paradigm. We have shown that at $T = 0$ there is a scenario that entails the formation of FC, manifested by the emergence of a completely flat portion of the single-particle spectrum. On the other hand, there are different kinds of instabilities related to the emergence of a multi-connected Fermi surface, see e.g., [1–7]. In such considerations, we analyze stability of a model fermion system with repulsive Landau interaction allowing to carry out an analytical studies of the emergence of a multi-connected Fermi surface [2, 3]. We show, in particular, that the Landau interaction given by the screened Coulomb law does not generate FC phase, but rather "iceberg" TT phase. For this model, we plot a phase diagram in the variables "screening parameter—coupling constant" displaying two kinds of TT: a 5/2-kind similar to the known Lifshitz transitions in metals, and a 2-kind characteristic for a uniform strongly interacting system. The Lifshitz transitions are topological transitions of the Fermi surface with no symmetry breaking [8].

The common ground state of isotropic LFL with density ρ_x is described at zero temperature by the stepwise Fermi function $n_F(p) = \theta(p_F - p)$, dropping discontinuously from 1 to 0 at the Fermi momentum p_F. The LFL theory states that

M.Y. Amusia et al., *Theory of Heavy-Fermion Compounds*, Springer Series in Solid-State Sciences 182, DOI 10.1007/978-3-319-10825-4_4

the quasiparticle distribution function $n(p)$ and its single particle spectrum $\varepsilon(p)$ are in all but name similar to those of an ideal Fermi gas with the substitution of real fermion mass m by the effective one M^*. These $n_F(p)$ and $\varepsilon(p)$ can become unstable under several circumstances. The best known example is Cooper pairing at arbitrarily weak attractive interaction with subsequent formation of the pair condensate and gapped quasiparticle spectrum [9]. However, a sufficiently strong repulsive Landau interaction can also generate non-trivial ground states. The first example of such restructuring for a Fermi system with model repulsive interaction is FC [10]. It reveals the existence of a critical value $\alpha_{\rm cr}$ of the interaction constant α such that at $\alpha = \alpha_{\rm cr}$ the stability criterion $s(p) = (\varepsilon(p) - E_F)/(p^2 - p_F^2) > 0$ fails at the Fermi surface $s(p_F) = 0$ (p_F-instability). We recall that in the case of this instability the single particle spectrum $\varepsilon(p)$ possesses the inflection point at the Fermi surface, see Sect. 6.3.1. Then at $\alpha > \alpha_{\rm cr}$ an exact solution of a variational equation for $n(p)$, following from the Landau functional $E(n(p))$ (2.15) (see also (4.1) below), can be found. This solution exhibits some finite interval $p_f - p_i$ (indices "f" and "i" stand for "final" and "initial" respectively) around p_F where the distribution function $n(p)$ varies continuously taking intermediate values between 1 and 0, while the single-particle excitation spectrum $\varepsilon(p)$ has a flat plateau. Equation (3.1) means actually that the roots of the equation $\varepsilon(p) = \mu$ form an uncountable set in the range $p_i \le p \le p_f$, see Fig. 4.1. It is seen from (3.1) that the occupation numbers $n(p)$ become variational parameters, deviating from the Fermi step function to minimize the energy E.

The other type of phase transition, corresponding to the so-called iceberg phase occurs when the equation $\varepsilon(p) = \mu$ has discrete countable number of roots, either

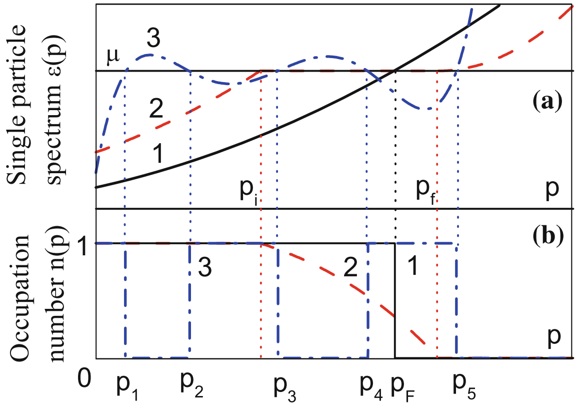

Fig. 4.1 Schematic plot of the single particle spectrum $\varepsilon(p)$ (**a**) and occupation numbers $n(p)$ (**b**), corresponding to LFL (curves 1), FC (curves 2, *dashed line*) and iceberg (curves 3, *dot-dashed line*) phases at $T = 0$. For LFL the equation, $\varepsilon(p) = \mu$, has a single root equal to Fermi momentum p_F. For iceberg phase, the above equation has countable set of the roots $p_1 ... p_N ...$, for FC phase the roots occupy the whole segment $(p_f - p_i)$. We note that $p_i < p_F < p_f$ and the states, where $\varepsilon(p) < \mu$ are occupied (n = 1), while those with $\varepsilon(p) > \mu$ are empty (n = 0)

finite or infinite. This is depicted in Fig. 4.1, and related to the situation when the Fermi surface becomes multi-connected. Note that the idea of multi-connected Fermi surface, with the production of new, interior segments, had already been considered [4–6].

Let us take the Landau functional $E(n(p))$ in the form

$$E(n(p)) = \int \frac{p^2}{2M} n(p) \frac{d\mathbf{p}}{(2\pi)^3} + \frac{1}{2} \int \int n(p) U(|\mathbf{p} - \mathbf{p}'|) n(p') \frac{d\mathbf{p} d\mathbf{p}'}{(2\pi)^6}, \tag{4.1}$$

which, by virtue of (2.3), leads to the following quasiparticles dispersion law:

$$\varepsilon(p) = \frac{p^2}{2M} + \int U(|\mathbf{p} - \mathbf{p}'|) n(p') \frac{d\mathbf{p}'}{(2\pi)^3}. \tag{4.2}$$

The angular integration with subsequent passing to the dimensionless variables $x = p/p_F$, $y = y(x) = 2M\varepsilon(p)/p_F^2$, $z = 2\pi^2 ME/p_F^5$, leads to simplification of the (4.1) and (4.2)

$$z[\nu(x)] = \int [x^4 + \frac{1}{2} x^2 V(x)] \nu(x) dx, \tag{4.3}$$

$$y(x) = x^2 + V(x), \tag{4.4}$$

where

$$V(x) = \frac{1}{x} \int x' \nu(x') u(x, x') dx',$$
$$u(x, x') = \frac{M}{\pi^2 p_F} \int\limits_{|x-x'|}^{x+x'} u(t) t dt. \tag{4.5}$$

In this chapter, we do not mention the renormalization constant z, and use z as the dimensional variable. Here $u(x) \equiv U(p_F x)$ and the distribution function $\nu(x) \equiv n(p_F x)$ is positive, obeys the normalization condition

$$\int x^2 \nu(x) dx = 1/3, \tag{4.6}$$

and the Pauli principle limitation $\nu(x) \leq 1$. The latter can be lifted using, e.g., the ansatz: $\nu(x) = [1 + \tanh \eta(x)]/2$. In the latter case the system ground state gives a minimum to the functional

$$f[\eta(x)] = \int [1 + \tanh \eta(x)] \Big\{ x^4 - \mu x^2 + x'[1 + \tanh \eta(x')] u(x, x') dx' \Big\} dx, \tag{4.7}$$

containing a Lagrange multiplier μ, with respect to an arbitrary variation of the auxiliary function $\eta(x)$. This allows to represent the necessary condition of extremum $\delta f = 0$ in the form

$$x^2 \nu(x)[1 - \nu(x)][y(x) - \mu] = 0. \tag{4.8}$$

This means that either $\nu(x)$ takes only the values 0 and 1 or the dispersion law is flat: $y(x) = \mu$ [10], in accordance with (3.1). The former possibility corresponds to iceberg phase, while the latter to FC. As it is seen from (3.1), the spectrum $\varepsilon(p)$ in this case cannot be an analytic function of complex p in any open domain, containing the FC interval $(p_f - p_i)$. In fact, all the derivatives of $\varepsilon(p)$ with respect to p along the strip $(p_f - p_i)$ should be zero, while this is not the case outside $(p_f - p_i)$. For instance, in the FC model with $U(p) = U_0/p$ [10] the kernel, (4.5), is nonanalytic

$$u(x, x') = \frac{MU_0}{\pi^2 p_F}(x + x' + |x - x'|), \tag{4.9}$$

which eventually causes nonanalyticity of the potential $V(x)$. It follows from (4.4), that the single particle spectrum is an analytic function on the whole real axis if $V(x)$ is such a function. In this case FC is forbidden and the only alternative to the Fermi ground state (if the stability criterion gets broken) is iceberg phase corresponding to TT between the topologically unequal states with $\nu(x) = 0, 1$ [11].

On the other hand, applying the technique of Poincaré mapping, it is possible to analyze the sequence of iterative maps generated by (2.14) for the single-particle spectrum at zero temperature [1]. If the sequence of maps converges, the multi-connected Fermi surface is formed. If it fails to converge, the Fermi surface swells into a volume that provides a measure of entropy associated with the formation of an exceptional state of the system characterized by partial occupation of single-particle states and dispersion of their spectrum proportional to temperature as seen from (3.12).

Generally, all such states related to the formation of iceberg phases are classified by the indices of connectedness (known as Betti numbers in algebraic topology [12, 13]) for the support of $\nu(x)$. In fact, for an isotropic system, these numbers simply count the separate (concentric) segments of the Fermi surface. Then the system ground state corresponds to the following multi-connected distribution shown in Fig. 4.2

$$\nu(x) = \sum_{i=1}^{n} \theta(x - x_{2i-1})\theta(x_{2i} - x), \tag{4.10}$$

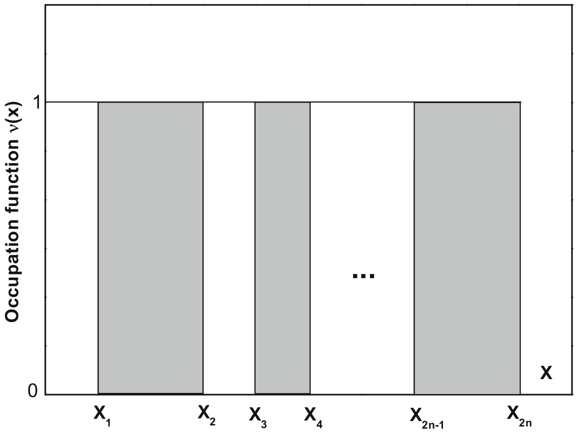

Fig. 4.2 Occupation function for a multiconnected distribution

where the parameters $0 \leq x_1 < x_2 < \cdots < x_{2n}$ obey the normalization condition

$$\sum_{i=1}^{n}(x_{2i}^3 - x_{2i-1}^3) = 1. \tag{4.11}$$

The function z, (4.3),

$$z = \frac{1}{2}\sum_{i=1}^{n}\int\limits_{x_{2i-1}}^{x_{2i}} x^2[x^2 + y(x)]dx, \tag{4.12}$$

has the absolute minimum with respect to $x_1, \ldots, x_{2n-1}$ and to $n \geq 1$. To obtain the necessary condition of extremum, we use the relations

$$\frac{\partial x_{2n}}{\partial x_k} = (-1)^{k-1}\left(\frac{x_k}{x_{2n}}\right)^2, \quad 1 \leq k \leq 2n-1, \tag{4.13}$$

following from (4.11) and the dependence of the potential $V(x)$ in the dispersion law $y(x)$ on the parameters $x_1, \ldots, x_{2n-1}$

$$V(x) = \frac{1}{x}\sum_{i=1}^{n}\int\limits_{x_{2i-1}}^{x_{2i}} x' u(x, x')dx'. \tag{4.14}$$

The differentiation of (4.12) with respect to the parameters $x_1, \ldots, x_{2n-1}$ with subsequent use of (4.13) and (4.14) yield the necessary conditions of extremum in the following form

$$\frac{\partial z}{\partial x_k} = (-1)^k x_k^2 [y(x_k) - y(x_{2n})] = 0, \quad 1 \le k \le 2n - 1. \tag{4.15}$$

This means that a multi-connected ground state is controlled by the evident rule of unique Fermi level $y(x_k) = y(x_{2n})$ for all $1 \le k \le 2n - 1$ (except for $x_1 = 0$). In principle, given the dispersion law $y(x)$, all the $2n - 1$ unknown parameters x_k can be found from (4.15). Then, the sufficient stability conditions $\partial^2 z/\partial x_i \partial x_j = \gamma_i \delta_{ij}$, $\gamma_i > 0$ yield the generalized stability criterion. Namely, the dimensionless function

$$\sigma(x) = 2Ms(p) = \frac{y(x) - y\,(x_{2n})}{x^2 - x_{2n}^2}, \tag{4.16}$$

should be positive within filled and negative within empty intervals, turning to zero at their boundaries in accordance with (4.15). It can be proved rigorously that, for given analytic kernel $u(x, x')$, (4.16) defines the system ground state uniquely.

Subsequently, we shall label each multi-connected state, (4.10), by an integer number related to the binary sequence of empty and filled intervals read from x_{2n} to 0. Thus, the Fermi state with a single filled interval ($x_2 = 1, x_1 = 0$) reads as unity, the state with a void at the origin (filled $[x_2, x_1]$ and empty $[x_1, 0]$) reads as $(10) = 2$, the state with a single gap: $(101) = 3$, etc. Note that all even phases have a void at the origin and odd phases have not.

For free fermions $V(x) = 0$, $y(x) = x^2$, (4.15) only yields the trivial solution corresponding to the Fermi state 1. To obtain non-trivial realizations of TT, we choose $U(p)$ to correspond to the common screened Coulomb potential:

$$U(p) = \frac{4\pi e^2}{p^2 + p_0^2}. \tag{4.17}$$

The related explicit form of the kernel,

$$u(x, x') = \alpha \ln \frac{(x + x')^2 + x_0^2}{(x - x')^2 + x_0^2}, \tag{4.18}$$

with the dimensionless screening parameter $x_0 = p_0/p_F$ and the coupling constant $\alpha = 2Me^2/\pi p_F$, evidently displays the necessary analytical properties for existence of iceberg phase. Equations (4.14) and (4.18) permit to express the potential $V(x)$ in elementary functions [2]. Then, the straightforward analysis of (4.15) shows that its nontrivial solutions appear only when the coupling parameter α exceeds a certain critical value α^*. This corresponds to the situation when the stability criterion [10] $\sigma(x) = (y_F(1) - y_F(x))/(1 - x^2) > 0$ calculated with the Fermi distribution, $y_F(x) = x^2 + V(x; 0, 1)$, fails in a certain point $0 \le x_i < 1$ within the Fermi sphere: $\sigma(x_i) \to 0$. There are two different types of such instabilities depending on the screening parameter x_0 (Fig. 4.3). For x_0 below a certain threshold value $x_{\text{th}} \approx 0.32365$ (weak screening regime, WSR) the instability point x_i sets rather close to the Fermi surface: $1 - x_i \ll 1$, while it drops abruptly to zero at $x_0 \to x_{\text{th}}$ and equals zero

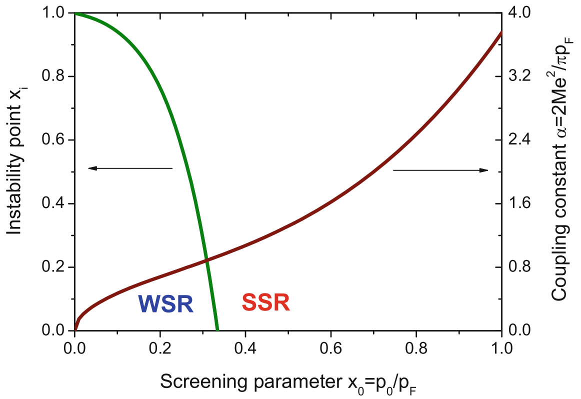

Fig. 4.3 Instability point x_i and critical coupling α^* as functions of screening. The regions of weak screening (WSR) and strong screening (SSR) are separated by the threshold value x_{th}. Note that a x_{th}, α_{th} is the triple point between the phases 1, 2, 3 in Fig. 4.4

for all $x_0 > x_{\text{th}}$ (strong screening regime, SSR). The critical coupling $\alpha^*(x_0)$ results in a monotonously growing function of x_0 with the asymptotics $\alpha^* \approx (\ln 2/x_0 - 1)^{-1}$ at $x_0 \to 0$ and staying analytic at $\alpha_{\text{th}} = \alpha^*(x_{\text{th}}) \approx 0.91535$, where it only exhibits an inflection point.

These two types of instabilities give rise to different types of TT from the state 1 at $\alpha > \alpha^*$: at SSR a void appears around $x = 0$ ($1 \to 2$ transition), and at WSR a gap opens around x_i ($1 \to 3$ transition). Further analysis of (4.15) shows that the point $x_{\text{th}}, \alpha_{\text{th}}$ represents a triple point in the phase diagram in the variables x_0, α (Fig. 4.3) where the phases 1, 2, and 3 meet one another. Similarly to the onset of instability in the Fermi state 1, each evolution of TT to higher order phases with growing α is manifested by a zero of $\sigma(x)$, (4.16), at some point $0 \le x_i < x_{2n}$ different from the existing interfaces. If this occurs at the very origin, $x_i = 0$, the phase number rises at TT by 1, corresponding to the opening of a void (passing from odd to even phase) or to emerging "island" (even $\to$ odd). For $x_i > 0$, either a thin spherical gap opens within a filled region or a thin filled spherical sheet emerges within a gap, so that the phase number rises by 2, living the parity unaltered. A part of the whole diagram shown in Fig. 4.4 demonstrates that with decreasing of x_0 (screening weakening) all even phases terminate at certain triple points. This, in particular, agrees with numerical studies of the considered model along the line $x_0 = 0.07$ at growing α [6], where only the sequence of odd phases $1 \to 3 \to 5 \to \ldots$ has been revealed (shown by the arrow in Fig. 4.3). The energy gain $\Delta(\tau_a)$ at TT as a function of small parameter $\tau_a = \alpha/\alpha^* - 1$ is evidently proportional to τ_a times the volume of a new emerging phase region (empty or filled). Introducing a void radius δ and expanding the energy gain $\Delta(\delta) = z[n(x,\delta)] - z[n_F(x)]$ in δ, one gets $\Delta = -\beta_1\tau_a\delta^3 + \beta_2\delta^5 + O(\delta^6)$, $\beta_1, \beta_2 > 0$. As a result, the optimum void radius is $\delta \sim \sqrt{\tau_a}$. Consequently we have $\Delta(\tau_a) \sim \tau_a^{5/2}$ indicating a resemblance to the known "${}^5/_2$-kind" phase transitions in the theory of metals [12]. The peculiar feature of our situation is that the new segment

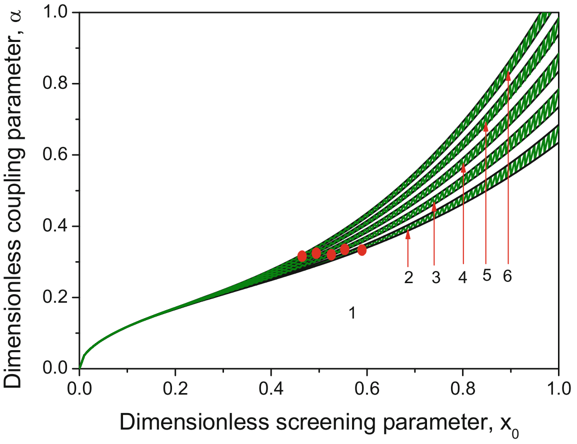

Fig. 4.4 Phase diagram in "screening-coupling" variables. Each phase with certain topology is labeled by the total number of filled and empty regions (see Fig. 4.2). Even phases (*shaded*) are separated from odd ones by "$^5/_2$-kind" topological transition (TT) lines, while odd phases are separated from each other by TT lines of 2 (second) kind odd phases. Triple points, where two $^5/_2$-TT and one 2-TT meet, are shown by *circles*

of the Fermi surface opens at very small momentum values, which can dramatically change the system response to, e.g., electron-phonon interaction. On the other hand, this segment may have a pronounced effect on the thermodynamical properties of ^{3}He at low temperatures, especially in the case of P-pairing, producing excitations with extremely small momenta.

For a TT with unchanged parity, the width of a gap (or a sheet) is found to be $\sim \tau_a$ so that the energy gain is $\Delta(\tau_a) \sim \tau_a^2$ and such TT can be related to the second kind. It follows from the above consideration that each triple point in the $x_0 - \alpha$ phase diagram is a point of confluence of two $^5/_2$-kind TT lines into one 2-kind line. The latter type of TT has already been discussed in the literature [4, 6]. Here we only mention that its occurrence on a whole continuous surface in the momentum space is rather specific for the systems with strong fermion-fermion interaction, while the known TT's in metals, under the effects of crystalline field, occur typically at separate points in the quasi-momentum space. It is interesting to note that in the limit $x_0 \to 0, \alpha \to 0$, reached along the line $\alpha = kx_0$, we attain the exactly solvable model: $U(p) \to (2\pi)^3 U_0 \delta(p)$ with $U_0 = k/(2Mp_F)$, which is known to display FC for all $U_0 > 0$ [10]. The analytic mechanism of this behavior is the disappearance of the poles of $U(p)$, (4.17), as $p_0 \to 0$, restoring the analytical properties necessary for FC. Otherwise, the FC regime corresponds to the phase order $\to \infty$, when the density of infinitely thin filled (separated by empty) regions approaches some continuous function $0 < \nu(x) < 1$ [6] and the dispersion law turns flat according to (4.15). Several remarks should be made at this point.

First, when the dispersion law starts to turn flat, the system of icebergs can transform into the FC state due to some admixture of a non-analytical interaction. In fact, even in the absence of such an admixture the difference in the energy between the ground state with FC and one with the system of icebergs is negligibly small. Therefore, at lowering temperature the system is "wandering" in the energy landscape trying to find the absolute minimum of its energy. We speculate that in such a case some of HF compounds can exhibit the dynamics of glasses when the dynamics is strongly suppressed becoming very slow down.

Second, the considered model formally treats x_0 and α as independent parameters, though in fact a certain relation between them can be imposed. Under such restriction, the system ground state should depend on a single parameter, say the particle density ρ_x, along a certain trajectory $\alpha(x_0)$ in the above phase diagram. For instance, with the simplest Thomas-Fermi relation for a free electron gas $\alpha(x_0) = x_0^2/2$, this trajectory stays fully within the Fermi state 1 over all the physically reasonable range of densities. Hence a faster growth of $\alpha(x_0)$ is necessary for realization of TT in any fermionic system with the interaction (4.17).

Third, at increasing temperatures, the stepwise form of the quasiparticle distribution is smearing. We call this the melting of icebergs. Therefore, as temperature moves away from zero, the concentric Fermi spheres are taken up by FC. In fact, these arguments do not work in the case of a few icebergs. Thus, it is quite possible to observe the two separate Fermi sphere regimes related to the FC and iceberg states.

There is a good reason to mention that neither in the FC phase nor in the other TT phases, the standard Kohn-Sham scheme [14, 15] is no longer valid. This is because in the systems with FC or TT phase transitions the occupation numbers of quasiparticles are indeed variational parameters. Thus, to get a reasonable description of the system, one has to consider the ground state energy as a functional of the occupation numbers $E[(n(p)]$ rather than a functional of the density $E[\rho_x]$ [16–18].

References

1. V.A. Khodel, J.W. Clark, M.V. Zverev, Phys. Rev. B **78**, 075120 (2008)
2. S.A. Artamonov, Y.G. Pogorelov, V.R. Shaginyan, JETP Lett. **68**, 942 (1998)
3. Y.G. Pogorelov, V.R. Shaginyan, in *Condensed Matter Theories*, vol. 18 (Nova Science Publishers Inc., NY, 2003), p. 191
4. M. de Llano, J.P. Vary, Phys. Rev. C **19**, 1083 (1979)
5. M. de Llano, A. Plastino, J.P. Zabolitsky, Phys. Rev. C **20**, 2418 (1979)
6. M.V. Zverev, M. Baldo, J. Phys. Condens. Matter **11**, 2059 (1999)
7. M.V. Zverev, M. Baldo, JETP **87**, 1129 (1998)
8. I.M. Lifshitz, Sov. Phys. JETP **11**, 130 (1960)
9. J. Bardeen, L.N. Cooper, J.R. Schrieffer, Phys. Rev. **108**, 1175 (1957)
10. V.A. Khodel, V.R. Shaginyan, JETP Lett. **51**, 553 (1990)
11. G.E. Volovik, JETP Lett. **53**, 222 (1991)
12. I.M. Lifshitz, Sov. Phys. JETP **11**, 1130 (1960)
13. M. Nakahara, *Geometry, Topology and physics* (IOP Publishing, Bristol, 1990)
14. W. Kohn, L.J. Sham, Phys. Rev. **140**, A1133 (1965)

15. W. Kohn, P. Vashishta, in *Theory of the Inhomogeneous Electron Gas*, ed. by S. Lundqvist, N. March (Plenum, New York, 1983)
16. V.R. Shaginyan, Phys. Lett. A **249**, 237 (1998)
17. M.Y. Amusia, V.R. Shaginyan, Phys. Lett. A **269**, 337 (2000)
18. V.R. Shaginyan, JETP Lett. **68**, 527 (1998)

Chapter 5
Appearance of Fermion-Condensation Quantum Phase Transition in Fermi Systems

Abstract As high-T_c superconductors are represented primarily by 2D layered structures, in Sect. 5.1 we discuss the superconducting state of a 2D liquid of heavy electrons, and within the framework of Gor'kov microscopic equations construct the Green functions of the FC state. On the other hand, our study can easily be generalized to the 3D case. To show that there is no fundamental difference between the 2D and 3D cases, we derive Green's functions for the 3D case in Sect. 5.1.1. In Sect. 5.2, we consider the dispersion law and lineshape of single-particle excitations. Section 5.3 is devoted to the behavior of heavy-electron liquid with FC in magnetic field. In Sect. 5.4, we analyze conditions which lead to the emergence of FC in Fermi systems composed of different fermions such as atoms of ^{3}He and electrons.

5.1 The Superconducting State with FC at $T = 0$

As we have seen in Sect. 3.1.1, the ground-state energy $E_{gs}(\kappa(\mathbf{p}), n(\mathbf{p}))$ of a 2D electron liquid is a functional of the superconducting order parameter $\kappa(\mathbf{p})$ and of the quasiparticle occupation numbers $n(\mathbf{p})$. This energy is determined by the well-known Bardeen-Cooper-Schrieffer (BCS) equations and in the weak-coupling superconductivity theory is given by [1–3]

$$E_{gs}(\kappa(\mathbf{p}), n(\mathbf{p})) = E(n(\mathbf{p})) + \lambda_0 \int V(\mathbf{p}_1, \mathbf{p}_2) \times \kappa(\mathbf{p}_1)\kappa^*(\mathbf{p}_2)\frac{d\mathbf{p}_1 d\mathbf{p}_2}{(2\pi)^4}. \tag{5.1}$$

Here

$$\kappa(\mathbf{p}) = \sqrt{n(\mathbf{p})(1 - n(\mathbf{p}))} \tag{5.2}$$

with $n(\mathbf{p}) = v^2(\mathbf{p})$, $u(\mathbf{p})$ and $v(\mathbf{p})$ are parameters of the Bogolubov transformation, which obey for fermions the normalization rule $v^2(\mathbf{p}) + u^2(\mathbf{p}) = 1$. It is assumed that the constant λ_0, which determines the magnitude of the pairing interaction $\lambda_0 V(\mathbf{p}_1, \mathbf{p}_2)$, is small. The superconducting gap is then defined

M.Y. Amusia et al., *Theory of Heavy-Fermion Compounds*, Springer Series
in Solid-State Sciences 182, DOI 10.1007/978-3-319-10825-4_5

$$\Delta(\mathbf{p}) = -\lambda_0 \int V(\mathbf{p}, \mathbf{p}_1)\kappa(\mathbf{p}_1)\frac{d\mathbf{p}_1}{4\pi^2}. \tag{5.3}$$

The (5.2) shows that the order parameter $\kappa(\mathbf{p})$ can be expressed equally well through coefficient $v(\mathbf{p})$ of the corresponding Bogolyubov transformation. Latter fact shows that the energy E_{gs} in (5.1) is a functional of $v(\mathbf{p})$. Minimizing this energy in $v(\mathbf{p})$ and using (5.3), we arrive at equations that relate the single-particle energy $\varepsilon(\mathbf{p})$ to $\Delta(\mathbf{p})$ and $E(\mathbf{p})$

$$\varepsilon(\mathbf{p}) - \mu = \Delta(\mathbf{p})\frac{1 - 2v^2(\mathbf{p})}{2\kappa(\mathbf{p})}, \quad \frac{\Delta(\mathbf{p})}{E(\mathbf{p})} = 2\kappa(\mathbf{p}). \tag{5.4}$$

Here the single-particle energy $\varepsilon(\mathbf{p})$ is determined by (2.3), and

$$E(\mathbf{p}) = \sqrt{\xi^2(\mathbf{p}) + \Delta^2(\mathbf{p})} \tag{5.5}$$

with $\xi(\mathbf{p}) = \varepsilon(\mathbf{p}) - \mu$. Substituting the expression for $\kappa(\mathbf{p})$ from (5.4) in (5.3), we obtain the well-known equation for $\Delta(\mathbf{p})$ of the BCS theory

$$\Delta(\mathbf{p}) = -\frac{\lambda_0}{2} \int V(\mathbf{p}, \mathbf{p}_1)\frac{\Delta(\mathbf{p}_1)}{E(\mathbf{p}_1)}\frac{d\mathbf{p}_1}{4\pi^2}. \tag{5.6}$$

As $\lambda_0 \to 0$, the maximum value Δ_1 of the superconducting gap $\Delta(\mathbf{p})$ tends to zero and each equation in (5.4) reduces to (3.1)

$$\frac{\delta E(n(\mathbf{p}))}{\delta n(\mathbf{p})} = \varepsilon(\mathbf{p}) - \mu = 0, \tag{5.7}$$

if $0 < n(\mathbf{p}) < 1$, or $\kappa(\mathbf{p}) \neq 0$, in the interval $p_i \leq p \leq p_f$. Equation (5.7) shows that the function $n_0(\mathbf{p})$ is determined from the solution of the standard problem of functional $E(n(\mathbf{p}))$ minimization [4–6]. Equation (5.7) specifies the quasiparticle distribution function $n_0(\mathbf{p})$ that ensures the minimum of the ground-state energy $E(\kappa(\mathbf{p}), n(\mathbf{p}))$. We can now study the relation between the state specified by (5.7) or (3.1) and the superconducting state.

At $T = 0$, (5.7) determines the specific state of a Fermi liquid with FC, the state for which the absolute value of the order parameter $|\kappa(\mathbf{p})|$ is finite in the momentum interval $p_i \leq p \leq p_f$ as $\Delta_1 \to 0$. Such a state can be considered superconducting with an infinitely small value of Δ_1. Hence, the entropy of this state at $T = 0$ is zero. Solutions $n_0(\mathbf{p})$ of (5.7) constitute a new class of solutions of both the BCS equations and the Landau Fermi-liquid equations. In contrast to the ordinary solutions of the BCS equations [2], the new solutions are characterized by an infinitely small superconducting gap $\Delta_1 \to 0$, with the order parameter $\kappa(\mathbf{p})$ remaining finite. On the other hand, in contrast to the standard solution of the Landau Fermi-liquid theory, the new solutions $n_0(\mathbf{p})$ determine the state of a heavy-electron liquid with a finite entropy S_0 as $T \to 0$ (see (3.8)). We arrive at an important conclusion that the solutions of (5.7) can be interpreted as the simultaneous general solutions of the BCS equations and the Landau Fermi-liquid theory equations, while (5.7) by itself can be derived either from the BCS theory or from the Landau Fermi-liquid theory. Thus, as it is shown in Sect. 3.1.1, both states of the system coexist at $T \to 0$. As the system passes into a state with the order parameter $\kappa(\mathbf{p})$, the entropy vanishes abruptly and the system undergoes the first-order transition. In vicinity of this point, the critical quantum and thermal fluctuations are suppressed so that the quasiparticles remain well-defined excitations (see also Chap. 8). It follows from (3.2) that FCQPT is related to a change in the topological structure of the Green's function and belongs to Lifshitz's topological phase transitions, which occur at absolute zero temperature [7]. This fact sets a relation between FCQPT and quantum phase transitions, under which the Fermi sphere splits into a sequence of Fermi layers [8, 9] (see Sects. 5.3 and 4.1). We note that in the state with the order parameter $\kappa(\mathbf{p})$, the system entropy $S = 0$ and the Nernst theorem holds in systems with FC.

If $\lambda_0 \neq 0$, the gap Δ_1 becomes finite, leading to a finite value of the effective mass M^*_{FC}, which may be obtained from (5.4) by differentiation its both sides over the momentum p with subsequent using of (2.6) [10–13]:

$$M^*_{FC} \simeq p_F \frac{p_f - p_i}{2\Delta_1}. \tag{5.8}$$

It follows from (5.8) that in the superconducting state the effective mass is always finite. Its energy scale is determined by the parameter E_0:

$$E_0 = \varepsilon(\mathbf{p}_f) - \varepsilon(\mathbf{p}_i) \simeq p_F \frac{(p_f - p_i)}{M^*_{FC}} \simeq 2\Delta_1. \tag{5.9}$$

5.1.1 Green's Function of the Superconducting State with FC at T = 0

We begin with the Gor'kov equations [14], determining the Green's functions $F^+(\mathbf{p},\omega)$ and $G(\mathbf{p},\omega)$ of a superconductor (see, e.g., [15]). For 3D case they read:

$$\begin{aligned} F^+ &= \frac{-\lambda_0 \Xi^*}{(\omega - E(\mathbf{p}) + i\,0)(\omega + E(\mathbf{p}) - i\,0)}; \\ G &= \frac{u^2(\mathbf{p})}{\omega - E(\mathbf{p}) + i\,0} + \frac{v^2(\mathbf{p})}{\omega + E(\mathbf{p}) - i\,0}, \end{aligned} \tag{5.10}$$

The gap Δ and the function Ξ are given by

$$\Delta = \lambda_0 |\Xi|, \quad i\Xi = \int \int_{-\infty}^{\infty} F^+(\mathbf{p},\omega) \frac{d\omega d\mathbf{p}}{(2\pi)^4}. \tag{5.11}$$

We recall that the function $F^+(\mathbf{p},\omega)$ has the meaning of the wave function of Cooper pairs and Ξ is the wave function of the motion of these pairs as a whole and is just a constant in a homogeneous system [15]. It follows from (5.4) and (5.11) that

$$i\Xi = \int_{-\infty}^{\infty} F_0^+(\mathbf{p},\omega)\frac{d\omega d\mathbf{p}}{(2\pi)^4} = i\int \kappa(\mathbf{p})\frac{d\mathbf{p}}{(2\pi)^3}. \tag{5.12}$$

With respect to (5.11) and (5.4), the (5.10) assume the form

$$\begin{aligned} F^+ &= -\frac{\kappa(\mathbf{p})}{\omega - E(\mathbf{p}) + i\,0} + \frac{\kappa(\mathbf{p})}{\omega + E(\mathbf{p}) - i\,0}; \\ G &= \frac{u^2(\mathbf{p})}{\omega - E(\mathbf{p}) + i\,0} + \frac{v^2(\mathbf{p})}{\omega + E(\mathbf{p}) - i\,0}. \end{aligned} \tag{5.13}$$

As $\lambda_0 \to 0$, the gap $\Delta \to 0$, but Ξ and $\kappa(\mathbf{p})$ remain finite if the spectrum becomes flat, $E(\mathbf{p}) = 0$, and (5.13) lead

$$\begin{aligned} F^+(\mathbf{p},\omega) &= -\kappa(\mathbf{p})\left[\frac{1}{\omega + i\,0} - \frac{1}{\omega - i\,0}\right]; \\ G(\mathbf{p},\omega) &= \frac{u^2(\mathbf{p})}{\omega + i\,0} + \frac{v^2(\mathbf{p})}{\omega - i\,0}. \end{aligned} \tag{5.14}$$

in the interval $p_i \le p \le p_f$. The parameters $v(\mathbf{p})$ and $u(\mathbf{p})$ are determined by the condition that the spectrum should be flat: $\varepsilon(\mathbf{p}) = \mu$. With respect to Landau equation (2.3), this condition again reduces to (3.1) and (5.7) for minimum of the functional $E(n(\mathbf{p}))$.

We construct the functions $F^+(\mathbf{p},\omega)$ and $G(\mathbf{p},\omega)$ in the case where the constant λ_0 is finite, but small, namely that $v(\mathbf{p})$ and $\kappa(\mathbf{p})$ can be found on the basis of the FC solutions of (3.1). Then $\kappa(\mathbf{p})$, Ξ, $E(\mathbf{p})$ and Δ are given by (5.2), (5.12), (5.11) and (5.4) respectively. Substituting the functions constructed in this manner into (5.13), we obtain $F^+(\mathbf{p},\omega)$ and $G(\mathbf{p},\omega)$ [16]. We note that (5.11) imply that the gap Δ is a linear function of λ_0 under the adopted conditions. As we shall see in Sect. 5.1.2, this gives rise to high-T_c at common values of the superconducting coupling constant.

5.1.2 The Superconducting State at Finite Temperatures

We assume that the region occupied by FC is small: $(p_f - p_i)/p_F \ll 1$ and $\Delta_1 \ll T_f$. Then, the order parameter $\kappa(\mathbf{p})$ is determined primarily by FC, i.e., the distribution function $n_0(\mathbf{p})$ [10–12]. To be able to solve (5.6) analytically, we adopt the BCS approximation for the interaction [2]: $\lambda_0 V(\mathbf{p},\mathbf{p}_1) = -\lambda_0$ if $|\varepsilon(\mathbf{p}) - \mu| \le \omega_D$ and the interaction is zero outside this region, with ω_D being a certain characteristic energy, proportional to the Debye temperature. As a result, the superconducting gap depends only on the temperature, $\Delta(\mathbf{p}) = \Delta_1(T)$ and (5.6) becomes

$$1 = N_{FC}\lambda_0 \int\limits_0^{E_0/2} \frac{d\xi}{\sqrt{\xi^2 + \Delta_1^2(0)}} + N_L\lambda_0 \int\limits_{E_0/2}^{\omega_D} \frac{d\xi}{\sqrt{\xi^2 + \Delta_1^2(0)}}. \tag{5.15}$$

Here $\xi = \varepsilon(\mathbf{p}) - \mu$ and N_{FC} is the density of states in the momentum interval $p_f - p_i$ or in the energy interval E_0. It follows from (5.8) that $N_{FC} = (p_f - p_F)p_F/(2\pi\Delta_1)$. Within the energy interval $\omega_D - E_0/2$, the density of states N_L has the standard form $N_L = M_L^*/2\pi$. As $E_0 \to 0$, (5.15) becomes the BCS equation. On the other hand, assuming that $E_0 \leq 2\omega_D$ and discarding the second integral on the right-hand side of (5.15), we obtain

$$\begin{aligned} \Delta_1(0) &= \frac{\lambda_0 p_F(p_f - p_F)}{2\pi} \ln\left(1 + \sqrt{2}\right) \\ &= 2\beta\varepsilon_F \frac{p_f - p_F}{p_F} \ln\left(1 + \sqrt{2}\right), \end{aligned} \tag{5.16}$$

where $\varepsilon_F = p_F^2/2M_L^*$ is the Fermi energy and $\beta = \lambda_0 M_L^*/2\pi$ is the dimensionless coupling constant. Using the standard value of $\beta \simeq 0.3$ for ordinary superconductors and assuming that $(p_f - p_F)/p_F \simeq 0.2$, we obtain from (5.16) a large value $\Delta_1(0) \sim 0.1\varepsilon_F$; for ordinary superconductors, this gap is much smaller: $\Delta_1(0) \sim 10^{-3}\varepsilon_F$. We recollect that in BCS theory the temperature of superconducting phase transition T_c equals to $T_c \approx \Delta_1(0)/3.52$. This, along with above expressions for $\Delta_1(0)$, permits to estimate T_c in the substances with FC. Note that in FC theory this is underestimation of T_c, see (5.21) below. This means that with accurate account of all factors in FC approach T_c will be even larger.

As the Fermi energy order of magnitude is around 1 eV $\approx 10^4$ K, we obtain that in the substances with FC $T_c \simeq 300$ K, which is around room temperature. At the same time, for ordinary superconductors the expression $\Delta_1(0) \sim 10^{-3}\varepsilon_F = 10$ K gives correct estimate for T_c. This means that the FC concept explains successfully the physics of high-T_c superconductors. The above calculations show that the explanation is very simple and do not require any exotic departure from weak coupling BSC-like theory. Moreover, we recollect that BCS theory of superconductivity uses the Fermi liquid as the normal state of the system. Since the presented FC approach is a generalization (in the sense of new quasiparticle concept) of Landau Fermi liquid theory, we conclude that it is capable to describe naturally the BSC pairing of new "fermi-condensed" quasiparticles thus lying a foundation for successful explanation of high-T_c superconductivity phenomenon.

With the integral discarded earlier taken into account, we find that

$$\Delta_1(0) \simeq 2\beta\varepsilon_F \frac{p_f - p_F}{p_F} \ln\left(1 + \sqrt{2}\right) + \Delta_1(0)\beta \ln\left(\frac{2\omega_D}{\Delta_1(0)}\right), \tag{5.17}$$

where $\Delta_1(0)$ is given by (5.16). As $E_0 \to 0$ and $p_f \to p_F$, the first term on the right-hand side of (5.15) is zero. Therefore, we obtain the ordinary BCS result with $\Delta_1 \propto \exp(-1/\lambda_0)$. The correction related to the second integral in (5.15) is small because the second term on the right-hand side of (5.17) contains the additional factor β. In what follows, we show that $2T_c \simeq \Delta_1(0)$. The isotopic effect is small in this case since T_c depends on ω_D logarithmically, but the effect is restored as $E_0 \to 0$.

At $T \simeq T_c$, (5.8) and (5.9) are replaced by (3.12) and (3.14), which also hold for $T_c \leq T \ll T_f$:

$$M^*_{FC} \simeq p_F \frac{p_f - p_i}{4T_c}, \quad E_0 \simeq 4T_c, \text{ at } T \simeq T_c, \tag{5.18}$$

$$M^*_{FC} \simeq p_F \frac{p_f - p_i}{4T}, \quad E_0 \simeq 4T, \text{ at } T < T_c. \tag{5.19}$$

For finite temperatures the (5.15) is replaced by its standard generalization

$$\begin{aligned} 1 = N_{FC}\lambda_0 \int\limits_0^{E_0/2} \frac{d\xi}{\sqrt{\xi^2+\Delta_1^2}} \tanh\frac{\sqrt{\xi^2+\Delta_1^2}}{2T} \\ + N_L\lambda_0 \int\limits_{E_0/2}^{\omega_D} \frac{d\xi}{\sqrt{\xi^2+\Delta_1^2}} \tanh\frac{\sqrt{\xi^2+\Delta_1^2}}{2T}. \end{aligned} \tag{5.20}$$

Because $\Delta_1(T \to T_c) \to 0$, (5.20) implies a relation that closely resembles the BCS result [17],

$$2T_c \simeq \Delta_1(0), \tag{5.21}$$

where $\Delta_1(T = 0)$ is found from (5.17). Comparing (5.8) and (5.9) with (5.18) and (5.19), we see that both M^*_{FC} and E_0 are temperature-independent for $T \leq T_c$.

5.1.3 Bogolyubov Quasiparticles

Equation (5.6) shows that the superconducting gap depends on the single-particle spectrum $\varepsilon(\mathbf{p})$. On the other hand, it follows from (5.4) that $\varepsilon(\mathbf{p})$ depends on $\Delta(\mathbf{p})$ if (5.7) has a solution that determines the existence of FC at $\lambda_0 \to 0$. We assume that λ_0 is so small that the pairing interaction $\lambda_0 V(\mathbf{p}, \mathbf{p}_1)$ leads only to a small perturbation of the order parameter $\kappa(\mathbf{p})$. Equation (5.8) implies that the effective mass and the density of states $N(0) \propto M^*_{FC} \propto 1/\Delta_1$ are finite. Thus, in contrast to the spectrum in the standard superconductivity theory, the single-particle spectrum

$\varepsilon(\mathbf{p})$ depends strongly on the superconducting gap, and (2.3) and (5.6) must be solved self-consistently.

We assume that (2.3) and (5.6) have been solved and the effective mass M^*_{FC} has been found. This means that we can find the quasiparticle dispersion law $\varepsilon(\mathbf{p})$ by choosing the effective mass M^* equal to the obtained value of M^*_{FC} and then solve (5.6) without (2.3), as it is done in the standard BCS superconductivity theory [2]. Hence, the superconducting state with FC is characterized by Bogolyubov quasiparticles [18] with dispersion (5.5) and the normalization condition $v^2(\mathbf{p}) + u^2(\mathbf{p}) = 1$ for the coefficients $v(\mathbf{p})$ and $u(\mathbf{p})$. Moreover, quasiparticle excitations of the superconducting state in the presence of FC coincide with the Bogolyubov quasiparticles in the BCS theory. This means that the superconductivity in FC state resembles BCS one, which points to the applicability of the modified BCS formalism to the description of the high-T_c superconducting state. At the same time, the maximum value of the superconducting gap set by (5.17) and other exotic properties are determined by the presence of FC. These results are in good agreement with the experimental observations for the high-T_c superconductor $Bi_2Sr_2Ca_2Cu_3O_{10+\delta}$ [19].

In constructing the superconducting state with FC, we returned to the foundations of the LFL theory, where the high-energy degrees of freedom had been eliminated by introduction of new quasiparticles. The main difference between the LFL, which forms the basis for constructing the superconducting state, and the Fermi liquid with FC is that in the latter case we should increase the number of low-energy degrees of freedom by introducing the new type of quasiparticles with the effective mass M^*_{FC} and the characteristic energy E_0 given by (5.9). Hence, the dispersion law $\varepsilon(\mathbf{p})$ in FC state is characterized by two types of quasiparticles with the effective masses M^*_L and M^*_{FC} and the scale E_0. The extended paradigm and new quasiparticles determine the properties of the superconductor, including the lineshape of quasiparticle excitations [10–12, 20], while the formal dispersion of the Bogolyubov quasiparticles has the standard form (5.5).

We note that for $T < T_c$, the effective mass M^*_{FC} and the scale E_0 are temperature-independent [20]. For $T > T_c$, the effective mass M^*_{FC} and the scale E_0 are given by (3.12) and (3.14). Obviously, we cannot directly relate these new quasiparticles (excitations) of the Fermi liquid with FC to excitations (quasiparticles) of an ideal Fermi gas, as is done in the standard LFL theory, because the system is beyond FCQPT. The properties and dynamics of quasiparticles are given by the extended paradigm and closely related to the properties of the superconducting state and are of a collective nature, formed by FCQPT and determined by the macroscopic number of FC quasiparticles with momenta in the interval $(p_f - p_i)$. Such a system cannot be perturbed by scattering on impurities and on lattice defects and, therefore, has the features of a quantum protectorate and demonstrates universal scaling behavior, forming a new state of matter [10–12, 21–24], see Chaps. 17 and 18.

Several remarks concerning the quantum protectorate and the universal behavior of superconductors with FC are in order. Similarly to the Landau Fermi liquid theory, the theory of high-T_c superconductivity based on FCQPT deals with quasiparticles that are elementary low-energy excitations. The theory provides general qualitative description of the superconducting and the normal states of high-T_c superconductors and HF metals. Of course, the proper choice of the phenomenological parameters like pairing coupling constant can yield a quantitative description of superconductivity similar to the case of Landau theory for an ordinary Fermi liquid like ^{3}He. Hence, any formalism capable of FC description and compatible with the BCS theory yields the same qualitative picture of normal and superconducting states in a substance with FCQPT. Obviously, both approaches may be coordinated on the level of numerical results by choosing the appropriate parameters. For instance, because the formation of FC is possible in the Hubbard model [25], it allows reproducing the results of the theory based on FCQPT.

5.1.4 The Dependence of Superconducting Phase Transition Temperature T_c on Doping

We examine the maximum value of the superconducting gap Δ_1 as a function of the number density x of mobile charge carriers, which is proportional to the degree of doping. Using (3.15), we can rewrite (5.16) as

$$\frac{\Delta_1}{\varepsilon_F} \sim \beta \frac{(x_{FC} - x)x}{x_{FC}}. \tag{5.22}$$

Here we take into account that the Fermi level $\varepsilon_F \propto p_F^2$ and the number density $x \sim p_F^2/(2M^*)$ with the result $\varepsilon_F \propto x$. It is realistic to assume that $T_c \propto \Delta_1$, because the curve $T_c(x)$ obtained in experiments with high-T_c superconductors [26] must be a smooth function of x. Hence, we can approximate $T_c(x)$ by a smooth bell-shape function [27]:

$$T_c(x) \propto \beta(x_{FC} - x)x. \tag{5.23}$$

To illustrate the application of the above analysis, we examine the main features of a superconductor that can hypothetically exist at room temperature. Such a superconductor should consist of two-dimensional layers similar to high-T_c superconducting cuprates. Equation (5.16) implies that $\Delta_1 \sim \beta\varepsilon_F \propto \beta/r_s^2$. Bearing in mind that FCQPT occurs at $r_s \sim 20$ in 3D systems and at $r_s \sim 8$ in 2D systems [28], we can expect that in 3D systems Δ_1 amounts to 10 % of the maximum size of the superconducting gap in 2D systems, which in our case amounts to 60 mV for weakly doped cuprates with $T_c = 70$ K [29]. On the other hand, (5.16) implies that Δ_1 may be even larger, $\Delta_1 \sim 75$ mV. We can expect that $T_c \sim 300$ K in the case of s-wave pairing, as the simple relation $2T_c \simeq \Delta_1$ implies. Indeed, we can take $\varepsilon_F \sim 500$ mV, $\beta \sim 0.3$, and $(p_f - p_i)/p_F \sim 0.5$. Thus, the hypothetical room temperature superconductor could have simple s-wave pairing. We note that the number density x of mobile charge carriers have to satisfy the condition $x \leq x_{FC}$ and should be varied to reach the optimum degree of doping $x_{opt} \simeq x_{FC}/2$.

5.1.5 The Gap and Heat Capacity Near T_c

We now calculate the gap and the heat capacity at temperatures $T \to T_c$. Our analysis is valid at $T_p^* \simeq T_c$ as otherwise the discontinuities in the heat capacity considered below are smeared over the temperature interval between T_p^* and T_c where T_p^* is the temperature at which the pseudogap is closed. Since the origin of the pseudogap is controversial and still subject to debate in the condensed matter community, we do not consider here this phenomenon. To simplify matters, we calculate the leading contribution to the gap and heat capacity related to FC. We use (5.20) to find the function $\Delta_1(T \to T_c)$ simply by expanding the first integral on its right-hand side in powers of Δ_1 and dropping the contribution from the second integral. This procedure leads to the equation [20]

$$\Delta_1(T) \simeq 3.4T_c\sqrt{1-\frac{T}{T_c}}. \tag{5.24}$$

Therefore, the gap in the single-particle excitations spectrum behaves in the ordinary BCS manner.

To calculate the heat capacity, we can use the standard expression for the entropy S [2]:

$$S(T) = -2\int\Big[f(\mathbf{p})\ln f(\mathbf{p}) + (1-f(\mathbf{p}))\ln(1-f(\mathbf{p}))\Big]\frac{d\mathbf{p}}{(2\pi)^2}, \tag{5.25}$$

where

$$f(\mathbf{p}) = \left(1+\exp\frac{E(\mathbf{p})}{T}\right)^{-1}, \ E(\mathbf{p}) = \sqrt{(\varepsilon(\mathbf{p})-\mu)^2 + \Delta_1^2(T)}. \tag{5.26}$$

The heat capacity C is given by

$$\begin{aligned} C(T) = T\frac{dS}{dT} &\simeq 4\frac{N_{FC}}{T^2}\int_0^{E_0} f(E)(1-f(E))\left[E^2 + T\Delta_1(T)\frac{d\Delta_1(T)}{dT}\right]d\xi \\ &+ 4\frac{N_L}{T^2}\int_{E_0}^{\omega_D} f(E)(1-f(E))\left[E^2 + T\Delta_1(T)\frac{d\Delta_1(T)}{dT}\right]d\xi. \end{aligned} \tag{5.27}$$

In deriving (5.27), we again use the variables ξ and $E = \sqrt{\xi^2 + \Delta_1^2(T)}$ and the above notation for the densities of states N_{FC} and N_L. Equation (5.27) describes a jump in heat capacity, $\delta C(T) = C_s(T) - C_n(T)$, where $C_s(T)$ and $C_n(T)$ are respectively the heat capacities of the superconducting and normal states at T_c; the jump is determined by the last two terms in the square brackets on the right-hand side of this equation. Using (5.24) to calculate the first term on the right-hand side of (5.27), we find [20]

$$\delta C(T_c) \simeq \frac{3}{2\pi^2}(p_f - p_i)p_F^n. \tag{5.28}$$

where $n = 1$ in the 2D case and $n = 2$ in the 3D case. This result differs from the ordinary BCS result, according to which the discontinuity in the heat capacity is a linear function of T_c. The jump $\delta C(T_c)$ is independent of T_c because, as (5.19) shows, the density of state varies in inverse proportion to T_c. We note that in deriving (5.28) we took the leading contribution coming from FC into account. This contribution disappears as $E_0 \to 0$, and the second integral on the right-hand side of (5.27) yields the standard result.

As we will show in Chap. 8 [see (8.6)], the heat capacity of a system with FC behaves as $C_n(T) \propto \sqrt{T/T_f}$. The jump in the heat capacity given by (5.28) is temperature-independent. As a result, we find that

$$\frac{\delta C(T_c)}{C_n(T_c)} \sim \sqrt{\frac{T_f}{T_c}}\frac{(p_f - p_i)}{p_F}. \tag{5.29}$$

In contrast to the case of normal superconductors, where $\delta C(T_c)/C_n(T_c) = 1.43$ [15], in our case (5.29) implies that the ratio $\delta C(T_c)/C_n(T_c)$ is not constant and may be very large when $T_f/T_c \gg 1$ [20, 30]. It is instructive to apply this analysis to CeCoIn$_5$, where T_c =2.3 K [30]. In this material [31], $\delta C/C_n \simeq 4.5$ is substantially higher than the BCS value, in agreement with (5.29).

5.2 The Dispersion Law and Lineshape of Single-Particle Excitations

Recently discovered gap in the quasiparticles dispersion at energies between 40 and 70 meV, resulting in quasiparticles velocity altering in this energy range [32–35], can hardly be explained by the marginal Fermi-liquid theory as it contains no additional energy scales or parameters that would allow taking the gap into account [36, 37]. One could assume that the gap, defining new energy scale, occurs due to the interaction of electrons and collective excitations. In this case, however, we would have to discard the idea of a quantum protectorate, which in its turn would contradict the experimental data [21, 22].

As shown in Sects. 3.1.3 and 5.1, a system with FC has two effective masses: M^*_{FC}, which determines the single-particle spectrum at low energies, and M^*_L, which determines the spectrum at high energies. The fact that there are two effective masses manifests itself in the form of a kink in the quasiparticle dispersion law. The dispersion law can be approximated by two straight lines intersecting at the binding energy $E_0/2$ [see (3.14) and (5.9)]. The kink in the dispersion law occurs at temperatures much lower than $T \ll T_f$, when the system is in the superconducting or normal state. Such behavior is in good agreement with the experimental data [35]. It is pertinent to note that at temperatures below $T < T_c$, the effective mass M^*_{FC} is independent of the momenta p_F, p_f, and p_i, as shown by (5.8) and (5.16):

$$M^*_{FC} \sim \frac{2\pi}{\lambda_0}. \tag{5.30}$$

This formula implies that M^*_{FC} is only weakly dependent on x, if a dependence of λ_0 on x is allowed. This result is in good agreement with the experimental data [38–40]. The same is true for the dependence of the Fermi velocity $v_F = p_F/M^*_{FC}$ on x because the Fermi momentum $p_F \sim \sqrt{n}$ is weakly dependent on the electron number density $n = n_0(1 - x)$ [38, 39]. Here, n_0 is the single-particle electron number density at half-filling.

Since λ_0 is the coupling constant that determines the magnitude of the pairing interaction, e.g., the electron-phonon one, we can expect a kink in the quasiparticle dispersion law to be caused by the electron-phonon interaction. The electron-phonon scenario could explain the constancy of the kink at $T > T_c$ as phonon contribution is temperature independent. On the other hand, it was found that the quasiparticle dispersion law distorted by the interaction with phonons has a tendency to restore itself to the ordinary single particle dispersion law when the quasiparticle energy becomes higher than the phonon energy [41]. However, there is no experimental evidence that such restoration of the dispersion law actually takes place [35].

The quasiparticle excitation curve $L(q, \omega)$ is a function of two variables. Measurements at a constant energy $\omega = \omega_0$, where ω_0 is the single particle excitation energy, determine the curve $L(q, \omega = \omega_0)$ as a function of the momentum q. We have shown above that M^*_{FC} is finite and constant at temperatures not exceeding T_c. Hence, at excitation energies $\omega < E_0$, the system behaves as an ordinary superconducting Fermi liquid with the effective mass determined by (5.8) [10–13]. At $T_c \leq T$, the effective mass M^*_{FC} is also finite and is given by (3.12). In other words, at $\omega < E_0$, the system behaves as a Fermi liquid whose single-particle spectrum is well defined and the width of the single-particle excitations is of the order of T [5, 10–12]. Such behavior has been observed in measurements of the quasiparticle excitation curve at fixed energy [33, 42, 43].

The quasiparticle excitation curve can also be described as a function of ω, at a constant momentum $q = q_0$. For small values of ω, the behavior of this function is similar to that described above, with $L(q = q_0, \omega)$ having a characteristic maximum and width. For $\omega \geq E_0$, the contribution provided by quasiparticles of mass M^*_L becomes significant and leads to an increase in the function $L(q = q_0, \omega)$. Thus, $L(q = q_0, \omega)$ has a certain structure of maxima and minima directly determined by the existence of two effective masses, M^*_{FC} and M^*_L [10–13]. We conclude that, in contrast to Landau quasiparticles, these quasiparticles have a more complicated spectral lineshape.

To calculate the imaginary part $\mathrm{Im}\,\Sigma(\mathbf{p}, \varepsilon)$ of the self-energy $\Sigma(\mathbf{p}, \varepsilon)$, we use the Kramers-Kronig relations. For that we first calculate its real part $\mathrm{Re}\,\Sigma(\mathbf{p}, \varepsilon)$, which determines the effective mass M^* [44],

$$\frac{1}{M^*} = \left(\frac{1}{m} + \frac{1}{p_F}\frac{\partial \mathrm{Re}\Sigma}{\partial p}\right) \Big/ \left(1 - \frac{\partial \mathrm{Re}\Sigma}{\partial \varepsilon}\right). \tag{5.31}$$

The corresponding momenta p and energies ε satisfy the inequalities $|p - p_F|/p_F \ll 1$, and $\varepsilon/\varepsilon_F \ll 1$. We take Re $\Sigma(\mathbf{p}, \varepsilon)$ in the simplest possible form that ensures the correct variation of the effective mass at the energy $E_0/2$,

$$\begin{aligned} \mathrm{Re}\Sigma(\mathbf{p}, \varepsilon) = &- \varepsilon \frac{M^*_{FC}}{m} + \left(\varepsilon - \frac{E_0}{2}\right) \frac{M^*_{FC} - M^*_L}{m} \\ &\times \left[\theta\left(\varepsilon - \frac{E_0}{2}\right) + \theta\left(-\varepsilon - \frac{E_0}{2}\right)\right], \end{aligned} \tag{5.32}$$

where $\theta(\varepsilon)$ is the step function. To ensure a smooth transition from the single-particle spectrum characterized by M^*_{FC} to the spectrum characterized by M^*_L, we must replace the step function by a smoothed one. Substituting (5.32) in (5.31), we see that $M^* \simeq M^*_{FC}$ within the interval $(-E_0/2,\ E_0/2)$, while $M^* \simeq M^*_L$ outside this interval. Applying the Kramers-Kronig relation to $\mathrm{Re}\Sigma(\mathbf{p}, \varepsilon)$, we express the imaginary part of the self-energy as [20]

$$\mathrm{Im}\Sigma(\mathbf{p}, \varepsilon) \sim \varepsilon^2 \frac{M^*_{FC}}{\varepsilon_F m} + \frac{M^*_{FC} - M^*_L}{m}\left[\varepsilon \ln\left|\frac{2\varepsilon + E_0}{2\varepsilon - E_0}\right| + \frac{E_0}{2}\ln\left|\frac{4\varepsilon^2 - E_0^2}{E_0^2}\right|\right]. \tag{5.33}$$

Clearly, with $\varepsilon/E_0 \ll 1$, the imaginary part is proportional to ε^2; at $2\varepsilon/E_0 \simeq 1$, we have $\mathrm{Im}\Sigma \sim \varepsilon$, and for $E_0/\varepsilon \ll 1$, the main contribution to the imaginary part is approximately constant.

It follows from (5.33) that as $E_0 \to 0$, the second term on its right-hand side vanishes and the single-particle excitations become well-defined, which resembles the situation with a normal Fermi liquid, while the pattern of minima and maxima eventually disappears. Now the quasiparticle renormalization factor $z(\mathbf{p})$ is given by the equation [44]

$$\frac{1}{z(\mathbf{p})} = 1 - \frac{\partial \mathrm{Re}\Sigma(\mathbf{p}, \varepsilon)}{\partial \varepsilon}. \tag{5.34}$$

Consequently, the (5.33) and (5.34) show that for $T \le T_c$, the interaction of a quasiparticle on the Fermi surface increases as the characteristic energy E_0 decreases. Equations (5.9) and (5.23) imply that $E_0 \sim (x_{FC} - x)/x_{FC}$. When $T > T_c$, it follows from (5.32) and (5.34) that the quasiparticle interaction increases as the effective mass M^*_{FC} decreases. So, from (3.12) and (3.15) $M^*_{FC} \sim (p_f - p_i)/p_F \sim (x_{FC} - x)/x_{FC}$. As a result, we conclude that the interaction increases with the doping level x and the single-particle excitations are better defined in heavily doped samples. As $x \to x_{FC}$, the characteristic energy $E_0 \to 0$ and the quasiparticles become normal excitations of LFL. We note that such behavior has been observed in experiments with heavily doped Bi2212, which demonstrates high-T_c superconductivity with the gap of about 10 mV [45]. The size of the gap suggests that the region occupied by FC is small because $E_0/2 \simeq \Delta_1$. For $x > x_{FC}$ and low temperatures, the HF liquid behaves as LFL (see Fig. 3.2 and Sect. 3.1.4). Experimental data show that, as expected, the LFL state exists in super-heavily doped nonsuperconducting $La_{1.7}Sr_{0.3}CuO_4$ [46, 47].

5.3 Electron Liquid with FC in Magnetic Fields

The behavior of heavy-electron liquid with FC in magnetic field is considered. At low temperatures and under the application of weak magnetic field the distribution function is to be reconstructed so that the order parameter vanishes, and a new distribution function is to deliver the same ground state energy. We show that the new distribution emerges as a result of topological phase transition, and is represented by multiply connected Fermi spheres. This topological phase transition and multiply connected Fermi spheres (icebergs) are considered in Chap. 4.

5.3.1 Phase Diagram of Electron Liquid in Magnetic Field

Let us assume that the coupling constant is nonzero, $\lambda_0 \neq 0$, but is infinitely small. We found in Sect. 5.1 that at $T = 0$ the superconducting order parameter $\kappa(\mathbf{p})$ is finite in the region occupied by FC and that the maximum value of the superconducting gap $\Delta_1 \propto \lambda_0$ is infinitely small. Hence, any weak magnetic field $B \neq 0$ is critical and destroys the order parameter and FC. Simple energy arguments suffice to determine the type of rearrangement of the FC state. On one hand, since FC state is destroyed, the energy gain $\Delta E_B \propto B^2$ vanishes as $B \to 0$. On the other hand, the function $n_0(\mathbf{p})$, which occupies the finite interval $(p_f - p_i)$ in the momentum space and is specified by (3.1) or (5.9), leads to a finite gain in the ground-state energy compared to that of a normal Fermi liquid [4]. Thus, the distribution function is to be reconstructed so that the order parameter is to vanish while a new distribution function is to deliver the same ground state energy. Thus, in weak magnetic fields, the new ground state without FC must have almost the same energy as the state with FC. As shown in Chap. 4, such a state is formed by multiply connected Fermi spheres resembling an onion, in which a smooth distribution function of quasiparticles, $n_0(\mathbf{p})$, is replaced in the interval $(p_f - p_i)$ with the distribution function [8, 48]

$$\nu(\mathbf{p}) = \sum_{k=1}^{n} \theta(p - p_{2k-1})\theta(p_{2k} - p). \tag{5.35}$$

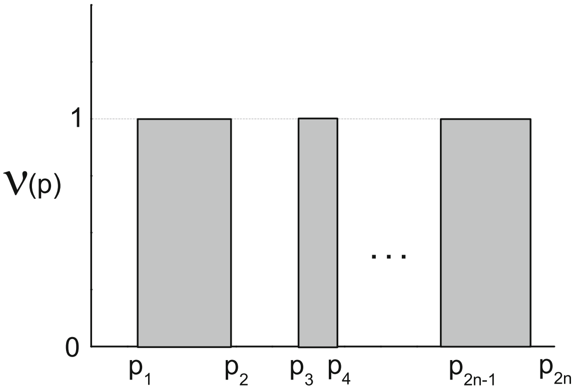

Fig. 5.1 The function $\nu(\mathbf{p})$ for the multiply connected distribution that replaces the function $n_0(\mathbf{p})$ in the region $(p_f - p_i)$ occupied by FC. The momenta satisfy the inequalities $p_i < p_F < p_f$. The outer Fermi surface at $p \simeq p_{2n} \simeq p_f$ has the shape of a Fermi step, and therefore the system behaves like LFL at sufficiently low temperatures

where the parameters $p_i \leq p_1 < p_2 < \cdots < p_{2n} \leq p_f$ are chosen so as to satisfy the conditions of normalization and conservation of the particles number:

$$\int\limits_{p_{2k-1}}^{p_{2k+3}} \nu(\mathbf{p})\frac{d\mathbf{p}}{(2\pi)^3} = \int\limits_{p_{2k-1}}^{p_{2k+3}} n_0(\mathbf{p})\frac{d\mathbf{p}}{(2\pi)^3}.$$

Figure 5.1 shows the corresponding multiply connected distribution. For definiteness, we present the most interesting case of a three-dimensional system. The two-dimensional case can be examined similarly. We note that the possibility of the existence of multiply connected Fermi spheres have been studied in [49–52].

We assume that the thickness of each inner slice of the Fermi sphere, $\delta p \simeq p_{2k+1} - p_{2k}$, is determined by the magnetic field B. Using the well-known rule for estimating errors of numerical calculation of definite integrals, we find that the minimum loss of the ground-state energy due to slice formation is approximately $(\delta p)^4$. This becomes especially clear if we take into account the fact that the continuous FC functions $n_0(\mathbf{p})$ ensure the minimum value of the energy functional $E[n(\mathbf{p})]$, while the approximation of $\nu(\mathbf{p})$ by steps of width δp leads to a minimal error of the order of $(\delta p)^4$. Recalling that the gain due to the magnetic field is proportional to B^2 and equating the two contributions, we obtain

$$\delta p \propto \sqrt{B}. \tag{5.36}$$

Therefore, as $T \to 0$, with $B \to 0$, the slice thickness δp also tends to zero and the behavior of a Fermi liquid with FC is replaced with that of LFL with the Fermi momentum p_f. Equation (5.7) implies that $p_f > p_F$ and the electron number density x remains constant, with the Fermi momentum of the multiply connected Fermi sphere $p_{2n} \simeq p_f > p_F$ (see Fig. 5.1). We will see subsequently in Chap. 8 that these observations play an important role in studying the behavior of both the Hall coefficients $R_H(B)$ and the second order phase transitions in HF metals as a function of B at low temperatures.

To calculate the effective mass $M^*(B)$ as a function of the applied magnetic field B, we first note that at $T = 0$ the field B splits the FC state into Landau levels, suppresses the superconducting order parameter $\kappa(\mathbf{p})$, and destroys FC, which leads to restoration of LFL [53, 54]. The Landau levels near the Fermi surface can be approximated by separate slices whose thickness in momentum space is δp. Approximating the quasiparticle dispersion law within a single slice, $\varepsilon(p) - \mu \sim (p - p_f + \delta p)(p - p_f)/M^*$, we find the effective mass $M^*(B) \sim M^*/(\delta p/p_f)$. The energy increment ΔE_{FC} caused by the transformation of the FC state can be estimated based on using the Landau formula [15]

$$\Delta E_{FC} = \int (\varepsilon(\mathbf{p}) - \mu)\delta n(\mathbf{p}) \frac{d\mathbf{p}^3}{(2\pi)^3}. \tag{5.37}$$

The region occupied by the variation $\delta n(\mathbf{p})$ has the thickness δp, with $(\varepsilon(\mathbf{p}) - \mu) \sim (p - p_f)p_f/M^*(B) \sim \delta p p_f/M^*(B)$. As a result, we find that $\Delta E_{FC} \sim p_f^3 \delta p^2/M^*(B)$. On the other hand, there is one more term in the energy E expression, $\Delta E_B \sim (B\mu_B)^2 M^*(B)p_f$, caused by the applied magnetic field, which decreases the energy and is related to the Zeeman splitting. Equating ΔE_B and ΔE_{FC} and recalling that $M^*(B) \propto 1/\delta p$ in this case, we obtain the chain of relations

$$\frac{\delta p^2}{M^*(B)} \propto \frac{1}{(M^*(B))^3} \propto B^2 M^*(B), \tag{5.38}$$

which implies that the effective mass $M^*(B)$ diverges as

$$M^*(B) \propto \frac{1}{\sqrt{B - B_{c0}}}. \tag{5.39}$$

where B_{c0} is the critical magnetic field, which places HF metal at the magnetic-field-tuned quantum critical point and nullifies the respective Nèel temperature, $T_{NL}(B_{c0}) = 0$ [54]. In our simple model of HF liquid, the quantity B_{c0} is a parameter determined by the properties of the specific metal with heavy fermions. We note that in some cases $B_{c0} = 0$, e.g., the HF metal $\mathrm{CeRu_2Si_2}$ has no magnetic order, exhibits no superconductivity, and does not behave like a Landau Fermi liquid even at the lowest reached temperatures [55].

Formula (5.39) and Fig. 5.1 shows that the application of a magnetic field $B > B_{c0}$ brings the FC system back to the LFL state with the effective mass $M^*(B)$ that depends on the magnetic field. This means that the following characteristic of LFL are restored: $C/T = \gamma_0(B) \propto M^*(B)$ for the heat capacity and $\chi_0(B) \propto M^*(B)$ for the magnetic susceptibility. The coefficient $A(B)$ determines the temperature-dependent part of the resistivity, $\rho(T) = \rho_0 + \Delta\rho$, where ρ_0 is the residual resistivity and $\Delta\rho = A(B)T^2$. Since this coefficient is directly determined by the effective mass, $A(B) \propto (M^*(B))^2$ [56], (5.39) yields

$$A(B) \propto \frac{1}{B - B_{c0}}. \tag{5.40}$$

Thus, the empirical Kadowaki-Woods relation [57] $K = A/\gamma_0^2 \simeq const$ is valid in our case [56]. Furthermore, K may depend on the quasiparticles degree of degeneracy. With this degeneracy, the Kadowaki-Woods relation provides a good description of the experimental data for a broad class of HF metals [58, 59]. In the simplest case, where HF liquid is formed by spin-$1/2$ quasiparticles with the degeneracy degree 2, the value of K turns out to be close to the empirical value [56] known as the Kadowaki-Woods ratio [57]. Hence, the system, subjected to a magnetic field, returns to the LFL state with constant Kadowaki-Woods relation. We note that when the system is located near FCQPT, the application of magnetic field brings it to the LFL state due to the Zeeman splitting, as it is discussed in Chap. 6.

At finite temperatures, the system remains in the LFL state, but when $T > T^*(B)$, the NFL behavior is restored. As regards to finding the function $T^*(B)$, we reminder that the transition region characterized by the function $T^*(B)$ can be determined in different measurements on HF compounds such as measurements of the maximums of the heat capacity C/T or maximums of the magnetic susceptibility χ, etc (see, Sect. 6.4). In the considered case, $T^*(B)$ is determined in measurements of the resistivity $\rho(T)$ in magnetic fields, see Sect. 6.3.1. We note that the effective mass M^*, characterizing the single-particle spectrum, cannot change at $T^*(B)$ because no phase transition occurs at this temperature. To calculate $M^*(T)$, we equate the effective mass $M^*(T)$ in (3.12) to $M^*(B)$ in (5.39), $M^*(T) \sim M^*(B)$,

$$\frac{1}{M^*(T)} \propto T^*(B) \propto \frac{1}{M^*(B)} \propto \sqrt{B - B_{c0}}. \tag{5.41}$$

Let us note that

$$T^*(B) \propto \sqrt{B - B_{c0}}. \tag{5.42}$$

At temperatures $T \geq T^*(B)$, the system returns to the NFL behavior with the effective mass M^* specified by (3.12). Thus, expression (5.42) determines the line in the $T - B$ phase diagram that separates the region where the effective mass depends on B and the heavy Fermi liquid behaves like a Landau Fermi liquid from the region where the effective mass is temperature-dependent. At $T^*(B)$, the temperature dependence of the resistivity ceases to be quadratic and becomes linear.

A schematic $T - B$ phase diagram of HF liquid with FC in magnetic field is shown in Fig. 5.2. At magnetic field $B < B_{c0}$ the FC state can be captured by FM, AFM and/or SC states lifting the degeneracy of the FC state. It follows from (5.42) that at a certain temperature $T^*(B) \ll T_f$, the heavy-electron liquid transits from its NFL state to LFL one acquiring the properties of LFL at $(B - B_{c0}) \propto (T^*(B))^2$. At temperatures below $T^*(B)$, as shown by the horizontal arrow in Fig. 5.2, the heavy-electron liquid demonstrates an increasingly metallic behavior as the magnetic field B increases. This is because the effective mass decreases, see (5.39). Such behavior

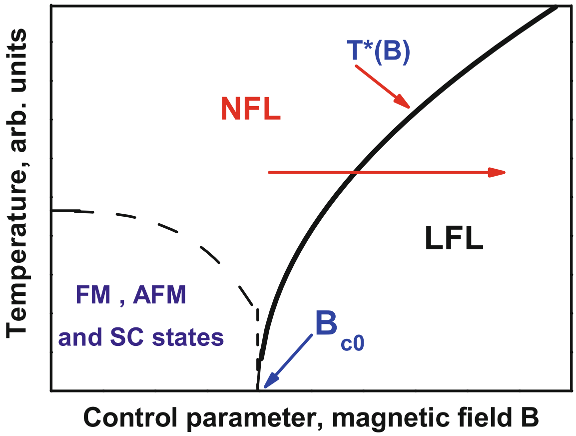

Fig. 5.2 Schematic $T - B$ phase diagram of heavy electron liquid. B_{c0} denotes the magnetic field at which the effective mass diverges according to (5.39). The *horizontal arrow* illustrates the system moving in the NFL-LFL direction along B at fixed temperature. As shown by the *dashed curve*, at $B < B_{c0}$ the system can be in its ferromagnetic (FM), antiferromagnetic (AFM) or superconducting (SC) states. The NFL state is characterized by the entropy S_0 given by (3.8). The *solid curve* $T^*(B)$ separates the NFL state and the weakly polarized LFL one and represents the transition regime

of the effective mass can be observed, for instance, in measurements of the heat capacity, magnetic susceptibility, resistivity, and Shubnikov-de Haas oscillations. The $T - B$ phase diagram in Fig. 5.2 shows that a unique possibility emerges where a magnetic field can be used to control the variations in the physical nature and type of behavior of the electron liquid with FC.

We briefly discuss the case where the system is extremely close to FCQPT on the ordered size of this transition, and hence $\delta p_{FC} = (p_f - p_i)/p_F \ll 1$. Because $\delta p \propto M^*(B)$, it follows from (5.36) and (5.39) that

$$\frac{\delta p}{p_F} \sim a_c \sqrt{\frac{B - B_{c0}}{B_{c0}}}, \tag{5.43}$$

where $a_c \sim 1$. As the magnetic field B increases, $\delta p/p_F$ becomes comparable to δp_{FC}, and the distribution function $\nu(\mathbf{p})$ disappears, being absorbed by the ordinary Zeeman splitting. As a result, we are dealing with HF liquid located on the disordered side of FCQPT. We show in Chap. 6 that the behavior of such a system differs essentially from that of a system with FC. Equation (5.43) implies that the relatively weak magnetic field B_{cr},

$$B_{red} \equiv \frac{B - B_{c0}}{B_{c0}} = (\delta p_{FC})^2 \sim B_{cr}, \tag{5.44}$$

where B_{red} is the reduced field, takes the system from the ordered side of the phase transition to the disordered if $\delta p_{FC} \ll 1$.

5.3.2 Magnetic Field Dependence of the Effective Mass in HF Metals and High-T_c Superconductors

Observations have shown that in the normal state both heavily $Tl_2Ba_2CuO_{6+\delta}$ [60] and optimally doped cuprates $Bi_2Sr_2CuO_{6+\delta}$ [61] exhibit no significant violations of the Wiedemann-Franz law. The normal state has been obtained by applying a magnetic field whose strength is higher than the maximum critical field B_{c2} that destroys superconductivity. Studies of the electron—doped superconductor $Pr_{0.91}LaCe_{0.09}Cu0_{4-y}$ ($T_c = 24$ K), revealed that when a magnetic field destroyed superconductivity in this material, the spin-lattice relaxation constant $1/T_1$ obeyed the relation $T_1T = const$, known as the Korringa law, down to temperatures about $T \simeq 0.2$ K [62, 63]. At higher temperatures and in magnetic fields up to 15.3 T perpendicular to the CuO_2 plane, the ratio $1/T_1T$ remains constant as a function of T for $T \leq 55$ K. In the temperature range from 50 to 300 K, the ratio $1/T_1T$ decreases as the temperature increases [63]. Measurements involving the heavily doped nonsuperconducting material $La_{1.7}Sr_{0.3}CuO_4$ have shown that the resistivity ρ varies with T as T^2 and that the Wiedemann-Franz law holds [46, 47].

As Korringa and Wiedemann-Franz laws strongly indicate the presence of the LFL state, experiments show that the observed elementary excitations cannot be distinguished from Landau quasiparticles in high-T_c superconductors. This places severe restrictions on models describing hole- or electron-doped high-T_c superconductors. For instance, for a Luttinger liquid [64, 65], for spin-charge separation [66], and in some $t - J$ models [67], a violation of the Wiedemann-Franz law was predicted, which is in contradiction with experimental evidence and points to the limited applicability of these models.

If the constant λ_0 is finite, then a HF liquid with FC is in the superconducting state. We examine the behavior of the system in magnetic fields $B > B_{c2}$. In this case, the system becomes LFL induced by the magnetic field, and the elementary excitations become quasiparticles that cannot be distinguished from Landau quasiparticles, with the effective mass $M^*(B)$ given by (5.39). As a result, the Wiedemann-Franz law holds as $T \to 0$, which agrees with the experimental data [60, 61]. Note, that violations of the Wiedemann-Franz law in HF metals are considered in Chap. 14.

The low-temperature properties of the system depend on the effective mass; in particular, the resistivity $\rho(T)$ obeys to (2.19) with $A(B) \propto (M^*(B))^2$. Assuming that for high-T_c superconductors the critical field $B = B_{c0}$, we deduce from (5.39) that

$$\gamma_0\sqrt{B - B_{c0}} = const. \tag{5.45}$$

Taking (5.40) and (5.45) into account, we find that

$$\gamma_0 \sim A(B)\sqrt{B - B_{c0}}. \tag{5.46}$$

At finite temperatures, the system remains LFL, but for $T > T^*(B)$ the effective mass becomes temperature-dependent, $M^* \propto 1/T$, and the resistivity becomes a linear function of the temperature, $\rho(T) \propto T$ [68]. Such behavior of the resistivity has been observed in the high-T_c superconductor $Tl_2Ba_2CuO_{6+\delta}$ ($T_c < 15$ K) [69]. At $B < 10$ T, the resistivity is a linear function of the temperature in the range from 120 mK to 1.2 K, and at $B = 10$ T the temperature dependence of the resistivity can be written in the form $\rho(T) \propto AT^2$ in the same temperature range [69, 70], clearly demonstrating that the LFL state is restored under the application of magnetic fields. The behavior of the resistivity of HF metals is studied in Chaps. 9, 10 and 11.

In LFL, the spin-lattice relaxation parameter $1/T_1$ is determined by the quasiparticles near the Fermi level, whose population is proportional to M^*T, whence $1/T_1T \propto M^*$, and is a constant quantity [62, 63]. When the superconducting state disappears as a magnetic field is applied, the ground state can be regarded as a field-induced LFL with field-dependent effective mass. As a result, $T_1T = const$, which implies that the Korringa law holds. According to (5.39), the ratio $1/T_1T \propto M^*(B)$ decreases as the magnetic field increases at $T < T^*(B)$, whereas in the case of a Landau Fermi liquid it remains constant, as noted above. On the other hand, at $T > T^*(B)$, the ratio $1/T_1T$ is a decreasing function of the temperature, $1/T_1T \propto M^*(T)$. These results are in good agreement with the experimental data [63]. Since $T^*(B)$ is an increasing function of the magnetic field [see (5.42)], the Korringa law remains valid even at higher temperatures and in stronger magnetic fields. Hence, at $T_0 \leq T^*(B_0)$ and high magnetic fields $B > B_0$, the system demonstrates distinct metallic behavior, because the effective mass decreases as B increases, see (5.39). For details, see Sect. 7.5.

The existence of FCQPT can also be verified experimentally, for at number densities $x > x_{FC}$ or beyond the FCQPT point, the system must become LFL at sufficiently low temperatures [53]. Experiments have shown that such a liquid indeed exists in the heavily doped non-superconducting compound $La_{1.7}Sr_{0.3}CuO_4$ [46, 47]. It is remarkable that for $T < 55$ K, the resistivity exhibits a T^2-behavior without an additional linear term and the Wiedemann-Franz law holds [46, 47]. At temperatures above 55 K, experimentalists have detected significant deviations from the LFL behavior. Observations [48, 71, 72] are in accord with these experimental findings showing that the system can again be returned to the LFL state by applying sufficiently strong magnetic fields (also see Chap. 6).

5.3.2.1 Common QCP in the High-T_c $Tl_2Ba_2CuO_{6+x}$ and the HF Metal $YbRh_2Si_2$

Under the application of magnetic fields $B > B_{c2} > B_{c0}$ and at $T < T^*(B)$, a high-T_c superconductor or HF metal can be driven to the LFL state with its resistivity given by (2.19). In that case measurements of the coefficient A produce information on its field dependence. We note that relationships between critical magnetic fields B_{c2} and B_{c0} are clarified in Sect. 7.6.

Precise measurements of $A(B)$ on the high-T_c compound $Tl_2Ba_2CuO_{6+x}$ [74] allow us to establish relationships between the physics of both high-T_c superconductors and HF metals and clarify the role of the extended quasiparticle paradigm. The

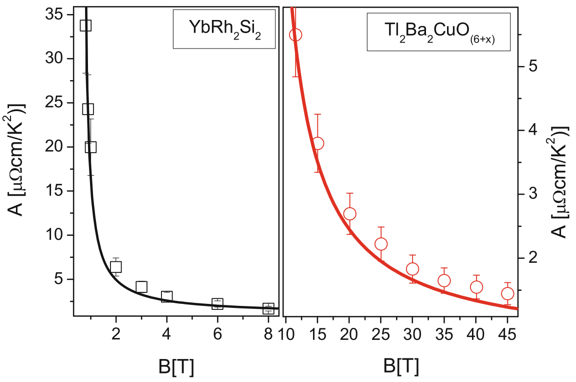

Fig. 5.3 The charge transport coefficient $A(B)$ as a function of magnetic field B obtained in measurements on $YbRh_2Si_2$ [73] and $Tl_2Ba_2CuO_{6+x}$ [74]. The different field scales are clearly seen. The *solid curves* represent our fit by (5.47)

$A(B)$ coefficient, being proportional to the quasiparticle—quasiparticle scattering cross-section, is found to be $A \propto (M^*(B))^2$ [56, 73]. With respect to (5.39), this implies that

$$A(B) \simeq A_0 + \frac{D}{B - B_{c0}}, \tag{5.47}$$

where A_0 and D are fitting parameters.

Figure 5.3 reports the fit of our theoretical dependence (5.47) to the experimental data for the measurements of the coefficient $A(B)$ for two different classes of substances: HF metal $YbRh_2Si_2$ (with $B_{c0} = 0.06$ T, left panel) [73] and high-T_c $Tl_2Ba_2CuO_{6+x}$ (with $B_{c0} = 5.8$ T, right panel) [74]. In Fig. 5.3, left panel, $A(B)$ is shown as a function of magnetic field B, applied both along and perpendicular to the c axis. For the latter the B values have been multiplied by a factor of 11 [73]. The different scales of field B_{c0} are clearly seen and demonstrate that B_{c0} has to be taken as an input parameter. Indeed, the critical field of $Tl_2Ba_2CuO_{6+x}$ with $B_{c0} = 5.8$ T is 2 orders of magnitude larger than that of $YbRh_2Si_2$ with $B_{c0} = 0.06$ T.

Figure 5.3 displays good coincidence of the theoretical dependence (5.40) with the experimental facts [74, 75]. This means that the physics underlying the field-induced reentrance into the LFL behavior, is the same for both classes of substances. To further corroborate this point, we rewrite (5.47) in the reduced variables A/A_0 and B/B_{c0}. Such rewriting immediately reveals the scaling nature of the behavior of these two substances—both of them are driven to common QCP related to FCQPT and induced by the application of magnetic field. As a result, (5.47) takes the form

$$\frac{A(B)}{A_0} \simeq 1 + \frac{D_N}{B/B_{c0} - 1}, \tag{5.48}$$

where $D_N = D/(A_0 B_{c0})$ is a constant. From (5.48) it is seen that upon applying the scaling to both coefficients $A(B)$ for $Tl_2Ba_2CuO_{6+x}$ and $A(B)$ for $YbRh_2Si_2$ they are reduced to a function depending on the single variable B/B_{c0} thus demonstrating universal behavior. To support (5.48), we replot both dependencies in reduced

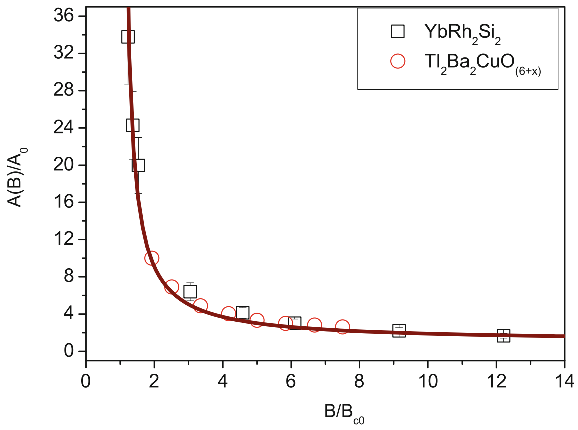

Fig. 5.4 Normalized coefficient $A(B)/A_0 \simeq 1 + D_N/(y-1)$ given by (5.48) as a function of normalized magnetic field $y = B/B_{c0}$ shown by *squares* for $YbRh_2Si_2$ and by *circles* for high-T_c $Tl_2Ba_2CuO_{6+x}$. D_N is the only fitting parameter

variables A/A_0 and B/B_{c0} in Fig. 5.4. Such replotting immediately reveals the universal scaling nature of the behavior of these two substances. It is seen from Fig. 5.4 that close to the magnetic induced QCP there are no "external" physical scales revealing the scaling. Therefore the normalization by the scales A_0 and B_{c0} immediately uncovers the common physical nature of these substances, allowing us to get rid of the specific properties of the system that define the values of A_0 and B_{c0}.

Based on the above analysis of the A coefficients, we conclude that there is at least one quantum phase transition inside the superconducting dome of high-T_c superconductors, and this transition is FCQPT [76].

5.4 Appearance of FCQPT in Fermi systems

We call the Fermi systems approaching QCP from a disordered side as highly correlated systems. We do that in order to distinguish them from strongly correlated systems (or liquids) that are already beyond FCQPT placed at the quantum critical line as shown in Fig. 3.2. A detailed description of the properties of highly correlated systems we give in Chap. 6, while the properties of strongly correlated systems are discussed in Chap. 8. In the present section, we discuss the behavior of the effective mass M^* as a function of the density x of the system as $x \to x_{FC}$.

The experimental data for high-density 2D ^{3}He [77–80] show that the effective mass becomes divergent when the density, at which the 2D liquid ^{3}He begins to solidify, is reached [78]. Also observed was a sharp increase in the effective mass in the metallic 2D electron system as the density x decreases and tends to the critical density of the metal-insulator transition [81]. We note that there is no ferromagnetic instability in the Fermi systems under consideration and the corresponding Landau interaction obeys the inequality $F_0^a > -1$ [78, 81], which agrees with the model of nearly localized fermions [82–84].

We examine the divergence of the effective mass in 2D and 3D highly correlated Fermi liquids at $T = 0$ as the density $x \to x_{FC}$ while approaching FCQPT from the disordered phase. We begin by calculating M^* as a function of the difference $(x - x_{FC})$ for a 2D Fermi liquid. To do this, we use the equation for M^* derived in [28], where the divergence of M^* related to the generation of density wave in various Fermi liquids was predicted [28]. As $x \to x_{FC}$, the effective mass M^* can be approximately written as

$$\frac{1}{M^*} \simeq \frac{1}{m} + \frac{1}{4\pi^2} \int_{-1}^{1} \int_{0}^{g_0} \frac{y\,dy\,dg}{\sqrt{1-y^2}} \frac{v(q(y))}{[1 - R(q(y), g)\chi_0(q(y))]^2}. \tag{5.49}$$

Here we use the notation $p_F\sqrt{2(1-y)} = q(y)$, where $q(y)$ is the momentum, $v(y)$ is the interaction, the integral over coupling constant g is taken from zero to the actual value g_0, $\chi_0(q, \omega)$ is the linear response function for the noninteracting Fermi liquid, and $R(q, \omega)$ is the effective interaction, with both functions taken at $\omega = 0$. The quantities R and χ_0 determine the response function for the system,

$$\chi(q, \omega, g) = \frac{\chi_0(q, \omega)}{1 - R(q, \omega, g)\chi_0(q, \omega)}. \tag{5.50}$$

Near the instability related to the generation of density wave at the density x_{cdw}, the singular part of the response function χ has the well-known form, see e.g., [26]

$$\chi^{-1}(q, \omega, g) \simeq a(x_{cdw} - x) + b(q - q_c)^2 + c(g_0 - g), \tag{5.51}$$

where a, b, and c are constants and $q_c \simeq 2p_F$ is the momentum of the density-wave. Substitution of (5.51) in (5.49) and integration permits to represent the equation for the effective mass M^* in the form

$$\frac{1}{M^*(x)} = \frac{1}{m} - \frac{c}{\sqrt{x - x_{cdw}}}, \tag{5.52}$$

where c is a positive constant. It follows from (5.52) that $M^*(x)$ diverges as a function of the difference $(x - x_{FC})$ and $M^*(x) \to \infty$ as $x \to x_{FC}$ [85, 86]

$$\frac{M^*(x)}{m} \simeq a_1 + \frac{a_2}{x - x_{FC}}, \tag{5.53}$$

where a_1 and a_2 are constants. We note that (5.52) and (5.53) do not explicitly contain the interaction $v(q)$, although $v(q)$ affects a_1, a_2 and x_{FC}. This result agrees with (2.21), which determines the same universal type of divergence (i.e. a divergence that is independent explicitly of the interaction type). Hence, both (2.21) and (5.53) can be applied to 2D ^{3}He, the electron liquid, and other Fermi liquids. We also see that FCQPT precedes the formation of density waves (or charge-density waves)

Fig. 5.5 The dependence of the effective mass $M^*(\mathrm{z})$ on dimensionless density $\mathrm{z} = x/x_{FC}$. Experimental data from [78] are shown by *circles* and *squares* and those from [80] are shown by *triangles*. The effective mass is fitted as $M^*(\mathrm{z})/M \propto b_1 + b_2/(1-\mathrm{z})$ (also see (2.21)), while the reciprocal one as $M/M^*(\mathrm{z}) \propto b_3\,\mathrm{z}$, where b_1, b_2 and b_3 are constants

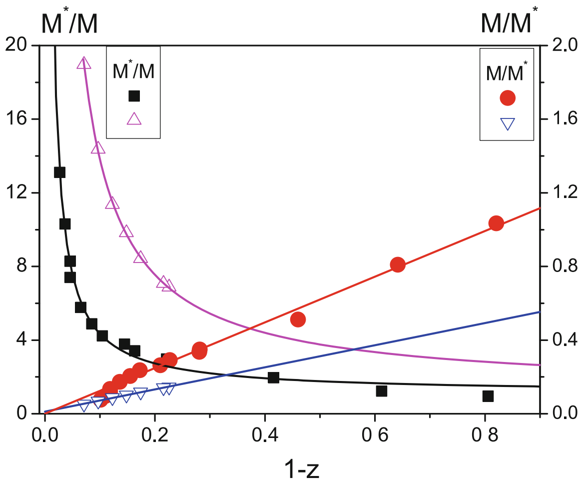

in Fermi systems. As we have seen in Sect. 5.1, the high-T_c superconductivity is explained within the framework of the fermion condensation theory. Therefore, one expect to observe charge-density waves in high-T_c compounds, and this expectation is in accordance with experimental facts, see e.g., [87]. We note that the difference $(x - x_{FC})$ must be positive in both cases, since the density x approaches x_{FC} when the system is on the disordered side of FCQPT with the finite effective mass $M^*(x) > 0$. In the case of ^{3}He, FCQPT occurs as the density increases, when the potential energy begins to dominate the ground-state energy due to the strong repulsive short ranged part of the interparticle interaction. Thus, for the 2D ^{3}He liquid, the difference $(x - x_{FC})$ on the right hand side of (5.53) must be replaced by $(x_{FC} - x)$. Experiments have shown that the effective mass indeed diverges at high densities for 2D ^{3}He and at low ones for 2D electron systems [78, 81].

In Fig. 5.5, we present the experimental values of the effective mass $M^*(\mathrm{z})$ obtained by the measurements on ^{3}He monolayer [78]. These measurements, in coincidence with those from [80], show the divergence of the effective mass at $x = x_{FC}$. To show, that our FCQPT approach is able to describe the above data, we represent the fit of $M^*(\mathrm{z})$ by the rational expression $M^*(\mathrm{z})/M \propto b_1 + b_2/(1-\mathrm{z})$ and the reciprocal effective mass by the linear fit $M/M^*(\mathrm{z}) \propto b_3\,\mathrm{z}$. We note here, that the linear fit has been used to describe the experimental data for bilayer ^{3}He [80, 88] and we use this function here for the sake of illustration. It is seen from Fig. 5.5 that the data of [80] (^{3}He bilayer) can be equally well approximated by both linear and rational functions, while the data in [78] cannot. For instance, both fitting functions give for the critical density in bilayer $x_{FC} \approx 9.8\,\mathrm{nm}^{-2}$, while for monolayer [78] these values are different $-x_{FC} = 5.56\,\mathrm{nm}^{-2}$ for linear fit and $x_{FC} = 5.15\,\mathrm{nm}^{-2}$. It is seen from Fig. 5.5, that linear fit is unable to properly describe the experiment [78] at small $1 - \mathrm{z}$ (i.e. near $x = x_{FC}$), while the fit describes the experiment very well.

This means that more detailed measurements are necessary in the vicinity $x = x_{FC}$ [89].

The effective mass as a function of the electron density x in a silicon MOSFET is shown in Fig. 2.1. We see that (5.52) provides a good description of the experimental results. The divergence of the effective mass $M^*(x)$ discovered in measurements involving 2D ^{3}He [77, 78, 80] is illustrated by Figs. 2.2 and 5.5. Figures 2.1, 2.2 and 5.5 show that the description provided by (2.21), (5.52) and (5.53) is in good agreement with the experimental data.

In the case of 3D systems, as $x \to x_{FC}$, the effective mass is given by the expression [28]

$$\frac{1}{M^*} \simeq \frac{1}{m} + \frac{p_F}{4\pi^2} \int_{-1}^{1} \int_{0}^{g_0} \frac{v(q(y))y dy dg}{[1 - R(q(y), g)\chi_0(q(y))]^2}. \tag{5.54}$$

Comparison of (5.49) and (5.54) shows that there is no essential difference between them, although they describe different cases, 2D and 3D. In the 3D case, we can derive equations similar to (5.52) and (5.53) just as we did in the 2D case, but the numerical coefficients are different, because they depend on the dimensionality. The only difference between 2D and 3D electron systems is that FCQPT occurs in 3D systems at densities much lower than in those corresponding to 2D systems. No such transition occurs in massive 3D ^{3}He because the FCQPT transition is presumably absorbed by the first-order liquid-solid phase transition [77, 78].

References

1. L.N. Oliveira, E.K.U. Gross, W. Kohn, Phys. Rev. Lett. **60**, 2430 (1988)
2. J. Bardeen, L.N. Cooper, J.R. Schrieffer, Phys. Rev. **108**, 1175 (1957)
3. D.R. Tilley, J. Tilley, *Superfluidity and Superconductivity* (Hilger, Bristol, 1985)
4. V.A. Khodel, V.R. Shaginyan, JETP Lett. **51**, 553 (1990)
5. J. Dukelsky, V. Khodel, P. Schuck, V. Shaginyan, Z. Phys. **102**, 245 (1997)
6. V.A. Khodel, V.R. Shaginyan, in *Condensed Matter Theories*, ed. by J. Clark, V. Plant (Nova Science Publishers Inc., New York, 1997), p. 221
7. G.E. Volovik, JETP Lett. **53**, 222 (1991)
8. S.A. Artamonov, Y.G. Pogorelov, V.R. Shaginyan, JETP Lett. **68**, 942 (1998)
9. Y.G. Pogorelov, V.R. Shaginyan,*in Condensed Matter Theories*, vol 18. (Nova Science Publishers Inc., New Yorhk, 2003), p. 191
10. M.Y. Amusia, V.R. Shaginyan, JETP Lett. **73**, 232 (2001)
11. M.Y. Amusia, V.R. Shaginyan, Phys. Rev. B **63**, 224507 (2001)
12. V.R. Shaginyan, Physica B **413**, 312–313C (2002)
13. S.A. Artamonov, V.R. Shaginyan, JETP **92**, 287 (2001)
14. L.P. Gor'kov, Sov. Phys. JETP **7**, 505 (1958)
15. E.M. Lifshitz, L.P. Pitaevskii, *Statisticheskaya Fizika (Statistical Physics), part 2*. Course of Theoretical Physics (Pergamon Press, Oxford, 1980)
16. V.R. Shaginyan, A.Z. Msezane, V.A. Stephanovich, E.V. Kirichenko, Europhys. Lett. **76**, 898 (2006)

17. V.I. Belyavsky, Y.V. Kopaev, Phys. Usp. **49**, 441 (2006)
18. N.N. Bogoliubov, Nuovo Cimento **7**, 794 (1958)
19. H. Matsui, T. Sato, T. Takahashi, S.C. Wang, H.B. Yang, H. Ding, T. Fujii, T. Watanabe, A. Matsuda, Phys. Rev. Lett **90**, 217002 (2003)
20. M.Y. Amusia, S.A. Artamonov, V.R. Shaginyan, JETP Lett. **74**, 396 (2001)
21. R.B. Laughlin, D. Pines, Proc. Natl. Acad. Sci. USA **97**, 28 (2000)
22. P.W. Anderson, Science **288**, 480 (2000)
23. M.Y. Amusia, V.R. Shaginyan, Contrib. Plasma Phys. **53**, 721 (2013)
24. D. Yudin, D. Hirschmeier, H. Hafermann, O. Eriksson, A.I. Lichtenstein, M.I. Katsnelson, Phys. Rev. Lett. **112**, 070403 (2014)
25. V.Y. Irkhin, A.A. Katanin, M.I. Katsnelson, Phys. Rev. Lett. **89**, 076401 (2002)
26. C.M. Varma, Z. Nussionov, W. van Saarloos, Phys. Rep. **361**, 267 (2002)
27. M.Y. Amusia, V.R. Shaginyan, JETP Lett. **76**, 651 (2002)
28. V.A. Khodel, V.R. Shaginyan, M.V. Zverev, JETP Lett. **65**, 242 (1997)
29. N. Miyakawa, J. Zasadzinski, L. Ozyuzer, P. Guptasarma, D.G. Hinks, C. Kendziora, K.E. Gray, Phys. Rev. Lett. **83**, 1018 (1999)
30. V.A. Khodel, M.V. Zverev, V.M. Yakovenko, Phys. Rev. Lett. **95**, 236402 (2005)
31. C. Petrovic, P.G. Pagliuso, M.F. Hundley, R. Movshovich, J.L. Sarrao, J.D. Thompson, Z. Fisk, P. Monthoux, J. Phys. Condens. Matter **13**, L337 (2001)
32. A. Kaminski, M. Randeria, J.C. Campuzano, M.R. Norman, H. Fretwell, J. Mesot, T. Sato, T. Takahashi, K. Kadowaki, Phys. Rev. Lett. **86**, 1070 (2001)
33. T. Valla, A.V. Fedorov, P.D. Johnson, B.O. Wells, S.L. Hulbert, Q. Li, G.D. Gu, N. Koshizuka, Science **285**, 2110 (1999)
34. T. Valla, A.V. Fedorov, P.D. Johnson, Q. Li, G.D. Gu, N. Koshizuka, Phys. Rev. Lett. **85**, 828 (2000)
35. P.V. Bogdanov, A. Lanzara, S.A. Kellar, X.J. Zhou, E.D. Lu, W.J. Zheng, G. Gu, J.I. Shimoyama, K. Kishio, H. Ikeda, R. Yoshizaki, Z. Hussain, Z.X. Shen, Phys. Rev. Lett. **85**, 2581 (2000)
36. C.M. Varma, P.B. Littlewood, S. Schmittrink, E. Abrahams, A.E. Ruckenstein, Phys. Rev. Lett. **63**, 1996 (1989)
37. C.M. Varma, P.B. Littlewood, S. Schmittrink, E. Abrahams, A.E. Ruckenstein, Phys. Rev. Lett. **64**, 497 (1990)
38. A. Ino, C. Kim, M. Nakamura, T. Yoshida, T. Mizokawa, A. Fujimori, Z.X. Shen, T. Kakeshita, H. Eisaki, S. Uchida, Phys. Rev. B **65**, 094504 (2002)
39. X.J. Zhou, T. Yoshida, A. Lanzara, P.V. Bogdanov, S.A. Kellar, K. Shen, W.L. Yang, F. Ronning, T. Sasagawa, T. Kakeshita, T. Noda, H. Eisaki, S. Uchida, C.T. Lin, F. Zhou, J.W. Xiong, W.X. Ti, Z.X. Zhao, A. Fujimori, Z. Hussain, Z.X. Shen, Nature **423**, 398 (2003)
40. W.J. Padilla, Y.S. Lee, M. Dumm, G. Blumberg, S. Ono, K. Segawa, S. Komiya, Y. Ando, D.N. Basov, Phys. Rev. B **72**, 060511 (2005)
41. T. Valla, A.V. Fedorov, P.D. Johnson, S.L. Hulbert, Phys. Rev. Lett. **83**, 2085 (1999)
42. J.D. Koralek, J.F. Douglas, N.C. Plumb, Z. Sun, A.V. Fedorov, M.M. Murnane, H.C. Kapteyn, S.T. Cundiff, Y. Aiura, K. Oka, H. Eisaki, D.S. Dessau, Phys. Rev. Lett. **96**, 017005 (2006)
43. D.L. Feng, A. Damascelli, K.M. Shen, N. Motoyama, D.H. Lu, H. Eisaki, K. Shimizu, J.I. Shimoyama, K. Kishio, N. Kaneko, M. Greven, G.D. Gu, X.J. Zhou, C. Kim, F. Ronning, N.P. Armitage, Z.X. Shen, Phys. Rev. Lett. **88**, 107001 (2002)
44. A.B. Migdal, *Theory of Finite Fermi Systems and Applications to Atomic Nuclei* (Wiley, New York, 1967)
45. Z.M. Yusof, B.O. Wells, T. Valla, A.V. Fedorov, P.D. Johnson, Q. Li, C. Kendziora, S. Jian, D.G. Hinks, Phys. Rev. Lett. **88**, 167006 (2002)
46. S. Nakamae, K. Behnia, N. Mangkorntong, M. Nohara, H. Takagi, S.J.C. Yates, N.E. Hussey, Phys. Rev. B **68**, 100502(R) (2003)
47. N.E. Hussey, M. Abdel-Jawad, A. Carrington, A.P. Mackenzie, L. Balicas, Nature **425**, 814 (2003)
48. Y.G. Pogorelov, V.R. Shaginyan, JETP Lett. **76**, 532 (2002)
49. M. de Llano, J.P. Vary, Phys. Rev. C **19**, 1083 (1979)

50. M. de Llano, A. Plastino, J.P. Zabolitsky, Phys. Rev. C **20**, 2418 (1979)
51. M.V. Zverev, M. Baldo, J. Phys. Condens. Matter **11**, 2059 (1999)
52. V.A. Khodel, J.W. Clark, M.V. Zverev, Phys. Rev. B **78**, 075120 (2008)
53. V.R. Shaginyan, A.Z. Msezane, M.Y. Amusia, Phys. Lett. A **338**, 393 (2005)
54. V.R. Shaginyan, JETP Lett. **79**, 286 (2004)
55. D. Takahashi, S. Abe, H. Mizuno, D. Tayurskii, K. Matsumoto, H. Suzuki, Y. Onuki, Phys. Rev. B **67**, 180407(R) (2003)
56. V.A. Khodel, P. Schuck, Z. Phys. B: Condens. Matter **104**, 505 (1997)
57. K. Kadowaki, S.B. Woods, Solid State Commun. **58**, 507 (1986)
58. N. Tsujii, H. Kontani, K. Yoshimura, Phys. Rev. Lett. **94**, 057201 (2005)
59. A.C. Jacko, J.O. Fjærestad, B.J. Powell, Nature Physics **5**, 422 (2009)
60. C. Proust, E. Boaknin, R.W. Hill, L. Taillefer, A.P. Mackenzie, Phys. Rev. Lett. **89**, 147003 (2002)
61. R. Bel, K. Behnia, Y. Nakajima, K. Izawa, Y. Matsuda, H. Shishido, R. Settai, Y. Onuki, Phys. Rev. Lett. **92**, 217002 (2004)
62. J. Korringa, Physica (Utrecht) **16**, 601 (1950)
63. G.Q. Zheng, T. Sato, Y. Kitaoka, M. Fujita, K. Yamada, Phys. Rev. Lett. **90**, 197005 (2003)
64. C.L. Kane, M.P.A. Fisher, Phys. Rev. Lett. **76**, 3192 (1996)
65. C.L. Kane, M.P.A. Fisher, Phys. Rev. B **55**, 15832 (1997)
66. T. Senthil, M.P.A. Fisher, Phys. Rev. B **62**, 7850 (2000)
67. A. Houghton, S. Lee, J.B. Marston, Phys. Rev. B **65**, 22503 (2002)
68. V.A. Khodel, M.V. Zverev, JETP Lett. **85**, 404 (2007)
69. A.P. Mackenzie, S.R. Julian, D.C. Sinclair, C.T. Lin, Phys. Rev. B **53**, 5848 (1996)
70. M.Y. Amusia, V.R. Shaginyan, Phys. Lett. A **315**, 288 (2003)
71. V.R. Shaginyan, M.Y. Amusia, K.G. Popov, Phys. Usp. **50**, 563 (2007)
72. V.R. Shaginyan, M.Y. Amusia, A.Z. Msezane, K.G. Popov, Phys. Rep. **492**, 31 (2010)
73. P. Gegenwart, J. Custers, C. Geibel, K. Neumaier, K.T.T. Tayama, O. Trovarelli, F. Steglich, Phys. Rev. Lett. **89**, 056402 (2002)
74. T. Shibauchi, L. Krusin-Elbaum, M. Hasegawa, Y. Kasahara, R. Okazaki, Y. Matsuda, Proc. Natl. Acad. Sci. USA **105**, 7120 (2008)
75. V.R. Shaginyan, K.G. Popov, JETP Lett. **88**, 183 (2008)
76. V.R. Shaginyan, M.Y. Amusia, K.G. Popov, V.A. Stephanovich, Phys. Lett. A **373**, 686 (2009)
77. A. Casey, H. Patel, J. Nyeki, B.P. Cowan, J. Saunders, Low Temp. Phys. **113**, 293 (1998)
78. A. Casey, H. Patel, J. Cowan, B.P. Saunders, Phys. Rev. Lett. **90**, 115301 (2003)
79. K.D. Morhard, C. Bauerle, J. Bossy, Y. Bunkov, S.N. Fisher, H. Godfrin, Phys. Rev. B **53**, 2658 (1996)
80. M. Neumann, J. Nyéki, B. Cowan, J. Saunders, Science **317**, 1356 (2007)
81. A.A. Shashkin, S.V. Kravchenko, V.T. Dolgopolov, T.M. Klapwijk, Phys. Rev. B **66**, 073303 (2002)
82. D. Vollhardt, Rev. Mod. Phys. **56**, 99 (1984)
83. M. Pfitzner, P. Wölfle, Phys. Rev. B **33**, 2003 (1986)
84. D. Vollhardt, P. Wölfle, P.W. Anderson, Phys. Rev. B **35**, 6703 (1987)
85. V.M. Yakovenko, V.A. Khodel, JETP Lett. **78**, 850 (2003)
86. V.R. Shaginyan, JETP Lett. **77**, 104 (2003)
87. R. Comin, A. Frano, M.M. Yee, Y. Yoshida, H. Eisaki, E. Schierle, E. Weschke, R. Sutarto, F. He, A. Soumyanarayanan, Y. He, M.L. Tacon, I.S. Elfimov, J.E. Hoffman, G.A. Sawatzky, B. Keimer, A. Damascelli, Science **343**, 390 (2014)
88. A. Benlagra, C. Pépin, Phys. Rev. Lett. **100**, 176401 (2008)
89. V.R. Shaginyan, A.Z. Msezane, K.G. Popov, V.A. Stephanovich, Phys. Rev. Lett. **100**, 096406 (2008)

Chapter 6
Highly Correlated Fermi Liquid in Heavy-Fermion Metals: The Scaling Behavior

Abstract In this chapter we show how the FCQPT theory works. We do that on the base of experimentally relevant examples. Namely, as noted in the Introduction (Chap. 1), the challenge for the theories is to explain the scaling behavior of the normalized effective mass $M^*_N(y)$ displayed in Fig. 1.3. The theories analyzing only the critical exponents characterizing $M^*_N(y)$ at $y \gg 1$ consider only a part of the problem. In this section we analyze and derive the scaling behavior of the normalized effective mass near QCP as reported in Fig. 1.3. We start with describing magnetic field dependence of the quasiparticle effective mass in Sect. 6.1. Quasiparticle damping and the temperature dependence of the effective mass is considered in Sect. 6.2. In Sect. 6.4 we study the energy scales and the general properties of the phase diagrams of strongly correlated Fermi systems, including HF metals like $\mathrm{YbRh_2Si_2}$, and consider the evolution of these diagrams under the application of negative/positive pressure. We have observed that at sufficiently high temperatures outside the AFM phase the transition temperature follows almost linear B-dependence, coinciding with the transition temperature, induced by the presence of FC.

6.1 Magnetic Field Dependence of the Quasiparticle Effective Mass

When the system approaches FCQPT from the disordered side, at sufficiently low temperatures (see Fig. 3.2) it remains LFL with the effective mass M^* that strongly depends on the distance $r = (x - x_{FC})/x_{FC}$ and magnetic field B. This state of the system with M^* being strongly dependent on r and B resembles the state of strongly correlated liquid described in Chap. 8. But in contrast to a strongly correlated liquid, the system in question does not have temperature independent entropy S_0 specified by (3.8) and at low temperatures becomes LFL with effective mass $M^* \propto 1/r$ [see (2.21) and (5.53)]. Such a system can be called a highly correlated liquid. We will see shortly, that its effective mass exhibits the scaling behavior. We will study this behavior when the system transits from LFL to NFL states.

We use Landau equation to study the effective mass $M^*(T, B)$ as a function of the temperature and magnetic field. For the model of homogeneous HF liquid at finite

M.Y. Amusia et al., *Theory of Heavy-Fermion Compounds*, Springer Series in Solid-State Sciences 182, DOI 10.1007/978-3-319-10825-4_6

temperatures and magnetic fields, this equation acquires the form [1]

$$\frac{1}{M^*(T,B)} = \frac{1}{m} + \sum_{\sigma_1} \int \frac{\mathbf{p}_F \mathbf{p}}{p_F^3} F_{\sigma,\sigma_1}(\mathbf{p_F},\mathbf{p}) \frac{\partial n_{\sigma_1}(\mathbf{p},T,B)}{\partial p} \frac{d\mathbf{p}}{(2\pi)^3}. \tag{6.1}$$

where $F_{\sigma,\sigma_1}(\mathbf{p_F},\mathbf{p})$ is the Landau interaction dependent, on momenta p_F, p and spin index σ. For the sake of definiteness, we assume that the HF sysmem is a 3D liquid. As seen in Sect. 5.4, the scaling behavior obtained in the HF liquid models, is independent of dimensionality and interparticle interaction, while the scales like M^*_M and T_M are dependent. To simplify matters, we suppress the spin dependence of the effective mass, because $M^*(T,B)$ is nearly independent of the spin in weak fields. The quasiparticle distribution function can be expressed as

$$n_\sigma(\mathbf{p},T) = \left\{1 + \exp\left[\frac{(\varepsilon(\mathbf{p},T) - \mu_\sigma)}{T}\right]\right\}^{-1}, \tag{6.2}$$

where $\varepsilon(\mathbf{p},T)$ is determined by (2.3). The single-particle spectrum is a variational derivative of the system energy $E[n_\sigma(\mathbf{p})]$ with respect to the quasiparticle distribution function or occupation numbers n,

$$\varepsilon(\mathbf{p}) = \frac{\delta E[n(\mathbf{p})]}{\delta n(\mathbf{p})}. \tag{6.3}$$

In our case the Landau interaction F is fixed by the condition that the system is situated at FCQPT. The variational procedure, being applied to the functional $E[n_\sigma(\mathbf{p},T)]$, gives

$$\frac{\partial \varepsilon_\sigma(\mathbf{p},T)}{\partial \mathbf{p}} = \frac{p}{M} + \sum_{\sigma_1} \int F_{\sigma,\sigma_1}(\mathbf{p},\mathbf{p}_1) \frac{\partial n_{\sigma_1}(\mathbf{p}_1,T)}{\partial \mathbf{p}} \frac{d^3 p_1}{(2\pi)^3}, \tag{6.4}$$

where $\varepsilon(\mathbf{p},T) = \varepsilon_\sigma(\mathbf{p},T) \equiv \varepsilon[n_\sigma(\mathbf{p},T)]$. Equations (6.2) and (6.4) constitute the closed set for self-consistent determination of $\varepsilon_\sigma(\mathbf{p},T)$ and $n_\sigma(\mathbf{p},T)$. The sole role of the Landau interaction is to bring the system to FCQPT point, where $M^* \to \infty$ at $T = 0$ and $H = 0$, and the Fermi surface alters its topology so that the effective mass acquires temperature and field dependence.

In our case, the single-particle spectrum depends on the spin only weakly, but the chemical potential may depend on the spin due to the Zeeman splitting. When this is important, we specifically indicate the spin dependence of physical quantities. We write the quasiparticle distribution function as $n_\sigma(\mathbf{p},T,B) \equiv n_\sigma(\mathbf{p},T=0,B=0) + \delta n_\sigma(\mathbf{p},T,B)$. Then (6.1) becomes

$$\frac{m}{M^*(T,B)} = \frac{m}{M^*(x)} + \frac{m}{p_F^2} \sum_{\sigma_1} \int \frac{\mathbf{p}_F \mathbf{p_1}}{p_F} F_{\sigma,\sigma_1}(\mathbf{p_F},\mathbf{p}_1) \frac{\partial \delta n_{\sigma_1}(\mathbf{p}_1,T,B)}{\partial p_1} \frac{d\mathbf{p}_1}{(2\pi)^3}. \tag{6.5}$$

We assume that the highly correlated HF liquid is close to FCQPT and the distance $r \to 0$, and therefore $M/M^*(x) \to 0$, as follows from (2.21). For normal metals, where the electron liquid behaves like LFL with the effective mass of several bare electron masses $M^*/m \sim 1$, at temperatures even near 1,000 K, the second term on the right hand side of (6.5) is of the order of T^2/μ^2 and is much smaller than the first term. The same is true, as can be verified, when a magnetic field $B \sim 100$ T is applied. Thus, the system behaves like LFL with the effective mass that is actually independent of the temperature or magnetic field, while $\rho(T) \propto AT^2$. This means that the corrections to the effective mass determined by the second term of the right-hand side of (6.5) are proportional to $(T/\mu)^2$ or $(\mu_B B/\mu)^2$.

Near QCP x_{FC}, with $m/M^*(x \to x_{FC}) \to 0$, the behavior of the effective mass alters dramatically as the first term on the right-hand side of (6.5) vanishes, the second term becomes dominant, and the effective mass is determined by the homogeneous version of (6.5) as a function of B and T. As a result, the LFL state vanishes and the system demonstrates the NFL behavior down to lowest temperatures.

We now qualitatively analyze the solutions of (6.5) at $x \simeq x_{FC}$ and $T = 0$. Application of magnetic field leads to Zeeman splitting of the Fermi surface, and the distance δp between the Fermi surfaces with spin "up" and spin "down" becomes $\delta p = p_F^{\uparrow} - p_F^{\downarrow} \sim \mu_B B M^*(B)/p_F$. We note that the second term of the right-hand side of (6.5) is proportional to $(\delta p)^2 \propto (\mu_B B M^*(B)/p_F)^2$, and therefore (6.5) reduces to [2–4]

$$\frac{m}{M^*(B)} = \frac{m}{M^*(x)} + c_1 \frac{(\mu_B B M^*(B))^2}{p_F^4}, \tag{6.6}$$

where c_1 is a constant. We also note that $M^*(B)$ depends on x and that this dependence disappears at $x = x_{FC}$. At this point, the term $m/M^*(x)$ vanishes and (6.6) becomes homogeneous and can be solved analytically [3–5]:

$$M^*(B) \propto \frac{1}{(B - B_{c0})^{2/3}}. \tag{6.7}$$

where B_{c0} is the critical magnetic field, regarded as a parameter (see the discussion of Fig. 5.3).

Equation (6.7) specifies the universal power-law behavior of the effective mass regardless the interaction type and is valid in 3D and 2D cases. For densities $x > x_{FC}$, the effective mass $M^*(x)$ is finite and we deal with the LFL state if the magnetic field is so weak that

$$\frac{M^*(x)}{M^*(B)} \sim 1, \tag{6.8}$$

and the effective mass M^* is practically independent of B. The second term in the right-hand side of (6.6), which is proportional to $(BM^*(B))^2$, is only a small correction. In the opposite case, at $T/T^*(B) \ll 1$, where

$$\frac{M^*(x)}{M^*(B)} \gg 1, \tag{6.9}$$

the electron liquid behaves as if it were at the quantum critical point in its LFL region, for $M^*(B)$ is given by (6.7). In the LFL state, the main thermodynamic and transport properties of the system are determined by the effective mass. It therefore follows from (6.7) that we have the unique possibility of controlling the magnetoresistance, resistivity, heat capacity, magnetization, thermal bulk expansion and other parameters by varying the magnetic field B. It should be noted that a large effective mass leads to a high density of states, which causes the emergence of a large number of competing states and phase transitions. We believe that such states can be suppressed by the external magnetic field, and we examine the thermodynamic properties of the system without considering such competition.

6.2 Quasiparticles and the Temperature Dependence of the Effective Mass

To examine qualitatively the dependence $M^*(T, B, x)$ at increasing temperatures, we simplify (6.5) by dropping the variable B and by mimicking the effect of an external magnetic field by a finite effective mass in the denominator of the first term of its right hand side. Then the effective mass $M^*(r)$ becomes a function of the distance r to the critical density, determined by the magnetic field B and x. At zero magnetic field $r = (x - x_{FC})/x_{FC}$. To obtain the equation, determining the temperature dependence of the effective mass, we first integrate the second term on the right-hand side of (6.5) over angular variables. Then we integrate the remaining equation by parts over p, replacing it by the variable $z = (\varepsilon(p) - \mu)/T$. In the case of a flat and narrow band, we can use the approximation $(\varepsilon(p) - \mu) \simeq p_F(p - p_F)/M^*(T)$. The result is

$$\frac{M}{M^*(T)} = \frac{m}{M^*(r)} - \alpha \int_0^\infty \frac{F(p_F, p_F(1+\alpha z))dz}{1+e^z} + \alpha \int_0^{1/\alpha} F(p_F, p_F(1-\alpha z))\frac{dz}{1+e^z}, \tag{6.10}$$

where we denote

$$F \sim m\frac{d(F^1 p^2)}{dp}, \ \alpha = \frac{TM^*(T)}{p_F^2} = \frac{TM^*(T)}{T_k M^*(r)}, \tag{6.11}$$

$T_k = p_F^2/M^*(r)$, and the Fermi momentum p_F is defined by the condition $\varepsilon(p_F) = \mu$.

We first consider the case $\alpha \ll 1$. Then, discarding terms of the order $\exp(-1/\alpha)$, we can set the upper limit in the second integral in (6.10) to infinity. This renders the sum of the second and third terms to be an even function of α. The resulting integrals involve the Fermi-Dirac function and are customary to LFL theory, which means that they can be evaluated by the standard procedure, see e.g., [6]. As we need only an estimate of the integrals, we present (6.10) as

$$\frac{m}{M^*(T)} \simeq \frac{m}{M^*(r)} + a_1\alpha^2 + a_2\alpha^4 + \cdots , \tag{6.12}$$

where a_1 and a_2 are constants of the order of unity and α is defined by (6.11).

Equation (6.12) is a typical equation of the LFL theory. The only exception is the effective mass $M^*(r)$, which depends strongly on the distance r and diverges as $r \to 0$. Nevertheless, (6.12) implies that as $T \to 0$, the corrections to $M^*(r)$ begin with terms of the order T^2 if

$$\frac{m}{M^*(r)} \gg \left(\frac{TM^*(T)}{T_k M^*(r)}\right)^2 \simeq \frac{T^2}{T_k^2}, \tag{6.13}$$

and the system behaves like LFL. Condition (6.13) implies that the behavior inherent in LFL disappears as $r \to 0$ and $M^*(r) \to \infty$. Then the free term in the right-hand side of (6.10) is negligible, $m/M^*(r) \to 0$, and (6.10) becomes homogeneous and determines the universal behavior of the effective mass $M^*(T)$. At a certain temperature $T^* \ll T_k$, the value of the sum on the right-hand side of (6.12) is determined by the second term and the relation (6.13) becomes invalid. Keeping only the second term in (6.12), we arrive at an equation for determining $M^*(T)$ in the transition region [3, 7]:

$$M^*(T) \propto \frac{1}{T^{2/3}}. \tag{6.14}$$

To estimate the transition temperature $T^*(B)$ where the effective mass becomes temperature dependent, we note that this quantity is a continuous function of the temperature and magnetic field: $M^*(B) \sim M^*(T^*)$. Combining (6.7) and (6.14), we obtain

$$T^*(B) \simeq \mu_B(B - B_{c0}). \tag{6.15}$$

As the temperature increases, the system transfers its into another mode. The coefficient α is then of the order of unity, $\alpha \sim 1$, the upper limit in the second integral in (6.10) cannot be set to be infinity, and odd terms begin to play a significant role. As a result, (6.12) breaks down and the sum of the first and second integrals on the right-hand side of (6.10) becomes proportional to $TM^*(T)$. Neglecting the first term $m/M^*(r)$ and approximating the sum of integrals by $TM^*(T)$, we obtain from (6.10) that

$$M^*(T) \propto \frac{1}{\sqrt{T}}. \tag{6.16}$$

We note that the dependence (6.16) for $M^*(T)$ can be also generated if the Landau interaction $F(p)$ is a nonanalytic function. In other words, in such case it cannot be expanded in Taylor series at $p \to 0$, see Sect. 4.1. The other possibilities leading to the dependence (6.16) will be considered in Chap. 18 and Sect. 18.2.

We therefore conclude that as the temperature increases and the condition $x \simeq x_{FC}$ is satisfied, the system demonstrates three kinds of regimes: (i) the Landau Fermi liquid regime at $\alpha \ll 1$, when (6.13) is valid and the effective mass is described by (6.7); (ii) the behavior defined by (6.14), when $M^*(T) \propto T^{-2/3}$ and $S(T) \propto M^*(T)T \propto T^{1/3}$; and (iii) the regime at $\alpha \sim 1$, when (6.16) is valid, $M^*(T) \propto 1/\sqrt{T}$, the entropy $S(T) \propto M^*(T)T \propto \sqrt{T}$, and the heat capacity $C(T) = T(\partial S(T)/\partial T) \propto \sqrt{T}$.

We illustrate the $S(T)$ behavior related to (6.16) (regime (iii)) using the model Landau functional [8, 9]

$$E[n(p)] = \int \frac{\mathbf{p}^2}{2M}\frac{d\mathbf{p}}{(2\pi)^3} + \frac{1}{2}\int V(\mathbf{p}_1 - \mathbf{p}_2)n(\mathbf{p}_1)n(\mathbf{p}_2)\frac{d\mathbf{p}_1 d\mathbf{p}_2}{(2\pi)^6}, \tag{6.17}$$

with nonanalytic Landau interaction

$$V(\mathbf{p}) = g_0 \frac{\exp(-\beta_0|\mathbf{p}|)}{|\mathbf{p}|}. \tag{6.18}$$

In the calculations below, we normalize the effective mass to m ($M^* = M^*/m$), the temperature T_0 to the Fermi energy ε_F^0 ($T = T_0/\varepsilon_F^0$) and use the dimensionless parameters: coupling constant $g = (g_0 m)/(2\pi^2)$ and $\beta = \beta_0 p_F$. FCQPT occurs when these parameters reach the critical values $\beta = b_c$ and $g = g_c$. On the other hand, a transition of this kind occurs as $M^* \to \infty$. This condition allows deriving a relation between b_c and g_c [8, 9]:

$$\frac{g_c}{b_c^3}(1 + b_c)\exp(-b_c)[b_c \cosh(b_c) - \sinh(b_c)] = 1. \tag{6.19}$$

This relation implies that the critical point of FCQPT can be reached by varying g_0 if β_0 and p_F are fixed, by varying p_F if β_0 and g_0 are fixed, etc. For definiteness, we vary g to reach FCQPT or to study the properties of the system beyond the critical point. Calculations of $M^*(T)$, $S(T)$, and $C(T)$ based on the model functional (6.17) with the parameters $g = g_c = 6.7167$ and $\beta = b_c = 3$ show that $M^*(T) \propto 1/\sqrt{T}$, $S(T) \propto \sqrt{T}$, and $C(T) \propto \sqrt{T}$. The temperature dependence of the entropy in this case is demonstrated in Fig. 6.1.

Let us now estimate the quasiparticle damping $\gamma(T)$. In the LFL theory, $\gamma(T)$ is given by [1]

$$\gamma \sim |\varGamma|^2 (M^*)^3 T^2, \tag{6.20}$$

where $\varGamma$ is the particle-hole interaction. In the case of highly correlated HF system with a high density of states caused by the enormous effective mass, $\varGamma$ cannot be approximated by the "bare" interaction between particles but can be estimated within

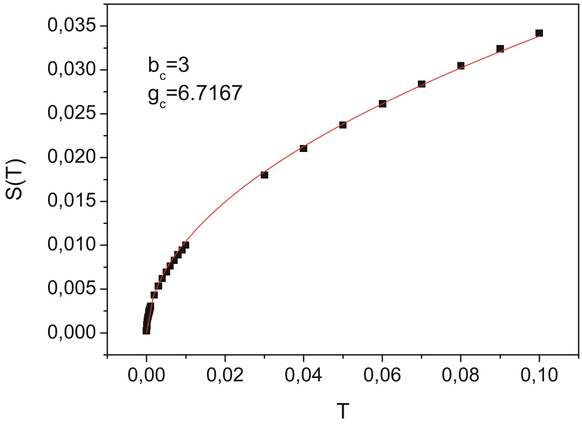

Fig. 6.1 The entropy $S(T)$ of a highly correlated Fermi liquid at the critical FCQPT point. The *solid line* represents the function $S(T) \propto \sqrt{T}$ and the *squares* mark the results of calculations

the "random phase approximation", which yields $|\Gamma| \sim 1/(p_F M^*(T))$ [10–12]. As a result, we find that $\gamma(T) \propto T^2$ in the LFL regime since M^* is temperature-independent. Then, $\gamma(T) \propto T^{4/3}$ in the $T^{-2/3}$ regime, and $\gamma(T) \propto T^{3/2}$ in the $1/\sqrt{T}$ regime. We note that in all these cases, the width γ is small compared to the characteristic quasiparticle energy, which is assumed to be of the order of T so that the quasiparticle concept is meaningful. A detailed consideration of both γ and the lifetime in magnetic fields in the case of HF compounds with FC is reserved for Chaps. 8–10.

The conclusion that can be drawn here is that when the HF liquid is localized near QCP of FCQPT and is on the disordered side, its low-energy excitations are quasiparticles with the effective mass $M^*(B, T)$. We note that at FCQPT, the quasiparticle renormalization z-factor remains approximately constant and the divergence of the effective mass that follows from (2.21) is not related to the fact that $z \to 0$ [13–15]. Therefore, the quasiparticle concept remains valid and it is these quasiparticles that constitute the extended paradigm and determine the transport, relaxation and thermodynamic properties of HF liquid.

6.3 Scaling Behavior of the Effective Mass and Energy Scales

Multiple energy scales are detected in measurements of the thermodynamic and transport properties heavy fermion metals. We demonstrate that the experimental data on the energy scales can be well described by the scaling behavior of the effective mass at FCQPT, and show that the dependence of the effective mass on temperature and applied magnetic fields gives rise to the non-Fermi liquid behavior. Our analysis is placed in the context of experimental results, obtained in remarkable measurements on the HF metal $YbRh_2Si_2$.

As it has been mentioned in the Introduction, to avoid difficulties associated with the anisotropy generated by the crystal lattice of HF metals, we study the universal behavior of HF metals using the model of the homogeneous HF (electron) liquid. The model is quite meaningful, because we consider the scaling behavior exhibited by the effective mass at low temperatures. The scaling behavior of the effective mass is determined by energy and momentum transfers that are small compared to the Debye characteristic temperature and momenta of the order of the reciprocal lattice constant a^{-1}. Therefore quasiparticles are influenced by the crystal lattice averaged over large distances compared to the length a so that we can safely use well-known jelly model. We note that the scales M^*_M, T_M, B_{c0} and B_{c2} etc. depend on the HF metal properties like its lattice symmetry, composition etc. For example, the critical magnetic field B_{c0} depends even on its orientation with respect to the lattice symmetry axes.

To explore the scaling behavior of M^*, we begin with qualitative analysis of (6.1). At FCQPT the effective mass M^* diverges and (6.1) becomes homogeneous determining M^* as a function of temperature as given by (6.14). If the system is located before FCQPT, M^* is finite, and at low temperatures the system demonstrates the LFL behavior $M^*(T) \simeq M^* + a_1 T^2$. As we have seen in Sect. 6.2, the LFL behavior takes place when the second term on the right hand side of (6.1) is small in comparison with the first one. Then, at increasing temperatures the system enters the transition regime, where M^* grows, reaching its maximum M^*_M at $T = T_M$, with subsequent diminishing. Near temperatures $T \geq T_M$ the last "traces" of LFL regime disappear, the second term starts to dominate, and again (6.1) becomes homogeneous so that the NFL behavior restores, manifesting itself in decreasing of M^* as $T^{-2/3}$. When the system is near FCQPT, it turns out that the solution of (6.1) $M^*(T)$ can be well approximated by a simple universal interpolating function [16]. The interpolation occurs between the LFL ($M^* \simeq M^* + a_1 T^2$) and NFL ($M^* \propto T^{-2/3}$) regimes, thus describing the above crossover. Introducing the dimensionless variable $y = T_N = T/T_M$, we obtain the desired expression

$$M^*_N(y) \approx c_0 \frac{1 + c_1 y^2}{1 + c_2 y^{8/3}}. \tag{6.21}$$

Here $M^*_N = M^*/M^*_M$ is the normalized effective mass, $c_0 = (1 + c_2)/(1 + c_1)$, c_1 and c_2 are fitting parameters, parameterizing the Landau interaction.

It follows from (6.7), that the application of magnetic field restores the LFL behavior, so that M^*_M depends on B as

$$M^*_M \propto (B - B_{c0})^{-2/3}, \tag{6.22}$$

while

$$T_M \propto \mu_B (B - B_{c0}). \tag{6.23}$$

Employing (6.22) and (6.23) to calculate M^*_M and T_M, we conclude that (6.21) is valid to describe the normalized effective mass in external fixed magnetic fields with $y = T/(B - B_{c0})$. On the other hand, (6.21) is valid when the applied magnetic field becomes a variable, while temperature is fixed at $T = T_f$. In that case, it is convenient to represent the variable as $y = (B - B_{c0})/T_f$.

6.3.1 Schematic Phase Diagram of a HF Metal

The schematic phase diagram of a HF metal is reported in Fig. 6.2, panel a. Magnetic field B is taken as the control parameter. In fact, the control parameter can be pressure P or doping (the number density) x as well. At $B = B_{c0}$, FCQPT takes place leading to a strongly degenerate state, where B_{c0} is the critical magnetic field, such that at $B > B_{c0}$ the system is driven towards the LFL state. We recall, that in our simple model B_{c0} is a parameter. The FC state is captured by the superconducting (SC), ferromagnetic (FM), antiferromagnetic (AFM) etc. states lifting the degeneracy. Below in Sect. 6.3.2 we consider the HF metal $YbRh_2Si_2$. In that case, $B_{c0} \simeq 0.06$ T ($B \perp c$) and at $T = 0$ and $B < B_{c0}$ the AFM state takes place with temperature dependent resistivity $\rho(T) \propto T^2$ [17]. At higher temperatures and fixed magnetic fields the

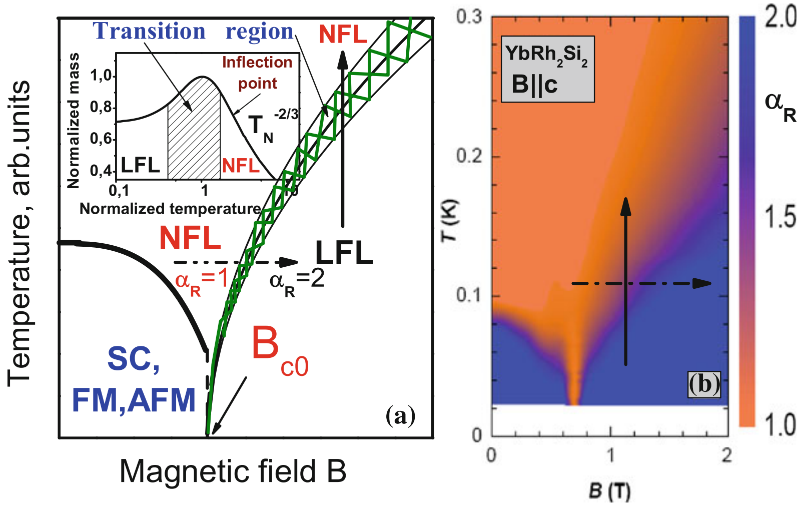

Fig. 6.2 The panel **a** represents a schematic phase diagram of HF metals. The effective mass diverges at magnetic field $B = B_{c0}$. The acronyms SC, FM and AFM denote the superconducting (SC), ferromagnetic (FM) and antiferromagnetic (AFM) states. At $B < B_{c0}$ the system can be in SC, FM or AFM states. The *vertical arrow* shows the transition from the LFL to the NFL state at fixed B along T with M^* depending on T. The *dash-dot horizontal arrow* illustrates the system moving from the NFL to LFL state along B at fixed T. The exponent α_R determines the temperature dependent part of the resistivity, see (2.19). In the LFL state the exponent $\alpha_R = 2$ and in the NFL $\alpha_R = 1$. In the transition regime the exponent evolves from its LFL value to the NFL one. The *inset* shows a schematic plot of the normalized effective mass versus the normalized temperature. Transition regime, where M^*_N reaches its maximum value M^*_M at $T = T_M$, is shown by the hatched area both in the panel **a** and in the *inset*. The *arrows* mark the position of inflection point in M^*_N and the transition region. The panel **b** shows the experimental $T - B$ phase diagram of the exponent $\alpha_R(T, B)$ as a function of temperature T versus magnetic field B [18]. The evolution of $\alpha_R(T, B)$ is shown by the *color*: the *orange color* corresponds to $\alpha_R(T, B) = 1$ (the NFL state) and the *blue color* corresponds to $\alpha_R(T, B) = 2$ (the LFL state). The NFL behavior occurs at the lowest temperatures right at QCP tuned by magnetic field. At rising magnetic fields $B > B_{c0}$ and $T \sim T^*(B)$, the broad transition regime from the NFL state to the field-induced LFL state occurs. The meaning of *arrows* is similar to panel **a**

NFL regime occurs, while rising B again drives the system from the NFL state to the LFL one as is shown by the dash-dot horizontal arrow in Fig. 6.2. We consider the transition region when the system moves from the NFL state to LFL one along the horizontal arrow and also moves from LFL state to NFL one along the vertical arrow as shown in Fig. 6.2. The inset to Fig. 6.2 demonstrates the scaling behavior of the normalized effective mass $M^*_N = M^*/M^*_M$ versus normalized temperature $T_N = T/T_M$, where M^*_M is the maximum value that M^* reaches at $T = T_M$. The $T^{-2/3}$ regime is marked as NFL since the effective mass depends strongly on temperature. The temperature region $T \simeq T_M$ signifies the crossover (or the transition region) between the LFL state with almost constant effective mass and NFL behavior, given by $T^{-2/3}$ dependence. Thus, temperatures $T \sim T_M$ can be regarded as the crossover region between the LFL and NFL states.

The transition (crossover) temperature $T^*(B)$ is not really the temperature of a phase transition. It is necessarily broad, very much depending on the criteria for determination of the point of such a crossover, as it is seen from the inset to Fig. 6.2a, see e.g., [17, 19]. As usual, the temperature $T^*(B)$ is extracted from the field dependence of charge transport, for example from the resistivity $\rho(T)$ given by (2.19). The LFL state is characterized by the power-law T^{α_R} dependence of the resistivity with $\alpha_R = 2$, see Sect. 7.2.3. The crossover (i.e. the transition regime shown by the hatched area both in the panel a of Fig. 6.2 and in its inset) takes place at temperatures where the resistance starts to deviate from the LFL behavior with $\alpha_R = 2$ so that the exponent becomes $1 < \alpha_R < 2$, see Sect. 7.2.3. As it will be shown in Sect. 7.2.3, in the NFL state $\alpha_R = 1$.

The panel b of Fig. 6.2 represents the experimental $T - B$ phase diagram of the exponent $\alpha_R(T, B)$ as a function of temperature T versus magnetic field B [18]. The evolution of $\alpha_R(T, B)$ is shown by the color: the orange color corresponds to $\alpha_R(T, B) = 1$ and the blue color corresponds to $\alpha_R(T, B) = 2$. It is seen from the panel that at the critical field $B_{c0} \simeq 0.66$ T ($B \| c$) the NFL behavior occurs down to the lowest temperatures while $YbRh_2Si_2$ transits from the NFL to LFL regimes under the application of magnetic field. It is worth noting that the phase diagram displayed in Fig. 6.2a coincides with that in the panel b.

A few remarks are in order here. As we shall see, the magnetic field dependence of the effective mass or other observables like the longitudinal magnetoresistance (LMR), see Sect. 7.2.1, do not have peculiarities like maxima. The normalization is to be performed in the other points like the inflection one at $T = T_{inf}$ (or at $B = B_{inf}$) shown in the inset to Fig. 6.2 by the arrow. Such a normalization is possible since it is established on the scales, $T_{inf} \propto T_M \propto (B - B_{c0})$. As a result, we obtain

$$\mu_B(B_{inf} - B_{c0}) \propto T_f. \tag{6.24}$$

It follows from (6.21) that in contrast to the Landau paradigm of quasiparticles, their effective mass strongly depends on T and B. This dependence leads to the extended quasiparticle paradigm and forms the NFL behavior. Also, the equation (6.21) reveals the scaling behavior of M^* near QCP by the proper choice of physical scales to measure the effective mass, magnetic field and temperature. At fixed magnetic fields, the characteristic scales of temperature and of the function $M^*(T, B)$ are defined by both T_M and M^*_M respectively. At fixed temperatures, the characteristic scales are $B_M - B_{c0}$ and M^*_M. It is seen from (6.22) and (6.23), that at fixed magnetic fields, $T_M \to 0$, and $M^*_M \to \infty$ and the width of the transition region shrinks to zero as $B \to B_{c0}$ when they are measured in "external" (dimensional) scales like T in Kelvins, magnetic field B in Teslas etc. It also follows from (6.14) and (6.24) that at fixed temperature T_f, $(B_{inf} - B_{c0}) \to 0$, and $M^*_M \to \infty$ so that the width of the transition region shrinks to zero as $T_f \to 0$. Thus, the application of the external scales obscure the scaling behavior of the effective mass and the thermodynamic and transport properties.

6.3.2 *Non-Fermi Liquid Behavior of* $\mathbf{YbRh_2Si_2}$

Here we analyze the transition regime and the NFL behavior of the HF metal $YbRh_2Si_2$. We demonstrate that experimental NFL thermodynamic and transport properties $YbRh_2Si_2$ can be successfully described by the scaling behavior of the normalized effective mass. This allows us to extract the thermodynamic and transport properties from the experimental data and represent them as functions of certain scaled variable. The validity of such scaling in the wide range (over three decades) of latter variable permits to conclude that the extended quasiparticles paradigm is perfectly valid. We show that peculiarities of the normalized effective mass give rise to the characteristic energy observed in the thermodynamic and transport properties of HF metals. The energy scales inherent in these functions are also explained.

Below we calculate the effective mass using (6.1) and employ (6.21) for estimations of the considered values. To compute the effective mass $M^*(T, B)$, we solve (6.1) with a quite general form of Landau interaction [3]. Choice of the interaction is dictated by the fact that the system has to be at QCP, which means that the first two p-derivatives of the single-particle spectrum $\varepsilon(\mathbf{p})$ should be equal to zero. Since the first derivative is proportional to the reciprocal quasiparticle effective mass $1/M^*$, its zero just signifies QCP of FCQPT. The second derivative must vanish; otherwise $\varepsilon(p) - \mu$ has the same sign below and above the Fermi surface, and the Landau state becomes unstable before $r \to 0$ [13]. Zeros of these two subsequent derivatives mean that the spectrum $\varepsilon(\mathbf{p})$ has an inflection point at p_F so that the lowest term of its Taylor expansion is proportional to $(p - p_F)^3$. After solution of (6.1), the obtained spectrum has been used to calculate the entropy $S(B, T)$, which, in turn, has been used to recalculate the effective mass $M^*(T, B)$ by virtue of the well-known LFL relation $M^*(T, B) = S(T, B)/T$. Our calculations of the normalized entropy as a function of the normalized magnetic field $B/B_{inf} = y$ and as a function of the normalized temperature $y = T/T_{inf}$ are depicted in Fig. 6.3. Here T_{inf} and B_{inf} are the corresponding inflection points in the function S. We normalize the entropy by its value at the inflection point $S_N(y) = S(y)/S(1)$. As it is seen from Fig. 6.3, our calculations corroborate the scaling behavior of the normalized entropy. Namely, the curves at different temperatures and magnetic fields merge into a single one in

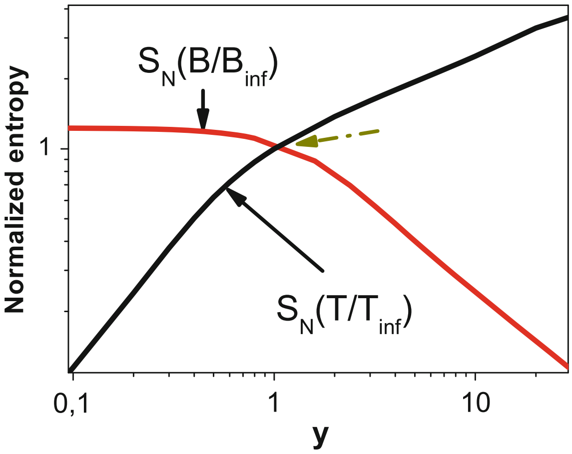

Fig. 6.3 The normalized entropy S_N versus $y = B/B_{inf}$ and $y = T/T_{inf}$, calculated at fixed temperature and magnetic field respectively. The inflection point is shown by the *dash-dot arrow*

terms of the variable y. The inflection point T_{inf} in $S(T)$ makes $M^*(T, B)$ to have its maximum as a function of T, while $M^*(T, B)$ versus B has no maximum. We note that our entropy calculations confirm the validity of (6.21) and the scaling behavior of the normalized effective mass shown in Fig. 6.2.

6.3.3 Heat Capacity and the Sommerfeld Coefficient

A large body of measurements of $C/T \propto M^*$, performed on the new generation of $YbRh_2Si_2$ samples at different magnetic fields B up to 1.5 T [20] allows to identify the scaling behavior of the effective mass M^* and observe different regimes of its behavior. Namely, the LFL regime, transition from the LFL one to the NFL one and the NFL regime itself can be traced. Under the application of magnetic field B, as it is seen from both (6.21) and from Fig. 1.2, the maximum in $C/T \propto M^*_M$ appears at T_M. The value of T_M shifts towards higher T at B increase. The Sommerfeld coefficient $C/T = \gamma_0$ is saturated at low temperatures. This saturation value decreases at higher magnetic fields.

The transition region corresponds to the temperatures where the vertical arrow in the main panel a of Fig. 6.2 crosses the hatched area. The width of the region, being proportional to $T_M \propto (B - B_{c0})$ shrinks, T_M moves to zero temperature and $\gamma_0 \propto M^*$ increases as $B \to B_{c0}$. These observations are in good agreement with experimental data [20].

To obtain the normalized effective mass M^*_N, the maximum structure in C/T was used to normalize C/T, and T was normalized by T_M. In Fig. 6.4, $M^*_N(T_N)$ ($T_N = T/T_M$ is the normalized temperature) is shown by different symbols, our calculations are shown by the solid line. Figure 6.4 reveals the scaling behavior of the normalized experimental curves—the scaled curves at different magnetic fields B merge into a

Fig. 6.4 The normalized effective mass M_N^* extracted from the measurements of the specific heat C/T on $\mathrm{YbRh_2Si_2}$ in magnetic fields B [20] listed in the legend. Our calculations are depicted by the *solid curve* tracing the scaling behavior of M_N^*

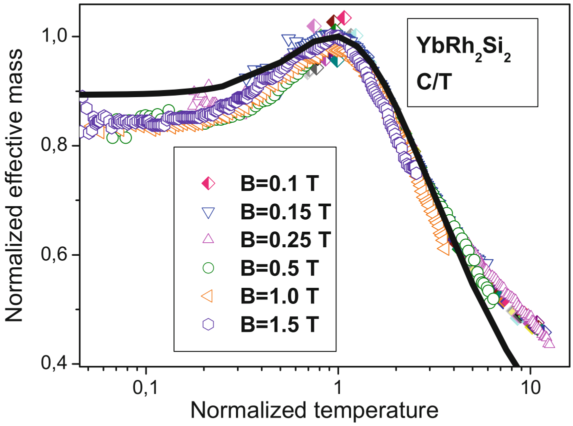

single one in terms of the normalized variable $y = T/T_M$. As seen, the normalized mass M_N^* extracted from the measurements is not a constant, as would be for LFL. The two regimes (the LFL and NFL regimes) separated by the transition region, as depicted by the hatched area in the inset to Fig. 6.2a, are clearly seen in Fig. 6.4 displaying good agreement between the theory and experiment. It is worth noting that the normalization procedure allows us to construct the scaled function C/T extracted from the experimental data in wide range of the normalized temperature. Indeed, it merges the measurements of C/T at different magnetic fields into single function of the normalized temperature. This function has a scaling behavior over three orders in its argument as it is seen from Fig. 6.4. Figure 1.2 shows that the NFL behavior extends at least to temperatures up to a few Kelvins. Thus, we conclude that the extended quasiparticle paradigm does take into account the remarkably large temperature ranges over which the NFL behavior is observed. We note that at these temperatures the contribution coming from phonons is still small.

6.4 General Properties of the Phase Diagrams of Heavy-Fermion Metals

We study the $T - B$ phase diagrams of HF metals, and show that at sufficiently high temperatures outside the ordered phase the crossover temperature $T^*(B)$ follows a linear B-dependence, and crosses the origin of the $T - B$ phase diagram. Upon analyzing the experimental $T - B$ phase diagram of $\mathrm{YbRh_2Si_2}$, we show that FCQPT represents QCP hidden in the AF phase. Our analysis agrees well with the experimental $T - B$ phase diagrams of the HF metals $\mathrm{YbRh_2Si_2}$, $\mathrm{Yb(Rh_{0.93}Co_{0.07})_2Si_2}$, and $\mathrm{Yb(Rh_{0.94}Ir_{0.06})_2Si_2}$. We calculate the isothermal magnetization M, and demonstrate that dM/dT exhibits a universal temperature over magnetic field scaling. Our results are in good agreement with data collected on $\mathrm{YbRh_2Si_2}$, and support our conclusion on the nature of the hidden QCP.

We start with considering energy scales observed in experimental measurements of the thermodynamics and transport properties on HF metals. Figure 6.5 presents $T_{inf}(B)$ and $T_M(B)$, shown by the solid and dash-dotted lines respectively. The boundary between the NFL and LFL regions is shown by the dashed line, and AFM marks the antiferromagnetic state. The corresponding data are taken from [21–23]. It is seen that our calculations are in good agreement with the experimental results. In Fig. 6.5, the solid and dash-dotted lines corresponding to the functions T_{inf} and T_M, respectively, represent the energy scales observed in LMR and in the heat capacity C/T. Thus, we can conclude that the energy scales are reproduced by (6.23) and (6.24) and related to the peculiarities T_M and T_{inf} of the normalized effective mass M^*_N, which are shown by the arrows in the inset to Fig. 6.2. As it is seen from Figs. 6.4 and 7.3, the experimental facts reflect back these peculiarities, while the normalization allows us to construct the unique scaled thermodynamic and transport functions extracted from the experimental data in a wide range of the scaled variable y. As seen from the aforementioned Figures, the constructed normalized thermodynamic and transport functions show the scaling behavior over three orders in the normalized variable. Note, that at $B \to B_{c0}$ both $T_{inf} \to 0$ and $T_M \to 0$, so that the LFL and the transition regimes in C/T and LMR are shifted to very low temperatures. Therefore due to experimental difficulties these regimes cannot be unambiguously identified in HF metals.

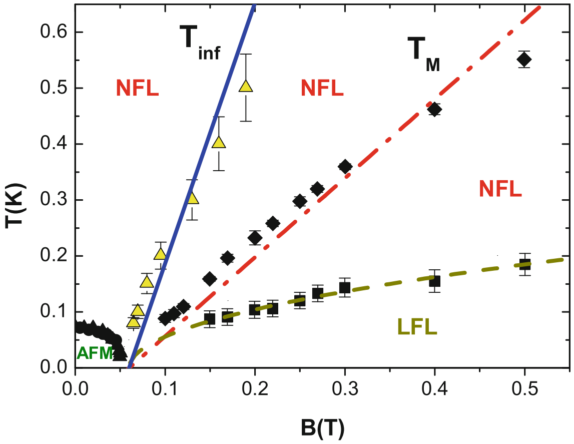

Fig. 6.5 Temperature—magnetic field $(T-B)$ phase diagram for $\mathrm{YbRh_2Si_2}$. *Solid circles* represent the boundary between AFM and NFL states. The *solid squares* denote the boundary of the NFL and LFL regime [17, 21, 22] shown by the *dashed line* approximated by $\sqrt{B-B_{c0}}$ [24]. *Diamonds* mark the maxima T_M of C/T [22] shown in Fig. 1.2. The *dash-dot line* is approximated by $T_M \propto a(B-B_{c0})$, a is a fitting parameter, see (6.23). *Triangles* along the *solid line* denote T_{inf} in LMR [21, 22] shown in Fig. 7.3, and the *solid line* represents the function $T_{inf} \propto b(B-B_{c0})$, b is a fitting parameter, see (6.24)

Now we are in position to consider the general properties of the $T - B$ phase diagram of HF metals. As we have seen, at $T = 0$ a quantum phase transition is driven by a nonthermal control parameter like number density x, magnetic field B or pressure P. At the QCP, situated at $x = x_{FC}$ and related to FCQPT, the effective mass M^* diverges. We note that there are different kinds of instabilities of normal Fermi liquids related to several perturbations of initial quasiparticle spectrum $\varepsilon(p)$ and occupation numbers $n(p)$, associated with the emergence of a multi-connected Fermi surface, see e.g., [13, 24–26]. Depending on the parameters and analytical properties of the Landau interaction, such instabilities lead to several possible types of restructuring of the initial Fermi liquid ground state. This restructuring generates topologically distinct phases. One of them is the FC, another one belongs to a class of topological phase transitions, where the sequence of rectangles $n(p) = 0$ and $n(p) = 1$ is realized at $T = 0$. In fact, at elevated temperatures the systems located at these transition points, exhibit the behavior typical to those located at FCQPT [24]. Therefore, we do not consider the specific properties of these topological transitions, but rather focus on the behavior of the experimentally important systems located near FCQPT.

Beyond FCQPT, the system forms FC that leads to the emergence of a topologically protected flat band [27, 28]. The schematic $T - x$ phase diagram of the system driven to the FC state by the number density x variation is reported in Fig. 6.6. Upon approaching the critical density x_{FC} the system remains in the LFL region at sufficiently low temperatures, as it is shown by the shadowed area. The temperature range of this area shrinks as the system approaches QCP, and $M^*(x \to x_{FC})$ diverges as it follows from (2.21). At this QCP shown by the arrow in Fig. 6.6, the system demonstrates the NFL behavior down to the lowest temperatures. Beyond the critical point at finite temperatures the behavior remains to be NFL one. It is determined by the temperature-independent entropy S_0 [24, 29]. In that case at $T \to 0$, the system again demonstrates the NFL behavior, and approaches a quantum critical line (QCL) (shown by the vertical arrow and the dashed line in Fig. 6.6) rather than a QCP. Upon reaching the QCL from above at $T \to 0$ the system undergoes the first order quantum phase transition that leads to vanishing S_0. As it is seen from Fig. 6.6, at rising temperatures the system located before QCP does not undergo a phase transition, and transits from the NFL to the LFL regime. At finite temperatures there is no boundary (or phase transition) between the states of the system located before or behind QCP, shown by the arrows. Therefore, at elevated temperatures the properties of systems with $x/x_{\mathrm{FC}} < 1$ or with $x/x_{FC} > 1$ become indistinguishable.

As seen from Fig. 6.6, the location of the system is controlled by the number density x. At rising x, $x/x_{FC} > 1$, the system is located before FCQPT, and demonstrates the LFL behavior at low temperatures. We suggest that such a state can be induced by the application of positive pressure, including positive chemical pressure. On the other hand, at diminishing x, $x/x_{FC} < 1$, the system is shifted beyond FCQPT, and is at the quantum critical line depicted by the dashed line. In that case the system demonstrates the NFL behavior at any finite temperatures. We assume that such a state can be induced by the application of negative pressure, including negative chemical pressure. At low temperatures and above the critical line, the

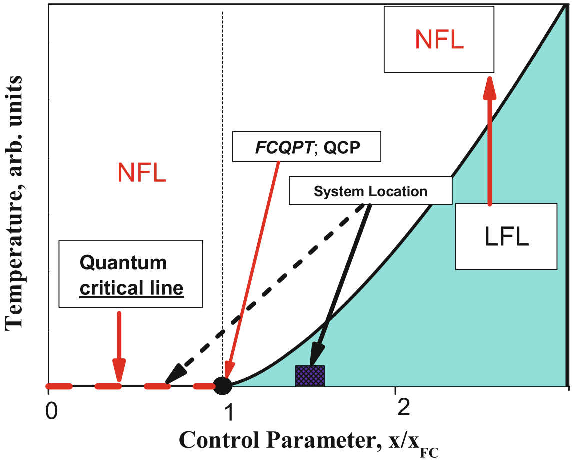

Fig. 6.6 Schematic $T - x$ phase diagram of system with FC. The number density x is taken as the control parameter and is depicted as x/x_{FC}. At $x/x_{FC} > 1$ and sufficiently low temperatures, the system is in the LFL state as shown by the shadowed area. This location of the system is depicted by both the *solid square* and the *arrow*. The *vertical arrow* illustrates the system moving in the LFL-NFL direction along T at fixed control parameter. At $x/x_{FC} < 1$ the system is shifted beyond the QCP, and is at the quantum critical line depicted by the *dashed line* and shown by the *vertical arrow*. This location of the system is shown by the *short dash arrow*. At any finite low temperatures $T > 0$ the system possesses finite entropy S_0 and exhibits the NFL behavior

system has the finite entropy S_0 and its NFL state is strongly degenerate. The degeneracy stimulates the emergence of different phase transitions, lifting it and removing the entropy S_0. The NFL state can be captured by other states such as superconducting (SC) (like SC state in $CeCoIn_5$), or antiferromagnetic (AF) (like AFM in $YbRh_2Si_2$) [24, 29, 30]. The diversity of phase transitions at low temperatures is one of the most spectacular features of the physics of many HF metals and strongly correlated compounds. Within the scenario of ordinary quantum phase transitions, it is hard to understand why these transitions are so different from each other and their critical temperatures are so extremely small. However, such diversity is endemic to systems with a FC, since the FC state should be altered as $T \to 0$ so that the excess entropy S_0 goes to zero before zero temperature is reached. At finite temperatures this takes place by means of some phase transitions, shedding the excess entropy [13, 24].

The schematic $T - B$ phase diagram of a HF liquid is reported in Fig. 6.7, with the magnetic field B serving as control parameter. At $B = 0$, the HF liquid acquires a flat band corresponding to a strongly degenerate state. The NFL regime reigns at elevated temperatures and fixed magnetic field. With increasing B, the system is driven from the NFL region to the LFL domain. As shown in Fig. 6.7, the system moves from the NFL regime to the LFL one along a horizontal arrow, and from the LFL to NFL along a vertical arrow. The magnetic-field-tuned QCP is indicated by the arrow and located at the origin of the phase diagram, since application of any magnetic field destroys

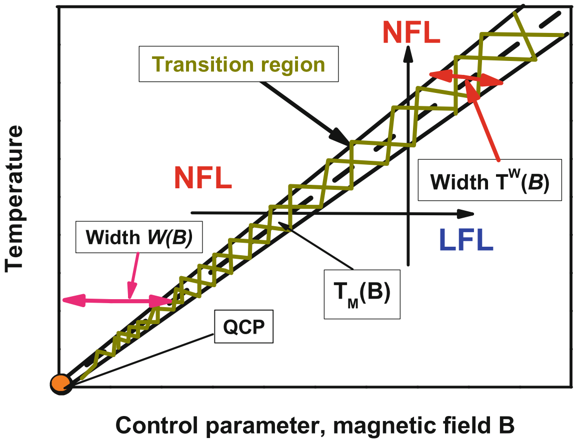

Fig. 6.7 Schematic $T-B$ phase diagram of HF liquid with magnetic field as the control parameter. The *vertical* and *horizontal arrows* show LFL-NFL and NFL-LFL transitions at fixed B and T, respectively. At $B = 0$ the system is in its NFL state, having a flat band, and demonstrates NFL behavior down to $T \to 0$. The *hatched area* separates the NFL phase and the weakly polarized LFL phase and represents the transition region. The *dashed line* in the *hatched area* represents the function $T_M(B) \simeq T^*_{FC}$ given by $T_m \simeq a_1\mu_B B$ (see (6.23)). The functions $W(B) \propto T$ and $T^W(B) \propto T$ shown by *two-headed arrows* define the width of the NFL state and the transition area, respectively. The QCP located at the origin and indicated by the *arrow* denotes the critical point at which the effective mass M^* diverges and both $W(B)$ and $T^W(B)$ tend to zero

the flat band and shifts the system into the LFL state [17, 24, 31–33]. The hatched area denoting the transition region separates the NFL state from the weakly polarized LFL state and contains the dashed line tracing the transition region, $T_M(B) \simeq T^*_{FC}$. Referring to (6.23), this line is defined by the function $T^*_{FC} \propto \mu_B B$, and the width $W(B)$ of the NFL state is seen to be proportional to T. It can similarly be shown that the width $T^W(B)$ of the transition region is also proportional to T.

Now we construct the $T-B$ schematic phase diagram of a HF metal like YbRh$_2$Si$_2$ shown in Fig. 6.8 [24, 34]. We start from observation that (6.21) reveals the scaling behavior of the normalized effective mass $M^*_N(T_N)$. Namely, the effective masses $M^*(T, B)$ at different magnetic fields B merge into a single value M^*_N in terms of the normalized variable $T_N = T/T_M$. The inset in Fig. 6.8 demonstrates the scaling of the normalized effective mass M^*_N versus the normalized temperature T_N. The LFL phase prevails at $T \ll T_M$, followed by the $T^{-\beta}$ regime at $T \gtrsim T_M$, with $\beta = 2/3$ or $\beta = 1/2$ as it follows from (6.14) and (6.16). The latter regime is designated as NFL due to the strong temperature dependence of the effective mass in it. The temperature region $T \simeq T_M$ encompasses the transition between the LFL regime with almost constant effective mass and the NFL behavior. Thus, $T^* \sim T_M(B)$ identifies the transition region featuring a crossover between LFL and NFL regimes. The transition (crossover) temperature $T^*(B)$ is not the actually temperature of a phase transition. Its specification is necessarily ambiguous, depending on the particularities

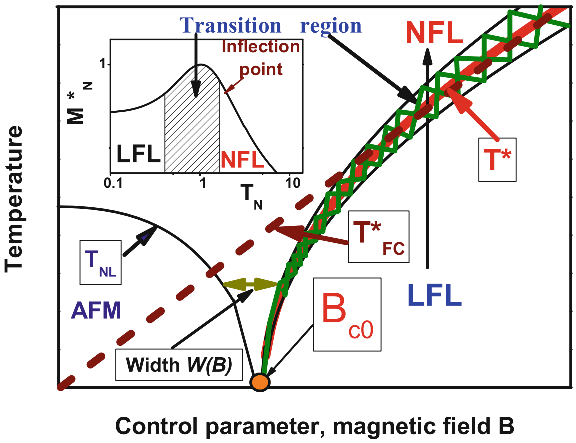

Fig. 6.8 Schematic $T - B$ phase diagram of a HF metal with magnetic field as control parameter. The antiferromagnetic (AFM) phase boundary line is shown by the *arrow* and plotted by the *solid curve*, representing the Néel temperature T_{NL}. The *vertical* and *horizontal arrows* show LFL-NFL and NFL-LFL transitions at fixed B and T, respectively. The *hatched area* separates the NFL phase and the weakly polarized LFL one and represents the transition region. The *solid curve* inside the *hatched area* represents the transition temperature T^*. The *solid short dash line* $T^*_{FC}(B) \propto B\mu_B$ shows the transition temperature provided that the AFM state were absent. The function $W(B) \propto T$ shown by *two-headed arrow* defines the total width of both the NFL state and the transition area. The *inset* shows a schematic plot of the normalized effective mass versus the normalized temperature. The transition region, where M^*_N reaches its maximum at $T_N = T/T_M = 1$, is shown as the *hatched area* in both the main panel and the *inset*. *Arrows* indicate the transition region and the inflection point T_{inf} in the M^*_N plot

of substance under consideration. As usual, the temperature $T^*(B)$ is extracted from the field dependence of charge transport phenomena like resistivity $\rho(T)$, given by

$$\rho(T) = \rho_0 + AT^{\alpha_R}, \tag{6.25}$$

where ρ_0 is the residual resistivity and A is a T-independent coefficient. The term ρ_0 is ordinarily attributed to impurity scattering. The LFL state is characterized by the T^{α_R} dependence of the resistivity with the index $\alpha_R = 2$. The crossover (through the transition regime shown as the hatched area in the main panel and inset of the Fig. 6.8) takes place at temperatures, where the resistivity starts to deviate from LFL behavior, with the exponent α_R shifting from 2 into the range $1 < \alpha_R < 2$. When constructing the phase diagram in Fig. 6.8, we assume that AFM order wins the competition, destroying the S_0 term at low temperatures. At $B = B_{c0}$, the HF liquid acquires a flat band corresponding to a strongly degenerate state. Here, B_{c0} is a critical magnetic field, such that at $T \to 0$ the application of magnetic field $B \gtrsim B_{c0}$ destroys the AFM state restoring the paramagnetic one with LFL behavior. In some cases $B_{c0} = 0$ as in the HF metal CeRu$_2$Si$_2$ (see e.g., [33]), while in YbRh$_2$Si$_2$, B$_{c0} \simeq 0.06$ T [17]. Obviously, B_{c0} is defined by the specific system properties, therefore we consider it as a parameter. The NFL regime reigns at elevated temperatures and fixed magnetic field. With increasing B, the system is driven from the NFL region to the LFL domain. As shown in Figs. 6.7 and 6.8, the system moves from the NFL regime to the LFL one along the corresponding arrows. The magnetic-field-tuned QCP is indicated by the arrow and located at $B = B_{c0}$. The hatched area denotes the transition region, and separates the NFL state from the weakly polarized LFL one. It contains both the dashed line tracing $T^*_{FC}(B)$ and the solid curve $T^*(B)$. Referring to (6.21), the latter is defined by the function $T^* \propto \mu_B B$ and merges with $T^*_{FC}(B)$ at relatively high temperatures, and $T^* \propto \mu_B(B - B_{c0})$ at lower $T \sim T_{NL}$, with $T_{NL}(B)$ being the Néel temperature. As seen from (6.21), both the width $W(B)$ of the NFL state and the width of the transition region are proportional to T [34]. The AFM phase boundary line is shown by the arrow and depicted by the solid curve. As it was mentioned above, the dashed line $T^*_{FC}(B) \propto B\mu_B$ represents the transition temperature provided that the AFM state were absent. In that case the FC state is destroyed by any weak magnetic field $B \to 0$ at $T \to 0$ and the dashed line T^*_{FC} crosses the origin of coordinates, as it is displayed in Figs. 6.7 and 6.8. At $T \gtrsim T_{NL}(B = 0)$ the transition temperature $T^*_{FC}(B)$ coincides with $T^*(B)$ shown by the solid curve, since the properties of the system are given by its local free energy, describing the paramagnetic state of the system. One might say that the system "does not" remember the AFM state that emerges at lower temperatures. This observation is in good agreement with experimental data collected on the HF metal $YbRh_2Si_2$. These findings are summarized in the phase diagrams of Fig. 6.9: At relatively high temperatures $T \gtrsim T_{NF}(B = 0)$ the transition temperature T^*, obtained in measurements on $YbRh_2Si_2$ [17, 21], is well approximated by the straight lines representing T^*_{FC}. In contrast to Fig. 6.5, it is also seen from Fig. 6.9 that the emphasis is placed on the relatively high temperatures, so the straight lines deviate from the experimental points at relatively low temperatures. It is seen from Fig. 6.9, that the slope of the line (representing the maxima of the specific heat C/T) is different from that of the solid line (representing maxima of the susceptibility $\chi(T)$). Such a behavior is determined by the fact that the maxima of C/T and $\chi(T)$ are given by the different relations, determining the inflection points of the entropy:

$$\frac{\partial^2 S}{\partial T^2} = 0, \quad \frac{\partial^2 S}{\partial B^2} = 0, \tag{6.26}$$

respectively. As it is seen from Fig. 6.3, based on the theory of FC, that the inflection points exist under the condition that the system is located near FCQPT [24].

Let us now corroborate the above consideration by experimental facts collected in measurements on HF metals. Panels a, b, c of Fig. 6.10 are focused on the behavior of the transition temperature $T^*(B)$ extracted from measurements of kinks in $\hat{\mathbf{M}}(B) = \mathbf{M}+\mathbf{B}(\mathbf{dM}/\mathbf{dB})$ [35, 36], where $\mathbf{M}$ is a magnetization. Positions of the kinks is shown by pentagons in Fig. 6.10. It is seen from panel a of Fig. 6.10, that at $T \gtrsim T_{NL}(B = 0)$, the transition temperature T^* of $YbRh_2Si_2$ is well approximated by the line T^*_{FC}. As mentioned above, upon using nonthermal tuning parameters like the number density x, the NFL behavior can be destroyed and the LFL one will be restored. In

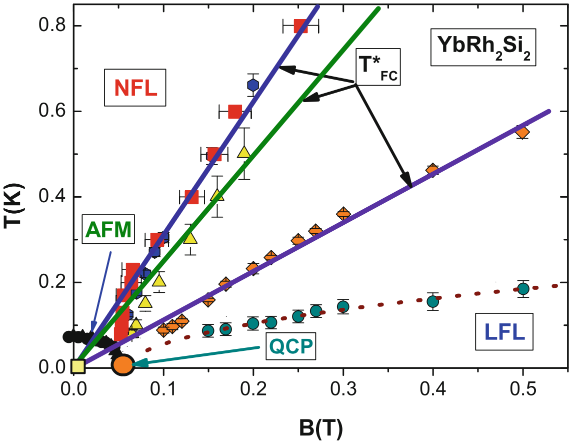

Fig. 6.9 $T-B$ phase diagram for $YbRh_2Si_2$. *Solid circles* represent the boundary between AFM and NFL states. The *solid circles* along the *short dash curve* denote the boundary of the NFL and LFL regions [17, 21]. The *curve* (*short dash*) is represented by the function $\sqrt{B-B_{c0}}$ [24]. The *solid lines* are approximated by $T^*_{FC} \propto B\mu_B$. *Diamonds* marking T^* along the line signify the maxima T_M of C/T [20] shown in Fig. 1.2. The transition temperature T^*, determined from magnetostriction (*solid squares*), longitudinal magnetoresistivity (*triangles*), and susceptibility (*solid circles*) [21] is also reported. The *solid lines* show the linear fit to T^*_{FC}

our simple model, the application of positive pressure P makes x to grow shifting the system from FCQPT to the LFL state. It is shown in Fig. 6.6 that above actions moves the electronic system of $YbRh_2Si_2$ into the shadow area characterized by the LFL behavior at low temperatures. The new location of the system, represented by $Yb(Rh_{0.93}Co_{0.07})_2Si_2$, is shown by the arrow pointing at the solid square. We note that the positive chemical pressure in the considered case is induced by Co substitution [35, 37–39]. As a result, the application of magnetic field $B \simeq B_{c0}$ does not drive the system to its FCQPT with the divergent effective mass because the QCP has already been destroyed by the positive pressure, as it is shown in panel b of Fig. 6.10. Here B_{c0} is the critical magnetic field that eliminates the corresponding AFM order. At relatively high temperatures both $YbRh_2Si_2$ and $Yb(Rh_{0.93}Co_{0.07})_2Si_2$ are in their paramagnetic states. As a result, in that case T^* is well approximated by the straight line T^*_{FC}. This observation coincides with experimental facts [35, 37] reported in panels a, b of Fig. 6.10.

The system located above QCL exhibits the NFL behavior down to lowest temperatures unless it is captured by a phase transition. The behavior exhibited by the system located above QCL agrees with the experimental observations of the QCP evolution in $YbRh_2Si_2$ under the application of negative chemical pressure induced by Ir substitution [35, 37–39]. To explain the latter behavior, we propose a simple model that the application of negative pressure reduces x so that the electronic system of $YbRh_2Si_2$ moves from QCP to a new position over QCL shown by the dash arrow in Fig. 6.6. Thus, the electronic system of $Yb(Rh_{0.94}Ir_{0.06})_2Si_2$ is located at

Fig. 6.10 $T - B$ phase diagrams for the three HF metals: $YbRh_2Si_2$ (**a**); $Yb(Rh_{0.93}Co_{0.07})_2Si_2$ (**b**); $Yb(Rh_{0.94}Ir_{0.06})_2Si_2$ (**c**). In panels **a** and **b**, the AFM phase boundaries [35] are shown by the *solid lines*. In panel **b**, the *diamonds* report the measurements [35]. In panel **c**, the phase boundary of possible phase transition is shown by *short dot curve*. *Pentagons* correspond to the measurements of $T^*(B)$ on the HF metals extracted from the analysis of $\hat{\mathbf{M}}(B)$ function [35]. The *solid straight lines* depict the transition temperature $T^*_{FC}(B)$. *Dash line* represents schematically the boundary between NFL and LFL regions

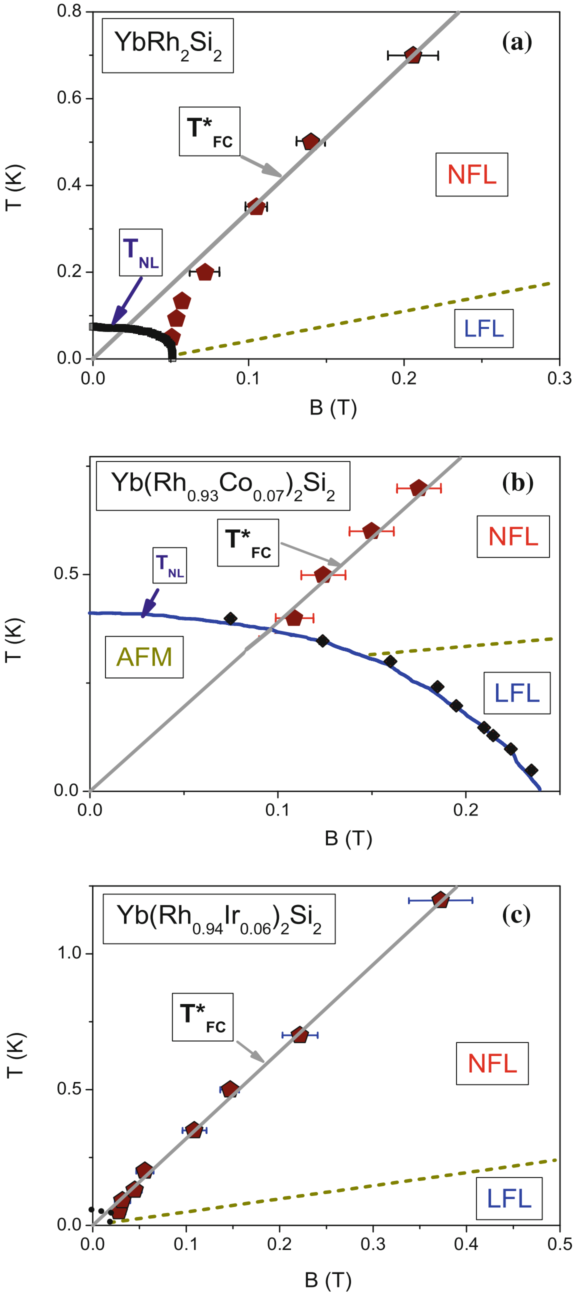

QCL and possesses a flat band, while the entropy includes S_0. We speculate that at lowering temperatures, the electronic system of Yb($Rh_{0.94}Ir_{0.06}$)$_2$$Si_2$ is captured by a phase transition, since the NFL state above QCL is strongly degenerate and the term S_0 should be eliminated. At temperature decrease, this degeneracy is to be lifted by some phase transition which can be possibly detected by the LFL state accompanying it. The tentative boundary line of that transition is shown by the short dot line in Fig. 6.10, panel c. It is also seen from panel c of Fig. 6.10, that at elevated temperatures T^* is well approximated by the function T^*_{FC}. Thus, at relatively high temperatures the curve $T^*_{FC}(B)$, shown in panels a, b, c of Fig. 6.10 by the solid lines, coincides with $T^*(B)$ depicted by the pentagons. The preceding discussion demonstrates that the local properties of the systems in question are given by their local free energy, formed by the NFL region related to FC, as it is reported in Fig. 6.6.

To confirm the above consideration of the phase diagrams, we describe both low temperature magnetization measurements carried out under pressure P and the $T - B$ phase diagram of $YbRh_2Si_2$ near its magnetic-tuned QCP [23, 37]. To carry out a quantitative analysis of the scaling behavior of $-\Delta M^*(B,T)/\Delta T$, we calculate the entropy $S(B,T)$ and employ the well-known thermodynamic equality $dM/dT = dS/dB \simeq \Delta M/\Delta T$, see for details Chap. 7 and particularly Sect. 7.3. Figure 6.11, panel a, reports the normalized $(dS/dB)_N$ as a function of the normalized magnetic field. The function $(dS/dB)_N$ is obtained by normalizing (dS/dB) by its maximum taking place at B_M, and the field B is scaled by B_M. It is seen from Fig. 6.11, panel a, that our calculations are in good agreement with the experimental data and the functions $-(\Delta M/\Delta T)_N$ show the scaling behavior over three decades in the normalized magnetic field. Figure 6.11, panel b, presents the temperature T_M,

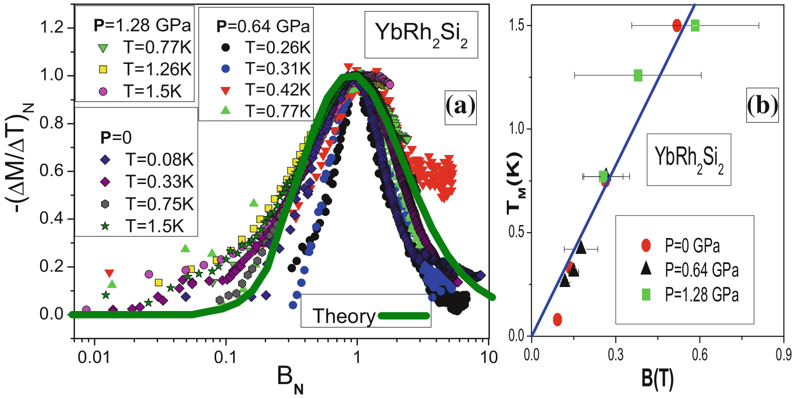

Fig. 6.11 Panel **a** normalized magnetization difference divided by temperature increment $-(\Delta M/\Delta T)_N$ versus normalized magnetic field at fixed temperature and pressure (listed in the legend in the *upper left* corner) is extracted from the data collected on $YbRh_2Si_2$ [23, 37]. Panel **b** T_M versus B is obtained under the application of hydrostatic pressure depicted in the legend and extracted from the measurements [23, 37]. The *solid line* shows the linear fit to $T^*(B)$, and represents T^*_{FC}

at which the maximum $-(\Delta M/\Delta T)$ takes place, as a function of magnetic field B. At $T_M \sim T_{NL}$ the line T^*_{FC} starts to deviate from the experimental data, where T_{NL} is shown in Fig. 6.10, panel a.

Thus, we conclude that carried out our theoretical study of the phase diagrams of strongly correlated Fermi systems, including HF metals like $\mathrm{YbRh_2Si_2}$, and considered the evolution of these diagrams under the application of negative/positive pressure are in good agreement with the experimental facts. We have observed that at sufficiently high temperatures outside the AFM phase the transition temperature $T^*(B)$ follows almost linear B-dependence, and coincides with $T^*_{FC}(B)$, induced by the presence of FCQPT. Thus, the influence of FCQPT extends over a wide range in the $T-B$ phase diagram. This is the regime of quantum criticality, which is of crucial importance for interpreting a wide variety of experiments, finds good explanations within the FC theory. As we shall show in Chaps. 17 and 18, the phase diagram of HF liquid (Fig. 6.7) describes those of quantum spin liquids and quasicrystals as well, while their scaling behavior is described in the same way. Thus, all above strongly correlated compounds exhibit the similar behavior and allow us to consider it as representing the main characteristic of the new state of matter [40, 41].

References

1. E.M. Lifshitz, L.P. Pitaevskii, *Statistical Physics, part 2: Theory of Condensed State* (Pergamon Press, Oxford, New York, Toronto, Sydney, Paris, Frankfurt, 1980)
2. V.R. Shaginyan, JETP Lett. **79**, 286 (2004)
3. J.W. Clark, V.A. Khodel, M.V. Zverev, Phys. Rev. B **71**, 012401 (2005)
4. V.R. Shaginyan, A.Z. Msezane, M.Y. Amusia, Phys. Lett. A **338**, 393 (2005)
5. V.R. Shaginyan, JETP Lett. **77**, 104 (2003)
6. L.D. Landau, E.M. Lifshitz, *Statistical Physics* (Elsevier, Oxford, 1980)
7. V.R. Shaginyan, JETP Lett. **80**, 263 (2004)
8. V.A. Khodel, V.R. Shaginyan, V.V. Khodel, Phys. Rep. **249**, 1 (1994)
9. V.A. Khodel, V.R. Shaginyan, Nucl. Phys. A **555**, 33 (1993)
10. V.A. Khodel, V.R. Shaginyan, P. Schuk, JETP Letters **63**, 752 (1996)
11. J. Dukelsky, V. Khodel, P. Schuck, V. Shaginyan, Z. Phys. **102**, 245 (1997)
12. V.A. Khodel, V.R. Shaginyan, in *Condensed Matter Theories*, vol. 12, ed. by J. Clark, V. Plant (Nova Science Publishers Inc., New York, 1997), p. 221
13. V.A. Khodel, J.W. Clark, M.V. Zverev, Phys. Rev. B **78**, 075120 (2008)
14. V.A. Khodel, JETP Lett. **86**, 721 (2007)
15. J.W. Clark, V.A. Khodel, M.V. Zverev, V.M. Yakovenko, Phys. Rep. **391**, 123 (2004)
16. V.R. Shaginyan, JETP Lett. **77**, 178 (2003)
17. P. Gegenwart, J. Custers, C. Geibel, K. Neumaier, K.T.T. Tayama, O. Trovarelli, F. Steglich, Phys. Rev. Lett. **89**, 056402 (2002)
18. J. Custers, P. Gegenwart, H. Wilhelm, K. Neumaier, Y. Tokiwa, O. Trovarelli, C. Geibel, F. Steglich, C. Pépin, P. Coleman, Nature **424**, 524 (2003)
19. T. Shibauchi, L. Krusin-Elbaum, M. Hasegawa, Y. Kasahara, R. Okazaki, Y. Matsuda, Proc. Natl. Acad. Sci. USA **105**, 7120 (2008)
20. N. Oeschler, S. Hartmann, A. Pikul, C. Krellner, C. Geibel, F. Steglich, Physica B **403**, 1254 (2008)
21. P. Gegenwart, T. Westerkamp, C. Krellner, Y. Tokiwa, S. Paschen, C. Geibel, F. Steglich, E. Abrahams, Q. Si, Science **315**, 969 (2007)

22. P. Gegenwart, T. Westerkamp, C. Krellner, M. Brando, Y. Tokiwa, C. Geibel, F. Steglich, Physica B **403**, 1184 (2008)
23. Y. Tokiwa, T. Radu, C. Geibel, F. Steglich, P. Gegenwart, Phys. Rev. Lett. **102**, 066401 (2009)
24. V.R. Shaginyan, M.Y. Amusia, A.Z. Msezane, K.G. Popov, Phys. Rep. **492**, 31 (2010)
25. S.A. Artamonov, Y.G. Pogorelov, V.R. Shaginyan, JETP Lett. **68**, 942 (1998)
26. M.V. Zverev, M. Baldo, J. Phys. Condens. Matter **11**, 2059 (1999)
27. G.E. Volovik, JETP Lett. **53**, 222 (1991)
28. G.E. Volovik, in *Quantum Analogues: From Phase Transitions to Black Holes and Cosmology*, ed. by W.G. Unruh, R. Schutzhold. Springer Lecture Notes in Physics, vol. 718 (Springer, Orlando, 2007), p. 31.
29. V.A. Khodel, M.V. Zverev, V.M. Yakovenko, Phys. Rev. Lett. **95**, 236402 (2005)
30. V.R. Shaginyan, M.Y. Amusia, K.G. Popov, Phys. Lett. A **373**, 2281 (2009)
31. V.R. Shaginyan, Physics of Atomic Nuclei **74**, 1107 (2011)
32. V.A. Khodel, J.W. Clark, M.V. Zverev, Physics of Atomic Nuclei **74**, 1237 (2011)
33. D. Takahashi, S. Abe, H. Mizuno, D. Tayurskii, K. Matsumoto, H. Suzuki, Y. Onuki, Phys. Rev. B **67**, 180407(R) (2003)
34. V.R. Shaginyan, A.Z. Msezane, K.G. Popov, J.W. Clark, M.V. Zverev, V.A. Khodel, JETP Lett. **96**, 397 (2012)
35. M. Brando, L. Pedrero, T. Westerkamp, C. Krellner, P. Gegenwart, C. Geibel, F. Steglich, Phys. Status Solidi B **459**, 285 (2013)
36. V.R. Shaginyan, A.Z. Msezane, K.G. Popov, G.S. Japaridze, V.A. Khodel, Europhys. Lett. **106**, 37001 (2014)
37. Y. Tokiwa, P. Gegenwart, C. Geibel, F. Steglich, J. Phys. Soc. Jpn. **78**, 123708 (2009)
38. S. Friedemann, T. Westerkamp, M. Brando, N. Öeschler, S. Wirth, P. Gegenwart, C. Krellner, C. Geibel, F. Steglich, Nat. Phys. **5**, 465 (2009)
39. J. Custers, P. Gegenwart, S. Geibel, F. Steglich, P. Coleman, S. Paschen, Phys. Rev. Lett. **104**, 186402 (2010)
40. M.Y. Amusia, V.R. Shaginyan, Contrib. Plasma Phys. **53**, 721 (2013)
41. D. Yudin, D. Hirschmeier, H. Hafermann, O. Eriksson, A.I. Lichtenstein, M.I. Katsnelson, Phys. Rev. Lett. **112**, 070403 (2014)

Chapter 7
Highly Correlated Fermi Liquid in Heavy-Fermion Metals: Magnetic Properties

Abstract In this chapter we show how the FCQPT theory works, when describing the behavior of HF metals under the application of magnetic field. We show that a large body of experimental data regarding the thermodynamic, transport and relaxation properties collected in measurements on HF metals can be well explained. It is demonstrated that the experimental data exhibit the scaling behavior.

7.1 Magnetization

Consider now the magnetization M as a function of magnetic field B at fixed temperature $T = T_f$

$$M(B, T) = \int_0^B \chi(b, T) db, \tag{7.1}$$

where the magnetic susceptibility χ is given by [1]

$$\chi(B, T) = \frac{\beta M^*(B, T)}{1 + F_0^a}. \tag{7.2}$$

Here, β is a constant and F_0^a is the Landau interaction related to the exchange interaction. In the case of strongly correlated systems the Landau interaction F_0^a is saturated at $F_0^a \geq -0.9$ [2–4]. As a result, it follows from (7.2) that $\chi \propto M^*$. Therefore, the behavior of the function $\chi(B, T)$ is similar to that of $M^*(B, T)$. Thus, we can normalize $\chi \propto M^*$ in the same way as it was done when deriving (6.21), see Sect. 6.3. As seen from (6.21) and (7.2), the coefficients β and $(1 + F_0^a)$ drop out from the normalized magnetic susceptibility χ_N, so that the normalized magnetic susceptibility $\chi_N = M_N^*$, see Sect. 7.4 for details. One could assume that F_0^a strongly depends on B. This is not the case [7, 8], since the Kadowaki-Woods ratio is conserved [9, 10], $A(B)/\gamma_0^2(B) \propto A(B)/\chi^2(B) \propto const$, for we have $\gamma_0 \propto M^* \propto \chi$. Note that the Sommerfeld coefficient does not depend on F_0^a.

Our calculations show that the magnetization exhibits a kink at some magnetic field $B = B_k$. The experimentally observed magnetization demonstrates the same

M.Y. Amusia et al., *Theory of Heavy-Fermion Compounds*, Springer Series
in Solid-State Sciences 182, DOI 10.1007/978-3-319-10825-4_7

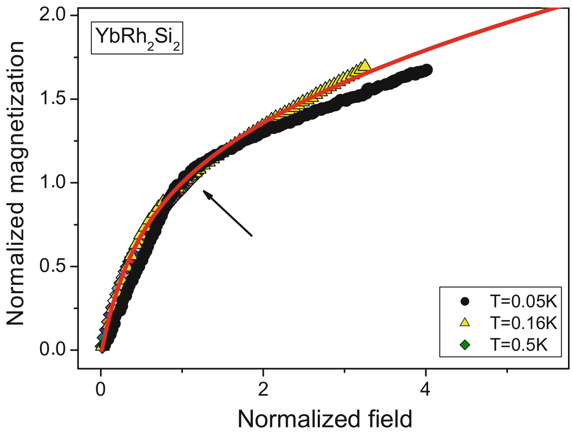

Fig. 7.1 The field dependencies of the normalized magnetization M at different temperatures, shown in the legend. The *curves* are extracted from measurements of YbRu$_2$Si$_2$ [5, 6]. The kink (*shown by the arrow*) is clearly seen at the normalized field $B_N = B/B_k \simeq 1$. The *solid curve* represents our calculations

behavior [5, 6]. We use B_k and $M(B_k)$ to normalize B and M respectively. The normalized magnetization $M(B)/M(B_k)$, extracted from experimental (shown with symbols) and calculated magnetization shown by the solid line, are reported in Fig. 7.1. It is seen that the scaled data at different T_f merge into a single curve in terms of the normalized variable $y = B/T_k$. It is also seen, that these data exhibit energy scales separated by a kink at normalized magnetic field $B_N = B/B_k = 1$. The kink is a crossover point from the fast to slow growth of M at rising magnetic field. Figure 7.1 shows that our calculations are in good agreement with the experimental data. In this case, all the data exhibit the kink (shown by the arrow) at $B_N \simeq 1$ taking place as soon as the system enters the transition region corresponding to the magnetic fields, where the horizontal dash-dot arrow in the main panel a of Fig. 6.2 crosses the hatched area. Indeed, as seen from Fig. 7.1, at lower magnetic fields M is a linear function of B since M^* is approximately independent of B. Then, (6.21) and (6.22) show that at elevated magnetic fields M^* becomes a decreasing function of B and generates the kink in $M(B)$ separating the energy scales, discovered experimentally in [5, 6]. It is seen from (6.24) that the magnetic field B_k at which the kink appears, $B_k \simeq B_M \propto T_f$, shifts to lower B as T_f is decreased. This observation coincides with experimental facts [5, 6].

Consider now the "average" magnetization $\underline{M} \equiv B\chi + M$ as a function of the magnetic field B at fixed temperature $T = T_f$ [5]. We again use B_k and $\underline{M}(B_k)$ to normalize B and $\underline{M}$ respectively. The normalized $\underline{M}$ versus the normalized field $B_N = B/B_K$ are shown in Fig. 7.2. Our calculations are represented by the solid line. The stars trace our calculations of $\underline{M}$ with $M^*(y)$ extracted from the data C/T shown in Fig. 6.4. It is seen from Fig. 7.2 that our calculations are in good agreement with the experiment. All experimental data have the kink (shown by arrow) at $B_N \simeq 1$ taking place as soon as the system enters the transition region corresponding to the magnetic fields where the horizontal dash-dot arrow in the main panel a of Fig. 6.2 crosses the hatched area. Indeed, as seen from Fig. 7.2, at lower magnetic fields $\underline{M}$ is a linear function of B since M^* is approximately independent of B. It follows from

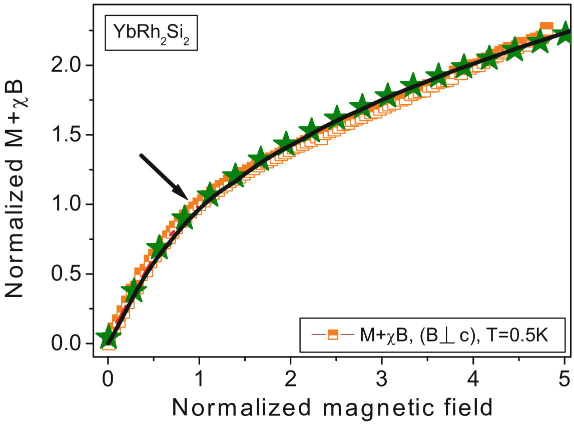

Fig. 7.2 The field dependence of the normalized "average" magnetization $\underline{M} \equiv M + B\chi$ is shown by *squares*. It has been extracted from measurements of YbRu$_2$Si$_2$ [5]. The kink (shown by the *arrow*) is clearly seen at $B_N = B/B_k \simeq 1$. The *solid curve* and *stars* (*see text*) represent our calculations

(6.22) that at elevated magnetic fields M^* becomes a diminishing function of B and generates a kink in $\underline{M}(B)$ separating the energy scales discovered in [5]. It is also seen from (6.24) that the magnetic field $B_k \simeq B_M$, where the kink appears, shifts to lower B as T_f is decreased.

7.2 Magnetoresistance

The magnetoresistance (MR) of a number of HF metals is notably different from that expected for orbital MR due to the Lorentz force and described by Kohler's rule, which holds in many conventional metals. We show that a pronounced crossover from negative to positive MR is determined by the dependence of the effective mass $M^*(B, T)$ on both magnetic field B and temperature T. Thus, the crossover is regulated by the universal behavior of $M^*(B, T)$ observed in heavy-fermion metals. This behavior is exhibited by $M^*(B, T)$, when a strongly correlated electron system transits from the Landau Fermi liquid behavior, induced by the application of magnetic field, to the non-Fermi liquid behavior taking place at rising temperatures.

7.2.1 *Longitudinal Magnetoresistance*

Consider the longitudinal magnetoresistance (LMR) $\rho(B, T) = \rho_0 + AT^2$ as a function of B at fixed T_f. In that case, the classical contribution to LMR due to orbital motion of carriers induced by the Lorentz force is small, while the Kadowaki-Woods relation [9–13], $K = A/\gamma_0^2 \propto A/\chi^2 = const$, allows us to employ M^* in constructing the coefficient A, since $\gamma_0 \propto \chi \propto M^*$. Omitting the classical contribution to LMR, we obtain, as it follows from (2.19), that $\rho(B, T) - \rho_0 \propto (M^*)^2$. Figure 7.3 reports

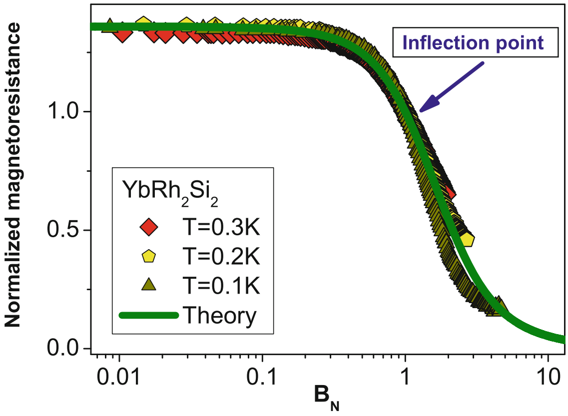

Fig. 7.3 Magnetic field dependence of the normalized magnetoresistance ρ_N, extracted from LMR of YbRh$_2$Si$_2$ at different temperatures [5, 6] listed in the legend. The inflection point is shown by the *arrow*, and the *solid line* represents our calculations

the normalized magnetoresistance

$$\rho_N(y) \equiv \frac{\rho(y) - \rho_0}{\rho_{inf}} = (M_N^*(y))^2 \tag{7.3}$$

versus normalized magnetic field $y = B/B_{inf}$ at different temperatures, shown in the legend. Here ρ_{inf} and B_{inf} are LMR and magnetic field, respectively, taken at the inflection point marked by the arrow in Fig. 7.3. Both theoretical (solid line) and experimental (symbols) curves have been normalized by their inflection points, which also reveal the scaling behavior: The scaled curves at different temperatures merge into a single one as a function of the variable y and show the scaling behavior over three orders in the normalized magnetic field. The transition region, where LMR starts to decrease is shown in the inset to Fig. 6.2a by the hatched area. Obviously, as seen from (6.24), the width of the transition region being proportional to $B_M \simeq B_{inf} \propto T_f$ decreases as the temperature T_f is lowered. Similar to that, the LMR inflection point, generated by that of M^* (arrow in the inset to Fig. 6.2) shifts towards lower B as T_f is decreased. All these observations are in good agreement with experimental data [5, 6].

7.2.2 *Transverse magnetoresistance in the HF Metal* CeCoIn$_5$

Our comprehensive theoretical study of both the longitudinal and transverse magnetoresistance (MR) shows that it is, similar to other thermodynamic characteristics like magnetic susceptibility, specific heat, etc. governed by the scaling behavior of the quasiparticle effective mass. The crossover from negative to positive MR occurs at elevated temperatures and fixed magnetic fields, when the system transits from the LFL behavior to NFL one and can be well captured by this scaling behavior.

By definition, MR is given by

$$\rho_{mr}(B,T)=\frac{\rho(B,T)-\rho(0,T)}{\rho(0,T)}, \tag{7.4}$$

We apply (7.4) to study MR of strongly correlated electron liquid versus temperature T as a function of magnetic field B. The resistivity $\rho(B,T)$ can be presented as

$$\rho(B,T)=\rho_0+\Delta\rho(B,T)+\Delta\rho_L(B,T), \tag{7.5}$$

where ρ_0 is a residual resistance, $\Delta\rho = c_1AT^2$, c_1 is a constant. The classical contribution $\Delta\rho_L(B,T)$ to MR due to orbital motion of carriers induced by the Lorentz force obeys the Kohler's rule. We note that $\Delta\rho_L(B) \ll \rho(0,T)$, as it is assumed in the weak-field approximation. To calculate A, we again use the quantities $\gamma_0 = C/T \propto M^*$ and/or $\chi \propto M^*$ as well as employ the fact that the Kadowaki-Woods ratio $K = A/\gamma_0^2 \propto A/\chi^2 = const$. As a result, we obtain $A \propto (M^*)^2$, so that $\Delta\rho(B,T) = c(M^*(B,T))^2T^2$ and c is a constant. Suppose that the temperature is not very low, so that $\rho_0 \leq \Delta\rho(B=0,T)$, and $B \geq B_{c0}$. Substituting (7.5) into (7.4), we find that [14]

$$\rho_{mr}\simeq\frac{\rho_0+\Delta\rho_L(B,T)}{\rho(0,T)}+cT^2\frac{(M^*(B,T))^2-(M^*(0,T))^2}{\rho(0,T)}. \tag{7.6}$$

Consider the qualitative behavior of MR described by (7.6) as a function of B at a certain temperature $T = T_0$. In weak magnetic fields, when the system exhibits NFL behavior (see Fig. 6.2), the main contribution to MR comes from the term $\Delta\rho_L(B)$, because the effective mass is independent of the applied magnetic field. Hence, $|M^*(B,T) - M^*(0,T)|/M^*(0,T) \ll 1$ and the leading contribution is made by $\Delta\rho_L(B)$. As a result, MR is an increasing function of B. When B becomes so high that $T^*(B) \sim \mu_B(B - B_{c0}) \sim T_0$, the difference $(M^*(B,T) - M^*(0,T))$ becomes negative because $M^*(B,T)$ is now the diminishing function of B, given by (6.22), while $T^*(B)$ is the crossover (transition temperature) shown in Fig. 5.2. Thus, MR as a function of B reaches its maximal value at $T^*(B) \sim T_N(B) \sim T_0$. At further increase of magnetic field, when $T_M(B) > T_0$, the effective mass $M^*(B,T)$ becomes a decreasing function of B. As B growth, one has

$$\frac{(M^*(B,T)-M^*(0,T))}{M^*(0,T)}\to -1, \tag{7.7}$$

and the magnetoresistance, being a decreasing function of B, can reach its negative values.

Now we study the behavior of MR as a function of T at fixed value B_0 of magnetic field. At low temperatures $T \ll T^*(B_0)$, it follows from (6.21) and (6.7) that $M^*(B_0,T)/M^*(0,T) \ll 1$, and it is seen from (7.7) that $\rho_{mr}(B_0,T) \sim -1$, because $\Delta\rho_L(B_0,T)/\rho(0,T) \ll 1$. We note that B_0 must be relatively high to guarantee that $M^*(B_0,T)/M^*(0,T) \ll 1$. As the temperature increases, MR increases, remaining negative. At $T \simeq T^*(B_0)$, MR is approximately zero, because at this point $\rho(B_0, T) \simeq \rho(0, T)$. This allows us to conclude that the change of the temperature dependence of resistivity $\rho(B_0, T)$ from quadratic to linear manifests itself in the transition from negative to positive MR. One can also say that the transition takes place when the system goes from the LFL behavior to the NFL one. At $T \geq T^*(B_0)$, the leading contribution to MR is made by $\Delta\rho_L(B_0, T)$ and MR reaches its maximum. At $T_M(B_0) \ll T$, MR is a decreasing function of the temperature, because

$$\frac{|M^*(B,T) - M^*(0,T)|}{M^*(0,T)} \ll 1, \tag{7.8}$$

and $\rho_{mr}(B_0, T) \ll 1$. Both transitions, from positive to negative MR with increasing B at fixed temperature T and from negative to positive MR with increasing T at fixed B value, have been detected in measurements of the resistivity of $\mathrm{CeCoIn_5}$ in a magnetic field [15].

Let us turn to quantitative analysis of MR [14]. As it was mentioned above, we can safely assume that the classical contribution $\Delta\rho_L(B, T)$ to MR is small as compared to $\Delta\rho(B, T)$. Omission of $\Delta\rho_L(B, T)$ allows us to make our analysis and results transparent and simple while the behavior of $\Delta\rho_L(B_0, T)$ is not known in the case of HF metals. Consider the ratio $R^\rho = \rho(B, T)/\rho(0, T)$ and assume for a while that the residual resistance ρ_0 is small in comparison with the temperature dependent terms. Taking into account (7.5) and $\rho(0, T) \propto T$, we obtain from (7.6) that

$$R^\rho = \rho_{mr} + 1 = \frac{\rho(B,T)}{\rho(0,T)} \propto T(M^*(B,T))^2, \tag{7.9}$$

and consequently, from (6.21) and (7.9) that the ratio R^ρ reaches its maximal value R^ρ_M at some temperature $T_{\mathrm{Rm}} \sim T_M$. If the ratio is measured in units of its maximal value R^ρ_M and T is measured in units of $T_{\mathrm{Rm}} \sim T_M$ then it is seen from (6.21) and (7.9) that the normalized MR

$$R^\rho_N(y) = \frac{R^\rho(B,T)}{R^\rho_M(B)} \simeq y(M^*_N(y))^2 \tag{7.10}$$

becomes a function of the only variable $y = T/T_{\mathrm{Rm}}$. The results of the normalization procedure of MR are depicted in Fig. 7.4. It is clearly seen that the data collapse into the same curve, indicating that the normalized magnetoresistance R^ρ_N obeys the scaling behavior well described by (7.10). This scaling behavior obtained directly from the experimental facts is a vivid evidence that MR behavior is predominantly governed by the effective mass $M^*(B, T)$.

Now we are in the position to calculate $R^\rho_N(y)$ given by (7.10). Using (6.21) to parameterize $M^*_N(y)$, we extract parameters c_1 and c_2 from measurements of the magnetic AC susceptibility χ on $\mathrm{CeRu_2Si_2}$ [16] and apply (7.10) to calculate the normalized ratio. It is seen that the calculations shown by the starred line in Fig. 7.4 start to deviate from experimental points at higher temperatures. To improve the

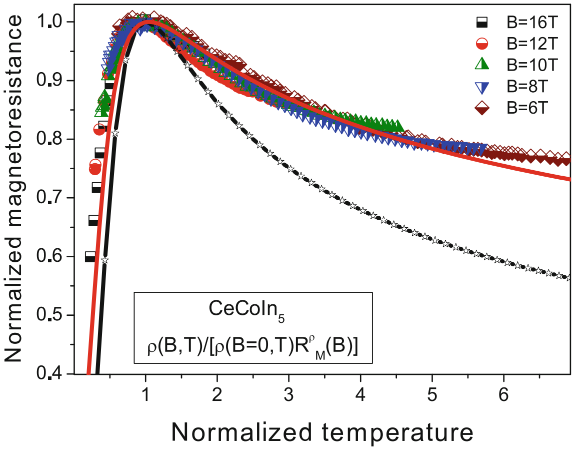

Fig. 7.4 The normalized magnetoresistance $R_N^\rho(y)$ determined by (7.10) versus normalized temperature $y = T/T_{\text{Rm}}$. The data have been extracted from MR shown in Fig. 7.6 and collected on CeCoIn_5 at fixed magnetic fields B [15] listed in the *right upper corner*. The *starred line* represents our calculations based on (6.21) and (7.10) with the parameters extracted from *AC* susceptibility of CeRu_2Si_2 (see the caption to Fig. 7.9). The *solid line* displays our calculations based on (7.11) and (7.10). Only one parameter was used to fit the data, while the other were extracted from the *AC* susceptibility measured on CeRu_2Si_2

coincidence, we employ (6.16), which describes the behavior of the effective mass at higher temperatures and ensures that at these temperatures the resistance behaves as $\rho(T) \propto T$. To correct the behavior of $M_N^*(y)$ at rising temperatures $M^* \sim T^{-1/2}$, we add a term to (6.21) and obtain

$$M_N^*(y) \approx \frac{M^*(x)}{M_M^*}\left[\frac{1 + c_1 y^2}{1 + c_2 y^{8/3}} + c_3 \frac{\exp(-1/y)}{\sqrt{y}}\right], \tag{7.11}$$

where c_3 is an adjustable parameter. The last term on the right hand side of (7.11) makes M_N^* satisfy (6.16) at temperatures $T/T_M > 2$. In Fig. 7.4, the fit of $R_N^\rho(y)$ by (7.11) is shown by the solid line. Constant c_3 is taken as a fitting parameter, while the other were extracted from *AC* susceptibility of CeRu_2Si_2 as described in the caption to Fig. 7.9.

Before discussing the magnetoresistance $\rho_{mr}(B, T)$ given by (7.4), we consider the magnetic field dependence of both the MR peak value $R_{\max}(B)$ and the corresponding peak temperature $T_{\text{Rm}}(B)$. It is possible to use (7.9) which relates the position and value of the peak with the function $M^*(B, T)$. Since $T_{\text{Rm}} \propto \mu_B(B - B_{c0})$, B enters (7.9) only as tuning parameter of QCP, as both $\Delta\rho_L$ and ρ_0 were omitted. At $B \to B_{c0}$ and $T \ll T_{\text{Rm}}(B)$, this omission is not correct since $\Delta\rho_L$ and ρ_0 become comparable with $\Delta\rho(B, T)$. Therefore, both $R_{\max}(B)$ and $T_{\text{Rm}}(B)$ are not characterized by any critical field, being continuous functions at the quantum critical field B_{c0}, in contrast to $M^*(B, T)$, whose peak value diverges and the peak temperature tends to zero at

B_{c0}, as it is seen from (6.22) and (6.23). Thus, we have to take into account $\Delta\rho_L(B,T)$ and ρ_0 which prevent $T_{\rm Rm}(B)$ from vanishing and make $R_{\max}(B)$ finite at $B \to B_{c0}$. As a result, we have to replace B_{c0} by some effective field $B_{eff} < B_{c0}$ and take B_{eff} as a parameter which imitates the contributions coming from both $\Delta\rho_L(B,T)$ and ρ_0. Upon modifying (7.9) by taking into account $\Delta\rho_L(B,T)$ and ρ_0, we obtain

$$T_{\rm Rm}(B) \simeq b_1(B - B_{eff}), \tag{7.12}$$

$$R_{\max}(B) \simeq \frac{b_2(B-B_{eff})^{-1/3}-1}{b_3(B-B_{eff})^{-1}+1}. \tag{7.13}$$

Here b_1, b_2, b_3 and B_{eff} are the fitting parameters. It is pertinent to note that to derive (7.13) we use (7.12) with substitution $(B - B_{eff})$ for T. Then, (7.12) and (7.13) are not valid at $B \lesssim B_{c0}$. In Fig. 7.5, we show the field dependence of both $T_{\rm Rm}$ and $R_{\max}$, extracted from MR measurements [15]. Clearly, both $T_{\rm Rm}$ and $R_{\max}$ are well described by (7.12) and (7.13) with $B_{eff} = 3.8$ T. We note that this value of B_{eff} is in good agreement with observations, obtained from the experimental T–B phase diagram of CeCoIn$_5$ [15].

To calculate $\rho_{mr}(B,T)$, we apply (7.10) to describe its universal behavior, (6.21) for the effective mass along with (7.12) and (7.13) for MR parameters. Figure 7.6 shows the calculated MR versus temperature as a function of magnetic field B together with the experimental points from [15]. We recall that the contributions coming from $\Delta\rho_L(B,T)$ and ρ_0 were omitted. As seen from Fig. 7.6, our description of the experiment is good.

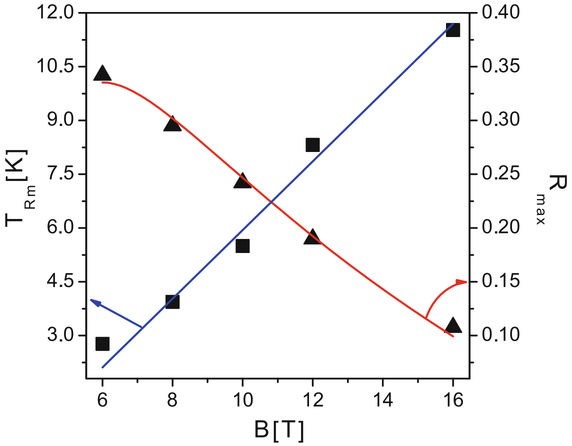

Fig. 7.5 The peak temperatures $T_{\rm Rm}$ (*squares*) and the peak values $R_{\max}$ (*triangles*) versus magnetic field B extracted from measurements of MR [15]. The *solid lines* represent our calculations based on (7.12) and (7.13)

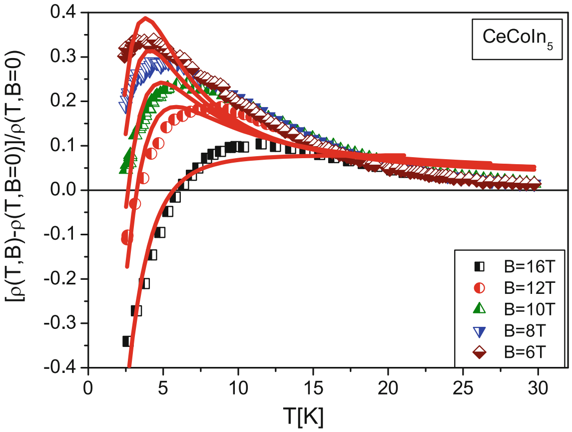

Fig. 7.6 MR versus temperature T as a function of magnetic field B. The experimental data on MR were collected on CeCoIn$_5$ at fixed magnetic field B [15] shown in the *right bottom corner* of the figure. The *solid lines* represent our calculations; (6.21) is used to fit the effective mass entering (7.10)

7.2.3 Electric Resistivity of HF Metals

Here we give a brief outline of the physical properties of HF metals resistivity, while its detailed analysis including the residual term ρ_0 is postponed to the Chaps. 9–11. We note that the role of Umklapp processes, violating momentum conservation and forming ρ_0, are briefly discussed in Sect. 10.2. The electric resistivity of strongly correlated Fermi systems, $\rho(T) = \rho_0 + \Delta\rho_1(B, T)$ is determined by the effective mass due to Kadowaki-Woods relation $\Delta\rho_1(B, T) = A(B, T)T^2 \propto (TM^*(B, T))^2$, see Sect. 7.2.1 and [11–13]. Therefore the above temperature dependence of the effective mass can be observed in measurements of HF metals resistivity. At temperatures $T \ll T^*(B)$, the system is in the LFL state, the behavior of the effective mass as $x \to x_{FC}$ is described by (6.7), and the coefficient $A(B)$ can be represented as

$$A(B) \propto \frac{1}{(B - B_{c0})^{4/3}}. \tag{7.14}$$

In this regime, the resistivity behaves as $\Delta\rho_1 = c_1T^2/(B-B_{c0})^{4/3} \propto T^2$. The second regime, a highly correlated Fermi liquid determined by (6.14), is characterized by the resistivity dependence $\Delta\rho_1 = c_2T^2/(T^{2/3})^2 \propto T^{2/3}$. The third regime at $T > T^*(B)$ is determined by (6.16). In that case we obtain $\Delta\rho_1 = c_3T^2/(T^{1/2})^2 \propto T$. If the system is above the quantum critical line shown in Fig. 6.7, the temperature dependence of the effective mass is given by (3.12) so that we obtain from (6.20) that the quasiparticle damping behaves as $\gamma(T) \propto T$ [17]. As a result, we see that the temperature dependence of resistivity is $\Delta\rho_1 = c_4T$ [18]. Here, $c_1 - c_4$ are constants. If the system is at the transition regime (arrows in Fig. 6.2), the temperature dependence of the effective mass cannot be characterized by a single exponent as it is clearly seen from the inset to Fig. 6.2a. So, we have $\Delta\rho_1 \propto T^{\alpha_R}$ with $1 < \alpha_R < 2$. Note that all temperature dependencies corresponding to these regimes have been observed experimentally in the HF metals CeCoIn$_5$, YbRh$_2$Si$_2$ and YbAgGe [15, 19–22].

7.3 Magnetic Entropy

The evolution of the derivative of magnetic entropy $dS(B,T)/dB$ as a function of magnetic field B at fixed temperature T_f is of great importance since it allows to study the scaling behavior of the effective mass derivative $TdM^*(B,T)/dB \propto dS(B,T)/dB$. While the scaling properties of the effective mass $M^*(B,T)$ can be analyzed via LMR, see Fig. 7.3, those of the effective mass derivative cannot. As seen from (6.21) and (6.24), at $y \leq 1$ the derivative $dM_N(y)/dy$ is determined as follows

$$-\frac{dM_N(y)}{dy} \propto y,\ \ y = (B - B_{c0})/(B_{inf} - B_{c0}) \propto (B - B_{c0})/T_f. \tag{7.15}$$

We note that the effective mass as a function of B does not have a maximum. At elevated y the derivative $-dM_N(y)/dy$ possesses a maximum at the inflection point and then becomes a decreasing function of y. Using the variable $y = (B-B_{c0})/T_f$, we conclude that at decreasing temperatures, the leading edge of the function $-dS/dB \propto -TdM^*/dB$ becomes steeper and its maximum at $(B_{inf} - B_{c0}) \propto T_f$ is higher. These observations are in quantitative agreement with the measurements of the quantity $-\Delta M/\Delta T$ as a function of magnetic field at fixed temperatures T_f collected on $YbRh_2Si_2$ [23]. We note that according to the well-known thermodynamic equality $dM/dT = dS/dB$ we have $\Delta M/\Delta T \simeq dS/dB$. To carry out a quantitative analysis of the scaling behavior of $-dM^*(B,T)/dB$, we calculate the entropy $S(B,T)$ shown in Fig. 6.3 as a function of B at fixed dimensionless temperatures T_f/μ shown in the right legend of Fig. 7.7. This figure demonstrates the normalized quantity $(dS/dB)_N$ as a function of the normalized magnetic field. The function $(dS/dB)_N$ is obtained

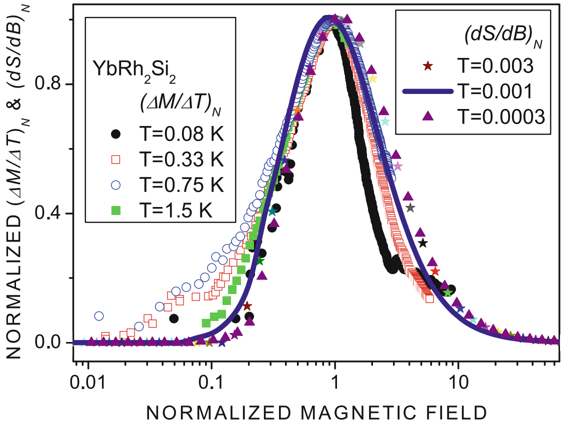

Fig. 7.7 The ratio of normalized magnetization difference and temperature increment $(\Delta M/\Delta T)_N$ versus normalized magnetic field at fixed temperatures, listed in the *left* legend. The *curves* are extracted from the measurements on $YbRh_2Si_2$ [23]. Our calculations of the normalized derivative $(dS/dB)_N \simeq (\Delta M/\Delta T)_N$ versus normalized magnetic field are reported at fixed dimensionless temperatures T/μ and are listed in the *right* legend. All the data are shown by the *symbols* explained in the legends

by normalizing $(-dS/dB)$ by its maximum at $B = B_M$, and the field B is scaled by B_M. The measurements of $-\Delta M/\Delta T$ are normalized similarly and reported in Fig. 7.7 as a function of normalized field. It is seen from Fig. 7.7 that our calculations are in good agreement with the experiment and both the experimental functions $(\Delta M/\Delta T)_N$ and the calculated $(dS/dB)_N$ show the scaling over three orders in the normalized magnetic field.

7.4 Magnetic Susceptibility

7.4.1 *Magnetic Susceptibility and Magnetization Measured on* $CeRu_2Si_2$

Experimental investigations of the magnetic properties of $CeRu_2Si_2$ down to the lowest achieved temperatures (170 mK) and ultrasmall magnetic fields (0.21 mT) have neither shown evidence of the magnetic ordering and/or superconductivity nor conventional LFL behavior [16]. These results imply that magnetic quantum critical point is absent in $CeRu_2Si_2$ and the critical field $B_{c0} = 0$. Even if the magnetic QCP were there it should maintain the NFL behavior over four orders in temperature. We believe that such a strong influence can hardly exist within the picture of conventional quantum phase transitions.

Temperature dependence in the logarithmic scale of the normalized AC susceptibility $\chi_N(B, T) = M_N^*$ as a function of the normalized temperature T_N is shown at different magnetic fields B as indicated in the panel a of Fig. 7.8. The panel b of this Figure shows the normalized static magnetization $M_B(B, T)$ (DC susceptibility) in the same normalized temperature range. The temperature is normalized to T_M. It is the temperature where the susceptibility reaches its peak value. The susceptibility is normalized to its peak value $\chi(B, T_M)$, and the magnetization is normalized to $M_B(B, T \to 0)$ for each value of the field [16]. If we use (7.1) and the definition of susceptibility (7.2), we conclude that the susceptibility and magnetization also demonstrate the scaling behavior and can be represented by the universal function (6.21) of the single variable y.

We see from panel a of Fig. 7.8 that at finite B, the curve $\chi(B, T)/\chi(B, T_M)$ has a peak at a certain temperature T_M, while $M_B(B, T)/M_B(B, T_M)$ has no such peak (panel b) [24–26]. This behavior agrees well with the experimental results [24–26] obtained for $CeRu_2Si_2$ [16]. We note that such behavior of the susceptibility is unusual for ordinary metals and cannot be explained by the theories accounting for only ordinary quantum phase transitions [16].

To verify (6.16) and illustrate the transition from LFL behavior to NFL one, we use the results of measurements of $\chi_{AC}(T)$ in $CeRu_2Si_2$ at magnetic field $B = 0.02$ mT where this HF metal demonstrates the NFL behavior down to lowest investigated temperatures [16]. Indeed, in this case we expect that LFL regime begins to appear at temperatures lower than $T_M \sim \mu_B B \sim 0.01$ mK, as it follows from (6.23). It is seen from Fig. 7.9 (panels a and b) that (6.16) gives good description of the experimental data in the extremely wide temperature range: the susceptibility $\chi_{AC}(T)$ does not

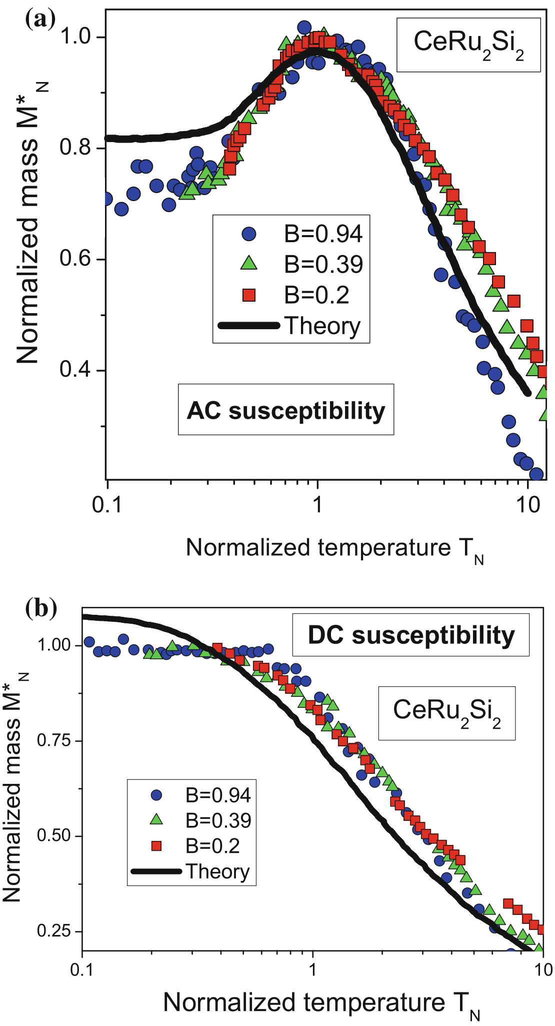

Fig. 7.8 Panel **a** the normalized magnetic susceptibility $\chi(B,T)/\chi(B,T_M)$, and panel **b** normalized magnetization $M_B(B,T)/M_B(B,T_M)$ (DC *susceptibility, right box*) for CeRu$_2$Si$_2$ in magnetic fields 0.20 mT (*squares*), 0.39 mT (*triangles*), and 0.94 mT (*circles*) as functions of the normalized temperature T/T_M [16]. The *solid lines* report the calculated scaling dependence [24] as described in Sect. 6.3.1

remain a constant upon cooling, as would be for a Fermi liquid, but shows a $1/\sqrt{T}$ divergence over almost four orders of temperature. The inset in Fig. 7.9 reports a fit for M^*_N extracted from measurements of $\chi_{AC}(T)$ at different magnetic fields, clearly indicating the transition from LFL behavior at $T_N < 1$ to NFL one at $T_N > 1$ when the system moves along the vertical arrow in Fig. 6.2. It is seen from Figs. 7.8 and 7.9 that the function presented by (6.21) is a good approximation for M^*_N within the extended quasiparticle paradigm. We have seen in Sect. 6.3.2 that the same is true for YbRh$_2$Si$_2$ with its AF quantum critical point. We conclude that both alloys, CeRu$_2$Si$_2$ and YbRh$_2$Si$_2$, demonstrate the universal NFL thermodynamic behavior, independent of their microscopic details like lattice structure, chemical composition and magnetic ground state. This conclusion implies also that numerous QCPs, related

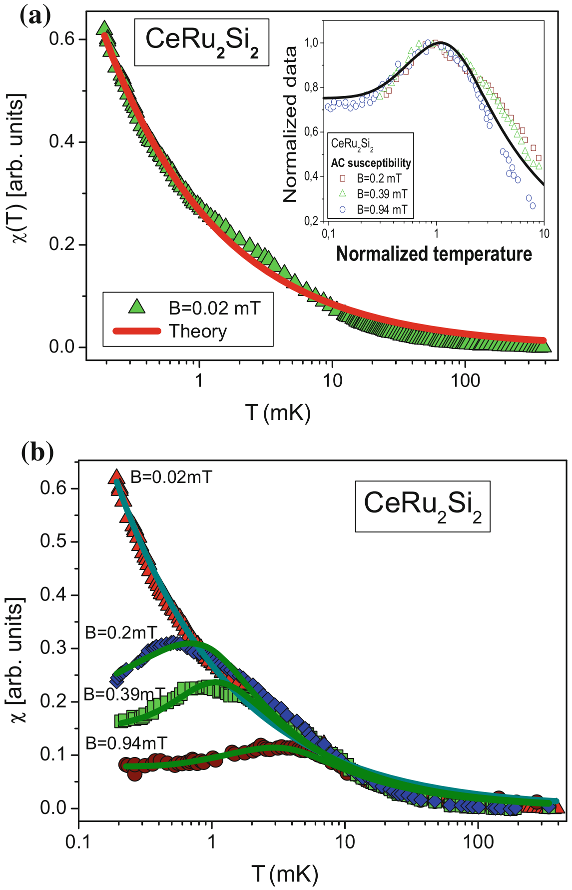

Fig. 7.9 Temperature dependence of the AC susceptibility. Panel **a** the *AC* susceptibility χ_{AC} for $\mathrm{CeRu_2Si_2}$. The *solid curve* is a fit for the data (*triangles*) at $B = 0.02\,\mathrm{mT}$ [16] and represented by the function $\chi(T) = a/\sqrt{T}$ given by (6.16) with a being a fitting parameter. The *inset* shows the normalized effective mass versus normalized temperature T_N extracted from χ_{AC} measured at different fields, as indicated in the *inset* legend [16]. The *solid curve* traces the universal behavior of $M^*_N(T_N)$ determined by (6.21). Parameters c_1 and c_2 are adjusted to fit the average behavior of the normalized effective mass M^*_N. Panel **b** temperature dependence of the *AC* susceptibility $\chi_{AC}(T, B)$ in the magnetic fields B shown near the *curves*

to conventional quantum phase transitions assumed to be responsible for the NFL behavior of different HF metals, can be well reduced to a single QCP related to FCQPT and accounted for within the extended quasiparticle paradigm [27].

7.5 Magnetic-Field-Induced Reentrance of the LFL Behavior and Spin-Lattice Relaxation Rates

A strong departure from the Landau-Fermi liquid (LFL) behavior have been revealed in observed anomalies in both the magnetic susceptibility χ and the muon and ^{63}Cu nuclear spin-lattice relaxation rates $1/T_1$ of $\mathrm{YbCu_{5-x}Au_x}$ ($x = 0.6$). We show that the above anomalies along with magnetic-field-induced reentrance of LFL properties are indeed determined by the dependence of the quasiparticle effective mass M^* on magnetic field B and temperature T and demonstrate that violations of the Korringa law also come from $M^*(B,T)$ dependence upon B and T. We obtain this dependence theoretically utilizing our approach based on fermion condensation quantum phase transition notion. The theoretical analysis of experimental data on the base of FCQPT approach permits not only to explain the above two experimental facts in a unified manner, but to unveil their universal properties, relating the peculiar features of longitudinal magnetoresistance in $YbRh_2Si_2$ to the behavior of spin-lattice relaxation rates.

One of the most interesting and puzzling issues in the research on HF metals is their anomalous dynamic and relaxation properties. It is important to verify whether quasiparticles with effective mass M^* still exist and determine the physical properties of the muon and ^{63}Cu nuclear spin-lattice relaxation rates $1/T_1$ in HF metals throughout their temperature—magnetic field phase diagram, see Fig. 6.2. This phase diagram comprises both LFL and NFL regions as well as NFL–LFL transition or the crossover region, where magnetic-field-induced LFL reentrance occurs. Measurements of the muon and ^{63}Cu nuclear spin-lattice relaxation rates $1/T_1$ in $YbCu_{4.4}Au_{0.6}$ have shown that it differs substantially from ordinary Fermi liquids obeying the Korringa law [28]. Namely, it was reported that for $T \to 0$ reciprocal relaxation time diverges as $1/T_1T \propto T^{-4/3}$ following the behavior predicted by the self-consistent renormalization (SCR) theory [29]. The static uniform susceptibility χ diverges as $\chi \propto T^{-2/3}$ so that $1/T_1T$ scales with χ^2. Latter result is at variance with SCR theory [28]. Moreover, the application of magnetic field B restores the LFL behavior from initial NFL one, significantly reducing $1/T_1$. These experimental findings are hard to explain within both the conventional LFL approach and in terms of other approaches like SCR theory [28, 29].

In this Section we show that the above anomalies along with magnetic-field-induced reentrance of LFL properties are indeed determined by the dependence of the quasiparticle effective mass M^* on magnetic field B and temperature T and demonstrate that the violation of the Korringa law also comes from $M^*(B,T)$ dependence. Our theoretical analysis of experimental data on the base of FCQPT approach permits not only to explain the above two experimental facts in a unified manner, but to unveil their universal properties, relating the peculiar features of both longitudinal magnetoresistance and specific heat in $YbRh_2Si_2$ to the behavior of spin-lattice relaxation rates.

To discuss the deviations from the Korringa law in light of NFL properties of $YbCu_{4.4}Au_{0.6}$, we notice that in LFL theory the spin-lattice relaxation rate $1/T_1$ is determined by the quasiparticles near the Fermi level. The above relaxation rate is related to the decay interaction of the quasiparticles, which in turn is proportional to the density of states at the Fermi level $N(E_F)$. Formally, the spin-lattice relaxation rate is determined by the imaginary part χ'' of the low-frequency dynamical magnetic susceptibility $\chi(\mathbf{q}, \omega \to 0)$, averaged over momentum $\mathbf{q}$

$$\frac{1}{T_1} = \frac{3T}{4\mu_B^2} \sum_{\mathbf{q}} A_{\mathbf{q}} A_{-\mathbf{q}} \frac{\chi''(\mathbf{q}, \omega)}{\omega}, \tag{7.16}$$

where $A_{\mathbf{q}}$ is the hyperfine coupling constant of the muon (or nuclei) with the spin excitations at wave vector $\mathbf{q}$ [29]. Theory of dynamic magnetic (spin) susceptibility of quantum spin liquid and heavy-fermion metals is discussed in Sect. 17.2.1. If $A_{\mathbf{q}} \equiv A_0$ is independent of q, then standard LFL theory yields the relation

$$\frac{1}{T_1 T} = \pi A_0^2 N^2(E_F). \tag{7.17}$$

Equation (7.17) can be viewed as Korringa law. Since in our FCQPT approach the physical properties of the system under consideration are determined by the effective mass $M^*(T, B, x)$, we express $1/T_1 T$ in (7.17) via it. This is accomplished with the standard expression [1] $N(E_F) = M^* p_F/\pi^2$, rendering (7.17) to the form

$$\frac{1}{T_1 T} = \frac{A_0^2 p_F^2}{\pi^3} M^{*2} \equiv \eta \left[M^*(T, B, x)\right]^2, \tag{7.18}$$

where $\eta = (A_0^2 p_F^2)/\pi^3 = \text{const}$. The empirical expression

$$\frac{1}{T_1 T} \propto \chi^2(T), \tag{7.19}$$

extracted from experimental data in $\mathrm{YbCu_{5-x}Au_x}$ [28], follows explicitly from (7.18) and well-known LFL relations $M^* \propto \chi \propto C/T$.

In what follows, we compute the effective mass as it was explained in Sect. 6.3.1 and employ (6.21) for estimations of obtained values [30]. The decay law given by (6.14) along with (7.18) permits to express the relaxation rate in this temperature range as

$$\frac{1}{T_1 T} = a_1 + a_2 T^{-4/3} \propto \chi^2(T), \tag{7.20}$$

where a_1 and a_2 are fitting parameters. The dependence (7.20) is reported in Fig. 7.10 along with experimental points for the muon and nuclear spin-lattice relaxation rates in $\mathrm{YbCu_{4.4}Au_{0.6}}$ at zero magnetic field [28]. It is seen from Fig. 7.10 that (7.20) gives good description of the experiment in the extremely wide temperature range. This means that the extended paradigm is valid and quasiparticles survive in close vicinity of FCQPT, while the observed violation of Korringa law comes from the temperature dependence of the effective mass.

Figure 7.11 displays magnetic field dependence of normalized muon spin-lattice relaxation rate $1/T_{1N}^{\mu}$ in $\mathrm{YbCu_{5-x}Au_x}$ (x = 0.6) along with our theoretical B—dependence. To obtain the latter theoretical curve for fixed temperature and in magnetic field B, we employ (7.18) and solve the Landau integral equation to calculate $M^*(T, B)$ in a way that has been described in Sect. 6.3.1. We note that the normalized effective mass $M_N^*(y)$ has been obtained by normalizing $M^*(T, B)$ at its inflection point shown in the inset to Fig. 6.2.

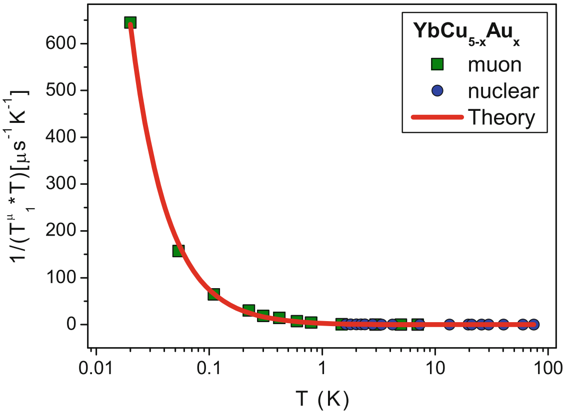

Fig. 7.10 Temperature dependence of muon (*squares*) and nuclear (*circles*) spin-lattice relaxation rates (*divided by temperature*) for $YbCu_{4.4}Au_{0.6}$ at zero magnetic field [28]. The *solid curve* represents our calculations based on (7.20)

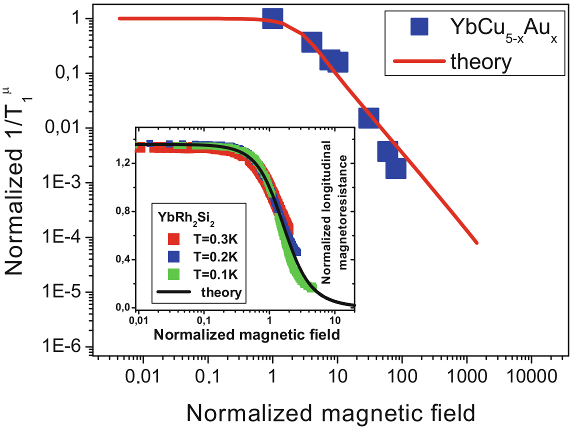

Fig. 7.11 Magnetic field dependence of normalized at the inflection point muon spin-lattice relaxation rate $1/T_{1N}^{\mu}$, extracted from measurements [28] on $YbCu_{4.4}Au_{0.6}$ along with our calculations of B-dependence of the quasiparticle effective mass. *Inset* shows the normalized LMR $R_N^{\rho}(y)$ versus normalized magnetic field. $R_N^{\rho}(y)$ was extracted from LMR of $YbRh_2Si_2$ at different temperatures [5] listed in the legend. The *solid curves* represent our calculations

It is instructive to compare the LMR analyzed in Sect. 7.2.1 and $1/T_1^{\mu}$. LMR $\rho(B,T) = \rho_0 + \rho_B + A(B,T)T^2$ is a function of B at fixed T, where ρ_0 is the residual resistance, ρ_B is the contribution to LMR due to orbital motion of carriers induced by the Lorentz force, and $A(B,T)$ is a function to be calculated. As we see in Sect. 7.2.1, ρ_B is small and we omit this contribution. The Kadowaki-Woods relation allows us to employ M^* in calculating $A(B,T)$. As a result, $\rho(B,T) - \rho_0 \propto (M^*)^2$, and $1/T_{1N}^{\mu} \propto (M^*)^2$ as seen from (7.18). Consequently, we see that LMR and the magnetic field dependence of normalized muon spin-lattice relaxation rate $1/T^{\mu}_{1N}$ can be evaluated from the same equation

$$R^{\rho}_{N}(y) = \frac{\rho(y) - \rho_0}{\rho_{\mathrm{inf}}} = \frac{1}{T^{\mu}_{1N}} = (M^*_N(y))^2. \tag{7.21}$$

Inset to Fig. 7.11 reports the normalized LMR versus normalized magnetic field $y = B/B_{\mathrm{inf}}$ at different temperatures, shown in the legend. Here ρ_{inf} and B_{inf} are, respectively, LMR and magnetic field taken at the inflection point. The inflection points of both LMR and $1/T_{1N}$ are generated by that of M^* shown in the inset to Fig. 6.2a by the arrow. The transition region where LMR starts to decrease is shown in the inset by the hatched area and takes place when the system moves along the horizontal dash-dot arrow. We note that the same normalized effective mass has been used to calculate both $1/T^{\mu}_{1N}$ in $\mathrm{YbCu_{4.4}Au_{0.6}}$ and the normalized LMR in $\mathrm{YbRh_2Si_2}$. Thus, (7.3) defines the intimate relationship between the quite different dynamic properties, showing the validity of the extended quasiparticle paradigm. In Fig. 7.11, both theoretical and experimental curves have been normalized by their inflection points, which also reveals the scaling behavior—the curves at different temperatures merge into a single one in terms of the scaled variable y. Figure 7.11 shows clearly that both, normalized magnetoresistance R^{ρ}_{N} and reciprocal spin-lattice relaxation time, obey the scaling law given by (7.21) well. This fact, obtained directly from the experimental findings, is a vivid evidence that the behavior of both above mentioned quantities is predominantly governed by the field and temperature dependence of the effective mass.

We note that the same normalized effective mass determines the behavior of the thermodynamic and transport properties in $\mathrm{YbRh_2Si_2}$, see Sect. 6.3.2. It is seen from the figures in Sect. 6.3.2 that our calculations of the effective mass offer good unified description for different quantities like the relaxation rates $(1/T_1T)$, the transport (LMR) and thermodynamic properties in such different HF metals as $\mathrm{YbCu_{5-x}Au_x}$ and $\mathrm{YbRh_2Si_2}$. It is pertinent to note that the obtained good description makes an impressive case in favor of the reliability of the extended quasiparticle paradigm.

7.6 The Relations Between Critical Magnetic Fields B_{c0} and B_{c2} in HF Compounds

In high-T_c superconductors, exciting measurements have been performed revealing their physics. One type of measurements demonstrate the existence of Bogoliubov quasiparticles (BQ) in their superconducting state [31–33], see Sect. 5.1.3. While in the pseudogap regime at $T > T_c$, when the superconductivity vanishes, a strong indication of the pairing of electrons or the formation of preformed electron pairs has been observed, while the gap continues to follow the simple d-wave form [32–34]. It is widely assumed that the pseudogap is a state where the Fermi surface of a strongly correlated compound possesses a partial energy gap. This state is very similar to the superconducting gap, which is an energy range that comprises no allowed states.

Another type of the measurement explored the normal state induced by the magnetic field application, when the transition from the NFL behavior to LFL one occurs [35]. As we have mentioned in Sect. 5.3.2.1, there are experimentally evident relations between the critical fields $B_{c2} \geq B_{c0}$, where B_{c2} is the field destroying the superconducting state, and B_{c0} is the critical field at which the (magnetic field induced) QCP takes place. Now we show that $B_{c2} \geq B_{c0}$. We note that to study the aforementioned transition experimentally in high-T_c superconductors, strong magnetic fields $B \geq B_{c2}$ are required. This means that such investigation had earlier been technically inaccessible. An attempt to study the transition experimentally had already been made in [36].

Let us now consider the T–B phase diagram of the high-T_c superconductor $Tl_2Ba_2CuO_{6+x}$ shown in Fig. 7.12. The substance is a superconductor with T_c from 15 to 93 K, being controlled by oxygen content [35]. In Fig. 7.12 open squares and solid circles show the experimental values of the crossover temperature from the LFL to NFL regimes [35]. The solid line given by (6.15) shows our fit with $B_{c0} = 6$ T that is in good agreement with $B_{c0} = 5.8$ T obtained from the field dependence of the charge transport [35].

As it is seen from Fig. 7.12, the linear behavior agrees well with the experimental data [14, 35]. The peak temperatures $T_{\max}$ shown in the inset to Fig. 7.12, depict the maxima of $C(T)/T$ and $\chi_{AC}(T)$, measured on $YbRh_2(Si_{0.95}Ge_{0.05})_2$ [37, 38]. It is

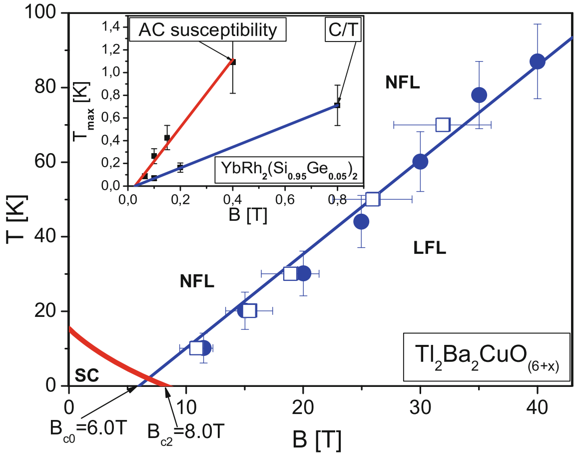

Fig. 7.12 T–B phase diagram of the superconductor $Tl_2Ba_2CuO_{6+x}$. The crossover from LFL to NFL *regime line* $T^*(B)$ is depicted by the *solid straight line*. *Open squares* and *solid circles* are experimental values [35]. *Thick line* represents the boundary between the superconducting and normal phases. The *arrows* near the bottom *left corner* indicate the critical magnetic field B_{c2} that destroys the superconductivity, and the critical field B_{c0}. *Inset* displays the peak temperatures $T_{\max}(B)$, extracted from measurements of C/T and χ_{AC} on $YbRh_2(Si_{0.95}Ge_{0.05})_2$ [37, 38] and approximated by *straight lines* (6.23). The *lines* intersect at $B \simeq 0.03$ T

seen from Fig. 7.12 that $T_{\max}$ shifts towards higher values with increase of the applied magnetic field and both functions can be represented by straight lines intersecting at $B \simeq 0.03$ T. This observation is in good agreement with experiments [37, 38]. It is clear from Fig. 7.12 that critical field $B_{c2} = 8$ T destroying the superconductivity is close to $B_{c0} = 6$ T. We will now show that this is more than a simple coincidence, and $B_{c2} \gtrsim B_{c0}$. Indeed, at $B > B_{c0}$ and low temperatures $T < T^*(B)$, the system is in its LFL state. The superconductivity is then destroyed since the superconducting gap is exponentially small, as we have seen in Sect. 5.1.2. At the same time, there is the FC state at $B < B_{c0}$ and this low-field phase has large prerequisites towards superconductivity, as in this case the gap is a linear function of the superconducting coupling constant λ_0 as that has been shown in Sect. 5.1.2. We note that this is exactly the case in $CeCoIn_5$ where $B_{c0} \simeq B_{c2} \simeq 5$ T [15], as it is seen from Fig. 7.13, while the application of pressure makes $B_{c2} > B_{c0}$ [40]. However, if the superconducting coupling constant is rather weak, then antiferromagnetic order wins the competition. As a result, $B_{c2} = 0$, while B_{c0} can be finite, as it is in $YbRh_2Si_2$ and $YbRh_2(Si_{0.95}Ge_{0.05})_2$ [19, 38].

Comparing the phase diagram of $Tl_2Ba_2CuO_{6+x}$ with that of $CeCoIn_5$, shown in Figs. 7.12 and 7.13, respectively, it is possible to conclude that they are similar in many respects. We note further that the superconducting boundary line $B_{c2}(T)$ acquires a step at decreasing temperatures, i.e. the corresponding phase transition becomes the transition of the first order [39, 41]. This permits us to speculate that the

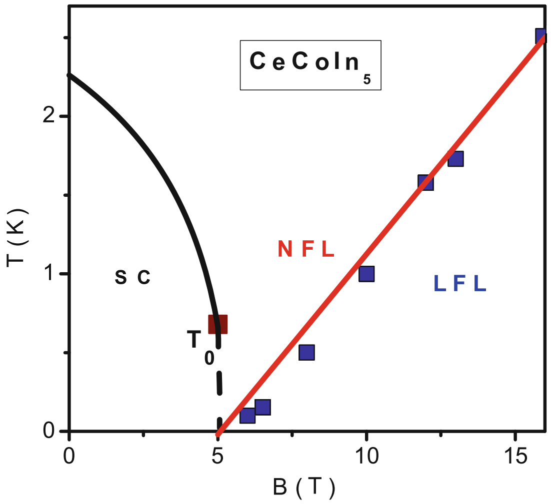

Fig. 7.13 *T–B* phase diagram of the HF metal $CeCoIn_5$. The interface between the superconducting and normal phases is shown by the *solid line* to the *square* where the phase transition becomes a first-order phase transition. At $T < T_0$, the phase transition is a first-order one [39]. The phase boundary between the superconducting and normal phases is shown by the *dashed line*. The *solid straight line*, represented by (6.23) with the experimental points [20] shown by *squares*, is the interface between the LFL and NFL states

same may be true for $Tl_2Ba_2CuO_{6+x}$. We expect that in the NFL state the tunneling conductivity is an asymmetric function of the applied voltage, while it becomes symmetric at the application of increased magnetic fields, when $Tl_2Ba_2CuO_{6+x}$ transits to the LFL phase, as it predicted to be in $CeCoIn_5$ [42].

It follows from (5.47) that it is impossible to observe the relatively high values of $A(B)$, since in our case $B_{c2} > B_{c0}$. We note that (5.47) is valid when the superconductivity is destroyed by the application of magnetic field: Otherwise the effective mass is also finite, since it is given by (5.8). Therefore, as was mentioned above, in high-T_c QCP is poorly accessible to experimental observations being "hidden beneath the superconductivity". Nonetheless, thanks to the experimental data [35], we have seen in Sect. 5.3.2.1, that it is possible to study QCP in high-T_c superconductors [43]. As it is seen from Fig. 5.4, the experiment gives evidences that the physics underlying the field-induced LFL behavior reentrance, is the same for both HF metals and high-T_c superconductors.

7.7 Scaling Behavior of the HF $CePd_{1-x}Rh_x$ Ferromagnet

QCP can arise by suppressing the transition temperature T_{NL} of a FM (or AFM) phase to zero by tuning some control parameter ζ other than temperature, such as pressure P, magnetic field B, or doping x as it takes place in the HF ferromagnet $CePd_{1-x}Rh_x$ [44, 45] or the HF metal $CeIn_{3-x}Sn_x$ [46].

The HF metal $CePd_{1-x}Rh_x$ evolves from ferromagnetism at $x = 0$ to a nonmagnetic state at some critical concentration x_{FC}. Utilizing the extended quasiparticle paradigm and the FCQPT concept, we address the question about the NFL behavior of the FM $CePd_{1-x}Rh_x$ and show that it coincides with that of the AFMs $YbRh_2(Si_{0.95}Ge_{0.05})_2$ and $YbRh_2Si_2$, and paramagnets $CeRu_2Si_2$, as well as $CeNi_2Ge_2$. We again conclude that the NFL behavior, being independent of the peculiarities of a specific alloy, is universal. Incidentally, numerous QCPs assumed by other approaches to be responsible for the NFL behavior of different HF metals can be well reduced to the only FCQPT related QCP [47, 48].

As we have seen above, the effective mass $M^*(T, B)$ can be measured in HF metals experimentally. For example, $M^*(T, B) \propto C(T)/T \propto \alpha(T)/T$ and $M^*(T, B) \propto \chi_{AC}(T)$ where $\chi_{AC}(T)$ is AC magnetic susceptibility. If the corresponding measurements are carried out at fixed magnetic field B (or at fixed x and B) then the effective mass reaches its maximum at some temperature T_M. Upon normalizing both, the effective mass by its peak value at each field B and the temperature by T_M, we observe that all the curves merge into a single one, given by (6.21), thus demonstrating a scaling behavior.

It is seen from Fig. 7.14, that the normalized AC susceptibility

$$\chi^N_{AC}(y) = \frac{\chi_{AC}(T/T_M, B)}{\chi_{AC}(T_M, B)} = M^*_N(T_N)$$

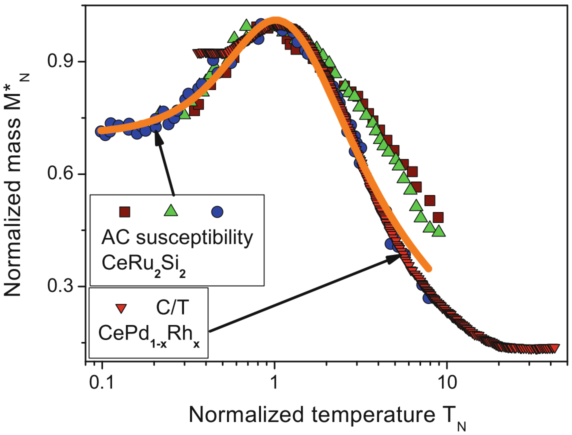

Fig. 7.14 Normalized magnetic susceptibility $\chi_N(T_N, B) = \chi_{AC}(T/T_M, B)/\chi_{AC}(1, B) = M^*_N(T_N)$ for CeRu$_2$Si$_2$ in magnetic fields 0.20 mT (*squares*), 0.39 mT (*upright triangles*) and 0.94 mT (*circles*) versus normalized temperature $T_N = T/T_M$ [16]. The susceptibility reaches its maximum $\chi_{AC}(T_M, B)$ at $T = T_M$. The normalized specific heat $(C(T_N)/T_N)/C(1)$ of the HF ferromagnet CePd$_{1-x}$Rh$_x$ with $x = 0.8$ versus T_N is shown by *downright triangles* [45]. Here T_M is the temperature at the peak of $C(T)/T$. The *solid curve* traces the universal behavior of the normalized effective mass determined by (6.21). Parameters c_1 and c_2 are adjusted for $\chi_N(T_N, B)$ at $B = 0.94$ mT

obtained in measurements on the HF paramagnet CeRu$_2$Si$_2$ [16] agrees with both, the approximation given by (6.21) and the normalized specific heat

$$\frac{C(T_N)/T_N}{C(T_M)} = M^*_N(T_N),$$

obtained in measurements on CePd$_{1-x}$Rh$_x$ [45]. We can also see from Fig. 7.14, that the curve given by (6.21) agrees perfectly with the measurements on CeRu$_2$Si$_2$ whose electronic system is placed at FCQPT [27].

Now let us consider the properties of $M^*_N(T)$, extracted from specific heat measurements on CePd$_{1-x}$Rh$_x$ under the magnetic field application [45] and shown in panel a of Fig. 7.15. It is seen that for $B \geq 1$ T M^*_N describes the normalized specific heat almost perfectly, demonstrating close agreement with that of CeRu$_2$Si$_2$. This coincides with the universal behavior of the normalized effective mass, given by (6.21). Thus, we conclude that the thermodynamic properties of CePd$_{1-x}$Rh$_x$ with $x = 0.8$ are determined by quasiparticles rather than by the critical magnetic fluctuations. On the other hand, one could expect the growth of the critical fluctuations contribution as $x \to x_{FC}$, so that the properties of the normalized effective mass would deviate from those given by (6.21). This is not the case, as observed from Fig. 7.15. It is also seen that at increasing magnetic fields B all the curves defining the normalized effective masses extracted from CePd$_{1-x}$Rh$_x$ with $x = 0.8$ merge into a single one, thus demonstrating a scaling behavior, in coincidence with equation

Fig. 7.15 Panel **a** the normalized effective mass M_N^* as a function of $y = T_N = T/T_M$ at elevated magnetic fields. The mass is extracted from the specific heat C/T of the HF FM $CePd_{1-x}Rh_x$ with $x = 0.8$ ([45]). It is shown at different magnetic fields B listed in the legend. At $B \geq 1$ T, $M_N^*(T_N)$ coincides with that of $CeRu_2Si_2$ (*solid curve*, see the caption to Fig. 7.14). Panel **b** the normalized specific heat $C(T_N)/C(T_M)$ of $CePd_{1-x}Rh_x$ at different magnetic fields B is shown in the *inset*. The kink in the specific heat is clearly seen at $y \simeq 2$. The *solid curve* represents the function $T_N M_N^*(T_N)$

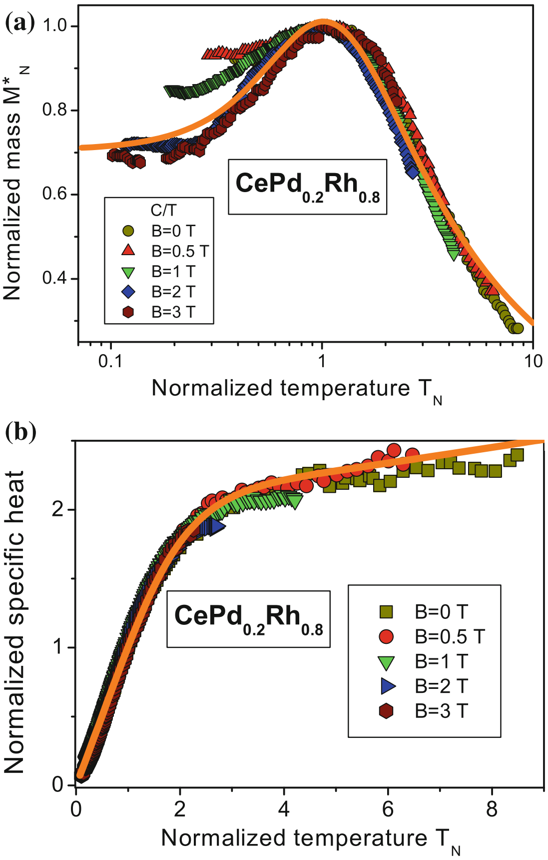

(6.21). We note that existing theories based on the quantum and thermal fluctuations predict that magnetic and thermal properties of FM $CePd_{1-x}Rh_x$ differ from those of the paramagnet $CeRu_2Si_2$, [45, 49–52]. The panel b of Fig. 7.15 shows the kink in the temperature dependence of the normalized specific heat $C(T_N)/C(T_M)$ of $CePd_{1-x}Rh_x$ appearing at $T_N \simeq 2$. In the panel, the solid line denotes the function $T_N M_N^*(T_N)$ with parameters c_1 and c_2, which are adjusted for the magnetic susceptibility at $B = 0.94$ mT. Since the function $T_N M_N^*(T_N)$ describes the normalized specific heat very well and its bend (or kink) comes from the crossover between LFL and NFL regimes, we reliably conclude that the kink emerges at temperatures, at which the system transits from the LFL behavior to the NFL one. As shown in Sect. 7.2.1, the magnetoresistance varies from positive to negative values at the same temperatures. One may speculate that there is an energy scale, which could make the kink coming from fluctuations of the order parameter [5]. In that case we should concede that such diverse HF metals as $CePd_{1-x}Rh_x$, $CeRu_2Si_2$ and $CeCoIn_5$ with different magnetic ground states have the same fluctuations, which exert coherent influence on the heat capacity, susceptibility and transport properties. Indeed, as

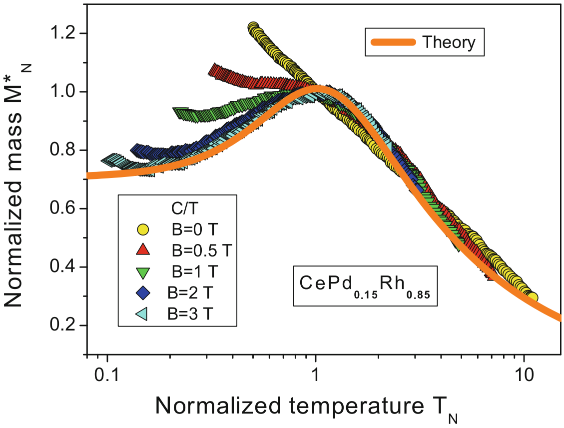

Fig. 7.16 The same as in Fig. 7.15 but for $x = 0.85$ [45]. At $B \geq 1$ T, $M^*_N(T_N)$ demonstrates the universal behavior (*solid curve*, see the caption to Fig. 7.14)

we have seen above and will also see below in this Subsection, the (6.21) allows to describe all above properties quantitatively. We safely conclude that the kink is defined by the universal scaling properties of the normalized effective mass M^*_N and represented by the function $T_N \times M^*_N(T_N)$.

In Fig. 7.16, the effective mass $M^*_N(T_N)$ is presented at fixed B. Since the curve shown by circles and extracted from measurements at $B = 0$ does not exhibit any maximum down to 0.08 K [45], we conclude that in this case x is very close to x_{FC} and the maximum is shifted to very low temperatures. As seen from Fig. 7.16, the application of magnetic field restores the scaling given by (6.21). Again, this permits us to conclude that the thermodynamic properties of $\mathrm{CePd_{1-x}Rh_x}$ with $x = 0.85$ are determined by quasiparticles rather than by the critical magnetic fluctuations.

The thermal expansion coefficient $\alpha(T)$ is given by $\alpha(T) \simeq M^*T/(p_F^2 K)$ [53]. The compressibility $K(\rho)$ is not expected to be singular at FCQPT and is approximately constant [54]. Taking into account (6.16), we find that $\alpha(T) \propto \sqrt{T}$ and the specific heat $C(T) = TM^* \propto \sqrt{T}$. Measurements of the specific heat $C(T)$ on $\mathrm{CePd_{1-x}Rh_x}$ with $x = 0.9$ show a power-law temperature dependence. It is described by the expression $C(T)/T = AT^{-q}$ with $q \simeq 0.5$ and $A =$ const [44].

Figure 7.17 shows that the value of doping $x = 0.90$ delivers the best agreement. Thus, this value tunes $\mathrm{CePd_{1-x}Rh_x}$ to the critical point. At this point $x = 0.90$, the FM critical temperature vanishes and the thermal expansion coefficient is well approximated by the dependence $\alpha(T) \propto \sqrt{T}$, as the temperature varies by almost two orders of magnitude. However, even a small deviation of the system from the critical point destroys the correspondence between this approximation and the experimental data. We note that it is possible to describe the critical behavior of two entirely different HF metals (one is a paramagnet and the other is a ferromagnet) by the function $\alpha(T) = c_1\sqrt{T}$ with only one fitting parameter c_1. This fact vividly shows that fluctuations are not responsible for the observable properties of $\alpha(T)$. Heat capacity measurements for $\mathrm{CePd_{1-x}Rh_x}$ with $x = 0.90$ have shown that $C(T) \propto \sqrt{T}$ [44]. Thus, the electron systems of both metals can be interpreted as being highly

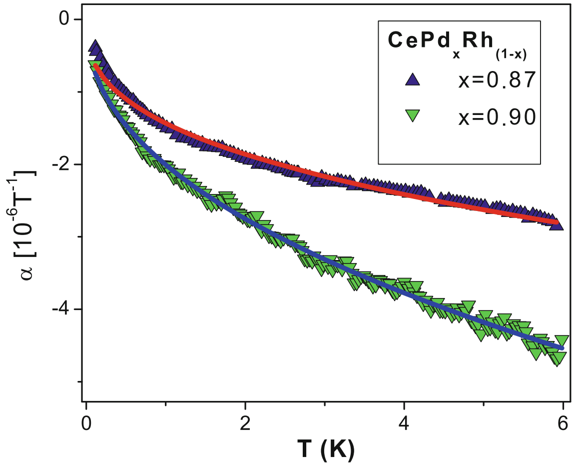

Fig. 7.17 Temperature dependence of the thermal expansion coefficient $\alpha(T)$ at $0.1 \leq T \leq 6$ K. The experimental doping levels $x = 0.90, 0.87$ are taken from [44]. The *solid lines* represent approximations of the experimental values of $\alpha(T) = c_1\sqrt{T}$, where c_1 is a fitting parameter

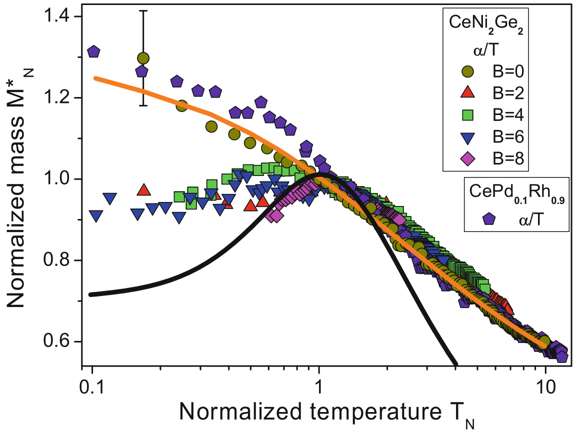

Fig. 7.18 The normalized thermal expansion coefficient $(\alpha(T_N)/T_N)/\alpha(1) = M^*_N(T_N)$ for CeNi$_2$Ge$_2$ [9] and for CePd$_{1-x}$Rh$_x$ with $x = 0.90$ [45] versus $T_N = T/T_M$. Data obtained in measurements on CePd$_{1-x}$Rh$_x$ at $B = 0$ are multiplied by some factor to adjust them at one point to the data for CeNi$_2$Ge$_2$. The *solid line* is a fit to the data shown by the *circles* and *pentagons* at $B = 0$; it is represented by the function $\alpha(T) = c_3\sqrt{T}$ with c_3 being a fitting parameter. The *solid curve* traces the universal behavior of the normalized effective mass determined by (6.21), see the caption to Fig. 7.14

correlated electron liquids. This permits us to conclude that the properties of the effective mass given by (6.16) agrees well with experimental data.

Figure 7.18 demonstrates the measurements of $\alpha(T)/T$ on both CePd$_{1-x}$Rh$_x$ with $x = 0.9$ [44] and CeNi$_2$Ge$_2$ [9]. It is seen that the approximation $\alpha(T) = c_3\sqrt{T}$ is in good agreement with the results of measurements of $\alpha(T)$ in CePd$_{1-x}$Rh$_x$ and CeNi$_2$Ge$_2$ over two orders of magnitude in T_N. It can be shown that measurements on CeIn$_{3-x}$Sn$_x$ with $x = 0.65$ [46] demonstrate the same behavior $\alpha(T) \propto \sqrt{T}$ (not shown in Fig. 7.18). As a result, we suggest that CeIn$_{3-x}$Sn$_x$ with $x = 0.65$, CePd$_{1-x}$Rh$_x$ with $x \simeq 0.9$, and CeNi$_2$Ge$_2$ are located at FCQPT. This becomes especially instructive if we recollect that CePd$_{1-x}$Rh$_x$ is a three dimensional FM [44, 45], CeNi$_2$Ge$_2$ has a paramagnetic ground state [9] and CeIn$_{3-x}$Sn$_x$ is AFM cubic metal [46].

The normalized effective mass $M^*_N(T_N)$ extracted from measurements on the HF metals YbRh$_2$(Si$_{0.95}$Ge$_{0.05}$)$_2$, CeRu$_2$Si$_2$, CePd$_{1-x}$Rh$_x$ and CeNi$_2$Ge$_2$ is reported in Fig. 7.19. It is seen that the scaling behavior of the effective mass given by (6.21) agrees well with the experimental data. Also, the values of $M^*_N(T_N)$ (inverted triangles), are extracted from the data collected on the HF metal YbRh$_2$(Si$_{0.95}$Ge$_{0.05}$)$_2$ [38], coincides with that collected on (upright triangles) the HF metal YbRh$_2$(Si$_{0.95}$Ge$_{0.05}$)$_2$ [38]. We note that in the case of LFL theory the corresponding normalized effective mass $M^*_{NL} \simeq 1$ is independent of both T and B as shown in Fig. 1.3.

The peak temperatures $T_{\max}$, where the maxima of $C(T)/T$, $\chi_{AC}(T)$ and $\alpha(T)/T$ occur, shift to higher values with increase of the applied magnetic field. In Fig. 7.20, $T_{\max}(B)$ are shown for C/T and χ_{AC}, measured on YbRh$_2$(Si$_{0.95}$Ge$_{0.05}$)$_2$. It is seen that both functions can be represented by straight lines intersecting at $B \simeq 0.03$ T. This observation [23, 38] as well as the measurements on CePd$_{1-x}$Rh$_x$, CeNi$_2$Ge$_2$

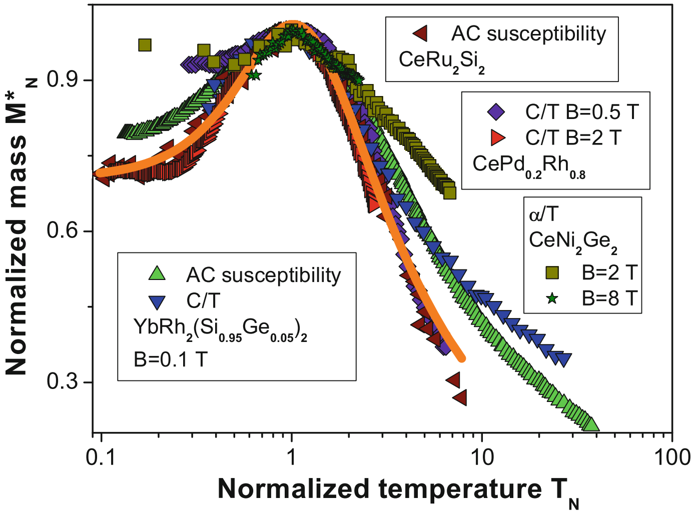

Fig. 7.19 The universal behavior of $M^*_N(T_N)$, extracted from $\chi_{AC}(T,B)/\chi_{AC}(T_M,B)$ for YbRh$_2$(Si$_{0.95}$Ge$_{0.05}$)$_2$ and CeRu$_2$Si$_2$ [16, 38], $(C(T)/T)/(C(T_M)/T_M)$ for YbRh$_2$(Si$_{0.95}$Ge$_{0.05}$)$_2$ and CePd$_{1-x}$Rh$_x$ with $x = 0.80$ [38, 45], and $(\alpha(T)/T)/(\alpha(T_M)/T_M)$ for CeNi$_2$Ge$_2$ [9]. All measurements have been performed under the magnetic field application; its values are listed in the legend. The *solid curve* reports the universal behavior of M^*_N determined by (6.21), see the caption to Fig. 7.14

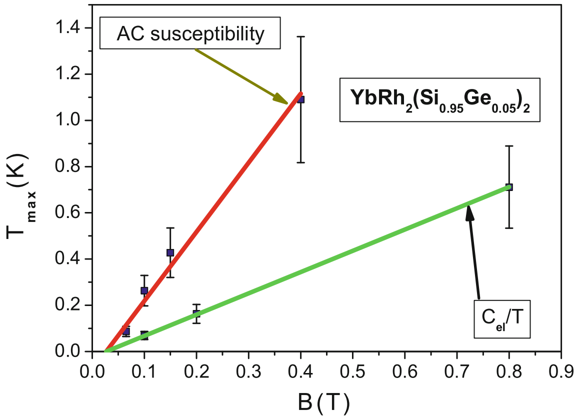

Fig. 7.20 The peak temperatures $T_{\max}(B)$, extracted from measurements of χ_{AC} and C/T on $YbRh_2(Si_{0.95}Ge_{0.05})_2$ [23, 38] and approximated by *straight lines* that are given by (6.23). The *lines* intersect at $B \simeq 0.03$ T

and $CeRu_2Si_2$ demonstrate similar behavior [9, 16, 45], which is well described by (6.23).

We conclude, that the treatment of various experimentally measured quantities (like $C(T)/T$, $\chi_{AC}(T)$, $\alpha(T)/T$ etc.) collected on different HF metals ($YbRh_2$ $(Si_{0.95}$ $Ge_{0.05})$ $_2$, $CeRu_2Si_2$, $CePd_{1-x}Rh_x$, $CeIn_{3-x}Sn_x$ and $CeNi_2Ge_2$) by the above employed normalization procedure immediately reveals their universal scaling behavior [48]. This is because all the above experimental quantities are indeed proportional to the normalized effective mass, thus exhibiting the scaling behavior. Since the effective mass determines the thermodynamic properties, we further conclude that the above HF metals demonstrate similar scaling behavior, independent of their microscopic details such as lattice structure, magnetic ground states, dimensionality etc.

References

1. E.M. Lifshitz, L.P. Pitaevskii, *Statisticheskaya Fizika (Statistical Physics), part 2*. Course of Theoretical Physics (Pergamon Press, Oxford, 1980)
2. D. Vollhardt, Rev. Mod. Phys. **56**, 99 (1984)
3. M. Pfitzner, P. Wölfle, Phys. Rev. B **33**, 2003 (1986)
4. D. Vollhardt, P. Wölfle, P.W. Anderson, Phys. Rev. B **35**, 6703 (1987)
5. P. Gegenwart, T. Westerkamp, C. Krellner, Y. Tokiwa, S. Paschen, C. Geibel, F. Steglich, E. Abrahams, Q. Si, Science **315**, 969 (2007)
6. P. Gegenwart, T. Westerkamp, C. Krellner, M. Brando, Y. Tokiwa, C. Geibel, F. Steglich, Physica B **403**, 1184 (2008)
7. V.R. Shaginyan, M.Y. Amusia, K.G. Popov, Phys. Lett. A **373**, 2281 (2009)
8. V.R. Shaginyan, M.Y. Amusia, K.G. Popov, S.A. Artamonov, JETP Lett. **90**, 47 (2009)
9. R. Kúchler, N. Oeschler, P. Gegenwart, T. Cichorek, K. Neumaier, O. Tegus, C. Geibel, J.A. Mydosh, F. Steglich, L. Zhu, Q. Si, Phys. Rev. Lett. **91**, 066405 (2003)
10. K. Kadowaki, S.B. Woods, Solid State Commun. **58**, 507 (1986)
11. V.A. Khodel, P. Schuck, Z. Phys. B: Condens. Matter **104**, 505 (1997)
12. N. Tsujii, H. Kontani, K. Yoshimura, Phys. Rev. Lett. **94**, 057201 (2005)

13. A.C. Jacko, J.O. Fjærestad, B.J. Powell, Nat. Phys. **5**, 422 (2009)
14. V.R. Shaginyan, M.Y. Amusia, A.Z. Msezane, K.G. Popov, V.A. Stephanovich, Phys. Lett. A **373**, 986 (2009)
15. J. Paglione, M. Tanatar, D. Hawthorn, E. Boaknin, R.W. Hill, F. Ronning, M. Sutherland, L. Taillefer, C. Petrovic, P. Canfield, Phys. Rev. Lett. **91**, 246405 (2003)
16. D. Takahashi, S. Abe, H. Mizuno, D. Tayurskii, K. Matsumoto, H. Suzuki, Y. Onuki, Phys. Rev. B **67**, 180407(R) (2003)
17. J. Dukelsky, V. Khodel, P. Schuck, V. Shaginyan, Z. Phys. **102**, 245 (1997)
18. V.A. Khodel, M.V. Zverev, JETP Lett. **85**, 404 (2007)
19. P. Gegenwart, J. Custers, C. Geibel, K. Neumaier, K.T.T. Tayama, O. Trovarelli, F. Steglich, Phys. Rev. Lett. **89**, 056402 (2002)
20. J. Paglione, M.A. Tanatar, D.G. Hawthorn, F. Ronning, R.W. Hill, M. Sutherland, L. Taillefer, C. Petrovic, Phys. Rev. Lett. **97**, 106606 (2006)
21. S.L. Bud'ko, E. Morosan, P.C. Canfield, Phys. Rev. B **69**, 014415 (2004)
22. A. Bianchi, R. Movshovich, I. Vekhter, P.G. Pagliuso, J.L. Sarrao, Phys. Rev. Lett. **91**, 257001 (2003)
23. Y. Tokiwa, T. Radu, C. Geibel, F. Steglich, P. Gegenwart, Phys. Rev. Lett. **102**, 066401 (2009)
24. J.W. Clark, V.A. Khodel, M.V. Zverev, Phys. Rev. B **71**, 012401 (2005)
25. V.R. Shaginyan, JETP Lett. **79**, 286 (2004)
26. V.R. Shaginyan, JETP Lett. **80**, 263 (2004)
27. V.R. Shaginyan, K.G. Popov, V.A. Stephanovich, Europhys. Lett. **79**, 47001 (2007)
28. P. Carretta, R. Pasero, M. Giovannini, C. Baines, Phys. Rev. B **79**, 020401 (2009)
29. T. Moriya, *Spin Fluctuations in Itinerant Electron Magnetism* (Springer, Berlin, 1985)
30. V.R. Shaginyan, A.Z. Msezane, K.G. Popov, V.A. Stephanovich, Phys. Lett. A **373**, 3783 (2009)
31. H. Matsui, T. Sato, T. Takahashi, S.C. Wang, H.B. Yang, H. Ding, T. Fujii, T. Watanabe, A. Matsuda, Phys. Rev. Lett. **90**, 217002 (2003)
32. M. Shi, J. Chang, S. Pailhes, M.R. Norman, J.C. Campuzano, M. Mansson, T. Claesson, O. Tjernberg, A. Bendounan, L. Patthey, N. Momono, M. Oda, M. Ido, C. Mudry, J. Mesot, Phys. Rev. Lett. **101**, 047002 (2008)
33. H.B. Yang, J.D. Rameau, P.D. Johnson, T. Valla, A. Tsvelik, G.D. Gu, Nature **456**, 77 (2008)
34. V. Mishra, U. Chatterjee, J.C. Campuzano, M.R. Norman, Nat. Phys. **10**, 357 (2014)
35. T. Shibauchi, L. Krusin-Elbaum, M. Hasegawa, Y. Kasahara, R. Okazaki, Y. Matsuda, Proc. Natl. Acad. Sci. USA **105**, 7120 (2008)
36. A.P. Mackenzie, S.R. Julian, D.C. Sinclair, C.T. Lin, Phys. Rev. B **53**, 5848 (1996)
37. J. Custers, P. Gegenwart, H. Wilhelm, K. Neumaier, Y. Tokiwa, O. Trovarelli, C. Geibel, F. Steglich, C. Pépin, P. Coleman, Nature **424**, 524 (2003)
38. P. Gegenwart, J. Custers, Y. Tokiwa, C. Geibel, F. Steglich, Phys. Rev. Lett. **94**, 076402 (2005)
39. A. Bianchi, R. Movshovich, N. Oeschler, P. Gegenwart, F. Steglich, J.D. Thompson, P.G. Pagliuso, J.L. Sarrao, Phys. Rev. Lett. **89**, 137002 (2002)
40. F. Ronning, C. Capan, E.D. Bauer, J.D. Thompson, J.L. Sarrao, R. Movshovich, Phys. Rev. B **73**, 064519 (2006)
41. V.R. Shaginyan, A.Z. Msezane, V.A. Stephanovich, E.V. Kirichenko, Europhys. Lett. **76**, 898 (2006)
42. V.R. Shaginyan, K.G. Popov, Phys. Lett. A **361**, 406 (2007)
43. V.R. Shaginyan, M.Y. Amusia, K.G. Popov, V.A. Stephanovich, Phys. Lett. A **373**, 686 (2009)
44. J.G. Sereni, T. Westerkamp, R. Kuchler, N. Caroca-Canales, P. Gegenwart, C. Geibe, Phys. Rev. B **75**, 024432 (2007)
45. A.P. Pikul, N. Caroca-Canales, M. Deppe, P. Gegenwart, J.G. Sereni, C. Geibel, F. Steglich, J. Phys. Condens. Matter **18**, L535 (2006)
46. R. Küchler, P. Gegenwart, K. Heuser, E.W. Scheidt, G.R. Stewart, F. Steglich, Phys. Rev. Lett. **93**, 096402 (2004)
47. V.R. Shaginyan, E.V. Kirichenko, V.A. Stephanovich, Phys. B **403**, 755 (2008)
48. V.R. Shaginyan, K.G. Popov, Phys. B **404**, 3179 (2009)
49. H.v. Löhneysen, A. Rosch, M. Vojta, P. Wölfle, Rev. Mod. Phys. **79**, 1015 (2007)

50. P. Coleman, arXiv:1001.0185v1 **1**, 1 (2010)
51. T.R. Kirkpatrick, D. Belitz, Phys. Rev. B **67**, 024419 (2003)
52. N.P. Butch, M.B. Maple, Phys. Rev. Lett. **103**, 076404 (2009)
53. L.D. Landau, E.M. Lifshitz, *Statistical Physics* (Elsevier, Oxford, 1980)
54. P. Nozières, J. Phys. I France **2**, 443 (1992)

Chapter 8
Metals with a Strongly Correlated Electron Liquid

Abstract In this chapter, we consider the main properties of strongly correlated Fermi systems, which are formed by the fermion condensate leading to the emergence of flat bands. Namely, we consider the residual entropy S_0 related to the flat bands that leads to the violation of the quasiparticle—hole symmetry. The presence of S_0 has a profound impact on the universality of second order phase transitions. In that case under the application of magnetic field the curve of the second order AF phase transitions passes into a curve of the first order ones at the tricritical point, thus leading to a violation of the critical universality of the fluctuation theory. We demonstrate that a jump in the Hall coefficient is determined by the presence of S_0. As we shall see in Chaps. 9, 10, and 11, the flat bands give rise to the linear in T resistivity, the magnetic field dependent residual resistivity, and quasi-classical behavior of HF fermion metals. We shall see in Chap. 13 that flat bands generate the particle-hole asymmetry leading to the asymmetry and other peculiarities of tunnel conductivity.

8.1 Entropy, Linear Expansion, and Grüneisen's Law

At $T_f \gg T$, where T_f is given by (3.11), the Fermi systems with FC have the distribution function $n_0(\mathbf{p})$ determined by (3.1). That function determines the entropy S given by (2.4) of the HF liquid, located above the quantum critical line shown in Fig. 3.2. It follows from (2.4) and (3.8), that the entropy contains a temperature-independent contribution S_0,

$$S_0 = -2\int \Big[n_0 \ln(n_0) + (1-n_0)\ln(1-n_0)\Big]\frac{d\mathbf{p}}{(2\pi)^3}. \tag{8.1}$$

As a result, we obtain the following estimate from (8.1)

$$S_0 \sim \frac{p_f - p_i}{p_F} \sim |r|, \tag{8.2}$$

where $r = (x - x_{FC})/x_{FC}$. Another specific contribution is related to the spectrum $\varepsilon(\mathbf{p})$, which ensures a link between the dispersionless region $(p_f - p_i)$ occupied by FC and the normal quasiparticles in the regions $p < p_i$ and $p > p_f$. This spectrum

M.Y. Amusia et al., *Theory of Heavy-Fermion Compounds*, Springer Series in Solid-State Sciences 182, DOI 10.1007/978-3-319-10825-4_8

has the form $\varepsilon(\mathbf{p}) \propto (p - p_f)^2 \sim (p_i - p)^2$. Such a shape of the spectrum, corroborated by exactly solvable models for systems with FC, leads to a contribution to the heat capacity $C \sim \sqrt{T/T_f}$ [1]. Therefore, at $0 < T \ll T_f$, the entropy can be approximated by the function [1, 2]

$$S_{NFL}(T) \simeq S_0 + a\sqrt{\frac{T}{T_f}} + b\frac{T}{T_f}, \tag{8.3}$$

where a and b are constants. The third term on the right-hand side of (8.3), which emerges due to the contribution of the temperature-independent part of the spectrum $\varepsilon(\mathbf{p})$, yields a relatively small addition to the entropy. In (8.3), we also omit terms $\propto T\ln(T)$ thar are considered in Sect. 10.2. As we will see shortly, the temperature-independent term S_0 determines the universal transport and thermodynamic properties of the heavy-electron liquid with FC, which we call a strongly correlated Fermi liquid. The properties of this liquid differ dramatically from those of highly correlated Fermi liquid that at $T \to 0$ becomes LFL. As a result, we can think of FCQPT as the phase transition that separates highly correlated and strongly correlated Fermi liquids. We note, that under the application of magnetic field the strongly correlated Fermi liquid transforms into the highly one, as it is shown in Sect. 5.3. Since the highly correlated liquid behaves like LFL as $T \to 0$, QCP separates LFL from a strongly correlated Fermi liquid. On the other hand, as was shown in Sect. 3.1.4, at elevated temperatures the properties of both liquids become indistinguishable. Thus, as we shall see below, both systems can be discriminated at low temperatures when the impact of both FCQPT and the quantum critical line on their physical properties become more pronounced.

Figure 8.1 shows the temperature dependence of $S(T)$ calculated on the basis of the model functional (6.17). The calculations were performed with $g = 7, 8, 12$ and $\beta = b_c = 3$. Let us recollect that the critical value of g is $g_c = 6.7167$. We see in Fig. 8.1 that in accord with (8.2) S_0 increases as the system moves away from QCP along the quantum critical line, see Fig. 3.2. Obviously, the term S_0 on the right-hand side of (8.3), which is temperature-independent, contributes nothing to the heat capacity; while second term in (8.3) gives the main contribution so that the heat capacity behaves as $C(T) \propto \sqrt{T}$.

8.1.1 Entropy, Linear Expansion, and Grüneisen's Law

The unusual temperature dependence of the entropy of a strongly correlated electron liquid specified by (8.3) determines the unusual behavior of the liquid. The existence of a temperature-independent term S_0 can be illustrated by calculating the thermal expansion coefficient $\alpha(T)$ [2, 3], which is given by [4, 5]

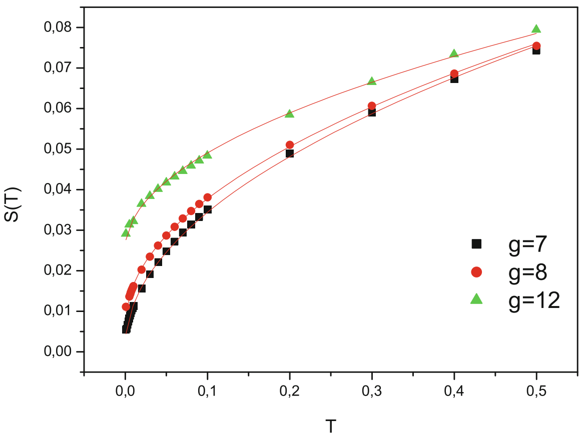

Fig. 8.1 The temperature dependence of the entropy $S(T)$. The *lines* represent the approximation for $S(T)$ (8.3); the symbols mark the results of calculations based on (6.17)

$$\alpha(T) = \frac{1}{3}\left(\frac{\partial(\log V)}{\partial T}\right)_P = -\frac{1}{3V}\left(\frac{\partial(S/x)}{\partial P}\right)_T, \tag{8.4}$$

where P is the pressure and V is the volume. We note that the compressibility $K = d\mu/d(Vx)$ does not develop a singularity at FCQPT and is approximately constant in systems with FC [6]. Substituting (8.3) in (8.4), we find that [2, 3, 6]

$$\frac{\alpha_{FC}(T)}{T} \simeq \frac{a_0}{T} \sim \frac{M^*_{FC}}{p_F^2 K}, \tag{8.5}$$

where $a_0 \sim \partial S_0/\partial P$ is temperature-independent. To derive (8.5), we consider the leading contribution to S_0 only. Recollecting that

$$C(T) = T\frac{\partial S(T)}{\partial T} \simeq \frac{a}{2}\sqrt{\frac{T}{T_f}}, \tag{8.6}$$

we obtain from (8.5) and (8.6) that the Grüneisen ratio $\Gamma(T)$ diverges as

$$\Gamma(T) = \frac{\alpha(T)}{C(T)} \simeq 2\frac{a_0}{a}\sqrt{\frac{T_f}{T}}. \tag{8.7}$$

This expression permits to conclude that Grüneisen's law does not hold in strongly correlated Fermi systems.

Measurements on $YbRh_2(Si_{0.95}Ge_{0.05})_2$ show, however, that $\alpha/T \propto 1/T$ and that the Grüneisen ratio diverges as $\Gamma(T) \simeq T^{-q}$, $q \simeq 0.33$, which allows classifying the electron system of this compound as a strongly correlated liquid [7]. Our estimate

$q = 0.5$, which follows from (8.7), is in satisfactory agreement with this experimental value. The behavior of $\alpha(T)/T$ given by (8.5) contradicts the LFL theory, according to which the thermal expansion coefficient $\alpha(T)/T = M^* = const$ as $T \to 0$. The $1/T$-dependence of the ration α/T predicted in [3] is in good agreement with the data collected on $\mathrm{YbRh_2(Si_{0.95}Ge_{0.05})_2}$ [7].

Equation (3.12) implies that $M^*(T \to 0) \to \infty$ and that the strongly correlated electron system behaves as if it were placed at the quantum critical point. Actually, as we have seen in Sect. 3.1.4, the system is at the quantum critical line $x/x_{FC} \leq 1$, and critical behavior is observed for all $x \leq x_{FC}$ as $T \to 0$. It was shown in Chap. 3 that as $T \to 0$, the strongly correlated electron liquid undergoes the first-order quantum phase transition as the entropy becomes a discontinuous function of the temperature: at finite temperatures, the entropy is given by (8.3), while $S(T = 0) = 0$. Hence, the entropy has a discontinuity $\delta S = S_0$ as $T \to 0$. This implies that, as a result of the first-order phase transition, there are no critical fluctuations along the quantum critical curve and the respective divergences like that of $\Gamma(T)$, are determined by the quasiparticles rather than by critical fluctuations, as could be expected for an ordinary quantum phase transition. We recall that according to the well-known inequality $q \leq T\delta S$ [5], in our case the heat q of the first order transition tends to zero as its critical temperature $T_{NL} \to 0$, see for details Sect. 3.1.1.

8.2 The $T - B$ Phase Diagram, the Hall Coefficient, and the Magnetic Susceptibility

To study the $T - B$ phase diagram of strongly correlated electron liquid, we examine the situation where NFL behavior emerges when the AF phase is suppressed by an external magnetic field B, which is the case for the HF metals $\mathrm{YbRh_2(Si_{0.95}Ge_{0.05})_2}$ and $\mathrm{YbRh_2Si_2}$ [7, 8].

The antiferromagnetic phase is LFL with the entropy vanishing as $T \to 0$. For magnetic fields higher than the critical value B_{c0}, at which the Néel temperature $T_{NL}(B \to B_{c0}) \to 0$, the antiferromagnetic phase transforms into a weakly polarized paramagnetic strongly correlated electron liquid [7, 8]. As shown in Sect. 5.3, a magnetic field applied to the system with $T = 0$ splits the FC state, occupying the interval $(p_f - p_i)$ into Landau levels, and suppresses the superconducting order parameter $\kappa(\mathbf{p})$. The new state is specified by a multiply connected Fermi sphere, on which a smooth quasiparticle distribution function $n_0(\mathbf{p})$ in the interval $(p_f - p_i)$ is replaced with another distribution $\nu(\mathbf{p})$, as it is seen from Fig. 5.1. Hence, the behavior of LFL is restored and characterized by quasiparticles with the effective mass $M^*(B)$ given by (5.39). When the temperature increases so high that $T > T^*(B)$ the system transits along the solid line from the LFL behavior to the NFL one, as it is shown by the arrow. In the NFL region, the entropy of the electron liquid is determined by (8.3). At sufficiently high T the system forgets about the AF transition, and T^* is represented by the straight line, see Sect. 6.4. The described behavior of the system is shown in the $T - B$ diagram in Fig. 8.2.

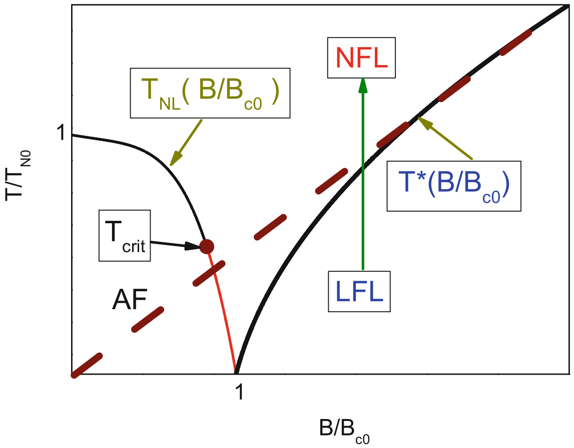

Fig. 8.2 The $T - B$ phase diagram of a strongly correlated electron liquid. The *line* $T_{NL}(B/B_{c0})$ represents the dependence of the Néel temperature on the field strength B. The dot at $T = T_{crit}$ marks the critical temperature where the second-order AF phase transition becomes a first-order one. For $T < T_{crit}$, the heavy *solid line* represents the function $T_{NL}(B/B_{c0})$, when the AF phase transition becomes a first-order one. The strongly correlated liquid in the NFL region is characterized by the entropy S_{NFL} given by (8.3). The *solid line* $T^*(B/B_{c0})$ separates the strongly correlated liquid (NFL) from the weakly polarized electron liquid, behaving like the Landau Fermi liquid. The *dashed line* shows the line T^* provided that the AF phase transition were absent, see Fig. 6.8 and Sect. 6.4

In accordance with the experimental data, we assume that at relatively high temperatures $T/T_{N0} \sim 1$, where T_{N0} is the Néel temperature in a zero magnetic field, the antiferromagnetic phase transition is of the second-order [8]. In this case, the entropy and other thermodynamic functions at the temperature $T_{NL}(B/B_{c0})$ are continuous. This means that the entropy S_{AF} of the antiferromagnetic phase coincides with the entropy S_{NFL} of the strongly correlated liquid given by (8.3):

$$S_{AF}(T \to T_{NL}(B)) = S_{NFL}(T \to T_{NL}(B)). \tag{8.8}$$

Since the antiferromagnetic phase behaves like LFL, with its entropy $S_{AF}(T \to 0) \to 0$, (8.8) cannot be satisfied at sufficiently low temperatures $T \leq T_{crit}$ because of the temperature-independent term S_0. Hence, the second order antiferromagnetic phase transition becomes the first order one at $T = T_{crit}$ [9, 10] as is shown by the arrow in Fig. 8.2. A detailed consideration of this problem is given in Sect. 8.3.

At $T = 0$, the critical magnetic field B_{c0}, in which the antiferromagnetic phase becomes LFL is determined by the condition that the ground-state energy of the antiferromagnetic phase is equal to the ground-state energy $E[n_0(\mathbf{p})]$ of the HF liquid with FC, since, as it was shown in Chap. 3, the heat of the transition $q = 0$. This means that the ground state of the antiferromagnetic phase is degenerate at $B = B_{c0}$. Hence, at $B \to B_{c0}$ the Néel temperature T_{NL} tends to zero and the behavior of the effective mass $M^*(B \geq B_{c0})$ is determined by (5.39), so that $M^*(B)$ diverges as $B \to B_{c0}$ from top. As a result, at $T = 0$, the phase transition separating the antiferromagnetic phase that exist at $B \le B_{c0}$ from LFL taking place at $B \ge B_{c0}$ is the first order quantum phase transition. The driving parameter of this phase transition is the magnetic field strength B. We note that the respective quantum and thermal critical fluctuations disappear at $T < T_{crit}$ because the first-order antiferromagnetic phase transition occurs at such temperatures.

We now examine the jump in the Hall coefficient detected in measurements involving $\mathrm{YbRh_2Si_2}$ [11]. The Hall coefficient $R_H(B)$ as a function of B experiences a jump as $T \to 0$, when the applied magnetic field reaches its critical value $B = B_{c0}$, and then becomes even higher than the critical value at $B = B_{c0} + \delta B$, where δB is an infinitesimal field variation [11]. As shown in Sect. 5.3, when $T = 0$, the application of the critical magnetic field B_{c0}, which suppresses the antiferromagnetic phase with the Fermi momentum p_F restores LFL with the Fermi momentum $p_f > p_F$. When $B < B_{c0}$, the ground-state energy of the antiferromagnetic phase is lower than that of the LFL state induced by the application of magnetic field, but for $B > B_{c0}$ we are confronted with the opposite case, where the LFL state has the lower energy. At $B = B_{c0}$ and $T = 0$, both phases have the same ground state energy and $T_{NL} = 0$ as the phases are degenerate, being separated by the first order phase transition as shown in Fig. 8.2.

Thus, at $T = 0$ and $B = B_{c0}$, an infinitesimal increase δB in the magnetic field leads to a finite discontinuity in the Fermi momentum. This is because the distribution function becomes multiply connected (see Fig. 5.1) and the number of mobile electrons does not change. Thus, the antiferromagnetic ground state can be viewed as having a “small” Fermi surface with Fermi momentum p_F, while the paramagnetic ground state at $B > B_{c0}$ has a “large” Fermi surface with $p_f > p_F$. As a result, the Hall coefficient experiences a sharp jump because $R_H(B) \propto 1/p_F^3$ in the antiferromagnetic phase and $R_H(B) \propto 1/p_f^3$ in the paramagnetic phase. Assuming that $R_H(B)$ is a measure of the Fermi momentum [11], as is in the case with a simply connected Fermi volume, we obtain

$$\frac{R_H(B = B_{c0} - \delta)}{R_H(B = B_{c0} + \delta)} \simeq 1 + 3\frac{p_f - p_F}{p_F} \simeq 1 + d\frac{S_0}{x_{FC}}, \tag{8.9}$$

where S_0/x_{FC} is the entropy per heavy electron and $d \sim 5$ is a constant. It follows from (8.9) that the discontinuity in the Hall coefficient is determined by the anomalous behavior of the entropy, which can be attributed to S_0. Hence, the discontinuity tends to zero as $r \to 0$ and disappears when the system is on the disordered side of FCQPT, where the entropy has no temperature-independent term [9].

We now turn to the magnetization which is determined by (7.1). For $T \ll T^*(B)$, the effective mass is given by (5.39) and the static magnetization is

$$M(B) \simeq a_M \sqrt{B - B_{c0}}. \tag{8.10}$$

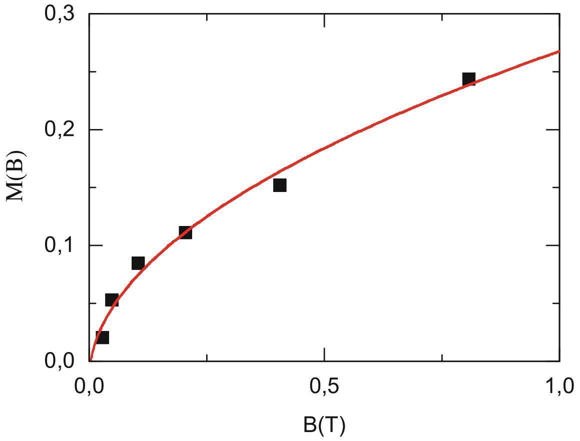

Fig. 8.3 The magnetization $M(B)$ obtained in measurements on $\mathrm{YbRh_2(Si_{0.95}Ge_{0.05})_2}$ (*black squares*) [12]. The *curve* represents the field-dependent function $M(B) = a_M\sqrt{B}$ given by (8.10), where a_M is a fitting parameter

Fig. 8.3 shows that the function $M(B)$ determined by (8.10) is in good agreement with the data obtained in measurements on $\mathrm{YbRh_2(Si_{0.95}Ge_{0.05})_2}$ [12]. We note that in this case $B_{c0} \simeq 0$.

We examine the experimental $T-B$ diagram of the heavy-fermion metal $\mathrm{YbRh_2Si_2}$ [8, 12] shown in Fig. 8.4. In the LFL state, the behavior of the metal is characterized by the effective mass $M^*(B)$, which diverges as $1/\sqrt{B-B_{c0}}$ [8]. It is quite evident that (5.39) provides a good description of this experimental fact: $M^*(B)$ diverges as $B \to B_{c0}$ at $T_{NL}(B = B_{c0}) = 0$ and, as Fig. 8.3 shows, the calculated behavior of the magnetization agrees with the experimental data. The magnetic field dependence of the coefficient $A(B)$, shown in the left panel of Fig. 5.3, is also in good agreement with experiment on $\mathrm{YbRh_2Si_2}$ [8]. Figure 8.4 demonstrates that in accordance with (5.42), the curve separating the LFL region from the NFL one can be approximated by the function $c_1\sqrt{B-B_{c0}}$ with a fitting parameter c_1. Bearing in mind that the behavior of $\mathrm{YbRh_2Si_2}$ is similar to that of $\mathrm{YbRh_2(Si_{0.95}Ge_{0.05})_2}$ [7, 12–14], we also conclude that the thermal expansion coefficient $\alpha(T)$ is temperature-independent and that the Grüneisen ratio diverges as a function of T in the NFL state [7]. We conclude that the entropy in the NFL state is determined by (8.3). Since the antiferromagnetic phase transition is of the second order at relatively high temperatures [8], we can predict that as the temperature decreases, the phase transition becomes the first order. The above description of the Hall coefficient $R_H(B)$ also agrees with the experimental data [11].

Thus, we conclude that the $T-B$ phase diagram of the strongly correlated electron liquid shown in Fig. 8.2 agrees with the experimental $T-B$ diagram obtained from experiments involving the heavy-fermion metals $\mathrm{YbRh_2Si_2}$ and $\mathrm{YbRh_2(Si_{0.95}Ge_{0.05})_2}$ and shown in Fig. 8.4.

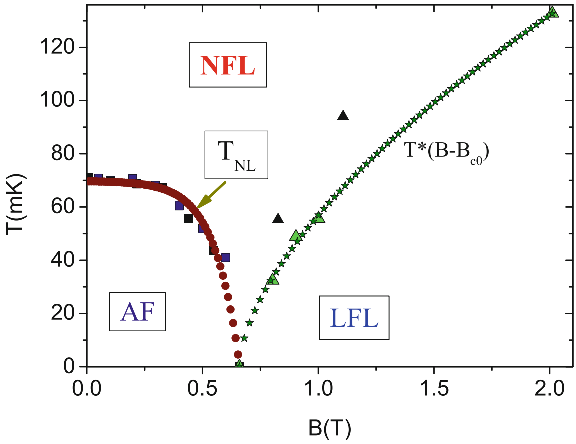

Fig. 8.4 $T - B$ phase diagram for $YbRh_2Si_2$ with magnetic fields applied parallel to the c axis. The symbols denote the experimental data [8, 12]. The line T_{NL} reports the field dependence of the Néel temperature $T_{NL}(B)$. In the NFL region, the strongly correlated liquid is characterized by the entropy S_{NFL} (8.3). The line, separating the NFL region from the LFL one, is approximated by the function $T^*(B - B_{c0}) = c_1\sqrt{B - B_{c0}}$, given by (5.42), where c_1 is a fitting parameter

8.3 The Impact of FCQPT on Ordinary Continuous Phase Transitions in HF Metals

We show that in HF metals with flat bands at $B \to B_{c1}$, where B_{c1} is the critical field, at which the tricritical point occurs, the second order phase transition becomes the first order one. In case of $CeCoIn_5$ the line of the second order superconducting phase transitions transits to the line of the first order one, while in case of $YbRh_2Si_2$ the line of the second order AF phase transitions transits to the line of the first order one.

The microscopic nature of quantum criticality, determining the NFL behavior in strongly correlated fermion systems of different types, is still unclear. Many puzzling and common experimental features of such seemingly different systems as two-dimensional (2D) electron systems and liquid ^{3}He as well as 3D heavy-fermion metals and high-T_c superconductors suggest that there is a hidden fundamental law of nature, which remains to be understood. To reveal this hidden law "the projection" of microscopic properties of the above materials on their observable, macroscopic characteristics is needed. One of such "projections" is the impact of the FCQPT phenomenon on the ordinary phase transitions in HF metals. As we have seen in Sect. 8.2, the main peculiarity here of the superconductive phase transition from the second order to the first one is the process of continuous magnetic field evolution [15–17]. The same changing of the order is valid for magnetic phase transitions.

The exciting measurements on $YbRh_2Si_2$ at the AF phase transition revealed a sharp peak in low-temperature specific heat, which is characterized by the critical exponent $\alpha = 0.38$ and therefore differs drastically from those of the conventional fluctuation theory of second order phase transitions [18], where $\alpha \simeq 0.1$ [5]. The obtained large value of α casts doubts on the applicability of the conventional theory and sends a real challenge for theories in describing the second order phase transitions in HF metals [18], stimulating impressive theoretical efforts to explain the violation of the critical universality in terms of the tricritical point [19–21].

The striking feature of FCQPT is that it has profound influence on thermodynamically driven second order phase transitions provided that they take place in the NFL region formed by FCQPT. As a result, the curve of second order phase transitions modifies into a curve of the first order ones at the tricritical point leading to a violation of the critical universality of the fluctuation theory. For example, as we have seen in Sect. 7.6 the second order superconducting phase transition in $\mathrm{CeCoIn_5}$ changes to the first order in the NFL region. It is this feature that provides the key to resolve the above described challenge.

8.3.1 The Comparison of $T - B$ Phase Diagrams for $\mathrm{YbRh_2Si_2}$ *and* $\mathrm{CeCoIn_5}$

In Fig. 8.4, the T_{NL} line represents temperature $T_{NL}(B)/T_{N0}$ versus field B/B_{c0} in the schematic phase diagram for $\mathrm{YbRh_2Si_2}$, with $T_{N0} = T_{NL}(B = 0)$. There $T_{NL}(B)$ is the Néel temperature as a function of the magnetic field B. The solid and dashed curves indicate the boundary of the AF phase at $B/B_{c0} \leq 1$ [8]. For $B/B_{c0} \geq 1$, the dash-dot line marks the upper limit of the observed LFL behavior. This dash-dot line coming from (5.42) separates the NFL state and the weakly polarized LFL one, being represented by

$$\frac{T^*}{T_{NL}} = a_1\sqrt{\frac{B}{B_{c0}} - 1}, \tag{8.11}$$

where a_1 is a parameter. We note that (8.11) is in good agreement with experimental facts [8]. Thus, $\mathrm{YbRh_2Si_2}$ demonstrates two different LFL states, where the temperature-dependent electrical resistivity $\Delta\rho$ follows the LFL behavior $\Delta\rho \propto T^2$, one being weakly antiferromagnetic ordered ($B \leq B_{c0}$ and $T < T_{NL}(B)$) and the other being the weakly polarized ($B \geq B_{c0}$ and $T < T^*(B)$) [8]. At increasing temperatures and fixed magnetic field, under that the system moves along the vertical arrow shown in Fig. 8.5, the NFL state occurs which is separated from the AF phase by the curve T_{NL} of the phase transitions. In consistence with the experimental data we assume that at relatively high temperatures $T/T_{NL}(B) \simeq 1$ the AF phase transition is of the second order [8, 18]. In that case, the entropy and the other thermodynamic functions are continuous at the line of the phase transitions T_{NL}, shown in Fig. 8.5. This means that the entropy of the AF phase $S_{AF}(T)$ coincides with the entropy $S_{NFL}(T)$ of the NFL state. Since the AF phase demonstrates the LFL behavior, that

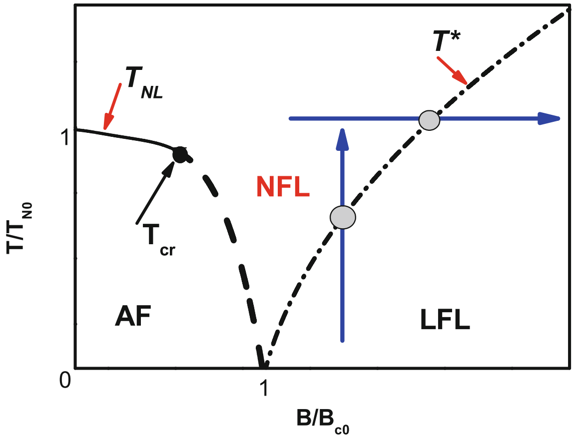

Fig. 8.5 Schematic $T - B$ phase diagram for $YbRh_2Si_2$. The *solid* and *dashed* T_{NL} *curves* separate the AF and NFL states representing the field dependence of the Néel temperature. The *black dot* at $T = T_{cr}$ and $B = B_{c1}$ shown by the *arrow* in the *dashed curve* is the tricritical point, where the curve of second order AF phase transitions (*solid line*) transits into the curve of the first ones. At $T < T_{cr}$, the *dashed line* represents the field dependence of the Néel temperature when the AF phase transition is of the first order. The NFL state is characterized by the entropy S_0 (8.2). The *dash-dot line* separating the NFL state and the weakly polarized LFL one is represented by T^* (8.11). The *horizontal solid arrow* represents the direction, along which the system transits from the NFL regime to the LFL one with increase of the magnetic field and fixed temperature. The *vertical solid arrow* represents the direction along which the system transits from the LFL regime to the NFL one at elevated temperature and fixed magnetic field. The *hatched circles* depict the transition temperature T^* from the NFL to LFL domains

is $S_{AF}(T \to 0) \to 0$, while $S_{NFL}(T)$ contains the temperature-independent term given by (3.8). Thus, in the NFL region formed by FCQPT, (8.8) cannot be satisfied at diminishing temperatures and the second order AF phase transition inevitably becomes the first order one at the tricritical point with $T = T_{cr}$, as shown in Fig. 8.5. At $T = 0$, the heat of the phase transition is zero, $q = 0$, as it was shown in Chap. 3. Thus, the critical field B_{c0} is determined by the condition that the ground state energy of the AF phase coincides with the ground state energy of the weakly polarized LFL, and the ground state of $YbRh_2Si_2$ becomes degenerate at $B = B_{c0}$. Therefore, the Néel temperature $T_{NL}(B \to B_{c0}) \to 0$. That means that at $T = 0$ the system moving along the horizontal arrow shown in Fig. 8.5 goes to its paramagnetic state, when the applied magnetic field reaches its critical value $B = B_{c0}$, and becomes even higher $B = B_{c0} + \delta B$, where δB is an infinitesimal magnetic field variation. As to the Hall coefficient, it experiences the jump, as it is seen from (8.9) [22].

The comparison of the phase diagrams of $YbRh_2Si_2$ (Fig. 8.5) and $CeCoIn_5$ (Figs. 7.13 and 10.1) permits to conclude that they are similar in many respects. Indeed, the line of the second order superconducting phase transitions transforms to the line of the first order ones at the tricritical point, shown by the square in Fig. 7.13. This transition takes place under the application of magnetic fields $B > B_{c2} \geq B_{c0}$

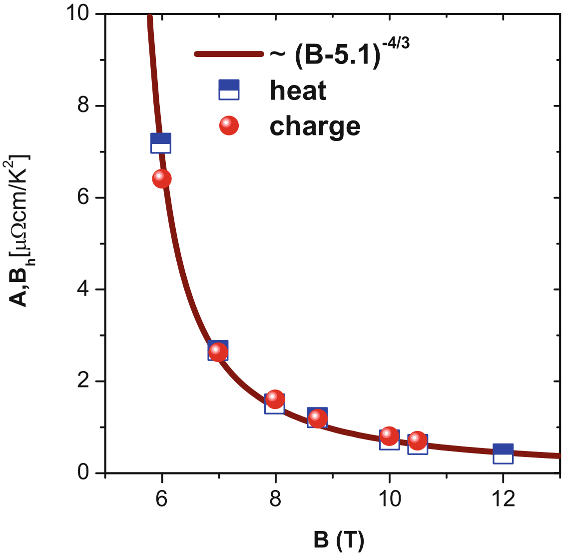

Fig. 8.6 The dependence of the charge and the heat transport on magnetic filed B. $A(B)$ and $B_h(B)$ determine the T^2-dependence of the resistance and the heat transfer in the LFL state induced by the magnetic field. The symbols mark the experimental data from [24, 25]

(see Sect. 7.6), where B_{c2} is the critical field destroying the superconducting state, and B_{c0} is the critical field, where QCP induced by the magnetic field takes place [15, 23]. We note that the superconducting boundary line $B_{c2}(T)$ at lower temperatures acquires the tricritical point, since (8.8) cannot be satisfied at diminishing temperatures $T \leq T_{cr}$, i.e. the corresponding phase transition becomes of first order [15]. This permits us to conclude that at lower temperatures, in the NFL region formed by FCQPT the curve of any second order phase transition transforms into the first order one at the tricritical point.

On the other hand, there is an important feature in the phase diagram of $CeCoIn_5$ that is not seen in that of $YbRh_2Si_2$, for the AF critical point is hidden in the superconducting dome. As a result, in contrast to the case of $YbRh_2Si_2$, the NFL behavior is not seen down to $T \to 0$ at $B \to B_{c2}$, see Sect. 10.2. Therefore, FC is destroyed by the application of magnetic field $B \to B_{c2}$ and $CeCoIn_5$ demonstrates the LFL behavior at sufficiently low temperatures. As Fig. 8.6 shows, in that case the behavior $A(B) \propto B_h(B) \propto M^*(B) \propto (B - B_{c0})^{-4/3}$ is specified by (6.7), and is in good agreement with the experimental results [24, 25]. The coefficient $B_h(B)$ determines the T^2-dependence of the thermal resistance, and the ratio $A(B)/B_H(B)$ is field-independent, with $A/B_H \simeq 0.70$ [24, 25].

8.3.2 *The Tricritical Point in the $B - T$ Phase Diagram of* $\mathrm{YbRh_2Si_2}$

Low-temperature specific-heat measurements on $\mathrm{YbRh_2Si_2}$ at the second order AF phase transition reveal a sharp peak at $T_{NL} = 72$ mK. The corresponding critical exponent α turns out to be $\alpha = 0.38$, which differs significantly from that obtained within the framework of the fluctuation theory of second order phase transitions based on the scale invariance, where $\alpha \simeq 0.1$. Under the application of magnetic field the curve of the second order AF phase transitions passes into a curve of the first order ones at the tricritical point leading to a violation of the critical universality of the fluctuation theory. This change of the phase transition is generated by FCQPT.

The Landau theory of the second order phase transitions becomes applicable as the tricritical point is approached, $T \simeq T_{cr}$, since the fluctuation theory can lead only to logarithmic corrections to the critical indices. Moreover, near the tricritical point, the difference $T_{NL}(B) - T_{cr}$ is a second order infinitesimal quantity, when entering the term defining the divergence of the specific heat [5]. As a result, upon using the Landau theory we obtain that the Sommerfeld coefficient $\gamma_0 = C/T$ varies as $\gamma_0 \propto |t-1|^{-\alpha}$ where $t = T/T_{NL}(B)$ with the exponent being $\alpha \simeq 0.5$ as the tricritical point is approached at fixed magnetic field [5].

We will see that $\alpha = 0.5$ gives a good description of the measurements of the specific heat on $\mathrm{YbRh_2Si_2}$. Taking into account that the specific heat increases in going from the symmetrical to the asymmetrical AF phase [5], we obtain

$$\gamma_0(t) = A_1 + \frac{B_1}{\sqrt{|t-1|}}. \tag{8.12}$$

Here, $B_1 = B_\pm$ are the proportionality factors, which are different for the two sides of the phase transition. The parameters $A_1 = A_\pm$, related to the corresponding specific heat $(C/T)_\pm$, are also different for the two sides, and "+" stands for $t > 1$, while "−" stands for $t < 1$.

The attempt to fit the available experimental data for $\gamma_0 = C(T)/T$ in $\mathrm{YbRh_2Si_2}$ at the AF phase transition in zero magnetic fields [18] by the function (8.12) is reported in Fig. 8.7. We show there the normalized Sommerfeld coefficient γ_0/A_+ as a function of the normalized temperature $t = T/T_{N0}$. It is seen that the normalized Sommerfeld coefficient γ_0/A_+ extracted from C/T measurements on $\mathrm{YbRh_2Si_2}$ [18] is well described in the entire temperature range around the AF phase transition by the formula (8.12) with $A_+ = 1$.

Now we transform (8.12) to the form

$$\frac{\gamma_0(t) - A_1}{B_1} = \frac{1}{\sqrt{|1-t|}}. \tag{8.13}$$

It follows from (8.13) that the ratios $(\gamma_0 - A_1)/B_1$ for $t < 1$ and $t > 1$ versus $|1-t|$ collapse into a single line on double logarithmic plot. The ratios (8.13), extracted

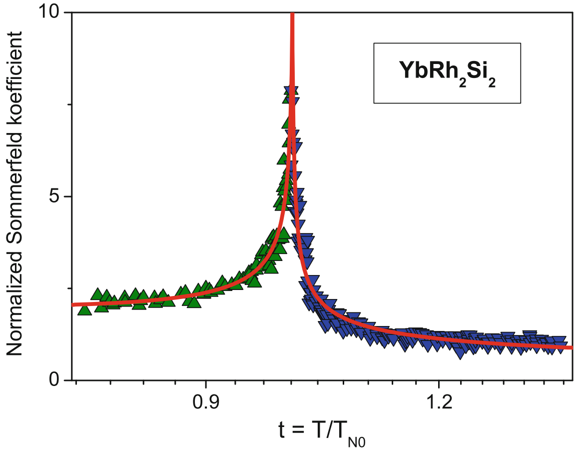

Fig. 8.7 The normalized Sommerfeld coefficient γ_0/A_+ as a function of the normalized temperature $t = T/T_{N0}$. The coefficient shown by the *solid curve* is given by the formula (8.12). It is extracted from the data on $\mathrm{YbRh_2Si_2}$ at the AF phase transition [18] and shown by the *triangles*

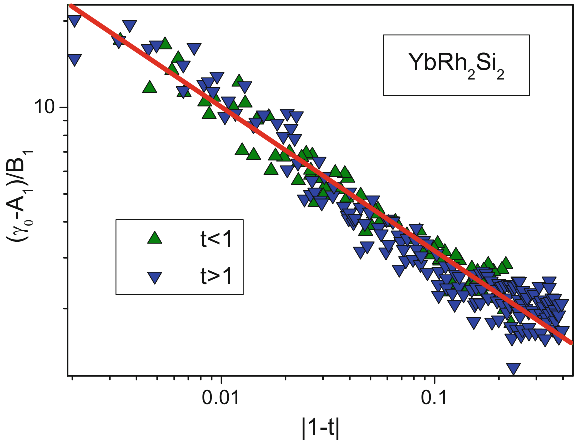

Fig. 8.8 The square root dependence at the tricritical point on the double logarithmic scale. *Solid line* shows the temperature dependence of the ratios $(\gamma_0 - A_1)/B_1$ for $t < 1$ and $t > 1$ versus $|1-t|$ given by (8.13). The ratios are extracted from measurements of γ_0 on $\mathrm{YbRh_2Si_2}$ at the AF phase transition [18] and depicted by the *triangles* as shown in the legend

from experimental data [18] are reported in Fig. 8.8. The coefficients A_1 and B_1 are taken from fitting of γ_0 presented in Fig. 8.7. It is seen from Fig. 8.8 that the ratios $(\gamma_0 - A_1)/B_1$ marked by the upward and downwards triangles for $t < 1$ and $t > 1$, respectively, do collapse into the single line shown by the solid straight line.

A few notes are here in order. The good fit (Figs. 8.7 and 8.8) of the experimental data by the functions (8.12) and (8.13) with the critical exponent $\alpha = 1/2$ allows to conclude that the specific heat measurements on $YbRh_2Si_2$ [18] are taken near the tricritical point and they predict that the second order AF phase transition in $YbRh_2Si_2$ changes to the first order one under the application of magnetic field, as it is shown by the arrow in Fig. 8.5 [10]. It is seen from Fig. 8.7 that at $t \simeq 1$ the peak is sharp, while one would expect that anomalies in the specific heat associated with the onset of magnetic order are broad [18, 26, 27]. Such a behavior reflects the fact that the phase transition has to change to the first order at the tricritical point, Fig. 8.5. As it is seen from Fig. 8.7, the Sommerfeld coefficient is larger below the phase transition than above it. This fact is in accord with the Landau theory, according to which the specific heat increases when passing from $t > 1$ to $t < 1$ [5].

8.3.3 *Low Temperature Entropy of* $YbRh_2Si_2$

It is instructive to analyze the low temperature evolution of the magnetic entropy in $YbRh_2Si_2$. We begin with considering the derivative of the magnetic entropy $dS(B,T)/dB$ as a function of magnetic field B at fixed temperature T_f, when the system goes from the NFL to LFL regime, as it is shown by the horizontal solid arrow in Fig. 8.5. Such a behavior is of great importance since the current measurements of the magnetic entropy in $YbRh_2Si_2$ [28] allow to analyze the reliability of the theory employed and to study the scaling behavior of the entropy, when the system is in its NFL, transition and LFL states, respectively.

The quantitative analysis of the scaling behavior of $dS(B,T)/dB$ is given in Sect. 7.3. Figure 7.7 reports the normalized $(dS/dB)_N$ as a function of the normalized magnetic field. It is seen from Fig. 7.7 that our calculations (solid line) are in good agreement with the measurements and the scaled functions $(\Delta M/\Delta T)_N$ extracted from the experimental data exhibit the scaling behavior in a wide range of the normalized magnetic fields B/B_M. The other thermodynamic and transport properties of $YbRh_2Si_2$ analyzed in Sect. 6.3.2 are also in good agreement with the measurements. These developments make our analysis of the AF phase transition quite substantial.

Now we are in a position to evaluate the entropy S at temperatures $T \lesssim T^*$ in $YbRh_2Si_2$. At $T < T^*$ the system in its LFL state, the effective mass is independent of T, is a function of the magnetic field B. As a result, (5.39) reads

$$\frac{m}{M^*(B)} = a_2\sqrt{\frac{B}{B_{c0}} - 1}, \tag{8.14}$$

where a_2 is a parameter. In the LFL state at $T < T^*$ when the system moves along the vertical arrow shown in Fig. 8.5, the entropy is given by the well-known relation, $S = M^*T\pi^2/p_F^2 = \gamma_0 T$ [5]. Taking into account (8.11) and (8.14) we obtain that at $T \simeq T^*$ the entropy is independent of both the magnetic field and temperature, $S(T^*) \simeq \gamma_0 T^* \simeq S_0 \simeq a_1 m T_{NL}\pi^2/(a_2 p_F^2)$. Upon using the data [8], we obtain that for fields that are applied along the hard magnetic direction $S_0(B_{c0} \parallel c) \sim 0.03R\ln 2$

(R is the universal gas constant), and for fields applied along the easy magnetic direction $S_0(B_{c0} \perp c) \sim 0.005R \ln 2$. Thus, as it follows from Fig. 8.4 and in accordance with the data collected on $YbRh_2Si_2$ [8], we conclude that the entropy contains the temperature-independent part S_0 [29–31], which gives rise to the tricritical point. As it is shown in Sect. 9.1, the presence of the term S_0 points directly to the existence of the heat capacity C independent of temperature. Such a behavior is observed in the HF metal $YbRh_2Si_2$ [32].

To summarize this subsection, we note that a theory, as it is in general, is an important tool in understanding what we observe. It is demonstrated here that the obtained value of α is in good agreement with the specific heat measurements on $YbRh_2Si_2$ and conclude that the critical universality of the fluctuation theory is violated at the AF phase transition since the second order phase transition is about to change to the first order one, making $\alpha \to 1/2$. We have also shown that in the NFL region formed by FCQPT the curve of any second order phase transition transforms into a curve of the first order ones at the tricritical point leading to the violation of the critical universality of the fluctuation theory. This change is generated by the temperature-independent entropy S_0 formed behind FCQPT.

References

1. V.A. Khodel, V.R. Shaginyan, JETP Lett. **51**, 553 (1990)
2. M.Y. Amusia, A.Z. Msezane, V.R. Shaginyan, Phys. Lett. A **320**, 459 (2004)
3. M.V. Zverev, V.A. Khodel, V.R. Shaginyan, M. Baldo, JETP Lett. **65**, 863 (1997)
4. E.M. Lifshitz, L.P. Pitaevskii, *Statisticheskaya Fizika (Statistical Physics), part 2*. Course of Theoretical Physics (Pergamon Press, Oxford, 1980)
5. L.D. Landau, E.M. Lifshitz, *Statistical Physics* (Elsevier, Oxford, 1980)
6. P. Nozières, J. Phys. I France **2**, 443 (1992)
7. R. Kúchler, N. Oeschler, P. Gegenwart, T. Cichorek, K. Neumaier, O. Tegus, C. Geibel, J.A. Mydosh, F. Steglich, L. Zhu, Q. Si, Phys. Rev. Lett. **91**, 066405 (2003)
8. P. Gegenwart, J. Custers, C. Geibel, K. Neumaier, K.T.T. Tayama, O. Trovarelli, F. Steglich, Phys. Rev. Lett. **89**, 056402 (2002)
9. V.R. Shaginyan, P.G. Popov, S.A. Artamonov, JETP Lett. **82**, 215 (2005)
10. V.R. Shaginyan, M.Y. Amusia, K.G. Popov, Phys. Lett. A **374**, 659 (2010)
11. S. Paschen, T. Lühmann, S. Wirth, P. Gegenwart, O. Trovarelli, C. Geibel, F. Steglich, P. Coleman, Q. Si, Nature **432**, 881 (2004)
12. J. Custers, P. Gegenwart, H. Wilhelm, K. Neumaier, Y. Tokiwa, O. Trovarelli, C. Geibel, F. Steglich, C. Pépin, P. Coleman, Nature **424**, 524 (2003)
13. P. Gegenwart, J. Custers, Y. Tokiwa, C. Geibel, F. Steglich, Phys. Rev. Lett. **94**, 076402 (2005)
14. C. Pépin, Phys. Rev. Lett. **94**, 066402 (2005)
15. A. Bianchi, R. Movshovich, N. Oeschler, P. Gegenwart, F. Steglich, J.D. Thompson, P.G. Pagliuso, J.L. Sarrao, Phys. Rev. Lett. **89**, 137002 (2002)
16. K. Izawa, H. Yamaguchi, Y. Matsuda, H. Shishido, R. Settai, Y. Onuki, Phys. Rev. Lett. **87**, 057002 (2001)
17. K. Maki, Phys. Rev. **148**, 362 (1966)
18. C. Krellner, S. Hartmann, A. Pikul, N. Oeschler, J.G. Donath, C. Geibel, F. Steglich, J. Wosnitza, Phys. Rev. Lett. **102**, 196402 (2009)
19. T. Misawa, Y. Yamaji, M. Imada, J. Phys. Soc. Jpn. **78**, 084707 (2009)
20. M. Imada, T. Misawa, Y. Yamaji, J. Phys. Condens. Matter **22**, 164206 (2010)

21. C. Klingner, C. Krellner, C. Geibel, J. Phys.: Conf. Ser. **200**, 012089 (2010)
22. V.R. Shaginyan, Phys. B: Condens. Matter **127**, 378–380 (2006)
23. N. Oeschler, P. Gegenwart, M. Lang, R. Movshovich, J.L. Sarrao, J.D. Thompson, F. Steglich, Phys. Rev. Lett. **91**, 076402 (2003)
24. J. Paglione, M. Tanatar, D. Hawthorn, E. Boaknin, R.W. Hill, F. Ronning, M. Sutherland, L. Taillefer, C. Petrovic, P. Canfield, Phys. Rev. Lett. **91**, 246405 (2003)
25. J. Paglione, M.A. Tanatar, D.G. Hawthorn, F. Ronning, R.W. Hill, M. Sutherland, L. Taillefer, C. Petrovic, Phys. Rev. Lett. **97**, 106606 (2006)
26. F. Steglich, B. Buschinger, P. Gegenwart, M. Lohmann, R. Helfrich, C. Langhammer, P. Hellmann, L. Donnevert, S. Thomas, A. Link, C. Geibel, M. Lang, G. Sparn, W. Assmus, J. Phys. Condens. Mat. **8**, 9909 (1996)
27. H. v. Löhneysen, J. Phys. Condens. Matter **8**, 9689 (1996)
28. Y. Tokiwa, T. Radu, C. Geibel, F. Steglich, P. Gegenwart, Phys. Rev. Lett. **102**, 066401 (2009)
29. V.R. Shaginyan, M.Y. Amusia, K.G. Popov, Phys. Usp. **50**, 563 (2007)
30. V.R. Shaginyan, M.Y. Amusia, A.Z. Msezane, K.G. Popov, Phys. Rep. **492**, 31 (2010)
31. V.A. Khodel, M.V. Zverev, V.M. Yakovenko, Phys. Rev. Lett. **95**, 236402 (2005)
32. P. Wölfle, E. Abrahams, Phys. Rev. B **84**, 041101(R) (2011)

Chapter 9
Quasi-classical Physics Within Quantum Criticality in HF Compounds

Abstract In this chapter, we explore how the fermion condensation paves the road for quasi-classical physics in HF compounds. This means simply that systems with FC admit partly the quasi-classical description of their thermodynamic and transport properties. This, in turn, simplifies a lot not only of their description but permits to gain more insights both in the puzzling NFL physics of HF compounds and of the physics of FC itself. The quasi-classical physics starts to be applicable near FCQPT, at which FC generates flat bands and quantum criticality, and makes the density of electron states in strongly correlated metals diverge. As we shall see, due to the formation of flat bands the strongly correlated metals exhibit the classical properties of elemental ones like copper, silver, aluminum, etc., for the strongly correlated metals demonstrate the quasi-classical behavior at low temperatures.

9.1 Second Wind of the Dulong-Petit Law at a Quantum Critical Point

We show that in the systems with quantum criticality like 2D ^{3}He, the group velocity of transverse zero sound depends strongly on temperature. It is this dependence that grants the Dulong - Petit Law a "second wind". In 2D liquid ^{3}He, the specific heat becomes temperature independent at some characteristic temperature of a few mK. In the same way, the heat capacity of the HF metal $YbRh_2Si_2$ contains the temperature independent term.

Almost 200 years ago, Pierre-Louis Dulong and Alexis-Thérèse Petit [1] discovered experimentally that the specific heat $C(T)$ of a crystal is close to constant, being independent of the temperature T. This behavior, attributed to lattice vibrations—i.e. phonons—is known as the Dulong-Petit Law. Later, Ludwig Boltzmann [2] reproduced the results of Dulong and Petit quantitatively in terms of the equipartition principle. However, subsequent measurements at low temperatures demonstrated that $C(T)$ drops rapidly as $T \to 0$, in sharp contrast to Boltzmann's theory. In 1912, Peter Debye [3] developed a quantum theory for evaluation of the phonon part of the specific heat of solids, correctly explaining the empirical behavior $C(T) \sim T^3$ of the lattice component as $T \to 0$. In the Debye theory, the T-independence of $C(T)$ is

M.Y. Amusia et al., *Theory of Heavy-Fermion Compounds*, Springer Series in Solid-State Sciences 182, DOI 10.1007/978-3-319-10825-4_9

recovered at $T \geq T_D$, where T_D is a critical temperature corresponding to the saturation of the phonon spectrum. With the creation of the Landau theory of quantum liquids [4], that predicted a linear-in-T dependence of $C(T)$ for the specific heat that is contributed by itinerant fermions, our understanding of the low-temperature thermodynamic properties of solids and liquids seemed to be firmly established. However, recent measurements [5, 6] of the specific heat of two-dimensional (2D) ^{3}He, realized as ^{3}He films absorbed on graphite preplated with a ^{4}He bilayer, reveal behavior strongly antithetical to established general view, that calls for a new understanding of the low-temperature thermodynamics of strongly correlated many-fermion systems [7].

Owing to its status as a fundamental specimen of the strongly interacting many-fermion systems, liquid ^{3}He remains a valuable touchstone for low-temperature condensed-matter physics. In recent years, interest in ^{3}He physics has been driven by the observation of non-Fermi-liquid (NFL) behavior of dense ^{3}He films at the lowest temperatures $T \simeq 1$ mK reached experimentally [5, 6, 8–12]. In particular, measurements of the specific heat $C(T)$ in the 2D ^{3}He system show the presence of a term β tending to a finite value as $T \to 0$. Such behavior contrasts sharply with that of its counterpart, three-dimensional (3D) liquid ^{3}He. Note, that here we do not consider superfluid phases of ^{3}He.

In seeking the origin of the anomalous contribution β remaining in $C(T)$ at the lowest temperatures attained, it is instructive to examine the schematic low-T phase diagram of 2D liquid ^{3}He shown in Fig. 9.1. The essential features of this picture are documented by the cited experiments on ^{3}He films. The effective coupling parameter

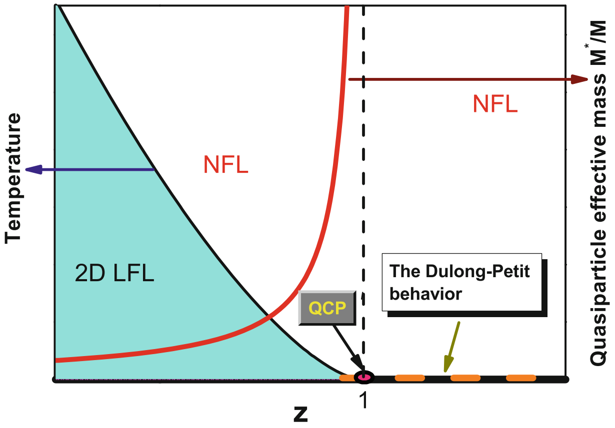

Fig. 9.1 Phase diagram of the 2D liquid ^{3}He system. The region defined by $z = \rho/\rho_{FC} < 1$ is divided into LFL and NFL domains separated by a *solid line*. The dependence $M^*(z) \propto (1-z)^{-1}$ is shown by the *solid line* approaching the *dashed asymptote*, thus depicting the divergence of the effective mass at the quantum critical point ($z = 1, T = 0$) indicated by the *arrow*. In the region $z \gtrsim 1$, the fermion condensate (FC) sets in and Dulong-Petit behavior of the specific heat is realized for the strongly correlated quantum many-fermion system (as represented by the *dash horizontal line* at $T = 0$)

is represented by $z = \rho/\rho_\infty$, where ρ is the number density of the system and ρ_∞ is the critical density at which a quantum critical point (QCP) occurs. This QCP is associated with a divergence of the effective mass $M^*(z)$, portrayed in Fig. 9.1 by the curve (in red on line) that approaches the dashed asymptote at $z = 1$. The $T - z$ phase plane is divided into regions of 2D LFL and NFL behavior. The part of the diagram where $z < 1$ consists of a FL region at lower T and a NFL region at higher T, separated by a solid curve. The regime where $z \gtrsim 1$ belongs to a NFL state with specific heat taking a finite value $\beta(\rho)$ at very low temperatures. The physical source of this excess heat capacity has not been established with certainty, although it is supposed that the β anomaly is related to peculiarities of the substrate on which the ^{3}He film is placed.

As indicated above, the most challenging feature of the NFL behavior of liquid ^{3}He films involves the specific heat $C(T)$. According to the Landau theory, $C(T)$ varies linearly with T, and at low film densities the experimental behavior of the specific heat of 2D liquid ^{3}He is in agreement with LFL theory. However, for relatively dense ^{3}He films, this agreement is found to hold only at sufficiently *high* temperatures. If T is lowered down to millikelvin region, the function $C(T)$ ceases to fall toward zero and becomes flat [5, 6, 12].

The common explanation [5, 6, 13] of the observed $C(T)$ flattening imputes the phenomenon to disorder associated with the substrate that supports the ^{3}He film. More specifically, it is considered that there exists weak heterogeneity of the substrate (namely, steps and edges on its surface), such that quasiparticles, being delocalized from it, give rise to the low-temperature feature β of the heat capacity [6].

Even if we disregard certain unjustified assumptions [13], there remains the disparate fact that the emergent constant term in $C(T)$ is of comparable order for different substrates [5, 6, 12]. Furthermore, the explanation posed in [13] implies that the departure of $C(T)$ from LFL predictions shrinks as the film density increases, since the effects of disorder are most prominent in weakly interacting systems. On the contrary, the anomaly in $C(T)$ makes its emerge in the density region where the effective mass M^* is greatly enhanced [6, 12] and the 2D liquid ^{3}He system becomes strongly correlated. This reasoning compels us to consider that the NFL behavior of $C(T)$ is an *intrinsic* feature of 2D liquid ^{3}He, which is associated with the divergence of the effective mass rather than with disorder. The flattening of the curve $C(T)$ as seen in ^{3}He films is by no means a unique phenomenon. Indeed, as expressed in the Dulong-Petit (DP) law, the specific heat $C(T)$ of solids remains independent of T as long as T exceeds the Debye temperature Ω_D, which is determined by the saturation of the phonon spectrum of the crystal lattice. Normally, the value of Ω_D is sufficiently high so that the DP law belongs to classical physics. However, we will argue that the DP behavior of $C(T)$ can also make its appearance at extremely low temperatures in strongly correlated Fermi systems, with zero sound playing the role of phonons.

To clarify the details of this phenomenon and calculate the specific heat $C(T)$, we evaluate a part F_B of the free energy F associated with the collective spectrum

$\omega(k) = ck$, based on the standard formula

$$F_B = \int_0^\infty \frac{d\omega}{\pi} \frac{1}{e^{\omega/T} - 1} \int \mathrm{Im}\left[\ln D^{-1}(k,\omega)\right] d\upsilon, \tag{9.1}$$

where $D(k,\omega)$ is the boson propagator, and $d\upsilon$ is an element of momentum space. Upon integration by parts this formula is recast to

$$F_B = T \int_0^\infty \frac{d\omega}{\pi} \ln\left(1 - e^{-\omega/T}\right) \int \mathrm{Im}\left(\frac{\partial D^{-1}(k,\omega)/\partial\omega}{D^{-1}(k,\omega)}\right) d\upsilon. \tag{9.2}$$

If the damping of the collective branch is negligible as in the case addressed here, then $D^{-1}(k,\omega) \simeq (\omega - ck)$ and $\partial D^{-1}(k,\omega)/\partial\omega \simeq 1$, while $\mathrm{Im}D^{-1}(k,\omega) \simeq \delta(\omega - ck)$, and we arrive at the textbook formula

$$F_B = T \int \ln\left(1 - e^{-ck/T}\right) \theta(\Omega_0 - ck) d\upsilon, \tag{9.3}$$

where Ω_0 is the characteristic frequency of zero sound. At $T \gg \Omega_0$, the factor $\ln(1 - e^{-\omega/T})$ reduces to $\ln(\omega/T)$, yielding the result

$$F_B(T) \propto T \ln(\Omega_0/T), \tag{9.4}$$

which, upon the double differentiation, leads to the DP law $C(T) = \mathrm{const}$. At first sight, this law has nothing to do with the situation in 2D liquid ^{3}He. Its Fermi energy ϵ_F^0 is around 1 K at densities where the Sommerfeld ratio $C(T)/T$ soars upward as $T \to 0$, while Ω_0 must be lower than $T \simeq 1$ mK. Indeed, in any conventional Fermi liquid, including 3D liquid ^{3}He, there is no collective degree of freedom, whose spectrum is saturated at such low ratios Ω_0/ε_F^0.

This conclusion remains valid *assuming* 2D liquid ^{3}He is an ordinary Fermi liquid. However, as it is seen from Fig. 9.1, if the QCP is reached at $T \to 0$ and at some critical density ρ_∞ where the effective mass $M^*(\rho_\infty)$ diverges, as it does in the present case [6, 8, 9, 12, 14], the situation changes dramatically. This is demonstrated explicitly in the results of standard LFL calculations of the velocity c_t of transverse zero sound, which satisfies [15, 16]

$$\frac{c_t}{2v_F} \ln \frac{c_t + v_F}{c_t - v_F} - 1 = \frac{F_1 - 6}{3F_1(c_t^2/v_F^2 - 1)}, \tag{9.5}$$

where $v_F = p_F/M^*$ is the Fermi velocity and $F_1 = p_F M^* f_1/\pi^2$ is a dimensionless version of the first Landau harmonic f_1 [15, 17]. The divergence of the effective mass M^* at the QCP implies that at the critical density determined by $f_1 p_F M/\pi^2 = 3$ [17], one has

$$c_t^2(\rho_\infty) \simeq \frac{p_F^2}{5M^*(\rho_\infty)M} \to 0, \tag{9.6}$$

whereas the sound velocity c_s remains finite in this limit [15, 16, 18].

We see then that in this case the effective mass M^* diverges, the group velocity c_t vanishes as $\sqrt{1/M^*}$. Flattening of the single-particle spectrum $\epsilon(p)$ prevails as long as $|p - p_F|/p_F < M/M^*$, implying that the transverse mode softens only for rather small wave numbers $k \sim p_F M/M^*$. Unfortunately, the associated numerical prefactor cannot be established, rendering the estimation of $\Omega_0 \sim (p_F^2/M)\sqrt{M/M^*}$ to be uncertain. Nevertheless, one cannot exclude a significant enhancement of the Sommerfeld ratio $C(T)/T$ at $T \simeq 1$ mK due to softening of the transverse zero sound in the precritical density region.

At $T \to 0$ and densities exceeding ρ_∞, the system undergoes a cascade of topological phase transitions in which the Fermi surface acquires additional sheets [19–22]. As indicated in Fig. 9.1, LFL theory continues to hold with quasiparticle momentum distribution $n(p)$ satisfying $n^2 = n$, until a larger critical density ρ_{FC} is reached where a new phase transition, known as FCQPT, takes place [18, 22–26]. Beyond the point of FCQPT, the single-particle spectrum $\varepsilon(p)$ acquires a flat portion. The range L of momentum space adjacent to the Fermi surface, where the FC resides, depends on the difference between the effective coupling constant and its critical value. As will be seen, L is a new dimensional parameter that serves to determine the key quantity Ω_0.

At finite T, the dispersion of the FC spectrum $\varepsilon(p)$, located in the vicinity of the chemical potential, acquires a nonzero value proportional to temperature [18, 22, 27]:

$$\varepsilon(p,T) = T \ln \frac{1 - n_*(p)}{n_*(p)}, \quad p_i < p < p_f, \tag{9.7}$$

where $0 < n_*(p) < 1$ is the FC momentum distribution and p_i and p_f are the lower and upper boundaries of the FC domain in momentum space. Consequently, in the whole FC region, the FC group velocity, given by

$$v(p,T) = \frac{\partial\varepsilon(p)}{\partial p} = -T\frac{\partial n_*(p)/\partial p}{n_*(p)(1 - n_*(p))}, \quad p_i < p < p_f, \tag{9.8}$$

is proportional to T. Significantly, in the density interval $\rho_\infty < \rho < \rho_{FC}$ the formula (9.7) describes correctly the single-particle spectrum $\varepsilon(p,T)$ in case the temperature T exceeds a very low transition temperature [22]. The FC itself contributes a T-independent term to the entropy S. Hence, its contribution to the specific heat $C(T) = TdS/dT$ is zero. Accordingly, we focus on the zero-sound contribution to $C(T)$ in systems having a FC.

Due to the fundamental difference between the FC single-particle spectrum and that of the remainder of the Fermi liquid, a system having FC is, in fact, a two-component system. Remarkably, the FC subsystem possesses its own set of zero-sound modes, whose wave numbers are relatively small, not exceeding $L = (p_f - p_i) > 0$. The mode of prime interest for our analysis is that of transverse zero sound. As may be seen by comparison of expressions (9.6) and (9.8), its velocity c_t *depends on temperature* so as to vanish like $\sqrt{T}$ as $T \to 0$.

To verify the latter property explicitly, we observe first that for systems with a rather small proportion of FC, evaluation of the spectrum of collective excitations may be performed by employing the familiar LFL kinetic equation [15, 28]

$$(\omega - \mathbf{kv})\, \delta n(\mathbf{p}) = -\mathbf{kn} \frac{\partial n(p)}{\partial p} \int \mathscr{F}(\mathbf{p}, \mathbf{p}_1) \delta n(\mathbf{p}_1) d\upsilon_1. \tag{9.9}$$

Focusing on transverse zero sound in 2D liquid ^{3}He, one need only retain the term in the Landau interaction $\mathscr{F}$ proportional to the first harmonic f_1. To proceed further we make the usual identification $(c_t - \cos\theta)\delta n(\mathbf{p}) = (\partial n(p)/\partial p)\, \phi(\mathbf{n})$, where $\cos\theta = \mathbf{kv}/kv$. Equation (9.9) then becomes

$$\phi(\theta) = -f_1 p_F \cos\theta \int \cos\chi \frac{\partial n(p_1)/\partial p_1}{c_t - v(T)\cos\theta_1} \phi(\theta_1) \frac{dp_1 d\theta_1}{(2\pi)^2}, \tag{9.10}$$

where $\cos\chi = \cos\theta\cos\theta_1 + \sin\theta\sin\theta_1$, while $v(T)$ is given by (9.8). The solution describing transverse zero sound is $\phi(\mathbf{n}) \sim \sin\theta\cos\theta$.

We see immediately that $c_t \gg v(T) \sim T$; therefore the transverse sound in question does not suffer Landau damping. In this situation, we are led to the simple result

$$c_t^2 = -\frac{p_F}{5M} \int \frac{\partial n(p)}{\partial p} v(p, T) dp \tag{9.11}$$

upon keeping just the leading relevant term $v(T)\cos\theta/c_t^2$ of the expansion of $(c_t - v(T)\cos\theta)^{-1}$ and executing straightforward manipulations. Factoring out an average value of the group velocity $v(p, T) \propto T/p_F$, we arrive at the stated behavior

$$c_t(k) \simeq \sqrt{\frac{T}{M}} \tag{9.12}$$

for wave numbers k not exceeding the FC range L. Transverse sound can of course propagate in the other, non-condensed subsystem of 2D liquid ^{3}He consisting of quasiparticles with normal dispersion [15, 16, 28]. However, its group velocity is T-independent, so the corresponding contribution to the free energy is irrelevant.

As noted above, the characteristic wave number of the soft transverse zero-sound mode is given by the FC range $L(\rho) = p_f - p_i$, treated here as an input parameter.

The key quantity Ω_0 is therefore estimated as $\Omega_0 \simeq k_{\max} c_t$, where $k_{\max}$ is the maximum value of the zero sound momentum at which the zero sound still exists. In our case the zero sound is associated directly with the FC. Hence, $k_{\max} \simeq \sqrt{Lp_F}$ and we have

$$\Omega_0 \simeq k_{\max} c_t \simeq \sqrt{\frac{TLp_F}{M}}. \tag{9.13}$$

As long as the inequality $Lp_F/M < T$ holds (or, equivalently, the relation $T/\epsilon_F^0 > L/p_F$ is valid), the ratio Ω_0/T is small, and we are led to the DP result $C(T) = \text{const}$. Then, in spite of the low temperature, C behaves as if the system were situated in the classical limit rather than at the QCP. Such a behavior is ensured by the fact that the system contains a macroscopic subsystem with heavy quasiparticles. As the temperature ultimately goes down to zero at the fixed density ρ, the inequality $Lp_F/M < T$ eventually fails, the quantum regime is restored and the dominant contribution to C comes from the "normal" fermions. In other words, there exists an extremely low temperature T_0 below which the usual LFL behavior of zero sound is recovered.

Interestingly, the value of the constant term in $C(T)$ can be evaluated in closed form in terms of the FC range L. Upon inserting $\omega_t(k) = c_t k$ into (9.3) and integrating, the T-independent term in the specific heat is found to be

$$\frac{C}{N} \simeq \frac{Lp_F}{8\pi\rho}, \tag{9.14}$$

where N is the number of atoms in a film. The FC range parameter L also enters the result obtained for the spin susceptibility χ, that is derived similarly to (9.14). The FC component of χ is given by [22, 29]

$$\chi_*(T) \simeq \chi_C(T)\frac{L}{p_F}, \tag{9.15}$$

where $\chi_C(T) = \mu_B^2\rho/T$.

The results (9.14) and (9.15) jointly establish an unambiguous relation within our model between the T-independent term in the specific heat $C(T)$ and the Curie component of the spin susceptibility $\chi(T)$ that has also been observed experimentally [8, 9]. This relation can be tested using existing experimental data [6]. The T-independent specific heat C/N exists in the density region around $\rho = 9.5\,\text{nm}^{-2}$. Being referred to one particle, it is readily evaluated from $\beta \simeq 0.25\,\text{mJ/K}$. One finds $C/N \simeq 0.01$, yielding $L/p_F \simeq 0.05$. On the other hand, the data for the spin susceptibility given in Fig. 2(B) of [6] supports a Curie-like component at $\rho = 9.25\,\text{nm}^{-2}$. The value of the corresponding numerical factor extracted from the data, which according to (9.15) is to be identified with the ratio L/p_F, is approximately 0.07. Given the uncertainties involved, our model is consistent with the experimental data reported in [6].

Thus, in two-dimensional liquid ^{3}He and HF metals, which are located in the vicinity of the quantum critical point associated with a divergent quasiparticle effective mass, the group velocity depends strongly on temperature, and vanishes at diminishing temperatures. The contribution to the specific heat coming from the boson part of the free energy follows the Dulong-Petit law. Accordingly, the specific heat becomes independent of temperature at some characteristic value of it. At sufficiently lower temperature the usual LFL behavior of zero sound is recovered. The other properties of ^{3}He at quantum criticality are considered in Sect. 18.4. We note that the heat capacity C of the HF metal YbRh$_2$Si$_2$ contains the temperature independent term C_0 as well [30].

9.2 Transport Properties Related to the Quasi-classical Behavior

We show that near FCQPT the quasi-classical approach remains applicable to the description of the resistivity ρ of strongly correlated metals due to the presence of a transverse zero-sound collective mode, reminiscent of the phonon mode in solids. These phonon-like soft and weakly damped branches of the transverse zero-sound mode are found to have extremely low effective Debye temperatures. Their contributions to the collision integral are shown to drive electron transport in the vicinity of the critical point toward a classical regime. A T-linear resistivity occurs due to a mechanism analogous to that affecting the resistivity in conventional metals at room temperature, giving rise to a quasi-classical regime of transport at extremely low temperatures in HF metals.

After a decade of comprehensive studies [31, 32], the prevalence of non-Fermi-liquid (NFL) behavior in strongly correlated Fermi systems is no longer a big surprise. However, various features of NFL phenomena still await satisfactory explanation, especially the puzzling observations pointing to characteristic quasi-classical behavior in a quantum-critical regime. For example, at extremely low temperatures around 1 mK, the results of experimental measurements of the specific heat of two-dimensional (2D) ^{3}He, as observed in dense ^{3}He films are described by the classical formula $C(T) = \beta + \gamma T$, where β and γ are constants, see Sect. 10.2. Also in contrast to LFL theory, it is perceived that the low-temperature resistivity $\rho(T)$ of many high-T_c compounds and certain HF metals vary linearly with T [33–35]. Hence these systems behave as if a major contribution to the collision term comes from the electron-phonon interaction, in spite of the fact that the phonon Debye temperature T_D exceeds measurement temperatures by a factor $10^2 - 10^3$.

In Sect. 9.1, we have attributed the presence of the classical term β in the specific heat $C(T)$ of 2D liquid ^{3}He to softening of the transverse zero-sound mode (TZSM), occurring near quantum critical point [6] (QCP) where the density of states $N(0)$, proportional to the effective mass M^*, diverges. Here we shall address the impact of the TZSM on transport properties in the QCP regime. The TZSM exists only in those correlated Fermi systems where the effective mass M^* exceeds the bare mass

M by a factor more than 3. This requirement is always met while approaching the QCP. In conventional Fermi liquids, the Fermi surface consists of a single sheet, so the TZSM has a single branch with velocity c_t exceeding the Fermi velocity v_F. Consequently, emission and absorption of sound quanta by electrons is forbidden, and the role of the TZSM in kinetics is of little interest. However, in heavy-fermion metals, it is usual for several bands to cross the Fermi surface simultaneously, thereby generating several zero-sound branches. For all branches but one the sound velocities are less than the largest Fermi velocity. Hence the aforementioned ban is lifted, and these branches of the TZSM spectrum experience damping, in a situation similar to that for zero-spin sound. In the latter instance, Landau damping is so strong that the mode cannot propagate through the liquid [15, 36]. It will be seen, however, that this is not the case for TZSM damping due to this mode softening close to the QCP. Due to the softening effect, the contribution of the damped TZSM to the collision integral has the same form as the electron-phonon interaction at room temperature. On the other hand, we will also find that in heavy-fermion metals, similar to the case of liquid ^{3}He films, softening of the TZSM acts to lower the characteristic temperature Ω_t that plays the role of the Debye temperature, setting the stage for the existence of a quasi-classical transport regime at extremely low temperatures.

In the canonical picture of quantum phase transitions, the QCP has been identified with an end point of the line T_N of a second-order phase transition, associated with violation of some Pomeranchuk stability condition. In its turn this violation is associated with divergence of the energy derivative $\partial\Sigma(p,\varepsilon)/\partial\varepsilon$ of the self-energy and consequent vanishing of the quasiparticle weight $z = (1 - \partial\Sigma(p,\varepsilon)/\partial\varepsilon)^{-1}$ in single-particle states at the Fermi surface, thus triggering [31, 32, 37] divergence of the effective mass M^* defined by $M/M^* = z(1 + \left(\partial\Sigma(\mathbf{p},\varepsilon)/\partial\epsilon^0_p\right)|_{p=p_F}$.

A number of important experimental studies, that were performed recently, fail to support the canonical view of the QCP. In 2D liquid ^{3}He, experimental data [6, 12] have not identified any phase transition that can be associated with the point of the divergence of the effective mass. It has been acknowledged [34, 38] that a similar situation also prevails for the QCPs of heavy-fermion metals. In essence, the point where the density of states diverges is *separated by an intervening NFL phase* from points, where lines of some second-order phase transition terminate. Furthermore, these transitions possess unusual properties such as hidden order parameters. Therefore within the standard collective scenario they can hardly qualify as triggers of the observed rearrangements.

We are, therefore, compelled to interchange the reason and the consequence in connection to the canonical scenario [39]. Following Sect. 9.1, we attribute the QCP to vanishing of the Fermi velocity v_F at a critical density ρ_∞, which occurs if $1 + \left(\partial\Sigma(\mathbf{p},\varepsilon)/\partial\epsilon^0_p\right)|_{p=p_F} = 0$. Accordingly, in this scenario for the QCP, it is the *momentum-dependent part* of the mass operator that plays the decisive role.

It is commonly accepted in the theory devoted to the QCP physics that switching on the interaction between particles never produces a significant momentum dependence in the effective interaction function f, and hence the option we propose and develop is irrelevant. However, this assertion cannot withstand scrutiny. The natural measure of the strength of momentum-dependent forces in the medium is provided by the dimensionless first harmonic $F_1 = f_1 p_F M^*/\pi^2$ of the Landau interaction function $f(\mathbf{p}_1, \mathbf{p}_2)$. In a system, such as 3D liquid ^{3}He, where the correlations are of moderate strength, the result $F_1 \geq 6.25$ for this measure extracted from specific-heat data is already rather large. The data on 2D liquid ^{3}He are yet more damaging to the claim of minimal momentum dependence, since the effective mass is found to *diverge* in dense films [6, 8, 12]. In the case of QCP phenomena occurring in strongly correlated systems of *ionic* crystals, it should be borne in mind that the electron effective mass is greatly enhanced due to electron-phonon interactions that subserve polaron effects [40, 41].

The change in sign of v_F at the QCP results not only in a divergent density of states, but also in a *rearrangement of the Landau state* beyond the QCP. As a rule, however, such a rearrangement already occurs *before* the system reaches QCP. This may be understood from simple arguments based on the Taylor expansion of the group velocity $v(p) = \partial\varepsilon(p)/\partial p$, which has the form

$$v(p) = v_F(\rho) + v_1(\rho)\frac{p - p_F}{p_F} + \frac{1}{2}v_2\frac{(p - p_F)^2}{p_F^2} \tag{9.16}$$

in the vicinity of the QCP. We assert that the last coefficient v_2 is positive, to ensure that the spectrum

$$\epsilon(p) = v_F(\rho)(p - p_F) + \frac{1}{2p_F}v_1(\rho)(p - p_F)^2 + \frac{1}{6p_F^2}v_2(p - p_F)^3 \tag{9.17}$$

derived from (9.16) exhibits proper behavior even far from the Fermi surface.

By its definition, the QCP is situated at a density ρ_∞ where $v_F(\rho)$ vanishes. The QCP must in fact correspond to an extremum of the function $v(p, \rho_\infty)$, which vanishes for the first time at $p = p_F$. Thus, the simultaneous vanishing of the coefficient $v_1(\rho_\infty) = (dv(p, \rho_\infty)/dp)|_{p=p_F}$ of the second term in the Taylor series is *crucial* to the QCP occurrence. Generally, v_1 does not meet this additional requirement. However, in relevant cases its finite value remains extremely small, making it possible to tune the QCP by imposing an external magnetic field.

When $v_1 \neq 0$ in (9.7), this equation unavoidably acquires two additional *real* roots at a critical density ρ_t where $v_F(\rho_t) = 3v_1^2/(8v_2)$, namely

$$p_{1,2} - p_F = -p_F\frac{3v_1}{2v_2}\left(1 \pm \sqrt{1 - \frac{8v_F(\rho)v_2}{3v_1^2}}\right). \tag{9.18}$$

Clearly, this transition, identified as a topological phase transition (TPT), see Chap. 4, takes place *already* on the disordered side of the QCP regime, where $v_F(\rho)$ is still positive. Accordingly, as it is discussed in Chap. 4, a new hole pocket opens and the Fermi surface gains two additional sheets, the new $T = 0$ quasiparticle momentum distribution being given by $n(p) = 1$ for $p < p_1$ and $p_2 < p < p_F$, and zero elsewhere. The emergence of new small pockets of the Fermi surface is an integral feature of the QCP phenomenon, irrespectively to whether the strongly correlated Fermi system is 2D liquid ^{3}He, a high-T_c superconductor, or a heavy-fermion metal.

At the TPT point ρ_t, the density of states, given by

$$N(T) = \int \frac{\partial n(\mathbf{p}, T)}{\partial \epsilon(\mathbf{p})} dv \tag{9.19}$$

with dv denoting an element of momentum space, is also divergent. Inserting the spectrum (9.17), straightforward calculation yields $N(T \to 0) \propto T^{-1/2}$, in contrast to the behavior $N(T \to 0, \rho_\infty) \propto T^{-2/3}$ obtained in the case where $v_1(\rho_\infty) = 0$.

Having tracked the initial evolution of the Fermi surface topology in the QCP region, our analysis turns next to the salient features of the TZSM spectrum in systems with a multi-connected (i.e. multi-sheet) Fermi surface. We first examine how the TZSM softens in 3D systems with a singly-connected Fermi surface, where the relation has the well-known form [15]

$$1 = \frac{F_1}{6}\left[1 - 3(s^2 - 1)\left(\frac{s}{2}\ln\frac{s+1}{s-1} - 1\right)\right] \tag{9.20}$$

with $s = c_t/v_F$ and $F_1 = f_1 p_F M^*/\pi^2$. The TZSM is seen to propagate only if $F_1 > 6$, i.e. $M^* > 3M$. Near the QCP where $M^*(\rho) \to \infty$, one has $v_F/c_t \to 0$, and (9.20) simplifies to

$$1 = \frac{F_1}{15}\frac{v_F^2}{c_t^2}, \tag{9.21}$$

which implies

$$c_t(\rho \to \rho_\infty) \to \sqrt{\frac{p_F v_F(\rho)}{M}} \propto \frac{p_F}{M}\sqrt{\frac{M}{M^*(\rho)}} \to 0, \tag{9.22}$$

an analogous formula being obtained for a 2D system.

To facilitate analysis of TZSM damping in the systems with *multi-connected* Fermi surface, we restrict consideration to the case of two electron bands. The TPT is assumed to occur at one of the bands, so that its Fermi velocity, denoted again by v_F, tends to zero, while the Fermi velocity v_o of the other band remains unchanged through the critical density region. The model dispersion relation for the complex sound velocity $c = c_R + ic_I$ becomes

$$1 = \frac{F_1}{6}\left[1 - 3\left(\frac{c_t^2}{v_F^2} - 1\right)\left(\frac{c_t}{2v_F}\ln\frac{c_t + v_F}{c_t - v_F} - 1\right)\right]$$
$$+ \frac{F_1}{6}\frac{v_F}{v_o}\left[1 - 3\left(\frac{c_t^2}{v_o^2} - 1\right)\left(\frac{c_t}{2v_o}\ln\frac{c_t + v_o}{c_t - v_o} - 1\right)\right]. \tag{9.23}$$

It can easily be verified that the contribution of the second term to the real part of the right-hand side of (9.23) is small compared to that of the first term, since $v_F/v_o \to 0$ toward the QCP. On the other hand, noting that

$$\ln\left[(c_R + ic_I + v_o)/(c_R + ic_I - v_o)\right] \simeq -i\pi,$$

the corresponding contribution $i\pi F_1 v_F c_R/(4v_o^2)$ to the imaginary part of the right-hand side cannot be ignored, else $c_I = 0$. By this reasoning, (9.23) assumes the simplified form

$$1 = \frac{F_1}{15}\frac{v_F^2}{(c_R + ic_I)^2} - i\frac{\pi}{4v_o^2}F_1 v_F c_R \tag{9.24}$$

analogous to (9.21). Its solution obeys

$$c_R \propto \sqrt{\frac{M}{M^*(\rho)}}, \quad c_I \propto \frac{M}{M^*(\rho)}. \tag{9.25}$$

Importantly, we see then that the ratio $c_I/c_R \propto \sqrt{M/M^*(\rho)}$ is *suppressed* in the QCP regime, which allows us to analyze the contribution of the TZSM to the collision term entering the resistivity along the same lines as in the familiar case of the electron-phonon interaction. By contrast, the group velocities of the damped branches of *longitudinal* zero sound are found to be insensitive to variation of the effective mass in the QCP region [15, 36]. No quenching by a small parameter M/M^* arises, so these modes cannot propagate in the Fermi liquid.

It is now clear that toward the QCP, the effective Debye temperature $\Omega_t = \omega(k_{\max}) = c_R k_{\max}$ *goes down to zero*, independently of the $k_{\max}$ value, characterizing the cutoff of the TZSM spectrum. Thus, the necessary condition $\Omega_t < T$ for quasi-classical behavior emergence is always met. However, another condition must also be satisfied, if there a well-pronounced classical domain at extremely low temperature exist. Take into account that the boson contribution

$$F_B = T\int \ln\left(1 - e^{-ck/T}\right)\theta(k - k_{\max})d\upsilon \tag{9.26}$$

to the free energy is proportional to some power of $k_{\max}$, depending on the dimensionality of the problem. The same is true for the corresponding contributions to kinetic phenomena. Therefore, the extra condition needed is that $k_{\max}$ should not be too small. We identify $k_{\max}$ with the new characteristic momentum arising beyond the point of the TPT, namely with the distance $d = p_2 - p_1$ between the new sheets of the Fermi surface. Indeed, for momenta p situated at distances from the Fermi surface significantly bigger than d, the single-particle spectrum $\epsilon(p)$ is no longer flat. The collective spectrum $\omega(k)$ determined from the corresponding Landau kinetic equation is no longer soft, and consequently the imaginary part c_I of c becomes of the same order as c_R, preventing propagation of the TZSM.

This scenario is illustrated by the key property of resistivity in electron systems of solids. The kernel of the electron-TZSM collision integral underlying the resistivity $\rho(T)$ contains terms $n_o(\mathbf{p}+\mathbf{k})(1-n_o(\mathbf{p}))N(\mathbf{k}) - n_o(\mathbf{p})(1-n_o(\mathbf{p}+\mathbf{k}))(1+N(\mathbf{k}))$ and $n_o(\mathbf{p}+\mathbf{k})(1-n_o(\mathbf{p}))(1+N(\mathbf{k})) - n_o(\mathbf{p})(1-n_o(\mathbf{p}+\mathbf{k}))N(\mathbf{k})$, in which $N(\mathbf{k})$ denotes a nonequilibrium TZSM momentum distribution and $n_o(\mathbf{p})$, a nonequilibrium electron momentum distribution of the band that can absorb and emit the TZSM. The explicit linearized electron-phonon-like form of the corresponding component of the collision integral is [42, 43]

$$I_{e,ph} \propto \int w(\mathbf{p},\mathbf{k})\omega(k)\frac{\partial N_0(\omega)}{\partial \omega}(\delta n_i - \delta n_f)\delta(\epsilon_i - \epsilon_f)d\upsilon. \qquad (9.27)$$

In this expression, w is the collision probability, $N_0(\omega) = [\exp(\omega(\mathbf{k})/T) - 1]^{-1}$ is the equilibrium TZSM momentum distribution, and $\delta n_{i,f}$ stands for the deviations of the real momentum distributions in the electron band labeled o to distinguish it from its nonequilibrium counterpart, with $n_i = n(\mathbf{p})$ and $n_f = n(\mathbf{p}+\mathbf{k})$. In the classical case of the electron-phonon interaction, at $T_D < T$ one has $\partial N_0(\omega)/\partial\omega \propto -T/\omega^2$ while all the other factors are T-independent, resulting [42, 43] in linear variation of the resistivity $\rho(T)$ with T.

Based on the analogy we have established between the roles of phonons and the TZSM, the resistivity of the strongly correlated electron system must obey the FL law $\rho(T) \propto T^2$ only at $T < \Omega_t$. In the opposite case $\Omega_t < T$, the resistivity exhibits a *linear* dependence on T. Imposition of a magnetic field cannot kill the soft mode of transverse zero sound as long as the flattening of the single-particle spectrum responsible for strong depression of the effective Debye temperature Ω_t persists.

These results and conclusions are in qualitative agreement with experimental data [34] on the low-temperature resistivity of the doped HF metal $\mathrm{YbRh_2(Si_{0.95}Ge_{0.05})_2}$. The data indicate that the linear-in-T dependence of the resistivity is robust, down to temperatures as low as 20 mK. Remarkably, the linearity of $\rho(T)$ continues to hold in external magnetic fields up to $B \simeq 2T$, far in excess of the critical value $B_c \simeq 0.3T$, at which this compound undergoes some phase transition with a hidden order parameter [34]. A linear T dependence of $\rho(T)$ is present as well in the Hertz-Millis spin-density-wave (SDW) scenario for the QCP in 2D electron systems [44, 45]. However, critical spin fluctuations die out at $B > B_c$, since the SDW transition is suppressed. Thus, the observed behavior of $\rho(T)$ contradicts the SDW scenario. As to our scenario, it is in fact compatible with the observed behavior, since the TZSM spectrum is less sensitive than the structure of critical spin fluctuations to the magnitude of the magnetic field. A linear T dependence of $\rho(T)$ can also emerge, if the light carriers are scattered by heavy bipolarons [40, 46]. However, there is no evidence for the presence of these quasiparticles in heavy-fermion metals.

Let us now briefly turn to the analysis of the soft TZSM contribution to the thermopower. One may recollect that in the classical situation, the phonon-drag thermopower $S_d(T)$ associated with nonequilibrium phonons is known [42, 43, 47] to account for a substantial part of the Seebeck coefficient $S(T)$. The same is true for the class of quantum-critical systems considered here, except that the domain, where the drag term $S_d(T)$ contributes appreciably, extends down to extremely low temperatures. Significantly, at $T \to 0$ the drag contribution increases as T^3, whereas at $T > \Omega_t$ it falls off as T^{-1}, producing a bell-like shape [42, 43] of $S_d(T)$ with a sharp maximum at $T \simeq \Omega_t$. Since the remaining contributions to S are rather smooth, this remarkable feature of S_d appears to be responsible for the change of sign of the full Seebeck coefficient $S(T)$ at extremely low T observed experimentally [48] in the heavy-fermion metal $\mathrm{YbRh_2Si_2}$, as well as the irregular behavior of $S(T \to 0)$ found in several heavy-fermion compounds [49]. The TZSM scenario proposed here predicts that the Seebeck coefficient in $\mathrm{YbRh_2(Si_{0.95}Ge_{0.05})_2}$ exhibits the same anomalous behavior at magnetic fields substantially exceeding a corresponding critical value B_c.

The conditions promoting the formation of soft damped collective modes play the same role in kinetic phenomena as phonons. Thus, such a damped soft branch belonging to the transverse zero-sound mode emerges when several bands cross the Fermi surface simultaneously, with one of the bands subject to a divergence of the effective mass of carriers. As a result, there are prerequisites for lowering the corresponding Debye temperature Ω_t, which makes the inequality $\Omega_t < T$ to be met near the quantum critical point, where the quasi-classical regime sets in at extremely low temperatures. As we shall see in the next Sect. 9.3, such a behavior illuminates unexpectedly close relationships existing between HF compounds and ordinary metals [50].

9.3 Quasi-classical Physics and T-Linear Resistivity

As it was demonstrated above, the Debye temperature T_D can be extremely low in the case of HF compounds. As a result, at $T > T_D$ the resistivity $\rho(T)$ varies linearly with T, since the mechanism, forming the dependence $\rho(T)$, is the same as the electron-phonon mechanism that prevails at high temperatures in ordinary metals. Thus, in the region of T-linear resistivity, the electron-phonon scattering yields almost material-independence of the lifetime τ_q of quasiparticles that is expressed as the ratio of Planck $\hbar$ and Boltzmann constants k_B, $T\tau_q \sim \hbar/k_B$. As an example, we analyze the resistivity of the HF metal $\mathrm{Sr_3Ru_2O_7}$.

Discoveries of surprising universality in the properties of both strongly correlated and ordinary metals provide unique opportunities to check and expand our understanding of quantum criticality in strongly correlated compounds. When exploring at different temperatures T the linear in temperature resistivity of these utterly different metals, an universality of their fundamental physical properties has been revealed [51]. On the one hand, at low T the linear T-resistivity

$$\rho(T) = \rho_0 + AT, \tag{9.28}$$

has been observed in many strongly correlated compounds like high-temperature superconductors and HF metals located near their QCP, and therefore exhibiting quantum criticality. Here ρ_0 is the residual resistivity and A is a T-independent coefficient. Explanations based on quantum criticality for the T-linear resistivity have been given in the literature, see e.g., [52–55] and references therein. On the other hand, at room temperatures the T-linear resistivity is exhibited by conventional metals such as Al, Ag or Cu. In case of a simple metal with a single Fermi surface pocket the resistivity is expressed as $e^2 n\rho \simeq p_F/(\tau_q v_F)$ [28], where e is the electronic charge, τ_q is the quasiparticles lifetime, n is the carrier concentration, and p_F and v_F are the Fermi momentum and the Fermi velocity, respectively. Writing the lifetime (or inverse scattering rate) τ_q of quasiparticles in the form [56, 57]

$$\frac{\hbar}{\tau_q} \simeq a_1 + \frac{k_B T}{a_2}, \tag{9.29}$$

we obtain

$$\frac{e^2 n\hbar}{p_F k_B}\frac{\partial\rho}{\partial T} = \frac{1}{a_2 v_F}, \tag{9.30}$$

where $\hbar = h/2\pi$ is Planck's constant, k_B is Boltzmann's constant, a_1 and a_2 are T-independent parameters. Figure 9.2 reports experimental measurements of $e^2 n\hbar/p_F k_B \partial\rho/\partial T$, that it is the left hand side of (9.30), versus $1/v_F$ [51]. One can see that the scattering rate per Kelvin is approximately constant across a wide range of materials [51], and (9.30) is in good agreement with the experimental facts. It is worth noting that elemental metals like copper, silver, aluminum, etc. are not strongly correlated. In contrast, as we have seen above, due to the formation of flat bands the strongly correlated metals exhibit the classical properties of elemental ones, for the strongly correlated metals demonstrate the quasi-classical behavior at low temperatures.

A challenging point for a theory is that experimental data confirm (9.30) for both strongly correlated and normal metals under the condition that latter demonstrate linear T-dependence of their resistivity [51]. Moreover, as it is seen from Fig. 9.2, the analysis of the data from the literature for the majority of compounds with the linear dependence of $\rho(T)$ shows that the coefficient a_2 is always close to unity, $0.7 \leq a_2 \leq 2.7$, despite huge distinction in the absolute value of ρ, T and Fermi velocities v_F, that are varying by two orders of magnitude [51]. As a result, it follows from (9.29) that the T-linear scattering rate is of universal form, $1/(\tau_q T) \sim k_B/\hbar$, valid for different systems displaying the T-linear dependence. Indeed, on the one

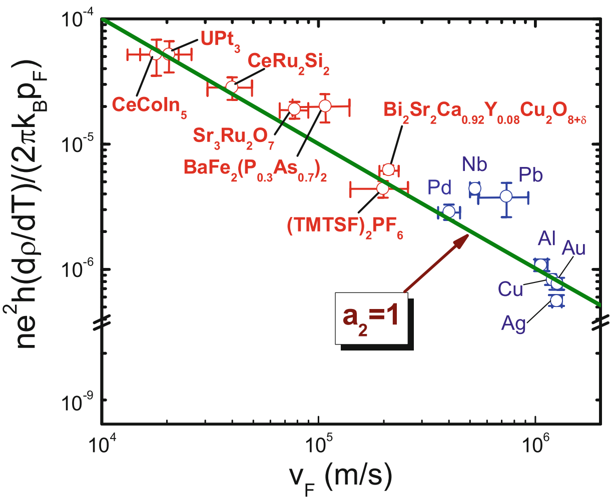

Fig. 9.2 Experimental measurements of $e^2n\hbar/p_Fk_B\partial\rho/\partial T$ (the *left hand side* of (9.30)) versus $1/v_F$ [51]. Ordinary metals are shown with *blue symbols*, strongly correlated metals are depicted with *red ones*. The line shown by the *arrow* represents the case $a_2 = 1$

hand this dependence is demonstrated by ordinary metals at $T \geq T_D$, where it is due to electron–phonon mechanism. On the other hand, it occurs in strongly correlated metals which are assumed to be fundamentally different from the ordinary ones. There, the linear dependence at their quantum criticality and temperatures of a few Kelvin is assumed to come from excitations of electronic origin rather than from phonons [51]. We note that in some of the cuprates the scattering rate has a momentum and doping dependence omitted in (9.30) [58–60]. Nonetheless, the fundamental picture outlined by (9.30) is strongly supported by measurements of the resistivity on $Sr_3Ru_2O_7$ for a wide range of temperatures: At $T \geq 100$ K, the resistivity becomes again T-linear at all applied magnetic fields, as it does at low temperatures and at the critical field $B_c \simeq 7.9$ T, but with the coefficient A lower than that seen at low temperatures. [51] Thus, the same strongly correlated compound exhibits the same behavior of the resistivity at both quantum critical regime and high temperature one, allowing us to expect that the same physics governs the T-linear resistivity in spite of possible peculiarities of some compounds.

To develop explanations of the constancy of the T-linear scattering rate $1/(\tau_qT)$, it is necessary to recollect the nature and consequences of flattening of single-particle excitation spectra $\varepsilon(\mathbf{p})$ ("flat bands") in strongly correlated Fermi systems [18, 23, 29, 61] (see [27, 62, 63] for recent reviews). At $T = 0$, the ground state of a system with a flat band is degenerate, and the occupation numbers $n_0(\mathbf{p})$ of single-particle states belonging to the flat band are continuous functions of momentum $\mathbf{p}$, in contrast to discrete standard LFL values 0 and 1, as it is seen from Fig. 9.3. Such behavior of $n_0(\mathbf{p})$ leads to a temperature-independent entropy term

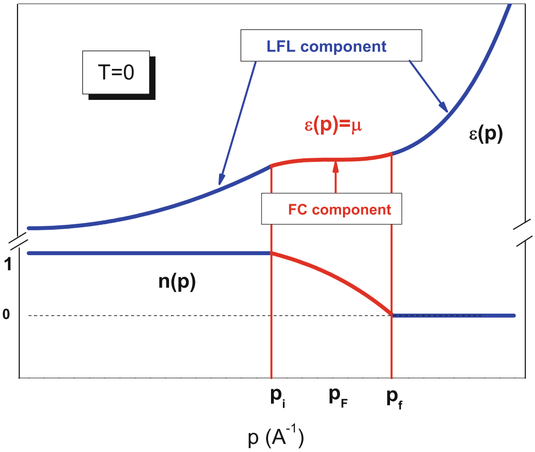

Fig. 9.3 Schematic plot of two-component electron liquid at $T = 0$ with FC. Due to the presence of FC, the system is separated into two components. The first component is a normal liquid with the quasiparticle distribution function $n_0(p < p_i) = 1$, and $n_0(p > p_f) = 0$. The second one is FC with $0 < n_0(p_i < p < p_f) < 1$ and the single-particle spectrum $\varepsilon(p_i < p < p_f) = \mu$. The Fermi momentum p_F satisfies the condition $p_i < p_F < p_f$

$$S_0 = -\sum_{\mathbf{p}} [n_0(\mathbf{p}) \ln n_0(\mathbf{p}) + (1 - n_0(\mathbf{p})) \ln(1 - n_0(\mathbf{p}))]. \tag{9.31}$$

Unlike the corresponding LFL entropy, which vanishes linearly as $T \to 0$, the term S_0 produces the NFL behavior that includes T-independent thermal expansion coefficient [27, 57, 64, 65]. T-independent behavior is observed in measurements on $CeCoIn_5$ [66–68] and $YbRh_2(Si_{0.95}Ge_{0.05})_2$ [69], while very recent measurements on $Sr_3Ru_2O_7$ indicate the same behavior [70, 71]. In the theory of fermion condensation, the degeneracy of the NFL ground state is removed at any finite temperature, with the flat band acquiring a small dispersion [18, 27]

$$\varepsilon(\mathbf{p}) = \mu + T \ln \frac{1 - n_0(\mathbf{p})}{n_0(\mathbf{p})} \tag{9.32}$$

proportional to T with μ being the chemical potential. The occupation numbers n_0 of FC remain unchanged at relatively low temperatures and, accordingly, so does the entropy S_0. Due to the fundamental difference between the FC single-particle spectrum and that of the remainder of the Fermi liquid, a system having FC is, in fact, a two-component system. The range L of momentum space adjacent to the Fermi surface where FC resides is given by $L \simeq (p_f - p_i)$, as seen from Fig. 9.3.

In strongly correlated metals at high temperatures, a light electronic band coexists with f or d-electron narrow bands, placed below the Fermi surface. At lower temperatures, when the quantum criticality is formed, a hybridization between this light band and f or d-electron bands results in its splitting into new flat bands, while some of the bands remain light, thus representing LFL states [72].

A flat band can also be formed by a van Hove singularity (vHs) [73–80]. We assume that at least one of these flat bands crosses the Fermi level and represents the FC subsystem that is shown in Fig. 9.3. Remarkably, the FC subsystem possesses its own set of zero-sound modes. The mode of interest for our analysis is that of transverse zero sound with its T-dependent sound velocity $c_t \simeq \sqrt{T/M}$ and the Debye temperature [81]

$$T_D \simeq c_t k_{max} \simeq \beta\sqrt{TT_F}. \tag{9.33}$$

Here, β is a numeric factor, M is the effective mass of electron generated by vHs or by the hybridization, T_F is the Fermi temperature, while M^* is the effective mass formed finally by some interaction, e.g., by the Coulomb interaction, that leads to flat bands [72]. The characteristic wave number k_{max} of the soft transverse zero-sound mode is estimated as $k_{max} \sim p_F$, since we assume that the main contribution forming the flat band comes from vHs or from the hybridization. Note that the numerical factor β cannot be established and is considered as a fitting parameter, rendering T_D value (9.33) to be uncertain. Estimating $T_F \sim 10\,\mathrm{K}$ and taking $\beta \sim 0.3$, and noting that the quasi-classical regime takes place at $T > T_D \simeq \beta\sqrt{TT_F}$, we obtain that $T_D \sim 1$ K and expect that strongly correlated Fermi systems can exhibit a quasi-classical behavior at their quantum criticality [39, 81] with the low-temperature coefficient A entering (9.28) $A = A_{LT}$. In case of HF metals with few bands crossing Fermi level and populated by LFL and HF quasiparticles, the transverse zero sound makes the resistivity possess the T-linear dependence at the quantum criticality, as the normal sound (or phonons) does in the case of ordinary metals [39]. It is quite natural to assume that the scattering of sound in these materials is almost material-independent, so that electron-phonon processes both in the low temperature limit at the quantum criticality and in the high temperature limit of ordinary metals have the same T-linear scattering rate that can be expressed as

$$\frac{1}{\tau_q T} \sim \frac{k_B}{\hbar}. \tag{9.34}$$

Thus, in case of the same material the coefficient $A = A_{HT}$, defining the classical linear T-dependence generated by the common sound (or phonons) at high temperatures, coincides with that of low-temperature coefficient A_{LT}, $A_{HT} \simeq A_{LT}$. As we shall see, this observation is in accordance with measurements on $\mathrm{Sr_3Ru_2O_7}$ [51]. It is worth noting that the transverse zero sound contribution to the heat capacity C follows the Dulong-Petit law, making C possess a T-independent term C_0 at $T \gtrsim T_D$, as it does in case of ordinary metals [81]. It is obvious that the zero sound contributes to the heat transport as the normal sound does in case of ordinary metals and its presence can violate the Wiedemann-Franz law. A detailed consideration of the emergence of transfers zero sound and its properties is presented in Sects. 9.1 and 9.2.

There is another mechanism contributing to the T-linear dependence at the quantum criticality that we name the second mechanism, in contrast to the first one described above and related to the transverse zero sound. We turn to consideration of the next contribution to the resistivity ρ in the range of quantum criticality, at which the dispersion of the flat band is governed by (9.32). It follows from (9.32) that the temperature dependence of $M^*(T)$ of the FC quasiparticles is given by

$$M^*(T) \sim \frac{\eta p_F^2}{4T}, \tag{9.35}$$

where $\eta = L/p_F$ [27, 62, 63]. Thus, the effective mass of FC quasiparticles diverges at low temperatures, while their group velocity, and hence their current, vanishes and the main contribution to the resistivity is provided by light quasiparticles bands. Nonetheless, the FC quasiparticles still play a key role in determining the behavior of both the T-dependent resistivity and ρ_0. The resistivity has the conventional dependence [28]

$$\rho(T) \propto M_L^* \gamma \tag{9.36}$$

on the effective mass and the damping of the normal quasiparticles. Based on the fact that all the quasiparticles have the same lifetime, one can show that in playing its key role, the FC makes all quasiparticles belonging to light and flat bands to have the same unique width γ and lifetime τ_q given by (9.29) [57, 82]. As a result, the first term a_0 on the right hand side of (9.29) forms an irregular residual resistivity ρ_0^c, while the second one forms the T-dependent part of the resistivity. The term “residual resistivity” ordinarily refers to impurity scattering. In the present case, the irregular residual resistivity ρ_0^c is, instead, determined by the onset of a flat band, and has no relation to scattering of quasiparticles by impurities, for details see Sect. 11.5. The two mechanisms described above contribute to the coefficient A on the right hand side of (9.28) and it can be represented as $A \simeq A_{LT} + A_{FC}$, where A_{LT} and A_{FC} are formed by the zero sound and by FC, respectively. Coefficients A_{LT} and A_{FC} can be identified and distinguished experimentally, for A_{LT} is accompanied by the temperature independent heat capacity C_0, while A_{FC} is escorted by the emergence of ρ_0^c. We note that the influence of FC on the residual resistivity is discussed in Chap. 10, and while for the case of $Sr_3Ru_2O_7$ in Chap. 11.

A few comments are in order here. As we have seen above, the presence of flat bands generates the characteristic behavior of the resistivity. Besides, it has a strong influence on the systems properties by creating the term S_0, making the spin susceptibility of these systems exhibit the Curie-Weiss law, as it is observed in the HF metal $CeCoIn_5$ [29]. The term S_0 serves as a stimulator of phase transitions that could lift the degeneracy and make S_0 vanish in accordance with the Nernst theorem. As we shall see, in case of $Sr_3Ru_2O_7$ the nematic transition emerges. If a flat band is absent, the T-dependence of the resistivity is defined by the dependence of the term γ, entering (9.36), on the effective mass $M^*(T)$ of heavy electrons, while the spin susceptibility is determined by $M^*(T)$ [27].

To illustrate the emergence of the both mechanisms contributing to the linear T-dependence of the resistivity, we now consider the HF compound $\mathrm{Sr_3Ru_2O_7}$. To achieve a consistent picture of the quantum critical regime underlying the quasi-classical region in $\mathrm{Sr_3Ru_2O_7}$, we have to construct its $T - B$ phase diagram. We employ the model [73–80] based on vHs that induces a peak in the single-particle density of states (DOS) and yields a field-induced flat band [83]. At fields in the range $B_{c1} < B < B_{c2}$, the vHs is moved through the Fermi energy and the DOS peak turns out to be at or near the Fermi energy. A key point in this scenario is that within the range $B_{c1} < B < B_{c2}$, a repulsive interaction (e.g., Coulomb) is sufficient to induce FC and the formation of a flat band with the corresponding DOS singularity is locked to the Fermi energy [27, 62, 63, 83]. Now, it is seen from (9.32) that finite temperatures, while removing the degeneracy of the FC spectrum, do not change the excess entropy S_0, threatening the violation of the Nernst theorem. To avoid such an entropic singularity, the FC state must be altered at $T \to 0$, so that S_0 is to be somehow removed before zero temperature is reached. This can take place by means of a specific phase transition or crossover, whose explicit consideration is beyond the scope of this book. In case of $\mathrm{Sr_3Ru_2O_7}$, this mechanism is naturally identified with the electronic nematic transition [73–75].

The schematic $T - B$ phase diagram of $\mathrm{Sr_3Ru_2O_7}$ based on the proposed scenario is presented in Fig. 9.4. Its main feature is the magnetic field-induced quantum critical domain created by quantum critical points that are situated at B_{c1} and B_{c2}, generating FC and associated flat band. It is seen that in contrast to the typical phase diagram of a HF metal [27], the domain occupied by the ordered phase in Fig. 9.4 is approximately symmetric with respect to the magnetic field $B_c \simeq (B_{c2} + B_{c1})/2 \simeq 7.9$ T [77]. The emergent FC and quantum critical points are considered to be hidden or concealed in a

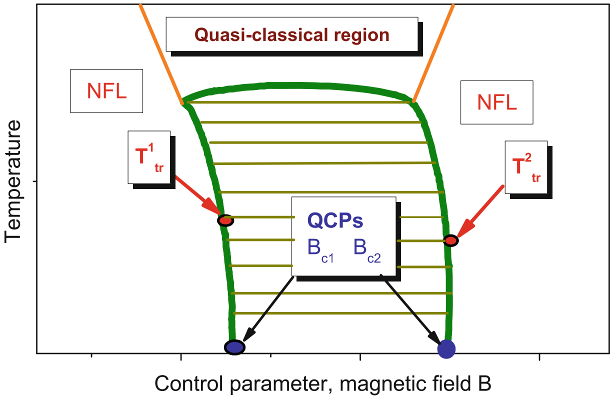

Fig. 9.4 Schematic phase diagram of the metal $\mathrm{Sr_3Ru_2O_7}$. The quantum critical points (QCPs) situated at the critical magnetic fields B_{c1} and B_{c2} are indicated by *arrows*. The ordered phase bounded by the *thick curve* and marked by *horizontal lines* emerges to remove the entropy excess given by (9.31). Two *arrows* label the tricritical points T^1_{tr} and T^2_{tr} where the *lines* of the second-order phase transitions change to the first order. Quasi-classical region is confined by two *lines* at the *top* of the figure and by the *top line* of the ordered phase

phase transition. The area occupied by this phase transition is indicated by horizontal lines and restricted by the thick boundary lines. At the critical temperature T_c, where new ordered phase sets in, the entropy is a continuous function. Therefore the top of the domain, occupied by the new phase, is a line of second-order phase transitions. As T is lowered, some temperatures $T^1_{\rm tr}$ and $T^2_{\rm tr}$ are reached, at which the entropy of the ordered phase becomes larger than that of the adjacent disordered phase, due to the remnant entropy S_0 from the highly entropic flat-band state. Therefore, under the influence of the magnetic field, the system undergoes a first-order phase transition upon crossing a sidewall boundary at $T = T^1_{\rm tr}$ or $T = T^2_{\rm tr}$, since entropy cannot be equalized there. It follows then that the line of the second-order phase transitions is changed to lines of the first-order transitions at tricritical points indicated by arrows in Fig. 9.4. It is seen from Fig. 9.4 that the sidewall boundary lines are not strictly vertical, due to the stated behavior of the entropy at the boundary and as a consequence of the magnetic Clausius-Clapeyron relation (as discussed in [75, 76]). Quasi-classical region is located above the top of the second order phase transition and restricted by two lines shown in Fig. 9.4. Therefore, the T-linear dependence is located in the same region, and is represented by AT dependence with $A \simeq A_{LT} + A_{FC}$. We predict that in this region the heat capacity C contains the temperature independent term C_0 as that of the HF metal $YbRh_2Si_2$ does, [30] while jumps of the residual resistivity, represented by ρ^c_0 in $Sr_3Ru_2O_7$, [73] are generated by the second mechanism.

The coefficients A_{FC}, A_{LT} and A_{HF} can be extracted from the results of measurements of the resistivity $\rho(T)$ shown in the left and right panels of Fig. 9.5 [51, 77]. For clarity, the left panel shows only a part of the data on $\rho(T)$ measured from 0.1 to 18 K at $B = B_c$. This part exhibits the T-linear dependence between 1.4 and 18 K

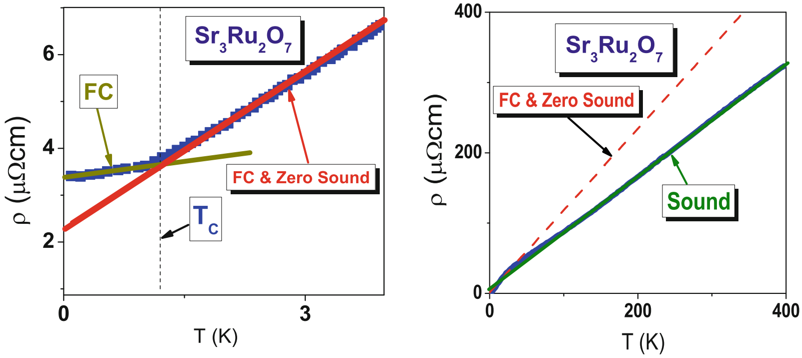

Fig. 9.5 Resistivity versus temperature. The *left panel* the resistivity $\rho(T)$ for $Sr_3Ru_2O_7$ at the critical field $B_c = 7.9\,$T [77]. Two *straight lines* display the T-linear dependence of the resistivity exhibiting a kink at $T = T_c$. At $T > T_c$ the T-linear resistivity is formed by zero sound and FC contributions, while at $T < T_c$ it comes from the FC contribution. The *right panel* the resistivity at B_c over an extended temperature range up to 400 K [51]. The *dashed line* shows the extrapolation of the low-T-linear resistivity at $T > T_c$, and the *solid line* shows the extrapolation of the high-T-linear resistivity formed at $T > 100$ K by the common sound (phonons)

and between 0.1 and 1 K [77]. The coefficient $A \simeq A_{LT} + A_{FC} \simeq 1.1$ μΩcm/K between 18 and 1.4 K. Since $T_D \sim 1$ K, we expect that between 1 and 0.1 K the coefficient A is formed by the second mechanism and $A_{FC} \simeq 0.25$ μΩcm/K. The right panel reports the measurements of $\rho(T)$ for $T > T_c$ up to 400 K [51]. The dash line shows the extrapolation of the low-temperature linear resistivity at $T < 20$ K and B_c with $A \simeq 1.1$ μΩcm/K, and the solid line shows the extrapolation of the high-temperature linear resistivity at $T > 100$ K with $A_{HT} \simeq 0.8$ μΩcm/K [51]. The obtained values of A allow us to estimate the coefficients A_{LT} and A_{FC}. Due to our assumption that $A_{LT} \simeq A_{HT}$, we have $A - A_{LH} \simeq A_{FC} \simeq 0.3$ μΩcm/K. This value is in good agreement with $A_{FC} \simeq 0.25$ μΩcm/K. As a result, we conclude that for $Sr_3Ru_2O_7$, where the measurements are precise, the scattering rate is given by (9.34), and does not depend on T, provided that $T \geq T_D$. The relatively small term A_{FC} is omitted. On the other hand, at $T < T_D$ $A_{HT}/A_{FC} \simeq 3$, and the constancy of the lifetime τ_q is violated, while the resistivity exhibits the T-linear dependence. It is seen from the left panel of Fig. 9.5, that the transition from the resistivity, characterized by the coefficient A_{LT}, to that with A_{FC} occurs as a kink at $T_c = 1.2$ K representing both the entry into the ordered phase and a transition region, where the resistivity alters its slope. We expect that the constancy of the scattering rate can also fail in such HF metals as $YbRh_2Si_2$ and the quasicrystal $Au_{51}Al_{34}Yb_{15}$ that exhibits the HF behavior [84, 85].

References

1. A.I. Petit, P.L. Dulong, Annales de Chimie ed de Physique **10**, 395 (1819)
2. L. Boltzmann, Wiener Berichte **74**, 553 (1877)
3. P. Debye, Annalen der Physik 39, 789 (1912). (Leipzig).
4. L.D. Landau, Zh Eksp, Teor. Fiz. **30**, 1058 (1956)
5. D.S. Greywall, Phys. Rev. B **41**, 1842 (1990)
6. M. Neumann, J. Nyéki, B. Cowan, J. Saunders, Science **317**, 1356 (2007)
7. V.A. Khodel, J.W. Clark, V.R. Shaginyan, M.V. Zverev, JETP Lett. **92**, 585 (2010)
8. C. Bäuerle, Y.M. Bunkov, A. Chen, S. Fisher, H. Godfrin, J. Low Temp. **110**, 333 (1998)
9. C. Bäuerle, Y.M. Bunkov, A.S. Chen, S.N. Fisher, H. Godfrin, J. Low Temp. **110**, 345 (1998)
10. M. Morishita, K. Ishida, K. Yawata, H. Nagatani, H. Fukuyama, J. Low Temp. **110**, 351 (1998)
11. M. Morishita, H. Nagatani, H. Fukuyama, J. Low Temp. **113**, 299 (1998)
12. A. Casey, H. Patel, J. Cowan, B.P. Saunders, Phys. Rev. Lett. **90**, 115301 (2003)
13. A. Golov, F. Pobell, Europhys. Lett. **38**, 353 (1997)
14. V.R. Shaginyan, A.Z. Msezane, K.G. Popov, V.A. Stephanovich, Phys. Rev. Lett. **100**, 096406 (2008)
15. I.M. Khalatnikov, *An Introduction to the Theory of Superfluidity* (Benjamin, New York, 1965)
16. A.A. Abrikosov, I.M. Halatnikov, Soviet Phys. Uspekhi **1**, 68 (1958)
17. M. Pfitzner, P. Wölfle, Phys. Rev. B **33**, 2003 (1986)
18. P. Nozières, J. Phys. I France **2**, 443 (1992)
19. M.V. Zverev, M. Baldo, JETP **87**, 1129 (1998)
20. M.V. Zverev, M. Baldo, J. Phys. Condens. Matter **11**, 2059 (1999)
21. S.A. Artamonov, Y.G. Pogorelov, V.R. Shaginyan, JETP Lett. **68**, 942 (1998)
22. V.A. Khodel, J.W. Clark, M.V. Zverev, Phys. Rev. B **78**, 075120 (2008)
23. V.A. Khodel, V.R. Shaginyan, JETP Lett. **51**, 553 (1990)

24. G.E. Volovik, JETP Lett. **53**, 222 (1991)
25. V.A. Khodel, V.R. Shaginyan, V.V. Khodel, Phys. Rep. **249**, 1 (1994)
26. V.R. Shaginyan, M.Y. Amusia, K.G. Popov, Phys. Usp. **50**, 563 (2007)
27. V.R. Shaginyan, M.Y. Amusia, A.Z. Msezane, K.G. Popov, Phys. Rep. **492**, 31 (2010)
28. A.A. Abrikosov, L.P. Gorkov, I.E. Dzyaloshinski, *Methods of Quantum Field Theory in Statistical Physics* (Dover, New York, 1975)
29. V.A. Khodel, M.V. Zverev, V.M. Yakovenko, Phys. Rev. Lett. **95**, 236402 (2005)
30. P. Wölfle, E. Abrahams, Phys. Rev. B **84**, 041101(R) (2011)
31. H. v. Löhneysen, A. Rosch, M. Vojta, P. Wölfle, Rev. Mod. Phys. **79**, 1015 (2007).
32. P. Gegenwart, Q. Si, F. Steglich, Nature Phys. **4**, 186 (2008)
33. P. Gegenwart, J. Custers, T. Tayama, K. Tenya, C. Geibel, O. Trovarelli, F. Steglich, K. Neumaier, Acta Phys. Pol. **34**, 323 (2003)
34. J. Custers, P. Gegenwart, S. Geibel, F. Steglich, P. Coleman, S. Paschen, Phys. Rev. Lett. **104**, 186402 (2010)
35. L. Taillefer, Ann. Rev. Cond. Matt. Phys. **1**, 51 (2010)
36. D. Pines, P. Noziéres, *Theory of Quantum Liquids* (Benjamin, New York, 1966)
37. D.M. Maslov, A.V. Chubukov, Phys. Rev. B **81**, 045110 (2010)
38. S.L. Bud'ko, E. Morosan, P.C. Canfield, Phys. Rev. B **69**, 014415 (2004)
39. J.W. Clark, V.A. Khodel, M.V. Zverev, Phys. Lett. A **377**, 647 (2013)
40. A.S. Alexandrov, N. Mott, *Polarons and Bipolarons* (World Scientific, Singapore, 1996)
41. A.S. Alexandrov, P.P. Kornilovitch, Phys. Rev. Lett. **82**, 807 (1999)
42. E.M. Lifshitz, L.P. Pitaevskii, *Physical Kinetics* (Pergamon Press, Oxford, 1981)
43. C. Kittel, *Introduction to Solid State Physics* (Wiley, New York, 1996)
44. J.A. Hertz, Phys. Rev. B **14**, 1165 (1976)
45. A.J. Millis, Phys. Rev. B **48**, 7183 (1993)
46. A.S. Alexandrov, Physica C **274**, 237 (1997)
47. R.D. Barnard, *Thermoelectricity in Metals and Alloys* (Taylor and Francis, London, 1972)
48. S. Hartmann, N. Oeschler, C. Krellner, C. Geibel, S. Paschen, F. Steglich, Phys. Rev. Lett. **104**, 096401 (2010)
49. K. Behnia, D. Jaccard, J. Flouquet, J. Phys.: Condens. Matter **16**, 5187 (2004)
50. V.R. Shaginyan, K.G. Popov, V.A. Khodel, Phys. Rev. B **88**, 115103 (2013)
51. A.N. Bruin, H. Sakai, R.S. Perry, A.P. Mackenzie, Science **880**, 339 (2013)
52. C.M. Varma, P.B. Littlewood, S. Schmittrink, E. Abrahams, A.E. Ruckenstein, Phys. Rev. Lett. **63**, 1996 (1989)
53. M.E. Simon, C.M. Varma, Phys. Rev. Lett. **89**, 247003 (2002)
54. P. Phillips, Phil. Trans. R. Soc. A **369**, 1572 (2011)
55. P. Phillips, Phil. Trans. R. Soc. A **369**, 1574 (2011)
56. P. Aynajian, E. Neto, A. Gyenis, R.E. Baumbach, J.D. Thompson, Z. Fisk, E.D. Bauer, A. Yazdani, Nature **486**, 201 (2012)
57. V.R. Shaginyan, A.Z. Msezane, K.G. Popov, J.W. Clark, M.V. Zverev, V.A. Khodel, Phys. Rev. B **86**, 085147 (2012)
58. D.C. Peets, D.G. Hawthorn, K.M. Shen, Y.J. Kim, D.S. Ellis, H. Zhang, S. Komiya, Y. Ando, G.A. Sawatzky, R. Liang, D.A. Bonn, W.N. Hardy, Phys. Rev. Lett. **103**, 087402 (2009)
59. M.M.J. French, J.G. Analytis, A. Carrington, L. Balicas, N.E. Hussey, New J. Phys. **11**, 055057 (2009)
60. J.W. Alldredge, J. Lee, K. McElroy, M. Wang, K. Fujita, Y. Kohsaka, C. Taylor, H. Eisaki, S. Uchida, P.J. Hirschfeld, J.C. Davis, Nature Phys. **4**, 319 (2008)
61. G.E. Volovik, in *Quantum Analogues: From Phase Transitions to Black Holes and Cosmology*, ed. by W.G. Unruh, R. Schutzhold, Springer Lecture Notes in Physics, 718 (Springer, Orlando, 2007), p. 31.
62. V.R. Shaginyan, Physics of Atomic Nuclei **74**, 1107 (2011)
63. V.A. Khodel, J.W. Clark, M.V. Zverev, Physics of Atomic Nuclei **74**, 1237 (2011)
64. M.V. Zverev, V.A. Khodel, V.R. Shaginyan, M. Baldo, JETP Lett. p. 863 (1997).
65. M.Y. Amusia, A.Z. Msezane, V.R. Shaginyan, Phys. Lett. A **320**, 459 (2004)

66. N. Oeschler, P. Gegenwart, M. Lang, R. Movshovich, J.L. Sarrao, J.D. Thompson, F. Steglich, Phys. Rev. Lett. **91**, 076402 (2003)
67. J.G. Donath, F. Steglich, E.D. Bauer, J.L. Sarrao, P. Gegenwart, Phys. Rev. Lett **100**, 136401 (2008)
68. S. Zaum, K. Grube, R. Schäfer, E.D. Bauer, J.D. Thompson, H. v. Löhneysen. Phys. Rev. Lett. **106**, 087003 (2011)
69. R. Kúchler, N. Oeschler, P. Gegenwart, T. Cichorek, K. Neumaier, O. Tegus, C. Geibel, J.A. Mydosh, F. Steglich, L. Zhu, Q. Si, Phys. Rev. Lett. **91**, 066405 (2003)
70. P. Gegenwart, F. Weickert, M. Garst, R.S. Perry, Y. Maeno, Phys. Rev. Lett. **96**, 136402 (2006)
71. C. Stingl, R.S. Perry, Y. Maeno, P. Gegenwart, Phys. Rev. Lett. **107**, 026404 (2011)
72. V.A. Khodel, J.W. Clark, H. Li, M.V. Zverev, Phys. Rev. Lett. **98**, 216404 (2007)
73. S.A. Grigera, P. Gegenwart, R.A. Borzi, F. Weickert, A.J. Schofield, R.S. Perry, T. Tayama, T. Sakakibara, Y. Maeno, A.G. Green, A.J. Millis, A.P. Mackenzie, Science **306**, 1154 (2004)
74. R.A. Borzi, S.A. Grigera, J. Farrell, R.S. Perry, S.J.S. Lister, S.L. Lee, D.A. Tennant, Y. Maeno, A.P. Mackenzie, Science **315**, 214 (2007)
75. A.W. Rost, R.S. Perry, J.F. Mercure, A.P. Mackenzie, S.A. Grigera, Science **325**, 1360 (2009)
76. S. Raghu, A. Paramekanti, E.A. Kim, R.A. Borzi, S.A. Grigera, A.P. Mackenzie, S.A. Kivelson, Phys. Rev. B **79**, 214402 (2009)
77. A.W. Rost, S.A. Grigera, J.A.N. Bruin, R.S. Perry, D. Tian, S. Raghu, S.A. Kivelson, A.P. Mackenzie, Proc. Natl. Acad. Sci. USA **108**, 16549 (2011)
78. B. Binz, M. Sigrist, Europhys. Lett. **65**, 816 (2004)
79. A.M. Berridge, S.A. Grigera, B.D. Simons, A.G. Green, Phys. Rev. B **81**, 054429 (2010)
80. A.P. Mackenzie, J.A.N. Bruin, R.A. Borzi, A.W. Rost, S.A. Grigera, Physica C **481**, 207 (2012)
81. V.A. Khodel, J.W. Clark, V.R. Shaginyan, M.V. Zverev, JETP Lett. **92**, 532 (2010)
82. V.R. Shaginyan, A.Z. Msezane, K.G. Popov, J.W. Clark, M.V. Zverev, V.A. Khodel, JETP Lett. **96**, 397 (2012)
83. V.R. Shaginyan, A.Z. Msezane, K.G. Popov, J.W. Clark, M.V. Zverev, V.A. Khodel, Phys. Lett. A **377**, 2800 (2013)
84. K. Deguchi, S. Matsukawa, N.K. Sato, T. Hattori, K. Ishida, H. Takakura, T. Ishimasa, Nature Materials **11**, 1013 (2012)
85. V.R. Shaginyan, A.Z. Msezane, K.G. Popov, G.S. Japaridze, V.A. Khodel, Phys. Rev. B **87**, 245122 (2013)

Chapter 10
Magnetoresistance in the HF Metal at Zero Temperature

Abstract In this chapter we consider the paradoxical behavior of the residual resistivity ρ_0 of HF metals in magnetic fields and under pressure. Our consideration is based on the idea of flattening of the single-particle spectrum $\varepsilon(\mathbf{p})$ that profoundly effects on the specific heat C, thermal expansion coefficient α and magnetic susceptibility χ in the normal state, the jump of C at the point of superconducting phase transition etc. We show that FC associated with flat bands contributes to the residual resistivity ρ_0, while the application of the magnetic field or pressure to the system with a flat band removes the flat band and leads to a strong suppression of ρ_0. Our analysis of the thermodynamic and transport properties gives direct evidences for the presence of the flat band in $CeCoIn_5$ (Sect. 10.2), $YbRh_2Si_2$ (Sect. 10.3), and $Sr_3Ru_2O_7$ (Chap. 11). It is further demonstrated that the application of magnetic field generates both the experimentally identifiable multiple energy scales and the scaling behavior of the effective mass in HF compounds.

10.1 Introduction

Measurements of the resistivity $\rho(T)$ in external magnetic fields H have displayed the diversity in the low-temperature behavior of this fundamental property in HF metals, when changing from LFL behavior to NFL one [1–4]. The resistivity $\rho(T)$ is frequently approximated by the formula,

$$\rho(T) = \rho_0 + AT^n, \tag{10.1}$$

where ρ_0 is the residual resistivity, A is a T-independent coefficient, the index $n = 1$ at NFL regime, $1 \lesssim n \lesssim 2$ at the crossover and $n = 2$ at LFL one, inherent in conventional metals.

The term ρ_0 is ordinarily attributed to scattering off impurities, being proportional to both the density of impurities and the transport cross section σ_{tr}. Assuming impurities to be structureless, one can infer that the application of a weak external magnetic field H that produces a small positive classical contribution to ρ, proportional to H^2 due to orbital motion of carriers induced by the Lorentz force, does not change σ_{tr} drastically, rendering ρ_0 almost H-independent. This conclu-

M.Y. Amusia et al., *Theory of Heavy-Fermion Compounds*, Springer Series
in Solid-State Sciences 182, DOI 10.1007/978-3-319-10825-4_10

sion is in agreement with the majority of available experimental data. However, in the HF metals, this picture fails, especially while dealing with the very clean compound $\mathrm{CeCoIn_5}$, where at any $T > T_c$ adjacent to the critical temperature $T_c = 2.3$ K of SC phase transition, the resistivity $\rho(T, H = 0)$ turns out to be a linear function of temperature. Furthermore, already at weak magnetic fields $H \geq H_{c2} \simeq 5\,\mathrm{T}$, where H_{c2} is the critical magnetic field terminating superconductivity of this metal at zero temperature, the term ρ_0 decreases dramatically: $\rho_0(H = 0) \simeq 1.5\,\mu\Omega\,\mathrm{cm}$, while $\rho_0(H = 6\,\mathrm{T}) \simeq 0.3\,\mu\Omega\,\mathrm{cm}$ [1, 3]. To resolve this paradox, we suggest that the electron system of $\mathrm{CeCoIn_5}$ contains a flat band. Flattening of the single-particle spectrum is directly related to the problem addressed here since, due to Umklapp processes, quasiparticles of the flat band produce a contribution to ρ_0 indistinguishable from that due to impurity scattering. We note, that necessary existence of Umklapp processes does not lead to any small factors, for electron quasi-momenta are large [5]. Furthermore, it is crucial that the flat band somehow becomes depleted at $T \to 0$ and $H = 6\,\mathrm{T}$. This depletion entails a dramatic suppression of the flat-band contribution to ρ_0.

Certainly, real impurities have a structure, and therefore σ_{tr} somehow depends on H. However, this dependence characterizes properties of the impurity system rather than those of the metal under consideration. On the contrary, as we will see, the suppression of ρ_0 in magnetic fields is an internal property of metals with flat bands. The key feature, which renders flattening of $\varepsilon(\mathbf{p})$ relevant to the suppression of $\rho_0(H)$ is that quasiparticles, belonging to the flat bands, scatter other quasiparticles like impurities [6, 7], producing an additional contribution to the part of ρ_0, coming from impurity scattering. However, the application of the magnetic field $H > H_{c2}$ results in the dramatic depletion of the flat band [8], implying, in its turn, the suppression of its contribution to ρ_0.

10.2 The HF Metal $\mathrm{CeCoIn_5}$

Here we propose an explanation of paradoxical behavior of the residual resistivity ρ_0 of the HF metal $\mathrm{CeCoIn_5}$ in magnetic fields and under pressure. The source of this behavior is identified as a flattening of the single-particle spectrum, which exerts profound effects on the physical properties of strongly correlated electron systems generally in solids and particularly in $\mathrm{CeCoIn_5}$. Namely, the above flattening affects such normal state properties as specific heat, thermal expansion coefficient, and magnetic susceptibility, as well as the specific heat jump at superconducting phase transition point.

Before proceeding to the analysis of the situation in $\mathrm{CeCoIn_5}$, let us make some remarks on the flattening of the spectra $\varepsilon(\mathbf{p})$ in strongly correlated Fermi systems, called swelling of the Fermi surface or FC. This phenomenon, discovered and initially elaborated more than 20 years ago [9–11] (see [8, 12] for recent reviews), has gained new impetus after considering *the topological matter*, characterized by nontrivial topology of the quasiparticle Green's function in momentum space, associated with topologically protected flat bands [13–17].

At $T = 0$, the ground states of the systems with flat bands are degenerate. Therefore, the occupation numbers $n_*(\mathbf{p})$ of states, belonging to the flat bands, who in total are sometimes called FC, are continuous functions of momentum that differ from standard LFL values 0 and 1. This leads to an entropy excess,

$$S_0 = -\sum_{\mathbf{p}}[n_*(\mathbf{p})\ln n_*(\mathbf{p}) + (1 - n_*(\mathbf{p}))\ln(1 - n_*(\mathbf{p}))], \tag{10.2}$$

that does not contribute to the specific heat $C(T)$. However, in contrast to the corresponding LFL value, vanishing linearly with $T \to 0$, S_0 produces a T-independent thermal expansion coefficient $\alpha \propto -\partial S_0/\partial P$ [18], where P is the pressure.

In the normal state of the HF metal CeCoIn$_5$ its thermal expansion coefficient α is, indeed, greatly enhanced and almost T-independent [19], signaling that this metal presumably has possessed a flat band. The analysis of experimental data on magnetic oscillations [20, 21] supports this assertion. CeCoIn$_5$ turns out to have two main Fermi surfaces. These two Fermi surfaces are represented by both the comparatively weakly renormalized α-sheet, which single-particle spectrum is observable at all fields down to $H_{c2} \simeq 5$ T, and by the β-sheet. Magnetic oscillations of the single particle spectrum of the β-sheet are undetectable at magnetic fields $H \leq 10$ T. Thus, we conclude that the β-sheet does possess a flat portion. Such a suppression is generated by the merging of the single particle levels [22], for details see Sect. 12.2.

Although in the FC theory, the above degeneracy is lifted at any finite temperatures, and FC acquires a small dispersion, proportional to T, with the spectrum [11],

$$\varepsilon(\mathbf{p}, n_*) = T \ln \frac{1 - n_*(\mathbf{p})}{n_*(\mathbf{p})} + \mu, \tag{10.3}$$

the FC occupation numbers $n_*(\mathbf{p})$ remain unchanged at small $T > 0$. Thus, lifting the degeneracy of the FC spectrum does not change the entropy excess S_0 that contradicts the Nernst theorem. To avoid the contradiction, FC must be completely eliminated at $T \to 0$. This can be done by means of crossover to a state with the multi-connected Fermi surface [8, 23–25] or by virtue of some phase transition, e.g., the SC one, where the cancelation of S_0 is associated with the emergence of the gap Δ in the single-particle spectrum [9, 26–29]. It is this transition that provides the elimination of the flat portion in the spectrum $\varepsilon(\mathbf{p})$ and the vanishing at $H \leq H_{c2}$ of the entropy excess S_0 in CeCoIn$_5$, whose schematic $T - H$ phase diagram is drawn in Fig. 10.1. Its key feature is a magnetic field-induced quantum critical point at H_{c0} hidden in the SC state [1]. As it is seen from Fig. 10.1, $H_{c2} > H_{c0}$ [8, 30] and the LFL behavior persists at $T \leq T_{cross}$ until the SC state emerges. If the SC state were absent, then at $H \geq H_{c0}$, the LFL behavior would persist in the domain $T \leq T_{cross}(H)$. The line $T_{cross}(H)$ describes crossover, shown by the hatched area, which separates the domain of NFL behavior from that of LFL one.

In accordance with this phase diagram, behavior of the dimensionless thermal expansion coefficient $\alpha_N(T, H) = \alpha(T, H)/\alpha(T_N, H)$, treated as a function of the

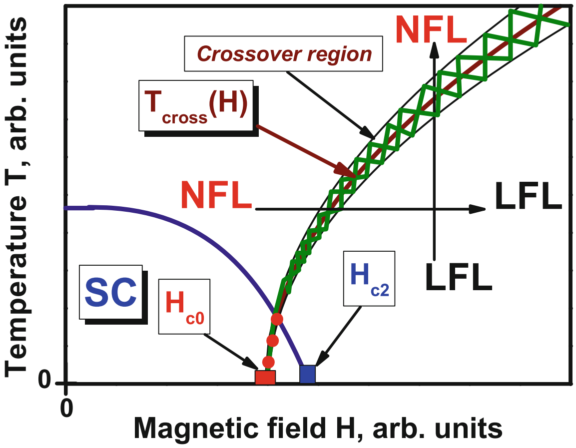

Fig. 10.1 Schematic $T-H$ phase diagram of CeCoIn$_5$. The *vertical* and *horizontal arrows*, crossing the transition region (*thick lines*), show the *LFL-NFL* and reverse transitions at fixed H and T, respectively. As shown by the *solid curve*, at $H < H_{c2}$ the system is in its superconducting (SC) state. H_{c0} denotes a QCP hidden beneath the SC dome where the flat band could exist at $H \leq H_{c0}$. The *hatched area* with the *solid curve* $T_{cross}(H)$ represents the crossover, separating *NFL* and *LFL* domains. A part of the crossover shown by the *dots* is hidden in the SC state. The NFL state is characterized by the entropy excess S_* (10.2)

dimensionless temperature $T_N = T/T_{cross}$, turns out to be almost universal. Indeed, as seen from Fig. 10.2, all the normalized data, extracted from measurements on CeCoIn$_5$ [31], collapse on the single scaled curve. At $T_N < 1$, α_N turns out to be a linear function of T_N as depicted by the dash–dot line, implying that at $T_N < 1$, CeCoIn$_5$ exhibits LFL behavior. At $T_N \simeq 1$ the system enters the narrow crossover region. Then at growing temperatures $T > 1$, NFL behavior prevails, and both α and the S_0 cease to depend on T, which is shown by the horizontal line. We note that the observed limited types of behaviors: The LFL one, with $\alpha \propto T$, and the NFL $\alpha = const$ are in accordance with recent experimental results [32]. Thus, we conlude that the experimental $T-H$ phase diagram of CeCoIn$_5$ agrees well with that drawn in Fig. 10.1.

In calculations of low-temperature transport properties of the normal state of CeCoIn$_5$, we employ a model with two bands, one of which is supposed to be flat, with the dispersion of $\varepsilon(\mathbf{p})$, given by (10.3), while the second band is assumed to possess the LFL single-particle spectrum having a finite T-independent dispersion. Let us start with the analysis of the case $H = 0$, where the resistivity of CeCoIn$_5$ is a linear function of T. We will see immediately that this kind of behavior is a peculiarity of electron systems with flat bands. Indeed, the conductivity $\sigma(T)$ is expressed in terms of the imaginary part of the polarization operator $\Pi(\mathbf{j})$ [33]

$$\sigma = \lim \omega^{-1}\mathrm{Im}\Pi(\mathbf{j}, \omega \to 0) \propto \frac{1}{T}\int\int |\mathscr{T}(\mathbf{j}, \omega = 0)|^2 \times \mathrm{Im}G_R(\mathbf{p}, \varepsilon)\mathrm{Im}G_R(\mathbf{p}, \varepsilon)\frac{d\upsilon d\varepsilon}{\cosh^2(\varepsilon/2T)}, \tag{10.4}$$

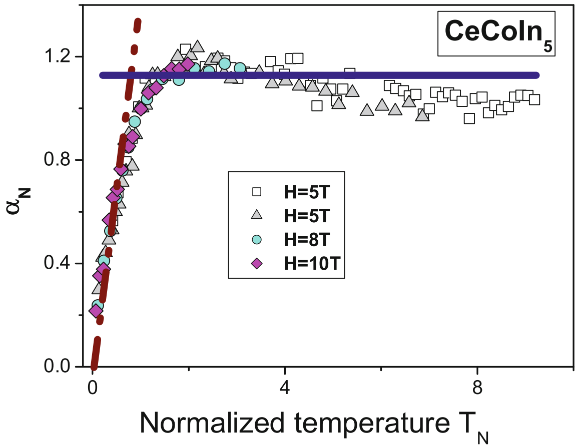

Fig. 10.2 Normalized low temperature thermal expansion coefficient α_N versus normalized temperature T_N of the normal state of CeCoIn$_5$. Different magnetic fields H are shown in the legend. All the data represented by the *symbols* are extracted from measurements on CeCoIn$_5$ [31]. The *dash–dot line* depicts the LFL regime taking place at low temperatures under the application of magnetic field. The high temperature NFL regime characterized by both $\alpha = const$ and S_0 (10.2) is noted by the *horizontal line*

where $d\upsilon$ is an element of momentum space, $\mathcal{T}(\mathbf{j}, \omega)$ is the vertex part, and $\mathbf{j}$ is the electric current. The imaginary part $\mathrm{Im}G_R(\mathbf{p}, \varepsilon)$ of the retarded quasiparticle Green's function G_R is given by

$$\mathrm{Im}G_R(\mathbf{p}, \varepsilon) = -\frac{\gamma}{(\varepsilon - \varepsilon(\mathbf{p}))^2 + \gamma^2}, \tag{10.5}$$

with the spectrum $\varepsilon(\mathbf{p})$ and damping γ, referring to the band with the finite value v_F of the Fermi velocity. Due to gauge invariance, $\mathcal{T}(\mathbf{j}, \omega)$ reads

$$\mathcal{T}(\mathbf{j}, \omega = 0) = e\frac{\partial \varepsilon(\mathbf{p})}{\partial \mathbf{p}}. \tag{10.6}$$

Upon inserting (10.6) into (10.4) and performing some algebra we arrive at the standard result

$$\sigma(T) = e^2 n \frac{v_F}{\gamma(T)}, \tag{10.7}$$

where n is the number density of electrons.

In conventional clean metals, obeying LFL theory, the damping $\gamma(T)$ is proportional to T^2, giving rise to (9.28) with $n = 2$. NFL behavior of $\sigma(T)$ is due to the NFL temperature dependence of $\gamma(T)$, associated with the presence of FC [6, 7]. In the standard situation, where the volume occupied by FC is rather small, overwhelming contributions to the transport, come from inelastic scattering, drawn in Fig. 10.3a.

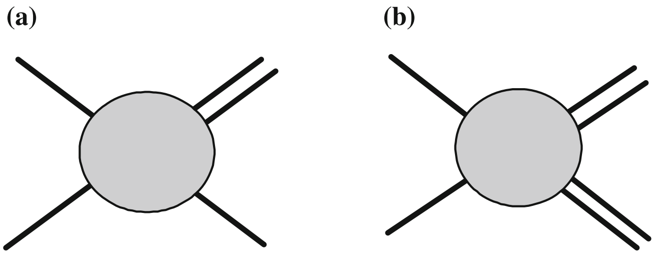

Fig. 10.3 Illustration of the scattering of electrons belonging to the light band off electrons belonging to the almost flat band. Scattering diagrams that contribute to the imaginary part of the mass operator $\Sigma(\varepsilon)$, referring to the band with finite value of the Fermi velocity. The *single line* corresponds to the quasiparticle of that band, and the *double line* corresponds to a FC quasiparticle. **a** The decay of a normal quasiparticle with the formation of a pair of normal quasiparticles and one quasiparticle belonging to the FC. **b** The decay of a normal quasiparticle with the formation of a pair of FC quasiparticles

In that case a FC quasiparticle, depicted by the double line, disappears, becoming a normal quasiparticle, or vice versa, the normal quasiparticle vanishes, turning into a FC quasiparticle. The second process illustrated in Fig. 10.3b contains two double lines, belonging to FC. The analytical expressions of the contributions of these processes to the damping γ are estimated on the base of a simplified formula,

$$\gamma(\mathbf{p},\varepsilon) \propto \int\int\int_0^{\varepsilon}\int_0^{\omega} |\Gamma(\mathbf{p},\mathbf{p}_1,\mathbf{q}|^2 \mathrm{Im}G_R(\mathbf{p}-\mathbf{q},\varepsilon-\omega) \\ \times \mathrm{Im}G_R(-\mathbf{p}_1,-\varepsilon)\mathrm{Im}G_R(\mathbf{q}-\mathbf{p}_1,\omega-\varepsilon)d\mathbf{p}_1 d\mathbf{q} d\omega d\varepsilon, \tag{10.8}$$

where now the element of volume in momentum space includes summation over different bands. The calculations (see [6] for details) yield

$$\gamma(\varepsilon) = \nu(\gamma_0 + \gamma_1\varepsilon), \quad \mathrm{Re}\Sigma(\varepsilon) = -\nu\gamma_1\varepsilon \ln\frac{1}{|\varepsilon|}, \tag{10.9}$$

where the factor ν stands for the volume in momentum space, occupied by the flat band. With this result, one finds that $\rho(T) = \rho_0 + AT$. Thus, in a system with FC, the term ρ_0 arises even if the metal has a perfect lattice with no impurities.

The presence of the flat band manifests itself not only in kinetics but also in thermodynamics of CeCoIn$_5$, e.g., in the occurrence of an additional term $\Delta C = C_s - C_n$ in the specific heat $C(T)$, given by the textbook formula

$$\Delta C = -\frac{1}{2T_c}\int\left(\frac{d\Delta^2(\mathbf{p})}{dT}\right)_{T_c} n(\mathbf{p})(1-n(\mathbf{p}))d\upsilon, \tag{10.10}$$

where C_s and C_n are the specific heat of the superconducting and normal states, correspondingly. The FC contribution to ΔC, being 0 in the normal state, is, in fact, concentrated in a narrow vicinity of the transition point at $T \leq T_c$. It is this contribution that endows CeCoIn$_5$ by a record value of the jump $\Delta C/C_n = 4.5$ [34] of the specific heat at T_c, (cf. LFL value 1.43). The enhancement factor is evaluated by setting $T = T_c$ in (10.10). Importantly, in systems with the flat bands, the quantity $q = -\left(\frac{d\Delta^2}{dT}\right)_c/2T_c$ has the same order [11], as in LFL theory where $q \simeq 5$. For illustration, let us assume the momentum distribution n to be dependent only on the absolute value of momentum $\mathbf{p}$. In this case, one obtains

$$\frac{\Delta C(T_c)}{C_n(T_c)} \simeq 1.43\frac{v_F}{T_c}\int n(p)\ (1-n(p))\,dp. \tag{10.11}$$

Thus the ratio $\Delta C(T_c)/C_n(T_c)$, proportional to a volume in momentum space occupied by the flat band, proves to be inversely proportional to T_c as well, implying that $\Delta C(T_c)/C_n(T_c)$ diverges at $T_c \to 0$, in agreement with data on CeCoIn$_5$ where T_c equals merely 2.3 K.

Curiously, the formula (10.10) can be recast to a different form [35],

$$\frac{\Delta C(T_c)}{C_n(T_c)} = q\mathscr{S}^{-1}(T_c)\frac{T_c\chi(T_c)}{C_n(T_c)}, \tag{10.12}$$

that allows one, with the aid of experimental data [36], to find the value of the Stoner factor $\mathscr{S}(T_c) = \chi(T_c)/\chi_0(T_c)$, indicating the enhancement or suppression of ferromagnetic fluctuations. One obtains $\mathscr{S}(T_c) < 0.1$. Thus, it is seen that in CeCoIn$_5$ the ferromagnetic fluctuations are greatly suppressed.

To confirm the statement that in systems with FC the quantity q has the same order, as it follows in accordance with the LFL theory, we proceed from the relation

$$\int \Delta^2(p)\left(\frac{\tanh\frac{E(p,T)}{2T}}{E(p,T)} - \frac{\tanh\frac{\varepsilon(p,T_c)}{2T_c}}{\varepsilon(p,T_c)}\right)d\upsilon = 0, \tag{10.13}$$

with the Bogoliubov quasiparticle energy $E(\mathbf{p}) = \sqrt{\varepsilon^2(\mathbf{p}) + \Delta^2(\mathbf{p})}$. At $T_c - T \ll T_c$ one has

$$\begin{aligned}\frac{\tanh\frac{E(\mathbf{p},T)}{2T}}{E(\mathbf{p},T)} - \frac{\tanh\frac{\varepsilon(\mathbf{p},T_c)}{T_c}}{\varepsilon(\mathbf{p},T_c)} &= \frac{(T_c - T)}{2T_c^2\cosh^2\frac{\varepsilon(\mathbf{p},T_c)}{2T_c}}\\ &+ \frac{\Delta^2(\mathbf{p})}{2\varepsilon^2(\mathbf{p},T_c)}\left(\frac{1}{2T_c\cosh^2\frac{\varepsilon(\mathbf{p},T_c)}{2T_c}} - \frac{\tanh\frac{\varepsilon(\mathbf{p},T_c)}{2T_c}}{\varepsilon(\mathbf{p},T_c)}\right).\end{aligned} \tag{10.14}$$

Inserting this relation into (10.13) and integrating over momentum with the aid of (10.3), we obtain

$$\Delta^2(T \to T_c) = cT(T - T_c), \tag{10.15}$$

with a numerical factor $c \simeq 10$, obtained in the analytically solvable model of FC [11]. These results can be straightforwardly applied to the analysis of the slope of the peak of the specific heat $C(T \to T_c)$ in the superconducting state of CeCoIn$_5$, described primarily by (10.10). More precisely, one has

$$\frac{dC(T \to T_c)/dT}{dC_{BCS}(T \to T_c)/dT} = \frac{\Delta C}{C_n(T_c)}. \tag{10.16}$$

Note, that the right hand side of this relation has been obtained with the help of (10.11). This narrowing of the shape of $C(T)$ toward the λ-point curve, observed in the case of superfluid ^{4}He, is in agreement with experimental data on CeCoIn$_5$.

The linear in the energy part of the damping γ, given by (10.9), is also responsible for a NFL logarithmic correction to the LFL specific heat value, observed in the normal state of CeCoIn$_5$ [36]. Indeed, one has for the entropy [33]:

$$S(T) \propto -\frac{1}{T} \int d\upsilon \int_{-\infty}^{\infty} d\varepsilon \frac{\partial f(\varepsilon)}{\partial \varepsilon} \varepsilon \frac{1}{i} \ln \frac{G_R(p,\varepsilon)}{G_A(p,\varepsilon)}, \tag{10.17}$$

where $f(\varepsilon) = [1 + e^{\varepsilon/T}]^{-1}$, while

$$\frac{1}{i} \ln(G_R/G_A) = \arctan \frac{\nu\varepsilon}{\varepsilon\left(1 + \nu \ln \frac{1}{|\varepsilon|}\right) - \varepsilon(p)}. \tag{10.18}$$

Here, $G_A(\mathbf{p},\varepsilon)$ is the advanced quasiparticle Green function, whose imaginary part is given by

$$\mathrm{Im} G_A(\mathbf{p},\varepsilon) = \frac{\gamma}{(\varepsilon - \varepsilon(\mathbf{p}))^2 + \gamma^2}. \tag{10.19}$$

Upon introducing new variables $w = \varepsilon(p)/\varepsilon \propto (p - p_F)/\varepsilon$ and $\varepsilon = zT$ and retaining only leading terms, this integral is recast to the sum $S = S_+ + S_-$ where

$$S_+ = T \int_0^{\infty} \frac{z^2 e^z dz}{(1+e^z)^2} \int_{-\infty}^{\infty} \arctan \frac{\nu}{1 + \nu \ln \frac{1}{T} - w} dw,$$

$$S_- = T \int_0^{\infty} \frac{z^2 e^z dz}{(1+e^z)^2} \int_{-\infty}^{\infty} \arctan \frac{\nu}{1 + \nu \ln \frac{1}{T} + w} dw.$$

Both integrals are evaluated analytically to yield the next contribution δS, $\delta S = S(T) - S_{LFL}(T) \propto \nu T \ln(T)$, in agreement with available experimental data on the specific heat of CeCoIn$_5$ [36].

Now we are in a position to show that the application of the magnetic field $H > H_{c2}$ on CeCoIn$_5$ generates a jump in the residual resistivity ρ_0. Indeed, as seen from Fig. 10.1, at low temperatures $T < T_{cross}$, the application of fields $H > H_{c2}$ drives the system from the SC state to the LFL one, where FC, or, equivalently, the flat portion of the spectrum $\varepsilon(\mathbf{p})$ are destroyed [8]. Thus, FC does not contribute any more to the residual resistivity ρ_0, thereby strongly reducing it. This conclusion is in agreement with experiment: at $H = 6$ T, one has $\rho_0 = 0.3\,\mu\Omega\,\text{cm}$, while at $H = 0$, $\rho_0 \simeq 1.5\,\mu\Omega\,\text{cm}$ [1]. Furthermore, we expect that the higher the quality of the CeCoIn$_5$ single crystal, the stronger is the suppression of ρ_0. In connection with this challenging behavior of the residual resistivity in magnetic fields, it makes sense to discuss the behavior of ρ_0 versus pressure P, studied in [37]. At $P > P^* = 1.6\,\text{GPa}$, ρ_0 drops reversibly by one order of magnitude to a very small value of about $0.2\,\mu\Omega\,\text{cm}$. Moreover, the experimental values of n in the coefficient AT^n of the resistivity, see (10.1), also increase strongly with increasing pressure for $P \to P^*$. Thus, the pressure P triggers an upward jump of the exponent n upon approaching P^* from below, and at $P \geq P^*$ $n = 2$ [37]. As result, at $P \simeq P^*$ CeCoIn$_5$ enters the LFL region, while the flat band vanishes. We can safely assume that the application of the pressure $P \geq P^*$ eliminates FC [38, 39], as it is demonstrated in Sect. 6.4 and depicted in Fig. 6.6. Indeed, as it is seen from Fig. 6.6, the system enters LFL region located above the critical density, and that region can be induced by the application of positive pressure. As a result, the application of the pressure removes the flat band, and makes ρ_0 jump to the very low value at $P \geq P^*$.

It should be emphasized that a nonzero contribution of FC to ρ_0 is associated with the presence of the crystal lattice, more precisely, with the Umklapp processes, violating momentum conservation. At the same time, such a restriction is absent in dealing with the thermal resistivity w_0. If, as usual, one normalizes the thermal resistivity by $w = \pi^2 T/(3e^2\kappa)$ where κ is the thermal conductivity, the famous Wiedemann-Franz relation then reads $\rho_0 = w_0$. The distinguished role of the Umklapp processes in the occurrence of ρ_0 in Fermi systems with FC implies that in the presence of FC, the Wiedemann-Franz law in some cases can be violated, so that $\rho_0 < w_0$.

10.3 The HF Metal YbRh$_2$Si$_2$

The nature of QCP dictates the NFL low-temperature properties of strongly correlated Fermi systems, notably HF metals, high-temperature superconductors, and quasi-two-dimensional ^{3}He. The experimental investigations of the much-studied compound YbRh$_2$Si$_2$ at very low temperatures probe the nature of its magnetic-field-tuned QCP. The jumps revealed both in the residual resistivity ρ_0 and in the Hall resistivity R_H, along with violation of the Wiedemann-Franz law, provide vitally important clues to the origin of such non-Fermi-liquid behavior. The experimental facts point unambiguously to association of the observed QCP with FCQPT.

The most fruitful strategy for exploring and revealing the nature of the QCP is to focus on those properties that exhibit the most spectacular deviations from the LFL behavior at the zero-temperature limit. In particular, incisive experimental measurements recently performed on the heavy-fermion metal $\mathrm{YbRh_2Si_2}$ have probed the nature of its magnetic-field-tuned QCP. It is found that at vanishingly low temperatures the residual resistivity ρ_0 experiences a jump across the magnetic QCP, with the crossover region proportional to T [40–43]. Jumps of the magnetoresistivity, the Hall coefficient, and the Lorenz number at zero temperature are in contradiction with the common behavior of Kondo systems, for which the width of the change region remains finite at zero temperature [42, 44]. Under the same experimental conditions in $\mathrm{YbRh_2Si_2}$, the Hall coefficient R_H is also found to experience a jump [41], while the data collected on heat and charge transport at the QCP can be interpreted as indicating a violation of the Wiedemann-Franz law [42]. The Wiedemann-Franz law defines the value of the Lorentz number $L = \kappa/T\sigma$ at $T \to 0$, i.e. $L = L_0$ with $L_0 = (\pi k_B)^2/3e^2$, where κ, σ, k_B, and e are respectively the thermal conductivity, the electrical conductivity, Boltzmann's constant, and the charge of the electron.

We begin with an analysis of the scaling behavior of the effective mass M^* and $T - B$ phase diagram of a homogeneous HF liquid, thereby avoiding complications associated with the crystalline anisotropy of solids [8]. Near the FCQPT, the temperature and magnetic field dependence of the effective mass $M^*(T, B)$ is governed by the Landau equation [33]

$$\begin{aligned}\frac{1}{M^*_\sigma(T,B)} =& \frac{1}{m} + \sum_{\sigma_1}\int \frac{\mathbf{p}_F\mathbf{p}}{p_F^3} F_{\sigma,\sigma_1}(\mathbf{p_F},\mathbf{p}) \\ & \times \frac{\partial n_{\sigma_1}(\mathbf{p},T,B)}{\partial p}\frac{d\mathbf{p}}{(2\pi)^3}. \qquad (10.20)\end{aligned}$$

We remind that $F_{\sigma,\sigma_1}(\mathbf{p_F},\mathbf{p})$ is the Landau interaction, p_F is the Fermi momentum, and σ is the spin label. To simplify matters, we ignore the spin dependence of the effective mass, noting that $M^*(T, B)$ is nearly independent of spin in weak fields. The quasiparticle distribution function n can be expressed as

$$n_\sigma(\mathbf{p},T) = \left\{1 + \exp\left[\frac{(\varepsilon(\mathbf{p},T) - \mu_\sigma)}{T}\right]\right\}^{-1}, \qquad (10.21)$$

where $\varepsilon(\mathbf{p}, T)$ is the single-particle (sp) spectrum. In the case under consideration, the sp spectrum depends on spin only weakly. However, the chemical potential μ_σ depends non-trivially on spin due to the Zeeman splitting, $\mu_\pm = \mu \pm B\mu_B$, where ± corresponds to states with the spin "up" or "down." Numerical and analytical solutions of this equation show that the dependence $M^*(T, B)$ of the effective mass gives rise to three different regimes with increasing temperature. In the theory of FC, if the system is located near the FCQPT on its ordered side, then the fermion condensate represents a group of quasiparticle states with dispersion given by [11]

$$\varepsilon(\mathbf{p}, n) - \mu = T \ln \frac{1 - n(\mathbf{p})}{n(\mathbf{p})}, \tag{10.22}$$

where μ is the chemical potential and $n(\mathbf{p})$ is the quasiparticle occupation number, which loses its temperature dependence at sufficiently low T. On the ordered side the sp spectrum of the HF liquid contains a flat portion embracing the Fermi surface. On the other hand, while the disordered side, at fixed, finite B and low temperatures we have a LFL regime with $M^*(T) \simeq M^* + aT^2$, where a is a positive constant [8]. Thus, the effective mass grows as a function of T, reaching its maximum M^*_M at some temperature T_M and subsequently diminishing according to [45]

$$M^*(T) \propto T^{-2/3}. \tag{10.23}$$

Moreover, the closer the control parameter B is to its critical value $B_{c0} = 0$, the higher is the growth rate. In this case, the peak value of M^*_M also grows, but the temperature T_M, at which M^* reaches its peak value decreases, so that $M^*_M(T_M, B \to B_{c0}) \to \infty$. At $T > T_M$, the last traces of LFL disappear. When the system is in the vicinity of the FCQPT, the approximate interpolative solution of (10.20) reads [8]

$$\frac{M^*}{M^*_M} = M^*_N(T_N) \approx c_0 \frac{1 + c_1 T_N^2}{1 + c_2 T_N^{8/3}}. \tag{10.24}$$

Here, $T_N = T/T_M$ is the normalized temperature, with $c_0 = (1 + c_2)/(1 + c_1)$ in terms of fitting parameters c_1 and c_2. Since the magnetic field enters (10.21) in the form of $\mu_B B/T$, we conclude that

$$T/T_M \propto \frac{T}{\mu_B B}, \tag{10.25}$$

where μ_B is the Bohr magneton. It follows from (10.25) that

$$T_M \simeq a_1 \mu_B B. \tag{10.26}$$

Equation (10.24) reveals the scaling behavior of the normalized effective mass $M^*_N(T_N)$. Indeed, the values of the effective mass $M^*(T, B)$ at different magnetic fields B merge into a single value of the mass M^*_N dependent upon the normalized variable $T_N = T/T_M$ [8]. The inset in Fig. 10.1 demonstrates the scaling behavior of the normalized effective mass M^*_N versus the normalized temperature T_N. The LFL phase prevails at $T \ll T_M$, followed by the $T^{-2/3}$ regime at $T \gtrsim T_M$. The latter phase is NFL due to the strong dependence of the effective mass on temperature. The temperature region $T \simeq T_M$ encompasses the transition between the LFL regime with almost constant effective mass and the NFL behavior described by (10.23). Thus, $T \sim T_M$ identifies the transition region featuring a crossover between LFL and NFL regimes. The inflection point T_{inf} of M^*_N versus T_N is depicted by an arrow in the inset of Fig. 10.4.

The transition (or crossover) temperature $T_M(B)$ is not actually the temperature of a phase transition. Its specification is necessarily ambiguous, depending as it does

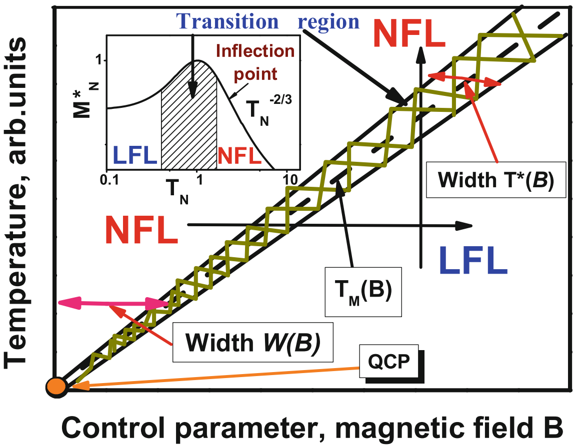

Fig. 10.4 Schematic $T - B$ phase diagram of HF liquid with magnetic field as the control parameter. The *vertical* and *horizontal arrows* show *LFL-NFL* and reverse transitions at fixed B and T, respectively. At $B = 0$ the system is in its *NFL* state having a flat band, and demonstrates NFL behavior down to $T \rightarrow 0$. The *hatched area* separates the *NFL* phase and the weakly polarized *LFL* one and represents the transition area. The *dashed line* in the *hatched area* represents the function $T_M(B)$ (10.26). The functions $W(B) \propto T$ and $T^*(B) \propto T$ shown by *two-headed arrows* define the *NFL* state width and the transition area, respectively. The *QCP* located at the origin and indicated by an *arrow* denotes the critical point, where the effective mass M^* diverges and both $W(B)$ and $T^*(B)$ tend to zero. The *inset* shows a schematic plot of the normalized effective mass versus the normalized temperature. The transition regime, where M^*_N reaches its maximum value at $T_N = T/T_M = 1$, is shown as the *hatched area* in both the main panel and the *inset*. *Arrows* indicate the transition region and the inflection point $T_{\rm inf}$ in the M^*_N plot

upon the criteria invoked for determination of the crossover point. As usual, the temperature $T^*(B)$ is extracted from the field dependence of charge transport, for example from the resistivity $\rho(T)$, given by

$$\rho(T) = \rho_0 + AT^{\alpha_R}, \tag{10.27}$$

where ρ_0 is the residual resistivity and A is a T-independent coefficient. The term ρ_0 is ordinarily attributed to impurity scattering. The LFL state is characterized by the T^{α_R} dependence of the resistivity with the index $\alpha_R = 2$. The crossover through the transition regime shown as the hatched area in both Fig. 10.1 and its inset takes place at temperatures, where the resistance starts to deviate from LFL behavior, with the exponent α_R shifting from 2 into the region, where it is in the range $1 < \alpha_R < 2$.

The schematic phase diagram of a HF metal is depicted in Fig. 10.4, with the magnetic field B serving as the control parameter. At $B = 0$, the HF liquid acquires a flat band corresponding to a strongly degenerate state. The NFL regime dominates at elevated temperatures and a fixed magnetic field. With increasing B, the system is driven from the NFL to LFL domain. As shown in Fig. 10.4, the system moves from

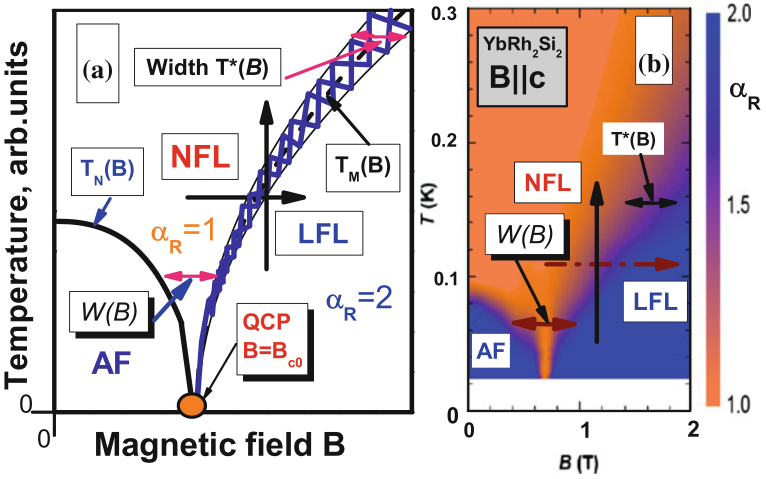

Fig. 10.5 The phase diagram of the HF metal YbRh$_2$Si$_2$. Panel **a** represents a schematic phase diagram of YbRh$_2$Si$_2$, with $T_N(B)$ denoting the Nèel temperature as a function of magnetic field B. The *QCP*, identified by an *arrow*, is now shifted to $B = B_{c0}$. At $B < B_{c0}$ the system is in its AF state. As in Fig. 10.4, the *vertical* and *horizontal arrows* show the transitions between the *LFL* and *NFL* states, the functions $W(B) \propto T$ and $T^*(B) \propto T$ indicated with *bi-directional arrows* define the width of the *NFL* state and that of the transition region, respectively. The *dashed line* in the *hatched area* represents the function $T_M(B)$ (10.26). The exponent α_R determines the temperature-dependent part of the resistivity (cf. (10.27)), with α_R taking values 2 and 1, respectively, in *LFL* and *NFL* states. In the transition regime the exponent evolves between *LFL* and *NFL* values. Panel **b** shows the experimental $T - B$ phase diagram [42, 49]. The evolution of α_R is depicted by *color* (coded in the *vertical stripe* on the *right-hand side* of the panel). The *NFL* behavior reaches to the lowest temperatures right at the *QCP*, tuned by the magnetic field. The transition regime between the *NFL* state and the field-induced *LFL* state broadens with rising magnetic fields $B > B_{c0}$ and $T \sim T^*(B)$. As in panel **a**, transitions from *LFL* to *NFL* state and from *NFL* to *LFL* state are indicated by the corresponding *arrows*, as are $W(B) \propto T$ and $T^*(B) \propto T$

the NFL to the LFL regime along the horizontal arrow, and from the LFL to NFL along the vertical arrow. The magnetic-field-tuned QCP is indicated by an arrow and located at the origin of the phase diagram, since application of a magnetic field destroys the flat band and shifts the system into the LFL state [8, 12, 38]. The hatched area denoting the transition region separates the NFL state from the weakly polarized LFL state and contains the dashed line tracing $T_M(B)$. Referring to (10.26), this line is defined by the function $T = a_1\mu_B B$, and the width $W(B)$ of the NFL state is seen to be proportional T. In the same way, it can be shown that the width $T^*(B)$ of the transition region is also proportional to T.

We focus on the HF metal YbRh$_2$Si$_2$, whose experimentally observed $T-B$ phase diagram is reproduced in panels a and b of Fig. 10.5. Panel a is similar to the main one of Fig. 10.4, but with the distinction that this HF compound possesses a finite critical magnetic field $B_{c0} \neq 0$ that shifts the QCP from the origin of the coordinates. To avert realization of a strongly degenerate ground state induced by the flat band, the FC must be completely eliminated at $T \to 0$. In a natural scenario, this occurs by means of an AF phase transition with an ordering temperature $T_N = 70$ mK, while application of a magnetic field $B = B_{c0}$ destroys the AF state at $T = 0$ [46]. In other words, the field B_{c0} places the HF metal at the magnetic-field-tuned QCP and nullifies the Nèel temperature $T_N(B_{c0}) = 0$ of the corresponding AF phase transition [8, 47]. Imposition of a magnetic field $B > B_{c0}$ drives the system to the LFL state. Thus, in the case of $YbRh_2Si_2$, the QCP is shifted from the origin to $B = B_{c0}$. In FC theory, the quantity B_{c0} is a parameter determined by the properties of the specific heavy-fermion metal. In some cases, notably the HF metal $CeRu_2Si_2$, B_{c0} does vanish [48], whereas in $YbRh_2Si_2$, $B_{c0} \simeq 0.06$ T, $B \perp c$ [46].

Panel b of Fig. 10.5 portrays the experimental $T - B$ phase diagram showing the evolution of the exponent $\alpha_R(T, B)$ [42, 49]. At the critical field $B_{c0} \simeq 0.66$ T ($B \| c$), the NFL behavior extends down to the lowest temperatures, while $YbRh_2Si_2$ transits from the NFL to LFL domain with the increase of the applied magnetic field. Vertical and horizontal arrows indicate the transition from the LFL to the NFL state and its reversal, respectively. The functions $W(B) \propto T$ and $T^*(B) \propto T$ associated with bi-directed arrows define the width of the NFL state and transition region, respectively. It is noteworthy that the schematic phase diagram displayed in panel a of Fig. 10.5 is in close qualitative agreement with its experimental counterpart in panel b.

To calculate the low-temperature dependence of ρ on the imposed magnetic field B in the normal state of $YbRh_2Si_2$, we employ a model of a HF liquid possessing a flat band with dispersion given by (10.22). Since the resistivity at $T \to 0$ is our primary concern, we concentrate on a special contribution to the residual resistivity ρ_0 which we call the critical residual resistivity ρ_0^c. Analysis begins with the case $B = 0$, for which the resistivity of the HF liquid at low temperatures is a linear function of T [8, 50]. This observation coincides with experimental data obtained from measurements on $YbRh_2Si_2$ indicating the presence of a flat band in $YbRh_2Si_2$ [8, 46, 50, 51]. In that case, the effective mass $M^*(T)$ of the FC quasiparticles takes the form

$$M^*(T) \sim \frac{\eta p_F^2}{4T}, \tag{10.28}$$

where $\eta = \delta p/p_F$ is determined by the characteristic size δp of the momentum interval L occupied by the FC. With the result (10.28) the width γ of FC quasiparticles is calculated in closed form, $\gamma \sim \gamma_0 + \eta T$, where γ_0 is a constant [52]. This result leads to the lifetime τ_q of quasiparticles

$$\frac{\hbar}{\tau_q} \simeq a_1 + a_2 T, \tag{10.29}$$

where a_1 and a_2 are parameters. Equation (10.29) is in excellent agreement with experimental observations [53]. In general, the electronic liquid in HF metals is represented by several bands, occupied by quasiparticles that simultaneously intersect the Fermi surface. FC quasiparticles never cover the entire Fermi surface. Thus, there exist LFL quasiparticles with the effective mass M_L^* independent of T and FC quasiparticles with M^* given by (10.28) at the Fermi surface, and all of them possess the same width γ. Upon appealing to the standard equation

$$\sigma \sim \frac{Ne^2}{\gamma M^*} \tag{10.30}$$

for the conductivity σ (see e.g., [33]) and taking into account the formulas specifying M^* and γ, we find that $\sigma \sim Ne^2/(p_F\eta)^2$, where N is the number density of electrons. With this result, we arrive at the critical residual resistivity ρ_0^c that is independent of T:

$$\rho_0^c \sim \frac{\eta^2}{p_F e^2}. \tag{10.31}$$

Derivation and examination of (10.30) and (10.31) is provided in Sect. 10.2. The term "residual resistivity" is usually attributed to impurity scattering. In our case, (10.31) shows that ρ_0^c is determined by the presence of a flat band and has no relation to the scattering of quasiparticles by impurities [52].

We next demonstrate that the application of a magnetic field to the HF liquid generates the observed step-like drop in the residual resistivity ρ_0. Indeed, Fig. 10.4 informs us that at a fixed temperature, application of the field B drives the system from the NFL state to the LFL state, the flat portion of $\varepsilon(\mathbf{p})$ being determined by (10.3) is destroyed at $T < T_M$ [8]. Thereupon, the factor η vanishes, nullifying ρ_0^c and strongly reducing ρ_0. Since both $W(B)$ and $T^*(B)$ widths are proportional to T, the imposition of the magnetic field causes a step-like drop in the residual resistivity ρ_0. Consequently two values of the residual resistivity must be introduced, namely ρ_0^{NFL} corresponding to the NFL state, and ρ_0^{LFL} corresponding to the LFL state induced under the application of magnetic field B. It follows from these considerations that $\rho_0^{NFL} > \rho_0^{LFL}$. This conclusion agrees with the experimental findings [40–42].

Figure 10.5 shows the $T-B$ phase diagram of $YbRh_2Si_2$, which maps faithfully onto the schematic phase diagram depicted in Fig. 10.4, except for the appearance of an AF phase at low temperatures. As seen from Fig. 10.5, at $T > T_N$ and $B = 0$ the system in its NFL state, while the LFL phase prevails at low temperature for magnetic fields beyond the critical value B_{c0}. The respective residual resistivities are measured at $\rho_0^{NFL} \simeq 0.55\,\mu\Omega\,\text{cm}$ (NFL) and $\simeq 0.5\,\mu\Omega\,\text{cm}$ (LFL) [40]. As T is lowered through T_N at $B = 0$ the system enters the AF state via a second-order phase transition. Accordingly, we expect that the residual resistivity does not change, remaining the same as that of the NFL state, ρ_0^{NFL}. On the other hand, under imposition of an increasing B-field, the system moves from the NFL state to the LFL state with the above value of ρ_0^{LFL}.

At this point it should be acknowledged that application of a weak magnetic field is known to produce a positive classical contribution $\propto B^2$ to ρ_0 arising from orbital motion of carriers induced by the Lorentz force. When considering spin-orbit coupling in disordered electron systems, where electron motion is diffusive, the magnetoresistivity may have both positive (weak localization) and negative (weak anti-localization) signs [54]. However, as studied experimentally, $YbRh_2Si_2$ is one of the purest heavy-fermion metals. Hence the applicable regime of electron motion

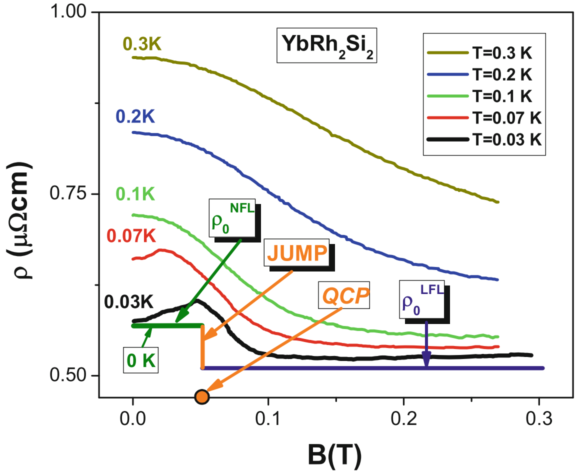

Fig. 10.6 Experimental results [40] for the longitudinal magnetoresistivity $\rho(T, B)$ of $\mathrm{YbRh_2Si_2}$ versus B at various temperatures T. The maxima of the *curves* for $T = 0.03$ and 0.07 K correspond to boundary points of the AF ordered state shown in Fig. 10.5b. The *solid line* marked with 0 K represent the schematic behavior of the residual resistivity ρ_0 as a function of B. The *arrows* pointing to the *horizontal solid lines* identify the residual resistivities ρ_0^{NFL} and ρ_0^{LFL} in $\mathrm{YbRh_2Si_2}$. The *jump* of ρ_0 occurs at the *QCP* identified by an *arrow*

is ballistic rather than diffusive. Both weak and anti-weak localization scenarios are irrelevant, and one expects the B-dependent correction to ρ_0 to be positive. We therefore conclude that the positive difference $\rho_0^c = \rho_0^{NFL} - \rho_0^{LFL}$ comes from the contribution related to the flat band. As seen from Fig. 10.6, when the system moves from NFL to the LFL state at fixed T and under application of elevated magnetic fields B, the step-like drop in its resistivity $\rho(T, B)$ becomes more pronounced, as it is seen from the experimental curves for $T = 0.3, 0.2, 0.1$ K.

This behavior is a simple consequence of the fact that the width of the crossover regime is proportional to T. By zooming the vicinity of QCP shown in Fig. 10.6, what corresponds, for example, to the experimental curves for $T = 0.07$ and 0.03 K, it may be seen that the crossover width remains proportional to temperature, ultimately shrinking to zero and leading to the abrupt jump in the residual resistivity at $T = 0$, when the system crosses the QCP at $B = B_{c0}$. In the same way, application of a magnetic field B to $\mathrm{CeCoIn_5}$ causes a step-like drop in its residual resistivity, as is in fact found experimentally [1]. Based on this reasoning, we expect that the higher the quality of both $\mathrm{CeCoIn_5}$ and $\mathrm{YbRh_2Si_2}$ single crystals, the greater is the ratio $\rho_0^{NFL}/\rho_0^{LFL}$, since the contribution coming from the impurities diminishes and ρ_0^{NFL} approaches ρ_0^c. It is also expected from (10.31) that the observed difference ρ_0^c in the residual resistivities will not show a marked dependence on the imperfections of the single crystal unless the impurities destroy the flat band. Finally, we point out that the jump of the magnetoresistivity at zero temperature contradicts the usual behavior of Kondo systems, with the width of the transition remaining finite at $T \to 0$ [41, 44]. Moreover, the Kondo systems has nothing to do with the asymmetrical tunnelling conductance as a function of the applied voltage V that has been predicted to emerge in such HF metals with the flat band as $CeCoIn_5$ and $YbRh_2Si_2$ [8, 55, 56]. Indeed, experimental observations have revealed that the conductance is the dissymmetrical function of V in both $CeCoIn_5$ [57] and $YbRh_2Si_2$ [51].

The emergence of a flat band entails a change of the Hall coefficient $R_H = \sigma_{xyz}/\sigma_{xx}^2$ [7, 58]. In homogeneous matter at $B \to 0$ one has $\sigma_{xx} = \sigma/3$, while σ_{xyz} is recast to

$$\sigma_{xyz} = \frac{e^3}{3\gamma^2} \int \left[\frac{dz}{dp}\right]^2 \frac{\partial n(z)}{\partial z} dz, \tag{10.32}$$

where $n(z)$ is the quasiparticle distribution function. Far from the QCP, these formulas lead to the standard result $R_H = 1/Ne$, whereas in the vicinity of the QCP, one finds $R_H = K/xe$ with $K \simeq 1.5$, x is the charge carrier density, and K is a coefficient [7]. We see then that the effective volume of the Fermi sphere shrinks considerably at the QCP. Importantly, in the LFL state where the effective mass stays finite, the value $K = 1$ holds even quite close to the QCP. As we have learned, the width $W(B)$ tends to zero at the QCP, implying that the critical behavior of K at $T \to 0$ emerges abruptly, producing a jump in the Hall coefficient, while the height of the jump remains finite. It is instructive to consider the physics of this jump of R_H in the case of $YbRh_2Si_2$. At $T = 0$, the critical magnetic field B_{c0} destroying the AF phase is determined by the condition that the ground-state energy of the AF phase is equal to the ground-state energy of the HF liquid in the LFL paramagnetic state. Hence, at $B \to B_{c0}$ the Néel temperature T_N tends to zero. In the measurements of the Hall coefficient R_H as a function of B, performed in $YbRh_2Si_2$ [41, 43, 59], a jump is detected in R_H as $T \to 0$ when the applied magnetic field reaches its critical value $B = B_{c0}$ and then goes infinitesimally higher: $B = B_{c0} + \delta B$. At $T = 0$, application of the critical magnetic field B_{c0}, which suppresses the AF phase whose Fermi momentum is p_F, restores the LFL phase with a Fermi momentum $p_f > p_F$. This occurs because the quasiparticle distribution function becomes multiply connected and the number of mobile electrons does not change [8]. The AF state can then be viewed as having a "small" Fermi surface characterized by the Fermi momentum p_F, whereas the LFL paramagnetic ground state at $B > B_{c0}$ has a "large" Fermi surface with $p_f > p_F$. As a result, the Hall coefficient experiences a sharp jump because $R_H(B) \propto 1/p_F^3$ in the AF phase and $R_H(B) \propto 1/p_f^3$ in the paramagnetic phase. Assuming that $R_H(B)$ is a measure of the Fermi momentum [58, 59] (as is the case with a simply connected Fermi volume), we arrive at (8.9) of Chap. 8.

Violation of the Wiedemann-Franz law at the QCP in HF metals has been predicted and estimated a few years ago [8, 61] and experimentally observed recently [42]. As it will be shown in Chap. 14, the predictions of LFL theory fail near QCP where the effective mass M^* diverges. The violation of the Wiedemann-Franz law takes place in the narrow segment of the $T - B$ phase diagram displayed in Fig. 14.2, panel a, having the width $W \to 0$ at $T \to 0$. In other words, at $T \to 0$ the ratio L/L_0 becomes abruptly $L/L_0 \sim 0.9$ at $B/B_{c0} = 1$, while $L/L_0 = 1$ at $B/B_{c0} \neq 1$ when the system is in its AF or LFL state shown in Fig. 14.2, panels a, b. The violation at

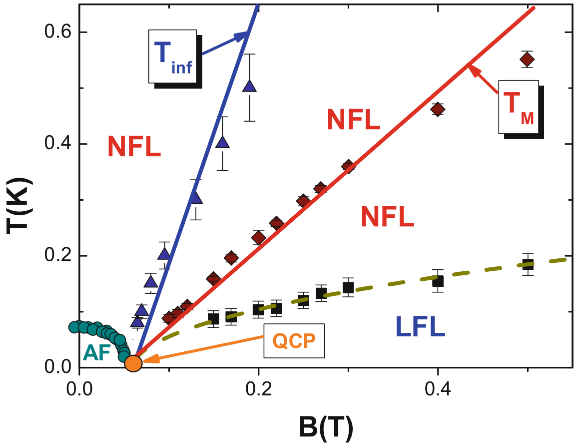

Fig. 10.7 Temperature–magnetic field ($T - B$) phase diagram of YbRh$_2$Si$_2$. *Solid circles* represent the boundary between *AF* and *NFL* states and the *QCP* is shown by the *arrow*. *Solid squares* refer to the boundary between *NFL* and *LFL* regimes [40, 41] represented by the *dashed line*, which is approximated by $(B - B_{c0})^{1/2}$ [8]. *Diamonds* mark the maxima T_M of the specific heat C/T [60], which are approximated by $T_M \propto b_1(B - B_{c0})$, with b_1 being a fitting parameter [8]. *Triangles* close to the *solid line* refer to the inflection points $T_{\rm inf}$ in the longitudinal magnetoresistivity [40, 41], while the *solid line* tracks the function $T_{\rm inf} \propto b_2(B - B_{c0})$, with b_2 being a fitting parameter

$B = B_{c0}$ and at $T \to 0$ seen in YbRh$_2$Si$_2$ thus suggests that a sharp Fermi surface does exist at $B/B_{c0} \neq 1$, but does not exist only at $B/B_{c0} = 1$ where the flat band emerges.

The application of magnetic field profoundly effects on the single-particle spectrum, and leads to the scaling behavior of the normalized effective mass, as it is demonstrated in Sect. 6.3. The peculiarities of the scaling behavior generates the energy scales shown in Fig. 10.7. Among other features, Fig. 10.7 includes results (solid lines) for the characteristic temperatures $T_{\rm inf}(B)$ and $T_M(B)$, which represent the positions of the kinks that separate the energy scales identified experimentally in [40, 41, 60]. The boundary between the NFL and LFL phases is indicated by a dashed line, while AF labels the antiferromagnetic phase. The corresponding data are taken from [40, 41, 60]. It is seen that our calculations coincide with the experimental data. In particular, we conclude that the energy scales and the widths W and T^* are reproduced by (10.24) and (10.26), and related to the special points $T_{\rm inf}$ and T_M associated with the normalized effective mass M^*_N, which are marked with arrows in the inset and the main panel of Fig. 10.4 [8, 62].

10.4 Main Results

In this Chapter, we have shown that imposition of a magnetic field on YbRh$_2$Si$_2$ and CeCoIn$_5$ leads to the emergence of the quantum critical point. With the increase of magnetic field, a strong suppression of the residual resistivity ρ_0 takes place.

In the case of CeCoIn_5 it is also explained that the same jump takes place under the application of both pressure and magnetic field. By considering the behavior of the thermal expansion coefficient and the specific heat we have unveiled the role of the flat band in forming thermodynamic properties of CeCoIn_5. Our consideration presents one of the direct evidences for the presence of the flat band in CeCoIn_5. The close similarity between the behaviors of the Hall coefficient R_H, magnetoresistivity ρ, and Lorenz number L at the QCP indicates that all transport measurements reflect the same underlying physics, which unambiguously entails an interpretation of the QCP as arising from the fermion condensation quantum phase transition leading to the formation of a flat band. The imposition of magnetic field is also led to the emergence of the energy scales, that is explained within the framework of FC theory.

References

1. J. Paglione, M. Tanatar, D. Hawthorn, E. Boaknin, R.W. Hill, F. Ronning, M. Sutherland, L. Taillefer, C. Petrovic, P. Canfield, Phys. Rev. Lett. **91**, 246405 (2003)
2. F. Ronning, C. Capan, A. Bianchi, R. Movshovich, A. Lacerda, M.F. Hundley, J.D. Thompson, P.G. Pagliuso, J.L. Sarrao, Phys. Rev. B **71**, 104528 (2005)
3. J. Paglione, M.A. Tanatar, D.G. Hawthorn, F. Ronning, R.W. Hill, M. Sutherland, L. Taillefer, C. Petrovic, Phys. Rev. Lett. **97**, 106606 (2006)
4. H.v. Löhneysen, A. Rosch, M. Vojta, P. Wölfle, Rev. Mod. Phys. **79**, 1015 (2007)
5. E.M. Lifshitz, L.P. Pitaevskii, *Physical Kinetics* (Pergamon Press, Oxford, 1981)
6. V.A. Khodel, M.V. Zverev, JETP Lett. **70**, 772 (1999)
7. V.A. Khodel, M.V. Zverev, J.W. Clark, JETP Lett. **81**, 315 (2005)
8. V.R. Shaginyan, M.Y. Amusia, A.Z. Msezane, K.G. Popov, Phys. Rep. **492**, 31 (2010)
9. V.A. Khodel, V.R. Shaginyan, JETP Lett. **51**, 553 (1990)
10. G.E. Volovik, JETP Lett. **53**, 222 (1991)
11. P. Nozières, J. Phys. I France **2**, 443 (1992)
12. V.A. Khodel, J.W. Clark, M.V. Zverev, Phys. Atom. Nuclei **74**, 1237 (2011)
13. G.E. Volovik, *The Universe in a Helium Droplet* (Clarendon Press, Oxford, 2003)
14. G.E. Volovik, JETP Lett. **59**, 830 (1994)
15. S.S. Lee, Phys. Rev. D **79**, 086006 (2009)
16. D. Green, L. Santos, C. Chamon, Phys. Rev. B **82**, 075104 (2010)
17. T.T. Heikkilä, N.B. Kopnin, G.E. Volovik, JETP Lett. **94**(252), 233 (2011)
18. M.V. Zverev, V.A. Khodel, V.R. Shaginyan, M. Baldo, JETP Lett. **65**, 863 (1997)
19. N. Oeschler, P. Gegenwart, M. Lang, R. Movshovich, J.L. Sarrao, J.D. Thompson, F. Steglich, Phys. Rev. Lett. **91**, 076402 (2003)
20. R. Settai, H. Shishido, S. Ikeda, Y. Murakawa, M. Nakashima, D. Aoki, Y. Haga, H. Harima, Y. Onuki, J. Phys.: Condens. Matter **13**, L627 (2001)
21. A. McCollam, J.S. Xia, J. Flouquet, D. Aoki, S.R. Julian, Physica B **403**, 717 (2008)
22. A.A. Shashkin, V.T. Dolgopolov, J.W. Clark, V.R. Shaginyan, M.V. Zverev, V.A. Khodel, Phys. Rev. Lett. **112**, 186402 (2014)
23. M.V. Zverev, M. Baldo, J. Phys. Condens. Matter **11**, 2059 (1999)
24. S.A. Artamonov, Y.G. Pogorelov, V.R. Shaginyan, JETP Lett. **68**, 942 (1998)
25. V.A. Khodel, J.W. Clark, M.V. Zverev, Phys. Rev. B **78**, 075120 (2008)
26. V.A. Khodel, V.R. Shaginyan, V.V. Khodel, Phys. Rep. **249**, 1 (1994)
27. G.E. Volovik, JETP Lett. **93**, 66 (2011)
28. N.B. Kopnin, T.T. Heikkilä, G.E. Volovik, Phys. Rev. B **83**, 220503(R) (2011)
29. G.E. Volovik, JETP Lett. **91**, 55 (2010)

30. F. Ronning, C. Capan, E.D. Bauer, J.D. Thompson, J.L. Sarrao, R. Movshovich, Phys. Rev. B **73**, 064519 (2006)
31. J.G. Donath, F. Steglich, E.D. Bauer, J.L. Sarrao, P. Gegenwart, Phys. Rev. Lett **100**, 136401 (2008)
32. S. Zaum, K. Grube, R. Schäfer, E.D. Bauer, J.D. Thompson, H. v. Löhneysen, Phys. Rev. Lett. **106**, 087003 (2011)
33. A.A. Abrikosov, L.P. Gorkov, I.E. Dzyaloshinski, *Methods of Quantum Field Theory in Statistical Physics* (Dover, New York, 1975)
34. C. Petrovic, P.G. Pagliuso, M.F. Hundley, R. Movshovich, J.L. Sarrao, J.D. Thompson, Z. Fisk, P. Monthoux, J. Phys. Condens. Matter **13**, L337 (2001)
35. V.A. Khodel, M.V. Zverev, V.M. Yakovenko, Phys. Rev. Lett. **95**, 236402 (2005)
36. J.S. Kim, J. Alwood, G.R. Stewart, J.L. Sarrao, J.D. Thompson, Phys. Rev. B **64**, 134524 (2001)
37. V.A. Sidorov, M. Nicklas, P.G. Pagliuso, J.L. Sarrao, Y. Bang, A.V. Balatsky, J.D. Thompson, Phys. Rev. Lett. **89**, 157004 (2002)
38. V.R. Shaginyan, Phys. Atom. Nuclei **74**, 1107 (2011)
39. V.R. Shaginyan, A.Z. Msezane, K.G. Popov, G.S. Japaridze, V.A. Khodel, Europhys. Lett. **106**, 37001 (2014)
40. P. Gegenwart, T. Westerkamp, C. Krellner, Y. Tokiwa, S. Paschen, C. Geibel, F. Steglich, E. Abrahams, Q. Si, Science **315**, 969 (2007)
41. S. Friedemann, N. Oeschlera, S. Wirtha, C. Krellnera, C. Geibela, F. Steglicha, S. Paschenb, S. Kirchnerc, Q. Sic, Proc. Natl. Acad. Sci. USA **107**, 14547 (2010)
42. H. Pfau, S. Hartmann, U. Stockert, P. Sun, S. Lausberg, M. Brando, S. Friedemann, C. ius Krellner, C. Geibel, S. Wirth, S. Kirchner, E. Abrahams, Q. Si, F. Steglich, Nature **484**, 493 (2012)
43. S. Friedemann, N. Oeschler, S. Wirth, C. Krellner, C. Geibel, F. Steglich, S. Paschen, S. Kirchner, Q. Si, J. Phys.: Condens. Matter **23**, 094216 (2011)
44. P. Schlottmann, Z. Phys, B **51**, 223 (1983)
45. J.W. Clark, V.A. Khodel, M.V. Zverev, Phys. Rev. B **71**, 012401 (2005)
46. P. Gegenwart, J. Custers, C. Geibel, K. Neumaier, K.T.T. Tayama, O. Trovarelli, F. Steglich, Phys. Rev. Lett. **89**, 056402 (2002)
47. V.R. Shaginyan, JETP Lett. **79**, 286 (2004)
48. D. Takahashi, S. Abe, H. Mizuno, D. Tayurskii, K. Matsumoto, H. Suzuki, Y. Onuki, Phys. Rev. B **67**, 180407(R) (2003)
49. J. Custers, P. Gegenwart, H. Wilhelm, K. Neumaier, Y. Tokiwa, O. Trovarelli, C. Geibel, F. Steglich, C. Pépin, P. Coleman, Nature **424**, 524 (2003)
50. V.A. Khodel, M.V. Zverev, JETP Lett. **85**, 404 (2007)
51. S. Ernst, S. Kirchner, C. Krellner, C. Geibel, G. Zwicknagl, F. Steglich, S. Wirth, Nature **474**, 363 (2011)
52. V.R. Shaginyan, A.Z. Msezane, K.G. Popov, J.W. Clark, M.V. Zverev, V.A. Khodel, Phys. Rev. B **86**, 085147 (2012)
53. P. Aynajian, E. Neto, A. Gyenis, R.E. Baumbach, J.D. Thompson, Z. Fisk, E.D. Bauer, A. Yazdani, Nature **486**, 201 (2012)
54. S. Hikami, A.I. Larkin, Y. Nagaoka, Prog. Theor. Phys. **63**, 707 (1980)
55. V.R. Shaginyan, JETP Lett. **81**, 222 (2005)
56. V.R. Shaginyan, K.G. Popov, Phys. Lett. A **361**, 406 (2007)
57. W.K. Park, L.H. Greene, J. Phys.: Condens. Matter **21**, 103203 (2009)
58. M.R. Norman, Q. Si, Y.B. Bazaliy, R. Ramazashvili, Phys. Rev. Lett. **90**, 116601 (2002)
59. S. Paschen, T. Lühmann, S. Wirth, P. Gegenwart, O. Trovarelli, C. Geibel, F. Steglich, P. Coleman, Q. Si, Nature **432**, 881 (2004)
60. N. Oeschler, S. Hartmann, A. Pikul, C. Krellner, C. Geibel, F. Steglich, Physica B **403**, 1254 (2008)
61. V.A. Khodel, V.M. Yakovenko, M.V. Zverev, JETP Lett. **86**(86), 772 (2007)
62. V.R. Shaginyan, M.Y. Amusia, A.Z. Msezane, K.G. Popov, V.A. Stephanovich, Phys. Lett. A **373**, 986 (2009)

Chapter 11
Zero Temperature Magnetoresistance of the HF Metal: Enigma of $Sr_3Ru_2O_7$

Abstract To understand the nature of field-tuned metamagnetic quantum criticality in the ruthenate $Sr_3Ru_2O_7$ is one of the significant challenges in the condensed matter physics. It is established experimentally that the entropy has a peak in the ordered phase. It is unexpectedly higher than that outside latter phase, while the magnetoresistivity varies abruptly near the ordered phase boundary. We demonstrate unexpected similarity between $Sr_3Ru_2O_7$ and HF metals expressing universal physics that transcends microscopic details. Our $T - B$ phase diagram of $Sr_3Ru_2O_7$ explains main features of the experimental situation. It gives an unambiguous interpretation of its extraordinary low-temperature thermodynamics in terms of FCQPT, leading to the flat band formation at the restricted range of magnetic fields B.

11.1 Introduction: Flat Bands and Enigma of Metamagnetic Quantum Critical Regime in $Sr_3Ru_2O_7$

Discoveries of surprising and exotic phenomena in strongly correlated metals provide unique opportunities for expanding our understanding of quantum critical physics. A case in point is the quantum critical metal $Sr_3Ru_2O_7$, a member of the Ruddlesden-Popper series of layered perovskite ruthenates consisting of RuO_2 *ab* planes forming bilayers, which are piled along the crystalline *c* axis, perpendicular to the *ab* axis, and weakly coupled to one another. In spite of numerous experimental and theoretical investigations [1–13], explanation of the puzzling low-temperature behavior of this material in external magnetic fields B remains an open problem in condensed matter theory, for reviews see e.g., [14, 15]. The observations indicate that the physics that determines the behavior of $Sr_3Ru_2O_7$, which resembles that of some HF metals, is not subsumed in the spin-Kondo picture [8–10]. In high quality crystals with residual resistivity $\rho_{\text{res}} \sim 0.4\,\mu\Omega\,\text{cm}$ measured at zero B-field and mean free path as big as approximately 3,000 Å, one observes a metamagnetic transition featuring a sudden and sharp rise in the magnetization $\mathbf{M}$ with a modest increase in the applied field [14, 15], accompanied by a bifurcation of the metamagnetic phase boundary. At low temperatures the bifurcation splits into two first-order metamagnetic transitions at critical magnetic field values $B_{c1} \simeq 7.8\,\text{T}$ and $B_{c2} \simeq 8.1\,\text{T}$ [2–4, 14, 15]. Conventionally, a phase that emerges at fields $B_{c1} < B < B_{c2}$ and temperatures $T \leq T_c \simeq 1.2\,\text{K}$

M.Y. Amusia et al., *Theory of Heavy-Fermion Compounds*, Springer Series in Solid-State Sciences 182, DOI 10.1007/978-3-319-10825-4_11

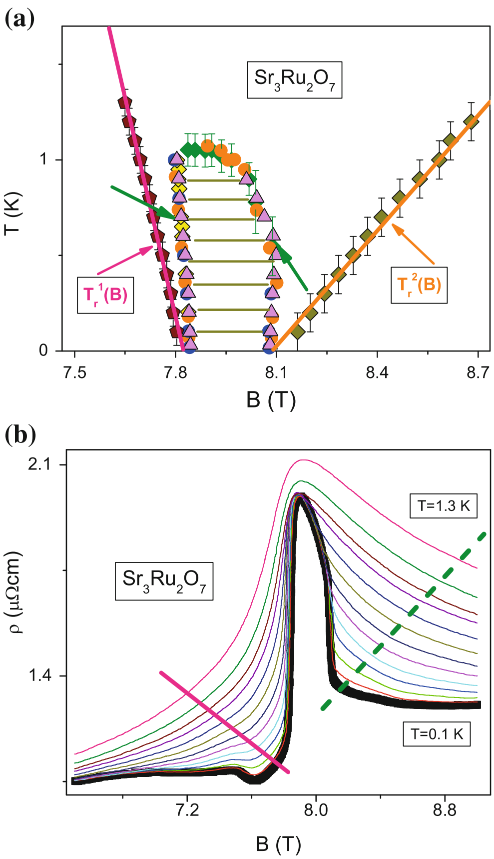

Fig. 11.1 The $T - B$ phase diagram and the magnetoresistivity $\rho(B)$. Panel **a** experimental phase diagram of $Sr_3Ru_2O_7$ in the $T - B$ plane with magnetic field B as the control parameter. Symbols, depicting data points derived from susceptibility, magnetostriction, thermal expansion and transport measurements, surround the area with *horizontal lines*, and represent transitions between equilibrium thermodynamic phases associated with a nematic ordered phase [3–5]. This phase is entered by the first-order phase transitions at low temperatures (the corresponding tricritical points is indicated by the *arrows*) and by the second-order phase transitions at high temperatures. The *solid lines* $T_r^1(B)$ and $T_r^2(B)$ on the low- and high-field sides of the plot, respectively, sketch the temperature-field dependence of the crossings of the resistivity $\rho(B, T)$ drawn in panel **b** with two *straight lines*, *solid* and *dashed*, respectively. Panel **b** the measured resistivity $\rho(B)$ of $Sr_3Ru_2O_7$ for temperatures between 0.1 and 1.3 K, in steps of 0.1 K [3, 4]

is identified as a nematic one [3–5, 7]. This phase breaks the discrete square lattice rotational symmetry, as witnessed by a large magnetoresistive anisotropy in the *ab* plane as the magnetic field B is rotated away from the c axis toward the *ab* plane [3–5]. The anisotropy vanishes as soon as the B-field is directed along the c axis, here we consider only this case denoted as $B \parallel c$. The two first-order transitions persist, but convert into two second-order phase transitions with rising temperature as is illustrated in Fig. 11.1a. The bifurcation is accompanied by the abrupt variation of the resistivity as it is shown in Fig. 11.1b. Moreover, the entropy S within the ordered phase, shown in Fig. 11.1a with horizontal lines, forms a peak, and is unexpectedly higher than that outside this phase, for one would expect that the entropy of the disorder phase should be higher than that of the ordered [7]. As result, we face the enigmatic behavior, exhibited by the thermodynamic and transport properties, of the quantum critical metal $Sr_3Ru_2O_7$. As it was shown in Chaps. 3, 8 and 10, such a behavior is associated with FC and the presence of flat bands, and we apply the theory of FC to resolve the enigma. For the reader convenience here we recapitulate some important points of preceding consideration.

11.2 Magnetoresistivity

The magnetoresistivity $\rho(B, T)$ as a function of the field and temperature is frequently approximated by the formula

$$\rho(B, T) = \rho_{\rm res} + \Delta\rho(B) + AT^n, \tag{11.1}$$

where $\Delta\rho$ is the correction to the resistivity produced by the field B and A is a T-independent coefficient. The index n takes the values 2 and 1, respectively, for Landau Fermi liquid (LFL) and non-Fermi liquid (NFL) states and values $1 \lesssim n \lesssim 2$ in the crossover region between them. Although both the large magnetoresistive anisotropy in the ab plane and the ordered phase are striking, the essential physics in $Sr_3Ru_2O_7$ seems to be that of a normal-phase electron fluid at fields $B < B_{c1}$ and $B > B_{c2}$, and at $T > T_c$ and $B_{c2} > B > B_{c1}$, i.e. outside of the ordered phase. Indeed, data on the low-temperature magnetoresistivity $\rho(B)$ with $B \parallel c$ collected for $Sr_3Ru_2O_7$ [3, 4] show that large changes of $\rho(B)$ occur as the ordered phase is approached. The straight lines indicated by arrows in Fig. 11.1a, crossing the pentagon data points on the low-field side and diamonds on the high-field side, represent the functions $T_r^1(B)$ and $T_r^2(B)$, respectively. In reference to panel b of Fig. 11.1, which shows the resistivity versus field strength at a series of temperatures, the straight line of panel a crossing pentagons [respectively, diamonds] delineates the intersection with the solid [dashed] line appearing in panel b. It is seen from Fig. 11.1 panel a, that $T_r^1(B = B_{c1}) \simeq 0$ and $T_r^2(B = B_{c2}) \simeq 0$. Thus, these functions show that the low-temperature sides of $\rho(B)$ at $T \to 0$ approach the steep sidewalls of the first-order phase transitions depicted in Fig. 11.1a. Accordingly $\rho(B)$ possesses two steep sidewalls as the critical fields B_{c1} and B_{c2} are approached at $T \to 0$, a behavior evident in both panels of Fig. 11.1.

The behavior at $B \simeq 7.9$ T and $T > T_c$ is equally striking in that ρ is precisely linear in T at least over the range $1.2 \leq T \lesssim 18$ K [10], see Sect. 9.3 and Fig. 9.5 therein, the left panel. This fact allows us to estimate the irregular residual resistivity $\rho_0^c(B)$. To evaluate $\rho_0^c(B)$, we extrapolate the data on the resistivity ρ [3, 4] to zero temperature, as if the ordered phase were absent in the range $B_{c2} > B > B_{c1}$.

In this way at $B = 7.9$ T one finds $\rho_0^c \sim 1.7\,\mu\Omega\,\text{cm}$, while the residual resistivity in the presence of the nematic phase is $\rho_0^{\text{nem}} \sim 2.0\,\mu\Omega\,\text{cm}$ in this range. On the other hand, at $B \simeq 7.6$ T the residual resistivity is $\rho_0^c(B) \simeq 1.1\,\mu\Omega\,\text{cm}$. Thus, even in the absence of the ordered phase, the field B triggers an upward jump of the resistivity upon approaching B_{c1} from below. The resistivity is approximately constant in the range $B_{c1} < B < B_{c2}$ and undergoes a second jump downward as B approaches B_{c2}. Such behavior, seen at the lowest accessible temperatures of 15 mK [16] and 70 mK [17], at which the term AT^n in (11.1) can be safely omitted, is consistent with both the jumps at QCPs and the constancy in the range $B_{c1} < B < B_{c2}$ of the irregular *residual* resistivity ρ_0^c. We conclude that it is ρ_0^c that are responsible for the observed behavior of ρ.

Let us evaluate possible causes for the jumps. When considering spin-orbit coupling in disordered electron systems, where electron motion is diffusive, the residual resistivity may have both positive (weak localization) and negative (weak anti-localization) signs [18]. However, since $Sr_3Ru_2O_7$ exhibits successive upward and downward jumps separated by the narrow range of magnetic fields $B_{c2} - B_{c1}$, it is unclear how weak localization at $B \simeq B_{c1}$ is changed to weak anti-localization at $B \simeq B_{c2}$. Moreover, $Sr_3Ru_2O_7$ is one of the purest compounds and the applicable regime of electron motion is ballistic rather than diffusive. Therefore, both weak and anti-weak localization scenarios are irrelevant. Accordingly, one expects the B-dependent correction $\Delta\rho$ to the residual resistivity to be positive and small. As we have seen, this is far from the real case.

Proposals for the origin of the jumps at finite temperatures may invoke band electrons close to the van Hove singularity (vHs), giving rise to the ordered phase [2, 5, 8, 12, 14, 15]. However, such scenarios should be rejected as the electrons involved must have very large effective mass M^* and hence contribute only weakly to transport properties at finite temperatures and not at all at $T = 0$, see e.g., [8]. Another possible source of the observed jumps might be resistivity associated with nematic domains that are thought to exist at $T \leq T_c$ for the fields tuning the system to a vHs [5, 8, 19, 20]. The jumps would be due to the extra scattering produced by such domains. This scenario is also problematic, since the domains would have to be present at least in the normal phase and at temperatures as high as $T \sim 18$ K, while the critical temperature for formation of both the nematic phase and the domains is estimated as $T_c \simeq 1.2$ K [5, 19, 20]. Due to the failing of such conventional explanations, we are faced with a challenging task that may well have broad implications for our understanding of unusual (notably, NFL) phenomena in condensed-matter systems: how does one unveil the QCPs that create the quantum critical regime of $Sr_3Ru_2O_7$, giving rise to the emergence of the resistivity jumps ρ_0^c and generating the entropy peak?

11.3 Fermion Condensation

To develop viable explanations of the resistivity jumps and entropy excess, it is necessary to recall the origin, nature, and consequences of *flattening* of single-particle excitation spectra $\varepsilon(\mathbf{p})$ ("flat bands") in strongly correlated Fermi systems, also called swelling of the Fermi surface or FC [21–25] (see [26–28] for recent reviews). At $T = 0$, the ground state of a system with a flat band is degenerate, and the occupation numbers $n_0(\mathbf{p})$ of single-particle states belonging to the flat band are continuous functions of momentum $\mathbf{p}$, in contrast to discrete standard LFL values 0 and 1. Such behavior of the occupation numbers leads to a T-independent entropy term

$$S_0 = -\sum_{\mathbf{p}}[n_0(\mathbf{p})\ln n_0(\mathbf{p}) + (1 - n_0(\mathbf{p}))\ln(1 - n_0(\mathbf{p}))] \tag{11.2}$$

that does not contribute to the specific heat $C(T) = TdS/dT$. Unlike the corresponding LFL entropy, which vanishes linearly as $T \to 0$, the term S_0 produces a T-independent thermal expansion coefficient [26, 29–31]. That T-independent behavior is observed in measurements on $\mathrm{CeCoIn_5}$ [32–34] and $\mathrm{YbRh_2(Si_{0.95}Ge_{0.05})_2}$ [35], while very recent measurements on $\mathrm{Sr_3Ru_2O_7}$ indicate the same behavior [36, 37] and confirm the existence of flat bands [13]. In the theory of fermion condensation, the degeneracy of the NFL ground state is removed at any finite temperature, since the flat band acquires a small dispersion proportional to T, see Sect. 3.1.3. The occupation numbers n_0 of FC remain unchanged at relatively low temperatures and, accordingly, so does the entropy S_0.

We now introduce these concepts to achieve a coherent picture of the quantum critical regime underlying the jump phenomena in $\mathrm{Sr_3Ru_2O_7}$. In constructing a field-induced flat band, we employ the model [5, 7, 8, 12, 38, 39] based on vHs that induces a peak in the single-particle density of states (DOS) and sharp rise of the magnetization $\mathbf{M}$ as the field sweeps across the metamagnetic transition. Upon increase of an applied magnetic field B, the vHs is moved through the Fermi energy. At fields in the range $B_{c1} < B < B_{c2}$ the DOS peak turns out to be at or near the Fermi energy. A key point in this scenario is that within the range $B_{c1} < B < B_{c2}$, a relatively weak repulsive interaction (e.g., Coulomb) is sufficient to induce FC and thus to form of a flat band with the corresponding DOS singularity locked in the Fermi energy [26–28]. Now, it is seen from (10.3) that finite temperatures, while removing the degeneracy of the FC spectrum, do not change S_0, threatening the violation of the Nernst theorem. To avoid such an entropic singularity, the FC state must be altered as $T \to 0$, so that the excess entropy S_0 is shed before zero temperature is reached. This can occur due to some phase transition or crossover, whose explicit consideration is beyond the scope of this book.

11.4 Phase Diagram

The schematic $T-B$ phase diagram of $Sr_3Ru_2O_7$ inferred from the proposed scenario is presented in Fig. 11.2. Its main feature is the magnetic field-induced quantum critical domain created by QCPs that are situated at B_{c1} and B_{c2} and supporting a FC and associated flat band induced by vHs (the double-headed arrow between the black dots). The low-field [high-field] QCP on the left [right] augurs the emergence of the flat band as $B \to B_{c1}$ [$B \to B_{c2}$] from below [above]. In contrast to the typical phase diagram of a HF metal [26], the domain occupied by the ordered phase in Fig. 11.2 is approximately symmetric with respect to the magnetic field $B_c = (B_{c2}+B_{c1})/2$. The emergent FC and QCPs are considered to be hidden or concealed in a phase transition, which is driven by the need for the system to avoid the entropic singularity that would be produced at $T \to 0$ by the T-independent entropy term S_0 of (11.2). The area occupied by this phase transition is indicated by horizontal lines and restricted by boundary lines ("sidewalls" and "roof"). At the critical temperature T_c where the new (ordered) phase sets in, the entropy is a continuous function. Therefore the "roof" of the domain occupied by the new phase is a line of second-order phase transitions. As T is lowered, some temperature T_{tr} is reached, where the entropy of the ordered phase becomes larger than that of the adjacent disordered one, due to the remnant entropy S_0 from the highly entropic flat-band state above T_c. Therefore, in the magnetic field, the system undergoes a first-order phase transition upon crossing a sidewall boundary at $T = T_{tr}$, since entropy cannot be equalized there. It follows,

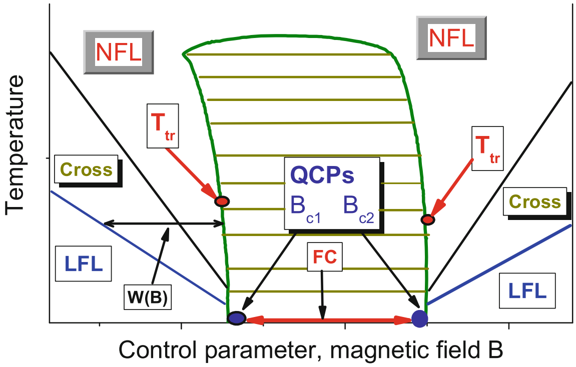

Fig. 11.2 Schematic phase diagram of the metal $Sr_3Ru_2O_7$. The QCPs situated at the critical magnetic fields B_{c1} and B_{c2} are indicated by *arrows*. The fermion condensation (FC) or flat band is present between these QCPs as depicted by the *double-headed arrow*. The ordered phase, bounded by the *curve* and demarcated by *horizontal lines*, emerges eliminating the entropy excess given by (11.2). *Two arrows* label the tricritical points T_{tr}, at which the lines of second-order phase transitions change to the first order. The total width of the NFL state and the crossover leading to the LFL state, $W(B) \propto T$, is denoted by the *arrow*. The LFL state occurs at the lowest temperatures below and above the critical values B_{c1} and B_{c2} of the tuned B-field. Rising temperature results in a broad crossover (labeled "Cross") from the LFL to the NFL state

then, that the line of second-order phase transitions is changed to a line of first-order ones at tricritical points indicated by arrows in Fig. 11.2. It is seen from Fig. 11.2 that the sidewall boundary lines are not strictly vertical due to the stated behavior of the entropy at the boundary and as a consequence of the magnetic Clausius-Clapeyron relation [7, 8]. Indeed, in our case the Clausius-Clapeyron equation reads,

$$\mu_0 \frac{dB_{cn}}{dT_c} = -\frac{\Delta S}{\Delta \mathbf{M}}. \tag{11.3}$$

Here, μ_0 is the permeability constant (in SI units) and B_{cn} stands for B_{c1} and B_{c2}. The advantage of (11.3) is that it defines the slope of the boundary lines shown in Fig. 11.2 from the basic principles of thermodynamics. Since the entropy S within the bounded region is higher than that outside it, the slopes of the phase boundaries point outwards as shown in Fig. 11.2. We conclude that the phase diagram 11.2 is in good agreement with the experimental one shown in panel a of Fig. 11.1. We note that the obtained agreement is robust and does not depend on the nature of the ordered phase, for our analysis is based on the thermodynamic consideration. For example, such a consideration allows one to establish the $T-B$ phase diagram of the HF metal $\mathrm{CeCoIn_5}$ that resembles that of $\mathrm{Sr_3Ru_2O_7}$ [31, 40].

On each flank of the region occupied by the ordered (nematic) phase, the system crosses over from the LFL state prevailing at the lowest temperatures to a NFL state under rising temperature. The total width $W(B)$ of the NFL state and crossover ("Cross") region on either flank (denoted with the double arrow in Fig. 11.2), is proportional to T [31, 41]. The behavior of $W(B)$ inferred from this phase diagram is also reflected in Fig. 11.1b, which depicts the dependence of the function $\rho(B)$ on field strength and temperature. Since the width $W(B)$ vanishes when the magnetic field tends to its critical values, $\rho(B)$ is represented by the two steep sidewalls seen in panel b of Fig. 11.1 as the critical field values B_{c1} and B_{c2} are respectively approached from below and above.

11.5 Jumps

Now we turn to calculations of the resistivity ρ in the range $B_{c1} < B < B_{c2}$, the dispersion of the flat band being governed by (10.3). The electronic liquid of $\mathrm{Sr_3Ru_2O_7}$ is described by several bands occupied by normal quasiparticles that simultaneously intersect the Fermi surface, along with heavy quasiparticles whose dispersion never covers the entire Fermi surface [5, 7, 8, 12, 38, 39, 42]. Based on (10.3), the temperature dependence of the effective mass $M^*(T)$ of the FC quasiparticles is given by

$$M^*(T) \sim \frac{\eta p_F^2}{4T}, \tag{11.4}$$

where $\eta = \delta p/p_F$ is determined by the characteristic size δp of the momentum domain occupied by the FC and p_F is the Fermi momentum [26–28]. It follows from this relation that the effective mass of FC quasiparticles diverges at low temperatures, while their group velocity, and hence their current, vanishes. Therefore the main contribution to the resistivity is provided by normal quasiparticles outside the FC having non-divergent effective mass M^*_L and finite group velocity at $T \to 0$. Nonetheless, it will be seen that FC quasiparticles still play a key role in determining the behavior of the irregular residual resistivity in the range $B_{c1} < B < B_{c2}$. Indeed, when analyzing the conductivity of HF metals, one should have in mind that the electronic liquid in them is anisotropic and, moreover, that several bands simultaneously intersect the Fermi surface so that FC never covers the entire Fermi surface. Hence, it follows that quasiparticles that do not belong to the FC make the main contribution to the conductivity. We call them normal, because their group velocity $v_F = p_F/M^*_L$ in the limit $T \to 0$ remains finite, while the group velocity of FC quasiparticles, as it follows from (11.4), and, hence, their current vanishes, as is mentioned above. These normal quasiparticles contribute to the conductivity in parallel with the FC quasiparticles. Therefore, they short out the contribution of the of FC carriers that are becoming heavy on the approach to FCQPT. We note that normal quasiparticles would short out the contribution coming from any heavy quasiparticles. As a result, one would conclude that the normal quasiparticles make a dominant contribution to the resistivity, and form its T^2 behavior. Now let us resolve the puzzle of the resistivity jumps at the critical fields B_{c1} and B_{c2}, as illustrated in panel b of Fig 11.1.

The resistivity has the conventional dependence [43]

$$\rho(T) \propto M^*_L \gamma \tag{11.5}$$

on the effective mass M^*_L and damping γ of the normal quasiparticles. As it is shown in Sect. 10.2, based on the relation (11.4), the behavior of γ is obtained in the present context in closed form as

$$\gamma(T) \sim \eta^2 \gamma_0 + \eta T, \tag{11.6}$$

where γ_0 is a constant [31, 41]. Let us illustrate the general consideration given in Sect. 10.2 by the following scenario [44]. Three processes make the main contribution to $\gamma(T)$. The first is the decay of a normal quasiparticle with the formation of a pair of normal quasiparticles and one quasiparticle belonging to FC. We label this contribution to the damping as γ_1. The second is the decay of a normal quasiparticle with the formation of a pair of FC quasiparticles, and the third is the elastic scattering of a normal quasiparticle by the FC quasiparticle. We label the contributions coming from these processes as γ_2 and γ_3, respectively. The two latter are topologically equivalent; therefore, their calculations can be combined. These three processes can be illustrated by the schematic diagrams shown in Fig. 10.3. Thus,

$$\gamma = \gamma_1 + \gamma_2 + \gamma_3, \tag{11.7}$$

where

$$\gamma_1(T) \propto W_1 T^2 (M_L^*)^2 M^*(T), \tag{11.8}$$

and

$$\gamma_2(T) \propto \gamma_3(T) \propto W_2 T^2 (M^*(T))^2 M_L^*. \tag{11.9}$$

Here, $M^*(T)$ is given by (11.4), W_1 and W_2 are the transition probabilities [43], given by integrals with atomic wave-functions integrated over two 4-momenta of the outgoing quasiparticles. Therefore, the temperature dependence of these probabilities is smeared due to the integration, and, neglecting this dependence, we obtain by using (11.4)

$$\gamma_1(T) \propto \eta (M_L^*)^2 T. \tag{11.10}$$

In the same way, we obtain

$$\gamma_3(T) \propto \gamma_2(T) \propto p_F^2 \eta^2 M_L^*, \tag{11.11}$$

and arrive at (11.6). We note that it is the temperature-independent part $\eta^2\gamma_0 \sim \gamma_2+\gamma_3$ of $\gamma(T)$, that mimics the scattering of normal quasiparticles by impurities, leads to the jumps in the magnetic field, giving rise to the irregular residual resistivity $\rho_0^c(B)$. It is seen from (11.6) that the coefficient A on the right hand side of (11.1) is partly formed by FC. We call this contribution to A, coming from FC, A_{FC}.

Let us now consider the additional contribution A_{TS} to the T-linear resistivity, formed by the zero sound modes, generated by the presence of FC, see Chap. 9 for details. The system with FC possesses its own set of zero sound modes. The mode of interest for our analysis contributes to the T-linear dependence of the resistivity, as the conventional sound mode does in the case of normal metals. The mode is that of transverse zero sound with its T-dependent sound velocity $c_t \simeq \sqrt{T/M_{\rm vHs}}$ and the Debye temperature given by [45, 46]

$$T_D \simeq c_t k_{max} \simeq \beta\sqrt{T T_F}. \tag{11.12}$$

Here, β is a factor, $M_{\rm vHs}$ is the effective mass formed by vHs, T_F is the Fermi temperature, while M^* on the left hand side of (11.4) is the effective mass formed finally by some relatively weak interaction, e.g., the Coulomb interaction, generating flat bands [47]. The characteristic wave number k_{max} of the soft transverse zero-sound mode is estimated as $k_{max} \sim p_F$, since we assume that the main contribution forming the flat band comes from vHs. We note that the numerical factor β cannot be established (if not using a very restrictive model), and is considered as a fitting parameter, making T_D given by (11.12) uncertain. Estimating $T_F \sim 10$ K and taking $\beta \sim 0.3$, and observing that the quasi-classical regime takes place at

$T > T_D \simeq \beta\sqrt{TT_F}$, we obtain that $T_D \sim 1$ K and expect that strongly correlated Fermi systems can exhibit a quasi-classical behavior with the low-temperature coefficient A, entering (11.1), $A = A_{FC} + A_{TS}$ [45, 46, 48].

Thus, in HF metals with few bands, crossing Fermi level and populated by LFL and HF quasiparticles, due to the transverse zero sound the resistivity is the T-linear dependent at the quantum criticality regime, as the normal sound (or phonons) do in the case of ordinary metals, while FC adds the quantum contribution A_{FC} to the coefficient A [46, 48]. The described contributions lead to the lifetime τ_q, formed by normal, FC quasiparticles, and the transverse zero sound in the form

$$\hbar/\tau_q \simeq a_1 + a_2 T, \tag{11.13}$$

where a_1 and a_2 are T-independent parameters. Relations (11.6) and (11.13) are in excellent agreement with recent experimental observations [49]. In playing its key role, the FC leads all quasiparticles to have the same unique width γ and lifetime τ_q. As we shall see, the T-independent width γ_0 forms the irregular residual resistivity ρ_0^c.

Using relations (11.1), (11.5) and (11.6) together with the standard treatment of possible corrections [50], we are led to conclusion that the resistivity of $Sr_3Ru_2O_7$ should behave as

$$\rho \sim \rho_{\rm res} + \Delta\rho(B) + \rho_0^c + AT \tag{11.14}$$

in the thermodynamic regime in question. The term "residual resistivity" ordinarily refers to impurity scattering. In the present case, as seen from (11.6) and (11.14), the irregular residual resistivity ρ_0^c is determined instead by the onset of a flat band, and has no relation to scattering of quasiparticles by impurities. Since the FC and the flat band manifest themselves in the region $B_{c1} < B < B_{c2}$, it is natural also to conclude that the QCPs indicated in Fig. 11.2 are responsible for the jumps in the irregular residual resistivity ρ_0^c. According to the relations (11.6) and (11.14), the resistivity ρ is a linear function of T [31, 41]. This feature of the flat-band scenario is in accordance with the relevant measurements on $Sr_3Ru_2O_7$ [10]. Moreover, experimental observations and their theoretical explanation show that the same physics describes the T-linear dependence of the resistivity of conventional metals and both HF metals and $Sr_3Ru_2O_7$, with the quasi-classical behavior formed by the zero-sound mode at their quantum criticality [48, 51].

As it was discussed above, heavy quasiparticles shaped by the flat band do not contribute directly to the transport properties. However, defining the lifetime τ_q instead, these quasiparticles specify the transport of the system. As a result, the magnetoresistivity jumps and their variation through the peak are defined by the variation of the irregular residual resistivity ρ_0^c. Indeed, increasing the temperature broadens and increases the resistivity in accordance with (11.14), but the minimal values of the jumps and the peak exhibit the spectacular independence of temperature, as it is seen from Fig. 11.1b. A prominent experimental feature supporting this conclusion is the occurrence of two jumps in the resistivity: The first is the upward jump at B_{c1}, where the FC is built up, followed by the second downward jump at B_{c2}, where the FC is destroyed. Thus, the scenario developed here reveals the genesis of the two steep sidewalls observed in the irregular residual resistivity ρ_0^c, arising from the formation of a flat band at QCPs.

One could attribute ρ_0^c to the influence of the magnetic field B, considering ρ_0^c as a magnetoresistivity. However, such a definition would obscure the physical mechanism responsible for forming ρ_0^c. Indeed, it is the flat band that forms the irregular residual resistivity, while the magnetic field represents an auxiliary parameter that tunes the system to the flat band.

11.6 Entropy

In the LFL state depicted in the Fig. 11.2, both the entropy S and the specific heat C of the electron liquid in $Sr_3Ru_2O_7$ behave in accordance with LFL theory $S/T = C/T \propto M^*$ [50]. The only but very essential specifics is that the effective mass M^* depends on magnetic field B according to $M^*(B) \propto |B - B_c|^{-2/3}$ [26, 52]. Here, B_c is the field at which the QCP occurs. In the present case of two QCPs, B_c for simplicity is taken equal to $B_c = (B_{c2} + B_{c1})/2 \simeq 7.9$ T. The entropy is then given by

$$S(B)/T = C/T \simeq A_s + D_s|B - B_c|^{-2/3}, \tag{11.15}$$

where A_s and D_s are fitting parameters for the low-field and high-field QCPs. The LFL behavior of C/T and S/T fitted by (11.15) are shown by the solid curve in Fig. 11.3, in

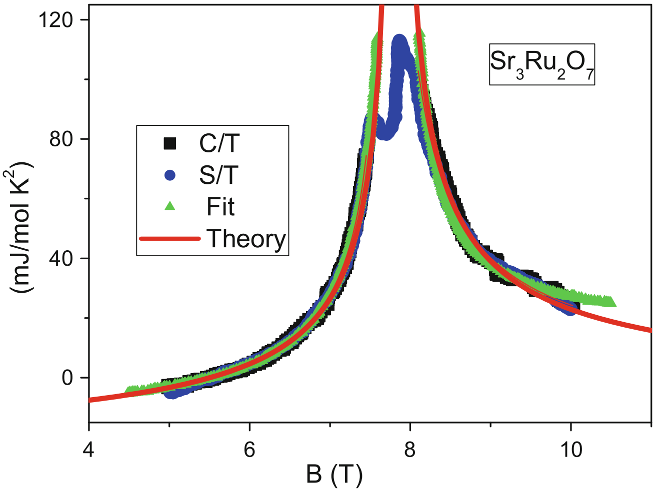

Fig. 11.3 The behavior of the specific heat C/T and the entropy S/T around the metamagnetic transition. Magnetic field dependence of C/T (*squares*) and S/T (*circles*) as obtained in measurements on $Sr_3Ru_2O_7$ and their divergent behavior as fitted by the function $B_c|B - B_c|^{\alpha}$ with $\alpha = -1$ (*triangles*) [7]. The theoretical fit of the current work is shown as the *solid curve* (11.15)

comparison with experimental results [7] for these quantities represented by squares and circle symbols, respectively. The triangles display the fit with exponent $\alpha = -1$ [7] rather than $\alpha - 2/3$. The two fits, namely, (the solid curve and the triangles) are seen to show similar behavior as functions of magnetic field. In contrast to the exponent $\alpha = -1$ obtained by the fitting of the experimental data over small variation of the magnetic field [7], the validity of the exponent $\alpha = -2/3$ is confirmed by the good agreement with the experimental data and internal consistency between the schematic phase diagram in Fig. 11.2 and the data in Figs. 11.1 and 11.3. Figure 11.3 shows that the entropy increases strongly on both the low-field and high-field sides of the ordered phase as the critical fields B_{c1} and B_{c2} are approached. Thus, the theory of FC allows us to explain, for the first time, the experimental data collected for $Sr_3Ru_2O_7$ [7, 37] on the evolution of the entropy and the heat capacity as the quantum critical point is approached. We note that the entropy jumps across the first-order phase transitions visible in Fig. 11.3 are in accord with the phase diagram sketched in Fig. 11.2.

11.7 Scaling Behavior

To reveal the signatures of the hidden QCPs, we conclude with an analysis of the thermodynamic properties of the C/T electronic specific heat measurements on $Sr_3Ru_2O_7$ [10]. As mentioned above, at $B = 7.9$ T the resistivity ρ is precisely linear in T over the range $T_c \leq T < 18$ K, with C/T varying as $\ln T$ over the same range [10]. These are typical fingerprints of a flat band generated by FC at QCPs [31, 41]. The experimentally derived temperature dependence of $C/T \propto M^*$ on magnetic field strength, shown in Fig. 11.4a, allows us to uncover the universal scaling behavior of the effective mass M^* that is the specific characteristic of HF metals. As shown in this Figure, the maximum of $C/T \propto M^*$ sharpens and shifts to lower temperatures as the field B approaches 7.9 T, where the maximum disappears. In contrast to HF metals, C/T exhibits a symmetry with respect to the area implicated by the ordering (nematic) transition. Indeed, the maximum appears upon approaching the QCPs and reappears on the high-field side of this transition region. This behavior of the maximum coincides with the phase diagram in Fig. 11.2, since the width $W(B)$ increases linearly with T and the maximum located in the transition region shifts toward zero temperature, while the effective mass $M^*(B)$ given by (11.15) diverges as B approaches the critical field.

To expose the scaling behavior, we normalize the measured C/T values to $(C/T)_N = (C/T)/(C/T)_M$ and the corresponding temperatures T to T_N, $T_N = T/T_M$, by dividing by their values T_M and $(C/T)_M$ at the maxima [26]. The elucidative values of T_M and $(C/T)_M$ at $B = 4$ T are depicted, as examples, by the arrows in panel a of Fig. 11.4. The spin AC susceptibility data $\chi(T) \propto M^*$ are normalized in the same way. At FQCPT, all the normalized χ_N and $(C/T)_N$ curves have to merge into a single one, $\chi_N = (C/T)_N = M^*_N(T_N)$, where M^*_N is the normalized effective mass represented by a universal function, being a solution of the Landau equation [26]. This solution $M^*_N(T_N)$ can be well approximated by a simple universal inter-

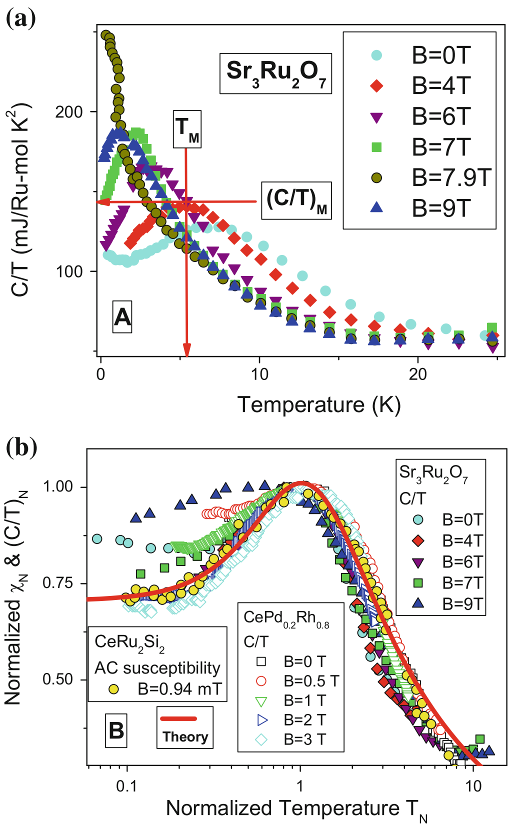

Fig. 11.4 The specific heat C/T versus magnetic field B and its scaling behavior. Panel **a** temperature dependence of the electronic specific heat for different magnetic field strengths (after Rost et al. [10]). The maximum at zero field increases and shifts to lower temperatures as the magnetic field approaches QCPs. At $B = 7.9$ T no maximum occurs. A maximum reappears on the high-field side of the transition, demonstrating a symmetrical behavior with respect to the critical region located between the two QCPs and occupied by the ordered phase. The illustrative values of $(C/T)_M$ and T_M at $B = 4$ T are shown by the *arrows*. Panel **b** universal scaling behavior of the normalized specific heat $\chi_N = (C/T)_N \propto M^*$, extracted from measurements on $\mathrm{CeRu_2Si_2}$ [53], $\mathrm{CePd_{1-x}Rh_x}$ with $x = 0.80$ [54], and $\mathrm{Sr_3Ru_2O_7}$ [10]. All the measurements displayed in panels **a** and **b** were performed under the application of magnetic fields as shown in the legends. The *solid curve* represents our calculation of the universal behavior

polating function. The interpolation occurs between the LFL and NFL regimes and represents the universal scaling behavior of M^*_N [26]

$$M^*_N(T_N) \approx c_0 \frac{1 + c_1 T_N^2}{1 + c_2 T_N^{8/3}}. \tag{11.16}$$

Here, $c_0 = (1 + c_2)/(1 + c_1)$, c_1, and c_2 are fitting parameters. Figure 11.4b reports the behavior of the normalized χ_N and $(C/T)_N$, thus extracted from measurements on $CeRu_2Si_2$ [53], $CePd_{0.8}Rh_{0.8}$ [54] and $Sr_3Ru_2O_7$ [10]. The solid curve shows the result of our calculation of the scaling behavior that can be well fit by (11.16). As is seen, the HF metals and $Sr_3Ru_2O_7$ exhibit the same scaling behavior, which can be understood within the framework of fermion condensation or flat-band theory [26–28].

11.8 Main Results

We have unveiled an interesting challenging relation in the behavior of $Sr_3Ru_2O_7$ and HF metals by establishing universal physics that straddles across the corresponding microscopic details. Our construction of the $T - B$ phase diagram of $Sr_3Ru_2O_7$ permits to explain main features of the experimental phase diagram, and unambiguously presents an interpretation of its unusual low-temperature thermodynamics in terms of FCQPT leading to the formation of a flat band at the restricted range of magnetic fields $B_{c1} \leq B \leq B_{c2}$. We have demonstrated that the obtained agreement with the experimental phase diagram is reliable and does not depend on the nature of the ordered phase, since our analysis is based on the thermodynamic (i.e. model independent) consideration. We have shown that it is the flat band that generates both the entropy peak and the resistivity jumps, as the critical fields B_{c1} and B_{c2} are approached. We have also detected the scaling behavior of the thermodynamic functions of $Sr_3Ru_2O_7$ coinciding with that of HF metals. We expect that the FC state breaks the discrete square lattice rotational symmetry and generates a large magnetoresistive anisotropy, as the magnetic field B is rotated away from the c axis towards the ab plane.

References

1. S.A. Grigera, R.S. Perry, A.J. Schofield, M. Chiao, S.R. Julian, G.G. Lonzarich, S.I. Ikeda, Y. Maeno, A.J. Millis, A.P. Mackenzie, Science **294**, 329 (2001)
2. R.S. Perry, K. Kitagawa, S.A. Grigera, R.A. Borzi, A.P. Mackenzie, K. Ishida, Y. Maeno, Phys. Rev. Lett. **92**, 166602 (2004)
3. S.A. Grigera, P. Gegenwart, R.A. Borzi, F. Weickert, A.J. Schofield, R.S. Perry, T. Tayama, T. Sakakibara, Y. Maeno, A.G. Green, A.J. Millis, A.P. Mackenzie, Science **306**, 1154 (2004)
4. J.A.N. Bruin, R.A. Borzi, S.A. Grigera, A.W. Rost, R.S. Perry, A.P. Mackenzie, Phys. Rev. B **87**, 161106 (2013)
5. R.A. Borzi, S.A. Grigera, J. Farrell, R.S. Perry, S.J.S. Lister, S.L. Lee, D.A. Tennant, Y. Maeno, A.P. Mackenzie, Science **315**, 214 (2007)
6. J. Farrell, R.S. Perry, A. Rost, J.F. Mercure, N. Kikugawa, S.A. Grigera, A.P. Mackenzie, Phys. Rev. B **78**, 180409(R) (2008)
7. A.W. Rost, R.S. Perry, J.F. Mercure, A.P. Mackenzie, S.A. Grigera, Science **325**, 1360 (2009)
8. S. Raghu, A. Paramekanti, E.A. Kim, R.A. Borzi, S.A. Grigera, A.P. Mackenzie, S.A. Kivelson, Phys. Rev. B **79**, 214402 (2009)

9. J. Lee, M.P. Allan, M.A. Wang, J. Farrell, S.A. Grigera, F. Baumberger, J.C. Davis, A.P. Mackenzie, Nat. Phys. **5**, 800 (2009)
10. A.W. Rost, S.A. Grigera, J.A.N. Bruin, R.S. Perry, D. Tian, S. Raghu, S.A. Kivelson, A.P. Mackenzie, Proc. Natl. Acad. Sci. USA **108**, 16549 (2011)
11. A.J. Millis, A.J. Schofield, G.G. Lonzarich, S.A. Grigera, Phys. Rev. Lett. **88**, 217204 (2002)
12. B. Binz, M. Sigrist, Europhys. Lett. **65**, 816 (2004)
13. M.P. Allan, A. Tamai, E. Rozbicki, M.H. Fischer, J. Voss, P.D.C. King, W. Meevasana, S. Thirupathaiah, E. Rienks, J. Fink, D.A. Tennant, R.S. Perry, J.F. Mercure, M.A. Wang, J. Lee, C.J. Fennie, E.A. Kim, M.J. Lawler, K.M. Shen, A.P. Mackenzie, Z.X. Shen, F. Baumberger, New J. Phys. **15**, 063029 (2013)
14. E. Fradkin, S.A. Kivelson, M.J. Lawler, J.P. Eisenstein, A.P. Mackenzie, Annu. Rev. Condens. Matter Phys. **1**, 153 (2010)
15. A.P. Mackenzie, J.A.N. Bruin, R.A. Borzi, A.W. Rost, S.A. Grigera, Physica C **481**, 207 (2012)
16. F. Weickert, P. Gegenwart, R.S. Perry, Y. Maeno, Physica C **460–462**, 520 (2007)
17. R.A. Borzi, A. McCollam, J.A.N. Bruin, R.S. Perry, A.P. Mackenzie, S.A. Grigera, Phys. Rev. B **84**, 205112 (2011)
18. S. Hikami, A.I. Larkin, Y. Nagaoka, Prog. Theor. Phys. **63**, 707 (1980)
19. J.F. Mercure, S.K. Goh, E.C.T. OFarrell, R.S. Perry, M.L. Sutherland, A.W. Rost, S.A. Grigera, R.A. Borzi, P. Gegenwart, A.P. Mackenzie, Phys. Rev. Lett. **103**, 176401 (2009)
20. C. Stingl, R.S. Perry, Y. Maeno, P. Gegenwart, Phys. Rev. Lett. **107**, 026404 (2011)
21. V.A. Khodel, M.V. Zverev, V.M. Yakovenko, Phys. Rev. Lett. **95**, 236402 (2005)
22. V.A. Khodel, V.R. Shaginyan, JETP Lett. **51**, 553 (1990)
23. G.E. Volovik, in *Quantum Analogues: From Phase Transitions to Black Holes and Cosmology*, ed. by W.G. Unruh, R. Schutzhold. Springer Lecture Notes in Physics (Springer, Orlando, 2007), p. 31
24. P. Nozières, J. Phys. I France **2**, 443 (1992)
25. T.T. Heikkilä, N.B. Kopnin, G.E. Volovik, JETP Lett. **94**(252), 233 (2011)
26. V.R. Shaginyan, M.Y. Amusia, A.Z. Msezane, K.G. Popov, Phys. Rep. **492**, 31 (2010)
27. V.R. Shaginyan, Phys. At. Nucl. **74**, 1107 (2011)
28. V.A. Khodel, J.W. Clark, M.V. Zverev, Phys. At. Nucl. **74**, 1237 (2011)
29. M.V. Zverev, V.A. Khodel, V.R. Shaginyan, M. Baldo, JETP Lett. **65**, 863 (1997)
30. M.Y. Amusia, A.Z. Msezane, V.R. Shaginyan, Phys. Lett. A **320**, 459 (2004)
31. V.R. Shaginyan, A.Z. Msezane, K.G. Popov, J.W. Clark, M.V. Zverev, V.A. Khodel, Phys. Rev. B **86**, 085147 (2012)
32. N. Oeschler, S. Hartmann, A. Pikul, C. Krellner, C. Geibel, F. Steglich, Phys. B **403**, 1254 (2008)
33. J.G. Donath, F. Steglich, E.D. Bauer, J.L. Sarrao, P. Gegenwart, Phys. Rev. Lett **100**, 136401 (2008)
34. S. Zaum, K. Grube, R. Schäfer, E.D. Bauer, J.D. Thompson, H.V. Löhneysen. Phys. Rev. Lett. **106**, 087003 (2011)
35. R. Kúchler, N. Oeschler, P. Gegenwart, T. Cichorek, K. Neumaier, O. Tegus, C. Geibel, J.A. Mydosh, F. Steglich, L. Zhu, Q. Si, Phys. Rev. Lett. **91**, 066405 (2003)
36. P. Gegenwart, F. Weickert, M. Garst, R.S. Perry, Y. Maeno, Phys. Rev. Lett. **96**, 136402 (2006)
37. C. Sting, R.S. Perry, Y. Maeno, P. Gegenwart, Phys. Status Solidi B **250**, 450 (2013)
38. A.M. Berridge, S.A. Grigera, B.D. Simons, A.G. Green, Phys. Rev. B **81**, 054429 (2010)
39. C.M. Puetter, J.G. Rau, H.Y. Kee, Phys. Rev. B **81**, 081105(R) (2010)
40. V.R. Shaginyan, A.Z. Msezane, V.A. Stephanovich, E.V. Kirichenko, Europhys. Lett. **76**, 898 (2006)
41. V.R. Shaginyan, A.Z. Msezane, K.G. Popov, J.W. Clark, M.V. Zverev, V.A. Khodel, JETP Lett. **96**, 397 (2012)
42. A. Tamai, M.P. Allan, F. Mercure, W. Meevasana, R. Dunkel, D.H. Lu, R.D.J. Singh, Z.X. Shen, F. Baumberger, Phys. Rev. Lett. **101**, 026407 (2008)
43. D. Pines, P. Noziéres, *Theory of Quantum Liquids* (Benjamin, New York, 1966)
44. V.A. Khodel, M.V. Zverev, JETP Lett. **85**, 404 (2007)

45. V.A. Khodel, J.W. Clark, V.R. Shaginyan, M.V. Zverev, JETP Lett. **92**, 532 (2010)
46. J.W. Clark, V.A. Khodel, M.V. Zverev, Phys. Lett. A **377**, 647 (2013)
47. V.A. Khodel, J.W. Clark, H. Li, M.V. Zverev, Phys. Rev. Lett. **98**, 216404 (2007)
48. V.R. Shaginyan, K.G. Popov, V.A. Khodel, Phys. Rev. B **88**, 115103 (2013)
49. P. Aynajian, E. Neto, A. Gyenis, R.E. Baumbach, J.D. Thompson, Z. Fisk, E.D. Bauer, A. Yazdani, Nature **486**, 201 (2012)
50. A.A. Abrikosov, L.P. Gorkov, I.E. Dzyaloshinski, *Methods of Quantum Field Theory in Statistical Physics* (Dover, New York, 1975)
51. A.N. Bruin, H. Sakai, R.S. Perry, A.P. Mackenzie, Science **880**, 339 (2013)
52. J.W. Clark, V.A. Khodel, M.V. Zverev, Phys. Rev. B **71**, 012401 (2005)
53. D. Takahashi, S. Abe, H. Mizuno, D. Tayurskii, K. Matsumoto, H. Suzuki, Y. Onuki, Phys. Rev. B **67**, 180407(R) (2003)
54. A.P. Pikul, N. Caroca-Canales, M. Deppe, P. Gegenwart, J.G. Sereni, C. Geibel, F. Steglich, J. Phys. Condens. Matter **18**, L535 (2006)

Chapter 12
Fermion Condensation in Finite Systems

Abstract Here we consider another example of systems, in which fermion condensation takes place. These are what is called finite Fermi systems, i.e. systems with finite number of fermions, contrary to a solid, where the number of electrons is practically infinite. An example of a finite Fermi system is an atomic nucleus, having finite number of nucleons, protons and neutrons, which are fermions. Here we show that the fermion condensation manifests itself in finite Fermi systems as a forced merger of all, discreet for finite systems, single-particle levels, lying near the Fermi surface. On the first sight, this merger contradicts the standard Landau quasiparticle picture. Nevertheless, similar to infinite systems, this is just the generalization of well-known Landau paradigm as for finite systems it is suitable to describe the restructuring (merging) of states at the Fermi surface. To demonstrate how this merging works, we show that the merging of the spin- and valley-split Landau levels at the chemical potential is an intrinsic property of a strongly-interacting two-dimensional electron system in silicon. Evidence for the level merging is given by available experimental data.

12.1 Finite Systems

In this section, we consider the problem of finite Fermi systems having a degenerate single-particle spectrum. We show that the Landau approach, applied to such a system, admits the possibility of single-particle levels merger. The salient feature of the phenomenon is the occurrence of noninteger quasiparticle occupation numbers, leading to a radical alteration of the standard quasiparticle picture. Implications of this alteration are considered for nuclear, atomic, and solid-state systems.

As we have seen in the preceding chapters, the most fruitful application of the FC notion was made to systems like HF compounds, where the concept of quasiparticles as well-defined excitations at the Fermi surface remains valid. The behavior of the electronic system in the above compounds is largely determined by the structure of single-particle (SP) levels. It seems therefore appropriate to renew the fundamental studies of single-particle aspects of finite Fermi systems as developed many years ago for atomic nuclei [1] in the expectation that the findings on the simple model

M.Y. Amusia et al., *Theory of Heavy-Fermion Compounds*, Springer Series
in Solid-State Sciences 182, DOI 10.1007/978-3-319-10825-4_12

systems may shed some light on the puzzling non-fermi liquid behavior of solids that are like heavy-fermion compounds.

In homogeneous matter, all the relevant measurable quantities, such as various susceptibilities, are functions of a single momentum transfer variable q. Inhomogeneous systems with a uniform distribution of SP levels possess basically the same properties. However, the situation changes, when the spectrum of their SP excitations is degenerate. This degeneracy implies the existence of a new energy scale D_{min}, given by the difference between the energies of the closest SP levels lying on opposite sides of the Fermi surface. The properties of such systems exhibit striking departures from what is found in homogeneous matter. To offer a prominent example, consider the ground-state energy $E_0(A)$ of atomic nuclei as a function of mass number A. For most nuclei, this quantity is well described by the Bethe-Weiszäcker liquid-drop formula. However, nuclei with a so-called magic number of protons or neutrons have spherical form [2], and the relevant energy scale D_{min} is several times larger than the average distance between neighboring SP levels in non-magic nuclei. This energy spacing provides a shell correction δE_s, lowering the liquid-drop binding energy, and guarantying the stability of the ground states of the known magic nuclei stable with respect to any mode of decay [2]. Another example is associated with the degeneracy of the SP spectrum of the two-dimensional electron gas in an external magnetic field. In this case, the degeneracy gives rise to a step-like behavior of the chemical potential $\mu(A)$, triggering oscillations of thermodynamic quantities [3].

Customary explanations of such extraordinary behavior do not take into account the alteration of key quantities due to interactions between added particles under variation of their number. In many cases such an approximation is justified, since these interactions do not affect the deviations that are mentioned above, even if the SP levels cross each other. However, we shall demonstrate that the dependence of SP energies $\varepsilon_s = E_s(A+1) - E_0(A)$ on quasiparticle occupation numbers n, inherent in Landau Fermi-liquid (LFL) theory, allows for an alternative scenario. The familiar energy level crossings of SP levels (Fig. 12.1) is shown in the panel a. This crossing changes to the "repelling", at which degenerate energy levels repel each other, as it is shown in panel b. In fact, the third possibility can take place: The repelling is replaced by an exact merging of these levels, a new phenomenon that leads to the disappearance of the energy distance between SP excitations, as it is shown in the panel c of Fig. 12.1. As we shall see below, the behavior of system exhibits drastic departures from predictions of standard LFL theory [4–7].

More then two decades ago [4] a new class of solutions was found for the equation of the Fermi-liquid theory [8, 9]

$$\varepsilon_{\mathbf{p}}(n_{\mathbf{p}}) - \mu - T \ln \frac{1-n_{\mathbf{p}}}{n_{\mathbf{p}}} = 0 \tag{12.1}$$

for the distribution function $n_{\mathbf{p}}$ of the quasiparticles with momenta $\mathbf{p}$. In this equation T is the temperature, μ is the chemical potential, and $\varepsilon_{\mathbf{p}} = \delta E/\delta n_{\mathbf{p}}$ is the quasiparticle energy, which, like the total energy E, is a functional of $n_{\mathbf{p}}$. The standard solution of (12.1) is obtained under the assumption that near the Fermi surface $\varepsilon_{\mathbf{p}}$ increases

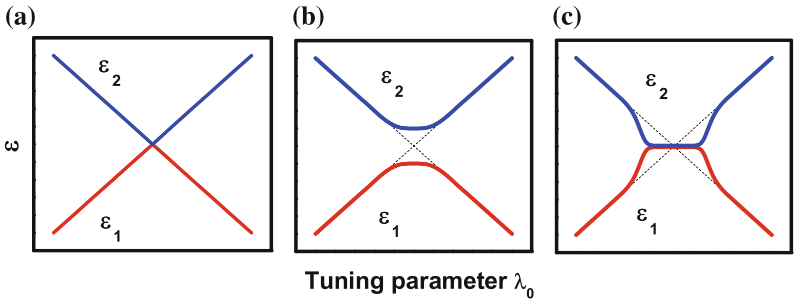

Fig. 12.1 Schematics of the behavior of the energies of single particle levels in a system with finite number of fermions (finite fermion system). The energy of levels $\varepsilon_1(\lambda_0)$ and $\varepsilon_2(\lambda_0)$ are functions of the tuning parameter λ_0. The panel **a** represents the levels crossing, the panel **b** represents the levels repelling, when the levels move apart, and panel **c** represents the levels merging, see (12.6). The case (**c**) is the analog of fermion condensation for finite fermion systems

monotonically with p growth. Then, at $T = 0$ the quasiparticles fill the Fermi sphere up to the radius $p_F = (3\pi^2 x)^{1/3}$ with x being the system density, and p_F is the Fermi momentum similar to that of an ideal Fermi gas, and, therefore, at low T the temperature dependence of the main characteristics of a Landau Fermi liquid is the same as in an ideal Fermi gas.

The new solutions of (12.1) have entirely different properties. The main one is that $n_{\mathbf{p}}$ is continuous near the Fermi surface. As a result, at $T = 0$ the term with the logarithm in (12.1) can be dropped, and then a plateau $\varepsilon_{\mathbf{p}} = \mu$ appears in the spectrum $\varepsilon_{\mathbf{p}}$. The quasiparticles with energies of chemical potential and lying on this plateau form the fermion condensate, see Chap. 3. From the mathematical standpoint the difference in the properties of the solutions is due to the location, where a minimum of the energy functional $E(n_{\mathbf{p}}, T = 0)$ is reached. The standard filling is realized in the systems with weak or moderate correlations. Then the minimum of E lies at the boundary of the functional space $[n_{\mathbf{p}}]$ determined by Pauli principle. A fermion condensate appears if the correlations are so strong that the minimum of E shifts into this space. This is easy to understand, if the equation $\varepsilon_{\mathbf{p}} = \mu$, which is valid in a homogeneous system in the interval $p_i < p < p_f$, is rewritten as a condition for a minimum

$$\frac{\delta E}{\delta n_{\mathbf{p}}} = \mu, \quad p_i < p < p_f. \tag{12.2}$$

It is worth noting that for $T \neq 0$ the plateau ceases to exist, and the derivative $d\varepsilon_{\mathbf{p}}/d\mathbf{p}$ becomes positive [10]. For low T the derivative is proportional to T, and for this reason in many respects a system with a fermion condensate behaves like a Fermi liquid in which the effective mass of the quasiparticles $M^* \sim 1/T$. This fact can be used to analyze the collisional damping of quasiparticle excitations of the condensate state. It has been found in [10] that the width $\gamma(T)$ of these states diverges in the perturbation theory as $1/T$ at small T. If this result were correct, the quasiparticle language would be unsuitable to describe the new solutions of (12.1). Actually, however, as we have seen in the preceding chapters, the quasiparticle formalism remains valid, and here, as often happens, a fiasco occurs in the perturbations beyond the phase transition point. To prove once more the first part of the assertion, let us analyze the problem of new solutions in a system of finite size, where the collisional width of the states in the discrete spectrum is completely absent. As an example, we study a spherical atomic nucleus with completely closed shells, which are separated from unfilled shells by a quite large energy "gap". Now we add to the nucleus a quite large number of particles $k \gg 1$ but small compared to the mass number A. Then the variation of the energy E of the system is given by a formula of the Landau Fermi-liquid theory

$$\delta E = \sum_{\lambda,\lambda_1} \left[\varepsilon_\lambda^m \delta n_\lambda \delta_{\lambda\lambda_1} + \frac{1}{2} F_{\lambda\lambda}^{\lambda_1\lambda_1} \delta n_\lambda \delta n_{\lambda_1} \right]. \tag{12.3}$$

The one-particle energies ε_λ^m appearing in (12.3) and the matrix elements of the effective interaction F are calculated in the initial nucleus, and $\lambda = n, l, j, m$ is the standard set of one-particle quantum numbers. In a spherical nucleus the levels are degenerate with respect to the magnetic quantum number m. If a level with total angular momentum j is filled, then there are $2j + 1$ quasiparticles in it: $\sum \delta n_\lambda = k$.

We recollect that the problem of the one-particle orbitals filling is ordinarily solved as follows. The main filling is the Hartree-Fock one giving a minimal energy E. However, if (12.2) possesses a solution which is consistent with the Pauli principle, then this solution delivers a deeper minimum. This is because in this case, according to (12.2), the occupation numbers $n_{\mathbf{p}}$ become variational parameters, and therefore the solution of the problem is sought on a wider class of functions than the Hartree-Fock ones. The case when there are only two one-particle levels in an unfilled shell is especially clear. In this case E is a function of only two variables $n_1 = \delta n_1(2j_1 + 1)$ and $n_2 = \delta n_2(2j_2+1)$, which are related by the condition $n_1+n_2 = k$. Equation (12.2) now becomes

$$\frac{\delta E}{\delta n_1} + \frac{\delta E}{\delta n_2}\frac{\delta n_2}{\delta n_1} = 0. \tag{12.4}$$

We introduce the one-particle energies in the nucleus in a standard manner

$$\begin{aligned} \varepsilon_1 &= \frac{\delta E}{\delta n_1} = \varepsilon_1^m + F_{11}^{11} n_1 + F_{22}^{11} n_2, \\ \varepsilon_2 &= \frac{\delta E}{\delta n_2} = \varepsilon_2^m + F_{11}^{22} n_1 + F_{22}^{22} n_2. \end{aligned} \tag{12.5}$$

In this case, the equation for the minimum can be represented in the different form

$$\varepsilon_1 = \varepsilon_2. \tag{12.6}$$

The second variation of the energy functional E should be positive, which is equivalent to the condition

$$F_{11}^{11} - 2F_{22}^{11} + F_{22}^{22} > 0.$$

For Fermi condensed state to exist, it should have the energy, which is lower then the initial ground state E_0. In other words, the difference $\varDelta E$ between E_0 and Hartree-Fock energy is negative if both quantities

$$n_1 = \frac{\varepsilon_2^m - \varepsilon_1^m + (F_{22}^{22} - F_{11}^{22})k}{F_{11}^{11} - 2F_{22}^{11} + F_{22}^{22}}, \quad n_2 = \frac{\varepsilon_1^m - \varepsilon_2^m + (F_{11}^{11} - F_{11}^{22})k}{F_{11}^{11} - 2F_{22}^{11} + F_{22}^{22}} \tag{12.7}$$

are positive so that

$$\varDelta E = -\frac{\left[\varepsilon_1^m - \varepsilon_2^m + (F_{11}^{11} - F_{11}^{22})k\right]^2}{2\left(F_{11}^{11} - 2F_{22}^{11} + F_{22}^{22}\right)}. \tag{12.8}$$

The analysis can be easily extended to a larger number of levels ε_λ^m. The main feature of the solution obtained is the forced "collapse" of all distances between levels which lie on the Fermi surface. An example of this kind for a system with infinite number of fermions is presented in [5]. It can be concluded from the above that in the systems where the temperature T is low compared to the one-particle levels splitting (so that there is no collisional damping of the states in the discrete spectrum), the quasiparticle formalism along with (12.4) and (12.6) can be used to describe the restructuring of the states at the Fermi surface. It is worth noting that it has not been assumed anywhere in the analysis that the input parameters are small, and if this is so, then the Landau Fermi-liquid approach is adequate to describe the fermion condensate, while the Hartree-Fock method is not. Moreover, if the effective interaction in the particle-particle channel is attractive, the above approach permits to take into account correctly the contribution of pair correlations with BCS gap $\varDelta$.

To gain more insight into FC scenario, we consider now one more schematic model involving three neutron levels in an open shell of a spherical nucleus [7]. The levels are denoted $-$, 0, and $+$ in ascending order of energy, and the distance between $-$ and 0 and between 0 and $+$ has the same value D. As usual, the SP energies and wave functions $\varphi_\lambda(\mathbf{r}) = R_{nl}(r)\varPhi_{jlm}(\mathbf{n})$, are solutions of equation $[p^2/2M + \varSigma(\mathbf{r},\mathbf{p})]\varphi_\lambda(\mathbf{r}) = \varepsilon_\lambda\varphi_\lambda(\mathbf{r})$, where $\varSigma$ stands for the self-energy. In even-even spherical nuclei, which have total angular momentum $J = 0$ due to pairing correlations, the energies ε_λ are independent of the magnetic quantum number m associated with the total SP angular momentum j. We suppose that the level $-$ is filled, the level $+$ is empty, and N neutrons are added to the level 0, changing the density by $\delta x(r) = NR_{n_0 l_0}^2(r)/4\pi$. We assume that $l_- \neq l_0 \neq l_+ \sim A^{1/3} \gg 1$.

It is our goal here to explore the consequences of the dependence of the SP energies $\varepsilon_\lambda(n)$ on the distribution n. In what follows, we shall retain only a major, spin- and momentum-independent part of the self-energy Σ and a primary, $\delta(r)$-like portion of the Landau-Migdal interaction function f [1, 8, 9, 11]. Accordingly, we simplify the LFL relation between Σ and the density x responsible for the variation of $\varepsilon_\lambda(n)$ over n to the form [1, 12] $\delta\Sigma(r) = f[x(r)]\delta x(\mathbf{r})$. For the sake of simplicity, we define the diagonal and nondiagonal matrix elements of f as follows

$$u = \int R^2_{nl}(r) f\,[x(r)]\, R^2_{nl}(r) r^2 dr/4\pi\,, \tag{12.9}$$

$$w = \int R^2_{nl}(r) f\,[x(r)]\, R^2_{n_1 l_1}(r) r^2 dr/4\pi\,, \tag{12.10}$$

independently of the quantum numbers $nl,\ n_1 l_1$.

A simple estimate of the ratio u/w is obtained using a semiclassical approximation $R_{nl}(r) \sim r^{-1}\cos\int p(r)dr$, with the result $u \simeq 3w/2$. We next observe that $f(x)$ is positive at densities close to equilibrium [1], but changes sign as $x \to 0$; hence the signs of u and w may depend on the quantum numbers of the SP levels in play.

Based on these results, the dimensionless shift $\xi_k(N) = [\varepsilon_k(N) - \varepsilon_k(0)]/D$ for $k = 0, +, -$ is given by

$$\xi_0(N) = n_0 U, \quad \xi_+(N) = n_0 W, \tag{12.11}$$

where $n_k = N_k/(2j_k + 1)$ is the occupation number of level k, $U = u(2j_0 + 1)/D$, and $W = w(2j_0 + 1)/D$. It is readily verified that if $fp_F M/\pi^2 \sim 1$, where $p_F = \sqrt{2M\varepsilon_F}$ and ε_F is the Fermi energy, then the integral (12.10) has a value $u \simeq \varepsilon_F/A$ and therefore $|U| \sim 1$, since $D \sim \varepsilon_F/A^{2/3}$ in spherical nuclei.

According to (12.11), the distance $\varepsilon_+(N) - \varepsilon_-(N)$ remains invariant when N increases. On the other hand, the difference $d_+(N) = \varepsilon_+(N) - \varepsilon_0(N)$ decreases with N when $U > W > 0$, as does the distance $d_-(N) = \varepsilon_0(N) - \varepsilon_-(N)$ in the opposite case, $U < W < 0$.

Now let us determine what happens when the functions $d_\pm(N)$ change their signs before SP level 0 is completely filled. We first examine the case $U < W < 0$. According to (12.11), the sign of $d_-(N)$ changes at $n_{0c} = 1/(W - U)$, which requires $W - U$ to be greater than 1 to meet the restriction $n < 1$. The usual Hartree-Fock scenario prescribes that for $n_0 > n_{0c}$, quasiparticles must leave the occupied level − and resettle into the unfilled level 0. Further, when the dependence $\varepsilon_\lambda = \varepsilon_\lambda(n)$ from (12.11) is brought into the picture, this effect is seen to promote the Hartree-Fock rearrangement.

In the opposite case, $U > W > 0$, the function $d_+(N)$ changes sign at $n_{0c} = 1/(U - W)$, implying $U - W > 1$. In order to satisfy this inequality, the repulsive part of the interaction f has to be sufficiently large, or else the scale D must be rather small. At $n_0 > n_{0c}$, the Hartree-Fock scenario requires the quasiparticles to leave the unfilled level 0 and move into the empty level +. Were this scenario the correct one, the rearranged SP energies would obey the equations $\varepsilon_0(N) = \varepsilon_0(N_c) + \delta N_c(w - u)$ and $\varepsilon_+(N) = \varepsilon_0(N_c) + \delta N_c(u - w)$, where δN_c is the number of quasiparticles shifted from level 0 to level +. The δ term in each of these equations arises due to the feedback of the immigrating quasiparticles. Upon subtracting one equation from the other, we find that $\varepsilon_+(N) - \varepsilon_0(N) > 0$ for any $\delta N_c > 0$, which says that the level $+$ lies above rather than below the level 0. We thus arrive at a contradiction that excludes the Hartree-Fock scenario in the case $U > W > 0$.

Under these conditions, a new ground state must form, denoted henceforth by M_s. As will now be shown, in the state M_s both of the levels 0 and $+$ are partially occupied. Solution of the problem for this case reduces to finding the minimum of the relevant energy functional

$$E = \varepsilon_0(0)N_0 + \varepsilon_+(0)N_+ + \frac{1}{2}\left[u(N_0^2 + N_+^2) + 2wN_0N_+\right] \tag{12.12}$$

with $N_k = \sum_m n_{km}$, through the variational conditions

$$\frac{\delta E}{\delta n_{0m}} = \frac{\delta E}{\delta n_{+m_1}} = \mu, \qquad \text{for all } m, m_1, \tag{12.13}$$

where μ is the chemical potential. Such a condition for characterization of a rearranged ground state first appeared in [4, 13], where homogeneous Fermi systems were addressed, without attention to degeneracy of SP levels. Equation (12.13) are conveniently rewritten as conditions for the coincidence of the SP energies ε_0 and ε_+,

$$\begin{aligned} \varepsilon_0(N) &= \varepsilon_0(0) + N_0u + N_+w = \mu\,, \\ \varepsilon_+(N) &= \varepsilon_+(0) + N_0w + N_+u = \mu\,, \end{aligned} \tag{12.14}$$

which, at $N > N_c = (2j_0 + 1)/(U - W)$, yield

$$\frac{N_0}{N} = \frac{1}{2}\left(1 + \frac{N_c}{N}\right), \quad \frac{N_+}{N} = \frac{1}{2}\left(1 - \frac{N_c}{N}\right). \tag{12.15}$$

Results of numerical calculations are plotted in Fig. 12.2, which consists of two columns, each made up of three plots. The uppermost panels show the dimensionless ratio $d_+(N) = (\varepsilon_+(N) - \varepsilon_0(N))/D$. The middle and lower panels give, respectively, the occupation numbers n_0 and n_+. Three different regimes can be seen. Two of them show well-defined SP excitations, and $d_+ \neq 0$. In the third regime, the energies of the levels 0 and $+$ coincide at zero. Passage through the three regimes can be regarded as a second-order phase transition, with the occupation number n_+ treated as an order parameter.

Inserting the above results into (12.12), we find

$$E_M - E_{HF}(N_0 = 0, N_+ = N) = -(u - w)(N - N_c)^2/4 < 0, \tag{12.16}$$

thereby verifying that the M_s state, having occupation numbers $0 < n < 1$ for both of the levels 0 and $+$, has lower energy than any Hartree-Fock state. Significantly,

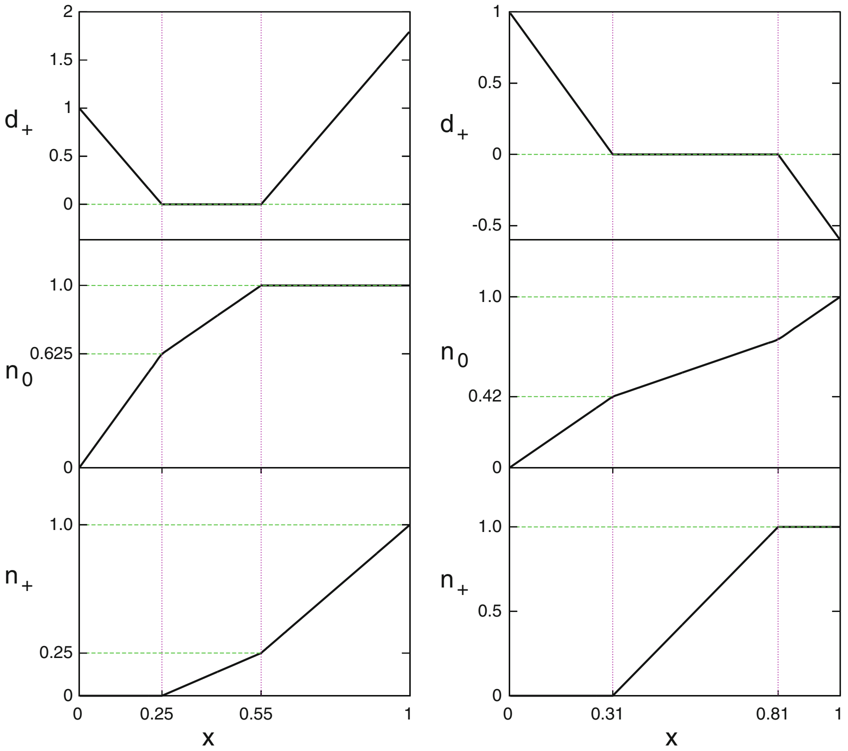

Fig. 12.2 *Top panels* Dimensionless distance $d_+ = (\varepsilon_+ - \varepsilon_0)/D$ between levels + and 0 as a function of the ratio $x = N/(2j_0 + 2j_+ + 2)$. *Middle* and *bottom panels* Occupation numbers n_k for levels 0 and +. Input parameters: $U = 4.0$, $W = 2.4$. For the *left* column, the ratio $r \equiv (2j_0 + 1)/(2j_+ + 1) = 2/3$; for the *right*, $r = 3.0$ [7]

the difference (12.16) is of the same order as a typical shell correction δE_s in heavy magic nuclei. In such systems, the chemical potential μ lies in the large gap between upper filled and lower unoccupied SP levels, while in the case of merging levels, μ is located at the place where the density of states attains its maximum.

The SP levels remain merged until one of them is completely filled. If the level 0 fills first, as in the left column of Fig. 12.2, then under further increase of N, quasiparticles fill the level +, signaling that the distance $d_+(N)$ again becomes positive. This behavior resembles the repulsion of two levels of the *same symmetry* in quantum mechanics, although here one deals with SP levels of *different symmetry*. In the opposite case where level + becomes fully occupied before level 0, as in the right column, the distance $d_+(N)$ becomes negative, and the two levels just cross each other at this point.

In the nuclear many-body problem, both types of SP level degeneracy—either initially present or arising in the scenario described above—are lifted when pairing correlations are explicitly involved. The role of D_{min} is played by the pairing gap

$\varDelta$ in the spectrum of SP excitations [14]. To illustrate this situation, we make BCS calculations in the above two-level model, under the assurance that realistic pairing forces are weak enough that the gap value remains smaller than the distance between neighboring SP levels in magic nuclei.

This two-level BCS problem is set up and solved as follows. First we rewrite the BCS gap equation as

$$\varDelta = gD\left[\sqrt{n_0(1-n_0)} + \sqrt{n_+(1-n_+)}\right]. \tag{12.17}$$

In doing so we have followed a sometimes used approximation introducing a common dimensionless pairing matrix element $g = (2j+1)\lambda\varepsilon_F/AD$, λ being a dimensionless pairing constant. A straightforward derivation, based on the BCS identity

$$4n_k(1-n_k) = \frac{\varDelta^2}{\varepsilon_k^2 + \varDelta^2}, \tag{12.18}$$

the definition $\varepsilon_\lambda = \delta E/\delta n_\lambda$ with E given by (12.12), and subtraction of one of Eqs. (12.14) from the other, leads to the key relation

$$\begin{aligned} 1 + (U-W)(N_0 - N_+) &= \frac{\varDelta}{D}\left[R(n_+) - R(n_0)\right], \\ R(n_k) &= \operatorname{sgn}(1-2n_k)\sqrt{\frac{1}{4n_k(1-n_k)} - 1}. \end{aligned} \tag{12.19}$$

The expression (12.19), along with obvious equalities $N_k = n_k(2j_k+1)$, form a closed system determining the occupation numbers n_0, n_+ and the gap value $\varDelta$. This set of equations should be solved numerically; some results are reported in Fig. 12.3. The inclusion of pairing correlations does indeed lift the degeneracy of the SP levels. However, the lowest value E_k of the Bogoliubov quasiparticles energies remains markedly less than D.

It is instructive to compare the structure of the pairing gap $\varDelta$ in two cases: when the above shrinkage of the distance between the SP levels + and 0 is taken into account, and when it is not. In the latter case, $\varDelta \sim [n_\lambda(1-n_\lambda)]^{1/2}$ shows two humps with a dip in between [14]. As it is seen in Fig. 12.3, the shrinkage effect fills in the dip. This increases the part of the ground-state energy associated with pairing correlations.

Let us now address the case $0 < w < u$ without pairing, existing for example in atoms and quantum dots. In this case, a pair of particles added to any SP level with $l \neq 0$ always have total angular momentum $J \neq 0$ (Hund's rule), in principle destroying spherical symmetry and lifting the m-degeneracy of the SP energies ε_{km}. This gives rise to spreading of the levels, the magnitudes of which are proportional to u for the level 0, and w for the level +. If the interaction function f has long-range character, we have $u/w \gg 1$, and hence the spread of level 0 is much larger than that

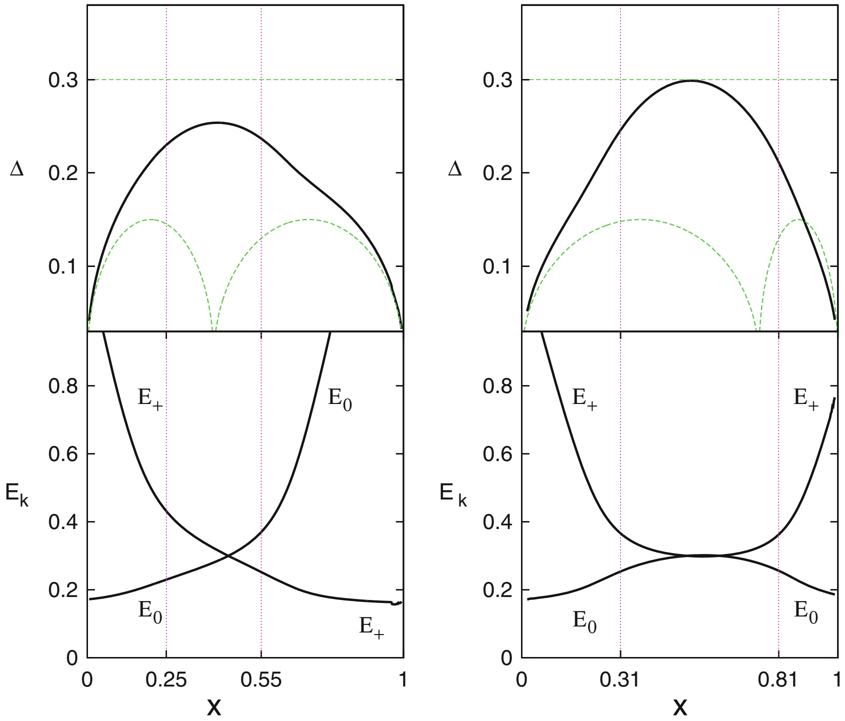

Fig. 12.3 *Top panels* Pairing gap Δ (in units of D) plotted versus $x = N/(2j_0 + 2j_+ + 2)$, both accounting for the shrinkage of the inter-level distance (*solid line*) and neglecting it (*dashed line*). *Bottom panels* Energies of Bogoliubov quasiparticles $E_k = \Delta/2\,[n_k(1-n_k)]^{1/2}$. Pairing constant: $g = 0.3$. Other input parameters for both columns are the same as those in Fig. 12.2 [7]

of level +. For the density δx associated with the added quasiparticles, we may write $\delta x(\mathbf{r}) = R^2_{n_0 l_0}(r) \sum_m |\Phi^2_{j_0 l_0 m}(\mathbf{n})|^2 n_{0m}$, which is applicable at least until the crossing of relevant orbitals begins. Upon inserting this formula into the relation $\delta\Sigma = f\delta x$, it is found that the spread does not affect the evolution of the centers of gravity $\varepsilon^0_k = \sum_m \varepsilon_{km}/(2j_k + 1)$ of the levels, since the isotropic part of δx has the same form $\delta_0 x = NR^2_{n_0 l_0}(r)/4\pi$ as if the degeneracy of the SP level were still in effect. This circumstance is especially important at the stage when the two families of SP levels begin to cross each other. Since at $0 < w < u$ the center of the gravity of the level + gets stuck close to the Fermi surface, our results provide a simple mechanism for pinning of the narrow bands in solids to the Fermi surface.

To exemplify this point, let us consider a model where the SP spectrum in local-density approximation (LDA) is exhausted by (i) a wide band, which disperses through the Fermi surface, and (ii) a narrow one, placed below the Fermi surface at a distance D_n. We assume that only the diagonal matrix element f_{nn} of the interaction function f referring to the narrow band is significant, the others being negligible. The shift $\delta\varepsilon_n$ in the location of the narrow band due to switching on the intraband interactions is given by a formula analogous to (12.11), namely $\delta\varepsilon_n = f_{nn} x_n$, where

x_n is the density of the band. If the correction $\delta\varepsilon_n$ exceeds the distance D_n then the Hartree-Fock scenario calls for the narrow band to be completely emptied; but then the shift $\delta\varepsilon_n$ must vanish. To eliminate this inconsistency, only a fraction of the particles leave the narrow band, in just the right proportion to equalize the chemical potentials of the two bands. The described feedback mechanism positions the narrow band exactly at the Fermi surface, resolving a long-standing problem with the LDA scheme.

In atoms, remnants of an accidental degeneracy of the Coulomb problem persist in the formation of electronic shells for which the distance between SP levels with different orbital momenta l is rather small. Recalling that matrix elements of the electron-electron interaction are quite sensitive to the l value, mergence of some SP levels cannot be excluded. To elucidate this situation, one needs to analyze the energy functional $E = \sum \varepsilon_k(0) n_{km} + \frac{1}{2} \sum u_{km,k_1m_1} n_{km} n_{k_1m_1}$, wherein the interaction matrix u_{km,k_1m_1} replaces the matrix element (12.10) and summation occurs over some states of the last unfilled shell. In this case, the variational equations generalizing (12.13), $\mu = \varepsilon_k(0) + \sum u_{km,k_1m_1} n_{k_1m_1}$, should be solved numerically.

The new many-body effect uncovered in the foregoing analysis resembles a previously studied fermion condensation, which involves wholesale mergence of SP levels in homogeneous Fermi fluids [13, 15–17]. In any conventional homogeneous Fermi liquid, e.g., liquid ^{3}He [18], the momentum $\mathbf{p}$ of an added particle can be associated with a certain quasiparticle. Similarly, in most spherical odd-A nuclei, the total angular momentum J in the ground state is carried by an odd quasiparticle. In atomic physics, the electronic configuration of ions of elements belonging to the principal groups of the periodic table repeats that of preceding atoms. From the microscopic perspective, in all such "open-shell" systems conforming to standard LFL theory, the single quasiparticle term $a^+_\lambda \Psi_0$ assumes a special role in the ground-state wave function, where Ψ_0 represents the ground state of a parent system. By contrast, in the case of merging of SP levels, the ground-state features a multitude of quasiparticle terms and therefore exhibits a more complicated, yet more balanced character. This implication of our analysis offers a qualitative explanation of the fact that the chemical properties of rare-earth elements differ little, in spite of marked variation in atomic numbers. In fact, a conventional explanation [19] based on resettling of electrons into the collapsed 4f-orbital, framed within the Thomas-Fermi (TF) method for the rare-earth elements having $Z > 60$, is flawed, because the TF self-consistent field, being a universal function of Z, does not change in case quasiparticles resettle from one SP level to another. However, proper accounting for the interaction between resettling electrons within a more sophisticated Landau theory of Fermi liquid demonstrates that the respective change of the self-consistent field exists, and it is large enough to give rise to merging of the collapsed $4f$-level with others in the open shell and hence level the SP properties of different electron systems that renders merging a complementary reason for the remarkable similarity of chemical properties of rare-earth elements.

In spite of evident similarities, there is a crucial difference between the conditions for the "level-mergence" phenomenon in homogeneous Fermi liquids and in finite Fermi systems with the degenerate SP levels. In the former, the presence of a significant velocity-dependent component in the interaction function f is needed to promote fermion condensation, while in the latter, SP levels can merge even if f is momentum-independent. The reason for this difference is simple: in the homogeneous case, the matrix elements u and w are equal to each other, implying zero energy gain due to the rearrangement when velocity-dependent forces are absent. We emphasize that the study of level mergence in finite systems has the advantage of transparency, in that (i) it is free of the complicated issue of SP excitations damping [20, 21], and (ii) it gives access to the precursor stage of the effect.

12.2 Merging of Landau Levels in Two-Dimensional Electron System in Silicon

Here we exemplify the merging of discrete levels by two-dimensional electron system in silicon. We show that the merging of the spin- and valley-split Landau levels at the chemical potential is an intrinsic property of a strongly-interacting two-dimensional electron system in silicon. Evidence for the level merging is given by available experimental data.

In a non-interacting fermion system with continuous spectrum, the occupation probability for a quantum state at fixed chemical potential and temperature is a function of the SP energy only [22]. If the temperature tends to zero, the energy interval separating the filled and empty quantum states also tends to zero. For free particles there appears a Fermi surface in momentum space with dimensionality $d - 1$, where d is the dimensionality of the fermionic space.

In general, this reasoning is not true for interacting fermions [4, 10, 17, 23–26]. In this case the single-particle energy depends on electron distributions, and the occupation numbers of quantum states at the chemical potential can be different, falling within the range between zero and one. As it was demonstrated in Chaps. 3 and 4, in strongly correlated Fermi systems at $T = 0$, a topological phase transition, related to the emergence of a flat portion of the single-particle spectrum $\varepsilon(p)$ at the chemical potential, has been predicted. This transition is associated with the band flattening or swelling of the Fermi surface in momentum space, which is preceded by an increasing quasiparticle effective mass m^* that diverges at the quantum critical point.

For an interacting fermion system with discrete spectrum, one expects a similar effect—the appearance of different fillings of quantum levels at the chemical potential. Given the energies of two quantum levels intersect each other when varying an external parameter, these can be the same as the chemical potential over a range of parameter values, i.e. the levels can merge at the chemical potential over this range [6, 7]. The level merging implies that there is attraction between the two partially-filled quantum levels. The merging interval is determined by a possibility of redistributing quasiparticles between the levels. It is clear that the effect of merging is in contrast to the simple crossing of quantum levels at some value of the external parameter, see Fig. 12.1.

Here, we show that the merging of the spin- and valley-split Landau levels at the chemical potential can be detected near the quantum critical point in a clean strongly-interacting two-dimensional (2D) electron system in (100) silicon [27]. In this electron system subjected to perpendicular magnetic fields, each Landau level is split into four quantum levels due to the spin and valley splitting. It has been experimentally observed that the Shubnikov-de Haas quantum oscillation minima at filling factor $\nu = 4i + 4$ (where $i = 0, 1, 2, \ldots$) disappear below some electron density n^* depending on ν, while the minima at $\nu = 4i + 2$ persist down to appreciably lower densities [28]. Although this behavior is consistent with the sharp increase of the effective mass with decreasing electron density n_s [29], the dependence of the density n^* on filling factor (or magnetic field) turns out to be anomalously strong and lacks explanation. We find that the anomalous behavior of the density where $\nu = 4i + 4$ oscillation minima vanish is described within the merging picture. This gives evidence for the level merging in a 2D electron system in silicon.

Imposition of the perpendicular magnetic field B on a homogeneous 2D electron system is known to create two subsystems of Landau levels numbered i and distinguished by ± projections of the electron spin on the field direction. The valley degeneracy is neglected for the sake of simplicity. The energy levels $\varepsilon_i^{\pm}$ in each set are spaced by the cyclotron splitting $\hbar\omega_c = \hbar eB/m^*c$, and the two sets of the Landau levels are shifted with respect to each other by the spin splitting $\Delta_Z = g\mu_B B$, where m^* and g are the values of mass and Lande factor renormalized by electron interactions and $\mu_B = e\hbar/2m_e c$ is the Bohr magneton, and m_e is an electron mass. Disregarding the anti-crossing effects, the Landau levels with opposite spin directions should intersect with changing electron density, as caused by the strong dependence of the effective mass on n_s, provided the g factor depends weakly on n_s. In particular, at high electron densities the cyclotron splitting usually exceeds the spin splitting, whereas at low densities the opposite case $\hbar\omega_c < \Delta_Z$ should occur due to the sharply increasing mass. Below, we obtain conditions when the level merging is possible.

Provided that the external magnetic field is fixed and weak, many quantum levels are occupied and the variation of the electron density in a quantum level is small compared to n_s. The variation of the energy ε_λ is evaluated using the Landau relation

$$\delta\varepsilon_\lambda = \sum_\sigma \Gamma_{\lambda\sigma}\delta n_\sigma, \tag{12.20}$$

where $\Gamma_{\lambda\sigma}$ is the electron-electron interaction amplitude that is a phenomenological ingredient of the Fermi liquid theory. Selecting the magnetic field at which the difference between the neighboring Landau levels ε_i^+ and ε_{i+1}^-

$$D = \varepsilon_i^+ - \varepsilon_{i+1}^- = \Delta_Z(n_s, B) - \hbar\omega_c(n_s, B) \tag{12.21}$$

zeroes at the filling factor $\nu = n_s hc/eB = 2i + 2$, we start from the higher density where both levels $(i + 1)^-$ and i^+ are completely filled at $\nu = N = 2i + 3$, the difference $D(N)$ being negative. Removing the electrons from the level $(i+1)^-$ implies that the electron density decreases and D increases. The above Landau relation reduces to the set

$$\begin{aligned} \varepsilon_i^+ - \varepsilon_i^+(N) &= -(N-\nu)n_0\Gamma^{+-}_{i,i+1}, \\ \varepsilon_{i+1}^- - \varepsilon_{i+1}^-(N) &= -(N-\nu)n_0\Gamma^{--}_{i+1,i+1}, \end{aligned} \tag{12.22}$$

where $\lambda, \sigma = i^+, (i+1)^-$ in the first equation, $\lambda, \sigma = (i+1)^-, (i+1)^-$ in the second one, and $n_0 = eB/hc$ is the level degeneracy. Upon subtracting the second equation from the first, one has

$$\varepsilon_i^+ - \varepsilon_{i+1}^- = D(N) + (N-\nu)n_0(\Gamma^{--}_{i+1,i+1} - \Gamma^{+-}_{i,i+1}). \tag{12.23}$$

The distance between the two levels vanishes as the level $(i+1)^-$ becomes empty, which corresponds to the relation

$$|D(N)| = n_0(\Gamma^{--}_{i+1,i+1} - \Gamma^{+-}_{i,i+1}). \tag{12.24}$$

Let us presume that at $\nu = 2i+2$ the level crossing occurs, i.e. the level i^+ becomes empty and the level $(i+1)^-$ is completely filled. Then, the set of (12.22) should be replaced by

$$\begin{aligned} \varepsilon_{i+1}^- - \varepsilon_{i+1}^-(N) &= -(N-\nu)n_0\Gamma^{-+}_{i+1,i} \\ \varepsilon_i^+ - \varepsilon_i^+(N) &= -(N-\nu)n_0\Gamma^{++}_{i,i} \end{aligned} \tag{12.25}$$

to yield

$$\varepsilon_i^+ - \varepsilon_{i+1}^- = D(N) + (N-\nu)n_0(\Gamma^{-+}_{i+1,i} - \Gamma^{++}_{i,i}). \tag{12.26}$$

Equations (12.23) and (12.26) are compatible with each other, favoring the level crossing, under the condition $\Gamma(i) = (\Gamma^{--}_{i+1,i+1} - \Gamma^{+-}_{i,i+1}) - (\Gamma^{-+}_{i+1,i} - \Gamma^{++}_{i,i}) \le 0$.

In the opposite case

$$\Gamma(i) > 0 \tag{12.27}$$

the single-particle levels attract to each other and merge at the chemical potential μ, as described by the merging equation $\varepsilon_{i+1}^- = \varepsilon_i^+ = \mu$. Both levels exhibit partial occupation with fractions of empty states $0 < \bar{f}_i < 1$ and $0 < \bar{f}_{i+1} < 1$ that obey the normalization condition $\bar{f}_i + \bar{f}_{i+1} = \bar{f} = N - \nu$. These fractions are determined from the set of equations

$$\begin{aligned} \varepsilon_{i+1}^- - \varepsilon_{i+1}^-(N) &= -n_0(\bar{f}_{i+1}\Gamma^{--}_{i+1,i+1} + \bar{f}_i\Gamma^{-+}_{i+1,i}) \\ \varepsilon_i^+ - \varepsilon_i^+(N) &= -n_0(\bar{f}_{i+1}\Gamma^{+-}_{i,i+1} + \bar{f}_i\Gamma^{++}_{i,i}) \end{aligned} \tag{12.28}$$

which yields

$$\begin{aligned}\varepsilon_i^+ - \varepsilon_{i+1}^- = D(N) &+ \bar{f}_{i+1} n_0 (\Gamma_{i+1,i+1}^{--} - \Gamma_{i,i+1}^{+-}) \\ &+ \bar{f}_i n_0 (\Gamma_{i+1,i}^{-+} - \Gamma_{i,i}^{++}).\end{aligned} \tag{12.29}$$

Using the merging equation and the normalization condition, we find

$$\begin{aligned}\bar{f}_i &= \frac{(\bar{f}-1)(\Gamma_{i+1,i+1}^{--} - \Gamma_{i,i+1}^{+-})}{\Gamma(i)} \\ \bar{f}_{i+1} &= \bar{f} - \frac{(\bar{f}-1)(\Gamma_{i+1,i+1}^{--} - \Gamma_{i,i+1}^{+-})}{\Gamma(i)}.\end{aligned} \tag{12.30}$$

The merging starts when the empty states appear in the level ε_i^+ and ends when this level is completely emptied. This corresponds to the increase of the fraction of empty states $\bar{f}$ in the range between $\bar{f} = 1$ (or $\nu = 2i + 2$) and $\bar{f} = \min(1 + \Gamma(i)/(\Gamma_{i+1,i+1}^{--} - \Gamma_{i,i+1}^{+-}), 2)$. Outside the merging region, the conventional Landau level diagram is realized. Note that the gap between the neighboring Landau levels ε_i^+ and ε_{i+1}^- proves to be invisible in transport and thermodynamic experiments. The upper boundary of the merging region $n_m(B)$ is written

$$\hbar\omega_c - \Delta_Z = 0. \tag{12.31}$$

Below, we compare the results of the calculations with the experimental data obtained in a strongly-interacting 2D electron system in (100) silicon. This electron system is characterized by the presence of two valleys in the spectrum so that each energy level $\varepsilon_i^\pm$ is split into two levels, as shown schematically in Fig. 12.4. One can easily see that the valley splitting Δ_v promotes the merging of quantum levels. The bigger the valley splitting, the higher the electron density at which the levels $(i+1)^-$ and i^+ with different valley numbers should merge at the chemical potential at filling factor $\nu = 4i + 4$. The upper boundary of the merging region $n_m(B)$ is determined by the relation

$$\hbar\omega_c - \Delta_Z - \Delta_v = 0, \tag{12.32}$$

which is different from (12.31) by the presence of the valley splitting. Since the electron density distributions corresponding to two valleys are spaced by distance α in the direction perpendicular to the Si-SiO$_2$ interface, the intervalley charge transfer creates an incremental electric field. In accordance with (12.29), we get $(\Gamma_{i+1,i+1}^{--} - \Gamma_{i,i+1}^{+-}) = (\Gamma_{i,i}^{++} - \Gamma_{i+1,i}^{-+})$ and $\Gamma(i) = 4\pi e^2\alpha/\kappa_d$, where κ_d is the dielectric constant. Although the distance $\alpha \sim 0.4$ Å is small compared to the thickness of the 2D electron system which is about 50 Å at densities $n_s \approx 1 \times 10^{11}$ cm^{-2} [30], the estimated interaction energy $n_0\Gamma(i) \sim 0.02$ meV at $B \approx 1$ T is comparable with the valley splitting $\Delta_v \approx 0.06$ meV. The value of Δ_v is calculated using the known

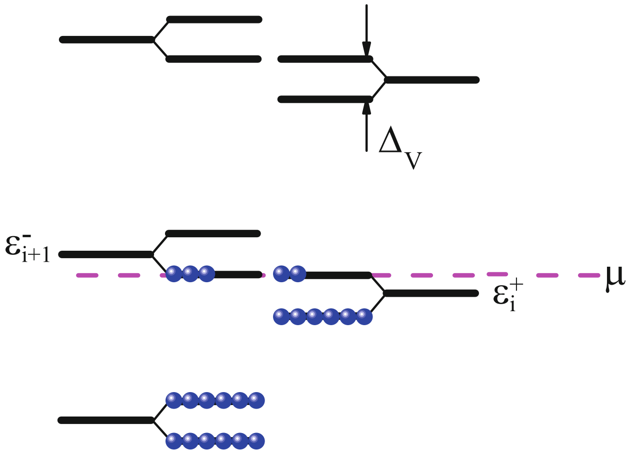

Fig. 12.4 Schematic diagram of merging of the spin- and valley-split Landau levels at the chemical potential. The occupied levels are indicated by *spheres*. The fillings of the two quantum levels at the chemical potential vary with changing electron density

formula $\Delta_v \approx 0.015(n_s + 32n_{depl}/11)$ meV, where $n_{depl} \approx 1 \times 10^{11}$ cm^{-2} is the depletion layer density and the densities are in units of 10^{11} cm^{-2} [30]. The strength of the merging effect being obviously determined by $\Gamma(i)$, the appreciable interaction energy should lead to a wide merging region.

In the high-density limit, where the effect of electron-electron interactions is negligible, the effective mass m^* and g factor are equal to $m_b = 0.19m_e$ and $g_0 = 2$ so that the cyclotron splitting significantly exceeds the spin splitting. At low electron densities, where the interaction effects are strong, the effective mass $m^*(n_s)$ is found to diverge as $m_b/m^* \simeq (n_s - n_c)/n_c$ at the quantum critical point close to the metal-insulator transition which occurs at $n_c \simeq 8 \times 10^{10}$ cm^{-2}, while the g factor stays close to g_0 [31–35]. The Landau level fan diagram for this electron system in perpendicular magnetic fields is represented in Fig. 12.5. The quantum oscillation minima at filling factor $\nu = 4i + 4$ disappear below some electron density n^* depending on ν, while the minima at $\nu = 4i + 2$ persist down to appreciably lower densities [28]. Although this behavior is consistent with the sharp increase of the effective mass with decreasing n_s, the dependence of the density n^* on filling factor (or B) turns out to be anomalously strong and lacks explanation. Particularly, this cannot be accounted by the impurity broadening of quantum levels in terms of $\omega_c\tau \sim 1$ (where τ is the elastic scattering time) in which case the drop of mobility $e\tau/m^*$ at low electron densities is controlled by the increasing mass [29].

Using the above expressions for m^* and Δ_v and $g = g_0$, we determine from (12.32) the expected upper boundary of the merging region $n_m(B)$, shown by the solid blue line in Fig. 12.5. The calculated boundary is in agreement with the experimental density $n^*(B)$ where the oscillation minima at $\nu = 4i + 4$ vanish. This fact gives evidence for the level merging in a 2D electron system in silicon.

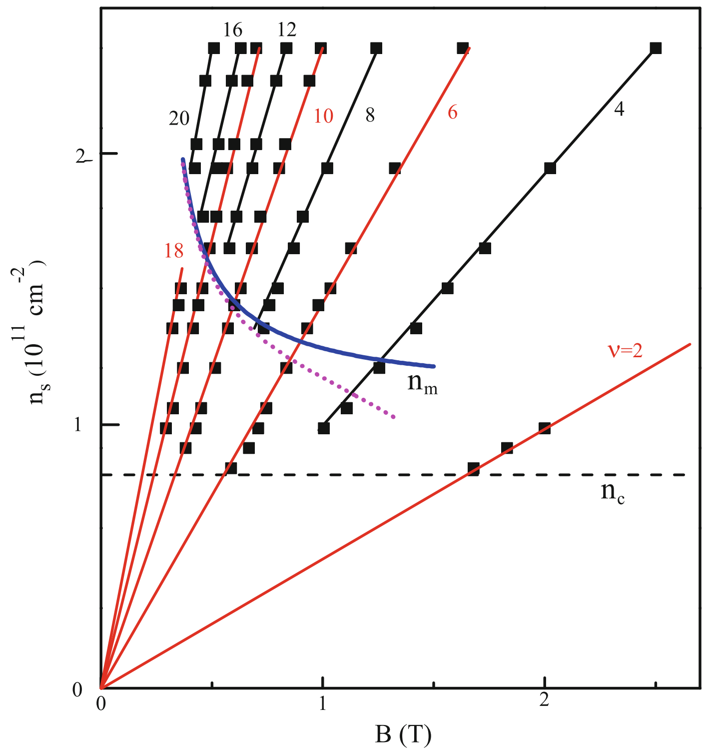

Fig. 12.5 Positions of the Shubnikov-de Haas oscillation minima in the (B, n_s) plane (*squares*) and the expected positions of the cyclotron and spin minima calculated according to the formula $n_s = \nu eB/hc$ (*solid lines*). The position of the metal-insulator transition, befalling at $n_c \simeq 8 \times 10^{10}$ cm^{-2}, in $B = 0$ is indicated by the *horizontal dash line*. The calculated merging boundary $n_m(B)$ is shown by the *solid blue line* for $\beta = 0$ and the *dotted violet line* for $\beta = 1$ in (12.35). This makes sense at filling factor $\nu = 4i + 4$

We now discuss the possibility that the description of the high-field data $n^*(B)$ improves within the merging picture if one takes account of nonlinear (cubic) corrections to the spectrum $\varepsilon(p)$ near the Fermi surface that lead naturally to a decrease of the effective mass with magnetic field. The cubic corrections should be important near the quantum critical point since the linear term is strongly suppressed, and the spectrum takes the form

$$\varepsilon(p) - \mu = \frac{p_F(p - p_F)}{m^*} + \beta \frac{(p - p_F)^3}{3m_b p_F}, \tag{12.33}$$

where $p_F = \hbar(\pi n_s)^{1/2}$ is the Fermi momentum and $\beta > 0$ is a coefficient. The cubic correction corresponds to an additional term in the single-particle Hamiltonian in magnetic fields. According to textbook rules, this term is written

$$\mathscr{H}_{add} = \beta \frac{\left[(\mathbf{p} - e\mathbf{A}/c)^2 - p_F^2\right]^3}{24 m_b p_F^4}, \tag{12.34}$$

where **A** is the vector potential. The resulting correction to the spectrum leads to a modification of (12.32) that describes the upper boundary of the merging region. The corrected equation reads

$$\hbar\omega_c - \Delta_Z - \Delta_\nu = -\beta \frac{(eB)^3}{3 m_b \hbar c^3 (\pi n_m)^2}. \tag{12.35}$$

Apparently, the right hand side of (12.35) can be important at high magnetic fields. Assuming that the coefficient $\beta = 1$, we estimate the influence of the correction and determine the corrected dependence $n_m(B)$, shown by the dotted violet line in Fig. 12.5. One concludes that the experimental data for the density $n^*(B)$ at which the oscillation minima at $\nu = 4i + 4$ disappear can be even better described within the concept of merging by taking into account cubic corrections to the spectrum at the Fermi surface near the quantum critical point.

References

1. A.B. Migdal, *Theory of Finite Fermi Systems and Applications to Atomic Nuclei* (Wiley, New York, 1967)
2. A. Bohr, B. Mottelson, *Nuclear Structure* (W. A. Benjamin, New York, 1969)
3. D. Shoenberg, *Magnetic Oscillations* (Cambridge University Press, Cambridge, 1984)
4. V.A. Khodel, V.R. Shaginyan, JETP Lett. **51**, 553 (1990)
5. Y. Sun, G. Kirczenow, Phys. Rev. Lett. **72**, 2450 (1994)
6. V.A. Khodel, V.R. Shaginyan, P. Schuk, JETP Lett. **63**, 752 (1996)
7. V.A. Khodel, J.W. Clark, H. Li, M.V. Zverev, Phys. Rev. Lett. **98**, 216404 (2007)
8. L.D. Landau, Zh Eksp, Teor. Fiz. **30**, 1058 (1956)
9. L.D. Landau, Zh Eksp, Teor. Fiz. **35**, 97 (1958)
10. P. Nozières, J. Phys. I Fr. **2**, 443 (1992)
11. E.M. Lifshitz, L. Pitaevskii, *Statistical Physics*, Part 2 (Butterworth-Heinemann, Oxford, 2002)
12. P. Ring, P. Schuck, *The Nuclear Many-Body Problem* (Springer, Berlin, 1980)
13. V.A. Khodel, V.R. Shaginyan, in *Condensed Matter Theories*, vol. 12, ed. by J. Clark, V. Plant (Nova Science Publishers, NY, 1997), p. 221
14. S.T. Belyaev, Mat. Fys. Medd. Dan. **31**(11) (1959)
15. V.A. Khodel, V.R. Shaginyan, V.V. Khodel, Phys. Rep. **249**, 1 (1994)
16. V.A. Khodel, M.V. Zverev, V.M. Yakovenko, Phys. Rev. Lett. **95**, 236402 (2005)
17. V.R. Shaginyan, M.Y. Amusia, A.Z. Msezane, K.G. Popov, Phys. Rep. **492**, 31 (2010)
18. V.R. Shaginyan, A.Z. Msezane, K.G. Popov, V.A. Stephanovich, Phys. Rev. Lett. **100**, 096406 (2008)
19. L.D. Landau, E.M. Lifshitz, *Quantum Mechanics, Non-relativistic Theory* (Pergamon, New York, 1965)
20. I.M. Khalatnikov, *An Introduction to the Theory of Superfluidity* (Benjamin, New York, 1965)
21. D. Pines, P. Noziéres, *Theory of Quantum Liquids* (Benjamin, New York, Amsterdam, 1966)
22. L.D. Landau, E.M. Lifshitz, *Statistical Physics* (Elsevier, Oxford, 1980)
23. G.E. Volovik, JETP Lett. **53**, 222 (1991)

24. V.A. Khodel, J.W. Clark, M.V. Zverev, Phys. Rev. B **78**, 075120 (2008)
25. J.W. Clark, M.V. Zverev, V.A. Khodel, Ann. Phys. **327**, 3063 (2012)
26. M.V. Zverev, V.A. Khodel, S.S. Pankratov, JETP Lett. **96**, 192 (2012)
27. A.A. Shashkin, V.T. Dolgopolov, J.W. Clark, V.R. Shaginyan, M.V. Zverev, V.A. Khodel, Phys. Rev. Lett. **112**, 186402 (2014)
28. S.V. Kravchenko, A.A. Shashkin, D.A. Bloore, T.M. Klapwijk, Solid State Commun. **116**, 495 (2000)
29. A.A. Shashkin, S.V. Kravchenko, V.T. Dolgopolov, T.M. Klapwijk, Phys. Rev. B **66**, 073303 (2002)
30. T. Ando, A.B. Fowler, F. Stern, Rev. Mod. Phys. **54**, 437 (1982)
31. E. Abrahams, S.V. Kravchenko, M.P. Sarachik, Rev. Mod. Phys. **73**, 251 (2001)
32. S.V. Kravchenko, M.P. Sarachik, Rep. Prog. Phys. **67**, 1 (2004)
33. A.A. Shashkin, Phys. Usp. **48**, 129 (2005)
34. V.T. Dolgopolov, Low Temp. Phys. **33**, 1 (2007)
35. A. Mokashi, S. Li, B. Wen, S.V. Kravchenko, A.A. Shashkin, V.T. Dolgopolov, M.P. Sarachik, Phys. Rev. Lett. **109**, 096405 (2012)

Chapter 13
Asymmetric Conductivity of Strongly Correlated Compounds

Abstract In this chapter, we show that the FC solutions for distribution function $n_0(\mathbf{p})$ generate NFL behavior, and violate the particle-hole symmetry inherent in LFL. This, in turn, yields dramatic changes in transport properties of HF metals, particularly, the differential conductivity becomes asymmetric. As it is demonstrated in Sect. 3.1, Fermi quasiparticles can behave as Bose one. Such a state is viewed as possessing the supersymmetry (SUSY) that interchanges bosons and fermions eliminating the difference between them. In the case of asymmetrical conductivity it is the emerging SUSY that violates the time invariance symmetry. Thus, restoring one important symmetry, the FC state violates another essential symmetry. As is shown in Sect. 5.3, the LFL behavior is restored under the application of magnetic field. Therefore, we expect that in magnetic fields SUSY is violated and the asymmetric part of the differential conductivity is suppressed. Scanning tunneling microscopy and point-contact spectroscopy closely related to the Andreev reflection are sensitive to both the density of states and the probability of the population of quasiparticle states determined by the function $n(\mathbf{p}, T)$ [1, 2]. Thus, the above experimental techniques are ideal tools for studying specific features of the NFL behavior of HF metals and high-T_c superconductors.

13.1 Normal State

The tunnelling current I flowing through a point contact of two ordinary metals is proportional to the applied voltage V and to the square of the modulus of the quantum mechanical transition interaction t. This is to be multiplied by the quantity $N_1(0)N_2(0)(n_1(\mathbf{p}, T) - n_2(\mathbf{p}, T))$ [3], where $N_1(0)$ and $N_2(0)$ are the densities of states of the metals 1 and 2 and $n_1(\mathbf{p}, T))$ and $n_2(\mathbf{p}, T))$ are, respectively, the distribution functions of these metals. On the other hand, in the semiclassical approximation, the wave function that determines the interaction t is proportional to $(N_1(0)N_2(0))^{-1/2}$. Therefore, the density of states cancels down in the final result and the tunnel current becomes independent of $N_1(0)N_2(0)$. Because the distribution $n(p, T \to 0) \to \theta(p_F - p)$ as $T \to 0$, where $\theta(p_F - p)$ is the step function, it can be verified that the differential tunnel conductivity $\sigma_d(V) = dI/dV$ is a symmetric

M.Y. Amusia et al., *Theory of Heavy-Fermion Compounds*, Springer Series
in Solid-State Sciences 182, DOI 10.1007/978-3-319-10825-4_13

or even function of V in the LFL theory. Actually, the symmetry of $\sigma_d(V)$ is obeyed if there is the (quasi)particle-hole symmetry, which is always present in the LFL theory. Hence, the fact that $\sigma_d(V)$ is symmetric is obvious and natural in the case of metal-metal contacts for ordinary metals that are in the normal or superconducting state.

We study the tunnelling current at low temperatures, which for ordinary metals is given by the expression [1, 3]

$$I(V) = 2|t|^2 \int [n(\varepsilon - V) - n(\varepsilon)]\, d\varepsilon. \tag{13.1}$$

Here we use again the atomic system of units $e = m = \hbar = 1$ and normalize the transition interaction to unity, $|t|^2 = 1$. Since the temperatures are low, we can approximate the distribution function $n(\varepsilon)$ by the step function $\theta(\mu - \varepsilon)$. Then, (13.1) yields $I(V) = a_1 V$ so that the differential conductivity $\sigma_d(V) = dI/dV = a_1 = const$ is a symmetric function of the applied voltage V.

To examine quantitatively the behaviour of the asymmetric part of the conductivity $\sigma_d(V)$, we differentiate both sides of (13.1) with respect to V. The result is the following equation for $\sigma_d(V)$:

$$\sigma_d = \frac{1}{T} \int n[\varepsilon(z) - V, T][1 - n(\varepsilon(z) - V, T)] \frac{\partial \varepsilon}{\partial z} dz, \tag{13.2}$$

We use the dimensionless momentum $z = p/p_F$ instead of ε in the integrand of (13.2), since for strongly correlated electron liquid n is no longer a function of ε. This is because for the latter case the energy-momentum dependence is no more linear (see panel a of Fig. 13.1), so that the proper dependence is upon momentum. Namely, the variable ε in the interval $(p_f - p_i)$ is equal to μ so that the quasiparticle distribution function varies within this interval. It is seen from (13.2) that the violation of the particle-hole symmetry makes $\sigma_d(V)$ to be asymmetric as a function of the applied voltage V [4–7].

The single particle energy $\varepsilon(\mathbf{k}, T)$ shown in Fig. 13.1a and the corresponding $n(\mathbf{k}, T)$ shown in the panel b evolve from the FC state characterized by $n_0(\mathbf{k}, T = 0)$ determined by the equation

$$\frac{\delta E}{\delta n(\mathbf{p})} = \varepsilon(\mathbf{p}) = \mu; \;\; p_i \le p \le p_f. \tag{13.3}$$

The momenta $p_i = k_i p_F$ and $p_f = k_f p_F$ are shown in Fig. 13.1a. It is seen from Fig. 13.1a, that at elevated temperatures the dispersion $\varepsilon(\mathbf{k}, T)$ becomes steeper, since the effective mass $M^*(T)$ diminishes, as it is seen from (3.12). At the Fermi level $\varepsilon(p, T) = \mu$, then from (2.5) the distribution function $n(p, T) = 1/2$. The vertical line in Fig. 13.1, crossing the distribution function at the Fermi level, illustrates the asymmetry of the distribution function with respect to the Fermi level at $T = 0.0001 E_F$. It is clearly seen that the FC state strongly violates the particle-hole

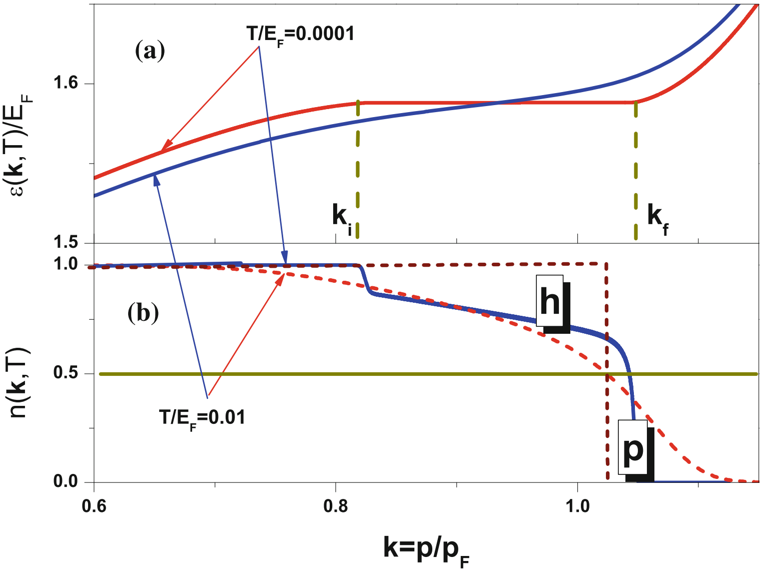

Fig. 13.1 The single particle energy $\varepsilon(\mathbf{k}, T)$ (**a**) and the distribution function $n(\mathbf{k}, T)$ (**b**) at finite temperatures as functions of the dimensionless variable $k = p/p_F$. The *arrows* show temperature measured in the units of E_F. At $T = 0.0001E_F$ the *vertical line* shows the position of the Fermi level E_F, at which $n(\mathbf{k}, T) = 0.5$ as depicted by the *horizontal line*. At $T \to 0$, the single particle energy $\varepsilon(\mathbf{k}, T)$ becomes more flat in the range $(p_f - p_i)$ so that the distribution function $n(\mathbf{k}, T)$ becomes more asymmetrical with respect to the Fermi level E_F, generating the particle-hole asymmetry related to the NFL behavior. To illuminate the asymmetry at $T = 0.01E_F$, the area bounded by the *short dash lines* and occupied by holes is marked by "**h**", and the area bounded by the *lines* and occupied by quasiparticles is marked by "**p**"

symmetry at decreasing temperatures. As a result, at low temperatures the asymmetric part of the differential conductivity becomes larger. On the hand, this state is viewed as the state possessing SUSY that interchanges bosons and fermions, and eliminates the difference between them, see Sect. 3.1. Thus, the asymmetrical conductivity is induced by the emerging SUSY, accompanying by the violation of the time invariance symmetry. Under the application of magnetic fields the system transits to the LFL state that strongly supports the particle hole symmetry, and violates SUSY. Therefore, the application of magnetic fields restoring the symmetry suppresses the asymmetric part of the differential conductivity.

Fairly simple transformations of (13.2) generate the following form for the asymmetric part of the differential conductivity

$$\Delta\sigma_d(V) = \frac{1}{2}[\sigma_d(V) - \sigma_d(-V)]. \tag{13.4}$$

Its explicit form yields

$$\varDelta\sigma_d(V) = \frac{1}{2}\int \frac{\alpha(1-\alpha^2)}{\Big[n(z,T)+\alpha[1-n(z,T)]\Big]^2} \times \frac{\partial n(z,T)}{\partial z}\frac{1-2n(z,T)}{\Big[\alpha n(z,T)+[1-n(z,T)]\Big]^2}dz,\ \alpha = \exp(-V/T). \tag{13.5}$$

Asymmetric tunnelling conductivity can be observed in the measurements involving metals, whose electron system is located near FCQPT or behind it. High-T_c superconductors and HF compounds like $\mathrm{YbRh_2(Si_{0.95}Ge_{0.05})_2}$, $\mathrm{CeCoIn_5}$, $\mathrm{YbCu_{5-x}Al_x}$ or $\mathrm{YbRh_2Si_2}$ are among such metals. The measurements should be done when the HF metal is in the superconducting or normal state. If the metal is in its normal state, the measurements of $\varDelta\sigma_d(V)$ can be done in a magnetic field $B > B_{c0}$ at temperatures $T^*(B) < T \leq T_f$ or in a zero magnetic field at temperatures higher than the corresponding critical temperature, when the electron system is in the paramagnetic state and its properties are determined by the entropy S_0. We note here that very often the experimentally measurable quantity is conductance (the characteristic of a specific sample) rather than conductivity, which is conductance multiplied by length and divided by cross-sectional area of a sample. Since in our theoretical considerations, the above length and cross-sectional area are kept constants, here we do not make a difference between conductance and conductivity. However, in the plots, related to experiment, we mention conductance as the quantity which has been actually measured.

We now derive an approximate expression to analyze the asymmetric part of the differential conductivity. It follows from (13.5) that for small V, the asymmetric part behaves as $\varDelta\sigma_d(V) \propto V$. We note here that the asymmetric part of the tunnelling conductivity is an odd function of V, $\varDelta\sigma_d(-V) = -\varDelta\sigma_d(V)$. The natural unit for measuring voltage is $2T$ as this quantity determines the characteristic energy for FC, as shown by (3.14). Actually, the asymmetric part should be proportional to the size $(p_f - p_i)/p_F$ of the region occupied by FC:

$$\varDelta\sigma_d(V) \simeq c_1\frac{V}{2T}\frac{p_f-p_i}{p_F} \simeq c\frac{V}{2T}\frac{S_0}{x_{FC}}. \tag{13.6}$$

where $S_0/x_{FC} \sim (p_f - p_i)/p_F$ is the temperature-independent part of the entropy [see (8.2)] and c_1 is a constant of the order of unity. For instance, calculations of c_1 with the distribution function displayed in Fig. 16.1 yield $c \sim 1$. From (13.6) we see that when $V \simeq 2T$ and FC occupies a sizable part of the Fermi volume, $(p_f - p_i)/p_F \simeq 1$, the asymmetric part becomes comparable to the differential tunneling conductivity $\varDelta\sigma_d(V) \sim V_d(V)$.

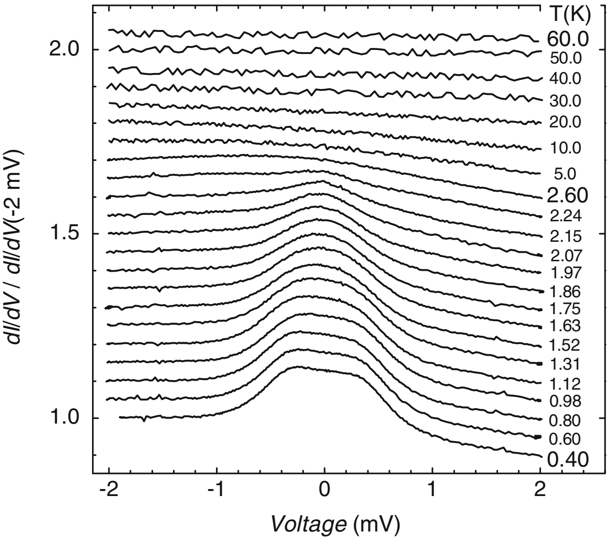

Fig. 13.2 Measured differential conductivity $\sigma_d(V)$ of point contacts Au/CeCoIn$_5$. The *curves* $\sigma_d(V)$ are displaced along the *vertical axis* by 0.05. The conductivity is normalized to its value at $V = -2\,\mathrm{mV}$. The asymmetry becomes noticeable at $T < 45\,\mathrm{K}$ and increases as the temperature decreases [8]

Figure 13.3a shows the results of calculations of the asymmetric part $\Delta\sigma_d(V)$ of the conductivity $\sigma_d(V)$ obtained from (13.5) [5]. In calculating the distribution function $n(z, T)$, we used the functional (6.17) with parameters $\beta = 3$ and $g = 8$. In this case, $(p_f - p_i)/p_F \simeq 0.1$. Figure 13.3a also shows that the asymmetric part $\Delta\sigma_d(V)$ of the conductivity (conductance) is a linear function of V for small voltages. Consistent with the Fig. 16.1 showing that the asymmetry of $n(\mathbf{k}, T)$ diminishes at elevated temperatures, the asymmetric part decreases with increasing temperature, which agrees with the behavior of the experimental curves in the panel b of Fig. 13.3. It is seen Fig. 13.3a, that (13.5) is in accordance with calculation based on (13.5): At low voltage the asymmetric conductance exhibits a linear dependence as a function of the voltage.

Recent measurements of the differential conductivity in CeCoIn$_5$ carried out by the point-contact spectroscopy technique [8] have clearly revealed its asymmetry in the superconducting ($T_c = 2.3\,\mathrm{K}$) and normal states. Figure 13.2 shows the results of these measurements. It is seen from Fig. 13.3b, that $\Delta\sigma_d(V)$ is nearly constant when the HF metal is in the superconducting state, experiencing no substantial variation near T_c, see also Fig. 13.7. Then it monotonically decreases as the temperature increases. Such a behavior of $\Delta\sigma_d(V)$ is related to the constancy of the effective mass at $T \leq T_c$, as it is discussed in Sect. 5.1.2. We pay attention to the fact that in the superconducting phase of CeCoIn$_5$ with $T \leq T_c = 2.3\,\mathrm{K}$ the asymmetric conductivity does not depend on temperature, see (13.9). Moreover, this independence

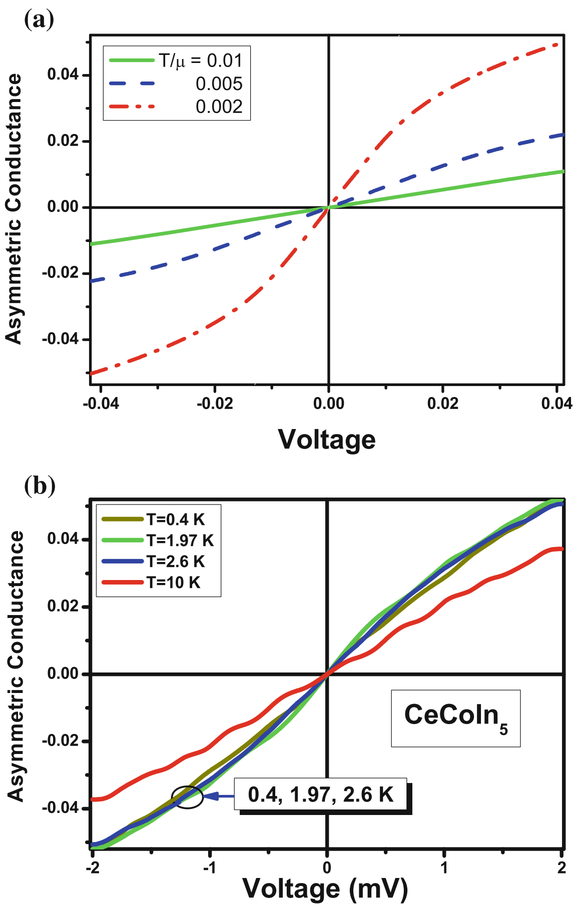

Fig. 13.3 Asymmetric conductance in CeCoIn$_5$. Panel **a** presents the asymmetric conductance $\Delta\sigma_d(V)$ as a function of V/μ for three normalized temperatures T/μ. Panel **b** shows the asymmetric conductance extracted from the data in Fig. 13.2. At $T \leq T_c$ ($T_c = 2.3$ K is the superconducting phase transition temperature) the conductance (and conductivity) becomes temperature independent

continues at $T \geq T_c$ K. Such a behavior suggests that there is the pseudogap in CeCoIn$_5$, resembling that of high-T_c superconductors. If we assume that there is the pseudogap, then we expect that $\Delta\sigma_d(V)$ remains approximately constant in the pseudogap state. It is seen from Fig. 13.3b, that $\Delta\sigma_d(V)$ is constant at $T \leq 2.6$ K, that is notably higher than T_c. This observation shows the existence of the pseudogap state in the HF compound CeCoIn$_5$. Thus, the study of the asymmetrical conductivity can be helpful in revealing the pseudogap state.

13.1.1 Suppression of the Asymmetrical Differential Resistance in YbCu$_{5-x}$Al$_x$ *in Magnetic Fields*

Now we consider the asymmetric part of the differential conductivity $\Delta\sigma_d(V)$ under the application of magnetic field B. Obviously, the differential conductivity being a scalar should not depend on the current I direction. Thus, the non-zero value of $\varDelta\sigma_d(V)$ manifests the violation of the particle-hole symmetry on a macroscopic scale. As we have seen in Sects. 5.3 and 6.1, at sufficiently low temperatures $T < T^*(B)$, the application of a magnetic field $B > B_{c0}$ leads to restoration of the LFL behavior eliminating the particle-hole asymmetry, and therefore the asymmetric part of the differential conductivity disappears [5, 6]. This prediction coincides with the experimental data on the differential resistance $dV/dI(V)$ under the application of magnetic fields in $\mathrm{YbCu_{5-x}Al_x}$ [9]. Representing the differential resistance as the sum of its symmetric $dV/dI^s(V)$ and asymmetric parts $dV/dI^{as}(V)$,

$$\frac{dV}{dI(V)} = \frac{dV}{dI^s(V)} + \frac{dV}{dI^{as}(V)},$$

we obtain the equation

$$\varDelta\sigma_d(V) \simeq -\frac{dV/dI^{as}(V)}{[dV/dI^s(V)]^2}. \tag{13.7}$$

To derive (13.7), we have assumed that $dV/dI^s(V) \gg dV/dI^{as}(V)$. Figure 13.4 [9] shows the temperature evolution of the symmetric $dV/dI^s(V)$ (a) and the asymmetric (b) $dV/dI^{as}(V)$ parts at zero value of the applied magnetic field. Also, the symmetric part does not show a decrease in $\rho(T)$, while the asymmetric one decreases at with growth of temperatures [9]. It is seen from Fig. 13.4 that the behavior of the asymmetric part of the differential resistance given by (13.6) and (13.7) is in accord with the experimental data. It is seen from Figs. 13.4 and 13.5 that the asymmetric part shows a linear behavior as a function of the voltage below about 1 mV [9], just as it was predicted in [5].

One can see from Fig. 13.5 [9] that with increase of magnetic fields the asymmetric part is suppressed. Thus, the application of magnetic fields destroys the NFL behavior and recovers both the LFL state and the particle-hole symmetry. We conclude that the particle-hole symmetry is macroscopically broken in the absence of applied magnetic fields, while the application of magnetic fields restores both the particle-hole symmetry and the LFL state. We note that the violation of the particle-hole symmetry makes broken the T-symmetry, that is the symmetry of physical laws under a time reversal transformation, as it is discussed in Chap. 16.

13.2 Superconducting State

Tunnel conductivity may remain asymmetric as a high-T_c superconductor or a HF metal passes into the superconducting state from the normal one. The reason is that the function $n_0(\mathbf{p})$ again determines the differential conductivity. As we have seen in Sect. 5.1, $n_0(\mathbf{p})$ is inessential distorted by the pairing interaction. This is because the latter interaction is weaker than the Landau one, which shapes the distribution function $n_0(\mathbf{p})$. Hence, the asymmetric part of the conductivity remains almost unchanged

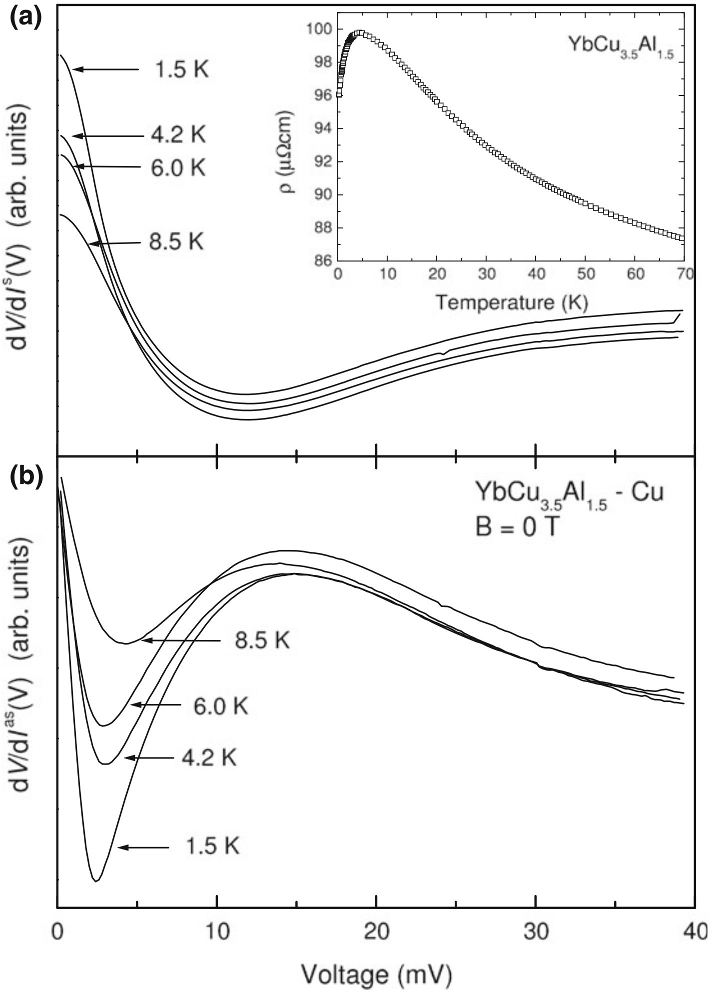

Fig. 13.4 Characteristic temperature behavior of **a** symmetric $dV/dI^s(V)$ and **b** asymmetric $dV/dI^{as}(V)$ parts of $dV/dI(V)$ for heterocontact YbCu$_{3.5}$Al$_{1.5}$ $-$ Cu at $B = 0$ and different temperatures shown by the *arrows*. The *inset* shows the bulk resistivity $\rho(T)$ of YbCu$_{3.5}$Al$_{1.5}$ [9]

for $T \leq T_c$, which agrees with the experimental results, see Fig. 13.2. In calculating the conductivity using the results of tunnelling microscopy measurements, we should keep in mind that the density of states of a superconductor

$$N_S(E) = N(\varepsilon - \mu)\frac{E}{\sqrt{E^2 - \Delta^2}} \tag{13.8}$$

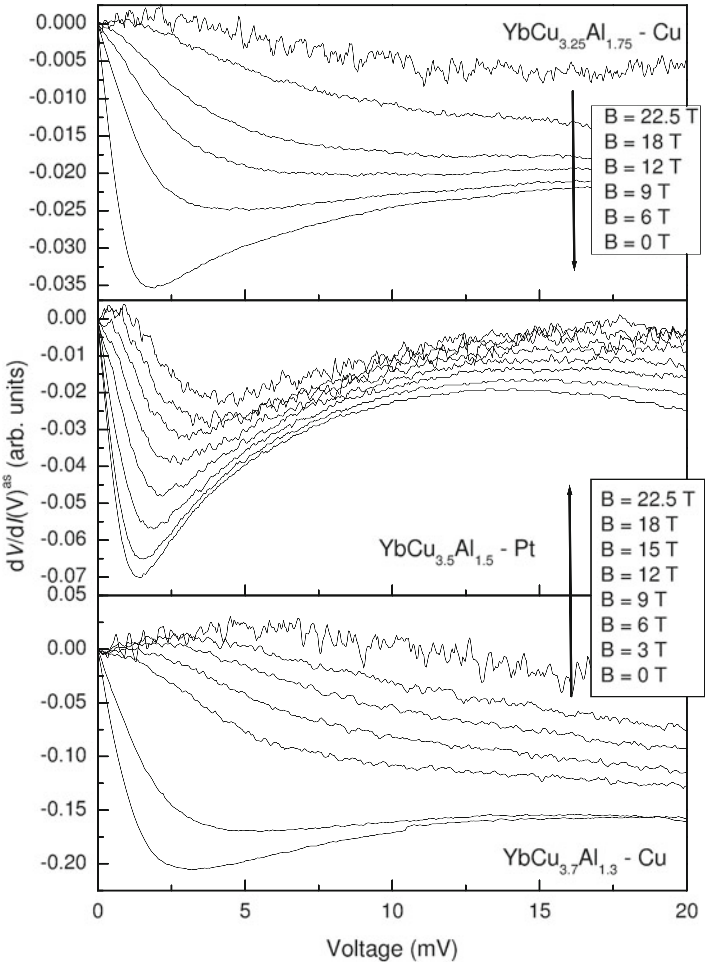

Fig. 13.5 Characteristic magnetic-field behavior of the asymmetric part $dV/dI^{as}(V)$ of the differential conductivity versus magnetic fields. The values of the field are displayed in the legends for heterocontacts with different $x = 1.3$, 1.5, and 1.75 at 1.5 K [9]

determines the conductivity, which is zero for $E \leq |\Delta|$, see, e.g., [10–12]. Here, E is the quasiparticle energy given by (5.5), and $\varepsilon - \mu = \sqrt{E^2 - \Delta^2}$. Equation (13.8) implies that the tunnel conductivity may be asymmetric, if the density of states in the normal state $N(\varepsilon)$ is asymmetric with respect to the Fermi level [13], which is the case for strongly correlated Fermi systems with FC. Our calculations of the above density of states based on model functional (6.17) (with the same parameters as those used in calculating $\Delta\sigma_d(V)$ shown in Fig. 13.3) corroborate this conclusion.

Figure 13.6 depicts the results of the calculated density of states $N(\xi, T)$. It is seen that $N(\xi, T)$ is strongly asymmetric with respect to the Fermi level. If the system

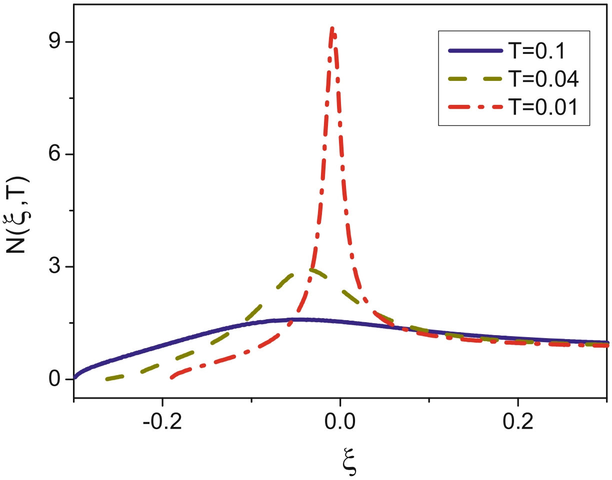

Fig. 13.6 Density of states $N(\xi, T)$ as a function of $\xi = (\varepsilon - \mu)/\mu$. $N(\xi, T)$ is calculated for three values of the temperature T, normalized to μ

is in the superconducting state, the normalized temperature listed in the legend, can be related to Δ_1. With $\Delta_1 \simeq 2T_c$, we find that $2T/\mu \simeq \Delta_1/\mu$. Since $N(\xi, T)$ is asymmetric, the first derivative $\partial N(\xi, T)/\partial\xi$ is finite at the Fermi level, and the function $N(\xi, T)$ can be written as $N(\xi, T) \simeq a_0 + a_1\xi$ for small values of ξ. The coefficient a_0 contributes nothing to the asymmetric part. Obviously, the value of $\Delta\sigma_d(V)$ is determined by the coefficient $a_1 \propto M^*(\xi = 0)$. In turn, $M^*(\xi = 0)$ is determined by (5.8). As a result, (13.6) assumes the form

$$\Delta\sigma_d(V) \sim c_1 \frac{V}{|\Delta|} \frac{S_0}{x_{FC}}, \tag{13.9}$$

because $(p_f - p_i)/p_F \simeq S_0/x_{FC}$, the energy E is replaced by the voltage V, and $\xi = \sqrt{V^2 - \Delta^2}$. The entropy S_0 here refers to the normal state of a heavy-fermion metal.

Actually, (13.9) coincides with (13.6) if we have in mind the fact that the characteristic energy of the superconducting state is determined by (5.9) and is temperature-independent. In studies of the universal behavior of the asymmetric conductivity, (13.9) has proven to be more convenient than (13.8). It follows from (13.6) and (13.9) that the measurements of the transport properties, for instance, the asymmetric part of the conductivity, allow the determination of the thermodynamic properties of the normal phase that are related to the entropy S_0. Equation (13.9) clearly shows that the asymmetric part of the differential tunnelling conductivity becomes comparable to the differential tunnelling conductivity at $V \sim 2|\Delta|$ if FC occupies a substantial part of the Fermi volume, $(p_f - p_i)/p_F \simeq 1$. In the case of the d-wave symmetry of the gap, the right-hand side of (13.9) must be averaged over the gap angular distribution $\Delta(\phi)$. This simple procedure amounts to redefining the gap size

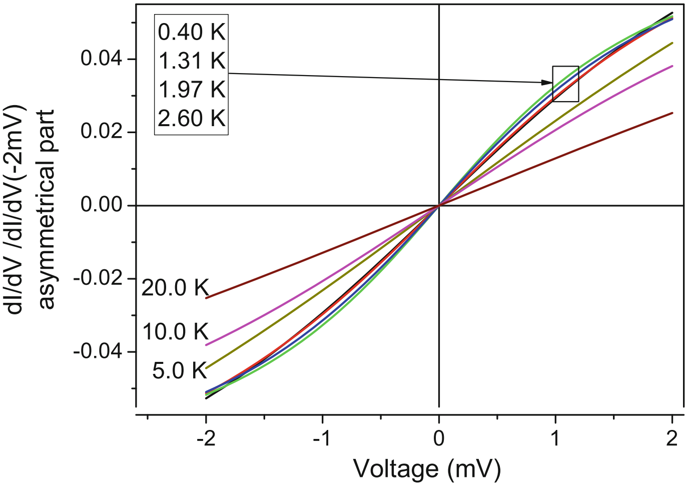

Fig. 13.7 Temperature dependence of the asymmetric parts $\Delta\sigma_d(V)$ of the conductance spectra extracted from measurements on $CeCoIn_5$ [8]. The temperatures are in the *box* and shown by the *arrow* for $T \leq 2.60$ K. Otherwise, the higher temperatures are given by numbers near the corresponding *curves*

or the constant c_1. As a result, (13.9) can also be applied when $V < \Delta_1$, where Δ_1 is the maximum size of the d-wave gap [6]. For the Andreev reflection [1–3], where the current is finite for any small V, (13.9) also holds for $V < \Delta_1$ in the case of the s-wave gap.

It is seen from Fig. 13.7 that the asymmetric part $\Delta\sigma_d(V)$ of the conductivity remains the same up to temperatures of about T_c, and persists up to temperatures well above T_c. At small voltages the asymmetric part is a linear function of V and starts to diminish at $T \geq T_c$. It follows from Fig. 13.7 that the above description of the asymmetric part based on (13.6) and (13.9) coincides with the the experimental data for $CeCoIn_5$.

Low-temperature tunneling microscopy and spectroscopy measurements have been used in [14] to detect an inhomogeneity in the electron density distribution in $Bi_2Sr_2CaCu_2O_{8+x}$. This inhomogeneity manifests itself as spatial variations in the local density of states in the low-energy part of the spectrum and in the size of the superconducting gap. The inhomogeneity observed in the integrated local density of states is not caused by impurities but is inherent in the system. Observation facilitates relating the integrated local density of states to the concentration x of local oxygen impurities.

Spatial variations in the differential tunneling conductivity spectrum are reported in Fig. 13.8. Clearly, the latter conductivity is highly asymmetric in the superconducting state of $Bi_2Sr_2CaCu_2O_{8+x}$. The differential tunneling conductivity shown in Fig. 13.8 may be interpreted as measured at different values of $\Delta_1(x)$ but at the same temperature, which allows studying the $\Delta\sigma_d(V)$ dependence on $\Delta_1(x)$. Figure 13.9 shows the asymmetric conductivity diagrams obtained from the data in Fig. 13.8.

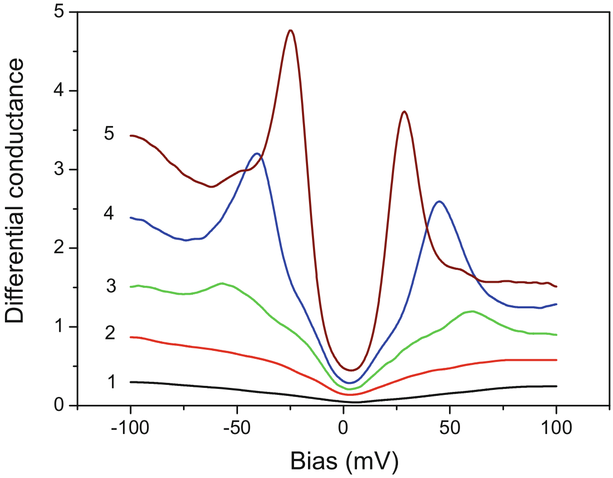

Fig. 13.8 Spatial variation of the differential tunnelling conductance spectra of the $Bi_2Sr_2CaCu_2O_{8+x}$. *Lines 1* and *2* belong to regions where the integrated local density of states is very low. Low differential conductivity and the absence of a gap show that we are dealing with an insulator. *Line 3* corresponds to a large gap (65 meV) with mildly pronounced peaks. The integrated value of the local density of states for *curve 3* is small, but is higher than that for *lines 1* and *2*. *Line 4* corresponds to a gap of about 40 meV, which is close to the average value. *Line 5* corresponds to the maximal integrated local density of states and the smallest gap of about 25 meV. Also, it has two sharp coherent peaks [14]

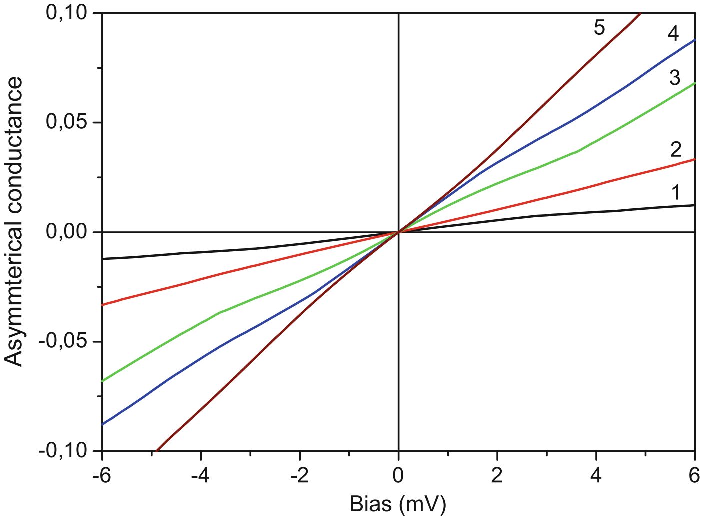

Fig. 13.9 The asymmetric part $\Delta\sigma_d(V)$ of the differential tunneling conductance in the high-T_c superconductor $Bi_2Sr_2CaCu_2O_{8+x}$. The corresponding values are extracted from the data in Fig. 13.8, and are presented as a function of the voltage V (mV). The lines numbering is consistent with that in Fig. 13.8

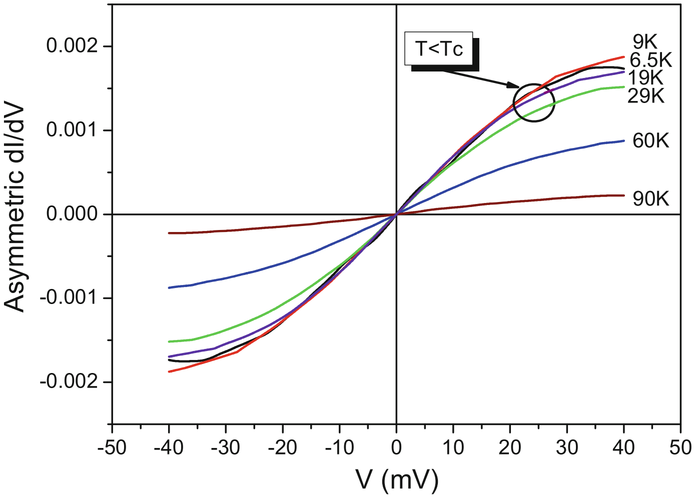

Fig. 13.10 Temperature dependence of the asymmetric part $\Delta\sigma_d(V)$ of the conductivity spectra. The data are obtained in measurements on $YBa_2Cu_3O_{7-x}/La_{0.7}Ca_{0.3}MnO_3$ by the contact spectroscopy method; the critical temperature $T_c \simeq 30\,K$ [15]

Clearly, for small voltages, $\Delta\sigma_d(V)$ is a linear function of V consistent with (13.9) and the slope of the respective straight lines $\Delta\sigma_d(V)$ is inversely proportional to the gap size Δ_1.

Figure 13.10 reports the variation of the asymmetric part $\Delta\sigma_d(V)$ with the temperature increase. The measurements have been performed on YBa_2 Cu_3O_{7-x} / $La_{0.7}Ca_{0.3}MnO_3$ with $T_c \simeq 30\,K$ [15]. It is seen that at $T < T_c \simeq 30\,K$, the asymmetric part $\Delta\sigma_d(V)$ depends on temperature only weakly in the region of the linear V-dependence. Such behavior agrees with (13.9). At $T > T_c$ the slope of the straight parts of $\Delta\sigma_d(V)$ dependence decreases with temperature increase. This behavior is described by (13.6). We conclude that the description of the universal behavior of $\Delta\sigma_d(V)$ based on the FCQPT is in good agreement with the results of the experiments presented in Figs. 13.3, 13.4, 13.5, 13.7, 13.9, and 13.10 and is valid for both high-T_c superconductors and HF metals.

13.3 Relation to the Baryon Asymmetry in the Early Universe

To finalize this chapter, we note that the demonstrated above particle-hole symmetry violation in the NFL state of HF compounds has its large-scale counterpart in the asymmetry between matter and antimatter in the early Universe [16]. In this case, the FCQPT concept delivers underlying physical mechanism for both above processes, which means that the FC phenomenon is rather general and not seldom in Nature.

As the details of matter-antimatter (baryon) asymmetry will be discussed in details in Chap. 16, here we present some general remarks regarding this question.

As it is well-known (see, e.g., [17–19]), the relation between particles and antiparticles in the Universe is governed by so-called CP (or more generally CPT) symmetry, which is the result of successive action of charge conjugation (C), transforming particle into antiparticle and parity (P), which reverses the directions of spatial coordinates. One more (T) symmetry results in time reversal, which reverses the time arrow. Simply speaking, the CPT symmetry is responsible for spin and charge conjugation, transforming particles into antiparticles. It is widely believed that at the initial stages of Universe, called Big Bang, creation the number of particles and antiparticles (or baryons and antibaryons, i.e. the rest mass carrying elementary particles, consisting of only either quarks or antiquarks, respectively [19]) was the same, while at the later stages, when the Universe began to cool down, this symmetry disappeared, giving rise to the current state where we have large clusters of visible matter (baryons) and the dark matter in their vicinity. The analogy between baryon-antibaryon and (quasi) particle-hole symmetry breaking can be obtained if we match baryon to a hole and antibaryon to a quasiparticle in a Fermi liquid. The standard observation in many ordinary metals is the symmetric character of their conductivity, which is a direct consequence of LFL theory, admitting complete particle-hole symmetry. As we have seen above, latter symmetry breaks down if we are going beyond LFL, which is the case, e.g., for HF compounds.

Indeed, recent experimental observations of low temperature electric conductivity in high-T_c superconductors [1] and in HF metals like $\mathrm{CeCoIn_5}$ and $\mathrm{YbCu_{5-x}Al_x}$ [8, 9] show that it is clearly asymmetric. Latter asymmetry vanishes as the temperature or magnetic field increases. We have demonstrated above, that the asymmetry cannot be explained in the framework of LFL theory since its particle-hole symmetry unavoidably leads to the step function for the fermion distribution function at low temperatures, which, in turn, results in a symmetric conductivity. To explain this asymmetry, the FCQPT notion has been invoked [16]. We note, that although fundamental microscopic interaction in FCQPT theory is fully symmetric with respect to quasiparticles and holes, at low temperatures it causes the spontaneous symmetry breaking [5, 20]. Asymmetry is due to the simple fact that, contrary to LFL, in strongly correlated fermion systems, the single-particle energy $\varepsilon(\mathbf{p})$ is temperature and magnetic field dependent. Thus, $n(\mathbf{p}, T)$ given by (16.3) does not reproduce the step function in the low temperature limit [21, 22]. The FCQPT approach of [16] is based on the observation that some condensed-matter systems like HF compounds, have topologically protected gapless and dispersionless fermions forming flat bands [23–25], which promote the FCQPT. This quantum phase transition, in turn, breaks the particle-hole symmetry, generating, among others, the observable asymmetric conductivity.

As is shown in Chap. 16, the same notion can be used to explain the baryon-antibaryon asymmetry in the Universe, which does not require any artificial extension of the standard models of cosmology. Namely, it is suggested that the initial state of the Universe was completely symmetric with the baryon number and CP conserved at the end of the inflation when the particle production started [16].

The observed asymmetry has been explained by suggesting that after the initial inflation, as the Universe cooled down in approximately 10 orders of magnitude, it came close to FCQPT similar to the situation in HF metals. At that time an excess of matter over the antimatter in the Universe had been generated by FC phenomenon. As the Universe cools down further, it has all NFL properties, dictated by FCQPT. We assume that this model describes the particle-antiparticle content of the Universe. At finite temperatures baryon-antibaryon asymmetry emerges as an inherent property of the system located in FC state. The asymmetry results from the distortion of the Fermi surface, or, in other words, because of the deviation of the distribution function $n(\mathbf{p})$ from the step function at low temperatures. At temperature lowering, the system approaches the quantum critical line which increases the asymmetry. Details of such increase depend on the model interparticle potential and other parameters. This interesting and important analogy is worth further extensive studies, which, in our opinion, can shed light not only on yet unsolved problems in condensed matter physics, but also on those in cosmology and particle physics.

References

1. G. Deutscher, Rev. Mod. Phys. **77**, 109 (2005)
2. A.F. Andreev, Zh Eksp, Teor. Fiz. **46**, 1823 (1964)
3. A.M. Zagoskin, *Quantum Theory of Many-Body Systems* (Springer, New York, 1998)
4. V.R. Shaginyan, M.Y. Amusia, K.G. Popov, Phys. Usp. **50**, 563 (2007)
5. V.R. Shaginyan, K.G. Popov, Phys. Lett. A **361**, 406 (2007)
6. V.R. Shaginyan, JETP Lett. **81**, 222 (2005)
7. V.R. Shaginyan, K.G. Popov, V.A. Stephanovich, E.V. Kirichenko, J. Alloy. Compd. **442**, 29 (2007)
8. W.K. Park, L.H. Greene, J.L. Sarrao, J.D. Thompson, Phys. Rev. B **72**, 052509 (2005)
9. G. Pristáš, M. Reiffers, E. Bauer, A.G.M. Jansen, D.K. Maude, Phys. Rev. B **78**, 235108 (2008)
10. L.N. Oliveira, E.K.U. Gross, W. Kohn, Phys. Rev. Lett. **60**, 2430 (1988)
11. J. Bardeen, L.N. Cooper, J.R. Schrieffer, Phys. Rev. **108**, 1175 (1957)
12. D.R. Tilley, J. Tilley, *Superfluidity and Superconductivity* (Hilger, Bristol, 1985)
13. P.W. Anderson, N.P. Ong, arXiv:0405518. pp. 1–5 (2004)
14. S.H. Pan, J.P. O'Neal, R.L. Badzey, C. Chamon, H. Ding, J.R. Engelbrecht, Z. Wang, H. Eisaki, S. Uchida, A.K. Gupta, K.W. Ng, E.W. Hudson, K.M. Lang, J.C. Davis, Nature **413**, 282 (2001)
15. S. Piano, F. Bobba, A.D. Santis, F. Giubileo, A. Scarfato, A.M. Cucolo, J. Phys: Conf. Ser. **43**, 1123 (2006)
16. V.R. Shaginyan, G.S. Japaridze, M.Y. Amusia, A.Z. Msezane, K.G. Popov, Europhys. Lett. **94**, 69001 (2011)
17. M. Sozzi, *Discrete Symmetries and CP Violation: From Experiment to Theory* (Oxford University Press, Oxford, 2008)
18. G.C. Branco, L. Lavoura, J.P. Silva, *CP Violation* (Clarendon Press, Oxford, 1999)
19. D.J. Griffiths, *Introduction to Elementary Particles* (Wiley, New York, 1987)
20. V.R. Shaginyan, M.Y. Amusia, A.Z. Msezane, K.G. Popov, Phys. Rep. **492**, 31 (2010)
21. V.A. Khodel, V.R. Shaginyan, JETP Lett. **51**, 553 (1990)
22. V.A. Khodel, V.R. Shaginyan, V.V. Khodel, Phys. Rep. **249**, 1 (1994)
23. G.E. Volovik, arXiv:1012.0905v3. (2010)
24. G.E. Volovik, J. Low Temp. Phys. **110**, 23 (1998)
25. G.E. Volovik, *The Universe in a Helium Droplet* (Clarendon Press, Oxford, 2003)

Chapter 14
Violation of the Wiedemann-Franz Law in HF Metals

Abstract Experimental observations of the much-studied compounds $CeCoIn_5$ and $YbRh_2Si_2$ at vanishing temperatures carefully probe the nature of their magnetic-field-tuned QCPs. The violation of Wiedemann-Franz (WF) law, along with jumps revealed both in the residual resistivity ρ_0 and the Hall resistivity R_H, provide vital clues to the origin of their non-Fermi-liquid behavior. The empirical facts point unambiguously to association of the observed QCP with FC forming flat bands.

As early as in 1853, German physicists Gustav Wiedemann and Rudolph Franz [1] discovered the empirical law stating that for different metals at low temperatures the ratio of its thermal conductivity $\kappa(T)$ to its electrical conductivity $\sigma(T)$ is the same, $\kappa(T)/\sigma(T) = \text{const}$. Later on, the Danish physicist Ludvig Valentin Lorenz showed that the above ratio is proportional to the temperature T, $\kappa(T)/\sigma(T) = LT$, the proportionality constant L is known as the Lorenz number. What is called Wiedemann-Franz (WF) law is indeed an independence of the Lorenz number L on temperature. However, it was firmly established that the WF law is obeyed both at room temperatures and at low ones (several Kelvins); while the intermediate temperatures $L = L(T)$.

Strictly speaking, the Lorenz number is temperature-independent only at low temperatures. Its theoretical value is

$$L_0 = \lim_{T\to 0} = \frac{\kappa(T)}{T\sigma(T)} = \frac{\pi^2}{3}\frac{k_B}{e^2}. \tag{14.1}$$

It had been calculated by Sommerfeld in 1927 [2] in the model of noninteracting electrons, obeying Fermi-Dirac statistics. The same result is obtained much later in LFL theory and reflects merely the fact that both thermal and electrical conductivities of a metal at low temperatures are determined by Landau quasiparticles. Due to this fact, possible deviations from the WF law can be regarded as a signature of NFL behavior in a considered compound.

Actually, (14.1) is usually referred to as the Wiedemann-Franz (WF) law. It was shown that at $T = 0$ (14.1) remains valid for arbitrarily strong scattering [3], disorder [4] and interactions [5]. This law holds for ordinary metals [6–9] and does not hold for HF metals [10–12] CeNiSn and $CeCoIn_5$ [12], $YbRh_2Si_2$ [13] (see also [14]), the electron-doped material [15] $Pr_{2-x}Ce_xCuO_{4-y}$, and the underdoped compound [16]

M.Y. Amusia et al., *Theory of Heavy-Fermion Compounds*, Springer Series
in Solid-State Sciences 182, DOI 10.1007/978-3-319-10825-4_14

$YbBa_2Cu_3O_y$. We note here, that WF law is also violated in mesoscopic systems, see [17] for review. In CeNiSn, the experimental value of the reduced Lorenz number $L(T)/L_0 \sim 1.5$ varies little at $T < 1\,\text{K}$. This rules out the phonon contribution to the violation of the WF law. In the electron-doped compound $Pr_{2-x}Ce_xCuO_{4-y}$ the departure of $L(T)$ from L_0 at $T > 0.3\,\text{K}$ is also considerably more then unity and even larger [15] than that in CeNiSn. Other experimental tests of the WF law have been undertaken in the normal state of cuprate superconductors. The phase diagram of these compounds shows evolution from Mott insulator for undoped materials towards metallic Fermi liquid behavior for overdoped cases. Upward shift $L/L_0 \simeq 2-3$ was found in underdoped cuprates at the lowest studied temperatures [15, 16, 18]. In strongly overdoped cuprates, the WF law was found to be perfectly correct [19].

The physical mechanism for the WF law violation is usually attributed to the NFL behavior, as it takes place in Luttinger and Laughlin liquids [20–23] or in the case of a marginal Fermi liquid [24]. Yet another possibility for the LFL theory and the WF law (14.1) violation occurs near QCPs where the effective mass M^* of a quasiparticle diverges. This is because at the QCP the Fermi liquid spectrum with finite Fermi velocity $v_F = p_F/M^*$ becomes meaningless as in this case $v_F \to 0$. Here we analyze the magnetotransport and violation of the WF law in HF compounds like $YbRh_2Si_2$ and $CeCoIn_5$ across a magnetic field tuned QCP. Close similarity between the properties of the Hall coefficient R_H and magnetoresistivity ρ at QCP discussed in Chaps. 8 and 10 indicates that all manifestations of magnetotransport stem from the same underlying physics. Thus, WF law violation along with the jumps of the Hall coefficient and magnetoresistivity in the zero-temperature limit provide unambiguous evidence for interpreting the QCP in terms of FCQPT forming a flat band in HF compounds.

The schematic phase diagram, demonstrating possible regions of the WF law violation, is depicted in Fig. 14.1, with the magnetic field B serving as the control parameter. At $B = 0$, the HF liquid acquires a flat band corresponding to a strongly degenerate state. The NFL regime reigns with increase temperatures and fixed magnetic field. With increasing B, the system is driven from the NFL region to the LFL domain. As it is shown in Fig. 14.1, the system moves from the NFL to the LFL regime along the horizontal arrow, and from the LFL to NFL along the vertical arrow. The magnetic-field-tuned QCP is indicated by the arrow and located at the origin of the phase diagram, since application of magnetic field destroys the flat band and shifts the system into the LFL state. The hatched area denotes the transition region that separates the NFL state from the weakly polarized LFL state and contains the dashed line tracing $T_M(B)$. Referring to Sect. 6.3.1, this line is defined by the function $T = a_1\mu_B B$, and the width $W(B)$ of the NFL state is seen to be proportional to T. In the same way, it can be shown that the width $T^*(B)$ of the transition region is also proportional to T. The regions, where WF law is violated and/or holds, are also shown.

We now focus on the empirical phase diagrams of HF compounds $YbRh_2Si_2$ (Fig. 14.2a, b) and $CeCoIn_5$ (Fig. 14.2c). Panel a of Fig. 14.2 is similar to the main panel of Fig. 14.1, but with the distinction that this HF compound possesses the AF state. To avert realization of a strongly degenerate ground state, induced by the flat

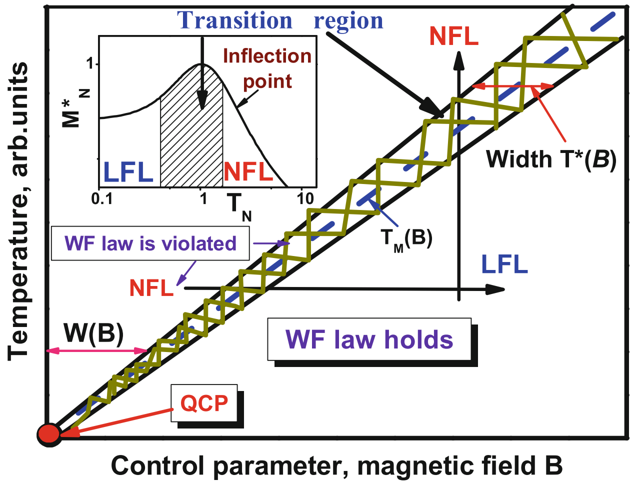

Fig. 14.1 Violation of the Wiedemann-Franz law and $T - B$ phase diagrams of HF metals. Schematic $T - B$ phase diagram of HF liquid with magnetic field as the control parameter. The *vertical* and *horizontal arrows* show LFL–NFL and NFL–LFL transitions at fixed B and T, respectively. At $B = 0$ the system is in its NFL state having a flat band down to $T \to 0$. The *hatched area* separates the NFL and the weakly polarized LFL phase and represents the transition state. The *dashed line* in the *hatched area* represents the function $T_M(B)$. The functions $W(B) \propto T$ and $T^*(B) \propto T$ shown by *two-headed arrows* define the widths of the NFL and the transition states, respectively. The QCP located at the origin denotes the critical point where the effective mass M^* diverges and both $W(B)$ and $T^*(B)$ tend to zero. The areas, where WF law holds (LFL state) and is violated (NFL and transition state) are also displayed. The *inset* shows a schematic plot of the normalized effective mass versus the normalized temperature. The transition regime, where M^*_N reaches its maximum value at $T_N = T/T_M = 1$, is shown as the *hatched area* in both the main panel and the *inset*. *Arrows* indicate the transition region and the inflection point $T_{\rm inf}$ in the M^*_N plot

band, the FC must be completely eliminated at $T \to 0$. In a general scenario, this occurs by means of an antiferromagnetic (AF) phase transition with an ordering temperature $T_{NL} = 70\,$mK, while application of a magnetic field $B = B_{c0}$ destroys the AF state at $T = 0$ [25]. In other words, the field B_{c0} places the HF metal at the magnetic-field-tuned QCP and nullifies the Nèel temperature $T_N(B_{c0}) = 0$ of the corresponding AF phase transition. Imposition of a magnetic field $B > B_{c0}$ drives the system to the LFL state. Thus, in the case of YbRh$_2$Si$_2$, the QCP is shifted from the origin to $B = B_{c0}$. In FC theory, the quantity B_{c0} is a parameter determined by the properties of the specific HF compound. In some cases, notably the HF metal CeRu$_2$Si$_2$, B_{c0} does vanish [26], whereas in YbRh$_2$Si$_2$, $B_{c0} \simeq 0.06$ T, $B \perp c$ [25]. Panel b of Fig. 14.2 portrays the experimental $T - B$ phase diagram in a manner showing the evolution of the exponent $\alpha_R(T, B)$ [13, 27]. At the critical field $B_{c0} \simeq 0.66$ T ($B \parallel c$), the NFL behavior extends down to the lowest temperatures, while YbRh$_2$Si$_2$ transits from the NFL to LFL behavior under increase of the applied magnetic field. Panel c of Fig. 14.2 depicts the $T - B$ phase diagram of compound

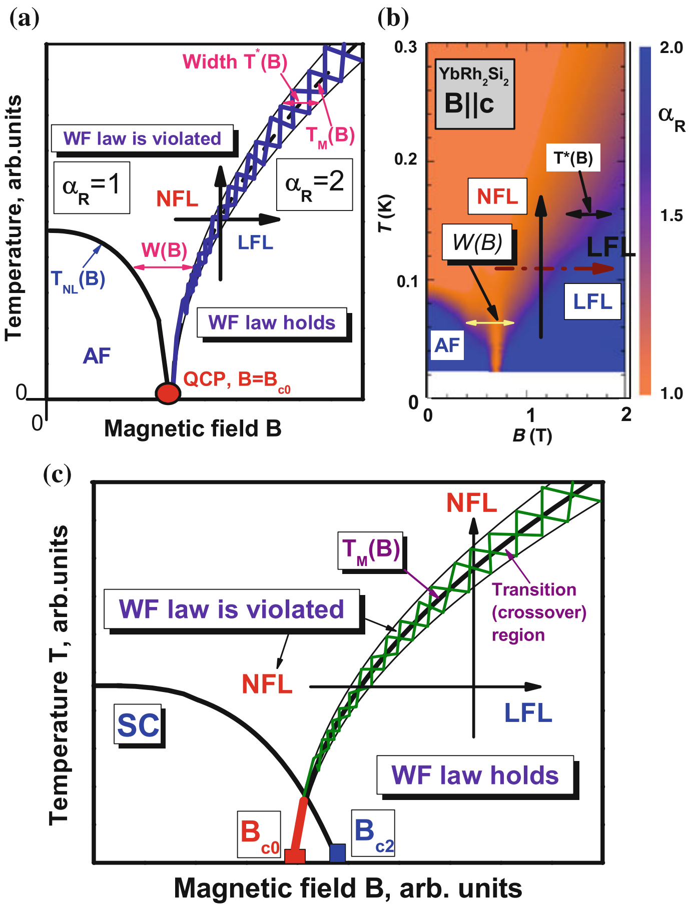

Fig. 14.2 Schematic phase diagrams of the HF compounds $\mathrm{YbRh_2Si_2}$ (panels **a**, **b**) and $\mathrm{CeCoIn_5}$ (panel **c**). In panel **a**, $T_{NL}(B)$ displays the Nèel temperature as a function of magnetic field B. The QCP, identified by the *arrow*, is now shifted from $B = 0$ to $B = B_{c0}$. At $B < B_{c0}$ the system is in its AF state. As in Fig. 14.1, the *vertical and horizontal arrows* show the transitions between the LFL and NFL states, the functions $W(B) \propto T$ and $T^*(B) \propto T$ indicated by the *two-sided arrows* define the width of the NFL state and of the transition region, respectively. The *dashed line* in the *hatched area* represents the function $T_M(B)$. The exponent α_R determines the temperature-dependent part of the resistivity, with α_R taking values 2 and 1, in LFL and NFL states. In the transition regime the exponent evolves between LFL and NFL values. Panel **b** shows the experimental $T - B$ phase diagram [13, 27]. The evolution of α_R is depicted by *color*. The NFL behavior reaches to the lowest temperatures *right* at the magnetic field tuned QCP. The transition regime between the NFL state and the field-induced LFL state broadens with rising magnetic fields $B > B_{c0}$ and $T \sim T^*(B)$. As in panel **a**, transitions from LFL to NFL state and from NFL to LFL state are indicated by the corresponding *arrows*, as are $W(B) \propto T$ and $T^*(B) \propto T$. In panel **c**, as shown by the *solid curve*, at $B < B_{c2}$ the system is in its superconducting state, with B_{c0} denoting a QCP hidden beneath the SC dome, where the flat band could exist at $B \leq B_{c0}$. The rest of the *lines* are similar to those from panel **a**. A part of the crossover above B_{c0} marked by *thick red line* is hidden in the SC state. The areas, where WF law holds (LFL state) and is violated (NFL and crossover region) are displayed in panels **a** and **c**

$\mathrm{CeCoIn_5}$. This phase diagram resembles those from the above panels a and b but with the difference that at low magnetic fields $\mathrm{CeCoIn_5}$ is in superconducting (SC) state, while its QCP is hidden beneath the superconducting dome. This implies the difference in the positions of critical fields B_{c0} in $\mathrm{CeCoIn_5}$ and $\mathrm{YbRh_2Si_2}$. In former compound this QCP is hidden under superconducting dome, $B_{c0} < B_{c2}$. It means that it lies in the superconducting state, which closes at $B = B_{c2}$, in latter one it corresponds to the QCP, comprising a boundary between NFL and magnetic—field—induced LFL parts of its phase diagram. Above the critical temperature T_c of the SC phase transition, the zero-field resistivity $\rho(T, B = 0)$ varies linearly with T. On the other hand, at $T \to 0$ and magnetic fields $B \geq B_{c2} \simeq 5$ T, the curve $\rho(T, B_{c2})$ is parabolic [10, 28]. Below we will show that WF law holds in LFL regime, while it is violated in NFL and transition regions of the phase diagram.

The violation of the WF law at the QCP in HF metals has been predicted and estimated a few years ago [29, 30] and observed recently [13]. Predictions of LFL theory fail in the vicinity of a QCP, where the effective mass M^* diverges, since the single-particle spectrum possesses a flat band at that point. In a once-standard scenario for such a QCP [31, 32], the divergence of the effective mass is attributed to vanishing of the quasiparticle weight z. However, as already indicated, this scenario is failed [33]. We therefore employ a different scenario for the QCP, in which the departure of the Lorenz number L from the Wiedemann-Franz value is associated with a rearrangement of sp degrees of freedom leading to a flat band. Within the quasiparticle paradigm, the relation between the Seebeck thermodynamic coefficient S and the thermal κ and electric σ conductivities has the form [34, 35]

$$\frac{\kappa(T)}{\sigma(T)T} + S^2(T) = \frac{1}{e^2}\frac{I_2(T)}{I_0(T)}. \tag{14.2}$$

Here

$$S(T) = \frac{1}{e}\frac{I_1(T)}{I_0(T)}, \tag{14.3}$$

with

$$I_k(T) = -\int \left(\frac{\varepsilon(p)}{T}\right)^k \left(\frac{d\varepsilon(p)}{dp}\right)^2 \tau(\varepsilon, T)\frac{\partial n(p)}{\partial \varepsilon(p)} d\upsilon, \tag{14.4}$$

where τ is the collision time, $d\upsilon$ is the volume element of momentum space. Overwhelming contributions to the integrals I_k come from a narrow vicinity $|\varepsilon| \sim T$ of the Fermi surface. In case of LFL, the Seebeck coefficient $S(T)$ vanishes linearly with T at $T \to 0$. The group velocity can be factored out from the integrals (14.4). The same is true for the collision time τ, which at $T \to 0$ depends merely on impurity scattering, and one obtains $I_1(T = 0) = 0$ and $I_2(T \to 0)/I_0(T \to 0) = \pi^2/3$. Inserting these results into (14.2), we find that the WF law holds, even if several bands cross the Fermi surface simultaneously [34].

It is worth illustrating the violation of the WF law by a numerical example [30]. As we have seen in Chap. 8, if the interaction function $F(k)$ has a singularity at $k = 0$, then at $g > g_c$ the system contains normal quasiparticles and FC fraction that grows linearly with the difference $g - g_c$. This situation is convenient for the demonstration of the impact of the particle-hole symmetry breaking in the systems with FC on the WF law violation. Below we address the model with the interaction function (see (6.18))

$$F(k) = g\frac{\exp(-\beta k)}{k}. \tag{14.5}$$

Since inside FC domain the single-particle spectrum $\varepsilon(p, T = 0) = \mu$, while outside it [36]

$$\frac{d\varepsilon(p, T = 0)}{dp} \propto \sqrt{|\varepsilon(p) - \mu|}, \tag{14.6}$$

such behavior results in a marked violation of the WF law. This conclusion is confirmed by results of numerical calculations, shown in Fig. 14.3.

The transport integrals I_k have been calculated numerically. We present the results of these calculations on Fig. 14.3. The calculations have been performed for $\beta p_F = 3$ and $\beta p_F = 30$. As it is seen from this figure, at the QCP and beyond it the integrals $I_0(T = 0)$ and $I_1(T = 0)$ has the same order, implying that in contrast to LFL theory, the $T = 0$ value of the Seebeck coefficient $S(0) = I_1(0)/eI_0(0)$ differs from 0. This is a fingerprint of particle-hole symmetry breaking, inherent in any system with FC. On the other hand, the ratio $L(0)/L_0$ turns out to be even larger than that at the QCP. Furthermore, calculations demonstrate that with increasing β, the value of this ratio increases as well, i.e. the longer the radius of the interaction function (14.5) in the coordinate space, the larger is the departure from the WF law. Thus, taking into account the fact that the reduction of the ratio L/L_0 occurs in the NFL state at the QCP [30], we conclude that the violation of the WF law takes place in the narrow segment of the $T - B$ phase diagram displayed in Figs. 14.1 and 14.2 with the width $W \to 0$ at $T \to 0$. In the other words, at $T \to 0$ the ratio L/L_0 becomes abruptly $L/L_0 \sim 0.9$ at $B/B_{c0} = 1$, while $L/L_0 = 1$ at $B/B_{c0} \neq 1$ when the system is in its AF or LFL state, shown in Fig. 14.2. This observation is in a good agreement with experimental data for $YbRh_2Si_2$ [13]. We conclude that at $T \to 0$, the WF law holds in the LFL state, at which the Fermi distribution function is reduced to the step function. The violation of the WF law at $B = B_{c0}$ and at $T \to 0$ seen in $YbRh_2Si_2$ thus suggests that a sharp Fermi surface does exist at $B/B_{c0} \neq 1$ but does not exist only at $B/B_{c0} = 1$, where the flat band emerges, the WF law is violated, and the jump of ρ_0 takes place, as it is shown in Fig. 14.4 by the arrow.

It was demonstrated in Chap. 10 that the application of a magnetic field to $YbRh_2Si_2$ makes the step-like drop in ρ_0 [37]. As it is seen from Fig. 14.4, when the system transits from the NFL state to the LFL at fixed T and under the application of growing magnetic fields B, the step-like drop in its resistivity $\rho(T, B)$ becomes more pronounced (see the experimental curves for $T = 0.3, 0.2$ and 0.1 K). It was

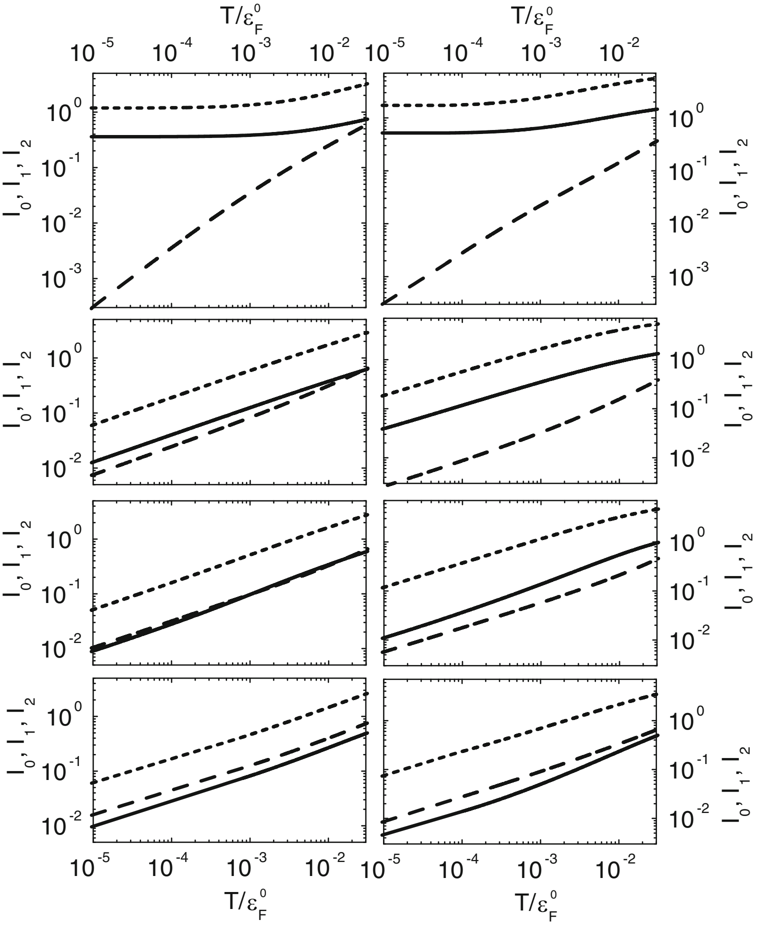

Fig. 14.3 The transport integrals (14.2) and (14.3). The transport integrals I_0 (*solid lines*), I_1 (*dashed lines*) and I_2 (*short-dashed lines*) in log-log scale as functions of reduced temperature T/ε_F^0, calculated with the interaction function (14.5) for $\beta p_F = 3$ (*left column*) and $\beta p_F = 30$ (*right column*) and four values of the parameter g corresponding to FL (*upper panels*), the QCP (*second line of panels*), and to the states with 10 % (*third line*) and 50 % (*lower panels*) of quasiparticles in the FC

shown in Sect. 10.3 that this behavior comes from the fact that $W \propto T$. As WF law is violated in the transition and NFL regions of the phase diagram, we conclude, that at $T = 0$ this law is violated in the narrow region of the ρ jump (see Fig. 14.4 with the arrow, showing the region of the WF law violation), while at higher temperatures this region widens and becomes diffuse. We also remark that at $T \to 0$ the NFL behavior can be captured by some states which destroy the flat band. For example, a short-range magnetic order prevents the NFL behavior from persisting down to $T \to 0$ by destroying the flat band. In that case at low temperatures the validity

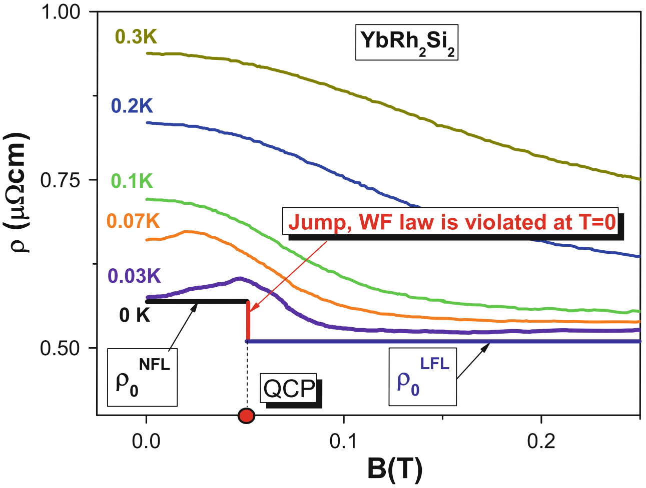

Fig. 14.4 Experimental results [37] for the longitudinal magnetoresistivity $\rho(T, B)$ of $\mathrm{YbRh_2Si_2}$ versus B at various temperatures T. The temperatures are indicated in the figure. The maxima of the *curves* for $T = 0.03$ and 0.07 K correspond to boundary points of the AF ordered state shown in Fig. 14.2b. The *solid lines marked* with 0 K represent the schematic behavior of the residual resistivity ρ_0 as a function of B. The *arrows* pointing to the *horizontal solid lines* identify the residual resistivities ρ_0^{NFL} and ρ_0^{LFL} in $\mathrm{YbRh_2Si_2}$. The jump of ρ_0 occurs at the QCP identified by an *arrow*. This is the point where WF law is violated at $T = 0$

of the WF law is restored. This means, in turn, that the experimental observation of deviation of L/L_0 ratio from unity (i.e. WF law violation) is extremely difficult. This observation is in agreement with experimental results, some of which directly point to the WF law violation in the case of the HF metal $\mathrm{YbRh_2Si_2}$ [13], while the others gives evidence that the WF holds [14, 38].

Not so long ago, the anisotropy of the WF law violation near the QCP has been experimentally observed in the HF metal $\mathrm{CeCoIn_5}$ [12]. In that paper, the above HF compound has been studied experimentally in external magnetic fields, close to the critical value H_{c2} that suppresses the superconductivity. Under these conditions, the WF law is violated. The violation is anisotropic and cannot be attributed to the above standard scenario of quasiparticle distraction by the fluctuation taking place at QCP. At the same time, close to the QCP, sufficiently large external magnetic fields reveal the anisotropy of the electrical conductivities $\sigma_{ik} \propto < v_i v_k >$ (v_i are the components of the group velocity vector) and thermal conductivities $\kappa_{ik} \propto < \varepsilon(\mathbf{p}) v_i v_k >$ of a substance. This is because the magnetic field does not affect the z-components of the group velocity $\mathbf{v}$ so that the QCP T-dependence of the transport coefficients holds, triggering the violation of the WF relation $L_{zz} = \sigma_{zz}/T\kappa_{zz} = \pi^2 k_B/3e^2$. On the other hand, the magnetic field $\mathbf{B}$ alters substantially the electron motion in the perpendicular direction, yielding considerable increase of the x and y components of the group velocity so that the corresponding components L_{ik} do not depart from their WF value.

Therefore, the flattening of the single particle spectrum $\varepsilon(\mathbf{p})$ of strongly correlated electron systems alters considerably their transport properties, especially beyond the FCQPT point due to particle-hole symmetry breaking. In topologically different "iceberg" phases the WF law is also violated near its QCP. The results of theoretical [30] and experimental investigations demonstrate that the FCQPT scenario with further occurrence of both "iceberg" and FC phases give natural and universal explanation of the NFL changes of the transport properties of HF compounds in general and of the WF law violation in particular. Therefore, as we have demonstrated above, to describe theoretically the violation of the WF law within the FCQPT formalism, it is sufficient to use the well-known LFL formulas for thermal and electrical conductivities, with the substitution of the modified single-particle spectrum into them. Such theory has been advanced in [30, 39]. The authors show that close to the QCP the Lorenz number $L_{\mathrm{QCP}}(T = 0) = 1.81\, L_0$. This result agrees well with the experimental values [11, 15]. Furthermore, the dependence $L(T)/L_0$ has been calculated for two topologically distinct phases (see Sect. 4.1)—"iceberg" phase and FC phase [30, 39]. Theoretical calculations have shown that in both phases the largest departure from the WF law occurs near QCP [30, 39]. Deep in the "iceberg" phase we have the reentrance of the "classical" WF law in a sense that $L = L_0$ while in the deep FC phase the Lorenz number is temperature independent at low temperatures, but its value is slightly larger than L_0. This is due to the particle-hole symmetry violation in FC phase [40–42].

References

1. G. Wiedemann, R. Franz, Ann. Phys. **89**, 497 (1853)
2. A. Sommerfeld, Naturwissenschaften **15**, 825 (1927)
3. G.V. Chester, A. Tellung, Proc. Phys. Soc. **77**, 1005 (1961)
4. M.J. Kearney, P.N. Butcher, J. Phys. C. Solid State Phys. **21**, L265 (1988)
5. C. Castellani, C. DiCastro, G. Kotliar, P.A. Lee, G. Strinati, Phys. Rev. Lett. **59**, 477 (1987)
6. H.R. Ott, O. Marti, F. Hulliger, Solid St. Comm. **49**, 1129 (1984)
7. A. Amato, D. Jaccard, E. Walker, J. Sierro, J. Flouquet, J. Magn. Magn. Mater. **63–64**, 300 (1987)
8. S. Kambe, H. Suderow, T. Fukuhara, J. Flouquet, T. Takimoto, J. Low Temp. Phys. **117**, 101 (1999)
9. R.T. Syme, M.J. Kelly, M. Pepper, J. Phys., Condenns. Matter **1**, 3375 (1989)
10. J. Paglione, M.A. Tanatar, D.G. Hawthorn, F. Ronning, R.W. Hill, M. Sutherland, L. Taillefer, C. Petrovic, Phys. Rev. Lett. **97**, 106606 (2006)
11. S. Paschen, B. Wand, G. Sparn, F. Steglich, Y. Echizen, T. Takabatake, Phys. Rev. B **62**, 14912 (2000)
12. M.A. Tanatar, J. Paglione, L. Taillefer, C. Petrovich, Science **316**, 1320 (2007)
13. H. Pfau, S. Hartmann, U. Stockert, P. Sun, S. Lausberg, M. Brando, S. Friedemann, C. ius Krellner, C. Geibel, S. Wirth, S. Kirchner, E. Abrahams, Q. Si, F. Steglich. Nature **484**, 493 (2012)
14. J.P. Reid, M.A. Tanatar, R. Daou, R. Hu, C. Petrovic, L. Taillefer (2013). arXiv:1309.6315v1
15. R.W. Hill, C. Proust, L. Taillefer, P. Fournier, R.L. Greene, Nature **414**, 711 (2001)
16. N. Doiron-Leyrand, M. Sutherland, S.Y. Li, L. Taillefer, R. Liang, D.A. Bonn, W.N. Hardy, Phys. Rev. Lett. **97**, 207001 (2006)

17. G.B. Lesovik, I.A. Sadovsky, Phys. Uspekhi **54**, 1007 (2011)
18. C. Proust, K. Behnia, R. Bel, D. Maude, S.I. Vedeneev, Phys. Rev. B **72**, 214511 (2005)
19. C. Proust, E. Boaknin, R.W. Hill, L. Taillefer, A.P. Mackenzie, Phys. Rev. Lett. **89**, 147003 (2002)
20. C.L. Kane, M.P.A. Fisher, Phys. Rev. Lett. **76**, 3192 (1996)
21. C.L. Kane, M.P.A. Fisher, Phys. Rev. B **55**, 15832 (1997)
22. L.G.C. Rego, G. Kirczenow, Phys. Rev. B **59**, 13080 (1999)
23. M.R. Li, E. Orignac, Europhys. Lett. **60**, 432 (2002)
24. C.M. Varma, P.B. Littlewood, S. Schmittrink, E. Abrahams, A.E. Ruckenstein, Phys. Rev. Lett. **63**, 1996 (1989)
25. P. Gegenwart, J. Custers, C. Geibel, K. Neumaier, K.T.T. Tayama, O. Trovarelli, F. Steglich, Phys. Rev. Lett. **89**, 056402 (2002)
26. D. Takahashi, S. Abe, H. Mizuno, D. Tayurskii, K. Matsumoto, H. Suzuki, Y. Onuki, Phys. Rev. B **67**, 180407(R) (2003)
27. J. Custers, P. Gegenwart, H. Wilhelm, K. Neumaier, Y. Tokiwa, O. Trovarelli, C. Geibel, F. Steglich, C. Pépin, P. Coleman, Nature **424**, 524 (2003)
28. J. Paglione, M. Tanatar, D. Hawthorn, E. Boaknin, R.W. Hill, F. Ronning, M. Sutherland, L. Taillefer, C. Petrovic, P. Canfield, Phys. Rev. Lett. **91**, 246405 (2003)
29. V.R. Shaginyan, M.Y. Amusia, A.Z. Msezane, K.G. Popov, Phys. Rep. **492**, 31 (2010)
30. V.A. Khodel, V.M. Yakovenko, M.V. Zverev, JETP Lett. **86**(86), 772 (2007)
31. P. Coleman, C. Pépin, Q. Si, R. Ramazashvili, J. Phys. Condens. Matter **13**, R723 (2001)
32. P. Coleman, C. Pepin, Phys. B **312–313**, 383 (2002)
33. V.A. Khodel, JETP Lett. **86**, 721 (2007)
34. E.M. Lifshitz, L.P. Pitaevskii, *Physical Kinetics* (Pergamon Press, Oxford, 1981)
35. N.W. Ashkroft, N.D. Mermin, *Solid State Physics* (HRW, Philadelphia, 1976)
36. V.A. Khodel, V.R. Shaginyan, V.V. Khodel, Phys. Rep. **249**, 1 (1994)
37. P. Gegenwart, T. Westerkamp, C. Krellner, Y. Tokiwa, S. Paschen, C. Geibel, F. Steglich, E. Abrahams, Q. Si, Science **315**, 969 (2007)
38. Y. Machida, K. Tomokuni, K. Izawa, G. Lapertot, G. Knebel, J.P. Brison, J. Flouquet, Phys. Rev. Lett. **110**, 236402 (2013)
39. V.A. Khodel, J.W. Clark, V.M. Yakovenko, M.V. Zverev, Phys. B **403**, 1227 (2008)
40. V.R. Shaginyan, K.G. Popov, Phys. Lett. A **361**, 406 (2007)
41. V.R. Shaginyan, JETP Lett. **81**, 222 (2005)
42. V.R. Shaginyan, V.A. Stephanovich, Phys. B **403**, 739 (2008)

Chapter 15
High Magnetic Fields Thermodynamics of Heavy Fermion Metals

Abstract In this chapter, we present the comprehensive theoretical analysis of thermodynamics of HF compounds at high magnetic fields. Such analysis permits to gain a deeper insight into the interplay of high magnetic field and temperature in suppressing and retrieving the Landau Fermi liquid state in these substances. Our analysis shows that although high magnetic fields and temperatures alter the properties of ordinary Landau quasiparticles, they survive, generating the experimentally observable anomalies in the thermodynamical quantities of HF compounds. We illustrate our theoretical findings by the example of the HF compound $\mathrm{YbRh_2Si_2}$.

15.1 Introduction

As we have seen in the previous chapters, the heavy fermion (HF) compounds play a distinctive role in modern condensed matter physics as many of their physical properties deviate substantially from those predicted by famous the LFL theory. The explanation of these puzzling NFL effects is of primary concern and challenge for existing theoretical approaches. The latter effects are especially surprising since their manifestations exist over a rather big region of temperature T and magnetic field B variations. For example, recent measurements of the specific heat C of $\mathrm{YbRh_2Si_2}$ under the application of magnetic field B show that the above temperature range extends at least up to twenty Kelvins, as it is reported in the inset to Fig. 15.1. As it is well-known from the LFL theory, the ratio C/T is proportional to quasiparticle effective mass M^*. The inset to Fig. 15.1 reports the dependence of $C(T)/T$, which has a maximum $M^*_{\max}(B)$ at some temperature $T_{\max}(B)$. It is seen, that $M^*_{\max}(B)$ decreases as magnetic field B grows, while $T_{\max}(B)$ shifts to higher T reaching 15 K at $B = 18\,\mathrm{T}$ [1].

A deeper insight into the behavior of C/T in the inset in Fig. 15.1 can be achieved using some "internal" scales. Namely, near QCP it is convenient to normalize the effective mass M^* and temperature T by their maximal values, $M^*_{\max}$ and $T_{\max}$, respectively. This generates the normalized effective mass $M^*_N = M^*/M^*_{\max}$ and temperature $T_N = T/T_{\max}$ [2]. The main panel of Fig. 15.1 reports the obtained dependence $M^*_N(T_N)$, which is shown by symbols, corresponding to different

M.Y. Amusia et al., *Theory of Heavy-Fermion Compounds*, Springer Series in Solid-State Sciences 182, DOI 10.1007/978-3-319-10825-4_15

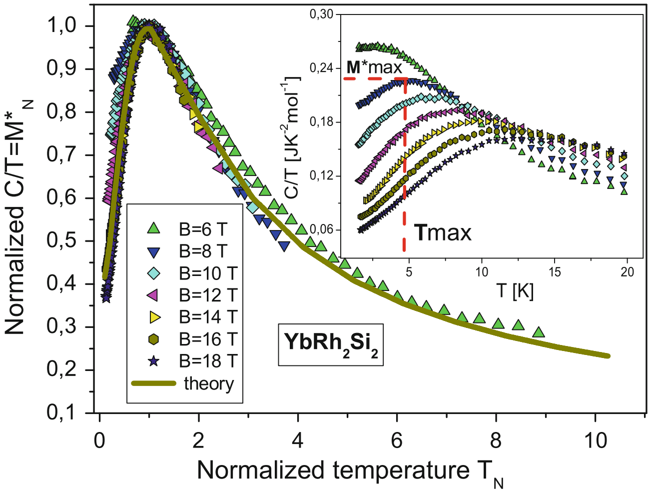

Fig. 15.1 The normalized effective mass $M_N^* = M^*/M_{\max}^*$ versus normalized temperature $T_N = T/T_{\max}$. M_N^* is extracted from the measurements (shown in the *inset*) of the specific heat C/T on $YbRh_2Si_2$ in magnetic fields B [1] listed in the legend. Our calculations (made at $B \simeq B^*$ when the quasiparticle band is fully polarized) are depicted by the solid curve tracing the scaling behavior of M_N^*. The *inset* reports the temperature dependence of the electronic specific heat C/T of $YbRh_2Si_2$ at different magnetic fields [1] shown in the main panel legend. The illustrative values of $M_{\max}^*$ and $T_{\max}$ at $B = 8$ T are also shown

magnetic fields. This immediately reveals the scaling in the normalized experimental curves: The curves at different magnetic fields B merge into a single one in terms of the normalized variable $T_N = T/T_{\max}$. It is seen from Fig. 15.1, that the normalized effective mass $M_N^*(T_N)$ is not a constant as it would be for LFL case. Rather, it shows the scaling behavior in terms of normalized temperature T_N. It is also seen from Fig. 15.1, both in the main panel and in the inset that the NFL behavior and the associated scaling extend at least to temperatures around twenty Kelvins.

It has been established experimentally [1], that at low magnetic fields B, $YbRh_2Si_2$ has a QCP related to the suppression of antiferromagnetic ordering at a critical magnetic field $B = B_{c0} \simeq 0.06$ T. Below, we will see that our calculations of the thermodynamic properties of $YbRh_2Si_2$ in broad magnetic field range, from $B_{c0} \simeq 0.06$ to $B \simeq 18$ T, allow us to straddle a possible metamagnetic transition region and probe the properties of both low-field HF liquid and high-field fully polarized one. Namely, high magnetic fields $B \sim B^* \sim 10$ T fully polarize corresponding quasiparticle band, so that quasiparticles spins become fully aligned along magnetic field direction. As a result, the LFL state is generated and the NFL one is, correspondingly, suppressed. The latter state can be restored at elevating temperatures.

Thus, we conclude that a complicated problem for theories considering the high magnetic field ($B \sim B^*$) NFL behavior of the HF metals is to explain both the scaling and the shape of $M_N^*(T_N)$. Another part of the same problem is the remarkably large temperature and magnetic field ranges, where the NFL behavior and scaling are observed, see above.

As we have shown above, the difference between our approach, related to FCQPT and the ordinary LFL approach, is a modification of the Landau paradigm, which generates the different behavior of a quasiparticle effective mass. Since in this Chapter we will heavily rely on this formalism, and have to take into account explicitly the spin dependence, and for the reader's convenience, we recapitulate the derivation of the main results. To be specific, in our FCQPT approach [2], in order to study the NFL behavior of the effective mass $M^*(T, B)$, we use the equation for the quasiparticle effective mass in a Fermi liquid. The only modification is that in our formalism the effective mass is no more constant but depends on temperature, magnetic field and other external parameters. For the model of homogeneous HF liquid at finite temperatures and magnetic fields, this equation acquires the form [2–4]

$$\frac{1}{M^*_\sigma(T, B)} = \frac{1}{M} + \sum_{\sigma_1} \int \frac{\mathbf{p}_F \mathbf{p}}{p_F^3} F_{\sigma,\sigma_1}(\mathbf{p_F}, \mathbf{p}) \frac{\partial n_{\sigma_1}(\mathbf{p}, T, B)}{\partial p} \frac{d\mathbf{p}}{(2\pi)^3}, \quad (15.1)$$

where M is a bare electron mass, $F_{\sigma,\sigma_1}(\mathbf{p}_F, \mathbf{p})$ is the Landau interaction, which depends on Fermi momentum $\mathbf{p}_F$, momentum $\mathbf{p}$, and spin projection σ. For definiteness, we assume that the HF liquid is 3D liquid. The Landau interaction is determined by the following relation [3, 4]

$$F_{\sigma,\sigma'}(\mathbf{p}, \mathbf{p}') = \frac{\delta^2 E[n]}{\delta n_\sigma(\mathbf{p}) \delta n_{\sigma'}(\mathbf{p}')}, \quad (15.2)$$

where $E[n]$ is the system energy, which is a functional of the quasiparticle distribution function n [2–4]. It can be expressed as

$$n_\sigma(\mathbf{p}, T) = \left\{1 + \exp\left[\frac{(\varepsilon_\sigma(\mathbf{p}, T) - \mu_\sigma)}{T}\right]\right\}^{-1}, \quad (15.3)$$

where $\varepsilon_\sigma(\mathbf{p}, T)$ is the single-particle spectrum. In our case, the chemical potential μ also depends on the spin due to Zeeman splitting $\mu_\sigma = \mu \pm \mu_B B$, μ_B is Bohr magneton.

In LFL theory, the single-particle spectrum is a variational derivative of the system energy $E[n_\sigma(\mathbf{p}, T)]$ with respect to the occupation number n_σ, $\varepsilon_\sigma(\mathbf{p}, T) = \delta E[n(\mathbf{p})]/\delta n_\sigma$. The choice of model of the interaction is determined by the fact that we consider the system has to be at the QCP of FCQPT. Namely, in this region the momentum-dependent part of Landau interaction can be taken in the form presented by truncated power series $F = a(\mathbf{p}-\mathbf{p}')^2 + b(\mathbf{p}-\mathbf{p}')^3 + c(\mathbf{p}-\mathbf{p}')^4 + \cdots$, where a, b and c are fitting parameters. We note that this interaction, being an analytical function of $(\mathbf{p}-\mathbf{p}')^2$, can generate topological phase transitions interfering with FCQPT [2]. In our case F does not depend on the number density x of the system as it is fixed by condition that the system is situated in QCP of FCQPT. Thus, the variational procedure, being applied to the functional $E[n_\sigma(\mathbf{p}, T)]$, leads to the following form for $\varepsilon(\mathbf{p}, T) = \varepsilon_\sigma(\mathbf{p}, T) \equiv \varepsilon[n_\sigma(\mathbf{p}, T)]$

$$\varepsilon_\sigma(\mathbf{p}, T) = \frac{p^2}{2M} + \sum_{\sigma_1} \int F_{\sigma,\sigma_1}(\mathbf{p}, \mathbf{p}_1) n_{\sigma_1}(\mathbf{p}_1, T) \frac{d^3 p_1}{(2\pi)^3}. \tag{15.4}$$

Equations (15.3) and (15.4) constitute the closed set of equations for self-consistent determination of $\varepsilon_\sigma(\mathbf{p}, T)$ and $n_\sigma(\mathbf{p}, T)$. The solutions of (15.4) generate the spectrum, where the first two p-derivatives are equal to zero. Since the first derivative is proportional to the reciprocal quasiparticle effective mass $1/M^*$, its zero just signifies QCP of FCQPT. The second derivative must vanish also. Otherwise $\varepsilon(p) - \mu$ has the same sign below and above the Fermi surface, and the Landau state becomes unstable [2, 5]. Zeros of these two subsequent derivatives mean that the spectrum $\varepsilon(\mathbf{p})$ has an inflection point at p_F so that the lowest term of its Taylor expansion is proportional to $(p - p_F)^3$. In the other words, close to FCQPT the single—particle spectrum does not have the usual form $v_F(p - p_F)$, with v_F being the Fermi velocity.

Having solved (15.3) and (15.4), we substitute their solution into (15.1) to obtain field and temperature dependence of Landau quasiparticle effective mass. We emphasize here, that in our approach the entire temperature and magnetic field dependence of the effective mass is brought to us by dependencies of $\varepsilon_\sigma(\mathbf{p}, T)$ and $n_\sigma(\mathbf{p}, T)$. The sole role of Landau interaction is to bring the system to FCQPT point, where Fermi surface alters its topology so that the effective mass acquires temperature and field dependence, see [2] and references therein for details.

Rewriting the quasiparticle distribution function as $n_\sigma(\mathbf{p}, T, B) \equiv n_\sigma(\mathbf{p}, T = 0, B = 0) + \delta n_\sigma(\mathbf{p}, T, B)$ yields more convenient form for the (15.1)

$$\frac{1}{M^*_\sigma(T, B)} = \frac{1}{M^*} + \frac{1}{p_F^2} \sum_{\sigma_1} \int \frac{\mathbf{p}_F \mathbf{p_1}}{p_F} F_{\sigma,\sigma_1}(\mathbf{p_F}, \mathbf{p}_1) \frac{\partial \delta n_{\sigma_1}(\mathbf{p}_1, T, B)}{\partial p_1} \frac{d\mathbf{p}_1}{(2\pi)^3}. \tag{15.5}$$

Our analysis shows, that near FCQPT the normalized solution of (15.5) $M^*_N(y = T_N)$ can be well approximated by a simple universal interpolating function. The interpolation occurs between the LFL ($M^* \propto a + bT^2$) and NFL ($M^* \propto T^{-2/3}$) regimes [2, 6]

$$M^*_N(y) \approx c_0 \frac{1 + c_1 y^2}{1 + c_2 y^{8/3}}. \tag{15.6}$$

Here a and b are constants, $c_0 = (1 + c_2)/(1 + c_1)$, c_1 and c_2 are fitting parameters, approximating the Landau interaction. Note, that our interpolative solution (15.6) is valid at low magnetic fields, where spin dependence of Landau interaction and single particle spectrum is not essential. At high fields, when this dependence is strong and we have full subband spin polarization, this interpolative solution is invalid and we should explicitly solve (15.5) with respect to (15.3) and (15.4). It can be shown that the magnetic field B enters Landau equation only in combination $B\mu_B/T$ making

$T_{\max} \propto B\mu_B$ [2, 6]. We conclude that under the application of magnetic field the variable

$$y = T/T_{\max} \propto \frac{T}{\mu_B(B - B_{c0})} \tag{15.7}$$

remains the same and the normalized effective mass is again determined by (15.6). Here B_{c0} is the critical magnetic field driving HF compound to its magnetic field tuned QCP and corresponding Néel temperature to $T = 0$. In some cases $B_{c0} = 0$. For example, the HF compound $CeRu_2Si_2$ has $B_{c0} = 0$ and shows neither magnetic ordering nor superconductivity [7]. In our simple model B_{c0} is taken as a parameter. In what follows, we compute the effective mass using (15.5) and employ (15.6) for qualitative analysis when considering the system at low magnetic fields.

15.2 Phase Diagram

Now we have everything to construct the schematic phase diagram of the HF metal $YbRh_2Si_2$ at $B \ll B^*$. The phase diagram is presented in Fig. 15.2. The magnetic field B plays the role of the control parameter, driving the system towards its QCP. In our case this QCP is of FCQPT type. The FCQPT peculiarity occurs at $B = B_{c0}$, yielding new strongly degenerate state at $B < B_{c0}$. To eliminate this degeneracy,

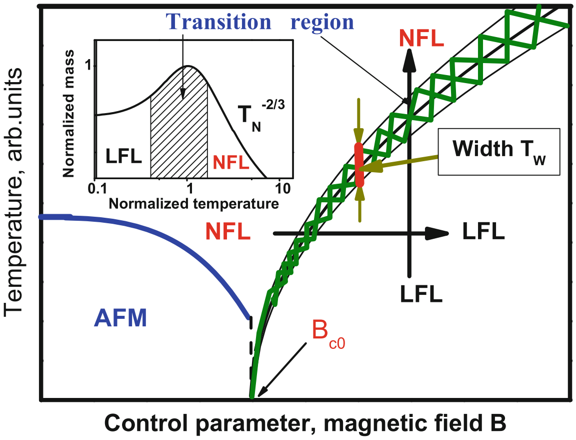

Fig. 15.2 Schematic phase diagram of $YbRh_2Si_2$ (15.6) with magnetic field as a control parameter. The *vertical* and *horizontal arrows* show LFL-NFL and reverse transitions at fixed B and T respectively. At $B < B_{c0}$ the system is in AFM state. The width of the transition region $T_w \propto T$ is shown by the segment between *two vertical arrows*. *Inset* shows the schematic plot of the normalized effective mass versus the normalized temperature. Transition region, where M_N^* reaches its maximum at $T/T_{\max} = 1$, is shown by the *hatched area* both in the main panel and in the *inset*

the system forms either superconducting (SC) or magnetically ordered FM, AFM, etc. states [2]. In the case of $\mathrm{YbRh_2Si_2}$, such a state is AFM one [1]. As it follows from (15.6) to (15.7) and seen from Fig. 15.2, at $B \geq B_{c0}$ the system is in either NFL or LFL states. At fixed temperatures the increase of B drives the system along the horizontal arrow from NFL to LFL state. On the contrary, at fixed magnetic field and raising temperatures the system transits along the vertical arrow from LFL state to NFL one. The inset to Fig. 15.2 demonstrates the behavior of the normalized effective mass $M^*_N = M^*/M^*_{\max}$ versus normalized temperature $y = T/T_{\max}$ that follows from (15.6). The $T^{-2/3}$ regime is marked as NFL one since contrary to LFL case, where the effective mass is constant, the effective mass depends strongly on temperature. It is seen that the temperature region $y \sim 1$ signifies a transition regime between the LFL behavior with almost constant effective mass and NFL one, given by $T^{-2/3}$ dependence. Thus, temperatures $T \simeq T_{\max}$, shown by arrows in the inset and main panel, can be regarded as a transition regime between LFL and NFL states. It is seen from (15.7) that the width of the transition regime $T_w \propto T$ is proportional to $(B - B_{c0})$. This is shown by the segment between two vertical arrows in Fig. 15.2. These theoretical results are in good agreement with the experimental data, as it is seen in Fig. 15.2 [1, 8].

15.3 Results and Discussion

Our calculations of the normalized effective mass $M^*_N(T_N)$ at fixed high magnetic field B^* are shown by the solid line in the main panel of Fig. 15.1. We recollect that in this case the quasiparticles spins are completely polarized. This reveals the above described scaling behavior of the normalized experimental curves in terms of the normalized variable $y = T/T_{\max}(B)$. It is seen from Fig. 15.1 that our calculations deliver a good description of the experiment [1]. Namely, at elevated temperatures $(y \simeq 1)$ the LFL state first converts into the transition one and then disrupts into the NFL state.

To perceive further the behavior of the system at high magnetic fields, in Fig. 15.3 we collect the curves $M^*_N(T_N)$ both at low (symbols in the upper box in Fig. 15.3) and high (symbols in the lower box) magnetic fields B. All curves have been extracted from the experimental data [1, 9]. It is seen that while at low fields the low-temperature ends $(T_N \sim 0.1)$ of the curves completely merge, at high fields this is not the case. Moreover, the low-temperature asymptotic value of $C/T = M^*_N$ at low fields is around two times bigger than that at high fields. The physical reason for low-field curves merging is that the effective mass does not depend on spin variable, so that the polarizations of subbands with $\sigma_\uparrow$ and $\sigma_\downarrow$ are almost equal to each other, where the arrows $\uparrow, \downarrow$ near σ denote the spin projection. The equality of the polarizations is reflected in our calculations, based on (15.6) for low magnetic fields $B \ll B^*$, at which the σ-dependence of the effective mass can be omitted. The result is shown by the dotted line in Fig. 15.3.

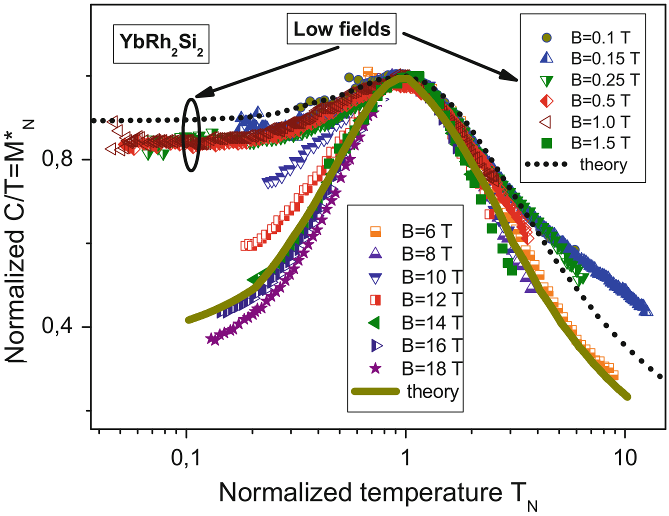

Fig. 15.3 Joint behavior of the normalized effective mass M^*_N at low (*upper box symbols*) and high (*lower box symbols*) magnetic fields. The data are extracted from the specific heat (C/T) measurements of the YbRh$_2$Si$_2$ [9]. Our low-field calculations are depicted by the *dotted line* tracing the scaling behavior of M^*_N. Our high-field calculations (*solid line*) are taken at $B \sim B^*$, when the quasiparticle band becomes fully polarized

It is also seen from Fig. 15.3 that all low-temperature differences between high- and low field behavior of the normalized effective mass disappear at high temperatures. In other words, while at low temperatures the values of M^*_N for low fields are two times bigger than those for high fields, at temperatures $T_N \geq 1$ this difference disappear. It is seen that these high temperatures lie about the transition region, marked by hatched area in the inset to Fig. 15.2. This means that the two states, LFL and NFL, separated by the transition region are clearly seen in Fig. 15.3 demonstrating good agreement between our calculations. The calculations are shown by the dotted line for low fields and by the thick line for high fields, while the experimental points are displayed by the symbols.

It is seen from Fig. 15.3, that at high fields $B \sim B^*$, symbols in the lower box, the curves $M^*_N(T_N)$ do not merge in the low temperature LFL state. Moreover, their values decrease as B grows, thus representing the full spin polarization of the HF band at the highest reached magnetic fields. This behavior is opposite to that at low fields. The corresponding theoretical curve has come from the explicit numerical solution of (15.5) with respect to (15.3) and (15.4). As we have mentioned above, at temperature raising, all effects of spin polarization smear down, yielding the restoration of NFL behavior at $T \simeq \mu_B B$. Our high-field calculations (the solid line in Fig. 15.3) reflect the latter fact and are also in good agreement with experimental facts. In order not to overload Fig. 15.3 with unnecessary details, we show the results of calculations only for the case of the complete spin polarization.

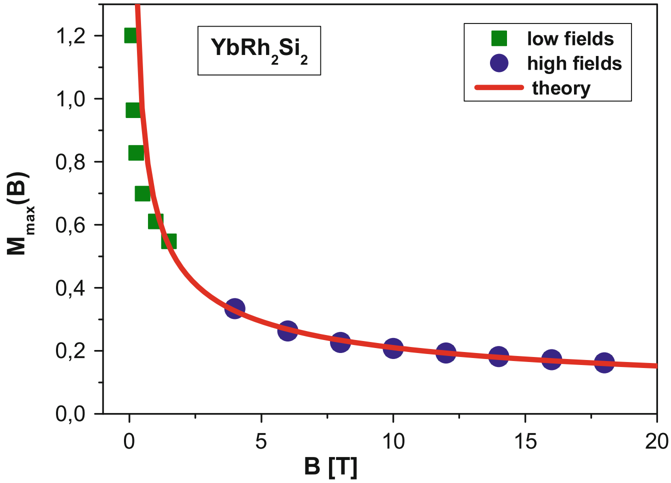

Fig. 15.4 The maxima $M^*_{\max}(B)$ of the functions C/T versus magnetic field B for $\mathrm{YbRh_2Si_2}$. The points for low [9] (*squares*) and high fields [1] (*circles*) are shown in the legend. The *solid curve* is approximated by $M^*_{\max}(B) \propto d/\sqrt{B - B_{c0}}$, where d is a fitting parameter

Figure 15.4 reports the maxima $M^*_{\max}(B)$ of the functions in the inset to Fig. 15.1 versus B. The solid line represents our approximation for these maxima $M^*_{\max}(B) \propto 1/\sqrt{B - B_{c0}}$ calculated within the framework of FCQPT theory [2, 10]. It is seen that our calculations are in good agreement with the experimental data in the entire magnetic field domain. Such good coincidence indicates that at $T \simeq \mu_B B$ the transition regime occurs and the NFL behavior restores at high temperatures $T \sim 20\,\mathrm{K}$.

In Fig. 15.5, the solid squares and circles denote temperatures $T_{\max}$ at which the maxima of C/T (from the inset to Fig. 15.1) occur. To fit the experimental data [1, 9] the function $T_{\max}(B) = b(B - B_{c0})$ defined by (15.7) with $b \simeq 0.74\,\mathrm{K/T}$ is used. It is seen from Fig. 15.5 that our calculations (solid line) coincide with experiment, and we conclude that the transition regime of $\mathrm{YbRh_2Si_2}$ is restored at temperatures $T \simeq \mu_B B$.

Consider now the magnetization $M(B, T)$ as a function of magnetic field B at fixed temperature T

$$M(B, T) = \int_0^B \chi(z, T) dz, \tag{15.8}$$

where the magnetic susceptibility χ is given by

$$\chi(B, T) = \frac{\beta M^*(B, T)}{1 + F_0^a}. \tag{15.9}$$

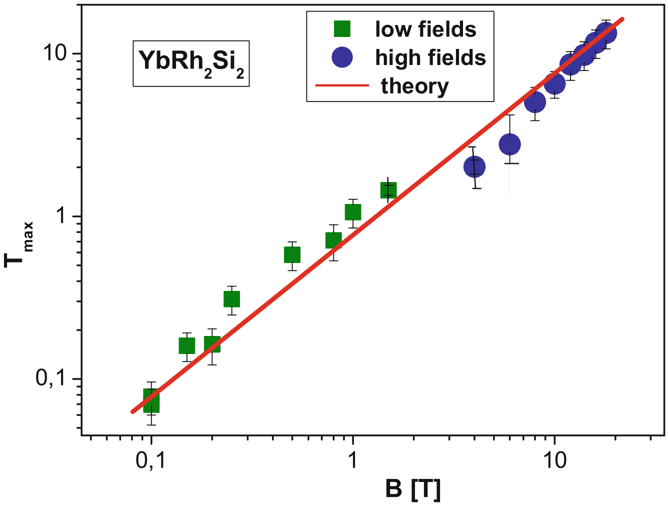

Fig. 15.5 The temperatures $T_{\max}(B)$ at which the maxima of C/T in YbRh$_2$Si$_2$ (inset to Fig. 15.1) are located. *Squares* correspond to low-field case [9] and *circles* to high fields one [1]. The *solid line* represents the function $T_{\max} \propto b(B - B_{c0})$, b being the fitting parameter, see (15.7)

Here, β is a constant and F_0^a is the spin-antisymmetric Landau interaction taken at orbital quantum number $L = 0$, see for details Sect. 7.1.

Our calculations show that the magnetization exhibits a kink at some magnetic field $B = B_k$. The experimental magnetization demonstrates the same behavior [11, 12]. Now we use the other internal scale, namely B_k and $M(B_k)$, to normalize B and M respectively. In the normalized variables, there are no coefficients β and $(1 + F_0^a)$ so that $\chi \propto M^*$ [2] and we can again use (15.5) to calculate the magnetic susceptibility χ. The normalized magnetization $M(B)/M(B_k)$, both extracted from experiment (symbols) and calculated by us (solid line), are reported in the inset to Fig. 15.6. It is seen that our calculations are in good agreement with the experiment. All the data exhibit the kink (shown by the arrow) at $B_N \simeq 1$ taking place as soon as the system enters the transition region. This region corresponds to the magnetic fields, where the horizontal arrow in Fig. 15.2 crosses the hatched area. To reveal the kink position, in Fig. 15.6 we present the $M(B)$ dependence in logarithmic—logarithmic scale. In that case the straight lines show clearly the change of the slope (power in logarithmic scale) of $M(B)$ at the kink point.

15.3.1 Kinks

At magnetic field $B \simeq B^*$ the quasiparticle band becomes fully polarized and a new kink appears [1, 13]. We name this kink the second one. Our calculations of the normalized magnetization (line) and the experimental points (squares) are shown in

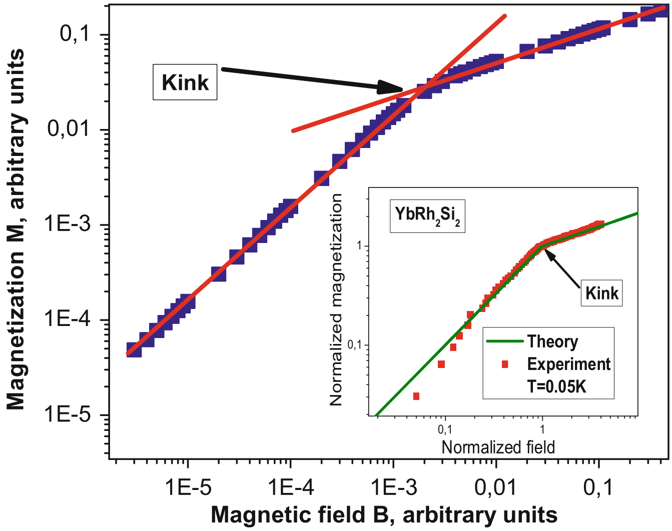

Fig. 15.6 The kink at the crossover region. The calculated magnetization $M(B)$ (*symbols*) and *straight lines* which are guides for the eye. The intersection of the *straight lines* visualize the kink at the crossover region in the Fig. 15.2. The *inset* The field dependencies of the normalized magnetization M of YbRu$_2$Si$_2$ [11] at $T = 0.05$ K. The kink (shown by the *arrow*) is clearly seen at the normalized field $B_N = B/B_k \simeq 1$. The *solid curve* represents our calculations

Fig. 15.7. In that case both the magnetization and the field are normalized by the corresponding values at the second kink position.

In Fig. 15.7, we plot our theoretical normalized (in the second kink point) magnetization along with the experimental data. Good coincidence is seen everywhere except the high-field part at $B_N \geq 1$. Here, the experimental normalized magnetization M_{nor} exhibits a linear dependence on B_N that is marked by two arrows, while the calculated magnetization is approximately constant. Such a behavior is the intrinsic shortcoming of the HF liquid model that accounts for only heavy electrons and omits the conduction electrons of other kind [14, 15]. Thus, we can consider the high-field (at $B_N > 1$) part of the magnetization as the contribution, which is not included in our theory. To separate this contribution from the experimental magnetization curve, we numerically differentiate it, then subtracting constant part at $B_N > 1$ and integrate back the resulting curve. The coincidence between our calculations (solid line) and processed experimental data (stars) is demonstrated in the inset in Fig. 15.7. As we can see now, the coincidence between the theory and experiment is good in the entire considered magnetic field domain. Taking into account the results displayed in Figs. 15.3, 15.4, 15.5, 15.6 and 15.7, we conclude that the HF system of YbRu$_2$Si$_2$ evolves continuously without any dramatic (metamagnetic) increase of magnetization under the application of external magnetic field. This fact agrees with the experimental observations [16].

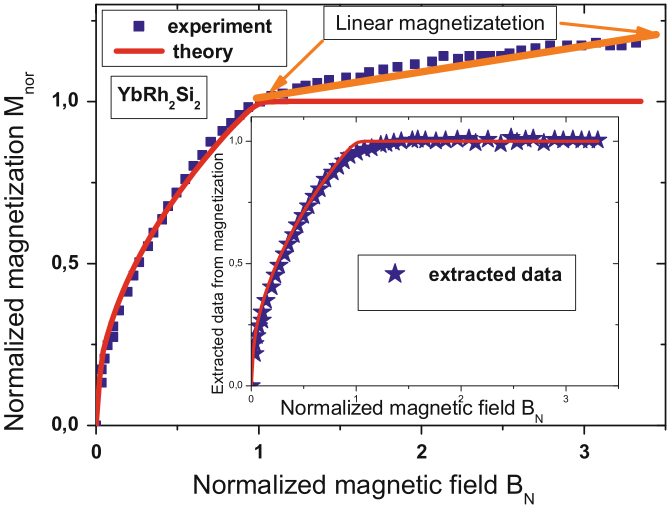

Fig. 15.7 The second kink. The normalized magnetization $M_{\rm nor}$ is displayed as a function of the normalized magnetic field B_N. The *line* represents our calculations and *squares* represent experimental points [1]. The linear dependence $M_{\rm nor}(B_N)$ is marked by the *arrows*. The *inset* demonstrates the experimental data (*stars*) with the subtracted high-field linear part. Our calculations are shown by the *solid line*

15.4 Main Results

The main physical content of this Chapter is that we have convincingly shown that the puzzle of non-Fermi liquid behavior in HF metals subjected to high magnetic fields, can be described successfully within our FCQPT approach. As the experimental data were available for YbRh$_2$Si$_2$, we apply our formalism to this HF compound. We note here, that although the physical interpretation of metamagnetism is ambiguous, see [17, 18], the common point of view is that it is related to the splitting of the Fermi surface in a paramagnetic system of itinerant electrons. This splitting, in turn, causes an energetically favorable transition to bulk magnetization near the transition to magnetically ordered state [17].

The above analysis of the thermodynamic properties of YbRh$_2$Si$_2$ at both low and high magnetic fields allows us to conclude that the HF metal YbRh$_2$Si$_2$ in strong magnetic field evolves continuously without the above discussed metamagnetic transition sand possible localization of heavy $4f$ electrons. Under the application of magnetic field at low temperatures, the HF system demonstrates the LFL behavior, while at increase temperatures the system enters the transition region followed by the NFL behavior. At low temperatures and high magnetic fields $B \simeq B^*$ the system is completely polarized and demonstrates the LFL behavior, while at high temperatures the NFL behavior is restored. The obtained results are in good agreement with the experimental data in the entire magnetic field (0.1–18 T) and temperature (40 mK–20 K) regions.

References

1. P. Gegenwart, Y. Tokiwa, T. Westerkamp, F. Weickert, J. Custers, J. Ferstl, C. Krellner, C. Geibel, P. Kerschl, K.H. Müller, F. Steglich, New J. Phys. **8**, 171 (2006)
2. V.R. Shaginyan, M.Y. Amusia, A.Z. Msezane, K.G. Popov, Phys. Rep. **492**, 31 (2010)
3. L.D. Landau, Zh Eksp, Teor. Fiz. **30**, 1058 (1956)
4. E.M. Lifshitz, L.P. Pitaevskii, *Statisticheskaya Fizika (Statistical Physics), part 2*. Course of Theoretical Physics (Pergamon Press, Oxford, 1980)
5. V.A. Khodel, J.W. Clark, M.V. Zverev, Phys. Rev. B **78**, 075120 (2008)
6. J.W. Clark, V.A. Khodel, M.V. Zverev, Phys. Rev. B **71**, 012401 (2005)
7. D. Takahashi, S. Abe, H. Mizuno, D. Tayurskii, K. Matsumoto, H. Suzuki, Y. Onuki, Phys. Rev. B **67**, 180407(R) (2003)
8. S. Friedemann, N. Oeschlera, S. Wirtha, C. Krellnera, C. Geibela, F. Steglicha, S. Paschenb, S. Kirchnerc, Q. Sic, Proc. Natl. Acad. Sci. USA **107**, 14547 (2010)
9. N. Oeschler, S. Hartmann, A. Pikul, C. Krellner, C. Geibel, F. Steglich, Phys. B **403**, 1254 (2008)
10. V.R. Shaginyan, JETP Lett. **79**, 286 (2004)
11. P. Gegenwart, T. Westerkamp, C. Krellner, M. Brando, Y. Tokiwa, C. Geibel, F. Steglich, Phys. B **403**, 1184 (2008)
12. P. Gegenwart, T. Westerkamp, C. Krellner, Y. Tokiwa, S. Paschen, C. Geibel, F. Steglich, E. Abrahams, Q. Si, Science **315**, 969 (2007)
13. S.V. Kusminskiy, K.S.D. Beach, A.C. Neto, D.K. Campbell, Phys. Rev. B **77**, 094419 (2008)
14. T. Saso, M. Itoh, Phys. Rev. B **53**, 6877 (1996)
15. H. Satoh, F.J. Ohkawa, Phys. Rev. B **63**, 184401 (2001)
16. P.M.C. Rourke, A. McCollam, G. Lapertot, G. Knebel, J. Flouquet, S.R. Julian1, Phys. Rev. Lett **101**, 237205 (2008)
17. E.P. Wohlfarth, P. Rhodes, Philos. Mag. **7**, 1817 (1962)
18. E. Stryjewski, N. Giordano, Adv. Phys. **26**, 487 (1977)

Chapter 16
Baryon Asymmetry Resulting from FCQPT in the Early Universe

Abstract This Chapter does not follow the main line of the book that is the theory of HF compounds but illustrates how the ideas of FC may be applicable to describe a very dissimilar system. Namely, here we consider a novel mechanism for explaining the matter-antimatter asymmetry of the universe. We assume that the universe starts from completely symmetric state and then, as it cools down, it undergoes a quantum phase transition, which in turn causes an asymmetry between matter and anti-matter. As we shall see the quantum phase transition is represented by FCQPT. The mechanism does not require the baryon number violating interactions or *CP* violation at a microscopic level. The state FC emerging behind FCQPT can be viewed as the state possessing the supersymmetry that interchanges bosons and fermions eliminating the difference between them. Thus restoring one important symmetry, the FC state violates another essential symmetry destroying matter—anti-matter symmetry. Our analysis of the matter antimatter asymmetry is in the context of remarkable experimental results obtained in the condensed matter physics.

16.1 Introduction

One of the important and long standing problems of modern cosmology and astrophysics is the matter-antimatter asymmetry: The observable part of the universe contains mostly baryons and antibaryons produced locally as the byproduct of nuclear reactions [1–4]. For the globally symmetric universe one can put a strong constraint on the size l of antimatter clusters [5], $l > 1{,}000$ Mpc. This number may be compared with the visible size of the universe, 3,000 Mpc.

A convenient dimensionless number, characterizing the baryon asymmetry magnitude is the ratio of the baryonic charge density $n_B - n_{\bar{B}}$ to the cosmic microwave background density n_γ [6]

$$\frac{n_B - n_{\bar{B}}}{n_\gamma} \leq 3 \times 10^{-10}. \tag{16.1}$$

M.Y. Amusia et al., *Theory of Heavy-Fermion Compounds*, Springer Series
in Solid-State Sciences 182, DOI 10.1007/978-3-319-10825-4_16

Estimate (16.1), excluding antimatter on scales of order $\sim$20 Mpc [6], may be obtained assuming that at earlier times, at temperatures well above 100 MeV, the universe had one extra quark per about 10^{10} quark-antiquark pairs and this tiny excess is responsible for the entire baryonic matter in the present universe.

Although there is no logical contradiction to assume that an excess of quarks over antiquarks is built in as an initial condition, this ad hoc hypothesis can not be justified within the inflationary scenario which does not provide such an initial condition [1–4]. Thus, it becomes necessary to explain baryon asymmetry without introducing the minute particle excess at the initial stage of the big bang.

Sakharov [7] was first to formulate the conditions necessary for generating the observed baryon asymmetry from an initially symmetric state. These are the baryon number non-conservation, *C* and *CP* violation, and a departure from the thermal equilibrium. Numerous possible scenarios incorporating Sakharov's conditions readily followed. The detailed discussion of these mechanisms such as electroweak baryogenesis, baryonic charge condensate, baryogenesis via lepto genesis, baryogenesis through evaporation of primordial black holes, out of equilibrium decays of massive particles, baryon number non-conservation caused by the triangle anomaly in baryonic current and baryogenesis in the presence of spontaneously broken Lorentz symmetry can be found in [1–4]. It is worth noting that all these scenarios require extension of the standard model of particle physics.

16.2 Model

We propose a mechanism for explaining the matter-antimatter asymmetry of the universe, which does not require any extension of the standard model of particle physics or the standard model of cosmology. Our approach is based on the observation that the condensed matter physics of strongly correlated Fermi systems and topologically protected dispersionless (i.e. flat bands forming) gapless fermions may offer opening for designing such a mechanism [8–11]. We propose that the universe began from a completely symmetric state with the baryon number and *CP* conserved at the end of inflation when the particle production started. The observed asymmetry may be explained by suggesting that in the post-inflation epoch, at baryogenesis, as the universe cooled down in approximately 10 orders of magnitude, it came near a quantum phase transition. At that time an excess of matter over the antimatter in the universe had been generated. This phase transition could wash out the antibaryons from the universe ground state wave function. Such a quantum phase transition can be represented by the fermion condensation quantum phase transition (FCQPT) that does not support quasiparticle-hole symmetry [12–16]. We note that flat bands related to FCQPT were observed in $2 + 1$ dimensional quantum field theory which is dual to a gravitational theory in the anti-de Sitter background [17]. For the detailed discussion of novel features exhibited by the strongly correlated Fermi systems see reviews [14, 15].

Our suggestion is based on the results of theoretical [14–16] and experimental [18–20] studies of novel systems of condensed matter physics—the strongly correlated Fermi systems and the quantum phase transitions within, forming their properties. These systems do not belong to the well known class of LFL [21], and exhibit the NFL features strikingly different from those of Landau Fermi liquids [22].

We propose that the universe exhibits NFL behavior and therefore shares the features of NFL, in particular the spontaneous breakdown of quasiparticle-hole symmetry. The quasiparticle-hole asymmetry manifests itself on a macroscopic scale as an asymmetric conductivity [18–20]. This phenomenon of quasiparticle-hole asymmetry serves as the guiding principle in our suggestion of explaining matter-antimatter asymmetry from the results of condensed matter physics of strongly correlated fermi systems. Below we briefly discuss the quasiparticle and hole properties in LFL and NFL which are necessary to illustrate our suggestion and provide the basis for interpreting the observed baryon asymmetry as resulting from a quantum phase transition. Throughout holes will represent the matter (baryons) and quasiparticles will serve as an analogy of antimatter (antibaryons).

As it is well known, the basic thermodynamic and transport properties of LFL are described in terms of quasiparticles—the weakly excited states over the Fermi sea (with “sea level” being equal to the Fermi level E_F) [21]. LFL is symmetric with regard to quasiparticles and holes. The latter are the “mirror images” of quasiparticles with the same mass but opposite charge; in particle physics terminology the quasiparticles above and the holes below the Fermi sea are fermions above and antifermions below the Dirac sea. The microscopic Hamiltonian of LFL is fully symmetric with respect to holes and quasiparticles, and this “matter-antimatter symmetry” holds on a macroscopic scale as well [21].

The theory of LFL is based on a representation of the system as a gas of interacting quasiparticles, the number of which is equal to the number N of particles [21]. The ground state energy E of a uniform Fermi system is treated as a functional of the quasiparticle distribution $n(\mathbf{p})$. Under arbitrary variation of $n(\mathbf{p})$, conserving the particle number density x, the energy E is changed according to the formula [12, 13]

$$\delta E = \int (\varepsilon(\mathbf{p}) - \mu)\delta n(\mathbf{p}) \frac{d\mathbf{p}}{(2\pi)^3}. \tag{16.2}$$

Here $\varepsilon(\mathbf{p}) = \delta E/\delta n(\mathbf{p})$ is the energy of a quasiparticle and μ is the chemical potential. Distribution $n(\mathbf{p})$ at $T = 0$ is a Fermi step $n(p) = \theta(p - p_F)$, p_F is the Fermi momentum, and $x = p_F^3/3\pi^2$. At finite temperatures $n(\mathbf{p})$ is given by the Fermi-Dirac distribution

$$n(\mathbf{p}, T) = \{1 + \exp[(\varepsilon(\mathbf{p}, T) - \mu)/T]\}^{-1}. \tag{16.3}$$

A necessary stability condition for LFL is that the group velocity of quasiparticles be nonnegative at the Fermi surface: $v_g(p) = d\varepsilon(p)/dp \geq 0$. In that case $\delta E \geq 0$ and we obtain that (16.2) admits the solution $\varepsilon(p) = \mu$. This condition can be reformulated as an equation for the minimum [12, 13]

$$\frac{\delta E}{\delta n(\mathbf{p})} = \varepsilon(\mathbf{p}) = \mu; \quad p_i \le p \le p_f. \tag{16.4}$$

The distribution function found from (16.4) differs from the step function in the interval from p_i to p_f; inside this interval $0 < n(\mathbf{p}) < 1$. Note that (16.4) describes pari passu both fermions and bosons, for inside the interval the distribution function is to automatically satisfy $0 < n(\mathbf{p}) < 1$. Outside this interval $n(\mathbf{p})$ coincides with the step function. When the density $x \to x_{FC}$ where x_{FC} is a quantum critical point (QCP) of FCQPT, a nontrivial solution of (16.4) emerges, see for details Chap. 3. We note that the state emerging behind FCQPT can be viewed as one possessing the supersymmetry (SUSY) that interchanges bosons and fermions eliminating the difference between them, see Sect. 3.1.

At finite T, a solution $n(\mathbf{p})$ of (16.4) and the corresponding single-particle spectrum $\varepsilon(\mathbf{p})$ are depicted in Fig. 16.1. At the Fermi level $\varepsilon(\mathbf{p}, T) = \mu$, then from (16.3) the distribution function $n(\mathbf{p}, T) = 1/2$. The vertical dashed and solid lines in Fig. 16.1 crossing the distribution function plot at the Fermi level illustrate the asymmetry of the corresponding distribution functions with respect to the Fermi level at $T = 0.01$ and $T = 0.0001$ respectively. As $T \to 0$ as seen from Fig. 16.1, the number density of holes $H = \sum_{\varepsilon(p)<E_F}(1 - n(p))$ is finite, while the number density of quasiparticles $P = \sum_{\varepsilon(p)>E_F} n(p)$ vanishes. Clearly the solutions of (16.4) strongly violate the particle-hole symmetry, and the asymmetry $R_A = (H - P)/(H + P)$ increases becoming more pronounced at diminishing temperatures.

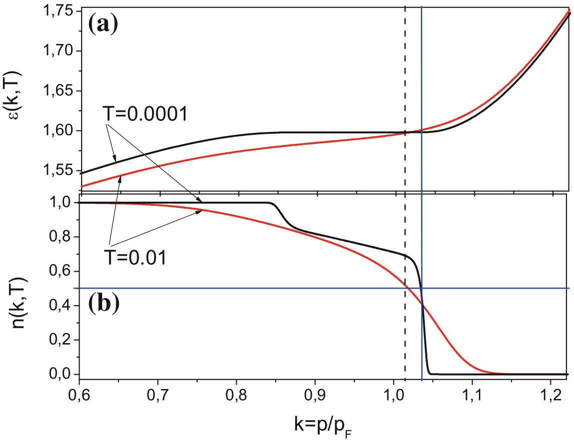

Fig. 16.1 The single particle energy $\varepsilon(\mathbf{k}, T)$ (**a**) and the distribution function $n(\mathbf{k}, T)$ (**b**) at finite temperatures as functions of the dimensionless variable $k = p/p_F$. Temperature is measured in units of E_F. At $T = 0.01$ and $T = 0.0001$ the *vertical dashed* and *solid lines* respectively show the position of the Fermi level E_F at which $n(\mathbf{k}, T) = 0.5$ as depicted by the *horizontal line*. As $T \to 0$ and consistent with (16.2), the single particle energy $\varepsilon(\mathbf{k}, T)$ becomes more flat in the region $(p_f - p_i)$ and the distribution function $n(\mathbf{k}, T)$ in this region becomes more asymmetric with respect to the Fermi level E_F producing the quasiparticle-hole asymmetry related to the NFL behavior

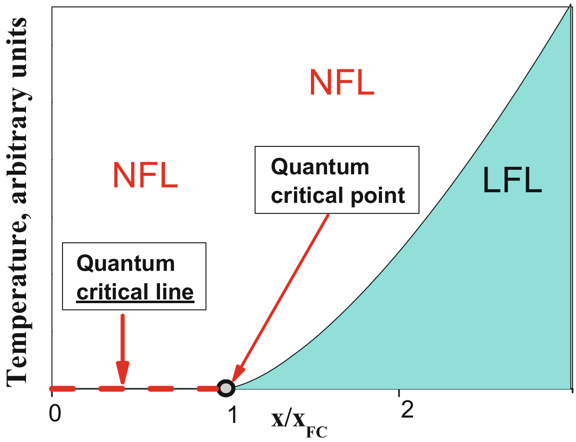

Fig. 16.2 Schematic phase diagram of a system with FCQPT. The number density x (in dimensionless form x/x_{FC}) is taken as the control parameter. The quantum critical point at $x/x_{FC} = 1$ of FCQPT is denoted by the *arrow*. At $x/x_{FC} > 1$ and sufficiently low temperatures, the system is in the LFL state as shown by the *shadow area*. At finite temperatures and beyond the critical point, $x/x_{FC} < 1$, the system is *above* the *quantum critical line* depicted by the *dashed line* and shown by the *vertical arrow*. The location of the system in the NFL region is characterized by the quasiparticle-hole asymmetry related to the NFL behavior

A schematic phase diagram of the system which is driven to FCQPT by variation of x is reported in Fig. 16.2. Upon approaching QCP of FCQPT at $x = x_{FC}$, the system remains in the LFL region at sufficiently low temperatures as is shown by the shadow area. The temperature range of the shadow area shrinks as the system approaches QCP. At x_{FC} shown by the arrow in Fig. 16.2, the system demonstrates the NFL behavior down to the lowest temperatures. Below QCP at finite temperatures the behavior remains the NFL one with the particle-hole asymmetry. In that case as $T \to 0$, the system is approaching a quantum critical line (shown by the vertical arrow and the dashed line in Fig. 16.2) rather than a quantum critical point. It is seen from Fig. 16.2 that at finite temperatures there is no boundary (or phase transition) between the states of systems located before or beyond QCP shown by the arrow. Therefore, at elevated temperatures the properties of systems with $x/x_{FC} < 1$ or with $x/x_{FC} > 1$ become indistinguishable, while the particle-hole symmetry is restored [14, 15]. In Fig. 16.3 we present the asymmetry R_A versus dimensionless temperature. At low temperatures $T/E_F \leq 1$ the asymmetry $R_A \simeq a_0 + a_1\sqrt{T}$ and the symmetry is restored at $T \simeq E_F$ since $R_A \simeq 0$. The function R_A is of universal form and the values of a_0 and a_1 are determined by the location of the system at the quantum critical line shown in Fig. 16.2. We note that a_0 is given by the temperature independent part S_0 of the entropy, $S(T \to 0) \to S_0$ [14–16].

One of the manifestations of the quasiparticle-hole symmetry on a macroscopic scale is the symmetric electric conductivity. It is straightforward to demonstrate that in LFL the differential conductivity σ_d

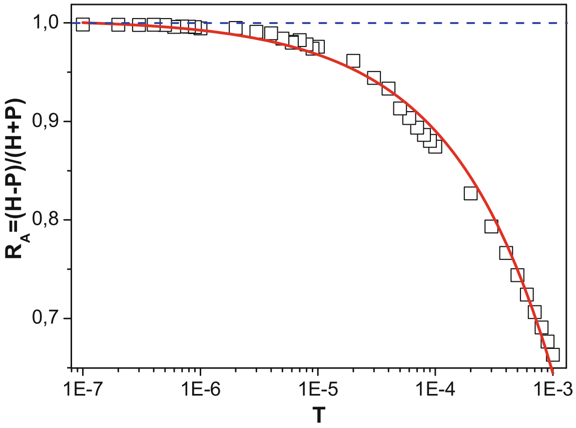

Fig. 16.3 R_A as a function of the dimensionless temperature measured in E_F. Our calculations are shown by *squares*. The *solid curve* represents a fit $R_A \simeq a_0 + a_1\sqrt{T}$

$$dI = \sigma_d \, dV \tag{16.5}$$

is a symmetric function of the voltage V, i.e. σ_d may depend on the absolute value of V, but not on its sign. It follows from (16.5), that when the conductivity is a symmetric function of voltage, reversing the sign of V results in $I \to -I$: Electric current maintains its magnitude and flows in the opposite direction. This reasonable feature may be readily derived in the framework of the LFL theory. Let us recollect that the electric current can be expressed in terms of the distribution function (16.3) as [18]

$$I(V) = \text{const} \int d\varepsilon \, [n(\varepsilon - V) - n(\varepsilon)]. \tag{16.6}$$

Now, it immediately follows from (16.5) to (16.6), that σ_d is a symmetric function of voltage V. This result is a direct consequence of the quasiparticle-hole symmetry which is an inherent feature of the LFL theory. The symmetric conductivity has been observed so many times that it lead to a perception that the conductivity can not be asymmetric.

This perception has been invalidated by recent experimental findings where it was shown that at low temperatures the electric conductivity in high-T_c superconductors [18] as well as in some heavy fermion metals, such as $\mathrm{CeCoIn_5}$ and $\mathrm{YbCu_{5-x}Al_x}$ [19, 20] is clearly asymmetric, this asymmetry vanishing as the temperature increases. Evidently, the asymmetry can not be explained in the framework of the LFL theory since the quasiparticle-hole symmetry unavoidably leads to the step function for the fermion distribution function in the low temperature regime which, in turn, results in a symmetric conductivity. Therefore, to explain the asymmetric conductivity, it is necessary to consider fermion systems more general than LFL.

Strongly correlated fermion systems may serve as one of the examples of such systems. These systems have many novel features which have been observed experimentally [14, 15, 22]. In our case the most attractive is the low temperature asymmetric conductivity, for details see Chap. 13. This macroscopic effect finds its explanation in the quasiparticle-hole asymmetry in theory of strongly correlated fermion systems. Fundamental microscopic interaction in this theory is fully symmetric with regard to quasiparticles and holes, but FCQPT at low temperatures causes the spontaneous symmetry breakdown [14–16]. Asymmetry is caused by the simple fact that in strongly correlated fermion systems, in contrast to LFL, the single-particle energy $\varepsilon(\mathbf{p})$ possesses a flat part that is T dependent. Thus $n(\mathbf{p}, T)$ given by (16.3) does not reproduce the step function in the low temperature limit [12, 13]. The asymmetric part of the conductivity,

$$\Delta\sigma_d(V) \equiv \frac{1}{2}\big[\sigma_d(V) - \sigma_d(-V)\big], \tag{16.7}$$

can be calculated [16] and comparison with experiments [19, 20] leads to good agreement. The estimate is

$$\Delta\sigma_d(V) \sim \frac{V}{2T}\frac{p_f - p_i}{p_F}. \tag{16.8}$$

It follows from (16.8), that a fairly large asymmetry is obtained when $(p_f - p_i)/p_F \approx 1$. When a magnetic field B is applied, the LFL behavior is restored, particle-hole asymmetry is eliminated, and therefore the asymmetric part of the differential conductivity disappears [14–16]. In other words, the particle-hole symmetry is macroscopically broken, or CP is violated, in the absence of applied magnetic fields. Conversely, the application of a magnetic field restores both the particle-hole symmetry and the LFL state. This agrees with the experimental facts collected in measurements on $\mathrm{YbCu_{5-x}Al_x}$ [14, 15, 20].

16.3 The Asymmetry of the Universe

Now we are in a position to formulate our approach to the baryon asymmetry of the universe. As it cools down, the universe behaves as a NFL. One of the manifestations of such systems is a strongly correlated Fermi system exhibiting FCQPT at $T = 0$, as it is shown in Fig. 16.2. We suggest that this model describes the particle-antiparticle content of the universe. As it is seen from Fig. 16.3, at finite temperatures the baryon-antibaryon asymmetry emerges as an inherent property of the system located above the quantum critical line. The asymmetry results from the distortion of the Fermi surface, in other words from the deviation of the distribution function $n(\mathbf{p})$ from the step function at low temperatures. At lowering temperature, the system approaches the quantum critical line so that the asymmetry increases. Details of this increase depend on the model chosen. The very existence and the universal qualitative behavior of the asymmetry is of great importance.

The picture for explaining baryon asymmetry emerging from the above is as follows. The initial excited state corresponding to the big bang with extremely high temperature possesses matter-antimatter symmetry. At the end of the inflation stage the dark matter emerges producing baryons (holes) and anti-baryons (quasiparticles). At this stage the temperature is high and the chemical potentials of baryons and antibaryons are zero, so that the asymmetry is also zero. As the temperature drops the state with the baryon (hole) asymmetry is formed. As a result, the universe approaches the quantum critical line which corresponds to the state with the maximum baryon (hole) asymmetry as it is seen from Fig. 16.3. This state is the eigenstate of the fully symmetric microscopic Hamiltonian with the eigenvalue lower than that for the state with matter-antimatter symmetry and contains the visible matter—baryons (holes), and the dark matter in the vicinity of the visible matter. In our approach, the visible matter is represented by the excitations (holes) of the dark matter. As there is almost no interaction between holes and the Fermi sea, we conclude that there is no direct interaction between dark and visible matter or, in the other words, the interaction (if any) is very weak. Then, proceeding along the universe-non-Fermi liquid analogy, since it takes about ten particles to create one quasiparticle [21], we estimate the ratio of the mass of visible matter to the mass of dark matter to be of order of ten which is close to the observed value $\Omega_{DM}/\Omega_b \approx 5$ [6, 23]. The ground state of the universe which we identify with the dark energy is interpreted in our approach as the vacuum.

Another result which comes as a bonus of our universe-non-Fermi liquid analogy is the high entropy of the universe. As it is seen from Fig. 16.1, $n(\mathbf{k}, T)$ of holes (the visible matter) even at $T \to 0$ is non-integer, $0 < n(\mathbf{k}, T) < 1$. The entropy $S(n(\mathbf{p}, T))$ is given by the well-known expression [21]

$$\begin{aligned} S(n(\mathbf{p}, T)) = & -2 \int [n(\mathbf{p}, T) \ln(n(\mathbf{p}, T)) + (1 - n(\mathbf{p}, T)) \\ & \times \ln(1 - n(\mathbf{p}, T))] \frac{d\mathbf{p}}{(2\pi)^3}. \end{aligned} \tag{16.9}$$

It follows from Fig. 16.1 and (16.9) that the entropy of the system is finite at $T \to 0$: $S(T \to 0) \to S_0$.

Let us introduce S_B, entropy per baryon, as S/x where S is given by (16.9) and x is the number density of baryons. Then it follows from the (16.9) that $S_B \sim 1$. This observation immediately explains the high entropy of the visible matter [24]. We also conjecture that the observed violation of *CP*-symmetry, leading to the violation of T-symmetry and making the finite term of the entropy, $S(T \to 0) = S_0$, may resolve the well-known problem of the time arrow.

It might seem that the presence of the Fermi level contradicts the relativistic invariance and the *CPT* theorem since the Fermi level and the Fermi sphere related to it are not transformed according to the invariance. As we shall see, at high energies the degrees of freedom related to the Fermi sphere become irrelevant and the relativistic symmetry is preserved in our approach. Let us assume that there are substantial gaps in the energy scales separating different states of the evolution of the Universe. One of these gaps separates the state behind FCQPT which produces *CP* violation and the symmetrical state laying above FCQPT. Consider the linear response function $\chi(\mathbf{q},\omega)$ (see, e.g., [25])

$$\chi(\mathbf{q},\omega)=\sum_n|\rho(q)_{n0}|^2\left[\frac{2\omega_{n0}}{(\omega+i\gamma)^2-\omega_{n0}^2}\right]. \tag{16.10}$$

Here $\rho(\mathbf{q})$ describes the fluctuations of the quasiparticle density, $\omega_{n0}=E_n-E_0$ is the difference between the ground state and the excited state energies. In our case E_n are the energies of excited states behind FCQPT. If ω is sufficiently high so that $\omega \gg (E_n-E_0)$ then (16.10) defines the linear response function of noninteracting particles [25]

$$\chi(\mathbf{q},\omega\to\infty)=\frac{xq^2}{m\omega^2}, \tag{16.11}$$

where m is the bare particle mass, for at $\omega \gg \omega_{n0}$ the effective mass $M^* \to m$ at such high energies. In our case, it means that these high energies render the system to be in the region of its phase diagram located well above the critical line shown in Fig. 16.2 where the *CP* symmetry is restored. Relativistic invariance is not yet restored since the very existence of quasiparticles ensures that Fermi sphere still remains relevant surface in phase space. Now we take into account that the linear response function of this system is again given by (16.10) with new ω'_{n0}. Again at $\omega \gg \omega'_{n0}$ the response function is given by (16.11) formed by particles that are not related to any Fermi sphere. Going this way, we ascend a level where the inflation takes place and the relevant degrees of freedom are now not quasiparticles but particles of the Standard Model. As a result, we conclude that at elevated energies ω the irrelevant degrees of freedom vanish and both the relativistic invariance and the *CPT* symmetry emerge. The details of reappearing of relativistic invariance are defined by the specific model chosen to describe baryogenesis.

The attractive feature of the above scenario is its “conservative” character—to introduce the matter-antimatter asymmetry it may suffice to suggest a mechanism based on analysis of quantum phase transitions in Fermi systems. There is no need to introduce baryon number non-conservation or *CP* violating interactions, as well as to invoke any extension of the standard cosmological model—ordinary quantum mechanics and statistics applied to a multi fermion system guarantee that the system starts from the symmetric state and at decreasing temperatures arrives at a maximally asymmetric one. This universal feature is present in strongly correlated Fermi systems with the FCQPT; the details depend on the specific microscopic Hamiltonian we begin with.

We note that typical current-current interactions lead to the formation of flat bands [26]. These bands located at the Fermi surface, being topologically protected from interaction and other disturbances, lead to the robustness of the generic properties of the quantum vacuum generated by their existence [8–10]. Due to the universal features of our model we have not concentrated on a particular picture that follows from some concrete dynamics, nor pursued the best quantitative description as the goal by itself. Rather, we demonstrate an opportunity to explain baryon asymmetry from the very general physics principles. Let us emphasize that the quasiparticle-hole asymmetry, which manifests itself at the macroscopic scale, is observed in experiments on HF metals and analyzed theoretically, is one of the few analogies of particle-antiparticle asymmetry observed in the universe, and thus deserves attention.

References

1. A.D. Dolgov, Phys. Rep. **222**, 309 (1992)
2. M.S. Turner, J.A. Tyson, Rev. Mod. Phys. **71**, S145 (1999)
3. M. Dine, A. Kusenko, Rev. Mod. Phys. **76**, 1 (2004)
4. M. Bartelmann, Rev. Mod. Phys. **82**, 331 (2010)
5. A.G. Cohen, A.D. Rujula, S.L. Glashow, Astrophy. J. **495**, 539 (1998)
6. G. Steigman, J. Cosmol. Astropart. Phys. **10**, 1 (2008)
7. A.D. Sakharov, Sov. Phys. JETP Lett. **5**, 24 (1967)
8. T.T. Heikkilä, N.B. Kopnin, G.E. Volovik, JETP Lett. **94**(252), 233 (2011)
9. G.E. Volovik, J. Low Temp. Phys. **110**, 23 (1998)
10. G.E. Volovik, *The Universe in a Helium Droplet* (Clarendon Press, Oxford, 2003)
11. V.R. Shaginyan, G.S. Japaridze, M.Y. Amusia, A.Z. Msezane, K.G. Popov, Europhys. Lett. **94**, 69001 (2011)
12. V.A. Khodel, V.R. Shaginyan, JETP Lett. **51**, 553 (1990)
13. V.A. Khodel, V.R. Shaginyan, V.V. Khodel, Phys. Rep. **249**, 1 (1994)
14. V.R. Shaginyan, M.Y. Amusia, K.G. Popov, Phys. Usp. **50**, 563 (2007)
15. V.R. Shaginyan, M.Y. Amusia, A.Z. Msezane, K.G. Popov, Phys. Rep. **492**, 31 (2010)
16. V.R. Shaginyan, K.G. Popov, Phys. Lett. A **361**, 406 (2007)
17. S.S. Lee, Phys. Rev. D **79**, 086006 (2009)
18. G. Deutscher, Rev. Mod. Phys. **77**, 109 (2005)
19. W.K. Park, L.H. Greene, J.L. Sarrao, J.D. Thompson, Phys. Rev. B **72**, 052509 (2005)
20. G. PristáŠ, M. Reiffers, E. Bauer, A.G.M. Jansen, D.K. Maude, Phys. Rev. B **78**, 235108 (2008)
21. L.D. Landau, Zh Eksp, Teor. Fiz. **30**, 1058 (1956)
22. G.R. Stewart, Rev. Mod. Phys. **73**, 797 (2001)
23. C. Amsler, M. Doser, M. Antonelli, D.M. Asner, K.S. Babu, H. Baer, H. Band, R. Barnett, E. Bergren, J. Beringer, G. Bernardi, W. Bertl, H. Bichsel, O. Biebel, P. Bloch, E. Blucher, S. Blusk, R. Cahn, M. Carena, C. Caso, A. Ceccucci, D. Chakraborty, M.C. Chen, R. Chivukula, G. Cowan, O. Dahl, G. D'Ambrosio, T. Damour, A. de Gouvéa, T. DeGrand, B. Dobrescu, M.D. nd D.A. Edwards, S. Eidelman, V.D. Elvira, J. Erler, V.V. Ezhela, J.L. Feng, W. Fetscher, B.D. Fields, B. Foster, T.K. Gaisser, L. Garren, H.J. Gerber, G. Gerbier, T. Gherghetta, G.F. Giudice, M. Goodman, C. Grab, A.V. Gritsan, J.F. Grivaz, D.E. Groom, M. Grünewald, A. Gurtu, T. Gutsche, H.E. Haber, K. Hagiwara, C. Hagmann, K.G. Hayes, J.J. Hernández-Rey, K. Hikasa, I. Hinchliffe, A. Höcker, J. Huston, P. Igo-Kemenes, J.D. Jackson, K.F. Johnson, T. Junk, D. Karlen, B. Kayser, D. Kirkby, S.R. Klein, I.G. Knowles, C. Kolda, R.V. Kowalewski, P. Kreitz, B. Krusche, Y.V. Kuyanov, Y. Kwon, O. Lahav, P. Langacker, A. Liddle, Z. Ligeti, C.J. Lin, T.M. Liss, L. Littenberg, J.C. Liu, K.S. Lugovsky, S.B. Lugovsky, H. Mahlke, M.L. Mangano, T. Mannel, A.V. Manohar, W.J. Marciano, A.D. Martin, A. Masoni, D. Milstead, R. Miquel, K. Mönig, H. Murayama, K. Nakamura, M. Narain, P. Nason, S. Navas, P. Nevski, Y. Nir, K.A. Olive, L. Pape, C. Patrignani, J.A. Peacock, A. Piepke, G. Punzi, A. Quadt, S. Raby, G. Raffelt, B.N. Ratcliff, B. Renk, P. Richardson, S. Roesler, S. Rolli, A. Romaniouk, L.J. Rosenberg, J.L. Rosner1, C.T. Sachrajda, Y. Sakai, S. Sarkar, F. Sauli, O. Schneider,

D. Scott, W.G. Seligman, M.H. Shaevitz, T. Sjöstrand, J.G. Smith, G.F. Smoot, S. Spanier, H. Spieler, A. Stahl, T. Stanev, S.L. Stone, T. Sumiyoshi, M. Tanabashi, J. Terning, M. Titov, N.P. Tkachenko, N.A. Törnqvist, D. Tovey, G.H. Trilling, T.G. Trippe, G. Valencia, K. van Bibber, M.G. Vincter, P. Vogel, D.R. Ward, T. Watari, B.R. Webber, G. Weiglein, J.D. Wells, M. Whalley, A. Wheeler, C.G. Wohl, L. Wolfenstein, J. Womersley, C.L. Woody, R.L. Workman, A. Yamamoto, W.M. Yao, O.V. Zenin, J. Zhang, R.Y. Zhu, P.A. Zyla, G. Harper, V.S. Lugovsky, P. Schaffner, Phys. Lett. B **667**, 1 (2008)

24. C.A. Egan, C.H. Lineweaver, Astrophys. J. **710**, 1825 (2010)
25. D. Pines, P. Noziéres, *Theory of Quantum Liquids* (Benjamin, New York, Amsterdam, 1966)
26. D.V. Khveshchenko, R. Hlubina, T.M. Rice, Phys. Rev. B **48**, 10766 (1993)

Chapter 17
Quantum Criticality of Spin Liquids in Novel Insulators and Magnets

Abstract Strongly correlated Fermi systems are among the most intriguing and fundamental systems in physics, whose realization in some compounds is still under consideration. Quantum spin liquids are a promising new phases, where exotic quantum states of matter could be realized. Exotic quantum spin liquid (QSL) made of such hypothetic particles as fermionic spinons which carry spin $1/2$ and no charge are considered in this chapter. Magnetic insulators with geometrical frustration produce important experimental facts shedding light on the nature of quantum spin liquid composed of spinons. We present a theory of the thermodynamic properties of quantum spin liquids, elucidating how their properties are affected by magnetic fields and describe as an example the experimental data for the herbertsmithite and HF metals. We show that the above insulators can be viewed as HF compounds, whose low temperature thermodynamics in magnetic fields is determined by a Fermi quantum spin liquid. These properties allow us to reveal their scaling behavior, which strongly resembles that observed in HF metals and two-dimensional ^{3}He. We also describe the dynamic magnetic susceptibility which allows us to reveal that at low temperatures quasiparticles excitations, or spinons, form a continuum, and populate an approximately flat band crossing the Fermi level. The obtained results show that the properties of compounds with quantum spin liquid are similar to those of HF metals. Thus, the compounds can be viewed as a new type of strongly correlated HF electrical insulator that possesses properties of HF metals with one exception: it resists a flow of electric charge. Transport properties of the compounds shed light on the nature of quantum spin liquid. Analysis of the heat conductivity detects its scaling behavior resembling those of both the spin–lattice relaxation rate and the magnetoresistivity. It reveals a strong magnetic field dependence of the spinons effective mass. As a result, the strongly correlated electrical insulator gains also a new magnetic feature of the matter, for the spins represented by the deconfined QSL get mobility. We show that the crystal keeps all properties of solids, but in the magnetic relation shows fluidity.

M.Y. Amusia et al., *Theory of Heavy-Fermion Compounds*, Springer Series
in Solid-State Sciences 182, DOI 10.1007/978-3-319-10825-4_17

17.1 Thermodynamic Properties of Quantum Spin Liquid in Insulators

An interesting and puzzling issue is the research of HF compounds and their non-Fermi liquid (NFL) behavior detected in their thermodynamic and transport properties. Under the application of magnetic field B, the system can be driven to a Landau Fermi liquid behavior (LFL). This behavior is observed in quite different objects such as HF metals, high-T_c superconductors, and 2D ^{3}He [1–4]. Recently, a natural object, the herbertsmithite $\mathrm{ZnCu_3(OH)_6Cl_2}$ has been exposed as a $S = 1/2$ kagome antiferromagnet [5]. New experimental investigations have revealed its unusual behavior [6–10] suggesting that herbertsmithite can be viewed as HF compound [11–14]. High-quality single crystals of $\mathrm{ZnCu_3(OH)_6Cl_2}$ were synthesized and characterized [9]. The bulk properties of that are consistent with the previously published powder results [6–9]. Observations have found no evidence of long range magnetic order or spin freezing, down to temperature of 50 mK [6–10, 15]. The specific heat C, arising from the Cu spin system, at $T < 1$ K appears to be governed by a power law with an exponent which is less than or equal to 1. At the lowest explored temperature, namely over the temperature range $100 < T < 400$ mK, C follows a linear temperature dependence, $C \propto T$, while for temperatures of $T \sim 10$ K and higher, $C(T) \propto T^3$ and is dominated by the lattice contribution [6–8]. At low temperatures the strong dependence of the specific heat C on magnetic field suggests that C is predominately magnetic in origin [6–8]. It is believed that the $S = 1/2$ model on the kagome lattice can be viewed as the gapless spin liquid [6–10, 15–19], while recent accurate calculations point to a fully gapped one, see [20] and references therein. Thus, it is of crucial importance to understand what kind of quantum spin liquid is formed in the herbertsmithite and determines its low temperature thermodynamic properties [11]. The sketch of the kagome lattice is shown in Fig. 17.1. The $S = 1/2$ spins of the Cu^{+2} ions occupying a highly symmetric kagome lattice are displayed by the arrows. As spins on the kagome lattice occupy a highly symmetric structure of corner-sharing triangles, the ground state energy does not depend on the spins configuration. As a result, spins located at the kagome hexagon, composed of the two triangles, form a frustrated pattern that is even more frustrated than the triangular lattice considered by Anderson [21].

17.1.1 Model

The magnetic susceptibility $\chi(T)$ of $\mathrm{ZnCu_3(OH)_6Cl_2}$ shown in Fig. 17.2 displays an unusual behavior [8]. At $B \geq 3$ T, $\chi(T)$ has a maximum $\chi_{\max}(T)$ at some temperature $T_{\max}(B)$. The maximum $\chi_{\max}(T)$ decreases as magnetic field B grows, while $T_{\max}(B)$ shifts to higher T reaching 15 K at $B = 14$ T. At $B \leq 1$ T, as seen from Fig. 17.2, where $\chi(T) \propto T^{-\alpha}$ with $\alpha = 2/3$. As it will be shown below, the calculated exponent is in good agreement with the experimental value $\alpha = 2/3 \simeq 0.66$ [8]. The observed behavior of χ strongly resembles that in HF metals and is associated

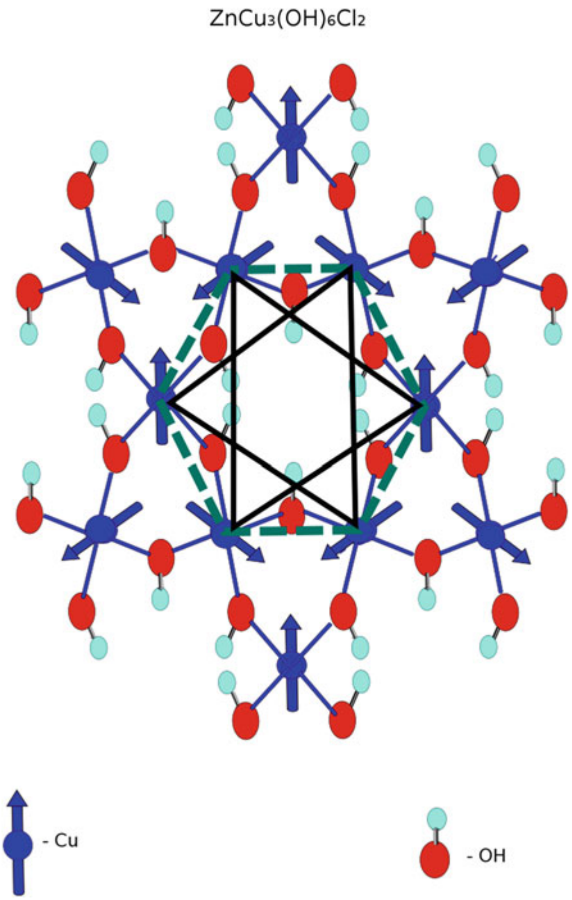

Fig. 17.1 The kagome frustrated lattice of $ZnCu_3(OH)_6Cl_2$. The Cu ions are shown by *blue circles* with *arrows* symbolizing the spins of the ions occupying the kagome lattice. The kagome *hexagon* is displayed by both the two *triangles* and the *lines*. The O−H group is represented by the big (O) and small (H) *circles*

with their proximity to QCP [4, 22, 23]. On this ground, we safely assume that a deconfined Fermi quantum spin liquid with essentially gapless excitations formed by neutral fermions is realized in $ZnCu_3(OH)_6Cl_2$ and located very near QCP [6]. Thus, $ZnCu_3(OH)_6Cl_2$ turns out to be located at its QCP without tuning this substance to QCP, using control parameter such as magnetic field, pressure, or chemical composition. This observation is in sharp contrast to the common practice applied to tune HF metals to their QCP's.

A simple kagome lattice has a dispersionless topologically protected branch of the spectrum with zero excitation energy that is the flat band [24, 25]. Therefore, FCQPT can be considered as QCP of the $ZnCu_3(OH)_6Cl_2$ quantum spin liquid. To study the low temperature thermodynamic and scaling behavior, we use the model of the homogeneous heavy-fermion liquid, see Sect. 6.3. This model permits to avoid complications associated with the crystalline anisotropy of solids. We propose that the quantum spin liquid is composed of fermions. These fermions with zero charge

Fig. 17.2 T-dependence of the magnetic susceptibility χ at different magnetic fields for $ZnCu_3(OH)_6Cl_2$ [8]. The illustrative values of $\chi_{\max}$ and $T_{\max}$ at $B = 7$ T are also shown. Our calculations made at $B = 0$ are depicted by the *solid curve* representing $\chi(T) \propto T^{-\alpha}$ with $\alpha = 2/3$

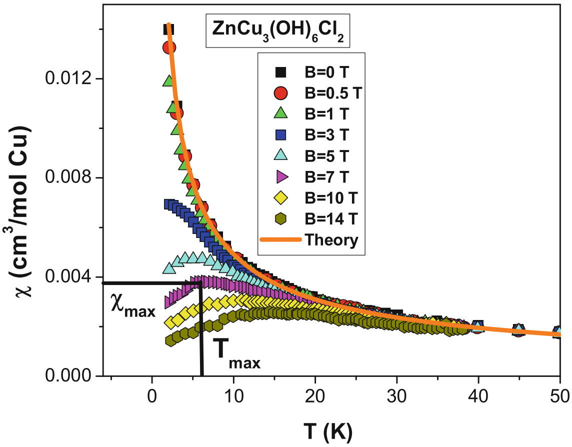

and spin $\sigma = 1/2$ occupy the corresponding Fermi sphere with the Fermi momentum p_F, and form the excitation spectrum typical for HF liquid located near FCQPT. As a result, spinons constitute the deconfined QSL, and gain mobility: The crystal keeps all properties of a solid, but in contrast to the two known classical types of magnetism, such as FM and AFM, in the magnetic relation shows fluidity—a new state that can be defined as one more magnetic state of matter.

The ground state energy $E(n)$ is given by the Landau functional depending on the quasiparticle distribution function $n_\sigma(\mathbf{p})$, where $\mathbf{p}$ is the momentum. Near FCQPT point, the effective mass M^* is governed by the Landau equation, see Sect. 6.1,

$$\frac{1}{M^*(T,B)} = \frac{1}{M^*} + \frac{1}{p_F^2}\sum_{\sigma_1}\int \frac{\mathbf{p}_F\mathbf{p}_1}{p_F} \times F_{\sigma,\sigma_1}(\mathbf{p_F},\mathbf{p}_1)\frac{\partial \delta n_{\sigma_1}(\mathbf{p}_1,T,B)}{\partial p_1}\frac{d\mathbf{p}_1}{(2\pi)^3}. \tag{17.1}$$

Here we have rewritten the quasiparticle distribution function as $n_\sigma(\mathbf{p},T,B) \equiv n_\sigma(\mathbf{p},T=0,B=0) + \delta n_\sigma(\mathbf{p},T,B)$. The Landau interaction F is completely defined by the fact that the system has to be at QCP of FCQPT, for we analyze the universal scaling behavior of the effective mass shown in the inset to Fig. 17.3. In that case, the sole role of the Landau interaction is to bring the system to FCQPT point, where Fermi surface alters its topology, so that the effective mass acquires temperature and field dependence. At this point, the term $1/M^*$ vanishes and (17.1) becomes homogeneous. It can then be solved analytically, as it is done in the case of HF metals, see Chap. 6. At $B = 0$, the effective mass strongly depends on T demonstrating the NFL behavior

$$M^*(T) \simeq a_T T^{-2/3}. \tag{17.2}$$

Fig. 17.3 Phase diagram of $ZnCu_3(OH)_6Cl_2$. The *vertical* and *horizontal arrows* show LFL-NFL and reverse transitions at fixed B and T respectively. *Inset* shows a plot of the normalized effective mass versus the normalized temperature. Transition region, where M^*_N reaches its maximum at $T_N = T/T_{\max} = 1$, is shown by the *arrows* and *hatched* area in both the main panel and in the *inset*

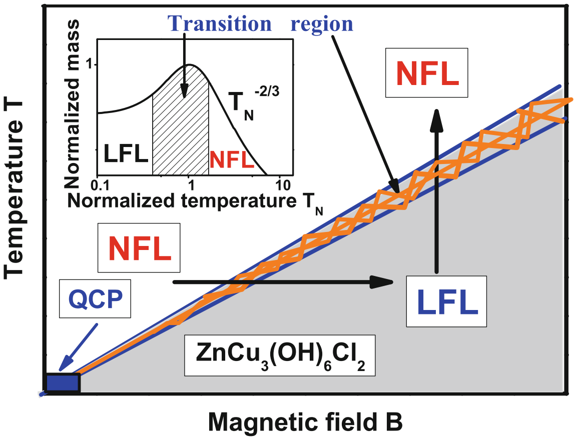

At finite T, the application of magnetic field B drives the system the to LFL region with

$$M^*(B) \simeq a_B B^{-2/3}. \tag{17.3}$$

At finite B and T near FCQPT, the solutions of (17.1) $M^*(B,T)$ can be well approximated by a simple universal interpolating function. The interpolation occurs between the LFL ($M^*(T) \propto const$) and NFL ($M^*(T) \propto T^{-2/3}$) regions [4, 22]. It is convenient to introduce the normalized effective mass M^*_N and the normalized temperature T_N dividing the effective mass M^* by its maximal values, M^*_M, and temperature T by $T_{\max}$, at which the maximum occurs. Equation (17.1) allows us to calculate the thermodynamic properties for the normalized susceptibility $\chi_N = \chi/\chi_{\max} = M^*_N$. Since $C/T \propto M^*$, the normalized $(C/T)_N = \chi_N = M^*_N$. We note that our calculations of M^*_N based on (17.1) do not contain any free fitting parameters. The normalized effective mass $M^*_N = M^*/M^*_M$ as a function of the normalized temperature $y = T_N = T/T_{\max}$ is given by the interpolating function (see Sect. 6.3)

$$M^*_N(y) \approx c_0 \frac{1 + c_1 y^2}{1 + c_2 y^{8/3}}. \tag{17.4}$$

Here $c_0 = (1 + c_2)/(1 + c_1)$, c_1 and c_2 are fitting parameters. Magnetic field B enters (17.1) only in the combination $\mu_B B/k_B T$, making $k_B T_{\max} \simeq \mu_B B$. Thus, in the presence of magnetic fields the variable y becomes

$$y = T/T_{\max} \simeq k_B T/\mu_B B. \tag{17.5}$$

The variables T and B enter (17.5) symmetrically; therefore (17.4) is valid for $y = \mu_B B/k_B T$. In what follows we use (17.4) to clarify our calculations based on (17.1). It follows directly from (18.10), (17.4) and (17.5) that $\chi(k_BT/\mu_BB)T^{2/3} \propto y^{2/3}M_N^*(y)$. Since on has for the magnetization $M(B,T) = \int \chi(B,T)dB$, we obtain that $M(B,T)T^{-1/3}$ depends on the only variable y. These observations confirm the scaling behavior of both $\chi T^{0.66}$ and $MT^{-0.34}$ experimentally established in [8].

17.1.2 Phase Diagram

We now construct the schematic phase diagram of $ZnCu_3(OH)_6Cl_2$. The phase diagram is depicted in Fig. 17.3. At $T = 0$ and $B = 0$ the system is located at QCP of FCQPT without tuning. Both magnetic field B and temperature T play the role of the control parameters, shifting the system from its QCP and driving it from the NFL to LFL regions as shown by the vertical and horizontal arrows. At fixed temperatures the increase of B leads the system along the horizontal arrow from NFL to LFL region. On the contrary, at fixed magnetic field and increasing temperatures the system moves along the vertical arrow from the LFL to NFL region. The inset to Fig. 17.3 demonstrates the behavior of the normalized effective mass M_N^* versus the normalized temperature T_N that follows from (17.4). It is seen that the temperature region $T_N \sim 1$ represents the transition region between the LFL behavior with almost constant effective mass and the NFL behavior, having the $T^{-2/3}$ dependence. It is seen from (17.4) and (17.5) and Fig. 17.3 that the width of the transition region is given by $T_w \propto T \propto B$.

17.1.3 The Thermodynamic Properties

The experimental data on the measurements of χ_N [8], $(C/T)_N = M_N^*$ [26] and our calculations of M_N^* at fixed magnetic field B that completely polarizes the quasiparticle band are shown respectively by the geometrical figures and solid curve in Fig. 17.4. It is clearly seen that the data collected on both $ZnCu_3(OH)_6Cl_2$ and $YbRh_2Si_2$ collapse into the same curve, obeying the scaling behavior. Consistent with the phase diagram displayed in Fig. 17.3, at growing temperatures ($y \simeq 1$) the LFL behavior first converts into the transition one and then disrupts into the NFL regime. This demonstrates that the spin liquid of $ZnCu_3(OH)_6Cl_2$ is close to QCP and behaves as the HF liquid of $YbRh_2Si_2$. On the other hand, that the low-temperature ends ($T_N \leq 0.5$) of the curves do not merge and their values decrease as B grows representing the total polarization of spins of the HF band at the highest reached magnetic fields [28], as it takes place in the case of $YbRh_2Si_2$ in strong magnetic fields, see Chap. 15. Indeed, at low T_N, χ_N at $B = 14$ T is close to $(C/T)_N$ at $B = 18$ T, while our calculations shown by the solid curve is close to each of the functions. Both the normalized magnetization $M_N(y) = M(B/B_k)/M(B_k)$, extracted from measurements of the magnetization $M(B)$ [8] depicted by the symbols, and calculated $M_N(y)$ shown by the solid line are reported in Fig. 17.5. Here, T_k is the temperature

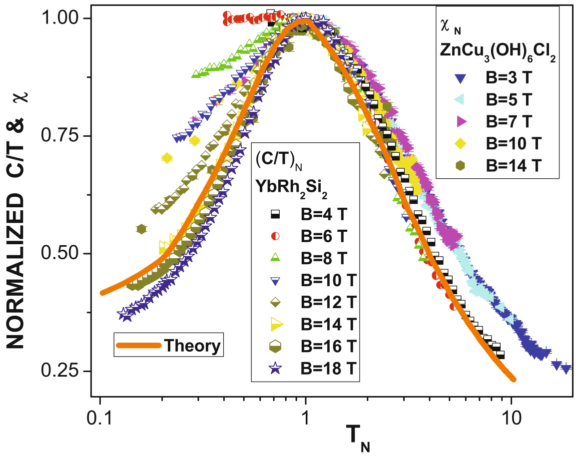

Fig. 17.4 Scaling behavior of the the magnetic susceptibility. Normalized susceptibility $\chi_N = \chi/\chi_{\max} = M_N^*$ is shown versus normalized temperature T_N. χ_N is extracted from the measurements of the magnetic susceptibility $\chi(B, T)$ [8] shown in Fig. 17.2. Normalized specific heat $(C/T)_N = M_N^*$ is extracted from the measurements of C/T on $YbRh_2Si_2$ in magnetic fields B [26]. The corresponding fields B are listed in the legends. Our calculations made at field B completely polarizing the quasiparticle band are depicted by the *solid curve* tracing the scaling behavior of M_N^*. It is clearly seen that the data collected on both $ZnCu_3(OH)_6Cl_2$ and $YbRh_2Si_2$ merge into the same *curve*, obeying the scaling behavior at $T_N \geq 1$ when the polarization vanish. In accordance with the phase diagram displayed in the panel **a**, at growing temperatures ($y \simeq 1$) the LFL regime first converts into the transition one and then disrupts into the NFL regime. This demonstrates that the spin liquid of herbertsmithite is close to QCP and behaves like HF liquid of $YbRh_2Si_2$ in strong magnetic fields

Fig. 17.5 Normalized magnetization $M_N(y)$ collected on measurements on $ZnCu_3(OH)_6Cl_2$ [8] and $YbRh_2Si_2$ [27] at different temperatures shown in the corresponding legends. The kink (*arrow*) is located at $y \simeq 1$. The normalized entropy $S_N(y)$ is extracted from measurements on 2D ^3He [2] at different densities x shown in the legend. The *solid curve* represents our calculations of the normalized magnetization

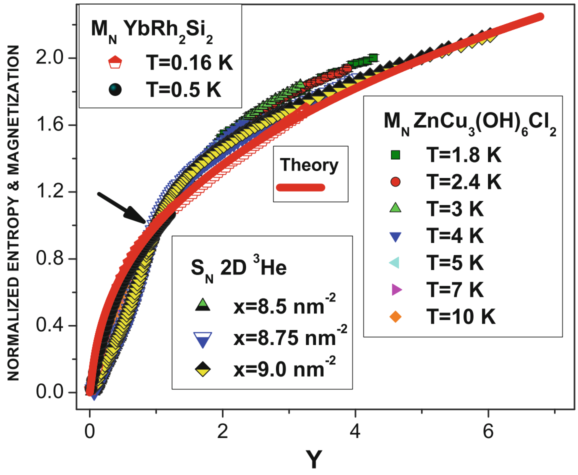

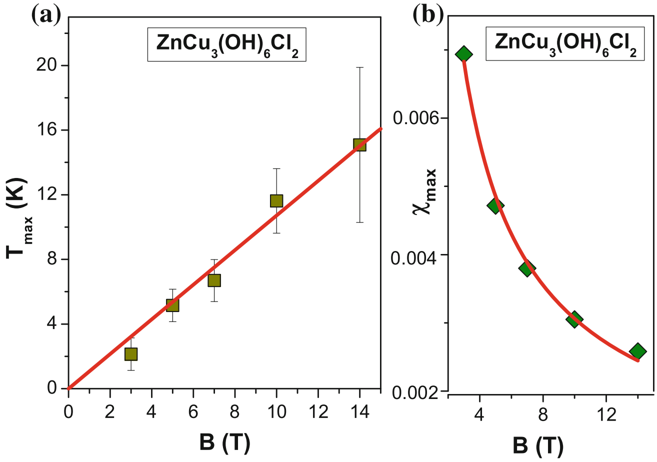

Fig. 17.6 $T_{\max}$ and $\chi_{\max}$ versus magnetic field B. Panel **a** The temperatures $T_{\max}(B)$ where the maxima of χ (see Fig. 17.2) are located. The solid line represents the function $T_{\max} \propto aB$, a being a parameter, see (17.5). Panel **b** The maxima $\chi_{\max}$ of $\chi(T)$ versus magnetic field B (see Fig. 17.2). The *solid curve* is approximated by $\chi_{\max}(B) = dB^{-2/3}$, see (17.3), where d is a parameter

where the magnetization has the kink, while the system enters the transition region [4] shown in Fig. 17.3. The normalized entropy $S_N(y) = S(T/T_{inf})/S(T_{inf})$ is obtained from measurements of the entropy S on 2D ^{3}He [2]. Here T_{inf} is the temperature where the system enters the transition region and S has its inflection point, clearly seen in the data, see Fig. 1.4. It is seen from (17.4) and from the inset in Fig. 17.3, that at $y < 1$, $S_N = M_N \propto y$, and at $y > 1$, $S_N = M_N \propto y^{1/3}$. This behavior produces the kink and makes the scaled data merge into a single curve dependent on the single variable y. Our calculations are in good agreement with the measurements. In Fig. 17.6, panel a, the solid squares denote temperatures $T_{\max}(B)$ at which the maxima of $\chi(T)$ occur versus magnetic field B. In the panel b, the corresponding values of the maxima $\chi_{\max}(B)$ are shown by the solid diamonds as a function of B. It is seen that the agreement between the theory and experiment is good in the entire magnetic field domain.

Our calculations of the specific heat $C(B, T)$ are shown in Fig. 17.7. For T of a few Kelvin, the lattice contribution to the specific heat is comparable with that of QSL, and at higher temperatures it becomes the most significant one. However, this contribution diminishes at low temperatures, and at $T \leq 1$ K C is predominately determined by the spin liquid contribution [6, 7]. It is seen from Fig. 17.7, that in the LFL region at $k_BT \lesssim \mu_BB$, $C(B, T) = a_1B^{-2/3}T \propto M^*T$ with a_1 being the only fitting parameter. The field B completely defines the $M^*(B)$ behavior given by (17.3). Clearly, our calculations are in good agreement with the measurements when the system demonstrates the LFL behavior. Indeed, at $T = 1$ K the system exhibits the LFL behavior at $B \geq 2$ T, while at $T = 0.5$ K the LFL behavior is observed even at lower values of B, namely $B \geq 1$ T.

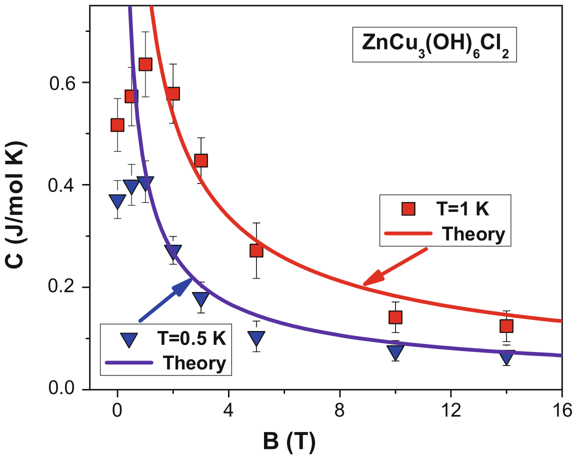

Fig. 17.7 The specific heat $C(B, T)$ versus magnetic field B measured on $ZnCu_3(OH)_6Cl_2$ [6]. The measurements were performed at two different temperatures T listed in the legends where they are shown by *triangles* and *squares*. Our calculations are depicted by the *solid curves* tracing the LFL behavior of $C(B, T) = a_1 B^{-2/3} T$, see (18.10), with a_1 being a parameter

The behavior of $M^*_N = M^*/M^*_M$ as a function of $y = T/T_M$ shown in the inset to Fig. 17.3 is independent of the specific features of corresponding strongly correlated Fermi system, while both M^*_M and T_M are determined by these features, as we have seen in Sect. 6.3. As a result, we obtain

$$\chi_N = (C_{mag}/T)_N = M^*_N, \tag{17.6}$$

where χ_N and $(C/T)_N$ are the normalized values of χ and C/T, respectively. The specific heat C, arising from the Cu spin system, at the lowest explored temperatures, $100 < T < 400\,\text{mK}$, follows a linear temperature dependence, $C \propto T$. As it is seen from Fig. 17.8, panel b, for temperatures of a few Kelvin and higher, the specific heat becomes $C(T) \propto T^3$ and is dominated by the lattice contribution. The strong magnetic field dependence of the specific heat C suggests that it is predominately formed by the specific heat C_{mag} of QSL,

$$C_{mag} = C - a_1 T^3, \tag{17.7}$$

since the lattice contribution is independent of B [6–8]. The above behavior of χ (Fig. 17.8, panel a) is a visible parallel to that of the HF metal $YbRh_2Si_2$ observed in measurements of C/T and displayed in the panel c. This coincidence becomes evident if we recollect that for HF liquid $\chi \propto C/T$ [4]. It is seen from the panel c that the electronic specific heat of $YbRh_2Si_2$ [26] is also strongly dependent on the applied magnetic field. It follows from Fig. 17.4 that in accordance with (17.6) the behavior of χ_N coincides with that of $(C/T)_N$ in $YbRh_2Si_2$. We will see below that both the specific heat C_{mag} and that of $YbRh_2Si_2$ exhibit the same behavior.

According to (17.6), in the case of QSL the behavior of the specific heat $(C_{mag}/T)_N$ must coincide with that of χ_N. To separate C_{mag} contribution, we approximate the general specific heat $C(T)$ at $T > 2$ K by the function

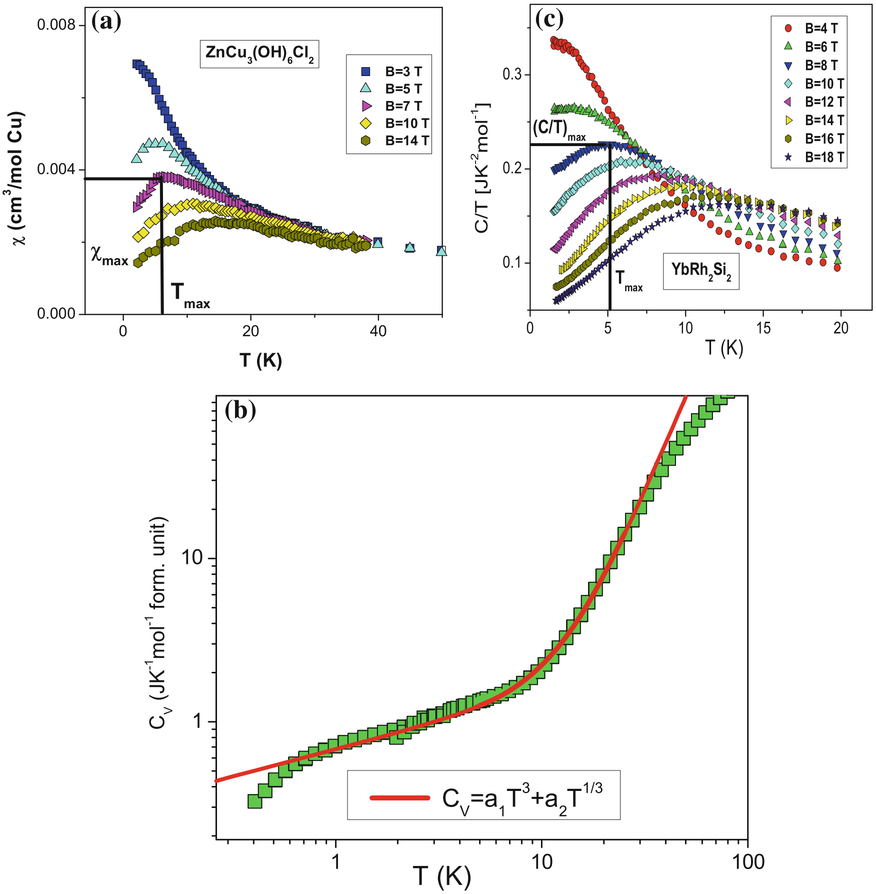

Fig. 17.8 Panel **a** T-dependence of the magnetic susceptibility χ at different magnetic fields B [8] shown in the legend. The values of $\chi_{\max}$ and $T_{\max}$ at $B = 7$ T are also shown. Panel **b** the heat capacity measured on $ZnCu_3(OH)_6Cl_2$ at zero magnetic field [7] is shown by *squares*. *Solid curve* corresponds to our theoretical approximation based on the function $C = a_1T^3 + a_2T^{1/3}$ with fitting parameters a_1 and a_2, see (17.8). Panel **c** reports the T-dependence of the electronic specific heat C/T of $YbRh_2Si_2$ at different magnetic fields [26] as shown in the legend. The values of $(C/T)_{\max}$ and $T_{\max}$ at $B = 8$ T are also shown

$$C(T) = a_1T^3 + a_2T^{1/3}. \qquad (17.8)$$

Here the first term proportional to a_1 presents the lattice (phonon) contribution, while the second one is determined by the QSL when it exhibits the NFL behavior, as it follows from (17.2). It is seen from Fig. 17.8, panel b, that the approximation (17.8) is valid in a wide temperature range. We note that the value a_1 is almost independent of a_2, the presence of which allows us to achieve a better approximation for C.

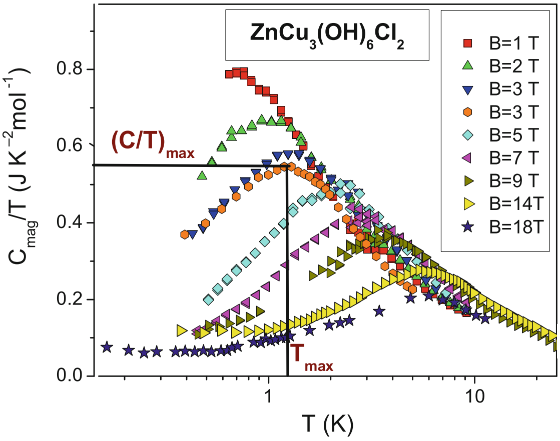

Fig. 17.9 The specific heat (C_{mag}/T) of QSL in $ZnCu_3(OH)_6Cl_2$ measured on powder samples [8] and on single crystal samples [29, 30]. (C_{mag}/T) is displayed versus temperature T as a function of the magnetic fields B shown in the legends. (C_{mag}/T) is extracted from the data [8, 29, 30] by using (17.9). The specific heat (C_{mag}/T) exhibits the same behavior as C/T of $YbRh_2Si_2$ demonstrated in the panel **c** of Fig. 17.8

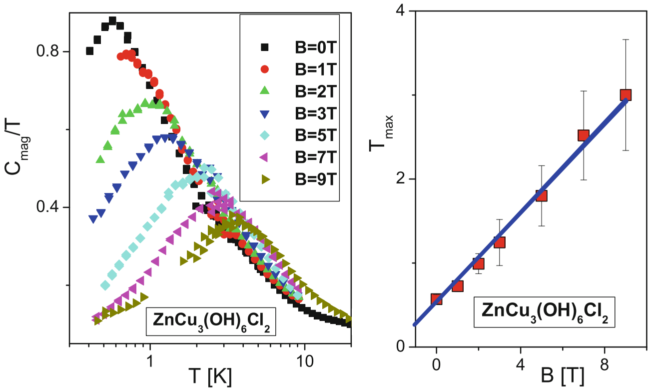

Fig. 17.10 *Left panel* The specific heat C_{mag}/T of QSL given by (17.8) is extracted from measurements of $C(B)$ on $ZnCu_3(OH)_6Cl_2$ at different magnetic fields shown in the legend [7]. *Right panel* The temperatures $T_{\max}(B)$ at which the maxima of C_{mag}/T (see the *left panel*) are located. The *solid line* represents the function $T_{\max} \propto B$, see (17.5)

The obtained heat capacity C_{mag}/T,

$$\frac{C_{mag}}{T} = \frac{C - a_1 T^3}{T}, \tag{17.9}$$

is displayed in Fig. 17.9 and in the left panel of Fig. 17.10, while the right panel of Fig. 17.10 demonstrates the maximum temperature as a function of the magnetic

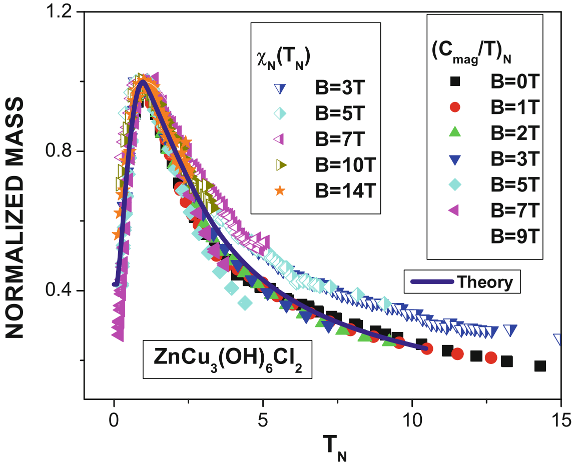

Fig. 17.11 The normalized susceptibility $\chi_N = \chi/\chi_{\max} = M^*_N$ and the normalized specific heat $(C_{mag}/T)_N = M^*_N$ of QSL effective mass versus normalized temperature T_N as a function of the magnetic fields shown in the legends. χ_N is extracted from the measurements of the magnetic susceptibility χ in magnetic fields B [8] shown in the panel **a** of Fig. 16.2. The normalized specific heat is extracted from the data displayed in Fig. 17.10, the *left panel*. Our calculations are depicted by the *solid curve* tracing the scaling behavior of M^*_N

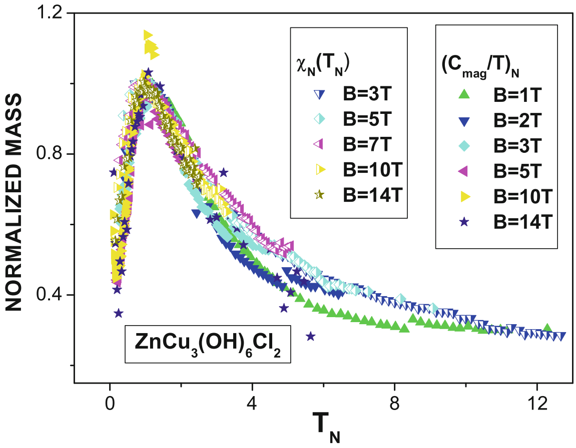

Fig. 17.12 The normalized susceptibility χ_N and the normalized specific heat $(C_{mag}/T)_N$ of QSL effective mass versus normalized temperature T_N as a function of the magnetic fields shown in the legends. χ_N and $(C_{mag}/T)_N$ are extracted from the data of [6, 8], respectively

field B. It is seen from Fig. 17.9 that $C_{mag}/T \propto M^*$ behaves like $\chi \propto M^*$ shown in Fig. 17.2. The normalized $(C_{mag}/T)_N$ and χ_N are depicted in Figs. 17.11, 17.12 and 17.16. It is seen from these figures that the results obtained on the different samples (powder samples and single crystal samples) and the measurements

[6, 7, 29, 30] exhibit similar properties. As it is seen from Figs. 17.11 to 17.12 that in accordance with (17.6), $(C_{mag}/T)_N \simeq \chi_N$ displays the same scaling behavior as $(C/T)_N$ measured on the HF metal $YbRh_2Si_2$. This observation rules out a scenario suggesting that extra Cu spins outside the kagome planes considered as weakly interacting impurities could be responsible for the divergent behavior of the low-temperature susceptibility seen from Fig. 17.2, see e.g., [10]. In that case the supposition is to lead to explanations of the observed scaling behavior of χ and C/T in strong magnetic fields shown in Figs. 17.11, 17.12 and 17.16. Obviously, it is impossible, for weakly interacting impurities would be polarized by relatively weak magnetic field, and would not contribute at higher magnetic fields. As a result, the scaling behavior were destroyed at the higher fields. Therefore, the scaling behavior of the thermodynamic functions of herbertsmithite is the intrinsic feature of the compound and has nothing to do with possible contribution coming from the magnetic impurities. Moreover, as it is seen from Fig. 17.9, the measurements on powder samples and on single crystal samples, demonstrating similar results, rule out noticeable contributions to the thermodynamic properties coming from defects of the lattice and impurities.

Thus, the kagome lattice of $ZnCu_3(OH)_6Cl_2$ can be viewed as a strongly correlated Fermi system whose thermodynamics is defined by the quantum spin liquid located at FCQPT. We conclude that in herbertsmithite the entire bulk susceptibility and the heat capacity obey the scaling behavior. The scaling behavior of the thermodynamic properties coincides with that observed in HF metals and 2D ^{3}He. Herbertsmithite $ZnCu_3(OH)_6Cl_2$ exhibits the LFL, NFL and the transition behavior as HF metals and 2D ^{3}He do, see Sects. 6.3.1 and 18.4.

17.2 Scaling in Dynamic Susceptibility of Herbertsmithite and HF Metals

In this Section we present a theory of the dynamic magnetic susceptibility of quantum spin liquid. The obtained results show that the dynamic magnetic susceptibility behaves as that of HF metals. Therefore, two known classical types of magnetism (ferro- and antiferromagnetism) can be augmented by one more, caused not by the order of the magnetic moments of atoms, ions or electrons, but by the “liquid” behavior of spins. A new magnetic state of matter emerges, which is characterized by a spins flow. This flow is described by means of virtual chargeless particles—spinons, behaving as HF liquid. The theory of the dynamic magnetic susceptibility allows us to reveal that at low temperatures quasiparticles excitations, or spinons, form a continuum, and populate an approximately flat band crossing the Fermi level. The obtained results are in good agreement with experimental facts collected on herbertsmithite $ZnCu_3(OH)_6Cl_2$ and as well as on HF metals, and allow us to predict a new scaling in magnetic fields in the dynamic susceptibility. Under the application of strong magnetic fields quantum spin liquid becomes completely polarized. We show that this polarization can be viewed as a manifestation of gapped excitations when investigating the spin–lattice relaxation rate.

The key point of the LFL theory is the existence of fermionic quasiparticles defining the thermodynamic, relaxation and dynamic properties of the considered material. However, strongly correlated Fermi systems encompassing a variety of systems that display behavior not easily understood within the LFL frame and called NFL. An important example of the NFL behavior is represented by HF metals. As we have demonstrated in Sect. 17.1, exotic QSL is formed with such hypothetic particles as fermionic spinons. The experimental studies of herbertsmithite $\mathrm{ZnCu_3(OH)_6Cl_2}$ and the organic insulator $\mathrm{EtMe_3Sb[Pd(dmit)_2]_2}$ have discovered gapless excitations, analogous to excitations near the Fermi surface in HF metals, indicating that $\mathrm{ZnCu_3(OH)_6Cl_2}$ and $\mathrm{EtMe_3Sb[Pd(dmit)_2]_2}$ are quite promising systems in investigating their QPTs and QSLs [5–11, 15–18]. The observed behavior of the thermodynamic properties of $\mathrm{ZnCu_3(OH)_6Cl_2}$ strongly resembles that in HF metals, since the kagome lattice being strongly frustrated has a dispersionless topologically protected branch of the spectrum with zero excitation energy [11, 12, 24, 25]. This indicates that QSL formed by the ideal kagome lattice is located near the ordered side of FCQPT that is characterized by the presence of the spectrum with zero excitation energy [4]. This observation allows us to establish a close similarity between QSL and HF metals whose HF systems are located near FCQPT and, therefore, exhibiting an universal scaling behavior [4, 11, 12].

Although, as we have seen in Sect. 17.1, experimental facts on the thermodynamic properties give conclusive evidence that the QSL does exist, the theoretical interpretation of other bunch of data, namely those on inelastic neutron scattering spectrum and spin–lattice relaxation rates on herbertsmithite can deliver additional information on close relationship between QSL and HF metals. Here, we employ the Landau transport equation to construct the dynamical spin susceptibility. We elucidate how the calculated susceptibility is affected by magnetic field and describe the experimental data for herbertsmithite and HF metals.

17.2.1 Theory of Dynamic Spin Susceptibility of Quantum Spin Liquid and Heavy-Fermion Metals

To construct the dynamic spin susceptibility $\chi(\mathbf{q},\omega,T) = \chi'(\mathbf{q},\omega,T) + i\chi''(\mathbf{q},\omega,T)$ as a function of momentum $\mathbf{q}$, frequency ω and and temperature T, we use the model of homogeneous HF liquid located near FCQPT [4]. To deal with the dynamic properties of Fermi systems, one can use the transport equation describing a slowly varying disturbance $\delta n_\sigma(\mathbf{q},\omega)$ of the quasiparticle distribution function $n_0(\mathbf{p})$, and $n = \delta n + n_0$. We consider the case when the disturbance is induced by the application of external magnetic field $B = B_0 + \lambda B_1(\mathbf{q},\omega)$ with B_0 being a static field and λB_1 a ω-dependent field with $\lambda \to 0$. As long as the transferred energy ω obeys the inequality, $\omega < qp_F/M^* << \mu$, where M^* is the effective mass and μ

is the chemical potential, the quasiparticle distribution function $n(\mathbf{q},\omega)$ satisfies the transport equation [31]

$$\begin{aligned}(\mathbf{q}\mathbf{v}_\mathbf{p}-\omega)\delta n_\sigma-\mathbf{q}\mathbf{v}_\mathbf{p}\frac{\partial n_0}{\partial\varepsilon_p}\sum_{\sigma_1\mathbf{p}_1}F_{\sigma,\sigma_1}(\mathbf{p}\mathbf{p}_1)\delta n_{\sigma_1}(\mathbf{p}_1)\\ =\mathbf{q}\mathbf{v}_\mathbf{p}\frac{\partial n_0}{\partial\varepsilon_p}\sigma\mu_B(B_0+\lambda B_1).\end{aligned}\tag{17.10}$$

We assume that B_0 is finite but not strong enough to lead to the total polarization of the corresponding quasiparticle band. In the field B_0, the two, the spin-up and spin-down, Fermi surfaces are displaced by opposite values of energy, $\pm B_0\mu_B$, and the magnetization is given by: $\mathscr{M}=\mu_B(\delta n_+-\delta n_-)$, where the two spin orientations with respect to the magnetic field are denoted by ±, and $\delta n_\pm=\sum_p\delta n_\pm(\mathbf{p})$. The spin susceptibility χ is given by $\chi=\partial\mathscr{M}/\partial B|_{B=B_0}$. The transport equation (17.10) is reduced to two equations, which can be solved for each direction ± independently and allows to calculate $\delta n_\pm$ and the magnetization. The response to $\lambda B_1(\mathbf{q},\omega)$ can be found by expanding the solution of (17.10) in a power series with respect to $M^*\omega/qp_F$. As a result, we obtain the imaginary part of the spin susceptibility

$$\chi''(\mathbf{q},\omega)=\mu_B^2\frac{\omega(M^*)^2}{2\pi q}\frac{1}{(1+F_0^a)^2},\tag{17.11}$$

where F_0^a is the dimensionless spin antisymmetric quasiparticle interaction [31]. The interaction F_0^a is found to saturate at $F_0^a\simeq-0.8$ [32, 33] so that $1+F_0^a$ is positive. It is seen from (17.11) that the second term is an odd function of ω. Therefore, it does not contribute to the real part χ' and forms the imaginary part χ''. Taking into account that at relatively high frequencies $\mu\gg\omega\geq qp_F/M^*$ in the hydrodynamic approximation one has $\chi'\propto 1/\omega^2$ [34], we conclude that the equation

$$\chi(\mathbf{q},\omega)=\frac{\mu_B^2}{\pi^2(1+F_0^a)}\frac{M^*p_F}{1+i\pi\frac{M^*\omega}{qp_F(1+F_0^a)}},\tag{17.12}$$

produces the simplest approximation for the susceptibility χ and satisfies the Kramers-Kronig relation connecting the real and imaginary parts of χ.

To understand how can χ'' and χ given by (17.11) and (17.12), respectively, depend on temperature T and magnetic field B, we recollect that near FCQPT point the effective mass M^* depends on T and B, and is given by the Landau equation (17.1). Magnetic field B enters it only in the combination $\mu_B B/k_B T$, making $k_B T_{\max}\simeq\mu_B B$ [4, 22]. Thus, in the presence of magnetic fields the variable y becomes $y=T/T_{\max}\simeq k_B T/\mu_B B$. Since the variables T and B enter symmetrically (17.4) is valid for $y=\mu_B B/k_B T$.

The schematic $T-B$ phase diagram of QSL and HF liquid is presented in Fig. 17.3. Magnetic field B and temperature T play the role of control parameters, the variation

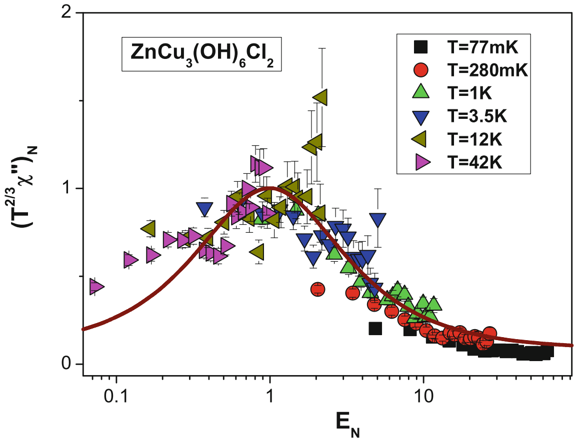

Fig. 17.13 The function $(T^{2/3}\chi'')_N$ plotted against the dimensionless ratio $E_N = \omega/((k_BT)^{2/3}E_{\max})$. The *solid curve* is the fit by the function (17.15). The data extracted from measurements on ZnCu$_3$(OH)$_6$Cl$_2$ are obtained for $0.077 < T < 42$ K [8]

of which leads to the transition from the NFL to LFL regions, as it is shown by the vertical and horizontal arrows. At fixed B and increasing T the system transits along the vertical arrow from LFL to NFL crossing the transition region. On the contrary, at fixed T the increase of B leads the system along the horizontal arrow from NFL region to LFL region.

17.2.2 Scaling Behavior of the Dynamic Susceptibility

To elucidate the scaling behavior of χ, we employ (17.2) to describe the temperature dependence of χ. It follows from (17.12) and (17.2) that

$$T^{2/3}\chi(T,\omega) \simeq \frac{a_1}{1+ia_2E}. \tag{17.13}$$

Here a_1 and a_2 are constants determined by irrelevant quantities, and $E = \omega/(k_BT)^{2/3}$. As a result, the imaginary part $\chi''(T,\omega)$ is given by the equation

$$T^{2/3}\chi''(T,\omega) \simeq \frac{a_3E}{1+a_4E^2}, \tag{17.14}$$

where a_3 and a_4 are constants. It is seen from (17.14) that $T^{2/3}\chi''(T,\omega)$ depends on the only variable E, and has a maximum $(T^{2/3}\chi''(T,\omega))_{\max}$ at some $E_{\max}$. Equation (17.14) confirms the scaling behavior of $\chi''T^{0.66}$ experimentally established in [8]. As the dimensionless function $M^*(y)$ was used when constructing (17.4), in the same way we introduce the dimensionless function $(T^{2/3}\chi'')_N = T^{2/3}\chi''/(T^{2/3}\chi'')_{\max}$ and the dimensionless variable $E_N = E/E_{\max}$, and (17.14) transforms into

$$(T^{2/3}\chi'')_N \simeq \frac{b_1 E_N}{1 + b_2 E_N^2}, \tag{17.15}$$

with b_1 and b_2 are fitting parameters which are to adjust the function on the right-hand side of (17.15) to reach its maximum value 1 at $E_n = 1$. We predict that if measurements of χ'' are taken at fixed T as a function of B, then by taking into account (18.10), we again obtain that the function $B^{2/3}\chi''(E)$ exhibits the scaling behavior with $E = \omega/(\mu_B B^{2/3})$. If the system is placed at FCQPT, the scaling described above is valid down to lowest temperatures.

In Figs. 17.13, 17.14 and 17.15, we depict the scaled normalized dynamic susceptibility $(T^{2/3}\chi'')_N$ extracted from the inelastic neutron scattering spectrum of herbertsmithite [8], $Ce_{0.925}La_{0.075}Ru_2Si_2$ with $Q_1 = 0.6910$ and $Q_1 = 0.4410$ [35]. It is seen that the scaled data are consistent with (17.15) and collapse fairly well onto a single curve over almost three orders of E_N. It is seen that our calculations

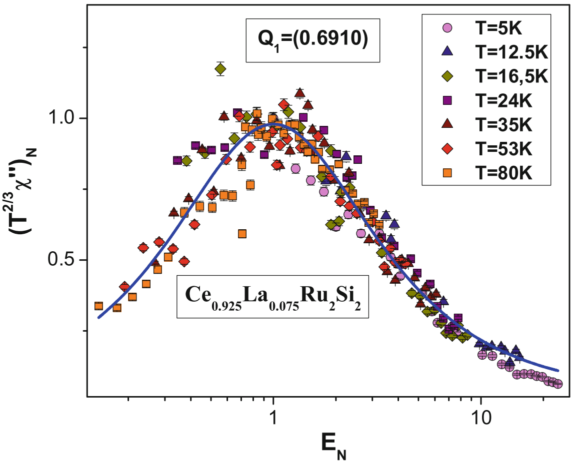

Fig. 17.14 Same as in Fig. 17.13, but for the HF metal $Ce_{0.925}La_{0.075}Ru_2Si_2$ obtained for $5 < T < 80$ K at $Q_1 = 0.6910$ [35]

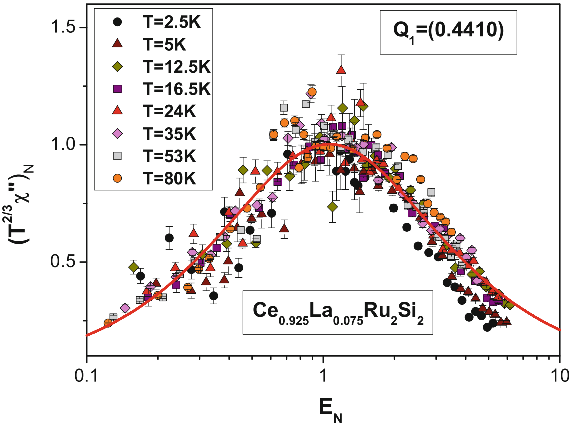

Fig. 17.15 Same as in Fig. 17.14, but for HF metal $Ce_{0.925}La_{0.075}Ru_2Si_2$ for $2.5 < T < 80$ K at $Q_1 = 0.4410$ [35]

(solid curves) are in good overall agreement with the experiment. Let us make some remarks on the role of both the disorder and the anisotropy. The anisotropy is supposed to be related to the Dzyaloshinskii-Moriya interaction, exchange anisotropy, or out-of-plane impurities. We note that the Hamiltonian of herbertsmithite includes a Heisenberg exchange term, with possible perturbations such as a Dzyaloshinskii-Moriya interaction. The measurements of the susceptibility on the single crystal of herbertsmithite have shown that the results closely follow that measured on a powder sample [9]. At low temperatures $T \lesssim 70\,\mathrm{K}$, the single-crystal data do not show magnetic anisotropy [9].

Figure 17.16 reports the normalized specific heat $(C_{mag}/T)_N$ of $\mathrm{ZnCu_3(OH)_6Cl_2}$ versus normalized temperature T_N as a function of the magnetic fields. $(C_{mag}/T)_N$ are extracted from the data of [8, 29, 30], our calculations are shown by solid curve. Measurements of the heat capacity C at magnetic fields $B = 0$–$14\,\mathrm{T}$ and $B = 0$–$18\,\mathrm{T}$ were carried out on single crystal samples [29, 30]. Good agreement among all the data is seen from Fig. 17.16. Thus, we conclude that the disorder does not significantly contribute to the heat capacity. The above facts confirm that the stoichiometry, disorder and anisotropy do not contribute significantly to the results at relatively low temperatures. Moreover, as we have seen, the scaling behavior of both the thermodynamic functions and the imaginary part of the magnetic susceptibility of herbertsmithite is the intrinsic feature and has nothing to do with the impurities [12]. These observations are in agreement with the general consideration of scaling behavior of HF metals, see Chaps. 6 and 7.

A few remarks regarding the imaginary part $\chi''(T, \omega)$ are in order here. Equation (17.14) is valid provided that the system approaches FCQPT from the disordered side as shown in the phase diagram Fig. 16.2. If the system is located on the orderedside

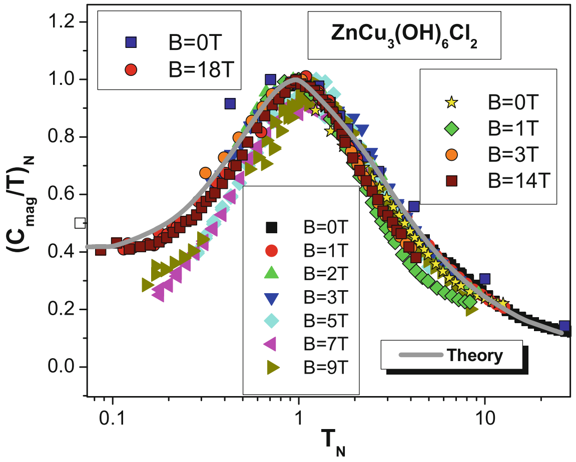

Fig. 17.16 The normalized specific heat $(C_{mag}/T)_N$ of QSL in $\mathrm{ZnCu_3(OH)_6Cl_2}$ versus normalized temperature T_N as a function of the magnetic fields shown in the legends. $(C_{mag}/T)_N$ are extracted from the data of [8, 29, 30]. Measurements of the heat capacity C were carried out on single crystal samples [29, 30]. *Solid curve* represents our calculations, and traces the scaling behavior of the effective mass

then at $B = 0$ the behavior of the effective mass as a function of T is given by [4]

$$M^*(T) \simeq a_\tau T^{-1}, \tag{17.16}$$

where a_τ is a constant. Upon taking into account (17.16) and acting in the same way as it was done in deriving (17.14), we obtain that the imaginary part $\chi''(T, \omega)$ is given by the equation

$$T\chi''(T, \omega) \simeq \frac{a_5 E}{1 + a_6 E^2}, \tag{17.17}$$

where a_5 and a_6 are constants, and $E = \omega/k_B T$. It is seen from (17.17) that $T\chi''(T, \omega)$ depends on the only variable $E = \omega/k_B T$. Thus, (17.14) and (17.17) establish two types of scaling behavior of $\chi''(\omega, T)$. Since the scaling behavior of $\chi''(\omega, T)$ is defined by the dependence of M^* on T, one may expect new types of scaling especially at the transition region shown in Figs. 6.2 and 17.3.

Figure 17.17 presents the dynamic susceptibility ($T\chi''$) extracted from measurements of the inelastic neutron scattering spectrum on the HF metal $YbRh_2Si_2$ [36]. The data ($T\chi''$) exhibit the scaling over three decades of the variation of both the function and the variable, thus confirming the validity of (17.17). The scaled data obtained in measurements on such quite different strongly correlated systems as $ZnCu_3(OH)_6Cl_2$, $Ce_{0.925}La_{0.075}Ru_2Si_2$ and $YbRh_2Si_2$ collapse fairly well onto a single curve over almost three decades of the scaled variables. It is seen that our calculations shown by the solid curves are in good agreement with the experimental data. Thus, the spin excitations in $ZnCu_3(OH)_6Cl_2$ exhibit the same behavior as electron excitations of the HF metal $Ce_{0.925}La_{0.075}Ru_2Si_2$, and, therefore form a continuum. This observation of the continuum is of great importance since it clearly reveals the presence of SCQSL in herbertsmithite. Thus, in contrast to ferromagnet (with

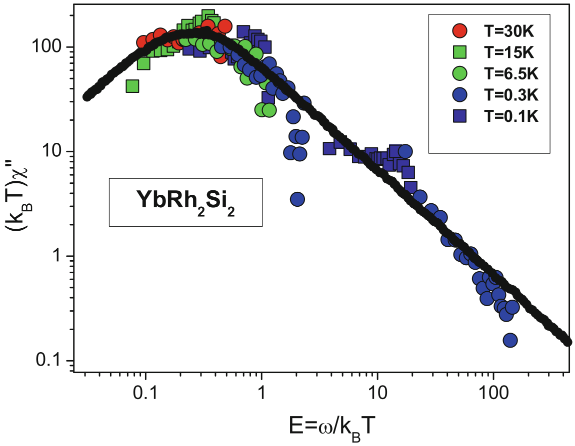

Fig. 17.17 $T\chi''$ plotted against $E = \omega/k_B T$. The data are extracted from measurements on $YbRh_2Si_2$ [36]. The *solid curve* is the fit by the function (17.17)

parallel direction of all atomic spins) and antiferromagnet (with opposite directions of atomic spins in its two sublattices), quantum spin liquid has the third type of magnetism—the direction of constituting spins is not fixed, but constantly rotated in time and space, being never ordered finally.

17.3 Spin–Lattice Relaxation Rate of Quantum Spin Liquid

A strong departure from LFL behavior have been revealed in the magnetic susceptibility χ and muon and ^{63}Cu nuclear spin–lattice relaxation rates $1/T_1$ of $\mathrm{YbCu_{5-x}Au_x}$ ($x = 0.6$). The above anomalies along with magnetic-field-induced reentrance of LFL properties are determined by the magnetic field B and temperature T dependence of the quasiparticle effective mass M^*. They demonstrate also that violations of the Korringa law (see Sect. 7.5) also come from $M^*(B, T)$ dependence. Our theoretical analysis of experimental data on the base of FCQPT approach permits not only to explain the above two experimental facts in a unified manner, but to unveil their universal properties, relating the peculiar features of both longitudinal magnetoresistance and specific heat in $\mathrm{YbRh_2Si_2}$ to the behavior of spin–lattice relaxation rates.

Consider the effect of B on the spin–lattice relaxation rate $1/T_1T$ determined by χ'' given by (17.11)

$$\frac{1}{T_1T} = \frac{3}{4\mu_B^2}\sum_{\mathbf{q}} A_{\mathbf{q}}A_{-\mathbf{q}}\frac{\chi''(\mathbf{q},\omega)}{\omega}|_{\omega\to 0} \propto (M^*)^2, \tag{17.18}$$

where $A_{\mathbf{q}}$ is the hyperfine coupling constant of the muon (or nuclei) with the spin excitations at wave vector $\mathbf{q}$ [4, 37, 38]. Figure 17.18 displays the normalized value $(1/T_1T)_N$ and the normalized longitudinal magnetoresistance ρ_N at fixed temperatures versus the normalized magnetic field B_N. It is seen from Fig. 17.18 that the magnetic field progressively reduces $1/T_1T$ and the longitudinal magnetoresistance (LMR), and these as a function of B possess an inflection point at $B = B_{inf}$ shown by the arrow. The normalized LMR obeys the equation [4]

$$\rho_N(B_N) = \frac{\rho(B_N) - \rho_0}{\rho_{inf}} = \left(\frac{1}{T_1T}\right)_N = (M_N^*)^2, \tag{17.19}$$

where ρ_0 is the residual resistance, ρ_{inf} is LMR taken at the inflection point, ρ is LMR, and $B_N = B/B_{inf}$. We normalize $(1/T_1T)$ and LMR by their values at the inflection point, and the magnetic field is normalized by B_{inf}. In accordance with the phase diagram Fig. 17.3, at $B > B_{inf}$, as it is seen from Figs. 17.5 and 17.18, QSL enters the LFL region with B-dependence of the effective mass defined by (17.3). It follows from (17.18) to (17.19) that $(1/T_1T)_N = \rho_N = (M_N^*)^2$ where $(M_N^*)^2$ is defined by (17.4), which shows that different strongly correlated Fermi

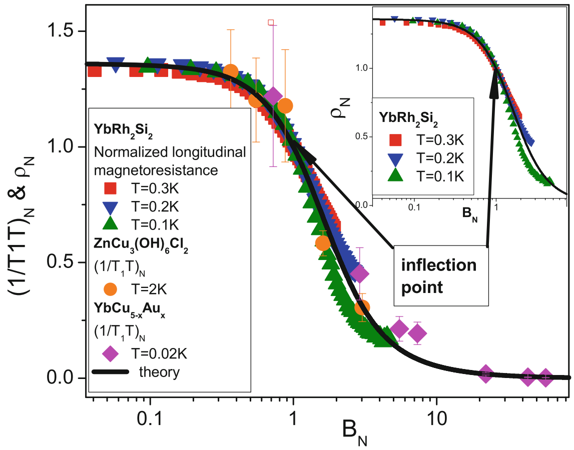

Fig. 17.18 The universal scaling behavior of the normalized muon spin-lattice relaxation rate. *Main panel* The dependence of normalized (see text for details) muon spin–lattice relaxation rate $(1/T_1T)_N$ extracted from measurements on $YbCu_{4.4}Au_{0.8}$ [39] and $ZnCu_3(OH)_6Cl_2$ [40] and presented along with the normalized longitudinal magnetoresistance ρ_N. The *arrows* indicate the inflection points. Our calculations are shown by the *solid line*. *Inset* ρ_N versus B_N. ρ_N is extracted from measurements on $YbRh_2Si_2$ at different temperatures [27] listed in the legend. The *solid curve* represents our calculations

systems have to exhibit the same scaling as $(M^*_N)^2$. It is seen from Fig. 17.18 and from the inset, that $YbCu_{5-x}Au_x$, herbertsmithite $ZnCu_3(OH)_6Cl_2$ and $YbRh_2Si_2$ demonstrate the similar behavior of $(M^*_N)^2$ resulting in the scaling of LMR and $1/T_1T$. Thus, (17.11), (17.18) and (17.19) determine the close relationship existing between the quite different dynamic properties and different HF compounds such as herbertsmithite and organic insulators (see Sect. 17.4) with QSL and HF metals, revealing their scaling behavior at FCQPT.

We note that one may be confused when applying (17.18) to describe $(1/T_1T)$ in strong magnetic fields. In that case both QSL and HF metals become fully polarized due to Zeeman splitting [11, 28, 37, 38]. As a result, one subband becomes empty, while the energy ε_F of spinons at the Fermi surface of the other subband lies below the chemical potential μ determined by the magnetic field B_0. It follows from (17.10) that $\chi'' = 0$ and (17.18) is not valid. The difference $\delta = \mu - \varepsilon_F$ can be viewed as a gap that makes $1/T_1T \propto \exp -(\delta/k_BT)$. At temperatures $k_BT \sim \delta$, the subbands are populated by spinons and the validity of (17.18) is restored. Thus, the presence of δ can be interpreted as the existence of gapped excitations. On the other hand, if there would be the gapped excitations, then the heat capacity would demonstrate the exponential decay rather than a linear T-dependence at low temperatures. Indeed, the analysis based on experimental data shows the presence of linear T-dependence even under the application of high magnetic fields [11], while measurements on $ZnCu_3(OH)_6Cl_2$ of $1/T_1T$ suggest that the excitations have a gap [41]. To clarify whether the gapped excitations could occur in $ZnCu_3(OH)_6Cl_2$, an accurate experimental measurement of the low temperature heat capacity in magnetic fields is necessary. Measurements under the application of magnetic field up to 18 T [29, 30] show the absence of the gap in the heat capacity C/T, while both the effective mass of spinons, $M^*_{mag} \propto C_{mag}/T$, and the normalized effective mass of spinons, $M^*_N = (C_{mag}/T)_N$, remain finite at the lowest accessible temperatures, as it is seen from Figs. 17.9 and 17.16.

17.4 Heat Transport in Magnetic Fields by Quantum Spin Liquid in Insulators

Measurements of the low-temperature heat (or thermal) conductivity performed on insulators with geometrical frustration produce important experimental facts shedding light on the nature of strongly correlated quantum spin liquid composed of spinons. We analyze here theoretically the results of measurements of the low-temperature heat conductivity in magnetic fields collected on the organic insulators $\mathrm{EtMe_3Sb[Pd(dmit)_2]_2}$ and $\kappa-\mathrm{(BEDT-TTF)_2Cu_2(CN)_3}$. To do this, we employ a model of strongly correlated quantum spin liquid located near the FCQPT. The properties of spin liquid strongly resemble those of the conventional electron liquid in HF metals.

The organic insulators $\mathrm{EtMe_3Sb[Pd(dmit)_2]_2}$ and $\kappa-\mathrm{(BEDT-TTF)_2Cu_2(CN)_3}$ have two-dimensional triangular lattices with the geometric frustration that prohibits spin ordering even at the lowest accessible temperatures T [42–46]. Therefore, being different form $\mathrm{ZnCu_3(OH)_6Cl_2}$, these insulators offer unique insights into the physics of quantum spin liquids (QSL). Indeed, measurements of the heat capacity on both considered insulators reveal a T-linear term indicating that the low-energy excitation spectrum from the ground state is gapless [42–44]. The excitation spectrum can be deduced from the measurements of the heat (thermal) conductivity $\kappa(T)$ in the low temperature regime. For example, at $T\to 0$ the residual value in κ/T signals that the excitation spectrum is gapless. The presence of the residual value is clearly resolved in $\mathrm{EtMe_3Sb[Pd(dmit)_2]_2}$, while measurements of κ/T on $\kappa-\mathrm{(BEDT-TTF)_2Cu_2(CN)_3}$ suggest that the low-energy excitation spectrum can have a gap [45, 46]. Taking into account the observed T-linear term of the heat capacity in $\kappa-\mathrm{(BEDT-TTF)_2Cu_2(CN)_3}$ with the static spin susceptibility remaining finite down to the lowest measured temperatures [47], the presence of a gap in the spin excitation becomes questionable. Thermal conductivity probe elementary itinerant excitations and is totally insensitive to localized ones, such as those responsible for Schottky contributions, which contaminates the heat capacity measurements at low temperatures [42–46]. The heat conductivity is formed primarily by both acoustic phonons and itinerant spinons, while the latter form QSL. Since the phonon contribution is insensitive to the applied magnetic field B, the elementary excitations of

QSL can be further explored by the magnetic field dependence of κ. Measurements under the application of magnetic field B of the heat conductivity κ in these insulators reveal strong dependence of $\kappa(B, T)$ on B at fixed T [45, 46]. The obtained dependence at low temperatures resembles that of the spin–lattice relaxation rate $(1/T_1T)$ at fixed temperature as a function of magnetic field [12]: $\kappa(B)$ at low fields is insensitive to B, displaying a response to increasing magnetic field B. On the other hand, it is suggested that the observed B-dependence implies that some spin-gap-like excitations coupling to the magnetic field are also present at low temperatures [45, 46]. As a result, we face a serious problem in interpretation of the experimental data in a consistent way, including the B-dependence of the heat conductivity [14].

Representing a special case of QSL, SCQSL is a quantum state of matter composed of spinons—chargeless fermionic particles with spin $1/2$ [12, 13, 35]. In insulating compounds such as the organic insulators $\mathrm{EtMe_3Sb[Pd(dmit)_2]_2}$ and $\kappa-\mathrm{(BEDT-TTF)_2Cu_2(CN)_3}$, SCQSL can emerge when interactions among the magnetic components are incompatible with the underlying crystal geometry, leading to a geometric frustration generated by the triangular and kagome lattices of magnetic moments, as it is in the case of $\mathrm{ZnCu_3(OH)_6Cl_2}$, see e.g., [48, 49]. In case of ideal 2D lattice, its frustration leads to a dispersionless topologically protected branch of the spectrum with zero excitation energy known as the flat band [24, 25, 50]. Thus, similar to the case of $\mathrm{ZnCu_3(OH)_6Cl_2}$, FCQPT can be considered as quantum critical point of SCQSL, composed of chargeless heavy spinons with $S = 1/2$ and the effective mass M^*_{mag}, occupying the corresponding Fermi sphere with the Fermi momentum p_F, see Sect. 17.1. Therefore, the properties of insulating compounds coincide with those of HF metals with one exception: it resists the flow of electric charges. Since we are dealing with compounds constituted of non-ideal triangular and kagome lattices, we have to bear in mind that the real magnetic interactions and possible distortion of the lattices can shift the SCQSL in the organic insulators from the exact FCQPT, positioning it somewhere near FCQPT. Therefore, the actual location in the phase diagram depicted in Fig. 17.19 of SCQSL can be established by analyzing the experimental data only. Indeed, in the case of systems located near FCQPT the energy landscape given by the Landau functional $E[n(p)]$ becomes very flat, see Chap. 4. As a result, numerical simulations of the ground state demonstrate their inefficiency.

In the vicinity FCQPT, pronounced deviations of physical properties from those in LFL are observed. These NFL effects are related to the action of strong enhancement of the effective mass M^*_{mag} associated with FCQPT. We note that there are different kinds of instabilities of LFL related to several perturbations of initial quasiparticle spectrum $\varepsilon(\mathbf{p})$ and occupation numbers $n(\mathbf{p})$, associated with strong enhancement of the effective mass and leading to the emergence of a multi-connected Fermi surface, see e.g., [4, 23, 51]. Depending on the parameters and analytical form of the Landau interaction, such instabilities lead to several possible types of restructuring of the initial LFL ground state. This restructuring generates topologically distinct phases, as it was shown in Chap. 4. One of them is the fermion condensation associated with FCQPT, another belongs to a class of topological phase transitions, where the sequence of rectangles $n(p) = 0$ and $n(p) = 1$ is realized at $T = 0$. In fact, at growing

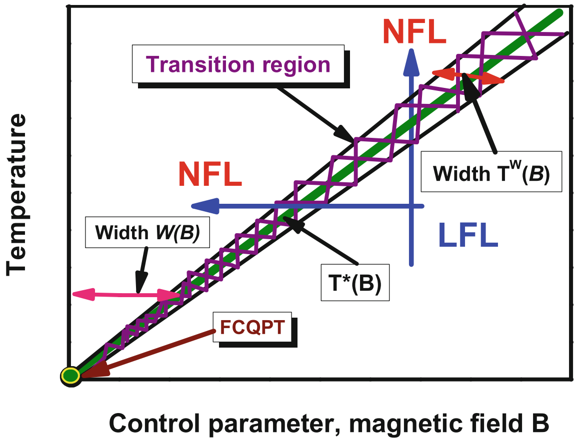

Fig. 17.19 Schematic $T-B$ phase diagram of SCQSL of the organic insulators with magnetic field as the control parameter. The *vertical* and *horizontal arrows* show LFL-NFL and reverse transitions at fixed B and T, respectively. The *hatched area* represents the transition region at $T^*(B)$. The *solid line* in the *hatched area* represents the function $T^*(B) \simeq T_M(B)$ given by (17.22). The functions $W(B) \propto T \propto T^*$ and $T^W(B) \propto T \propto T^*$ shown by *two-headed arrows* define the widths of the NFL state and the transition area, respectively. At FCQPT indicated by the *arrow* the effective mass M^* diverges, and leads both $W(B)$ and $T^W(B)$ to zero

temperatures the systems located at these transitions exhibit behavior typical to that determined by FCQPT. Therefore, we do not consider the specific properties of these topological transitions, and focus on the behavior of systems located near FCQPT.

We start with a brief outline of the effective mass dependence on magnetic field and temperature, $M^*_{mag}(B,T)$, while the dependence of the effective mass on T at fixed B is considered in Sect. 17.1. The key points of the employed formalism is the extended quasiparticle paradigm when the effective mass is no more constant but depends on temperature T, magnetic field B and other external parameters such as pressure P, are described in Sect. 17.1.3. To study the low temperature transport properties, scaling behavior, and the effective mass $M^*_{mag}(B,T)$ of SCQSL, we use the model of homogeneous HF liquid, that permits to avoid complications associated with the crystalline anisotropy of solids, while the effective mass M^* is given by (17.1). The distribution function n can be expressed as

$$n_\sigma(\mathbf{p},T) = \left\{1 + \exp\left[\frac{(\varepsilon(\mathbf{p},T)-\mu_\sigma)}{T}\right]\right\}^{-1}, \qquad (17.20)$$

In our case, the chemical potential μ depends on the spin due to Zeeman splitting $\mu_\sigma = \mu \pm \mu_B B$. The single-particle spectrum is a variational derivative of the system energy $E[n_\sigma(\mathbf{p},T)]$ with respect to occupation number n, $\varepsilon(\mathbf{p},T) = \delta E[n(\mathbf{p})]/\delta n$. The variational procedure, being applied to the functional $E[n_\sigma(\mathbf{p},T)]$, gives the following form for $\varepsilon_\sigma(\mathbf{p},T)$, see Sect. 2.3.1,

$$\frac{\partial \varepsilon_\sigma(\mathbf{p},T)}{\partial \mathbf{p}} = \frac{\mathbf{p}}{M} - \sum_{\sigma_1} \int \frac{\partial F_{\sigma,\sigma_1}(\mathbf{p},\mathbf{p}_1)}{\partial \mathbf{p}} n_{\sigma_1}(\mathbf{p}_1,T) \frac{d^3 p_1}{(2\pi)^3}, \tag{17.21}$$

As in the case of $ZnCu_3(OH)_6Cl_2$, (17.20) and (17.21) constitute the closed set for self-consistent determination of $\varepsilon_\sigma(\mathbf{p},T)$, $n_\sigma(\mathbf{p},T)$, and the effective mass M^*_{mag}, $p_F/M^*_{mag} = \partial\varepsilon(p)/\partial(p)|_{p=p_F}$. We emphasize here, that in our approach the entire temperature and magnetic field dependence of the effective mass is introduced by the dependencies of $\varepsilon_\sigma(\mathbf{p})$ and $n_\sigma(\mathbf{p})$ on T and B. At $B=0$, the effective mass strongly depends on T, thus demonstrating the NFL behavior given by (17.2). At finite T, the application of magnetic field B leads the system to the LFL region with $M^*(B)$ given by (17.3).

The behavior of $M^*(B,T)$ is defined again by (17.4). Magnetic field B enters (17.1) only in the combination $\mu_B B/T$, making $T_M \sim \mu_B B$. It follows from (17.4) that

$$T_M \simeq a_1 \mu_B B, \tag{17.22}$$

where a_1 is a dimensionless factor. Thus, in the presence of fixed magnetic field the variable y (see (17.4)) becomes $y = T/T_M \sim T/\mu_B B$. Taking into account (17.22), we conclude that (17.4) describes the scaling behavior of the effective mass as a function of T versus B: The curves M^*_N at different magnetic fields B merge into a single one in terms of the normalized variable $y = T/T_M$. Since the variables T and B enter symmetrically, (17.4) describes the scaling behavior of $M^*_N(B,T)$ as a function of B versus T.

The normalization procedure deserves here a comment. Namely, since the magnetic field dependence of $M^*_N(B,T)$ at fixed T does not have a maximum, the normalization is performed at its inflection point, occurring at $B = B_{inf}$. As a result, we have $y = B/B_{inf}$ and $M^*_N = M^*(B,T)/M^*(B_{inf},T)$. In other words, the curves M^*_N at different T merge into a single one in terms of the normalized variable $y = B/B_{inf}$, while (17.22) transforms into the equation

$$\mu_B B_{inf} \simeq a_2 T, \tag{17.23}$$

with a_2 is a dimensionless factor.

Let us create a more detailed schematic phase diagram of SCQSL of the organic insulators $EtMe_3Sb[Pd(dmit)_2]_2$ and $\kappa-(BEDT-TTF)_2Cu_2(CN)_3$ than that of $ZnCu_3(OH)_6Cl_2$. This phase diagram is reported in Fig. 17.19. We assume that at $T=0$ and $B=0$ the system is approximately located at FCQPT without tuning. Both magnetic field B and temperature T play the role of the control parameters, shifting the system from FCQPT and driving it from the NFL to LFL regions, as it is shown by the vertical and horizontal arrows. At fixed temperatures the increase of B drives the system along the horizontal arrow from the NFL to LFL region. On the contrary, at fixed magnetic field and increasing temperatures the system transits along the vertical arrow from the LFL region to the NFL one. The hatched area denoting the transition region separates the NFL state from the weakly polarized LFL state and contains the solid line tracing the transition region, $T^*(B) \simeq T_M(B)$. Referring to (17.22), this line is defined by the function $T^* \propto \mu_B B$, and the width $W(B)$ of the NFL state is seen to be proportional to T. In the same way, it can be shown that the width $T^W(B)$ of the transition region is also proportional to T.

As it was mentioned above, SCQSL plays an important role of HF liquid in organic insulators. Thus, we expect that SCQSL in organic insulators behaves like the electronic HF liquid in HF metals, provided that the charge of an electron were zero. In that case, the thermal resistivity w of SCQSL is related to the thermal conductivity κ

$$w = \frac{L_0 T}{\kappa} = w_0 + A_w T^2. \tag{17.24}$$

In magnetic fields, the resistivity w behaves like the electrical magnetoresistivity $\rho_B = \rho_0 + A_\rho T^2$ of the electronic liquid, since A_w represents the contribution of spinon-spinon scattering to the thermal transport, being analogous to the contribution A_ρ to the charge transport, defined by electron-electron scattering. Here, L_0 is the Lorenz number, ρ_0 and w_0 are residual resistivity of electronic liquid and QSL, respectively, and the coefficients $A_w \propto (M^*_{\rm mag})^2$ and $A_\rho \propto (M^*)^2$ [4]. Thus, in the LFL region the coefficient A_w of the thermal resistivity of SCQSL under the application of magnetic fields at fixed temperature behaves like the spin–lattice relaxation rate shown in Fig. 17.20, $A_w(B) \propto A_\rho \propto 1/T_1T(B) \propto (M^*(B)_{\rm mag})^2$ [28]. In accordance with (17.3), as it is seen from Fig. 17.20, panel a, the magnetic field B progressively reduces $1/T_1T$ [39, 40], and $1/T_1T$ as a function of B possesses an inflection point at some $B = B_{inf}$ shown by the arrow. The same behavior is seen from Fig. 17.20, panel b: The magnetic field B diminishes the longitudinal magnetoresistivity [27], and as a function of B it possesses an inflection point shown by the arrow. This behavior is consistent with the phase diagram displayed in Fig. 17.19. Namely, with the growing of magnetic fields the NFL behavior at first converts into the transition one and then transforms into the LFL behavior.

The panels a and b of Fig. 17.20 display, respectively, the normalized spin–lattice relaxation rates $(1/T_1T)_N$ and the longitudinal magnetoresistivity ρ_B at fixed temperature versus normalized magnetic field B_N. To clarify the universal scaling behavior of the herbertsmithite and the HF metal $\rm YbCu_{5-x}Au_x$, we normalize functions $1/T_1T$ and $(\rho_B - \rho_0)$ as well as the magnetic field. Namely, we normalize the functions by their values at the inflection point, and magnetic field is normalized by B_{inf}, $B_N = B/B_{inf}$. Since $(1/T_1T)_N = \rho_B - \rho_0 = (M^*_N(B))^2$ [4, 28], we expect that the different strongly correlated Fermi systems located near FCQPT exhibit the same behavior of the effective mass, as it is seen from panels a and b of Fig. 17.20. We shall see below that the heat conductivity of the organic insulators behaves similarly.

Study of the thermal resistivity w given by (17.24) allows one to reveal spinons as itinerant excitations. It is important that the data on w is not mixed with contributions coming from localized excitations. The temperature dependence of thermal resistivity w represented by the finite term w_0 directly shows that the behavior of SCQSL is similar to that of metals, and there is a finite residual term κ/T in the zero-temperature

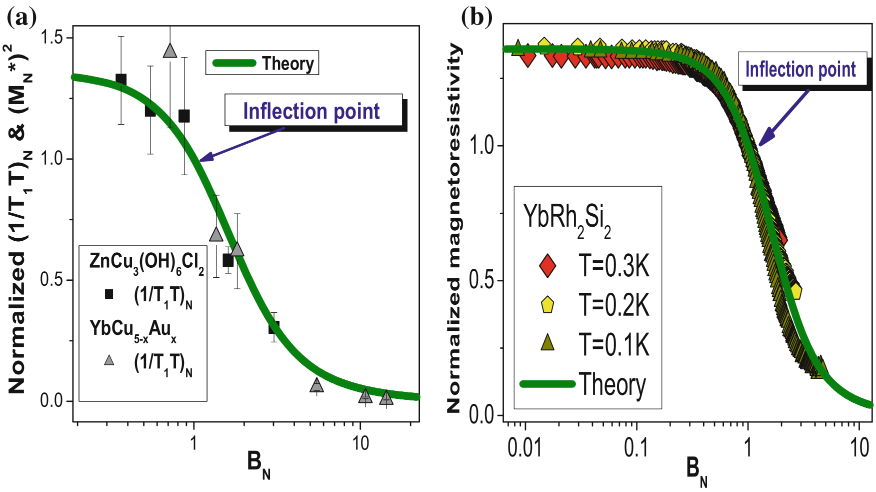

Fig. 17.20 The relaxation properties of the herbertsmithite versus those of HF metals. Panel **a** the normalized spin–lattice relaxation rate $(1/T_1T)_N$ at fixed temperature as a function of magnetic field: *Squares* correspond to the data on $(1/T_1T)_N$ extracted from measurements on $ZnCu_3(OH)_6Cl_2$ [40], while the *triangles* represent to those extracted from measurements on $YbCu_{5-x}Au_x$ with the doping of $x = 0.4$ [39]. The inflection point, representing the transition region, where the normalization is taken is marked by the *arrow*. Our calculations based on (18.5) and (17.4) are depicted by the *solid curve*, tracing the scaling behavior of $(M_N^*)^2$ and representing the B-dependence of the thermal resistivity w, see main text and (17.24). Panel **b** the normalized longitudinal magnetoresistivity ρ_N versus B_N. ρ_N is extracted from measurements on $YbRh_2Si_2$ at different temperatures [27] that are listed in the legend. The *solid curve* represents our calculations of $(M_N^*)^2$

limit of κ. The presence of this term immediately proves that there are gapless excitation associated with the property of normal and HF metals, in which gapless electrons govern the heat and charge transport, revealing the connection between classical physics and quantum criticality [52], see Chaps. 9 and 11. The finite value of w_0 means that in QSL both κ/T and $C_{mag}/T \propto M^*_{\rm mag}$ remain nonzero at $T \to 0$. Therefore, gapless spinons, forming the Fermi surface, determine the specific heat and the heat/thermal transport. Key information on the nature of spinons is further provided by the B-dependence of the coefficient A_w. The specific B-dependence of $(1/T_1T)_N \propto (M^*_{\rm mag})^2$, shown in Fig. 17.20, panel a, and given by (17.3), establishes the behavior of QSL as SCQSL. We note that the heat transport is polluted by the phonon contribution. On the other hand, the phonon contribution is not affected by the magnetic field B. Therefore, we expect the B-dependence of the heat conductivity to be governed by $A_w(B,T)$. Consider the approximate relation,

$$\begin{aligned} 1-\frac{A_w(B,T)}{A_w(0,T)} &= 1-\left(\frac{M^*(B,T)_{\rm mag}}{M^*(0,T)_{\rm mag}}\right)^2 \\ &\simeq a(T)\frac{\kappa(B,T)-\kappa(0,T)}{\kappa(0,T)} \equiv a(T)I(B,T), \end{aligned} \tag{17.25}$$

where the coefficient $a(T)$ is B-independent. To derive (17.25), we employ (17.24), and obtain

$$\frac{\kappa}{L_0 T} = \frac{1}{w_0 + A_w T^2} + bT^2. \tag{17.26}$$

Here the term bT^2 describes the phonon contribution to the heat transport. Upon carrying out simple algebra and assuming that $[1 - A_w(B,T)/A_w(0,T)] < 1$, we arrive at (17.25). It is seen from both panels of Fig. 17.20, that the effective mass $M^*_N(B) \propto M^*_{\rm mag}(B)$ is a diminishing function of magnetic field B. Then, it follows from (18.10), (17.4) and (17.25) that the reduced heat conductivity given by the function $I(B,T) = [\kappa(B,T) - \kappa(0,T)]/\kappa(0,T)$ increases at growing field B in the LFL region, while $I(B,T) \simeq 0$ in the NFL region, as this function is approximately independent of B in that case.

Recent measurements of $\kappa(B)$ in the organic insulators EtMe$_3$Sb[Pd(dmit)$_2$]$_2$ and $\kappa-$(BEDT $-$ TTF)$_2$Cu$_2$(CN)$_3$ [45, 46] are displayed in Figs. 17.21 and 17.22, panels a. The measurements show that the heat is carried by phonons and SCQSL, since the heat conductivity is well fitted by $\kappa/T = b_1 + b_2 T^2$, where b_1 and b_2 are constants. The finite value of b_1 term implies that spinon excitations are gapless in EtMe$_3$Sb[Pd(dmit)$_2$]$_2$, while in ($\kappa -$BEDT $-$ TTF)$_2$Cu$_2$(CN)$_3$ such excitations are questionable [46].

A simple estimation indicates that the ballistic propagation of spinons seems to be realized in the case of EtMe$_3$Sb[Pd(dmit)$_2$]$_2$ [45, 46]. It is seen from Figs. 17.21 and 17.22, panels a, that the function $I(B,T) = [\kappa(B,T) - \kappa(B=0,T)]/\kappa(B=0,T)$ demonstrates a strong B-dependence. Namely, the field dependence shows an increase of the thermal conductivity with growth of field B. Such a behavior is in agreement with (17.3) and Fig. 17.20, that demonstrates that $(M^*_{mag}(B))^2$ is a diminishing function of B. As a result, it follows from (17.25) that $I(B,T)$ is an increasing function of B. Our calculations based on (17.21) and (17.25) are depicted by geometrical symbols in Figs. 17.21 and 17.22, panels a. Since we cannot calculate $a(T)$ entering (17.25) we use it as a fitting parameter. Temperature T was also used to fit the data at temperatures, shown in the legend in Figs. 17.21 and 17.22. It is seen from Figs. 17.21 and 17.22, panels a, that $I(B,T)$ as a function of B has an inflection point at some $B = B_{inf}$. To reveal the scaling behavior of the heat conductivity of the organic insulators, we normalize both the function $I(B,T)$ and the magnetic field by their values at the inflection points, as it was done in the case of $(1/T_1T)$, see Fig. 17.20. The normalized reduced heat conductivity $I_N(B_N,T)$ does not depend on the factor $a(T)$, entering (17.25). Therefore, calculations of $I_N(B_N,T)$ do not have any fitting parameters. It is seen from Figs. 17.21, panel b and 17.22, panel b, that, in accordance with (17.4), $I_N(B_N,T)$ exhibits scaling behavior and becomes a function of a single variable B_N. It is instructive to compare the normalized values of the function $(1 - 1/T_1T)_N \equiv (1 - [M^*(B,T)/M^*(B=0,T)]^2)_N$ extracted from measurements of $(1/T_1T)_N$ shown in Fig. 17.20, panel a, with $I_N(B_N,T)$. The extracted values are normalized by their values at the inflection points and magnetic field is normalized by B_{inf}, as it is done in the case of $(1/T_1T)_N$. It is

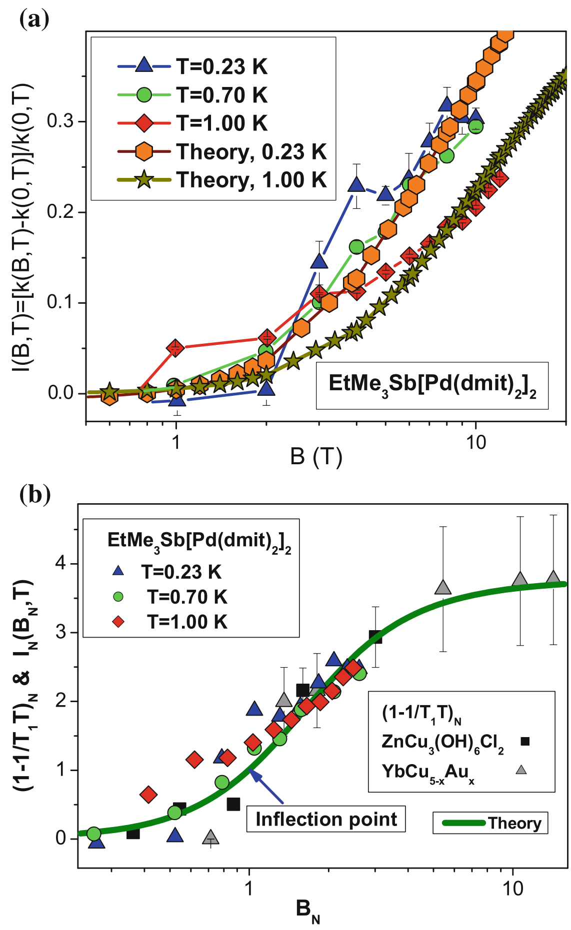

Fig. 17.21 Magnetic field B dependence of both the reduced thermal conductivity $I(B, T)$ and the normalized reduced thermal conductivity $I_N(B_N, T)$ of the organic insulator EtMe$_3$Sb[Pd(dmit)$_2$]$_2$. Panel **a**: $I(B, T)$ is standardized by its zero field value of κ, $I(B, T) = [\kappa(B, T) - \kappa(B = 0, T)]/\kappa(B = 0, T)$ at temperatures shown in the legend [45, 46]. Our calculations (17.25) are shown by hexagons and stars. Panel **b**: The normalized reduced thermal conductivity $I_N(B_N, T)$ versus B_N (symbols) is extracted from the data shown in the panel **a** of this figure. The inflection point is noted by the *arrow*. The magnetic field dependence of the function $(1-1/T_1T)_N$ is extracted from measurements of $(1/T_1T)_N$ shown in panel **a** of Fig. 17.20. The *solid curve* is obtained from the theoretical curve in Fig. 17.20

seen from panel b of Figs. 17.21 and 17.22, that $(1 - 1/T_1T)_N$ and $I_N(B_N, T)$ are in good overall agreement with the solid curve depicting the theoretical function $(1 - [M^*(B, T)/M^*(B = 0, T)]^2)_N$, obtained from our calculations represented by the solid curves in Fig. 17.20. This function demonstrates a flat dependence at low B_N, for at $B_N < 1$ the system in its NFL state and the B-dependence under discussion

Fig. 17.22 Same as in Fig. 17.21, but for organic insulator $\kappa-(\mathrm{BEDT\text{-}TTF})_2\mathrm{Cu}_2(\mathrm{CN})_3$

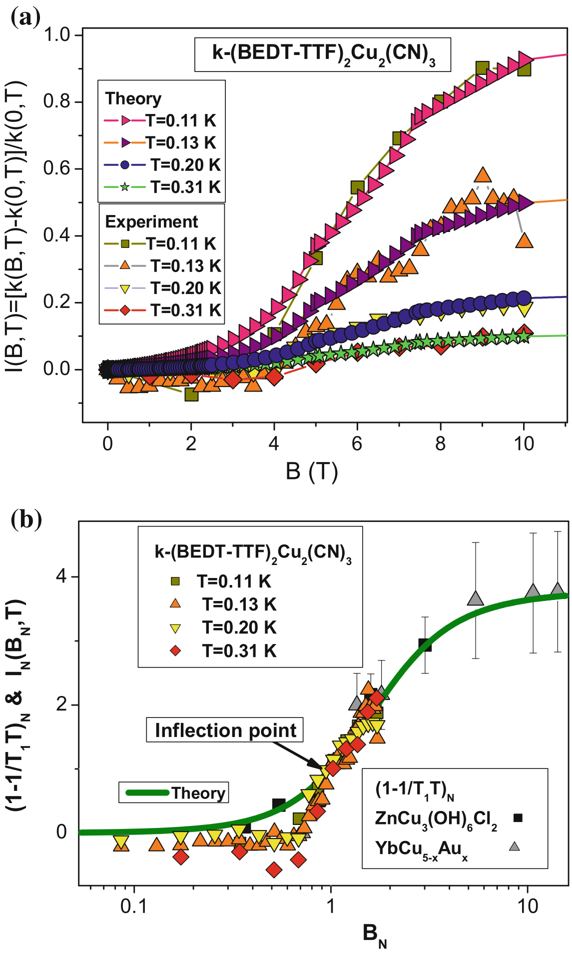

is weak. Thus, there is no need to introduce additional quasiparticles activated by the application of magnetic field in order to explain the growth of $I(B, T)$ at high B [45, 46]. It is also seen from panels b of Figs. 17.21 and 17.22, that the organic insulators demonstrate the same universal scaling behavior as $\mathrm{ZnCu}_3(\mathrm{OH})_6\mathrm{Cl}_2$, $\mathrm{YbCu}_{5-x}\mathrm{Au}_x$, and $\mathrm{YbRh}_2\mathrm{Si}_2$.

References

1. H. v. Löhneysen, A. Rosch, M. Vojta, P. Wölfle, Rev. Mod. Phys. **79**, 1015 (2007)
2. M. Neumann, J. Nyéki, B. Cowan, J. Saunders, Science **317**, 1356 (2007)
3. V.R. Shaginyan, A.Z. Msezane, K.G. Popov, V.A. Stephanovich, Phys. Rev. Lett. **100**, 096406 (2008)

4. V.R. Shaginyan, M.Y. Amusia, A.Z. Msezane, K.G. Popov, Phys. Rep. **492**, 31 (2010)
5. M.P. Shores, E.A. Nytko, B.M. Bartlett, D.G. Nocera, J. Am. Chem. Soc. **127**, 13462 (2005)
6. J.S. Helton, K. Matan, M.P. Shores, E.A. Nytko, B.M. Bartlett, Y. Yoshida, Y. Takano, A. Suslov, Y. Qiu, J.H. Chung, D.G. Nocera, Y.S. Lee, Phys. Rev. Lett. **98**, 107204 (2007)
7. M.A. DeVries, K.V. Kamenev, W.A. Kockelmann, J. Sanchez-Benitez, A. Harrison, Phys. Rev. Lett. **100**, 157205 (2008)
8. J.S. Helton, K. Matan, M.P. Shores, E.A. Nytko, B.M. Bartlett, Y. Qiu, D.G. Nocera, Y.S. Lee, Phys. Rev. Lett. **104**, 147201 (2010)
9. T.H. Han, J.S. Helton, S. Chu, A. Prodi, D.K. Singh, C. Mazzoli, P. Müller, D.G. Nocera, Y.S. Lee, Phys. Rev. B **83**, 100402(R) (2011)
10. F. Bert, P. Mendels, J. Phys. Soc. Jpn. **79**, 011001 (2010)
11. V.R. Shaginyan, A.Z. Msezane, K.G. Popov, Phys. Rev. B **84**, 060401(R) (2011)
12. V.R. Shaginyan, A.Z. Msezane, K.G. Popov, G.S. Japaridze, V.A. Stephanovich, Europhys. Lett. **97**, 56001 (2012)
13. V.R. Shaginyan, A.Z. Msezane, K.G. Popov, V.A. Khodel, Phys. Lett. A **376**, 2622 (2012)
14. V.R. Shaginyan, A.Z. Msezane, K.G. Popov, G.S. Japaridze, V.A. Khodel, Europhys. Lett. **103**, 67006 (2013)
15. F. Mila, Phys. Rev. Lett. **81**, 2356 (1998)
16. S. Lee, P. Lee, Phys. Rev. Lett. **95**, 036403 (2005)
17. O.I. Motrunich, Phys. Rev. B **72**, 045105 (2005)
18. Y. Ran, M. Hermele, P.A. Lee, X.G. Wen, Phys. Rev. Lett. **98**, 117205 (2007)
19. S. Ryu, O.I. Motrunich, J. Alicea, M.P.A. Fisher, Phys. Rev. B **75**, 184406 (2007)
20. S. Yan, D.A. Huse, S.R. White, Science **332**, 1173 (2011)
21. P.A. Lee, Science **321**, 1306 (2008)
22. J.W. Clark, V.A. Khodel, M.V. Zverev, Phys. Rev. B **71**, 012401 (2005)
23. V.A. Khodel, J.W. Clark, M.V. Zverev, Phys. Rev. B **78**, 075120 (2008)
24. D. Green, L. Santos, C. Chamon, Phys. Rev. B **82**, 075104 (2010)
25. T.T. Heikkilä, N.B. Kopnin, G.E. Volovik, JETP Lett. **94**(252), 233 (2011)
26. P. Gegenwart, Y. Tokiwa, T. Westerkamp, F. Weickert, J. Custers, J. Ferstl, C. Krellner, C. Geibel, P. Kerschl, K.H. Müller, F. Steglich, New J. Phys. **8**, 171 (2006)
27. P. Gegenwart, T. Westerkamp, C. Krellner, Y. Tokiwa, S. Paschen, C. Geibel, F. Steglich, E. Abrahams, Q. Si, Science **315**, 969 (2007)
28. V.R. Shaginyan, K.G. Popov, V.A. Stephanovich, V.I. Fomichev, E.V. Kirichenko, Europhys. Lett. **93**, 17008 (2011)
29. T.H. Han, S. Chu, Y.S. Lee, Phys. Rev. Lett. **108**, 157202 (2012)
30. T.H. Han, R. Chisnell, C.J. Bonnoit, D.E. Freedman, V.S. Zapf, N. Harrison, D.G. Nocera, Y. Takano, Y.S. Lee, arXiv:1402.2693 (2014)
31. D. Pines, P. Noziéres, *Theory of Quantum Liquids* (Benjamin, New York, 1966)
32. M. Pfitzner, P. Wölfle, Phys. Rev. B **33**, 2003 (1986)
33. D. Vollhardt, P. Wölfle, P.W. Anderson, Phys. Rev. B **35**, 6703 (1987)
34. D. Forster,*Hydrodynamic Fluctuations, Broken Symmetry, and Correlation Functions. Frontiers in Physics*, vol 47, XIX, 326 S. (W. A. Benjamin Inc, London, 1975).
35. W. Knafo, S. Raymond, J. Flouquet, B. Fák, M.A. Adams, P. Haen, F. Lapierre, S. Yates, P. Lejay, Phys. Rev. B **70**, 174401 (2004)
36. C. Stock, C. Broholm, F. Demmel, J.V. Duijn, J.W. Taylor, H.J. Kang, R. Hu, C. Petrovic, Phys. Rev. Lett. **109**, 127201 (2012)
37. J. Korringa, Physica (Utrecht) **16**, 601 (1950)
38. T. Moriya, *Spin Fluctuations in Itinerant Electron Magnetism* (Springer, Berlin, 1985)
39. P. Carretta, R. Pasero, M. Giovannini, C. Baines, Phys. Rev. B **79**, 020401 (2009)
40. T. Imai, E.A. Nytko, B.M. Bartlett, M.P. Shores, D.G. Nocera, Phys. Rev. Lett. **100**, 077203 (2008)
41. M. Jeong, F. Bert, P. Mendels, F. Duc, J.C. Trombe, M.A. de Vries, A. Harrison, Phys. Rev. Lett. **107**, 237201 (2011)

42. S. Yamashita, Y. Nakazawa, M. Oguni, Y. Oshima, H. Nojiri, Y. Shimizu, K. Miyagawa, K. Kanoda, Nat. Phys. **4**, 459 (2008)
43. M. Yamashita, N. Nakata, Y. Kasahara, T. Sasaki, N. Yoneyama, N. Kobayashi, S. Fujimoto, T. Shibauchi, Y. Matsuda, Nat. Phys. **5**, 44 (2009)
44. S. Yamashita, T. Yamamoto, Y. Nakazawa, M. Tamura, R. Kato, Nat. Commun. **2**, 275 (2011)
45. M. Yamashita, N. Nakata, Y. Senshu, M. Nagata, H.M. Yamamoto, R. Kato, T. Shibauchi, Y. Matsuda, Science **328**, 1246 (2010)
46. M. Yamashita, T. Shibauchi, Y. Matsuda, ChemPhysChem **13**, 74 (2012)
47. Y. Shimizu, K. Miyagawa, K. Kanoda, M. Maesato, G. Saito1. Phys. Rev. Lett. **91**, 107001 (2003)
48. T.H. Han, J.S. Helton, S. Chu, D.G. Nocera, J.A. Rodriguez-Rivera, C. Broholm, Y.S. Lee, Nature **492**, 406 (2012)
49. L. Balents, Nature **464**, 199 (2010)
50. N.B. Kopnin, T.T. Heikkilä, G.E. Volovik, Phys. Rev. B **83**, 220503(R) (2011)
51. M.V. Zverev, M. Baldo, JETP **87**, 1129 (1998)
52. V.R. Shaginyan, K.G. Popov, V.A. Khodel, Phys. Rev. B **88**, 115103 (2013)

Chapter 18
Quantum Criticality of Heavy-Fermion Compounds

Abstract Chapter 17 is devoted to the quantum criticality of quantum spin liquids. In this chapter we continue to consider the nature of quantum criticality in HF compounds. The quantum criticality induced by the fermion condensation quantum phase transition extends over a wide range in the $T - B$ phase diagram. As we shall see, the quantum criticality in all such different HF compounds, as high-T_c superconductors, HF metals, compounds with quantum spin liquids, quasicrystals, and 2D quantum liquids, is of the same nature. This challenging similarity between different HF compounds expresses universal physics that transcends the microscopic details of the compounds. This uniform behavior, induced by the universal quantum critical physics, allows us to view it as the main characteristic of new state of matter. We construct the $T - B$ phase diagrams, and explain main features of experimental facts of low-temperature thermodynamic properties in terms of FCQPT that leads to the formation of flat bands.

18.1 Quantum Criticality of High-Temperature Superconductors and HF Metals

At low temperatures the normal state (which is Landau Fermi liquid) of high-T_c superconductors and HF metals is recovered by the application of a magnetic field larger than the critical field. In this state, the Wiedemann–Franz and Korringa laws are held and the elementary excitations are Landau quasiparticles. Contrary to what one might expect from the LFL, the effective mass of quasiparticles depends on the magnetic field. We show that the magnetic-field-induced transition from NFL to LFL in high-temperature superconductors is similar to the transition observed in HF metals.

The extended quasiparticles paradigm supports quasiparticles that define the major part of the low-temperature properties of high-T_c superconductors, including their NFL behavior. At sufficiently low temperatures, as soon as the order parameter $\kappa(\mathbf{p})$ is suppressed by magnetic field $B > B_{c2}$, the field induced LFL emerges, see the Chap. 5. It was reported that in the normal state obtained by applying

M.Y. Amusia et al., *Theory of Heavy-Fermion Compounds*, Springer Series
in Solid-State Sciences 182, DOI 10.1007/978-3-319-10825-4_18

a magnetic field greater than the upper critical filed B_{c2}, in a hole-doped cuprates at overdoped concentration ($Tl_2Ba_2CuO_{6+\delta}$) [1] and at optimal doping concentration ($Bi_2Sr_2CuO_{6+\delta}$) [2], there are no sizable violations of the Wiedemann–Franz (WF) law. Since the validity of the WF law is a robust signature of LFL, these experimental facts demonstrate that the observed elementary excitations can be considered as Landau quasiparticle. At a constant magnetic field, the low energy elementary excitations are characterized by $M^*(B)$ and cannot be distinguished from Landau quasiparticles. On the other hand, in contrast to the LFL theory, the effective mass $M^*(B)$ depends on the magnetic field. As it was shown in Sect. 5.3.1, in this case the magnetic field B plays the role of the control parameter determining the effective mass

$$M^*(B) \propto \frac{1}{\sqrt{B - B_{c0}}}. \tag{18.1}$$

We recall that B_{c0} is the critical magnetic field driving corresponding AF phase transition towards $T = 0$. Since $B_{c0} > B_{c2}$, as it is discussed in Sect. 7.6, (18.1) is valid at $B > B_{c2}$. In that case, the effective mass $M^*(B)$ is finite, and the system is driven back to LFL and acquires the LFL behavior induced by the magnetic field.

Equation (18.1) shows that by applying a magnetic field $B > B_c$ the system can be driven back into LFL with the effective mass $M^*(B)$, which is finite and temperature independent. This means that the low temperature properties of the considered compounds depend on the effective mass in accordance with the LFL theory. In particular, the resistivity $\rho(T)$ as a function of the temperature behaves as $\rho(T) = \rho_0 + \Delta\rho(T)$ with $\Delta\rho(T) = AT^2$, where the factor A behaves as: $A \propto (M^*)^2 \propto 1/(B - B_{c0})^2$. At finite temperatures, the system persists as LFL, but there is the transition region (crossover) from the LFL behavior to the non-Fermi liquid behavior at temperature $T^*(B) \propto \mu_B(B - B_{c0})$. At $T \sim T^*(B)$, the system is located in the transition region, the effective mass starts to depend on the temperature, and the resistivity possesses the non-Fermi liquid behavior with a substantial T-linear term, $\Delta\rho(T) = aT + bT^2$. Here, $T^*(B)$ is the transition temperature. Since magnetic field enters the Landau equation as $\mu_B B/T$, we have

$$T^*(B) \sim \mu_B(B - B_{c0}). \tag{18.2}$$

The transition temperature is not really a phase transition. It is necessarily broad, very much depending on the criteria for determination of the point of such a transition. As it is seen from the $T - B$ phase diagram reported in Fig. 18.1, at raising magnetic field the system enters the LFL regime, and as a result, the T-linear term vanishes. Such a behavior of the resistivity was observed in the cuprate superconductors $Tl_2Ba_2CuO_{6+\delta}$ ($T_c < 15$ K) [4] and $La_{2-x}Ce_xCuO_4$ [5]. For example, at B = 10 T, $\Delta\rho(T)$ is a linear function of the temperature between 120 mK and 1.2 K, whereas at B = 18 T, the temperature dependence of the resistivity is consistent with $\rho(T) = \rho_0 + AT^2$ over the same temperature range [4].

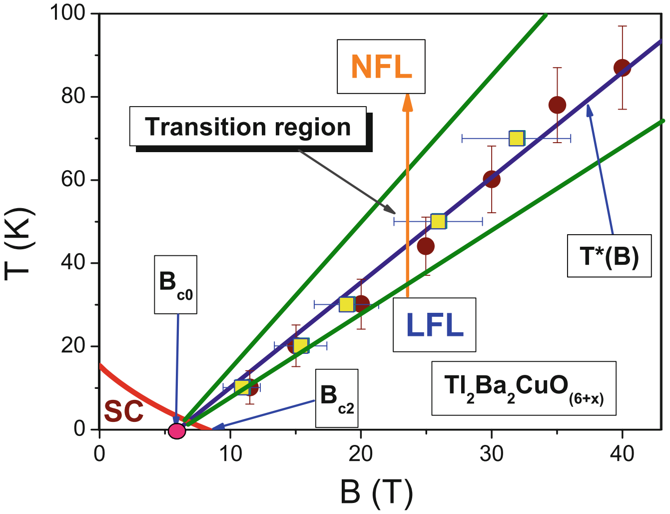

Fig. 18.1 $B-T$ phase diagram of superconductor $Tl_2Ba_2CuO_{6+x}$. The transition region from LFL to NFL regime marked by the *line* $T^*(B)$ is shown by the *arrow*. The corresponding transition temperature $T^*(B)$ is given by (18.2), while the *squares* and the *circles* are the experimental points [3]. *Thick line* is a boundary between the superconducting and normal phases. The *arrows* near the *bottom left* corner indicate the critical magnetic fields B_{c2} destroying the superconductivity and B_{c0} destroying the AF order

It has been shown in Sect. 7.5, that in the LFL phase, the nuclear spin-lattice relaxation rate $1/T_1$ is determined by the quasiparticles near the Fermi level, whose population is proportional to M^*T, so that $1/T_1T \propto (M^*)^2$ is a constant [6, 7]. When the superconducting state is removed by the application of a magnetic field, the underlying ground state can be seen as the field induced LFL with effective mass depending on the magnetic field. As a result, the rate $1/T_1$ follows the $T_1T = constant$ relation, that so the Korringa law is held. Unlike the behavior of LFL, as it follows from (18.1), $1/T_1T \propto (M^*(B))^2$ decreases with increasing the magnetic field at $T < T^*(B)$. Note that at $T > T^*(B)$, we observe that $1/T_1T$ is a decreasing function of the temperature, $1/T_1T \propto M^* \propto 1/T$. These observations are in good agreement with the experimental facts [6]. Since $T^*(B)$ is an increasing function of the magnetic field, the Korringa law retains its validity to higher temperatures at higher magnetic fields.

Let us now turn to the $B-T$ phase diagram of a high-T_c superconductor. The corresponding $T-B$ phase diagram of $Tl_2Ba_2CuO_{6+x}$ is shown as an example in Fig. 18.1. The substance is a superconductor with T_c from 15 to 93 K depending on oxygen content x. In Fig. 18.1, open squares and solid circles show the experimental values of the crossover temperature from the LFL to NFL regimes. The transition region between LFL and NFL regimes is shown by the arrow. The solid line shows our fit using (18.2) with $B_{c0} = 6$ T that is in good agreement with $B_{c0} = 5.8$ T obtained from the field dependence of the charge transport, see Sect. 5.3.2.1. As it is seen from Fig. 18.1, the linear behavior agrees well with experimental data [3]. Now we consider the field-induced reentrance of LFL behavior in $Tl_2Ba_2CuO_{6+x}$ at $B \geq B_{c2}$. In that case, the effective mass M^* depends on magnetic field B that becomes the control parameter, while the system is in the LFL regime as it is shown by the dashed horizontal arrow in Fig. 6.2. The LFL regime is characterized by the temperature dependence of the resistivity $\rho(T) = \rho_0 + A(B)T^2$, see also above. The coefficient A, being proportional to the quasiparticle–quasiparticle scattering cross-section, is found to be $A \propto (M^*(B))^2$. With respect to $M^* \propto B^{-1/2}$ (see (5.39)), this implies that

$$A(B) \simeq A_0 + \frac{D}{B - B_{c0}}, \tag{18.3}$$

where A_0 and D are parameters. It seen from Fig. 18.1 and follows from (18.3), that it is impossible to observe the relatively high values of $A(B)$ since in our case $B_{c2} > B_{c0}$, see the Sect. 7.6. Therefore, as was mentioned above, in high-T_c superconductors, their QCP is poorly accessible to experimental observations being "*hidden under superconducting dome*". Nonetheless, it is possible to study QCP by exploring the quantum criticality.

Figure 18.2 reports the fit of our theoretical dependence (18.3) to the experimental data for two different classes of substances: HF metal $YbRh_2Si_2$ and

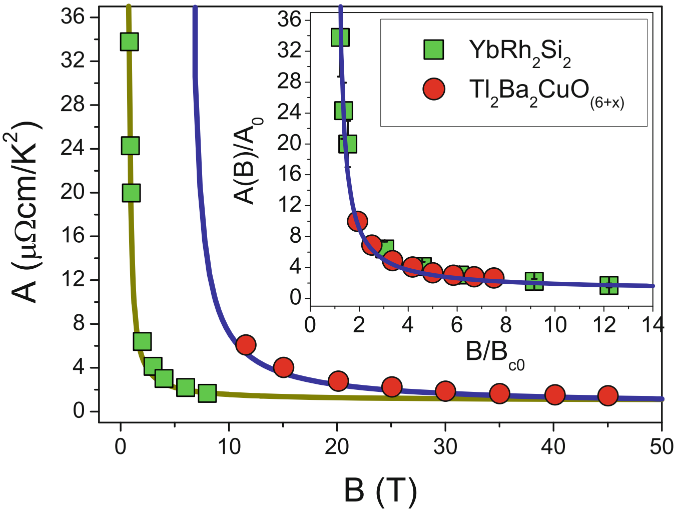

Fig. 18.2 The universal behavior of the charge transport coefficient $A(B)$ in the LFL state induced by the application of magnetic field B. *Main panel* $A(B)$ obtained in measurements on $YbRh_2Si_2$ (*squares*) [8] and $Tl_2Ba_2CuO_{6+x}$ (*circles*) [3]. Our calculations of $A(B)$ based on (18.3) are depicted by the *solid lines*. The *inset* Normalized coefficient $A(B)/A_0 \simeq 1 + D_N/(y-1)$ as a function of normalized magnetic field $y = B/B_{c0}$ is given by (18.4), and is shown by *squares* for $YbRh_2Si_2$ and by *circles* for $Tl_2Ba_2CuO_{6+x}$

HTSC $Tl_2Ba_2CuO_{6+x}$. The different scale of fields is clearly seen as well as good coincidence with the theoretical dependence determined by (18.3). This means that the physics underlying the field-induced reentrance of LFL behavior, is the same for both classes of substances. To corroborate this point further, let us rewrite (18.3) in reduced variables A/A_0 and B/B_{c0}. This rewriting immediately reveals the universal nature of the behavior of these two substances: Both of them are driven to common QCP, related to FC and induced by the application of magnetic field. In reduced values (18.3) takes the form

$$\frac{A(B)}{A_0} \simeq 1 + \frac{D_N}{B/B_{c0} - 1}, \tag{18.4}$$

where $D_N = D/(A_0 B_{c0})$ is the only fitting parameter. It is seen from (18.4) that upon applying the scaling in these variables, the quantities $A(B)$ for $Tl_2Ba_2CuO_{6+x}$ and $YbRh_2Si_2$ are described by a function of the single variable B/B_{c0}, thus demonstrating universal behavior. To support (18.4), we replot both dependencies in reduced variables A/A_0 and B/B_{c0} as it is depicted in the inset to Fig. 18.11. Such replotting immediately reveals the universal nature of the behavior of these two quite different substances. Indeed, in the case of $Tl_2Ba_2CuO_{6+x}$ the critical field $B_{c0} \simeq 6$ T, while the value of the critical field of $YbRh_2Si_2$ is $B_{c0} \simeq 0.06$ T. Nonetheless, it is seen from the inset to Fig. 18.2 that close to magnetic QCP there is no external physical scales, so that the normalization by internal scales A_0 and B_{c0} shows straightforwardly the common quantum criticality of HF metals and high-T_c superconductors.

Thus, our theoretical study of high-T_c superconductors and HF metals clearly demonstrates their generic family resemblance. We have shown that the physics underlying the field-induced reentrance of LFL behavior is the same for both high-T_c compounds and HF metals. It follows from our study that there is at least one quantum phase transition inside the superconducting dome, and this transition is FCQPT, for details see Chaps. 5 and 7.

18.2 Quantum Criticality of Quasicrystals

New exotic materials named quasicrystals and characterized by noncrystallographic rotational symmetry and quasiperiodic translational properties have attracted scrutiny. Studies of quasicrystals may shed light on the most basic notions related to the quantum critical state observed in HF metals. We show here that the electronic system of some quasicrystals is already located at the FCQPT point without any tuning. Therefore, the quasicrystals possess the quantum critical state with NFL phase, which in magnetic fields transforms into the LFL one. Remarkably, the quantum critical state is robust despite the strong disorder experienced by the electrons. Quasicrystals exhibit the typical scaling of their thermodynamic properties like magnetic susceptibility, belonging also to the family of HF metals.

When we encounter the exciting behavior of strongly correlated metals, we anticipate to learn more about quantum critical physics. Such an opportunity is provided by quasicrystals (QCs) [9, 10]. These substances, characterized by the absence of translational symmetry in combination with good ordered atomic arrangement and rotational symmetry, can be viewed as materials located between crystalline and disordered solids. QCs, their crystalline approximants and related complex metallic phases reveal very unusual mechanical, magnetic, electronic transport and thermodynamic properties. The mentioned crystalline approximants are the arrangements of atoms which within their unit cells closely approximate the local atomic structures in QCs [10]. The aperiodicity of QCs plays an important role in the formation of the properties since the band electronic structure governed by the Bloch theorem cannot be well defined. As an example, QCs exhibit a high resistivity although DOS at the Fermi energy is not small [11]. One expects the transport properties are defined by a small diffusivity of electrons which occupy a new class of states denoted as "critical states", neither being extended nor localized, and making the velocity of charge carriers very low [11]. Associated with these critical states, characterized by an extremely degenerate confined wave function, are the so-called "spiky" DOS [12, 13]. The presence of latter predicted DOS is confirmed by experiments revealing that the single particle spectra of the local DOS demonstrate a spiky DOS, [14, 15]. Clearly, these spiky states are associated with flat bands [16, 17]. On one hand, we expect the properties related to the itinerant states governed by the spiky ones of QCs to coincide with those of HF metals, while on the other hand, the pseudo localized states may result in those of amorphous materials. Therefore, the question of how quasicrystalline order influences the electronic properties of QCs, whether they resemble those of HF metals or amorphous materials, is of crucial importance.

Experimental measurements on the gold-aluminium-ytterbium quasicrystal $Au_{51}Al_{34}Yb_{15}$ with a six-dimensional lattice parameter $a_d = 0.7448$ nm have revealed quantum critical behavior with the unusual exponent $\alpha \simeq 0.51$ defining the divergency of the magnetic susceptibility $\chi \propto T^{-\alpha}$ as temperature $T \to 0$ [18]. The measurements have also exposed that the observed NFL behavior transforms into LFL under the application of a tiny magnetic field H, while it exhibits the robustness against hydrostatic pressure; the quasicrystal shows also metallic behavior with the $T-$dependent part $\Delta\rho$ of the resistivity, $\Delta\rho \propto T$, at low temperatures [18].

We start with constructing a model to explain the behavior of the gold-aluminum-ytterbium QC [19]. Taking into account that the spiky states are associated to flat bands [16, 20, 21], which are the generic signature of FCQPT, we safely assume that the electronic system of the gold-aluminum-ytterbium QC $Au_{51}Al_{34}Yb_{15}$ is located very near FCQPT [20]. Thus, $Au_{51}Al_{34}Yb_{15}$ turns out to be located at FCQPT without tuning this substance by pressure, magnetic field etc. Then, the system exhibits the robustness of its critical behavior against the hydrostatic pressure since the this pressure does not change the topological structure of QC leading to the spiky DOS and, correspondingly, flat bands. As we will see, the spiky DOS cannot prevent the field-induced LFL state.

To study the low temperature thermodynamic and scaling behavior, we use again the model of homogeneous HF liquid [20]. This model avoids the complications associated with the anisotropy of solids and considering both the thermodynamic properties and NFL behavior by calculating the effective mass $M^*(T, H)$ as a function of temperature T and magnetic field H. To study the behavior of the effective mass $M^*(T, H)$, we use the Landau equation for the quasiparticle effective mass. The only modification is that in our formalism the effective mass is no longer constant but depends on temperature and magnetic field. For the model of homogeneous HF liquid at finite temperatures and magnetic fields, this equation takes the form [20–23]

$$\frac{1}{M^*_\sigma(T, H)} = \frac{1}{M} + \sum_{\sigma_1} \int \frac{\mathbf{p}_F \mathbf{p}}{p_F^3} F_{\sigma,\sigma_1}(\mathbf{p_F}, \mathbf{p}) \frac{\partial n_{\sigma_1}(\mathbf{p}, T, H)}{\partial p} \frac{d\mathbf{p}}{(2\pi)^3}. \tag{18.5}$$

The single-particle spectrum is a variational derivative of the system energy $E[n_\sigma(\mathbf{p})]$ with respect to the quasiparticle distribution function or occupation numbers n,

$$\varepsilon_\sigma(\mathbf{p}) = \frac{\delta E[n(\mathbf{p})]}{\delta n_\sigma(\mathbf{p})}. \tag{18.6}$$

In our case F is fixed by the condition that the system is situated at FCQPT. The sole role of the Landau interaction is to bring the system to FCQPT point, where $M^* \to \infty$ at $T = 0$ and $H = 0$, and the Fermi surface alters its topology so that the effective mass acquires temperature and field dependence [20–22, 24]. Provided that the Landau interaction is an analytical function, at the Fermi surface the momentum-dependent part of the Landau interaction can be taken in the form of truncated power series $F = aq^2 + bq^3 + cq^4 + \cdots$, where $\mathbf{q} = \mathbf{p}_1 - \mathbf{p}_2$, a, b and c are fitting parameters which are defined by the condition that the system is at FCQPT.

A direct inspection of (18.5) shows that at $T = 0$ and $H = 0$, the sum of the first term and the second one on the right side vanishes, since $1/M^*(T \to 0) \to 0$ provided that the system is located at FCQPT [20, 24]. In case of analytic Landau interaction with respect to the momenta variables, at finite T the right hand side is proportional $F'(M^*)^2T^2$, where F' is the first derivative of $F(q)$ with respect to q at $q \to 0$. Calculations of the corresponding integrals can be found in textbooks, see e.g., in [25]. Thus, we have $1/M^* \propto (M^*)^2T^2$, and obtain [20, 24]

$$M^*(T) \simeq a_T T^{-2/3}. \tag{18.7}$$

At finite temperatures, the application of magnetic field H drives system to the LFL region with

$$M^*(H) \simeq a_H H^{-2/3}. \tag{18.8}$$

On the other hand, an analytic function $F(q)$ can lead to the general topological form of the spectrum $\varepsilon(p) - \mu \propto (p - p_b)^2(p - p_F)$ with $(p_b < p_F)$ and $(p_F - p_b)/p_F \ll 1$, that makes $M^* \propto T^{-1/2}$, and creates a quantum critical point [26]. As we shall see below, the same critical point is generated by the interaction $F(q)$

represented by an integrable over x nonanalytic function with $q = \sqrt{p_1^2 + p_2^2 - 2xp_1p_2}$ and $F(q \to 0) \to \infty$ [20, 27]. The both cases lead to $M^* \propto T^{-1/2}$, and (18.7) becomes

$$M^*(T) \simeq a_T T^{-1/2}. \tag{18.9}$$

In the same way, we obtain

$$M^*(H) \simeq a_H H^{-1/2}, \tag{18.10}$$

with a_T and a_H are parameters. Taking into account that (18.9) leads to the spiky DOS with the vanishing of spiky structure with increasing temperature T [28], as it is observed in quasicrystals [15, 18], we assume that the general form of $\varepsilon(p)$ produces the behavior of M^*, given by (18.9) and (18.10). This is realized in quasicrystals, which can be viewed as a generalized form of common crystals [29]. We note that the behavior $1/M^* \propto \chi^{-1} \propto T^{1/2}$ is in good agreement with $\chi^{-1} \propto T^{0.51}$ observed experimentally [18]. Our explanation is consistent with the robustness of the exponent 0.51 against the hydrostatic pressure [18] since the robustness is guaranteed by the unique singular DOS of QCs that survives under the application of pressure [12, 13, 15, 16, 18]. Then, the nonanalytic Landau interaction $F(q)$ can also serve as the good approximation, generating the observed behavior of the effective mass. We speculate that the nonanalytic interaction is generated by the nonconservation of the quasimomentum in QCs, making the Landau interaction $F(q)$ a nonlocal function of momentum q. Such a function can be approximated by a nonanalytic one.

A few remarks on the transport properties of QC are in order here. In calculations of low-temperature resistivity, we employ a two-band model, one of which is occupied by heavy quasiparticles, with the effective mass given by (18.9), while the second band possesses a LFL quasiparticles with a T−independent effective mass [30]. As a result, we find that the quasiparticles width $\gamma \propto T$ and that the T−dependent part of the resistivity $\Delta\rho \propto T$. This observation is in accordance with experimental facts [18].

At finite H and T near FCQPT, the solutions of (18.5) $M^*(T, H)$ can be well approximated by a simple universal interpolating function. A deeper insight into the behavior of $M^*(T, H)$ can be achieved using some “internal” scales. Namely, near FCQPT the solutions of (18.5) exhibit a universal scaling behavior so that $M^*(T, H)$ reaches it maximum value M^*_M at some temperature $T_{\max} \propto H$ [20, 24]. It is convenient to introduce the internal scales M^*_M and $T_{\max}$ to measure the effective mass and temperature, respectively. Thus, we divide the effective mass M^* and the temperature T by their maximal values, M^*_M and $T_{\max}$ respectively. This generates the normalized effective mass $M^*_N = M^*/M^*_M$ and temperature $T_N = T/T_{\max}$ [20]. Near FCQPT the normalized solution of (18.5) $M^*_N(T_N)$ with a nonanalytic Landau interaction can be well approximated by a simple universal interpolating function. The interpolation occurs between the LFL ($M^* \propto a + bT^2$) and NFL ($M^* \propto T^{-1/2}$) regimes and represents the universal scaling behavior of $M^*_N(T_N)$

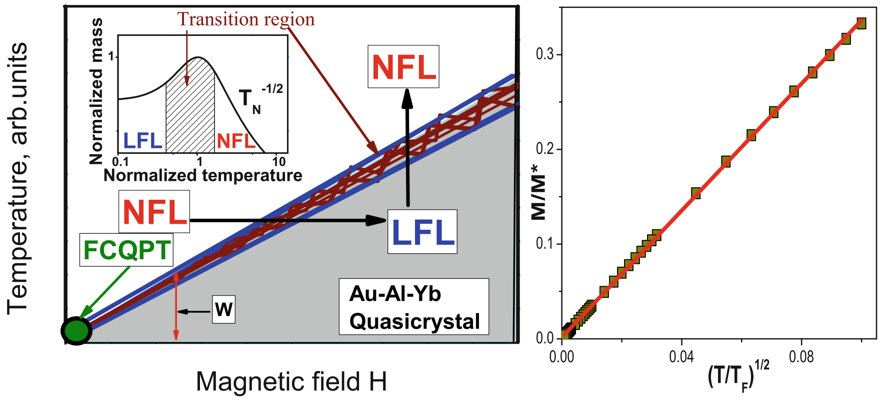

Fig. 18.3 The $T - H$ phase diagram of $Au_{51}Al_{34}Yb_{15}$ with the effective mass $M^*(T) \propto T^{-1/2}$. *Left panel* The $T - H$ phase diagram of $Au_{51}Al_{34}Yb_{15}$. Magnetic field H is the control parameter. The *vertical* and *horizontal arrows* show LFL-NFL and reverse transitions at fixed H and T, respectively. At $H = 0$ and $T = 0$ the system is at FCQPT shown by the *solid circle*. The total width of the LFL and the transition regions $W \propto T$ are shown by the *double arrows*. *Inset* shows a schematic plot of the normalized effective mass versus the normalized temperature. Transition region, where M_N^* reaches its maximum at $T/T_{\max} = 1$, is marked by the *hatched area*. The *right panel* reports the dimensionless inverse effective mass M/M^* versus dimensionless temperature $(T/T_F)^{1/2}$. The line is a linear fit

$$M_N^*(T_N) \approx c_0 \frac{1 + c_1 T_N^2}{1 + c_2 T_N^{5/2}}. \tag{18.11}$$

Here a and b are constants, $c_0 = (1 + c_2)/(1 + c_1)$, c_1 and c_2 are fitting parameters. The inset to the left panel of Fig. 18.3 shows the scaling behavior of the normalized effective mass. It is seen from the inset, that the total width W of the LFL and the transition region $W \propto T$ vanish as $H \to 0$ since $T_{\max} \propto H$. In the same way, the common width of the NFL and the transition region tends to zero as soon as $T \to 0$.

Now we construct the schematic phase diagram of the gold-aluminum-ytterbium QC $Au_{51}Al_{34}Yb_{15}$. The phase diagram is reported in Fig. 18.3, left panel. The magnetic field H plays the role of the control parameter, driving the system outwards FCQPT that occurs at $H = 0$ and $T = 0$ without tuning since the QC critical state is formed by singular density of states [12, 13, 15, 16, 18]. It follows from (17.4) and seen from the left panel of Fig. 18.3, that at fixed temperatures the increase of H drives the system along the horizontal arrow from NFL state to LFL one. On the contrary, at fixed magnetic field and increasing temperatures the system transits along the vertical arrow from LFL state to NFL one. The inset to the left panel demonstrates the behavior of the normalized effective mass M_N^* versus normalized temperature T_N following from (17.4). The $T^{-1/2}$ regime is marked as NFL since contrary to the LFL case, where the effective mass is constant, the effective mass depends strongly on temperature. It is seen that the temperature region $T_N \sim 1$ signifies a transition regime between the LFL behavior with almost constant effective mass and the NFL one, given by $T^{-1/2}$ dependence. Thus, temperatures $T \simeq T_{\max}$, shown by arrows in the inset and the main panel, can be regarded as the transition regime between LFL and NFL states. The common width W of the LFL transition regions $W \propto T$ is shown by the heavy arrow. These theoretical results are in good agreement with the experimental facts [18]. The right panel of Fig. 18.3 illustrates the behavior of the dimensionless inverse effective mass M/M^* versus the dimensionless temperature $(T/T_F)^{1/2}$, where T_F is the Fermi temperature of electron gas. To calculate M/M^*, we use a model Landau functional [20, 27]

$$E[n(p)] = \int \frac{\mathbf{p}^2}{2M}\frac{d\mathbf{p}}{(2\pi)^3} + \frac{1}{2}\int V(\mathbf{p}_1 - \mathbf{p}_2)n(\mathbf{p}_1)n(\mathbf{p}_2)\frac{d\mathbf{p}_1 d\mathbf{p}_2}{(2\pi)^6},$$

with the Landau interaction

$$V(\mathbf{q}) = g_0 \frac{\exp(-\beta_0\sqrt{\mathbf{q}^2 + \gamma^2})}{\sqrt{\mathbf{q}^2 + \gamma^2}}, \tag{18.12}$$

where the parameters g_0 and β_0 are fixed by the requirement that the system is located at FCQPT, see for details Sect. 6.2. At $\gamma = 0$, the interaction becomes nonanalytic function of q. Note that the other investigated nonanalytic interactions lead to the same behavior of M/M^*, see e.g., [27].

To demonstrate this, we apply (18.6) to construct $\varepsilon(p)$ using the functional (18.12). Taking into account that $\varepsilon(p \simeq p_F) - \mu \simeq p_F(p - p_F)$ and integrating over the angular variables, we obtain

$$\frac{1}{M^*} = \frac{1}{M} + \frac{\partial}{\partial p}\int \left[\Phi(p + p_1) - \Phi(|p - p_1|)\right]\frac{n(p_1, T)p_1 dp_1}{2p_F^2\pi^2}. \tag{18.13}$$

Here the derivative on the right hand side of (18.13) is taken at $p = p_F$ and

$$\int\limits_{|p-p_1|}^{p+p_1} V(z, \gamma = 0)z dz = \Phi(p + p_1) - \Phi(|p - p_1|). \tag{18.14}$$

The derivative $\partial\Phi(|p - p_1|)/\partial p|_{p\to p_F} = (p_F - p_1)/(|p_F - p_1|)\partial\Phi(z)/\partial z$ becomes a discontinuous function at $p_1 \to p_F$, provided that $\partial\Phi(z)/\partial z$ is finite (or integrable if the function tends to infinity) at $z \to 0$. As a result, the right hand side of (18.13) becomes proportional M^*T and (18.13) reads $1/M^* \propto M^*T$, making $M^* \propto T^{-1/2}$.

The analytic Landau interaction (18.12) with $\gamma > 0$ makes $M/M^* \propto T^{0.5}$ at raising temperatures, while at $T \to 0$ the system demonstrates the LFL behavior [20, 26]. This interaction can serve as model one to describe the behavior of the quasicrystal's crystalline approximant $Au_{51}Al_{35}Yb_{14}$ [18]. The approximant $Au_{51}Al_{35}Yb_{14}$ shows the LFL behavior at low temperatures, $\chi^{-1} \propto a + bT^{0.51}$ with the conventional LFL behavior of the resistivity [18]. We interpret this behavior of

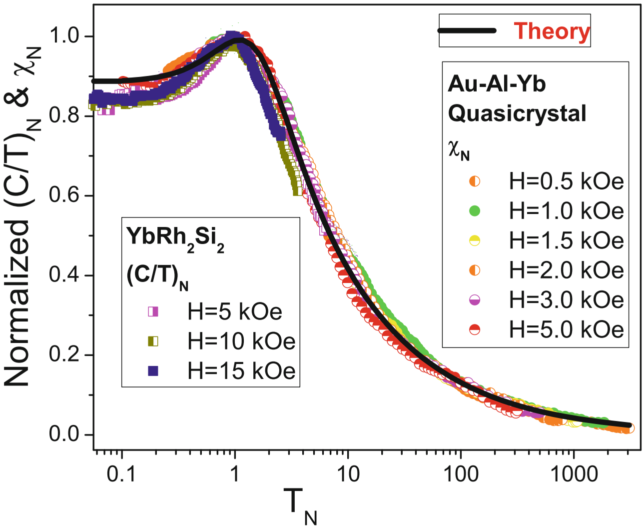

Fig. 18.4 The normalized specific heat $(C/T)_N$ and magnetic susceptibility χ_N extracted from measurements in magnetic fields H (shown in the legends) on YbRh$_2$Si$_2$ [31] and Au$_{51}$Al$_{34}$Yb$_{15}$ [18], respectively. Our calculations are depicted by the *solid curve* (17.4) tracing the scaling behavior of $(C/T)_N = \chi_N = M^*_N$

χ^{-1} through the absence of the unique electronic state of QCs, which results in the shift of the electronic system of the approximant from FCQPT into the LFL region. Such a behavior is achieved by making the interaction (18.12) an analytic function with $\gamma > 0$ as soon as the quasicrystal is transformed into its crystalline approximant. The finite γ, creating the LFL behavior at $T = 0$, makes $T_{\max}$ finite even at $H = 0$. Then, it follows from (17.4) that $1/M^* \propto \chi^{-1} \propto a + bT^{1/2}$ and the approximant is to demonstrate the conventional LFL behavior: $\Delta\rho \propto T^2$. The same result is acquired by transforming the spectrum as $\varepsilon(p) - \mu \propto ([p - p_b]^2 + \gamma^2)(p - p_F)$ [26].

We now investigate the behavior of χ as a function of temperature at fixed magnetic fields. The effective mass $M^*(T, H)$ can be measured in experiments for $M^*(T, H) \propto \chi$ where χ is the AC or DC magnetic susceptibility. If the corresponding measurements are carried out at fixed magnetic field H then, as it follows from (17.4), χ reaches the maximum $\chi_{\max}$ at some temperature $T_{\max}$. Upon normalizing both χ and the specific heat C/T by their peak values at each field H and the corresponding temperatures by $T_{\max}$, we observe from (17.4) that all the curves merge into a single one, thus demonstrating a scaling behavior typical for HF metals [20]. As seen from Fig. 18.4, χ_N extracted from measurements on Au$_{51}$Al$_{34}$Yb$_{15}$ [18] shows the scaling behavior given by (17.4) and agrees well with the normalized specific heat $(C/T)_N$ extracted from measurements in magnetic fields H on YbRh$_2$Si$_2$ [31]. Our calculations shown by the solid curve are in good agreement with χ_N over four orders of magnitude in the normalized temperature.

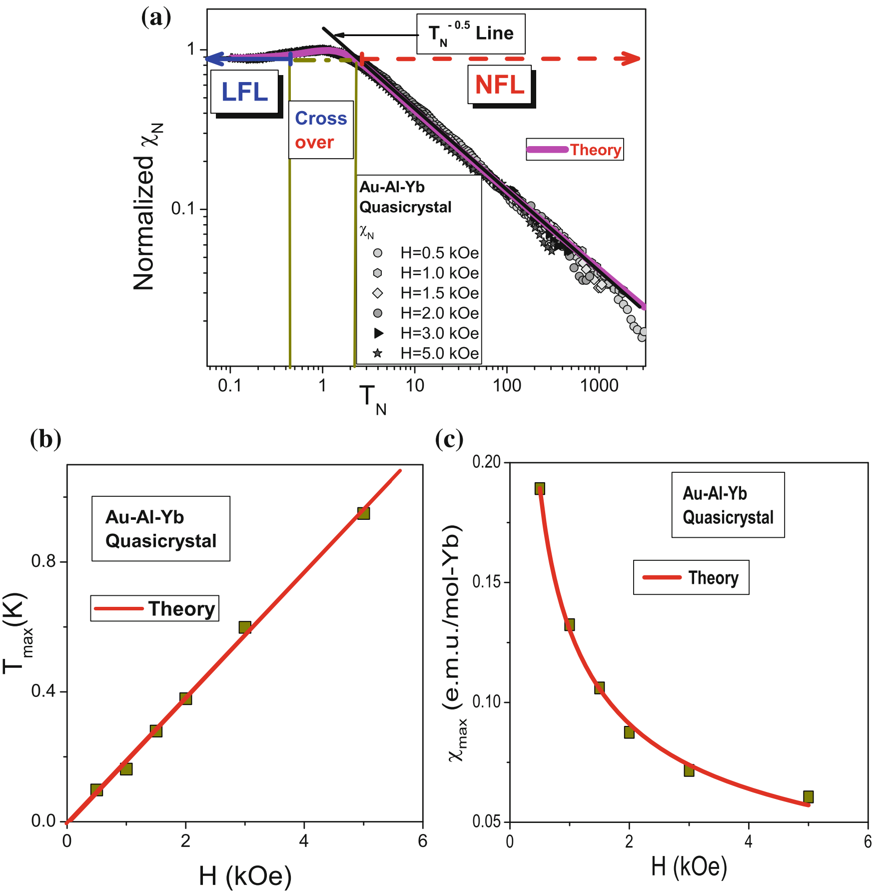

Fig. 18.5 The thermodynamic properties of the magnetic susceptibility. Panel **a**, temperature dependence in log-log scale of the magnetic susceptibility χ_N at different magnetic fields [18] given in the legend. The LFL and NFL regions are marked by the *solid* and *dashed arrows*, respectively. The *solid line* depicts $\chi_N \propto T_N^{-0.5}$ behavior. Panel **b**, the temperatures $T_{\max}$ where the maxima of χ (see Fig. 18.3) are located. The *solid line* represents the function $T_{\max} = aH$, a is a fitting parameter. Panel **c**, the maxima $\chi_{\max}$ versus magnetic field H. The *solid curve* is approximated by $\chi_{\max} = tH^{-1/2}$, see (18.10), t is a fitting parameter

To validate the phase diagram in Fig. 18.3, we focus on the LFL, NFL and the transition LFL-NFL regions exhibited by the QC. To this end, in Fig. 18.5a, we report the normalized χ_N in the log-log scale. As seen from Fig. 18.5a, χ_N extracted from the measurements is not a constant, as would be for LFL. Two (NFL and LFL) regions, separated by the transition one, as depicted by the hatched area in the inset in Fig. 18.3, are clearly seen in Fig. 18.5a, illuminating good agreement between the theory and measurements. The straight lines in Fig. 18.5a outline both the LFL and NFL behaviors of $\chi_N \propto const$ and $\chi_N \propto T_N^{-1/2}$, and are in good agreement with the behavior of M_N^* displayed in the inset of Fig. 18.3. In Fig. 18.5b, the solid squares denote temperatures $T_{\max}(H)$ at which the maxima $\chi_{\max}$ of $\chi(T)$ and, (c), the corresponding values of the maxima $\chi_{\max}(H)$ occur. It is seen that the agreement between the theory and experiment is good in the entire magnetic field domain. It is also seen from Fig. 18.5b that $T_{\max} \propto H$; thus a tiny magnetic field H destroys the NFL behavior hereby driving the system to the LFL region. This behavior is consistent with the phase diagram displaced in Fig. 18.3: at increasing temperatures ($T_N \simeq 1$) the LFL state first converts into the transition one and then disrupts into the NFL state, while at given magnetic field H the width $W \propto T$.

Thus, the quasicrystal $Au_{51}Al_{34}Yb_{15}$ exhibits typical scaling behavior of its thermodynamic properties, thus belonging in fact to the HF metals family, while the quantum critical physics of the quasicrystal is universal and emerges regardless its underlying microscopic details.

18.3 Quantum Criticality at Metamagnetic Phase Transitions

The nature of field-tuned metamagnetic quantum criticality in HF metals is a significant challenge for condensed matter physics. Here we center our attention on the role of the applied magnetic field B in the formation of quantum criticality within a restricted range of B at low temperatures T. Theoretical study of the HF compound $Sr_3Ru_2O_7$ fulfilled in Chap. 11 gives quantative insights into the quantum criticality, and reveal a close relation of the metamagnetic phase transition in $Sr_3Ru_2O_7$ and that of HF metals. Here we use this study to analyze quantum criticality and metamagnetic phase transitions in HF metals.

18.3.1 Typical Properties of the Metamagnetic Phase Transition in $Sr_3Ru_2O_7$

The coherent picture of both the quantum critical regime and the metamagnetic phase transition in $Sr_3Ru_2O_7$ was introduced in Chap. 11. Now we take $Sr_3Ru_2O_7$ as an example of quantum criticality formed at metamagnetic phase transition to outline its main features. In constructing both the field-induced quantum criticality and the corresponding metamagnetic phase transition, we employ the model based on a vHs that induces a peak in the single-particle DOS. At fields in some range $B_{c1} < B < B_{c2}$ the DOS peak turns out to be at or near the Fermi energy. As a result, a relatively weak repulsive interaction (e.g., Coulomb) is sufficient to move the system to FCQPT, or even to induce FC and formation of a flat band, as it takes place in the case of $Sr_3Ru_2O_7$.

To reveal signatures of the quantum criticality, we resume with an analysis of the properties of the C/T electronic specific heat observed in $Sr_3Ru_2O_7$ [33, 34].

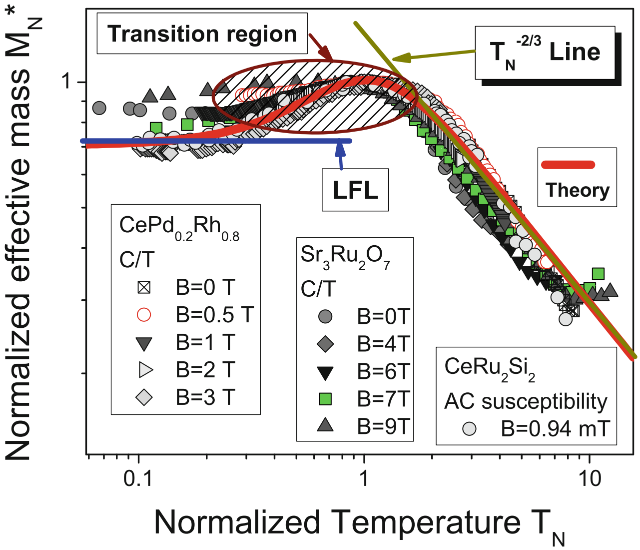

Fig. 18.6 The universal scaling behavior of the normalized effective mass M_N^* versus T_N. M_N^* is extracted from the measurements of χ and C/T (in magnetic fields B shown in the legends) on $CeRu_2Si_2$ [32], $CePd_{1-x}Rh_x$ with $x = 0.80$ [31], and $Sr_3Ru_2O_7$ [33]. The LFL and NFL regimes (latter having $M_N^* \propto T_N^{-2/3}$) are shown by the *arrows* and *straight lines*. The transition regime is depicted by the *shaded area*. The *solid curve* represents our calculation of the universal behavior of $M_N^*(T_N)$

The measurements of $C/T \propto M^*$ in magnetic fields on $Sr_3Ru_2O_7$ allow us to uncover the universal scaling behavior of the effective mass M^* that is characteristic of HF metals. As it is seen from Fig. 11.4, the maximum of $C/T \propto M^*$ sharpens and shifts to lower temperatures as the field B approaches the critical value $B = B_m \simeq (B_{c1} + B_{c2})/2$, where the maximum disappears. In contrast to HF metals, the maximum of the function C/T exhibits a symmetry with respect to B_m: the maximum appears at $B \to B_m$ and reappears on the high-field side at $B > B_m$. To reveal the scaling behavior of C/T, we normalize the measured C/T and T values (obtaining $(C/T)_N$ and T_N, respectively) by their maxima T_M and $(C/T)_M$ respectively [20]. The spin susceptibility data $\chi(T)$ are normalized in the same way. The behavior of the normalized effective mass extracted from measurements of χ and (C/T) on $CeRu_2Si_2$ [32], $CePd_{0.8}Rh_{0.8}$ [31] and $Sr_3Ru_2O_7$ [33], are presented in Fig. 18.6. The figure displays the main features of scaling behavior of the normalized effective mass M_N^* shown in Fig. 6.2. Namely, at low temperatures $T_N < 1$ the normalized effective mass is in the LFL region, then it enters the transition region, and finally disrupts into the NFL regime. The solid curve shows the result of our calculation of the scaling behavior. It is seen from Fig. 18.6, that $Sr_3Ru_2O_7$ located at the metamagnetic transition and HF metals exhibit the same scaling behavior, which exhibit the other HF compounds and which can be understood within the framework of fermion condensation or flat-band theory.

18.3.2 Metamagnetic Phase Transition in HF Metals

As we have seen above, a HF metal can be driven to FCQPT when narrow (flat) bands situated close to the Fermi surface are formed by the application of a critical magnetic field B_m. The emergence of such state is known as metamagnetism that occurs when this transformation comes abruptly at B_m [34], as it was discussed in Chap. 11 and Sect. 18.3.1.

Thus, the magnetic field B_m is similar to that of B_{c0} that moves a HF metal to its magnetic field tuned QCP. In our simple model both B_{c0} and B_m are taken as parameters. To apply (17.4) when the critical magnetic field is not zero, we have to replace B by $(B - B_m)$. Acting as above, we can extract the normalized effective mass $M^*_N(T_N)$ from data collected on HF metals at their metamagnetic quantum phase transition. In Fig. 18.7 the extracted normalized mass is displayed. $M^*_N(T_N)$ is extracted from measurements of C/T collected on $URu_{1.92}Rh_{0.08}Si_2$, $CeRu_2Si_2$ and $CeRu_2Si_{1.8}Ge_{0.2}$ at their metamagnetic QCP with $B_m \simeq 35$ T, $B_m \simeq 7$ T and $B_m \simeq 1.2$ T respectively [35, 36]. As it is seen from Fig. 18.7, the effective mass $M^*_N(T_N)$ in different HF metals reveals the same form, both in the high magnetic field and in low

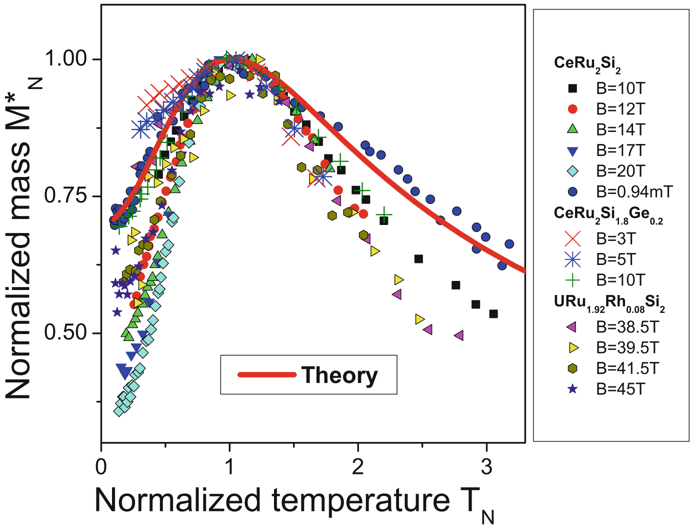

Fig. 18.7 The normalized effective mass versus the normalized temperature at different magnetic fields B, shown in the legend. $M^*_N(T_N)$ is extracted from measurements of C/T collected on $URu_{1.92}Rh_{0.08}Si_2$, $CeRu_2Si_2$ and $CeRu_2Si_{1.8}Ge_{0.2}$ [35, 36]. The *solid curve* gives the universal behavior of M^*_N, (17.4). See also the caption to Figs. 15.3 and 17.4

ones as soon as the corresponding bands become flat, that is the electronic system of HF metals is driven to FCQPT. This observation is extremely significant as it allows us to check the universal behavior in HF metals, when these are under the application of essentially different magnetic fields. Namely, the magnitude of the applied field ($B \sim 10$ T) at the metamagnetic point is four orders of magnitude larger than that of the field applied to tune $CeRu_2Si_2$ to the LFL behavior ($B \sim 1$ mT). Relatively small values of $M^*_N(T_N)$ observed in $URu_{1.92}Rh_{0.08}Si_2$ and $CeRu_2Si_2$ at the high fields and small temperatures can be explained by taking into account that the narrow band is completely polarized [35]. As a result, at low temperatures the summation over spin projections "up" and "down" reduces to a single direction producing the coefficient $1/2$ in front of the normalized effective mass. At high temperatures the polarization vanishes and the summation is restored. As it is seen from Fig. 18.7, these observations are in accord with the experimental facts.

18.4 Universal Behavior of Two-Dimensional ^{3}He at Low Temperatures

On the example of 2D ^{3}He we demonstrate that the main universal features of its experimental temperature T—density x phase diagram and its quantum criticality look like those in HF metals. Our detailed theoretical analysis of experimental situation in 2D ^{3}He allows us to propose a simple expression for effective mass $M^*(T, x)$, describing all diverse experimental facts in 2D ^{3}He in unified manner and demonstrating that the universal behavior of $M^*(T, x)$ coincides with that observed in HF metals.

It was discussed above that the electronic system of HF metals demonstrates the universal low-temperature behavior irrespectively of their magnetic ground state [37]. Therefore it is of crucial importance to check whether this behavior can be observed in 2D Fermi systems. Fortunately, the measurements on 2D ^{3}He are available [38, 39]. Their results are extremely significant as they allow to check the presence of the universal behavior in the system formed by ^{3}He atoms, which are essentially different from electrons [39]. Namely, atoms of 2D ^{3}He are neutral fermions with spin $S = 1/2$. They interact with each other by van-der-Waals forces with strong hardcore repulsion and a weakly attractive tail. The different character of interparticle interaction along with the fact, that a mass of He atom is 3 orders of magnitude larger than that of an electron, makes ^{3}He to have drastically different microscopic properties than that of 3D HF metals that constitute the most essential for our consideration. Because of this difference nobody can be sure that the macroscopic physical properties of both above fermionic systems will be more or less similar to each other.

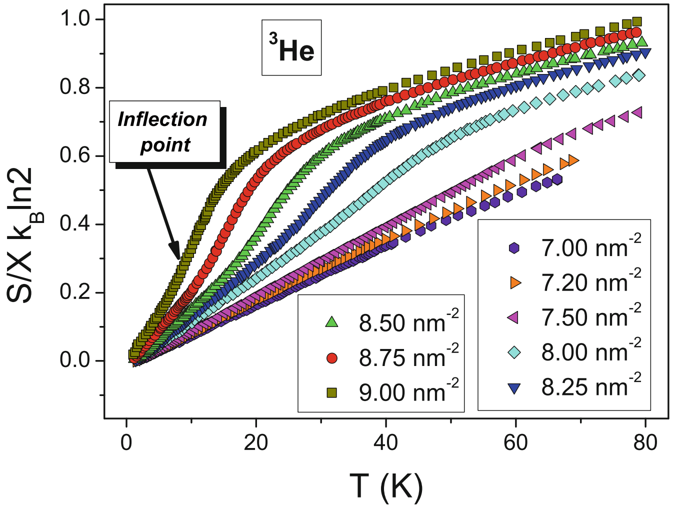

Fig. 18.8 Temperature dependence of the entropy S of 2D ^{3}He at different densities x (shown in the legends) [38]. The inflection point of S at $x = 9.00\ \mathrm{nm}^{-2}$ is shown by the *arrow*

The bulk liquid ^{3}He is historically the first object, to which a Landau Fermi-liquid (LFL) theory had been applied [23]. This substance, being intrinsically isotropic Fermi-liquid with negligible spin-orbit interaction is an ideal object to test the LFL theory. 2D films of ^{3}He have been fabricated and its thermodynamic properties have been thoroughly investigated [38, 38]. Among these properties are measurements of the entropy S as a function of the number density x versus T. As it is seen from Fig. 18.8, at $x \geq 8.00\ \mathrm{nm}^{-2}$ the entropy is no more a linear function of temperature T, exhibiting the NFL behavior.

The NFL properties manifest themselves in the power-law behavior of the physical quantities of strongly correlated Fermi systems located close to their QCPs, with exponents, characterizing the power-law behavior, different from those of a Fermi liquid. It is common belief that the main output of theory should be the explanation of these exponents, which are at least depended on the magnetic character of QCP and dimensionality of the system. On the other hand, the observed behavior of the thermodynamic properties cannot be described entirely by these exponents, as it is seen from Figs. 18.8 and 18.9. The behavior of the entropy $S(T)$ of two-dimensional (2D) ^{3}He [38] shown in Fig. 18.8 is positively different from that described by a simple function $a_1 T^{a_2}$ where a_1 is a constant and a_2 is the exponent. One sees from Fig. 18.8 that at low densities $x \simeq 7\ \mathrm{nm}^{-2}$ the entropy demonstrates the LFL behavior characterized by a linear function of T with $a_2 = 1$. The behavior becomes quite different at higher densities, where $S(T)$ has an inflection point. Obviously, at the inflection point $S(T)$ cannot be fit by the simple function $a_1 T^{a_2}$, as in the case of HF metals, see Sect. 6.3.1.

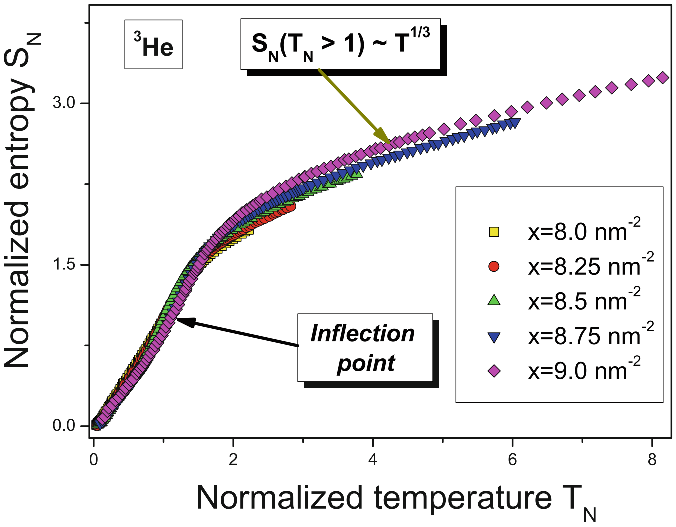

Fig. 18.9 The normalized entropy $S_N(T_N)$, extracted from the experimental data of Fig. 18.8. Densities x are shown in the legend. The *arrow* shows the inflection point

In order to show that the behavior of S displayed in Figs. 18.8 and 18.9 is of generic character, let us recollect that in the vicinity of QCP it is helpful to use "internal" scales to measure the effective mass $M^* \propto S/T$ and temperature T [20]. The internal scales of the thermodynamic functions, such as S or C/T, are related to "peculiar points" Peculiar points like the inflection or maximum. Since the entropy has no maxima, its normalization is to be performed at the inflection point that takes place at $T = T_{inf}$, see (6.26). Note that T_{inf} is a function of x, and it is seen from Fig. 18.8 that the inflection point moves towards lower temperatures with increase of x. The normalized entropy S_N as a function of the normalized temperature $T_N = T/T_{inf} = y$ is reported in Fig. 18.9. We normalize the entropy by its value at the inflection point $S_N(y) = S(y)/S(1)$. As it is seen from Fig. 18.9, the normalization reveals the scaling behavior of S_N. As we have seen previously, this means that the curves at different temperatures and densities x merge into a single one in terms of the variable y. We have excluded the experimental data taken at $x \leq 8\,\mathrm{nm}^{-2}$ since the corresponding curves do not contain the inflection points. It is seen from Fig. 18.9 that $S_N(y)$ extracted from the measurements is not a linear function of y, as would be for a LFL, and shows the scaling behavior in the normalized temperature T_N.

Thus, our above preliminary analysis of the experimental measurements has shown that the behavior of 2D ^{3}He is very close to that of 3D HF compounds with various ground state magnetic properties. Because of van-der-Waals interparticle interaction, ^{3}He has an important and specific feature that, generally speaking, cannot be realized in full in HF metals. This feature is that it is possible to change the total density of ^{3}He film. This change allows one to drive 2D film towards its QCP at which the quasiparticle effective mass M^* diverges [38, 40]. This peculiarity permits to plot the experimental temperature-density phase diagram, which in turn can be directly compared with theoretical predictions.

Let us consider HF liquid at $T = 0$ characterized by the effective mass M^* [20, 27, 41–44]. Upon applying the well-known equation, we can relate M^* to the bare gas mass M [23, 45] $M^*/M = 1/(1 - N_0 F^1(p_F, p_F)/3)$, see Sect. 2.3.1. Here N_0 is the density of states of a free gas, p_F is Fermi momentum, and $F^1(p_F, p_F)$ is the p-wave component of Landau interaction F. Since LFL theory implies that the number density has the form $x = p_F^3/3\pi^2$, we can rewrite the interaction as $F^1(p_F, p_F) = F^1(x)$. When at some critical point $x = x_c$, $F^1(x)$ achieves certain threshold value, the denominator tends to zero so that the effective mass diverges at $T = 0$ and the system undergoes FCQPT. The leading term of this divergence looks as

$$\frac{M^*(x)}{M} = A + \frac{B}{1-z}, \; z = \frac{x}{x_c}. \tag{18.15}$$

Equation (18.15) is valid in both 3D and 2D cases, while the values of factors A and B depend on dimensionality and inter-particle interaction [44]. At $x > x_c$ the fermion condensation takes place. However, we consider at first the case $x < x_c$.

When the system approaches FCQPT, the dependence $M^*(T, x)$ is governed by the Landau equation

$$\frac{1}{M^*(T,x)} = \frac{1}{M} + \int \frac{\mathbf{p}_F \mathbf{p}}{p_F^3} F(\mathbf{p_F}, \mathbf{p}) \frac{\partial n(\mathbf{p}, T, x)}{\partial p} \frac{d\mathbf{p}}{(2\pi)^3}, \tag{18.16}$$

where $n(\mathbf{p}, T, x)$ is the distribution function of quasiparticles. The approximate solution of this equation is of the form [37, 39]

$$\frac{M}{M^*(T)} = \frac{M}{M^*(x)} + \beta f(0) \ln\{1 + \exp(-1/\beta)\} + \lambda_1 \beta^2 + \lambda_2 \beta^4 + \cdots, \tag{18.17}$$

where $\lambda_1 > 0$ and $\lambda_2 < 0$ are constants of order unity, $\beta = TM^*(T)/p_F^2$ and $f(0) \sim F^1(x_c)$. It follows from (18.17) that the effective mass $M^*(T)$ as a function of T and x reveals three different regimes at growing temperature. At the lowest temperatures we have LFL regime with $M^*(T) \simeq M^*(x) + aT^2$ with $a < 0$ since $\lambda_1 > 0$. This observation coincides with experimental situation [38, 40]. The effective mass as a function of T decreases up to a minimum and afterward grows, reaching its maximum $M^*_M(T, x)$ at some temperature $T_{\max}(x)$ with subsequent diminishing as $T^{-2/3}$ [24, 44]. Moreover, the closer is the number density x to its threshold value x_c, the higher is the growth rate. The peak value M^*_M grows also, but the maximum temperature $T_{\max}$ lowers. Near this temperature the last "traces" of LFL regime disappear, manifesting themselves in the divergence of above low-temperature series and substantial growth of $M^*(x)$. The temperature region that starts near above minimum and continuing up to $T_{\max}(x)$ signifies the crossover between LFL regime with almost constant effective mass and NFL behavior, given by $T^{-2/3}$ dependence, given by (6.14). Thus, the $T_{\max}$ point can be regarded as the crossover between LFL and NFL regimes. The latter regime sets up at $T \leq T_{\max}$, when $M^*(x) \to \infty$, giving rise to the effective mass decrease

$$M^*(T) \propto T^{-2/3}. \tag{18.18}$$

It turns out that $M^*(T, x)$ in the entire T and x range can be well approximated by a simple universal interpolating function similar to the case of the application of magnetic field. The interpolation occurs between LFL ($M^* \propto T^2$) and NFL ($M^* \propto T^{-2/3}$) regimes thus describing the above crossover. Introducing the dimensionless variable $y = T/T_{\max}$, we present the desired expression

$$\frac{M^*(T,x)}{M^*_M} = \frac{M^*(y)}{M^*_M} = M^*_N(y) \approx \frac{M^*(x)}{M^*_M}\frac{1+c_1y^2}{1+c_2y^{8/3}}. \tag{18.19}$$

Here $M^*_N(y)$ is the normalized effective mass, c_1 and c_2 are parameters, obtained from the condition of best fit to experiment. Equation (18.15) shows that the maximum value M^*_M of the effective mass $M^*_M \propto 1/(1-z)$. On the other hand, it follows from (18.18) that $M^*_M \propto T^{-2/3} \sim T_{\max}^{-2/3}$. As a result, we obtain

$$T_{\max} \propto (1-z)^{3/2}. \tag{18.20}$$

We note that obtained results are in agreement with numerical calculations [24, 39, 44].

$M^*(T)$ can be measured in experiments on strongly correlated Fermi-systems. For example, $M^*(T) \propto C(T)/T \propto S(T)/T \propto M_0(T) \propto \chi(T)$ where $C(T)$ is the specific heat, $S(T)$—entropy, $M_0(T)$—magnetization and $\chi(T)$—AC magnetic susceptibility. If the measurements are performed at fixed x, then, as it follows from (18.19), the effective mass reaches the maximum at $T = T_{\max}$. Upon normalizing both, $M^*(T)$ by its peak value at each x and the temperature by $T_{\max}$, we see from (18.19) that all the curves merge into single one demonstrating a scaling behavior.

In Fig. 18.10, we show the phase diagram of 2D ^{3}He in the variables $T - z$ (see (18.15)). For the sake of comparison the plot of the effective mass versus z is shown by dashed line. The part of the diagram where $z < 1$ corresponds to HF behavior and consists of LFL and NFL parts, divided by the line $T_{\max}(z) \propto (1-z)^{3/2}$. We pay attention here, that our exponent $3/2 = 1.5$ is exact as compared to that from [38] 1.7 ± 0.1. The agreement between theoretical and experimental exponents suggests that our FCQPT scenario takes place both in 2D ^{3}He and in HF metals. The regime for $z > 1$ consists of low-temperature LFL piece, (shadowed region, beginning in the intervening phase $z \leq 1$ [38]) and NFL regime at higher temperatures. The former LFL piece is assigned to the peculiarities of substrate on which 2D ^{3}He film is placed. Namely, it is related to weak substrate heterogeneity (steps and edges on its surface) so that Landau quasiparticles, being localized (pinned) on it, give rise to LFL behavior [38, 38]. On the other hand, the intervening phase, shown in

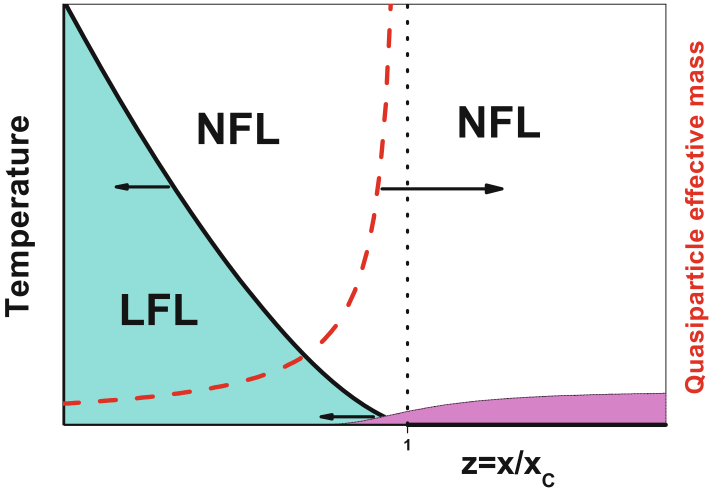

Fig. 18.10 The phase diagram of 2D ^{3}He. The part for $z < 1$ corresponds to HF behavior divided to the LFL and NFL parts by the line $T_{\max}(z) \propto (1-z)^{3/2}$, where $T_{\max}$ is the effective mass maximum temperature. The exponent $3/2 = 1.5$ coming from (18.20) is in good agreement with the experimental value 1.7 ± 0.1 [38]. The dependence $M^*(z) \propto (1-z)^{-1}$ is shown by the *dashed line*. The regime for $z \geq 1$ consists of LFL piece (the *shadowed region*, beginning in the intervening phase $z \leq 1$ [38], which is probably due to the quasi-classical behavior of the heat capacity C, see text) and NFL regime at higher temperatures

Fig. 18.10, can be related to the quasi-classical behavior of the heat capacity C that leads to a temperature independent contribution to C, as it is discussed in Sect. 9.1. This important observation deserves a further investigation that would prompt new theoretical work, supporting the idea that the physics of quantum criticality seen in HF compounds is universal.

In Fig. 5.5, the experimental values of effective mass $M^*(z)$ obtained by the measurements on ^{3}He monolayer are reported [40]. These measurements, in agreement with those from [38], demonstrate the divergence of the effective mass at $x = x_c$. To show, that our FCQPT approach is able to describe the above data, we present the fit of $M^*(z)$ by the rational expression $M^*(z)/M \propto A + B/(1-z)$ and the reciprocal effective mass by the linear fit $M/M^*(z) \propto A_1 z$. We note here, that the linear fit has been used to describe the experimental data for bilayer ^{3}He [38] and we use this function here for the sake of illustration. It is seen from Fig. 5.5 that the data in [38] (^{3}He bilayer) can be equally well approximated by both linear and rational functions, while the data in [40] cannot. For instance, both fitting functions give for the critical density in bilayer $x_c \approx 9.8$ nm^{-2}, while for monolayer [40] these values are different $-x_c = 5.56$ for linear fit and $x_c = 5.15$ for fractional fit. It is seen from Fig. 5.5, that linear fit is unable to properly describe the experiment [40] at small $1-z$ (i.e. near $x = x_c$), while the fractional fit describes the experiment pretty good. This means that the more detailed measurements are necessary in the vicinity $x = x_c$.

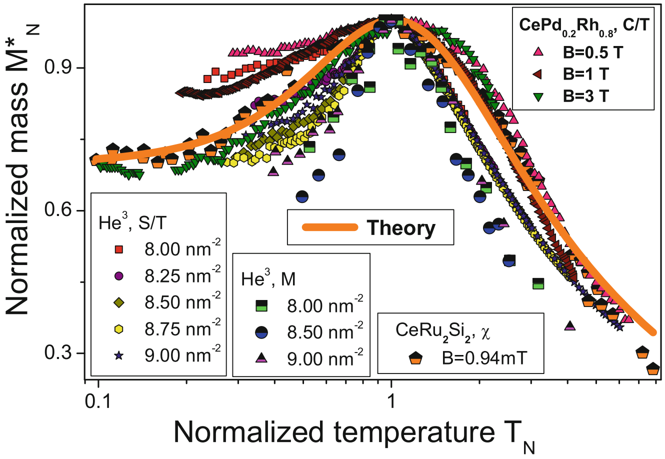

Fig. 18.11 The normalized effective mass M_N^* as a function of the normalized temperature $T/T_{\max}$ at densities shown in the *left down* corner. The behavior M_N^* is extracted from experimental data for $S(T)/T$ in 2D ^{3}He [38] and 3D HF compounds with different magnetic ground states, such as $\mathrm{CeRu_2Si_2}$ and $\mathrm{CePd_{1-x}Rh_x}$ [31, 32], fitted by the universal function (18.19)

Now we apply the universal dependence, given by (17.4) and (18.19), to fit the experiment not only in 2D ^{3}He but in 3D HF metals as well. $M_N^*(y)$ extracted from the entropy measurements on the ^{3}He film [38] at different densities $x < x_c$ smaller than the critical point $x_c = 9.9 \pm 0.1$ nm^{-2} is reported in Fig. 18.11. In the same figure, the data extracted from heat capacity of ferromagnet $\mathrm{CePd_{0.2}Rh_{0.8}}$ [31] and AC magnetic susceptibility of paramagnet $\mathrm{CeRu_2Si_2}$ [32] are plotted for different magnetic fields. It is seen that the universal behavior of the effective mass given by (18.19) (solid curve in Fig. 18.11) is in accord with experimental data. All substances are located at $x < x_c$, where the system progressively disrupts its LFL behavior at elevated temperatures. In that case the control parameter, driving the system towards its critical point x_c is merely a number density x. It is seen that the behavior of the effective mass $M_N^*(y)$, extracted from $S(T)/T$ in 2D ^{3}He (the entropy $S(T)$ is reported in Fig. 18.8) looks very much like that in 3D HF compounds. As we shall see from Fig. 18.13, the interaction and positions of the maxima of magnetization $M_0(T)$ and $S(T)/T$ in 2D ^{3}He follow nicely the interpolation formula (18.19). We conclude that (18.19) allows us to reduce a four variable function describing the effective mass to a function of a single variable. Indeed, the effective mass depends on magnetic field, temperature, number density and the composition so that all these parameters can be merged in the single variable by means of interpolating function like (18.19), see also [37].

The attempt to fit the available experimental data for $C(T)/T$ in ^{3}He [40] by the universal function $M_N^*(y)$ is reported below in Fig. 18.12. Here, the data extracted from heat capacity $C(T)/T$ for ^{3}He monolayer [40] and magnetization M_0 for bilayer [38], are reported. It is seen that the effective mass extracted from

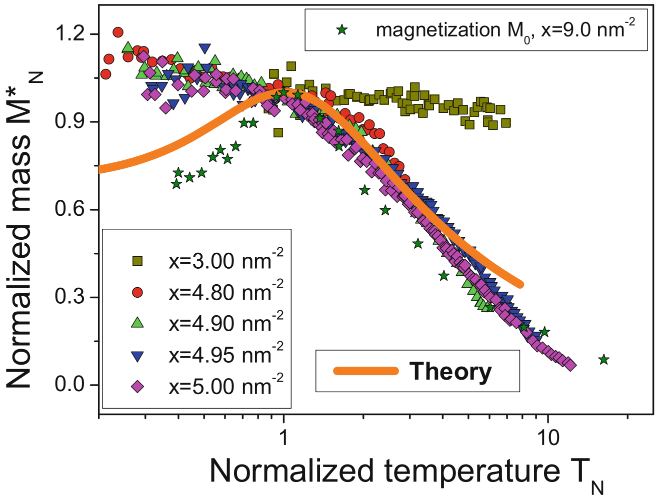

Fig. 18.12 The dependence of $M_N^*(T/T_{\rm max})$ versus T at densities shown in the *left down* corner. The behavior M_N^* is extracted from experimental data for $C(T)/T$ in 2D ^{3}He [40] and for the magnetization M_0 in 2D ^{3}He [38]. The *solid curve* shows the universal function, see the caption to Fig. 18.11

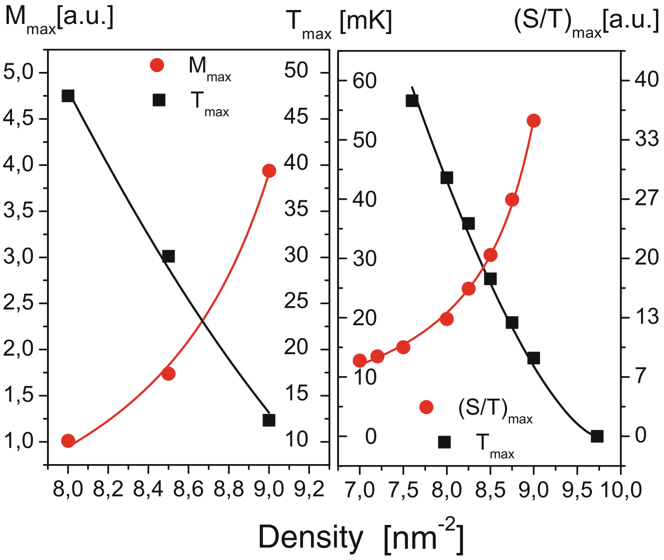

Fig. 18.13 *Left panel*, the peak temperatures $T_{\rm max}$ and values $M_{\rm max}$ extracted from measurements of the magnetization M_0 in ^{3}He [38]. *Right panel* shows $T_{\rm max}$ and the peak values $(S/T)_{\rm max}$ extracted from measurements of $S(T)/T$ in ^{3}He [38]. We approximate $T_{\rm max} \propto (1-z)^{3/2}$ and $(S/T)_{\rm max} \propto M_{\rm max} \propto A/(1-z)$

these thermodynamic quantities can be well described by the universal interpolation formula (17.4). We note the qualitative similarity between the double layer [38] and monolayer [40] of ^{3}He seen from Fig. 18.12.

On the left panel of Fig. 18.13, we show the density dependence of $T_{\max}$, extracted from measurements of the magnetization $M_0(T)$ on ^{3}He bilayer [38]. The peak temperature is fitted by (18.20). At the same figure, we have also presented the maximal magnetization $M_{\max}$. It is seen that $M_{\max}$ is well described by the expression $M_{\max} \propto (S/T)_{\max} \propto (1-z)^{-1}$, see (18.15). The right panel of Fig. 18.13 reports the peak temperature $T_{\max}$ and the maximal entropy $(S/T)_{\max}$ versus the number density x. They are extracted from the measurements of $S(T)/T$ on ^{3}He bilayer [38]. The fact that both the left and right panels have the same behavior shows once more that there are indeed the quasiparticles, determining the thermodynamic behavior of 2D ^{3}He (and also 3D HF compounds [37]) near their QCP.

We conclude that despite absolutely different microscopic nature of 2D ^{3}He and 3D HF metals, their main universal macroscopic features and quantum criticality are the same [39]. As a result, the main features of ^{3}He experimental $T-x$ phase diagram look like those in HF metals and can be well captured utilizing our notion of FCQPT, based on the extended quasiparticles paradigm, and described in details in Chap. 2. The modification is that in contrast to the Landau quasiparticle effective mass, the ^{3}He effective mass $M^*(T,x)$, as well as that of HF metals, become temperature and density dependent. We have demonstrated that the universal behavior of $M^*(T,x)$ coincides with that observed in HF metals.

18.5 Scaling Behavior of HF Compounds and Kinks in the Thermodynamic Functions

In this section we visualize kinks or energy scales in the thermodynamic functions measured on HF compounds such as HF metals, 2D ^{3}He, quasicrystals, etc. The kink is a crossover point from the fast to slow growth of the thermodynamic function of HF compound at raising magnetic field and at fixed temperature and vise versa.

To better visualize kinks or energy scales in the thermodynamic functions measured in HF metals [47] and 2D ^{3}He, we present the normalized effective mass M^*_N extracted from the thermodynamic functions versus normalized temperature and the normalized thermodynamic functions proportional to $T_N M^*_N$ in Figs. 18.14 and 18.15, respectively.

$M^*_N(y)$ extracted from the entropy $S(T)/T$ and magnetization M measurements on the ^{3}He film [38] at different densities x are presented in Fig. 18.14. The data are extracted from the heat capacity C of the ferromagnet $\mathrm{CePd_{0.2}Rh_{0.8}}$ [31], $\mathrm{CeCoIn_5}$ [46] and the AC magnetic susceptibility of the paramagnet $\mathrm{CeRu_{2Si_2}}$ [32], and are plotted for different magnetic fields. It is seen that the universal behavior of the

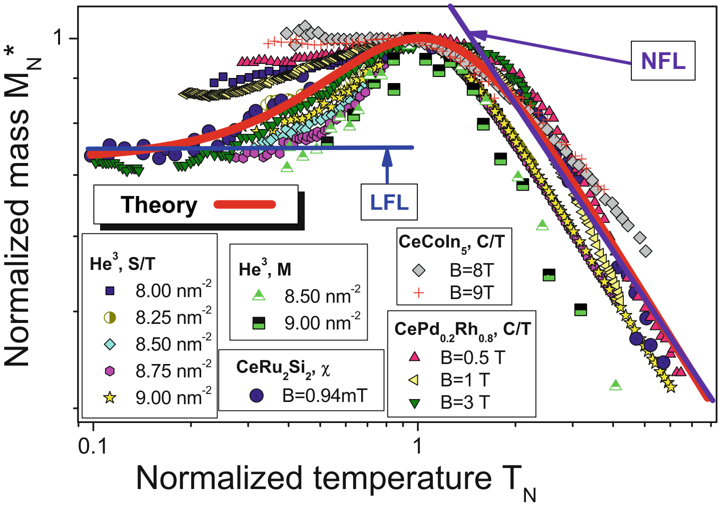

Fig. 18.14 Energy scales in HF metals and 2D ^{3}He. Normalized effective mass M_N^* versus normalized temperature $T_N = T/T_M$. The dependence $M_N^*(T_N)$ is extracted from measurements of $S(T)/T$ and magnetization M of 2D ^{3}He [38]), from AC susceptibility $\chi(T)$ of CeRu$_2$Si$_2$ [32] and from $C(T)/T$ of both CePd$_{1-x}$Rh$_x$ [31] and CeCoIn$_5$ [46]. The data are collected for different densities and magnetic fields shown in the legends. The *solid curve* traces the universal behavior of the normalized effective mass (18.19). Parameters c_1 and c_2 are adjusted for $\chi_N(T_N, B)$ at $B = 0.94$ mT. The LFL and NFL regions are shown by the *straight lines*, and are marked by the *arrows*

normalized effective mass given by (18.19) and shown by the solid curve is in accord with the experimental data. Note that the behavior of $M_N^*(y)$, extracted from $S(T)/T$ and magnetization M of 2D ^{3}He looks very much like that of 3D HF compounds. The LFL and NFL regimes are shown by the arrows. As it is seen from Fig. 18.14, the transition area is located between the LFL and NFL, and is relatively broad. In Fig. 18.15 we present the normalized data on $C(y)$, $S(y)$, $y\chi(y)$ and $\underline{M} = M(y) + y\chi(y)$ extracted from data collected on CePd$_{1-x}$Rh$_x$ [31], ^{3}He [38], CeRu$_{2Si_2}$ [32], CeCoIn$_5$ [46] and YbRu$_2$Si$_2$ [47], respectively. Note that in the case of YbRu$_2$Si$_2$, the variable $y = (B - B_{c0})\mu_B/T_M$ can be viewed as effective normalized temperature. We remind that $\underline{M}$ as a function of magnetic field has been calculated in Sect. 7.1. It is worth noting that upon comparing Figs. 17.15, 17.16,17.18 and 18.3 we observe that these quite various HF compounds exhibit the same behavior as that shown in Fig. 18.14. Again, we see that despite absolutely different microscopic nature of these HF compounds, their main universal macroscopic features and quantum criticality are of the same nature, generated by FCQPT.

It is seen from Fig. 18.15 that all the data exhibit the kink shown by arrow and taking place as soon as the system enters the transition region from the LFL state to the NFL one. This region corresponds to the temperatures where the vertical arrow in Fig. 6.2 crosses the hatched area separating the LFL from NFL. It is also seen in Fig. 18.15 that the low temperature LFL scale of the thermodynamic functions, as a

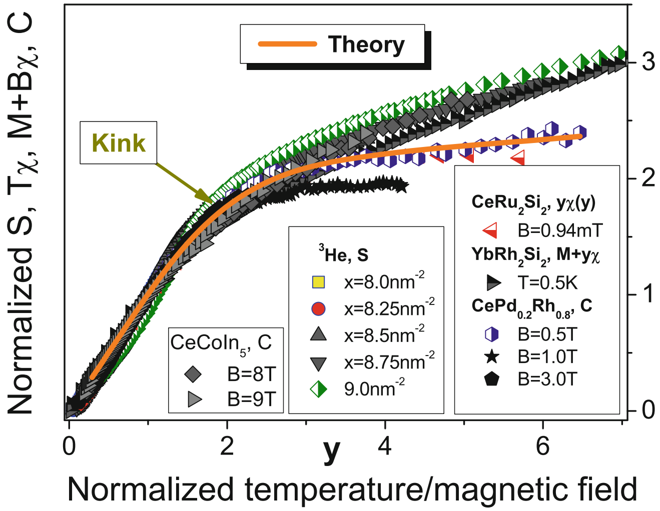

Fig. 18.15 Energy scales in HF metals and 2D ^{3}He. We plot the normalized specific heat $C(y)$ of $CePd_{1-x}Rh_x$ and $CeCoIn_5$ at different magnetic fields B, and the normalized entropy $S(y)$ of ^{3}He at different number densities x, and the normalized $y\chi(y)$ at $B = 0.94$ mT versus normalized temperature $y = T_N$ or magnetic field $y = B_N$. The normalized "average" magnetization $\underline{M} = M + B\chi$ is collected on $YbRu_2Si_2$ [47]. The kink (shown by the *arrow*) in all the data is clearly seen at the transition region. The *solid curve* represents $yM_N^*(y)$ with parameters c_1 and c_2 adjusted for the magnetic susceptibility of $CeRu_2Si_2$ at $B = 0.94$ mT

function of y, is characterized by fast growth, and the high temperature scale related to the NFL region is characterized by slow growth. As a result, we can identify the energy scales near QCP, discovered in [47, 48]: The thermodynamic characteristics exhibit kinks, i.e. crossover points from the fast to slow growth at elevated temperatures, which separate the low temperature LFL scale and high temperature one related to the NFL state.

18.6 New State of Matter

In Chaps. 17 and 18, we have described the diverse experimental facts related to temperature, magnetic field, and number density dependencies of thermodynamic characteristics of HF compounds. This universal behavior is also inherent to HF metals with different magnetic ground states. We also analyzed the interaction and positions of the maxima of magnetization M and the entropy S in 2D ^{3}He as the functions of the number density. These data could be obtained for ^{3}He only, while they were inaccessible for analysis in HF metals and other compounds. As a result, we were able to show the universality of the quantum criticality and the observed scaling behavior. Thus, by bringing the experimental data collected on different strongly correlated Fermi-systems to the above form related to the internal scales immediately, we reveal their universal scaling behavior. As we have seen above, FCQPT takes place in many compounds, generating the quantum critical state with the NFL behavior by forming flat bands. We have carried out a systematic theoretic study of the phase diagrams of strongly correlated Fermi systems, including HF metals, the new type of insulators with strongly correlated quantum spin liquid, and quasicrystals. We have demonstrated that these diagrams have universal features. The obtained results are in good agreement with experimental data. We have shown both theoretically and using arguments based entirely on the experimental grounds that the data collected on very different HF compounds, such as HF metals, compounds with quantum spin liquid, quasicrystals, and 2D ^{3}He have a universal scaling behavior at the quantum criticality domain in spite of their microscopic diversity. Thus, the quantum critical physics of different HF compounds is universal, and emerges regardless of the underlying microscopic details of the compounds. This uniform behavior, induced by the universal quantum critical physics, allows us to view it as the main characteristic of the new state of matter [49, 50]. Our analysis of HF compounds relies on numerous experimental results and on the calculations of the physical properties, related to NFL behavior. It is seen, that the FC theory, based on fermion condensation paradigm, delivers pretty good description of the NFL behavior of different strongly correlated Fermi systems. Moreover, FCQPT can be considered as the universal reason for the NFL behavior observed in various HF metals, liquids, insulators with quantum spin liquids, and quasicrystals.

References

1. C. Proust, E. Boaknin, R.W. Hill, L. Taillefer, A.P. Mackenzie, Phys. Rev. Lett. **89**, 147003 (2002)
2. R. Bel, K. Behnia, Y. Nakajima, K. Izawa, Y. Matsuda, H. Shishido, R. Settai, Y. Onuki, Phys. Rev. Lett. **92**, 217002 (2004)
3. T. Shibauchi, L. Krusin-Elbaum, M. Hasegawa, Y. Kasahara, R. Okazaki, Y. Matsuda, Proc. Natl. Acad. Sci. USA **105**, 7120 (2008)
4. A.P. Mackenzie, S.R. Julian, D.C. Sinclair, C.T. Lin, Phys. Rev. B **53**, 5848 (1996)
5. N.P. Butch, K. Jin, K. Kirshenbaum, R.L. Greene, J. Paglione, PNAS **109**, 8440 (2012)
6. G.Q. Zheng, T. Sato, Y. Kitaoka, M. Fujita, K. Yamada, Phys. Rev. Lett. **90**, 197005 (2003)
7. J. Korringa, Phys. (Utrecht) **16**, 601 (1950)
8. P. Gegenwart, J. Custers, C. Geibel, K. Neumaier, K.T.T. Tayama, O. Trovarelli, F. Steglich, Phys. Rev. Lett. **89**, 056402 (2002)
9. D. Shechtman, I. Blech, D. Gratias, J.W. Cahn, Phys. Rev. Lett. **53**, 1951 (1984)
10. A.I. Goldman, R.F. Kelton, Rev. Mod. Phys. **65**, 213 (1993)
11. D. Mayou, G.T. de Laissardière, in *Quasicrystals*, ed. by T. Fujiwara, Y. Ishii. Handbook of Metal Physics (Elsevier Science, Amsterdam, 2008), p. 209
12. T. Fujiwara, T. Yokokawa, Phys. Rev. Lett. **66**, 333 (1991)
13. T. Fujiwara, in *Physical Properties of Quasicrystals*, ed. by S.Z. M. Springer Series in Solid-State Sciences (Springer, Berlin, 1999), p. 438
14. R. Widmer, O. Gröning, P. Ruffieux, P. Gröning, Phil. Mag. **86**, 781 (2006)
15. R. Widmer, P. Gröning, M. Feuerbacher, O. Gröning, Phys. Rev. B **79**, 104202 (2009)
16. T. Fujiwara, S. Yamamoto, G.T. de Laissardière, Phys. Rev. Lett. **71**, 4166 (1993)

17. G.T. de Laissardière, Z. Kristallogr. **224**, 123 (2009)
18. K. Deguchi, S. Matsukawa, N.K. Sato, T. Hattori, K. Ishida, H. Takakura, T. Ishimasa, Nat. Mat. **11**, 1013 (2012)
19. V.R. Shaginyan, A.Z. Msezane, K.G. Popov, G.S. Japaridze, V.A. Khodel, Phys. Rev. B **87**, 245122 (2013)
20. V.R. Shaginyan, M.Y. Amusia, A.Z. Msezane, K.G. Popov, Phys. Rep. **492**, 31 (2010)
21. V.R. Shaginyan, Phys. At. Nuclei **74**, 1107 (2011)
22. V.A. Khodel, J.W. Clark, M.V. Zverev, Phys. At. Nuclei **74**, 1237 (2011)
23. L.D. Landau, Zh Eksp, Teor. Fiz. **30**, 1058 (1956)
24. J.W. Clark, V.A. Khodel, M.V. Zverev, Phys. Rev. B **71**, 012401 (2005)
25. E.M. Lifshitz, L. Pitaevskii, *Statistical Physics, Part 2* (Butterworth-Heinemann, Oxford, 2002)
26. V.A. Khodel, M.V. Zverev, J.W. Clark, JETP Lett. **81**, 315 (2005)
27. V.A. Khodel, V.R. Shaginyan, V.V. Khodel, Phys. Rep. **249**, 1 (1994)
28. J. Dukelsky, V. Khodel, P. Schuck, V. Shaginyan, Z. Phys. **102**, 245 (1997)
29. R. Lifshitz, Z. Phys. **51**, 1156 (2011)
30. V.R. Shaginyan, A.Z. Msezane, K.G. Popov, J.W. Clark, M.V. Zverev, V.A. Khodel, Phys. Rev. B **86**, 085147 (2012)
31. N. Oeschler, S. Hartmann, A. Pikul, C. Krellner, C. Geibel, F. Steglich, Phys. B **403**, 1254 (2008)
32. D. Takahashi, S. Abe, H. Mizuno, D. Tayurskii, K. Matsumoto, H. Suzuki, Y. Onuki, Phys. Rev. B **67**, 180407(R) (2003)
33. A.W. Rost, S.A. Grigera, J.A.N. Bruin, R.S. Perry, D. Tian, S. Raghu, S.A. Kivelson, A.P. Mackenzie, Proc. Natl. Acad. Sci. USA **108**, 16549 (2011)
34. R.A. Borzi, S.A. Grigera, J. Farrell, R.S. Perry, S.J.S. Lister, S.L. Lee, D.A. Tennant, Y. Maeno, A.P. Mackenzie, Science **315**, 214 (2007)
35. A.V. Silhanek, N. Harrison, C.D. Batista, A.L.M. Jaime, H. Amitsuka, J.A. Mydosh, Phys. Rev. Lett. **95**, 026403 (2005)
36. J.S. Kim, B. Andraka, G. Fraunberger, G.R. Stewart, Phys. Rev. B **41**, 541 (1990)
37. V.R. Shaginyan, K.G. Popov, V.A. Stephanovich, Europhys. Lett. **79**, 47001 (2007)
38. M. Neumann, J. Nyéki, B. Cowan, J. Saunders, Science **317**, 1356 (2007)
39. V.R. Shaginyan, A.Z. Msezane, K.G. Popov, V.A. Stephanovich, Phys. Rev. Lett. **100**, 096406 (2008)
40. A. Casey, H. Patel, J. Cowan, B.P. Saunders, Phys. Rev. Lett. **90**, 115301 (2003)
41. V.A. Khodel, V.R. Shaginyan, JETP Lett. **51**, 553 (1990)
42. M.Y. Amusia, V.R. Shaginyan, Phys. Rev. B **63**, 224507 (2001)
43. G.E. Volovik, in *Quantum Analogues: From Phase Transitions to Black Holes and Cosmology*, ed. by W.G. Unruh, R. Schutzhold. Springer Lecture Notes in Physics, vol. 718 (Springer, Orlando, 2007), p. 31
44. V.R. Shaginyan, M.Y. Amusia, K.G. Popov, Phys. Usp. **50**, 563 (2007)
45. M. Pfitzner, P. Wölfle, Phys. Rev. B **33**, 2003 (1986)
46. R. Movshovich, M. Jaime, J.D. Thompson, C. Petrovic, Z. Fisk, P.G. Pagliuso, J.L. Sarrao, Phys. Rev. Lett. **91**, 5152 (2001)
47. P. Gegenwart, T. Westerkamp, C. Krellner, Y. Tokiwa, S. Paschen, C. Geibel, F. Steglich, E. Abrahams, Q. Si, Science **315**, 969 (2007)
48. V.R. Shaginyan, M.Y. Amusia, A.Z. Msezane, K.G. Popov, V.A. Stephanovich, Phys. Lett. A **373**, 986 (2009)
49. M.Y. Amusia, V.R. Shaginyan, Contrib. Plasma Phys. **53**, 721 (2013)
50. D. Yudin, D. Hirschmeier, H. Hafermann, O. Eriksson, A.I. Lichtenstein, M.I. Katsnelson, Phys. Rev. Lett. **112**, 070403 (2014)

Chapter 19
Conclusions

Abstract This chapter concludes our book, serves as a road map for material presented and discusses what else can and should be done. Main emphasis is put on the fact that HF compounds feature universal scaling behavior in the wide range of the variation of magnetic fields, temperatures, number density, etc., which permits us to suggest that they form a new state of matter. Another emphasis in the book has been put on the ubiquity of the fermion condensation phenomenon. This phenomenon is ubiquitous as it is capable to describe equally well both the non-Fermi liquid behavior in HF compounds, the level merging in finite Fermi systems and baryon asymmetry in the early Universe. We conclude the monograph discussing possible avenues of future research in this extremely interesting field.

More than 2 decades have passed since first ideas appeared that led to the development of fermion condensation (extended Landau quasiparticle) paradigm [1–4]. During this time many theoretical papers appeared using this paradigm to study numerous strongly correlated electron systems, ranging from heavy-fermion (HF) compounds and high-T_c superconductors to the systems like 2D liquid ^{3}He, quantum spin liquids, quasicrystals, and even baryons in the early Universe [5]. The basic idea of fermion condensation (FC) paradigm is the new type of instability of ordinary Landau Fermi liquid (LFL) relatively toward the infinite growth of quasiparticle's effective mass. To avoid such unphysical situation, the system rearranges its energy spectrum in a way that Landau quasiparticle's kinetic energy becomes infinitely small near the Fermi surface and the distribution function $n(\mathbf{p})$ minimizing the ground state energy $E(n(\mathbf{p}))$ is mainly determined by the potential energy. In other words, the Fermi surface at $p = p_F$ transforms into the Fermi volume at $p_i \leq p \leq p_f$ suggesting that the single-particle spectrum is absolutely "flat" within this interval, i.e. the single-particle energies equal to the chemical potential μ. This state, where all quasiparticles with momenta $p_i \leq p \leq p_f$, have the same energy, closely resembles the Bose-condensed state. That is why the above state had been called Fermi condensate [1]. It had been shown by Volovik [3], that the FC state possesses different (than that of ordinary Fermi liquid) topology of the Fermi surface and thus cannot be reached from LFL without the phase transition. This phase transition had been called the Fermion condensation quantum phase transition (FCQPT), see [5] and references therein. The main physical effect of the FC theory is aforementioned extended quasiparticle paradigm. Namely, the notion of FCQPT is compatible with

M.Y. Amusia et al., *Theory of Heavy-Fermion Compounds*, Springer Series
in Solid-State Sciences 182, DOI 10.1007/978-3-319-10825-4_19

the idea of quasiparticles, for quasiprticles survive but they become different from those in ordinary Fermi liquid. More precisely, if in ordinary LFL the quasiparticle effective mass M^* is a constant, in FC state this quantity starts to depend on the external parameters like temperature T and external magnetic field B. This dependence is a key feature for explaining enigmatic NFL behavior of many strongly correlated electron systems and HF compounds in particular that are analyzed in this book.

Note that numerous theoretical models describing NFL behavior assume that quasiparticles are absent at the quantum critical points (QCP) of HF compounds, see Chap. 1, Introduction. Arguments that quasiparticles in strongly correlated electron systems "get heavy and die" at the QCP commonly employ the assumption that the quasiparticle weight factor z vanishes at the point of an associated second-order phase transition [6, 7]. Numerous experimental results have been discussed in terms of such an approach, but it can not explain neither qualitatively nor quantitatively main features of the physics of HF metals, see Chap. 1. Extensive studies have shown that above discussed FC approach, which preserves quasiparticles while being intimately related to the unlimited growth of M^*, delivers an adequate theoretical explanation of vast majority of experimental results in different HF metals. The essential point is that—as before—well-defined quasiparticles determine the thermodynamic and transport properties of strongly correlated Fermi systems, while the dependence of the effective mass M^* on T and B gives rise to the observed NFL behavior [5]. The most fruitful strategy for exploring and revealing the nature of the QCP is to focus on those properties that exhibit the most spectacular deviations from LFL behavior in the zero-temperature limit.

It turns out that the FC occurs in many compounds, generating the NFL behavior by forming flat bands. In this monograph we have shown both analytically (within FC approach) and using arguments based entirely on the experimental grounds that the data collected on extremely diverse HF compounds, such as HF metals, compounds with quantum spin liquid and quasicrystals, have a universal scaling behavior. This means that different materials with strongly correlated fermions can unexpectedly have a similar behavior despite their microscopic (like lattice symmetry and structure, magnetic ground state, dimensionality etc) diversity. Thus, the physics of quantum criticality of different HF compounds is universal and emerges regardless of the underlying microscopic details of the compounds. This identical behavior, taking place at relatively low temperatures and induced by the universal quantum critical physics, allows us to interpret it as a main characteristic of the new state of matter [3, 4, 8, 9]. Our analysis of strongly correlated systems is in the context of salient experimental results, and our calculations of the NFL physical properties are in good agreement with a broad variety of experimental data. Moreover, the fermion condensate can be considered as a defining cause for the NFL behavior observed in various HF metals, liquids, insulators with quantum spin liquids, and quasicrystals. As we have seen, a large diversity of the HF compounds exhibit the universal scaling behavior at their quantum criticality. Thus, whichever mechanism drives the system to FCQPT, the system demonstrates the universal behavior. There are lots of such mechanisms or tuning parameters like pressure, number density, magnetic field, chemical doping, frustration and etc.

We have described the effect of FCQPT on the properties of various Fermi systems and presented substantial evidence in favor of the existence of such a transition. We have demonstrated that FCQPT supporting the extended quasiparticle paradigm forms strongly correlated Fermi systems with their unique NFL behavior. Vast body of experimental facts gathered in studies of various materials, such as high-T_c superconductors, HF metals, and correlated 2D Fermi liquids like thin films of ^{3}He, can be explained by a theory based on the FCQPT concept. Description in terms of quasiparticles guarantees that Kadowski-Woods relation is conserved and that after magnetic field is applied, LFL behavior is restored.

We have also shown that in finite magnetic fields, in the NFL region formed by FCQPT, any second-order phase transition transforms into a first order one at the tricritical point leading to violation of universality in the framework of theory of critical fluctuations. This change is driven by the temperature independent part of entropy formed behind FCQPT. The quantum and thermal critical fluctuations corresponding to second-order phase transitions disappear and have a little effect on the low-temperature behavior of the system, so that the thermodynamics of HFmetals in this temperature range is mainly determined by quasiparticles.

We have found that the differential conductivity between a metal point contact and aHF compound or a high-T_c superconductor can be highly asymmetric as a function of the applied voltage. This asymmetry is observed when a strongly correlated metal is in its normal or superconducting state. We have shown that the application of magnetic field restoring the LFL behavior suppresses the asymmetry. We conclude therefore that the particle-hole symmetry is macroscopically broken in the absence of applied magnetic fields, while the application of magnetic fields restores both the LFL state and the particle-hole symmetry. The above features determine the universal behavior of strongly correlated Fermi systems and are related to the anomalous low-temperature behavior of the entropy, which contains the temperature independent term.

We have shown how the fermion condensation paves the road for quasi-classical physics in HF compounds. This means simply that systems with FC admit partly the quasi-classical description of their thermodynamic and transport properties. This description permits to gain more insights in the puzzling low-temperature NFL physics. The quasi-classical physics starts to be applicable near FCQPT, at which FC generates flat bands and quantum criticality, and makes the density of electron states in strongly correlated metals diverge. Due to the formation of flat bandsHF compounds exhibit the classical properties of elemental ones like copper, silver, aluminum, etc. In that case HF compounds demonstrate the quasi-classical behavior at low temperatures rather than elemental metals exhibit a quantum criticality.

The FC state represents the topologically protected new state of matter. In the case of Bose system the equation $\delta E/\delta n(p) = \mu$ describes the ground state. In the case of Fermi systems such an equation, generally speaking, would not be correct. Thus, it is the FC state, taking place behind FCQPT, that makes this equation applicable for Fermi systems. As a result, Fermi quasiparticles can behave as Bose one, occupying the same energy level $\varepsilon = \mu$. This state is viewed as the state possessing the supersymmetry (SUSY) that interchanges bosons and fermions eliminating the difference between them. We have seen that SUSY emerges naturally in condensed matter systems known as HF compounds. The FC state accompanied by SUSY violates the time invariance symmetry, while emerging SUSY violates the baryon symmetry of the Universe. Thus, restoring one important symmetry, the FC state violates another essential symmetry. In the future, the domain of problems should be broadened and certain efforts should be made to describe the other macroscopic features of FCQPT that could strongly modify the thermoelectric effects like Seebeck, Peltier etc. due to their relation to the entropy.

In addition to the already known materials whose properties not only provide information on the existence of FC but also almost shout aloud for such a condensate, there are other materials of enormous interest which could serve as possible objects for studying the phase transition in question. Among such objects are neutron stars, atomic clusters and fullerenes, ultra cold gases in traps, nuclei, and quark plasma. Another possible area of research is related to the structure of the nucleon, in which the entire "sea" of non-valence quarks may be in FC state. The combination of quarks and gluons that hold them together is especially interesting because gluons, quite possibly, can be in the gluon-condensate phase, which could be qualitatively similar to the pion condensate proposed by Migdal long ago [10]. We believe that FC can be observed in traps, where there is a possibility to control the emergence of a quantum phase transition accompanied by the formation of FCQPT by altering the particle number density.

In general, the ideas associated with this new phase transition in one area of research stimulates intensive studies of the possible manifestation of such a transition in other areas. This has happened in the case of metal superconductivity, whose ideas were fruitful in description of atomic nuclei and in a possible explanation of the origin of the mass of elementary particles. This, quite possibly, could be the case with FCQPT.

Finally, our general discussion shows that the FC theory, based on extended quasiparticle paradigm, develops unexpectedly simple, yet good qualitative as well as quantitative description of the NFL behavior of various strongly correlated Fermi systems. Moreover, the FC phenomenon can be considered as the universal reason for both the NFL behavior and the quantum criticality, observed in various heavy-fermion compounds, such as HFmetals, liquids like 2D ^{3}He, quantum spin liquids, strongly correlated insulators, quasicrystals and other Fermi systems. This observation permits us to suggest that FCQPT forms the new state of matter in heavy-fermion compounds and presents an almost unlimited area of research.

References

1. V.A. Khodel, V.R. Shaginyan, JETP Lett. **51**, 553 (1990)
2. P. Nozières, J. Phys. I France **2**, 443 (1992)
3. G.E. Volovik, JETP Lett. **53**, 222 (1991)

4. G.E. Volovik, in *Quantum Analogues: From Phase Transitions to Black Holes and Cosmology*, ed. by W.G. Unruh, R. Schutzhold. Springer Lecture Notes in Physics, vol. 718 (Springer, Orlando, 2007), p. 31
5. V.R. Shaginyan, M.Y. Amusia, A.Z. Msezane, K.G. Popov, Phys. Rep. **492**, 31 (2010)
6. P. Coleman, C. Pépin, Q. Si, R. Ramazashvili, J. Phys. Condens. Matter **13**, R723 (2001)
7. P. Coleman, C. Pepin, Phys. B **312–313**, 383 (2002)
8. M.Y. Amusia, V.R. Shaginyan, Contrib. Plasma Phys. **53**, 721 (2013)
9. D. Yudin, D. Hirschmeier, H. Hafermann, O. Eriksson, A.I. Lichtenstein, M.I. Katsnelson, Phys. Rev. Lett. **112**, 070403 (2014)
10. A.B. Migdal, *Theory of Finite Fermi Systems and Applications to Atomic Nuclei* (Wiley, New York, 1967)

Index

Symbols
2D ^{3}He, 83, 286, 291, 332, 336
3D ^{3}He, 44, 156, 164
Ag, 169
Al, 169
$Au_{51}Al_{34}Yb_{15}$, 176, 322, 325, 327
$Au_{51}Al_{35}Yb_{14}$, 326
Bi2212, 73
$Bi_2Sr_2CaCu_2O_{8+x}$, 245, 246
$Bi_2Sr_2Ca_2Cu_3O_{10+\delta}$, 67
$Bi_2Sr_2CuO_{6+\delta}$, 78, 318
$CeCoIn_5$, 40, 102, 116, 119, 129, 130, 147–149, 171, 173, 179, 240, 245, 258, 340, 341
CeNiSn, 251, 252
$CeNi_2Ge_2$, 130,134–136
$CeRu_2Si_2$, 40, 104, 131, 132, 135, 136
$CeRu_2Si_{1.8}Ge_{0.2}$, 331
$Ce_{0.925}La_{0.075}Ru_2Si_2$, 301, 303
Cu, 169, 286, 287, 293, 297
CuO_2, 78
Cu^{+2}, 286
$EtMe_3Sb[Pd(dmit)_2]_2$, 298, 306, 309
$La_{1.7}Sr_{0.3}CuO_4$, 73, 78, 79
$La_{2-x}Sr_xCuO_4$, 318
MOSFET, 27, 48
$Pr_{0.91}LaCe_{0.09}Cu0_{4-y}$, 78
$Pr_{2-x}Ce_xCuO_{4-y}$, 251, 252
$Sr_3Ru_2O_7$, 171–175,179,199,200
$Tl_2Ba_2CuO_{6+x}$, 79, 80
$URu_{1.92}Rh_{0.08}Si_2$, 331, 332
$YBa_2Cu_3O_{7-x}/La_{0.7}Ca_{0.3}MnO_3$, 247
YbAgGe, 119
$YbBa_2Cu_3O_y$, 252
$YbCu_{5-x}Al_x$, 248
$YbCu_{5-x}Au_x$, 123, 125, 127, 304
$YbRh_2Si_2$, 14, 40, 80, 93,96–100,102,103, 105–109,119,120,122,124,127, 144,145,147–150, 151–153, 175,179,187,188,192–195,251, 261, 262, 265, 266, 268, 269
$ZnCu_3(OH)_6Cl_2$, 286–290, 293, 295, 297, 300, 302, 303, 305–307,309, 311
^{4}He, 156, 186
^{63}Cu, 124, 304
$k--(BEDT--TTF)_2Cu_2(CN)_3$, 306, 309, 314
$CePd_{0.2}Rh_{0.8}$, 340
$CePd_{1-x}Rh_x$, 131–133, 341, 342 130, 132, 211,330,131–133,341,342
$YbRh_2(Si_{0.95}Ge_{0.05})_2$, 129, 135
2+1 dimensional quantum field theory, 274
2-kind TT, 58
2D Fermi liquid, 17, 82, 347
2D Fermi system, 12, 18, 332
2D lattice, 307
3D Fermi system, 165
5/2-kind TT, 58

A
Ab-initio methods, 4, 6
Ab-initio numerical electronic structure simulations, 2
Amorphous materials, 322
Andreev reflection, 235, 245
Anisotropy, 18, 93, 200, 258, 302, 323
Anti-de Sitter gravitational theory, 274
Anti-weak localization, 193, 202
Antiferromagnetic state, 100, 252, 254
Antiparticle, 9, 248, 282

M.Y. Amusia et al., *Theory of Heavy-Fermion Compounds*, Springer Series
in Solid-State Sciences 182, DOI 10.1007/978-3-319-10825-4

Antisymmetric wave function, 3
Atomic clusters, 17, 348
Atomic nuclei, 3, 216, 348
Atomic system of units, 8, 236
Average magnetization, 112, 113, 342

B
Ballistic electron motion, 202
Band theory of solids, 1
Bardeen-Cooper-Schrieffer, 61
  equations, 61
  approximation, 64
  gap, 219, 223
  pairing interaction, 34, 65
  theory, 61–63, 65, 67, 68
Baryogenesis via lepto genesis, 274
Baryon asymmetry, 33, 247, 274, 275, 280, 282, 345
Baryon number non conservation, 274, 281
Baryon-antibaryon symmetry breaking, 248
Baryonic charge condensate, 274
Bethe-Weizsäcker formula, 216
Betti numbers, 54
Bifurcation of the metamagnetic phase boundary, 199
Bloch theorem, 322
Bogolyubov quasiparticles, 67
Bohr
  magneton, 26, 227, 263
  radius, 38
Boltzmann constant, 168
Boltzmann's theory, 155
Bose
  condensed, 2, 345
  particles, 2, 3
Boson atoms ensemble, 2
Boson propagator, 48, 158

C
Characteristic energy, 65, 72, 97, 238
Charge, 2, 4, 8, 26, 46, 96, 149, 273, 285, 310, 319
Charge conjugation, 248
Charge density wave, 38
Charge transport coefficient, 320
Chemical composition, 2, 36
Chemical potential, 22, 32, 44, 88, 159, 171, 189, 216, 217, 221, 225–227, 229, 230, 275, 280, 299
Chemical pressure, 101, 106
Clausius-Clapeyron relation, 175, 205
Clusters, 3, 273
Coarse-grained model, 17
Coherent collective excitations, 9
Collective phenomena, 4
Collective response, 9
Collective state, 36
Collision integral, 24, 162, 163
Composition, 12, 94, 338
Compressibility, 133, 141
Computational complexity, 6
Condensed matter physics, 8, 10, 21, 249, 261, 273–275, 329
Condensed matter systems, 33, 348
Conductivity, 129, 182, 206, 239, 245, 247, 248, 278, 306
Control parameter, 12, 39, 95, 102, 104, 189, 190, 253, 265, 290, 308, 318, 325, 338
Cooper pairing, 52
Correlation effects, 3, 5
Correlation length, 12, 13, 42
Coulomb
  field, 3
  interaction, 1, 2, 4, 5, 172, 207
  law, 51
  potential, 56
  problem, 48, 225
  repulsion, 2, 4–6
CP symmetry, 248
CPT symmetry, 248, 281
Creation and annihilation operators, 5, 34
Critical domain, 174, 204
Critical exponent, 15, 147, 152
Critical field, 78, 96, 117, 128, 129, 148, 149, 175, 205, 210, 317, 321
Critical magnetic field, 75, 89, 95, 106, 128, 144, 180, 318
Critical magnetic fields Bc_2 and Bc_0, 319
Critical quantum and thermal fluctuations, 12, 63
Critical temperature, 40, 133, 142, 175, 202, 238
Crossover point, 112, 190, 340, 342
Crystal structure, 2
Crystalline field, 58
Crystalline structure, 17, 18
Crystalline symmetry, 4
Curie-like component, 161
Curie-Weiss law, 173

D
d and f electron shells, 2
Dark energy, 280

Dark matter, 280
Defects, 18, 67, 297
Degenerate, 38, 40, 102, 104, 144, 181, 191, 203, 215, 216, 218, 322
Delocalized nature of electrons, 2
Density functional theory, 4
Density functional theory for superconductors, 25, 33
Density of electrons, 183, 193
Density of states, 24, 26, 37, 42, 49, 65, 66, 70, 90, 92, 124, 162–165, 174, 235, 242–246, 325, 335
Density waves, 82
Differential conductivity, 235, 237, 238, 240, 241, 277, 347
Dirac sea, 275
Discrete square lattice rotational symmetry, 200
Disordered phase, 82, 175
Dispersion law, 54, 56, 59, 67, 70, 71, 75
Dispersionless plateau, 37
Dissymmetrical tunnelling conductance, 195
Divergence of the effective mass, 10, 26, 31, 48, 83, 93, 157, 163, 168, 255
Doping, 24, 68, 72, 95, 130, 133, 311
Dulong-Petit Law, 155, 162, 172
Dynamic properties, 127, 298, 305
Dynamic spin susceptibility, 298
Dynamical Mean-Field Theory, 6
Dzyaloshinskii-Moriya interaction, 302

E
Earth, 3
Effective impurity problem, 6
Effective interaction, 9, 164
Effective potential, 4
Effective single-impurity problem, 6
Electric current, 278
Electric resistivity, 13, 119
Electrical conductivity, 251
Electrodynamic properties, 9
Electron liquid, 10, 22, 36, 37, 61, 62, 73, 76, 77, 82, 89, 90, 115, 134, 140, 142, 143, 145, 171, 209, 236, 306
Electron liquid with FC, 37, 61, 73, 77
Electron quantum numbers, 22
Electron-phonon interaction, 58, 71, 162, 163, 166, 167
Electron-phonon scattering, 168
Electroweak baryogenesis, 274
Elementary excitations, 21, 78, 317, 318
Elementary particles, 1, 9
Energy and momentum conservation, 9
Energy functional, 4, 32, 74, 217, 221
Energy gain, 57, 73, 226
Energy scales, 70, 87, 93, 97, 100, 112, 280, 340–342
Ensemble of the particles, 1
Ensembles of interacting particles, 1
Entropy, 13, 15, 25, 35, 48, 62, 120, 139, 142–145, 152, 159, 171, 175, 186, 199, 201, 203–205, 209, 210, 238, 280, 333, 334, 338, 347
Entropy peak, 202, 212
Equipartition principle, 155
Evaporation of primordial black holes, 274
Exactly solvable models, 140
Exchange interaction, 111
Exchange-correlation energy, 4, 111
Excitation spectrum, 52, 288, 306
External parameters, 2, 10, 16, 308, 346

F
Fermi
  finite systems, 215
  function, 51
  layer, 63
  level, 5, 56, 124, 172, 208, 243, 319
  liquid, 1, 10–15, 17, 21, 22, 31–33, 35, 36, 41, 44–46, 48, 51, 62, 65, 67, 68, 70–74, 76, 79, 82, 92, 93, 101, 113, 119, 122–124, 140, 143, 158, 160, 163, 166, 171, 201, 217, 225, 248, 252, 261, 263, 275, 286, 317, 333, 345–347
    highly correlated, 82, 93, 119, 140
    normal, 21, 31, 51, 72, 73
    spectrum, 51, 101, 252
    state, 216
    strongly correlated, 12, 31, 140
    theory, 1, 11, 21, 35, 41, 62, 63, 65, 67, 70, 216, 218, 225, 227
    topology, 49, 345
  momentum, 195, 206, 217, 231, 335
  particles, 7
  sea, 275, 280
  step, 7, 34, 74, 275
  surface, 9, 17, 24, 31, 32, 37, 41, 46, 47, 49, 51–54, 56, 58, 74, 88, 97, 127, 159, 163, 165, 167, 171, 180, 181, 189, 192, 195, 216, 217, 219, 224–226, 231, 232, 255, 264, 275, 279, 298, 305, 307, 311, 323, 331, 345
    multi-connected, 45–47, 51, 53, 101, 181, 307

        swelling, 180
        topology, 49, 88
    velocity, 71, 163, 165, 169, 184, 264
    volume, 32, 144, 195
Fermi-Dirac distribution, 22, 25, 275
Fermion condensate, 17, 51, 188, 217, 346
Fermion condensation quantum phase transition, 197, 274
Fermionic spinons, 285, 298
Ferromagnetic state, 38, 266
First order phase transition, 34, 35, 39, 144, 175, 200, 204
Flat and narrow conductivity band, 27, 90
Flat bands, 17, 170, 172, 179–182, 185, 199, 201, 203, 207, 248, 251, 274, 281, 317, 322, 343, 346, 347
Flattening of the single-particle spectrum, 159, 179, 180
Flowing of spins, 285
Fluidity, 285, 288
Free energy, 22, 25, 105, 157, 162
Fullerenes, 3, 348

G
Gluon, 1, 348
Gluon-condensate, 348
Gorkov equations, 63
Gravitational interaction, 3
Greens function, 6, 32, 46, 61
Ground state, 5, 7, 9, 10, 21–23, 25, 34, 35, 46, 51–54, 56, 59, 73, 79, 101, 122, 132, 135, 136, 143, 144, 148, 170, 171, 203, 216, 221, 225, 252, 275, 280, 281, 286, 306, 307, 319, 332, 334, 338, 342, 346, 347
Ground state energy, 7, 22, 25, 34, 46, 59, 73, 144, 148, 288, 345
Group velocity, 44, 45, 155, 160, 162, 173, 206, 255, 258, 275
Grüneisen
    ratio, 141, 145

H
Hall
    coefficient, 74, 139, 142, 144, 145, 148, 188, 195, 252
        jump, 139, 144, 148
    effect, 2
        quantum, 2
    resistivity, 187, 251
Hartree contribution, 4
Hartree-Fock energy, 219
Hartree-Fock equation, 3
Hartree-Fock rearrangement, 220
Hartree-Fock scenario, 220, 221, 225
Heat capacity, 10, 18, 28, 69, 70, 76, 100, 140, 153, 155, 157, 162, 172, 173, 175, 294, 297, 302, 305, 306, 337, 338
Heat conductivity, 285, 306, 310, 312
Heat transport coefficient, 312
Heavily hole-overdoped, 318
Heavy bipolarons, 168
Heavy electron, 61, 77, 144, 173, 270
Heavy fermion, 1, 2, 11–13, 15–18, 24–28, 33, 34, 40, 44, 59, 68, 73–80, 87–89, 92–95, 97, 99–105, 107, 109, 113, 114, 116, 119, 121, 123, 124, 127, 129–133, 135, 136, 139, 142, 143, 146, 147, 153, 162, 167–169, 172, 174–176, 261, 278, 345–348
    compounds, 1, 11, 12, 16, 18, 28, 33, 59, 76, 93, 127, 168, 174, 191, 240, 252, 253, 258, 261, 265, 271, 286, 329, 340, 345–348
    liquid, 18, 25, 34, 73, 75–78, 87–89, 93, 102–104, 139, 143
        homogeneous, 18, 25, 87, 93, 188, 263, 287, 298, 308, 322, 323
    metals, 11–13, 15–18, 24, 26, 27, 40, 44, 68, 74–76, 78–80, 87, 93–95, 97, 99–105, 107, 109, 113, 114, 116, 119, 121, 123, 124, 127, 129, 130, 132, 133, 135, 136, 139, 142, 146, 147, 153, 162, 167–169, 172–176, 180, 181, 187, 190–192, 204, 205, 238, 239, 241, 253, 258, 265, 271, 278, 293, 297, 301, 303, 310, 320, 331, 346–348
    system, 2, 12, 92
Heavy quasiparticles, 205, 206, 208, 324
Heavy spinon, 307
Herbertsmithite, 285, 286, 291, 297, 298, 301–303, 305, 310
Hertz-Millis spin-density-wave, 167
Heterogeneity of the substrate, 157
High-T_c superconductivity, 65, 67, 73, 83
High-energy degrees of freedom, 21, 67
High-temperature superconductors, 187, 317
Highly correlated liquid, 87, 140
Highly correlated systems, 81
Hohenberg-Kohn theorem, 4
Hole-doped and electron-doped high-temperature superconductors, 78
Hubbard
    Hamiltonian, 5

  model, 6, 68
Hund's rule, 223
Hybridization, 171, 172
Hydrostatic pressure, 108, 322, 324
Hyperfine coupling constant of the muon, 125, 304

I
Iceberg phase, 52, 54, 56
Imaginary energy, 9
Impurities, 67, 173, 179, 180, 184, 193, 194, 207, 208, 245, 297, 302
Infinite correlation range, 12
Inflection point, 15, 52, 57, 97, 98, 105, 114, 120, 127, 264, 292, 304, 309, 310, 312, 313, 333, 334
Insulator, 11, 12, 16, 81, 246, 285, 286, 306, 307, 343, 346
Insulators with geometrical frustration, 285
Interatomic interaction potentials, 4
Internal degrees of freedom, 2
Interparticle correlations, 3
Ionic crystals, 164

J
Jelly model, 18, 94

K
Kadowaki-Woods relation, 13, 76, 113, 126
Kagome antiferromagnet, 286
Kagome hexagon, 286, 287
Kagome lattice, 286, 287, 297, 298, 307
Kinetic energy, 2, 4, 31, 36
Kink, 70, 71, 105, 112, 113, 132, 133, 175, 176, 196, 269, 270, 292, 340, 342
Kohler's rule, 113, 115
Kohn-Sham
  equations, 4, 5, 59
  potential, 4, 5
Kondo, 11, 13, 188, 194
Korringa law, 78, 79, 124, 125, 304, 317, 319
Kramers-Kronig transformation, 71, 299

L
Lagrange multiplier, 54
Landau
  damping, 160, 163
  energy functional, 32, 217
  equation, 9, 23, 25, 41, 188, 210, 264, 288, 299, 318, 323, 335
  formula, 47, 75
  functional, 52, 53, 92, 288, 307, 326
  interaction, 21–24, 26, 36, 51, 52, 88, 91, 97, 111, 188
  kinetic equation, 167
  level, 75, 142, 215, 226, 227, 229, 230
  quasiparticle, 7, 8, 10, 21, 24, 33, 40, 215, 251, 264, 317, 318, 336, 345
  quasiparticle paradigm, 7
  state, 31, 45, 49, 264
  the second order phase transitions theory, 40, 150
  transport equation, 298
Landau Fermi liquid, 1, 11, 14, 15, 22, 33, 62, 63, 65, 67, 68, 73–80, 87, 89–91, 113, 123, 143, 317
  behavior, 15, 16, 28, 40, 79, 80, 94, 96, 101, 104, 106, 113, 114, 123, 148, 149, 161, 162, 190
  state, 13, 51, 73, 75, 76, 78, 79, 89, 90, 261
  theory, 1, 11, 62, 63, 65, 67, 68, 90, 91
Landau-Migdal interaction, 220
Lattice symmetry axes, 94
Lattice vibrations, 155
Laughlin Fermi liquid, 252
Layered perovskite ruthenates, 199
Legendre polynomials, 23
Lepton, 1
Level-mergence phenomenon, 225
Lifshitz transitions, 51
Linear response function, 82, 281
Liquid-drop, 216
Local density approximation, 4
Local electronic charge density, 4
Local magnetic moments, 2
Local spin density approximation, 4
Long range magnetic order, 286
Longitudinal magnetoresistance, 113, 124, 304, 305
Longitudinal zero sound, 166
Lorentz
  force, 113, 115
  number, 188
  symmetry, 274
Lorentzian, 38
Low-temperature thermodynamic properties, 287, 317, 322
Luttinger Fermi liquid, 32

M
Macroscopic correlated coherent phenomena, 7
Macroscopic properties, 332

Magic number of protons, 216
Magnetic entropy, 120, 152
Magnetic field values, 199
Magnetic oscillations, 181
Magnetic quantum phase transitions, 12
Magnetic states, 5, 106, 288
Magnetic susceptibility, 13, 48, 76, 111, 123, 130, 180, 269, 285, 288, 291, 296, 297, 302, 321, 327, 342
Magnetically ordered state, 2, 271
Magnetization, 28, 105, 111, 112, 120, 121, 144, 203, 269, 270, 290, 299, 336, 338, 340, 341
Magnetoresistive anisotropy, 200, 212
Many-body effects, 3
Many-body Hamiltonian, 5, 6
Many-body problem, 3, 222
Many-body theory, 1, 8, 44
Marginal Fermi liquid, 33, 44, 70, 252
Mass number, 216, 218
Material-independence of the lifetime, 168
Matter and antimatter, 9, 247
Maximum value of the superconducting gap, 67, 68
Mean free path, 199
Metal-insulator transition, 81, 231
Metamagnetic phase transition, 329, 331
Metamagnetic quantum criticality, 199, 329
Metamagnetic transition, 199, 203, 209, 262, 271, 331
Metamagnetism, 271, 331
Microscopic characteristics, 4
Microscopic length scale, 12, 13
Minimum condition, 22
Model Hamiltonian approach, 5
Model of nearly localized fermions, 81
Model theoretical treatment, 2
Molecules, 1, 4, 5
Momentum transfer, 42, 94, 216
Moon, 3
Mott insulator, 252
Multi-component systems, 8
Multi-atomic object, 3
Muon spin-lattice relaxation rates, 125–127, 305

N
Narrow orbitals, 2, 171
Nematic phase, 202
Nernst theorem, 63, 174, 181
Neutron scattering spectrum, 298
Neutron stars, 17, 348
New state of matter, 16, 17, 33, 67, 109, 317, 342, 345, 346
Newton
  gravitation law, 3
  mechanics, 3
Non-Fermi liquid, 10
  behavior, 17, 93, 113, 216, 271, 318, 345
  effect, 210
  state, 201
Non-perturbative part of interparticle interaction, 3
Nonanalytic function, 91, 324, 326
Noncrystallographic rotational symmetry, 321
Normalized effective mass, 14–16, 87, 94–98, 100, 103, 123, 125, 127, 131, 134, 196, 253, 265, 289, 325, 331, 332, 336, 341
Nuclear spin-lattice relaxation rates, 124
Nuclei, 1, 216, 304, 348
Number density, 12, 25, 27, 38–40, 68, 71, 74, 101, 183, 193, 275–277, 333, 335, 338, 342, 345, 348
Numerical calculations, 221, 336
Nèel temperature, 75, 104, 105, 142, 143, 146–148, 191, 192, 195, 253, 254, 265

O
Occupation numbers, 25, 37, 45, 52, 59, 88, 101, 171, 203, 215, 226
Ohm’s law, 157
On-site fluctuations, 6
Optical lattice, 2
Optimally doped cuprates, 78
Orbital momentum, 2
Orbital motion of carriers, 113, 115, 126, 179
Order parameter, 13, 34, 39, 62, 63, 66, 73, 75, 163, 317
Order parameter fluctuations, 12, 15
Ordered phase, 12, 99, 174–176, 199–202, 204, 205, 211, 212
Ordinary particles densities, 21
Ordinary quantum phase transitions, 12, 13, 16, 40, 102
Organic insulators, 305–307, 309, 310, 312
Out of equilibrium decays of massive particles, 274
Overdoped, 252, 318

P
Pair interaction, 34, 61
Pairing interaction, 34, 61, 66, 71, 241

Paramagnetic, 106, 142, 148, 195, 238, 271
Particle distribution functions, 171
Particle-hole interaction, 92
Particle-hole symmetry, 237
Particles and antiparticles, 248
Pauli principle, 53
Peculiar points, 15
Peltier effect, 348
Periodic potential, 2
Phase diagram, 31, 38, 39, 47, 57, 76, 87, 95, 96, 102, 103, 108, 109, 124, 149, 181, 182, 190–192, 195, 196, 199, 204, 205, 210, 212, 252–255, 257, 265, 277, 289–291, 302, 307, 309, 310, 319, 325, 328, 329, 335–337, 340, 343
Phenomenological potential, 1
Phonon mode in solids, 162
Photoemission spectroscopy, 13
Photon, 1, 47
Pion condensate, 348
Plane waves, 2
Poincaré mapping, 54
Point-contact spectroscopy, 239
Polarization operator, 182
Polaron effects, 164
Pomeranchuk conditions, 10
Potential energy, 31, 38, 39, 83, 345
Power laws of the temperature dependence, 11
Power-law exponents, 299
Probability of the population, 235
Propagation velocity, 9
Pseudogap, 69, 127, 240

Q
Quantum critical line, 37, 39, 81, 102, 119, 140, 142, 249, 277, 279, 280
Quantum critical point, 11, 12, 16, 17, 40, 49, 75, 90, 122, 142, 156, 162, 174, 181, 196, 210, 226, 230, 231, 276, 277, 307, 323
Quantum criticality, 10–12, 15–18, 109, 146, 155, 162, 169, 170, 172, 173, 199, 208, 311, 317, 320, 321, 329, 330, 332, 340, 341, 343, 346–348
Quantum liquid, 10, 156, 317
Quantum mechanic, 2
Quantum mechanical transition interaction, 235
Quantum phase transition, 1, 2, 10–13, 16, 17, 21, 31, 34, 38, 40, 63, 81, 101, 102, 121, 123, 124, 142, 144, 163, 248, 273–275, 281, 317, 321, 348
Quantum protectorate, 36, 67, 70
Quantum spin liquid, 16, 17, 109, 125, 286–288, 292–298, 300, 302, 304–307, 311, 343, 345, 346, 348
Quark, 1, 17, 248, 274, 348
Quark plasma, 17, 348
Quasi-classical behavior, 11, 162, 169, 172, 208, 337, 347
Quasi-hole, 9
Quasi-momentum space, 58
Quasicrystals crystalline approximant, 326
Quasiparticle
  damping, 87, 92, 119
  decay, 8, 124, 206
  distribution function, 7, 22, 24, 27, 31–33, 35, 52, 62, 88, 142, 188, 195, 236, 263, 264, 288, 298, 299, 323, 335
  effective interaction, 7, 9, 21, 218, 219
  effective mass, 10, 24, 87, 97, 114, 124, 126, 173, 192, 217, 226, 252, 261, 263, 264, 304, 317, 323, 324, 334, 340, 345, 346
  excitation curve, 38, 71
  extended paradigm, 67, 93, 125
  lifetime, 9, 192
  weight, 12, 40, 49, 163, 255, 346
  width, 9, 208, 324
Quasiperiodic translational properties, 321

R
Random phase approximation, 93
Reciprocal lattice constant, 94
Reentrance of LFL behavior, 320, 321
Relaxation properties, 6, 16, 17, 111, 124, 311
Renormalization-group approach, 13
Residual entropy, 139
Residual heat conductivity, 306, 310
Residual interaction, 3
Residual resistance, 116, 126, 304
Resistivity jumps, 202, 206, 212
Resonance phenomena, 3
Restoration of the LFL behavior, 13, 241
Rotational symmetry, 200, 212, 322
Ruddlesden-Popper series, 199

S
Sakharov's conditions, 274
Scaling behavior, 15–18, 25, 27, 28, 87, 88, 93, 94, 96–100, 103, 108, 109, 114, 116, 120, 121, 127, 130, 131, 135, 136, 152, 210–212, 262, 266, 267, 285, 287, 290, 291, 297, 300–303, 305,

308, 309, 312, 322, 325, 327, 329, 330, 334, 336, 340, 342
Scanning tunnel microscopy, 235
Scattering cross-section, 320
Schrödinger equation, 3, 4
Second order phase transition, 34, 74, 139, 146, 147, 149, 150, 153, 163, 174, 175, 347
Seebeck coefficient, 168, 255, 256
Seebeck effect, 348
Self-consistent field, 3, 225
Self-consistent renormalization theory, 124
Self-energy, 6, 71, 219, 220
Semiclassical approximation, 220, 235
Shubnikov-de Haas oscillations, 27, 77
Single-electron eigen energies, 5
Single-electron spectrum, 37
Single-electron wave functions, 4
Single-particle and many body effects, 1
Single-particle levels, 17, 215, 228
Single-particle spectrum, 7, 32, 34, 44, 45, 52, 54, 66, 71, 76, 88, 159, 167, 171, 179–182, 215, 255, 259, 263, 264, 276, 308, 345
Slater determinants, 4
Small perturbation, 3, 66
Solar system, 3
Solid state, 215
Solids, 4, 10, 17, 47, 155, 157, 167, 216, 287, 323
Sommerfeld coefficient, 13, 14, 98, 111, 150, 151
Spatial confinement, 2
Spatial fluctuations, 6
Specific microscopic mechanisms of quantum criticality, 17
Spiky DOS, 322, 324
Spiky state, 322
Spiky structure, 324
Spin, 2, 4, 5, 11, 16, 23, 34, 88, 161, 188, 210, 226, 227, 248, 263, 267, 285–287, 291, 295, 298, 305, 311, 332
Spin density wave scenario, 13
Spin freezing, 286
Spin susceptibility, 26, 161, 173, 298, 299
Spin-gap like excitations, 307
Spin-lattice relaxation parameters, 79
Spin-lattice relaxation rate, 123–127, 285, 298, 304, 310
Spin-orbit coupling, 193, 202
Stability conditions, 10, 22, 23, 27, 41
Standard Model, 281
State of matter, 11, 16, 17, 33, 36, 67, 109, 288, 297
Static mean field, 5
Static spin susceptibility, 306, 359
Step function, 23, 27, 32, 35, 36, 52, 72, 235, 236, 248, 249, 256, 276, 278, 279
Step-like drop, 193, 194, 256
Stoner factor, 48, 185
Strong screening regime, 57
Strongly correlated
  electron systems, 2, 6, 113, 167, 180, 259, 345, 346
  insulators, 11, 348
  quantum spin liquid, 306, 343
  solids, 180
  substances, 1, 322
  systems, 1–4, 6, 7, 10, 11, 13, 16, 17, 38, 81, 87, 109, 111, 119, 139, 141, 156, 157, 162, 164, 165, 170, 172, 303, 346
Strongly interacting electrons, v
Strongly interacting fermions, 21
Strongly interacting ions, v
Strongly interacting system, 51
Substrate inhomogeneities, 245
Sun, 3
Superconducting gap, 34, 36, 61, 62, 66, 67, 73, 129, 245
Superconducting phase transition, 65, 68, 147, 180
Superconducting state, 37, 38, 61, 63, 67, 79, 186, 236, 239, 241, 244, 245, 254, 255, 319, 347
Superconductivity, 2, 3, 7, 17, 35, 61, 65–68, 73, 75, 78, 83, 121, 127–130, 258, 265, 319, 348
Superfluidity, 7, 10
Supersymmetry, 33, 273
Susceptibility, 10, 75, 106, 117, 121–123, 125, 132, 173, 210, 297, 299, 306, 340

T
T—density x phase diagram, 332
T symmetry, 248, 280
T-B phase diagram, 188, 190, 191, 193, 200, 204, 253, 254, 256, 300, 308, 317–319
t-J models, 78
T-linear resistivity, 162,168–170, 175, 207 175
Taylor series, 35, 164
Temperature independence, 10
Temperature-independent entropy, 35, 40, 87, 101, 153, 170

Thermal conductivity, 2, 188, 251, 310, 312, 313
Thermal expansion coefficient, 18, 133, 140, 142, 181, 203
Thermodynamic consideration, 205
Thermodynamic potential, 33, 34
Thermodynamic properties, 11, 16, 36, 90, 93, 127, 131, 133, 136, 140, 156, 197, 210, 262, 271, 285, 286, 289, 290, 297, 298, 321–323, 328, 329, 333
Third law of thermodynamics, 63, 173, 174, 181, 203
Thomas-Fermi approach, 4
Topological class, 32
Topological invariant, 33
Topological matter, 180
Topological phase transitions, 44, 63, 101, 159, 263, 307
Topological transitions, 45, 46, 51, 101, 308
Topologically protected flat band, 101, 181
Transforming particle into antiparticle and parity, 248
Transition regime, 13, 14, 16, 28, 94, 95, 100, 119, 190, 191, 253, 266, 268, 325, 326, 330
Translational symmetry, 322
Transport equation, 24, 298, 299
Transport properties, 16, 17, 22, 24, 25, 36, 90, 93, 97, 100, 127, 132, 152, 155, 162, 182, 201, 202, 208, 235, 244, 259, 285, 286, 322, 324, 346, 347
Transverse magnetoresistance, 114
Transverse zero sound, 159, 160, 172, 173, 207, 208
Transverse zero sound collective model, 162
Triangle anomaly in baryonic current, 274
Tricritical point, 147–150, 152, 175, 200, 205, 347
Triple point, 57, 58
Tuning parameter, 16, 40, 117, 217
Tunneling conductivity, 130, 238, 245
Tunnelling current, 235, 236
Two-body dynamics, 3

U
Ultra-cold gases in traps, 17
Umklapp processes, 24, 119, 180, 187
Universal interpolating function, 94, 211, 289, 324, 336
Universal scaling behavior, 16, 17, 67, 136, 210, 211, 288, 298, 305, 310, 314, 324, 330, 343, 345, 346
Universality of second order phase transitions, 139
Universe, 17, 33, 248, 249, 273–275, 279, 280, 282
Universe inflation, 249

V
Vacuum ground state, 7
Valence electron orbitals, 5
van Hove singularity, 172, 174, 202–204, 207, 329
van-der-Waals
  forces, 38, 332
  interaction, 334
Variational principle, 33
Vertex part of Green function, 183
Visible matter, 248, 280

W
Wave vectors, 18
Weak anti-localization, 193, 202
Weak localization, 193
Weak perturbations, 10
Weak screening regime, 56
Weak-coupling superconductivity theory, 61
Weak-field approximation, 115
Weakly correlated particles, 2
Weakly correlated solids, 1
Weakly interacting system, 157
Weakly polarized, 77, 103, 105, 143, 148, 190, 191, 252, 253
Wiedemann-Franz law, 78, 79, 187, 195, 253

Z
z-factor, 12, 40, 44, 93
Zeeman splitting, 75–77, 88, 89, 188, 263, 305, 308
Zero sound, 158, 161, 166, 172, 175, 207, 208